University of Strathclyde

Department of Chemical and Process

Engineering

Development of Novel Redox Stable Anode

Materials and their Suitability for Use in

Intermediate Temperature Solid Oxide Fuel Cells

by

Peter Ian Cowin

Degree of Doctor of Philosophy

2015

Declaration of Authors Rights

'This thesis is the result of the author's original research. It has been composed by the author and has not been previously submitted for examination which has led to the award of a degree.'

'The copyright of this thesis belongs to the author under the terms of the United Kingdom Copyright Acts as qualified by University of Strathclyde Regulation 3.50. Due acknowledgement must always be made of the use of any material contained in, or derived from, this thesis.'

Signed:

Date:

Preface of Publications

Published Manuscripts

Peter I. Cowin, Christophe T.G. Petit, Rong Lan, John T.S. Irvine and Shanwen Tao "Recent Progress in the Development of Anode Materials for Solid Oxide Fuel Cells" Advanced Energy Materials **2011** *1* 314-332.

Peter I. Cowin, Rong Lan, Christophe T.G. Petit, Lei Zhang and Shanwen Tao "Conductivity and Stability of Cobalt Pyrovanadate" Journal of Alloys and Compounds **2011** *509* 4117-4121.

Peter I. Cowin, Rong Lan, Lei Zhang, Christophe T.G. Petit, Arno Kraft and Shanwen Tao "Study on Conductivity and Redox Stability of Iron Orthovanadate" Materials Chemistry and Physics **2011** *126* 614-618.

Peter I. Cowin, Christophe T.G. Petit, Rong Lan, Carl J. Schaschke and Shanwen Tao "Structure and Conductivity of Rutile Niobium Iron Titanate" Solid State Ionics **2013** *236* 48-53.

Christophe T.G. Petit, Rong Lan, Peter I. Cowin, Shanwen Tao, "Structure and conductivity of strontium-doped cerium orthovanadates $Ce_{1-x}Sr_xVO_4$ ($x = 0 - 0.175$)" Journal of Solid State Chemistry **2010** *183* 1231-1238.

Christophe T.G. Petit, Rong Lan, Peter I. Cowin, John T.S. Irvine and Shanwen Tao "Novel redox reversible oxide, Sr-doped cerium orthovanadate to metavanadate" Journal of Materials Chemistry **2011** *21 (2)* 525-531.

Christophe T.G. Petit, Rong Lan, Peter I. Cowin, Arno Kraft and Shanwen Tao "Structure, conductivity and redox stability of solid solution $Ce_{1-x}Ca_xVO_4$ ($0 \leq x \leq 0.4125$)" Journal of Materials Science **2011** *46 (2)* 316-326.

Christophe T.G. Petit, Rong Lan, Peter I. Cowin, John T.S. Irvine and Shanwen Tao "Structure, conductivity and redox reversibility of Ca-doped cerium metavanadate" Journal of Materials Chemistry **2011** *21 (24)* 8854-8861.

Lei Zhang, Rong Lan, Peter I. Cowin and Shanwen Tao "Fabrication of solid oxide fuel cell based on doped ceria electrolyte by one-step sintering at 800 °C" Solid State Ionics **2011** *203* 47-51.

Yinzhu Jiang, Teci Matthieu, Rong Lan, Xiaoxiang Xu, Peter I. Cowin, Shanwen Tao "A stable NH_4PO_3-glass proton conductor for intermediate temperature fuel cells" Solid State Ionics **2011** *192* 108-112.

Acknowledgments

I would like to thank my supervisor, Professor Shanwen Tao, for his guidance and support throughout the project. Thanks also go to the members of the fuel cell group; Christophe Petit, Greg Mann, Ibrahim Amar, Bing Tao, Dr Lei Zhang, Dr Zhe Tang and Dr Rong Lan for all their help, guidance and friendship throughout this project.

Further thanks are given to the departmental lecturers, secretarial staff and the laboratory technicians from the Department of Chemical and Process Engineering for all their valuable assistance. For their friendship and enjoyable company, I would like to thank all the PhD students and Postdoctoral researchers with whom I have shared time with in both Glasgow and Edinburgh.

Finally, thanks go to my family and friends for their guidance, support and patience over the years.

Contents

List of Figures

List of Tables

List of Equations

Acronyms and Abbreviations

AFC – Alkaline fuel cell

AMFC – Alkaline membrane fuel cell

APS – Atmospheric plasma spray

ASD – A-site deficient

ASR – Area specific resistance

BSD – B-site deficient

EPD – Electrophoretic deposition

DFT – Density functional theory

FC – Fuel cell

GDC – Gadolinium doped ceria – Electrolyte – $Gd_xCe_{1-x}O_{2-\delta}$

LCO – Lanthanum doped ceria - $La_xCe_{1-x}O_{2-\delta}$

LSCF – Perovskite cathode – $La_{0.6}Sr_{0.4}Co_{0.8}Fe_{0.2}O_{3-\delta}$

LSCM – Perovskite anode – $La_{0.75}Sr_{0.25}Cr_{0.5}Mn_{0.5}O_{3-\delta}$

LSCNi – Perovskite anode - $La_{0.75}Sr_{0.25}Cr_{1-x}Ni_xO_{3-\delta}$

LSCRu – Perovskite anode - $La_{0.75}Sr_{0.25}Cr_{1-x}Ru_xO_{3-\delta}$

LSGM – Perovskite electrolyte – $La_{1-x}Sr_xGa_{1-y}Mn_yO_{3-\delta}$

LSSM – Perovskite cathode – $La_{0.8}Sr_{0.2}Sc_{0.2}Mn_{0.8}O_{3-\delta}$

LST – Lanthanum doped strontium titanate – Anode – $Sr_{1-x}La_xTiO_{3-\delta}$

MCFC – Molten Carbonate Fuel Cell

MIEC – Mixed ionic electronic conductor

Metal/Electrolyte – An anode cermet comprising of a metal and ceramic electrolyte

PEMFC – Polymer electrolyte membrane fuel cell

pO2 – Partial pressure of oxygen

Redox – Reduction and Oxidation

Rp – Polarisation resiatance

ScSZ – Scandium doped zirconia – Electrolyte – $Sc_xZr_{1-x}O_{2-\delta}$

SDC – Samarium doped ceria – Electrolyte – $Sm_xCe_{1-x}O_{2-\delta}$

SMMO – Perovskite anode – $Sr_2Mg_{1-x}Mn_xMoO_{6-\delta}$

SOFC – Solid oxide fuel cell

STO – Strontium titanate – Anode – SrTiO$_{3-\delta}$

TEC – Thermal expansion coefficient

TPB – Triple phase boundary

TPR – Temperature programmed reduction

YST – Yttrium doped strontium titanate – Anode – Sr$_{1-x}$Y$_x$TiO$_{3-\delta}$

YSZ – Yttrium stabilised zirconia– Electrolyte – Y$_x$Zr$_{1-x}$O$_{2-\delta}$

Abstract

Due to the material benefits in the reduction of the operating temperatures of SOFCs, development of novel electrolyte and electrode materials is deemed to be essential for SOFC performance optimisation at intermediate temperatures. Iron-based perovskites were previously overlooked as anode materials due to their instability in reducing atmospheres at SOFC operating temperatures, although substantial research has been conducted into the use of these materials as SOFC cathodes [1, 2]. The reduction in operating temperature allows for use of materials, such as iron-based perovskites, which lack the requisite thermal or redox stability for high temperature operation.

Synthesis of iron rich strontium molybdenum ferrite double perovskites determined that the previously observed performance of these materials was intrinsically linked to initial high temperature reduction, thus reducing the utility of these materials at intermediate temperatures. XRD and DC conductivity measurements determined that doping of $SrFeO_{3-\delta}$ with titanium and niobium produced the optimal balance between conductivity and stability for $SrFe_{0.9}(Ti,Nb)_{0.1}O_{3-\delta}$. Introduction of transition metal dopants further increased the electronic conductivity with copper doping exhibiting the highest electronic conductivity of the redox stable $SrFe_{0.8-x}(TM)_x(Ti,Nb)_{0.1}O_{3-\delta}$ materials. Increasing the copper content of $SrFe_{0.8-x}Cu_{0.1+x}Nb_{0.1}O_{3-\delta}$ resulted in a reduction of the electronic conductivity. A-site doping with lanthanum replicated the structure and conductivity observed previously in the literature [1, 3], with redox stability at intermediate temperature observed for both $La_{0.6}Sr_{0.4}FeO_{3-\delta}$ and $La_{0.8}Sr_{0.2}FeO_{3-\delta}$. Replacement of lanthanum with yttrium elicited a reduction in the electronic conductivity, with $Y_{0.3}Sr_{0.7}FeO_{3-\delta}$ exhibiting the highest electronic conductivity of the redox stable materials.

Symmetrical fuel cell testing with 60:40 $SrFe_{0.9}Ti_{0.1}O_{3-\delta}$-$Gd_{0.2}Ce_{0.8}O_{2-\delta}$, 55:45 $La_{0.6}Sr_{0.4}FeO_{3-\delta}$-$Gd_{0.2}Ce_{0.8}O_{2-\delta}$ and $SrFe_{0.8}Cu_{0.1}Nb_{0.1}O_{3-\delta}$ electrodes recorded performances of 22 $mWcm^{-2}$, 80 $mWcm^{-2}$ and 306 $mWcm^{-2}$ respectively at 700 °C. The fuel cell performance of a symmetrical $SrFe_{0.8}Cu_{0.1}Nb_{0.1}O_{3-\delta}$–$Gd_{0.2}Ce_{0.8}O_{2-\delta}$- $SrFe_{0.8}Cu_{0.1}Nb_{0.1}O_{3-\delta}$ fuel cell was an improvement on the symmetrical fuel cell performance from the literature [4-6].

1. Introduction

This chapter includes an introduction to the basics of fuel cell operation and a discussion of the important properties of SOFC anode materials and their relation to fuel cell operation. A review of the electrolyte, interconnect and cathode materials is followed by an in-depth literature review on anode materials and an overview of the objectives of this thesis.

1.1. Fuel Cells

Fuel cells (FCs) can be strictly defined as devices which convert chemical energy into electrical energy through a series of electrochemical reactions. These devices perform with a significantly higher efficiency than traditional fossil fuel combustion based generators. In addition to this, some systems can operate at low temperatures, have fuel flexibility, high power density and little to no carbon emissions with certain fuels [7]. Many of these systems currently operate with hydrogen fuels, produced mainly from fossil fuel sources, although the direct use of alternative energy carriers, such as methanol, hydrazine and syngas, has already been proven viable [8-10].

Fuel cells have been investigated in various forms for over 170 years. The first demonstration of a working example of a fuel cell, a sulphuric acid based cell, is a matter of some controversy, either being developed by Christian Friedrich Schönbein or Sir William Robert Grove in the 1830s [11]. The basic design consists of a gas tight, electronically insulating, ion-conducting membrane separating two electrodes, connected through an external circuit. For an oxygen-ion conducting FC, the oxygen from the air is dissociated and ionised at the cathode, the oxygen ions are transported through the electrolyte; these then react at the anode with the fuel gas, producing electrons which are transported round an external circuit to the cathode, generating electricity, as can be observed in Figure 1.1.
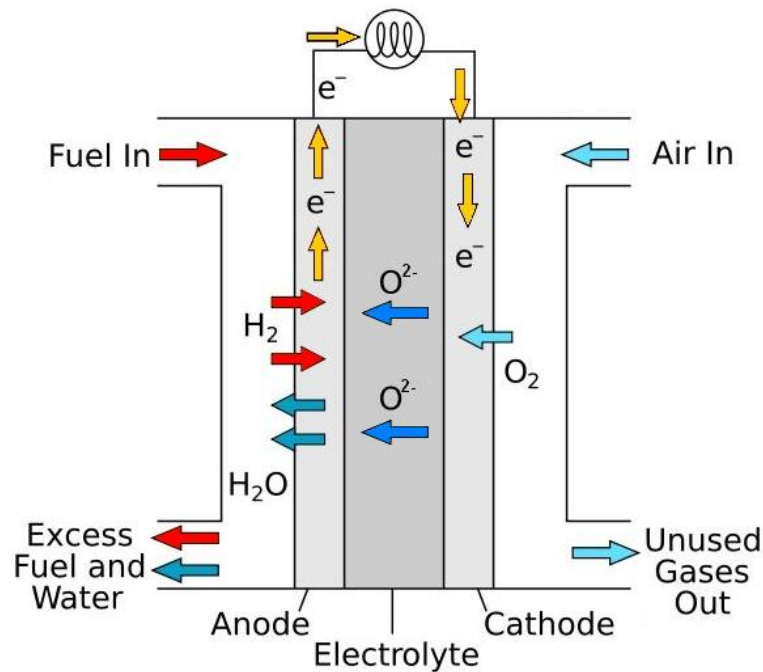
Figure 1.1: Diagram of an oxygen ion conducting fuel cell

For all other anions, such as OH^- and CO_3^{2-}, the process is similar to that for an oxygen ion conducting fuel cell. For a hydrogen ion conducting fuel cell, the fuel is dissociated into hydrogen ions and electrons at the anode, the protons are conducted through the electrolyte and combine at the cathode with oxygen from the air, while the electrons are conducted through the external circuit to the cathode. Technically hydrogen-ion conducting fuel cells have an advantage over traditional oxygen-ion conducting fuel cells in that, when using pure hydrogen fuel, fuel circulation is unnecessary and the anode compartment could be pressurised, increasing the fuel efficiency.

Fuel cells exist in a variety of different configurations, separated primarily by the differing composition of their electrolytes. The most notable, and most widely researched, of the fuel cell types are polymer electrolyte membrane, alkaline membrane, phosphoric acid, molten carbonate and solid oxide, although other, less well developed, fuel cell types, such microbial fuel cells [12], also exist.

1.1.1. *Polymer Electrolyte Membrane Fuel Cells (PEMFCs)*

Polymer electrolyte membrane fuel cells, also known as proton exchange membrane fuel cells, utilise a hydrogen ion-conducting polymer membrane as an electrolyte. PEMFCs operate optimally at approximately 80°C with pure hydrogen fuels, with a severe intolerance to fuel impurities noted for many current anode catalysts [13]. Additionally, membrane hydration is a significant concern, as either dehydration or flooding of the electrolyte will significantly degrade cell performance. Despite some drawbacks, these systems have quick start-up, high current densities and are thought to have great promise for small scale applications, such as automotive transport [14].

A subtype of PEMFCs is the direct methanol fuel cell (DMFC) which utilises methanol as a fuel at the anode. These cells are less attractive for large scale applications due to a lower efficiency than PEMFCs, however the use of liquid fuel has made these fuel cells attractive as possible battery replacements for mobile applications, i.e. mobile phones and laptop computers [8].

1.1.2. Alkaline Membrane Fuel Cells (AMFCs)

Alkaline membrane fuel cells have a similar construction to PEMFCs, although the membrane is a hydroxide ion conductor. Due to the improved reaction kinetics in a basic environment, AMFCs do not require the expensive electrode catalysts that are used in PEMFC construction. Original alkaline fuel cells utilised liquid electrolytes, such as potassium hydroxide, however problems with carbon dioxide poisoning meant that significant gas processing, for both anode and cathode, was required. The introduction of a solid electrolyte membrane was found to alleviate the effect of gas impurity poisoning, however the electrolytes are susceptible to oxygen or hydroxyl attack, resulting in membrane degradation [15]. The use of alkaline membranes has also allowed the use of alternative fuels, such as hydrazine [9] and urea [16]. Despite the option to use non-noble metal catalysts, the performance of these cells with hydrogen is much lower with alternative electrodes. AMFCs are still in an early stage of development and, as such, have worse performance than PEMFCs, however the use of alternative fuels may increase the commercial viability of AMFCs in the future.

1.1.3. Phosphoric Acid Fuel Cells (PAFCs)

Phosphoric acid fuel cells utilise a liquid phosphoric acid electrolyte immobilised in a solid matrix, such as silicon carbide, to transport hydrogen ions between anode and cathode. These cells operate between 150 °C and 200 °C and, to a lesser degree than PEMFCs, require fuel processing to avoid electrode poisoning [17]. The corrosive nature of the electrolyte causes significant problems with material selection and therefore PAFCs are more expensive than PEMFCs due to the additional cost associated with corrosion resistant materials. PAFCs have already found commercial application for stationary power generation, however further cost reductions, particularly of the platinum catalyst, are deemed necessary for widespread use [17].

1.1.4. Molten Carbonate Fuel Cells (MCFC)

Molten carbonate fuel cells use CO_3^{2-} ion-conducting electrolytes, in the form of molten carbonate salts immobilised in a ceramic matrix. The high temperature of operation, 600 °C – 700 °C, allows greater fuel flexibility and the use of inexpensive electrode catalysts whilst maintaining high efficiencies, although the start-up times are markedly longer. Combined heat and power (CHP) technology can also be used at these temperatures, which can significantly increase the overall system efficiency. The use of molten carbonates does cause additional problems with long term operation as corrosion of separator plates and electrolyte losses can cause serious performance degradation [18]. Additionally, at high temperatures, sulphurous impurities can cause significant poisoning of current state of the art anode materials [19]. Despite these drawbacks, MC-FCs have found commercial use as medium and large scale stationary power generation.

1.1.5. Solid Oxide Fuel Cells (SOFCs)

Solid oxide fuel cells operate at high efficiencies using a solid oxide, ceramic, electrolyte at high temperatures, between 500 °C and 1000 °C. The inherent advantages in high temperature operation apply for SOFCs without the associated electrolyte problems found for MCFCs, although the slightly higher operating temperature causes additional thermal stresses on the fuel cell components. SOFCs have also been proven to have stable long term operation, > 30,000 hours [20], with the addition of CHP pushing the theoretical efficiency to ~ 90 % [21]. The current scale of commercial systems ranges from household 1 kW systems such as those developed by Ceres Power to larger scale power generation on the 1 MW scale developed by Rolls Royce. Despite high temperature operation. SOFCs have been found to exhibit significant performance degradation with sulphurous and hydrocarbon impurities in the fuel gas, caused sulphur poisoning and coking, deposition of carbon, at the anode, respectively [22, 23]. These can be alleviated by the use of steam reforming at the anode, although this causes a subsequent reduction in fuel cell performance [24]. Coking and poisoning at the anode can also be eliminated by the use of alternative anode materials, although many of these have diminished fuel cell performance [22, 25].

Solid oxide fuel cells, despite problem with lengthy start up times, have shown significant promise for utility power generation and, with the highest possible efficiencies for any fuel cell type [21], could prove an ideal alternative to current large scale fossil fuel generators.

1.1.6. Fuel Cell Operation

The basic reactions which drive fuel cells operation are the two redox reactions which occur at the anode and cathode. The anodic and cathodic redox reactions for an oxygen ion conducting fuel cell operating with hydrogen fuel are given in Equations 1.1 and 1.2.

$$O_2 + 4e^- \rightarrow 2O^{2-} \qquad \text{(a)} \qquad (1.1)$$

$$2H_2 + 2O^{2-} \rightarrow 2H_2O + 4e^- \qquad \text{(b)} \qquad (1.2)$$
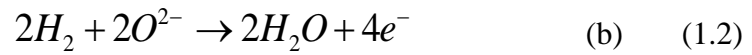
Half cell electrochemical reactions at the cathode (1.1) and anode (1.2) of a fuel cell operating on hydrogen fuel

The theoretical thermodynamic efficiency of a fuel cell is determined from the reactants, with the Gibbs free energy of the reaction determining the maximum achievable efficiency. The theoretical cell voltage achievable (E) can be determined using Equation 2, in which ΔG is the change in Gibbs free energy, n is the number of electrons transferred in the reaction and F is the Faraday constant.

$$\Delta G = -nFE \qquad (1.3)$$

Gibbs free energy for an electrochemical reaction

Comparison of the Gibbs free energy for the fuel cell reaction can only be made to the energy gained from the combustion of the reactant, to give a theoretical efficiency for the fuel cell reaction. The energy from fuel combustion can be found from the enthalpy of formation of the reaction product (Q_{react}), which can produce two values depending on the physical state of the product, in which case the higher heating value (HHV) is used. In the case of the hydrogen fuelled oxygen ion conducting fuel cell, the higher heating value corresponds to the formation of liquid H_2O while the lower heating value corresponds to the formation of gaseous H_2O.

$$\eta = \frac{\Delta G}{Q_{react}} = \frac{nFE}{HHV} \qquad (1.4)$$

Efficiency of an electrochemical cell

The theoretical efficiency of the cell, Equation 1.4, is dependent on the fuel used at the anode, as the energy available (Q_{react}) and the Gibbs free energy (G) will differ significantly.

Fuel cells do not often reach close to the maximum theoretical efficiency as actual cell performance is affected by losses from various electrochemical processes, as demonstrated in Equation 1.5, in which E_0 is the Nernst potential of the reactants, I is the current through the cell, R is the ohmic resistance of the cell and $\eta_{cathode}$ and η_{anode} are the cathodic and anodic polarisation losses.

$$V = E_0 - IR - \eta_{cathode} - \eta_{anode} \qquad (1.5)$$

Potential difference losses under fuel cell operating conditions

These losses can be further broken down into separate polarisation losses, as exhibited on Figure 1.2.
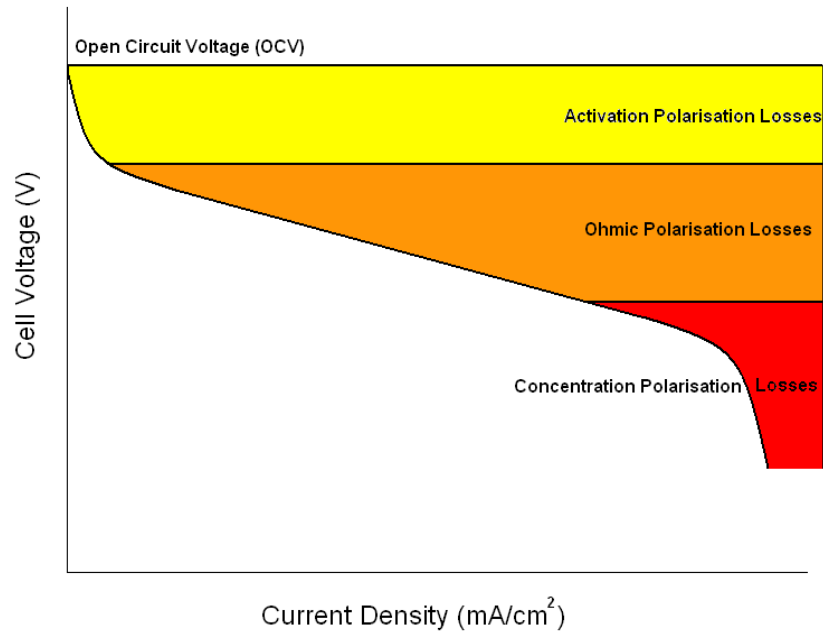
Figure 1.2: Fuel cell losses exhibited on a current-voltage (I-V) curve [26]

Fuel cell polarisation losses occur in three main forms: activation polarisation, ohmic polarisation and concentration polarisation. Activation polarisation is a combination of the limitations on the reaction rate and the electron/ion transfer for both the cathodic and anodic reactions. Ohmic polarisation is a combination of resistances to electron and ion transport throughout the fuel cell, although is dominated by electrolytic ionic resistance. Concentration polarisation is caused by constraints on the transport of the fuel and waste gases to and from the anode-electrolyte interface respectively. Low temperature operation also can lead to losses through fuel crossover, when the fuel passes through the electrolyte without reacting. These losses can be minimised through optimisation of the fuel cell structure and use of optimal materials.

1.2. Material Properties

Losses during fuel cell operation, from anode, cathode or electrolyte, are highly dependent on material properties and design of materials for these components requires detailed knowledge of material properties. For fuel cell materials, the most important of these properties are electronic and ionic conductivity, catalytic activity and chemical and thermal stability. As this work focuses on intermediate temperature oxygen ion conducting SOFCs, this section concentrates on the properties of ceramic and metallic materials for these applications.

1.2.1. Electronic Conductivity

Conduction through a solid, electrical conductivity can be separated by the type of charge carrier, with electrons, electronic conduction, or ions, ionic conduction, producing separate contributions to the total conductivity. High electronic conductivity is essential for anode, cathode and interconnect materials to minimise the ohmic polarisation losses throughout the cell, although negligible electronic conductivity is a requirement for electrolyte materials.

The conductivity of a compound is determined by the number of charge carriers, the charge of the carrier, e, and the mobility of the carriers, μ, as shown in Equation 1.6.

$$\sigma = ne\mu \tag{1.6}$$

General equation for conductivity

For electronic conductors the electron charge is constant, however both the number of charge carriers and the charge carrier mobility are determined by the activation energy and the temperature. The number of electrons available for conduction is given in Equation 1.7 where n_0 is the total number of electrons, E_a is the

activation energy for conduction, k_B is the Boltzmann constant and T is the temperature.

$$n = n_0 \exp(\frac{-E_a}{k_B T})$$

(1.7)

Equation for the number of mobile charge carriers in a solid

These general terms can be combined to give the Arrhenius equation for conductivity, Equation 1.8, in which A is the pre-exponential term and combines n_0, e and μ.

$$\sigma = A \exp(-\frac{E_a}{k_B T})$$

(1.8)

Arrhenius equation for conductivity

Consideration of the electronic conductivity of a solid also requires knowledge of the band structure of the material. Calculation of the band structure involves the application of molecular orbital theory to an infinite three dimensional structure. The application of molecular orbital theory to a diatomic molecule with sufficient atomic orbital overlap results in the formation of a lower energy bonding molecular orbital and a higher energy anti-bonding molecular orbital delocalised over the contributing atoms. For each atomic orbital incorporated into the system an additional molecular orbital is formed. As the number of molecular orbitals increases, the energy difference between molecular orbitals decreases, therefore when this is applied to an infinite structure the delocalised molecular orbitals merge to form a continuous band of energy levels. For simple structures this approach produces bands of energy levels which can be associated with the overlap of atomic orbitals, however for more complex structures the band structure becomes more difficult to predict. Formation of bands between different atoms will depend on the orbital overlap and the energy of the orbitals, with the structure of the compound also having an effect on the band structure.

The Fermi level (E_{Fermi}) is a hypothetical level of potential energy in a crystalline solid at which there is a 50% chance of the energy level being occupied by an electron at absolutely zero. Within a molecular orbital diagram, the Fermi level occurs at a level between the lowest occupied molecular orbital (LUMO) and the highest occupied molecular orbital (HOMO). As the temperature increases thermally activated promotion of electrons from the valence band to the conduction band will occur and energy levels above the Fermi level will be occupied.
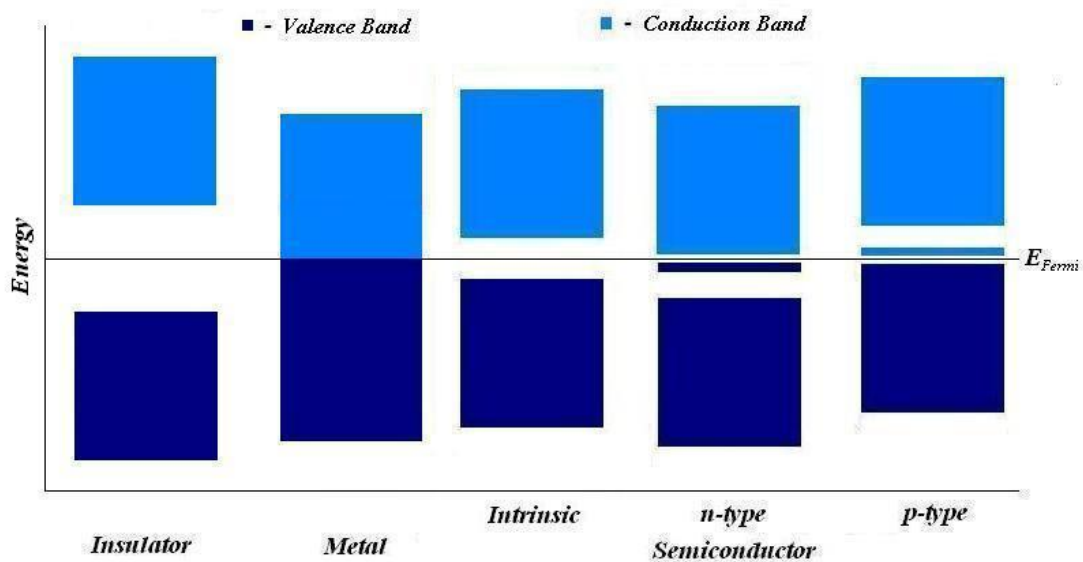
Figure 1.3. Basic energy level diagram for an insulator (a), metal (b), intrinsic semiconductor (c), n-type semiconductor (d) and p-type semiconductor (e) at low temperature

In terms of electronic conductivity, materials can be separated into three categories: metallic conductors, semiconductors and insulators, as illustrated by Figure 1.3. Generally insulators have a large band gap and therefore negligible numbers of electrons reach the thermal energy required for promotion to the conduction band, as is required for electrolyte materials. As valence electrons are delocalised over the band which they occupy, the energy required for promotion within the band is minimal. For metallic conductors the Fermi level occurs within a band thus the resistance for conduction is small and the number of charge carriers is large. Resistance in metallic conductors occurs as thermal vibrations in the structural lattice, known as polarons,

11

thus conductivity decreases with increasing temperature for these compounds. Semiconductors have a relatively small band gap so that electrons from the valence band, with sufficient thermal energy, can be promoted to the conduction band. The conductivity of semiconductors increases with increasing temperature, with the actual increase dependant on the activation energy for conduction, as demonstrated by Equation 1.8.

Introduction of a dopant to a semiconductor can significantly increase the conductivity, although at higher temperatures the conductivity of intrinsic and extrinsic semiconductors should, in theory, align. The number of electrons promoted over the intrinsic band gap will increase with increasing temperature until it becomes the dominant pathway for electron promotion, whilst the electron promotion to or from the dopant is limited by the number of electrons/holes provided by the dopant. Extrinsic semiconductors can be further classified into either p-type or n-type according to the effect of the dopant. Dopants in p-type semiconductors introduce an additional band between the conduction and valence band, at a slightly higher energy than the valence band. This induces promotion of the valence electrons to the dopant band, creating electron holes in the valence band. N-type dopants introduce the additional band slightly below the conduction band, with promotion of electrons from the dopant band to the conduction band increasing the conductivity of the compound.

The behaviour of n-type and p-type semiconductors differs significantly upon changes in the partial pressure of oxygen (pO_2). As n-type conductors introduce an electron band below the valence band, reduction of the compound is likely to remove electrons from this band, reducing the number of charge carriers and reducing the conductivity. As p-type semiconductors induce conductivity through the introduction of electrons holes, removal of electrons from the valence band will increase the number of mobile charge carriers and therefore increase the conductivity. Due to the behaviour of p-type semiconductors upon exposure to reducing atmospheres, these materials are of significant interest as SOFC anode materials.

Some transition metal compounds do not behave as predicted by band theory, instead behaving as if the electrons are localised on individual atoms. This is thought

to be due to increased nuclear attraction in the d-orbitals and the electrons instead hop between atoms given sufficient energy. These hopping semiconductors exhibit similar behaviour to intrinsic semiconductors.

1.2.2. Ionic Conductivity

Defect formation in crystalline solids is driven by reduction of the Gibbs free energy of the system, Equation 1.9, where H is the enthalpy, T is the temperature and S is the entropy.

$$\Delta G = \Delta H - T\Delta S \qquad (1.9)$$

Gibbs free energy of a crystalline solid

As the temperature increases the entropy has a larger effect on the free energy of the crystal and defect formation is favoured, as the energy required for defect formation is more than offset by the entropy reduction. Intrinsic defects, such as Schottky and Frenkel defects, occur naturally in most crystalline solids. Schottky defects consist of both an anion and cation vacancy, often associated within the structure, while Frenkel defects occur when an atom is displaced onto an interstitial site, leaving a vacant lattice site. Both Schottky and Frenkel defects leave a vacancy into which neighbouring atoms can move, encouraging ion migration.

Defects are not solely the product of intrinsic entropy effects, as they may also be formed by bombardment with high energy radiation or through substitution using aliovalent dopants. As high energy radiation is not an efficient effect method for formation, or reduction, of vacancies, many researchers use dopants to alter the proportion of ion vacancies through charge compensation mechanisms. As stabilisation of materials requires a balance of the overall positive and negative charges, any change in either the cationic or anionic charge will cause a subsequent alteration of the balancing ion, where possible. Charge compensation can be used to later the cation-anion ratio and substantially affect the material properties.

Charge compensation mechanisms may not affect the cation-anion ratio if the oxidation state of the cations in the material can be altered instead. This is observed in lanthanum manganese oxide perovskites, where aliovalent doping of the A-site will change the oxidation state of the manganese but not significantly alter the proportion of oxygen vacancies.

The formation of lattice defects, either cationic or anionic, is essential for the production of ionically conductive compounds. Conduction of ions in a solid occurs as migration of an ion from one lattice site to a neighbouring vacant site. There are two main mechanisms for ion migration in crystalline solids; vacancy conduction or interstitial conduction. Vacancy conduction requires the presence of lattice ion vacancies, as can be formed intrinsically or through introduction of aliovalent dopants. The conducting ions can then migrate from occupied to vacant lattice sites. Intrinsic formation of Frenkel defects allows for interstitial ion conduction, with the interstitial ion either hopping to a vacant interstitial site, or displacing an ion into an interstitial site from a neighbouring lattice site, which it then occupies.

As for electronic conduction, the equation for conductivity, Equation 1.6, can be applied to elucidate factors affecting ionic conduction. As the number of ionic vacancies is small, in comparison to the number of occupied lattice sites, the number of charge carriers for ionic conductors is generally proportional to the number of ionic vacancies. The mobility of ions in a solid is governed by the diffusivity, D, as exhibited in Equation 1.10 and derived from the Nernst-Einstein relationship [27].

$$\mu = \frac{qD}{kT} \tag{1.10}$$

Equation for the mobility of ions in a solid

$$D = a^2 v_0 \exp(\frac{\Delta S_m}{k}) \exp(-\frac{\Delta H_m}{kT}) \tag{1.11}$$

Equation for the diffusivity of ions in a solid

The diffusivity of an ion in a solid can be described as in Equation 1.11, where a is the jump distance, v_0 is the lattice vibration frequency and ΔS_m and ΔH_m are the

activation entropy and enthalpy of diffusion [27]. The jump distance and the activation energies for diffusion are highly dependent on the structure of the material. Migration between occupied and vacant lattice sites requires movement between neighbouring ions in the structure, which will narrow to a critical point as exhibited in Figure 1.4. The critical radius can be calculated, however the actual critical radius is likely to be larger than the calculated value as this not take into account localised structural distortions which are likely to occur with the presence of the lattice vacancy and the polarisability of the neighbouring ions.
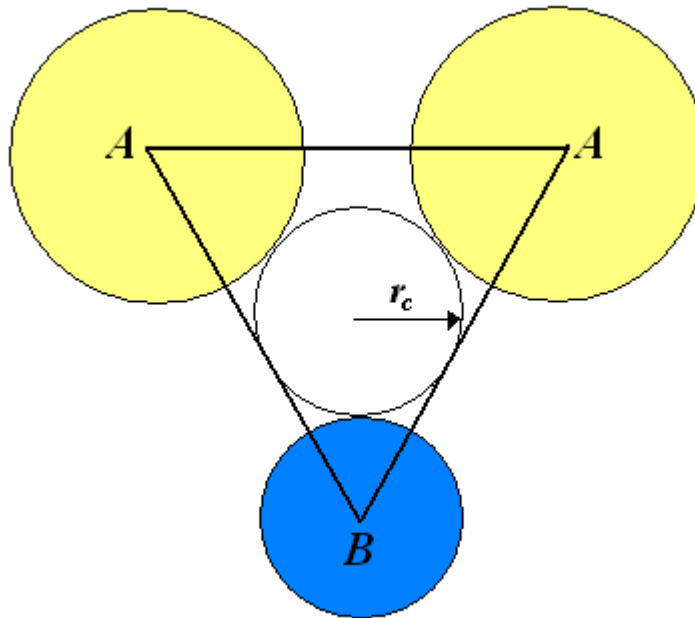
Figure 1.4: Diagram of the critical radius for oxygen ion conduction in a perovskite structure.

As for semiconductors, ionic conduction will exhibit different conduction behaviour depending on the temperature. Many ionic conductors utilise dopants to increase the number of lattice vacancies, improving the ionic conductivity, these compounds will exhibit a lower temperature extrinsic conduction region, where the number of extrinsic vacancies is higher than intrinsic vacancies and thus the conductivity is dependent on the dopant. A higher temperature intrinsic conduction region, where the number of intrinsic vacancies outweighs extrinsic vacancies and the conductivity is governed by intrinsic material properties.

Oxygen ion conductivity is an essential property of SOFC electrolyte, cathode and anode materials. Most oxygen ion conductors utilise the vacancy conduction mechanism, with the production of lattice oxygen vacancies necessary for the promotion of ionic conductivity. Some interstitial oxygen ion conductors do exist, although these materials utilise oxygen hyper-stoichiometry to promote the formation of Frenkel defects, which can utilise ions channels present in the structure to reduce the activation energy for interstitial-interstitial oxygen ion conduction. The production of Frenkel defects in oxide materials requires structures without unfavourable interstitial oxygen environments, which are much less common than those compounds which can favourably integrate oxygen vacancies.

As was briefly touched upon previously, the structure of compounds has a significant effect on the ionic conductivity, with polymorphs of some highly conductive electrolyte materials exhibiting minimal ionic conductivity [28]. Aliovalent doping is frequently utilised to optimise both the desired structure and the oxygen vacancy concentration. As the jump distance and the critical point can have a significant effect on the ionic conductivity, minimisation of the jump distance and maximisation of the critical point are likely to enhance the oxygen ion conductivity. Therefore, within a certain structural series, an optimum structure for oxygen ion conduction is likely to exist, partially independent of compositional concerns.

For fluorite structured materials, introduction of the minimum amount of dopant to stabilise the conductive polymorph, whilst minimising lattice deformation, will generally produce the highest conductivity [28]. Hayashi *et. al.* [29] suggested that, for perovskite materials, a balance between the tolerance factor and the lattice free volume can be achieved to optimise the ionic conductivity. As with fluorite materials, it was found that minimisation of lattice distortion upon aliovalent substitution generally improves conductivity, with maximisation of the lattice free volume noted to have a similar effect. The lattice free volume was found to decrease with a reduction in the tolerance factor, a measure of how close to the ideal perovskite structure the compound is, with compounds with t ~ unity exhibiting the ideal perovskite structure. Significant deviation of the structure from the ideal perovskite was found to reduce

stability and oxygen site equivalency, thus a balance between these tolerance factor and lattice free volume must be achieved to optimise the conductivity of perovskite compounds. From structural consideration of vacancy conductors, likely materials with high oxygen ion conductivity can be identified, although a balance between high electronic and ionic conductivities still must be considered.

The information for the effect of structural variations on the ionic conductivity of interstitial conductors is limited, therefore conclusions on material structure optimisation is currently difficult. Additionally, whether the conduction mechanism for interstitial conduction utilises interstitial-interstitial hopping, as found for apatite materials [30], or interstitial displacement, as found for K_2NiF_4-structured compounds [31], further complicates elucidation of structural factors. It is likely that optimisation of the number of oxygen interstitials can be achieved through charge compensation mechanisms.

Protonic conduction forms the cornerstone of alternative research into solid oxide fuel cells [32]. Hydrogen ion conductivity in these compounds requires the presence of oxygen vacancies, but does not operate as a vacancy conduction mechanism. Gas phase water dissociates into a hydroxide ion and a proton, with the hydroxide ion occupying an oxygen vacancy site whilst the proton combines with lattice oxygen to form another hydroxide defect. Hydrogen migration, after hydroxide defect formation, occurs through rotational diffusion of the hydrogen, followed by proton transfer to a neighbouring lattice oxygen. The ionic conductivity of current intermediate temperature solid oxide proton conductors is comparable to that of oxygen ion conductors at intermediate temperatures [32].

1.2.3. Catalytic Activity

Catalysis in fuel cells is ideally confined to the cathodic and anodic reactions, which differ depending on the fuel and conducting ion. For oxygen ion conducting fuel cells, the cathodic reaction consists of oxygen reduction, Equation 1.1, whilst the anodic reaction consists of fuel oxidation, Equation 1.2. The catalytic efficiency of

either electrode is dependent on three main components: the size of the three phase boundary, the composition of the catalyst and the operating conditions.
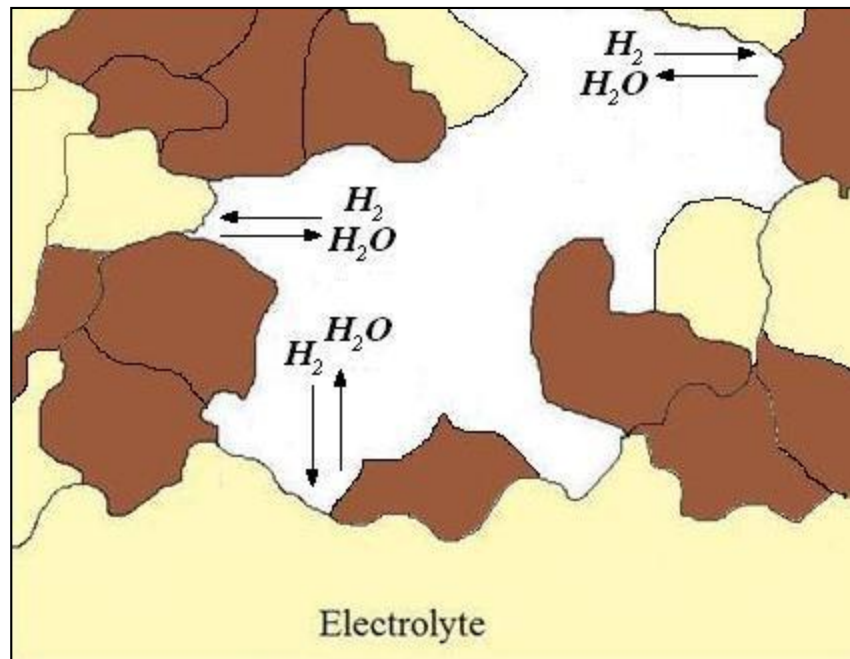
Figure 1.5. Graphical representation of the electrode three phase boundary in SOFCs [33]

In fuel cells the electrode reaction occurs over a catalytic three phase boundary (TPB), the area in which the fuel, electronically conductive phases and ionically conductive phases all interact, as exhibited in Figure 1.5. The length of the TPB in solid oxide fuel cells is dictated by the ionic conductivity, electronic conductivity, and the microstructure of the electrode [34]. Both electronic and ionic conduction through the electrode increases the effective catalytic area by increasing the proportion of the electrode over which the catalytic reaction can effectively occur. Gas diffusion to and from the catalytic sites is dictated by the electrodic microstructure, with increases in porosity increasing reactant concentration but reducing the catalytic surface area and conductivity [35]. Mixed electronic and ionic conducting materials can increase the area of the TPB by increasing the surface over which ionic conductors and electronic conductors interact.

Mechanistic modelling of both the cathodic and anodic reactions has been extensively investigated with the intention of developing an accurate model of the reaction mechanism and kinetics to allow accurate determination of efficient electrode catalysts [36, 37].

Catalysis at the cathode consists of a number of steps which are thought to determine the rate of the oxygen reduction reaction: gas diffusion to the catalyst surface, adsorption of oxygen onto the electrode surface, oxygen reduction, surface or bulk diffusion of reaction intermediates and incorporation of oxygen ions into the ionically conductive phase [38]. The general cathodic reaction is given in Equation 1.12, where the main electronic (LSM) and ionic (YSZ) conducting elements are separated. Further elucidation of the reaction mechanism is problematic as there are a number of different models for the reduction reaction, none of which have been proven for all cathode systems due to differences in preparation or testing conditions [37].

$$O_{2(Gas)} + 4e^-{}_{(LSM)} \Leftrightarrow 2O^{2-}{}_{(LSM-YSZ)} \tag{1.12}$$
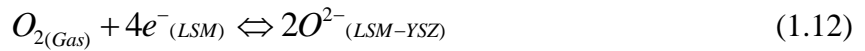
General reaction for oxygen reduction over a LSM-YSZ cathode

Similar processes as occur for the cathode reaction are posited to occur at the anode: gas diffusion to the anode, fuel adsorption on the anode surface, fuel oxidation, diffusion of reaction intermediates and desorption of products [39]. As the hydrogen oxidation reaction occurs at the three phase boundary, the general reaction for a cermet anode can be written as in Equation 1.13 [40].

$$H_{2(Gas)} + O^{2-}{}_{(YSZ)} \Leftrightarrow H_2O_{(Gas)} + 2e^-{}_{(Ni)} + V_O^{\bullet\bullet}{}_{YSZ} \tag{1.13}$$
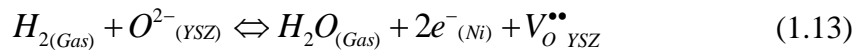
General reaction for hydrogen oxidation over a Ni/YSZ anode

Whilst most models of the anode reaction agree on the adsorption and desorption of gases and hydroxyl formation, the mechanism, and site, of the charge transfer reaction is still indeterminate. As current standard anode materials are a

composite of ionically conductive ceramic and electronically conductive metallic materials, modelling of these reactions has mainly focused on these anodes, although the reaction mechanism over mixed ionic-electronic conducting materials will differ considerably.

There are five main reaction mechanisms proposed for the the hydrogen oxidation reaction for a cermet anode: oxygen spillover, hydroxide spillover, hydrogen spillover, interstitial hydrogen transfer and the reactive electrolyte mechanism [40].

$$O_{YSZ}^{2-} + []_{Ni} \Leftrightarrow O_{Ni} + []_{YSZ} + 2e^- \qquad (1.14)$$

$$O_{YSZ}^{2-} + []_{Ni} \Leftrightarrow O^-_{Ni} + []_{YSZ} + e^- \qquad (1.15)$$

$$O_{YSZ}^- + []_{Ni} \Leftrightarrow O_{Ni} + []_{YSZ} + e^- \qquad (1.16)$$

$$OH_{YSZ}^- + []_{Ni} \Leftrightarrow OH_{Ni} + []_{YSZ} + e^- \qquad (1.17)$$
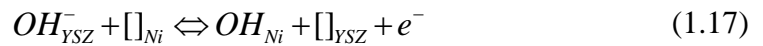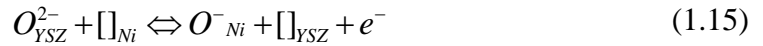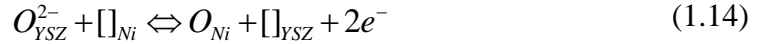
Oxygen and hydroxide spillover reactions over a Ni/YSZ anode

$$H_{Ni} + O_{YSZ}^{2-} \Leftrightarrow OH_{YSZ}^- + []_{Ni} + e^- \qquad (1.18)$$

$$H_{Ni} + OH_{YSZ}^- \Leftrightarrow H_2O_{YSZ} + []_{Ni} + e^- \qquad (1.19)$$

$$H_{i\ Ni}^x \Leftrightarrow H_{i\ YSZ}^\bullet + e^- \qquad (1.20)$$
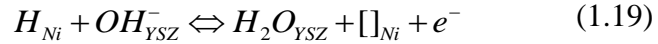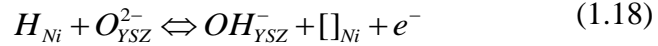
Hydrogen spillover and interstitial hydrogen transfer reactions over a Ni/YSZ anode

Oxygen spillover, as exhibited in Equations 1.14 to 1.17, involves transfer of surface oxygen or hydroxide ions from YSZ to vacant nickel surface sites, denoted by $[]_{Ni}$. The mechanism of transfer of adsorbed hydrogen from the nickel surface to react with oxygen or hydroxide ions on YSZ is known as hydrogen spillover, demonstrated in Equations 1.18 and 1.19. Both of these charge transfer mechanisms have found adherents with collaborating experimental data [41, 42], although, whilst these are generally considered to be the two main reaction mechanisms, other alternative hydrogen oxidation mechanisms exist.

Transfer of interstitial hydrogen ions between nickel and YSZ interstitial sites, as exhibited in Equation 1.20, has been proposed as a possible charge transfer step in

hydrogen oxidation [36, 43]. Whilst originally posited by Mogensen *et. al.* [36], Vogler and Bessler [44] concluded that the interstitial hydrogen transfer mechanism cannot explain the experimental current densities without increased diffusivities and thus this mechanism is not favoured without the presence of impurity phases, with surface spillover mechanisms favoured over clear three phase boundaries. Promotion of this mechanism may occur through humidification of the fuel, as interstitial hydrogen and hydroxide ions in YSZ can also be formed by surface-bulk exchange of adsorbed water [45].

In the reactive electrolyte mechanism all reactions occur on the electrolyte surface with charge transfer occurring between the electrolyte and metal phase, although, as with the hydrogen interstitial mechanism, this is thought to only be favourable in the presence of boundary impurity phases [42]. A decrease in the polarisation resistance of the anode is also observed with increasing fuel humidification, which is indicative of improved catalytic activity for fuel oxidation. Mogensen *et. al.* [36] originally suggested that the presence of impurity phases may explain the improved anodic performance in the presence of water, as glassy foreign phases may exhibit increased protonic conduction with increasing humidification.

Originally Bessler *et. al.* [40] concluded that the most likely rate determining step in hydrogen oxidation was hydrogen spillover, although this was contradicted by a later paper by Rossmeisl and Bessler [41] which drew the conclusion that the oxygen spillover was the likely hydrogen oxidation reaction mechanism over metal-YSZ cermets. A comparison between theoretical calculations and experimental results in the original paper by Bessler *et. al.* [40] indicated that the reaction mechanism may change according to the reaction conditions. Vogler *et. al.* [42] later concluded that hydrogen spillover onto both oxygen and hydroxide ions proved to be the best fit to experimental measurements over patterned Ni-YSZ anodes.

No general consensus has been reached over the exact mechanism of hydrogen oxidation, mainly due to differences in testing and preparation methods [36], although further research may manage to elucidate mechanisms for specific anode compositions and reaction conditions.

Alternative fuels, such as methane [46], methanol [47] and ammonia [48], are also of interest for SOFCs due to improvements in energy density and ease of storage over hydrogen. Oxidation catalysis of these compounds can occur through a variety of different mechanisms, all of which are temperature, atmosphere and catalyst dependant [49]. The complexity of the reactions which can occur at the anode increase considerably with increasing size of the hydrocarbon, as demonstrated in Equations 1.21 to 1.23 and Equations 1.24 to 1.28 [77].

$$CH_4 + 2O_2 \Leftrightarrow CO_2 + 2H_2O \qquad (1.21)$$

$$CH_4 + \frac{1}{2}O_2 \Leftrightarrow CO + 2H_2 \qquad (1.22)$$

$$CH_4 \Leftrightarrow C + 2H_2 \qquad (1.23)$$
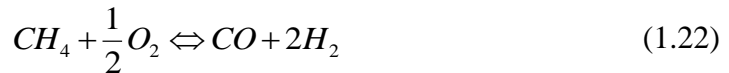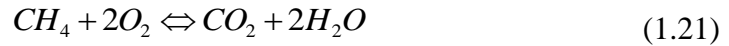
Oxidation and cracking reactions of methane under dry anodic conditions

$$C_2H_6 + \frac{7}{2}O_2 \Leftrightarrow 2CO_2 + 3H_2O \qquad (1.24)$$

$$C_2H_6 + O_2 \Leftrightarrow 2CO + 3H_2 \qquad (1.25)$$

$$C_2H_6 + \frac{1}{2}O_2 \Leftrightarrow C_2H_4 + H_2O \qquad (1.26)$$

$$C_2H_6 \Leftrightarrow C_2H_4 + H_2 \qquad (1.27)$$

$$C_2H_6 \Leftrightarrow 2C + 3H_2 \qquad (1.28)$$
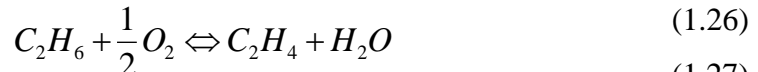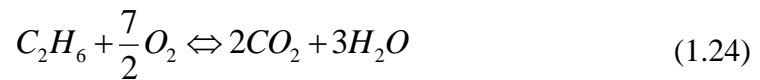
Oxidation and cracking reactions of ethane under dry anodic conditions

Direct hydrocarbon utilisation, used in this context to describe the use of hydrocarbons without fuel reforming, oxidises hydrocarbons through various surface catalysed reactions, as exhibited in Equations 1.21 to 1.28. The exact oxidation mechanism of hydrocarbons is highly dependent on the anodic conditions, with changes in the oxygen flow from the electrolyte, the temperature and the fuel gas composition all shifting the primary reaction mechanism.

$$2CO \Leftrightarrow CO_2 + C \qquad\qquad (1.29)$$

The Boudouard reaction

$$CO + H_2 \Leftrightarrow H_2O + C \qquad\qquad (1.30)$$
$$CO_2 + 2H_2 \Leftrightarrow 2H_2O + C \qquad\qquad (1.31)$$

Carbon formation mechanisms at low temperatures

Residues from using alternative fuels, especially those which contain carbon, can have a detrimental effect on anode performance, with carbon deposition, or coking, observed to occur for some materials [49]. Carbon deposition on the anode surface has been shown to block catalytic active sites, considerably reducing the catalytic activity of the anode. This is particularly observed for direct utilisation of hydrocarbons, as little pre-reforming of the fuel occurs, which allows for hydrocarbon cracking on the catalyst surface, as exhibited in Equations 1.23, 1.27 and 1.28, resulting in anodic coking.

Carbon deposition does not solely occur through cracking reactions, as carbon monoxide may react through the Boudouard reaction, Equation 1.29, to form surface carbon deposits at high temperatures. Coking may also occur though the reaction of adsorbed reaction intermediates with hydrogen, as exhibited in Equation 1.30 and 1.31. The kinetics of carbon formation differ significantly depending on the catalyst composition and reaction conditions with a considerable reduction in coking able to be achieved by alteration of the reaction conditions to suppress carbon formation, promotion of internal fuel reforming or use of alternative anode materials [49].

$$CH_4 + H_2O \Leftrightarrow CO + 3H_2 \qquad\qquad (1.32)$$
$$CH_4 + CO_2 \Leftrightarrow 2CO + 2H_2 \qquad\qquad (1.33)$$
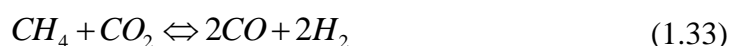
Steam reforming and carbon dioxide reforming of methane under anodic conditions

Fuel reforming of hydrocarbons to form syn-gas, a mixture of hydrogen and carbon monoxide, is achieved through addition of water, Equation 1.32, or carbon dioxide, Equation 1.33, to the fuel stream. This can be done prior to anode exposure, through external reforming or indirect internal reforming, or within the anode, through direct internal reforming. External reforming of the fuel is the most common fuel processing technique, which uses an external catalyst to form the syn-gas prior to anode exposure. External reforming produces higher fuel cell efficiencies than for internal reforming, however the process is highly endothermic and requires considerable amounts of undesirably bulky equipment. Internal reforming improves the thermal efficiency of the fuel cell, reduces the need for cell cooling, improves fuel distribution and reduces capital outlay, however the chance of anodic carbon formation is higher than for external reforming and large intra-anodic thermal gradients may form. Indirect internal reforming, which uses a catalytic functional layer atop the anode to reform the fuel prior to anode exposure, has similar advantages and drawbacks to direct internal reforming, however, whilst the chance of anode coking is reduced substantially, the thermal gradients formed in this process may induce fracture formation in the cell [50].

$$H_2O + CO \Leftrightarrow H_2 + CO_2 \qquad (1.34)$$

The water-gas shift reaction

Variation of the fuel/water ratio in steam reforming effects both the fuel conversion and carbon deposition on the catalyst [47]. In general, increasing the steam content of the anode gas will reduce the coking level, through Equations 1.32, 1.33 and 1.34, although with a subsequent reduction in fuel cell performance due to fuel dilution.

The addition of carbon dioxide to the fuel gas stream, Equation 1.33, has a comparable effect to that of steam addition, although with additional dilution of the fuel. Additionally, prevention of carbon formation on the anode requires a higher carbon dioxide content in the fuel than steam content for steam reforming [51] and therefore this technique is less effective than steam reforming [52].

24

Partial oxidation of hydrocarbon fuels can be achieved through addition of air, or oxygen, to the fuel gas stream, as exhibited in Equations 1.22 and 1.25. Partial oxidation is highly exothermic but produces high levels of carbon monoxide, thus combination with either steam reforming or carbon dioxide reforming can mitigate problems with each process. Whilst this process is likely to be more efficient than traditional steam reforming, similar problems with direct internal reforming will occur for autothermal reforming, although the use of an integrated internal reforming catalytic layer has been theoretically proven to be feasible with autothermal reforming [53].

Catalytic functional layers have been utilised to affect fuel catalysis prior to the anode exposure. This is generally utilised to protect the anode from exposure to gases which may cause coking, such as octane [54], or catalytic poisoning, such as hydrogen sulphide [55]. Addition of nanosized catalytic material into the anode has also been utilised for anode protection or to improve the catalytic activity of the anode. Infiltration of a small amount of catalyst into porous electrodes has been shown to significantly increase catalytic activity, due to the formation of uniformly distributed catalyst nanoparticles throughout the electrode [56].

1.2.4. *Material Stability*

When constructing a multi-component system, the stability of all the materials in the system must be taken into account. Chemical reactions between contacting materials depend on both components and are difficult to predict, however at higher temperatures, such as those attained during fuel cell preparation, these reactions become more commonplace. In addition to modification of material properties, chemical reactions at the interface can affect the microstructure of the anode and cause degradation of the electrode-electrolyte interface [57]. Formation of non-conductive compounds at interfaces within fuel cells can have a catastrophic effect on fuel cell performance [58, 59] and therefore testing of compound reactivity prior to fuel cell preparation is essential.

Even without observation of a direct chemical reaction, inter-diffusion may take place between contacting components, causing a modification in material properties [60]. Atomic diffusion occurs through substitutional migration across both bulk materials and grain boundaries and has also been observed through reaction preventing interlayer materials [61]. Diffusion is a gradual process and therefore is only observed upon long term operation of fuel cell materials, although in many cases the extent of diffusion is small and does not significantly affect bulk material properties.

Chemical stability is not limited to interactions between contacting components, as reactions may occur with various gases in the fuel or air streams. In some cases the reactive gases may be removed from the gas stream prior to use, although with the development of alternative fuels this is more difficult due to the extensive fuel processing that this would require. Compound reaction with gases in the air stream are more unusual due to the formation of most fuel cell components at high temperature in air, although some barium oxide based electrodes are known to react with CO_2 [62]. Anode components are exposed to a variety of reactive impurities in the fuel gas stream and therefore are more likely to exhibit instability under fuel cell operating conditions. These impurities are fuel dependent and can vary significantly depending on the feedstock, in the case of syn-gas and biogas, or the source, in the case of natural gas. A significant number of gaseous compounds have been observed to exhibit deleterious effects on fuel cell performance [63].

The temperature of operation of solid oxide fuel cells causes a variety of problems for material design as compound degradation, phase changes and phase transitions are significantly more likely at high temperatures. For most ceramic materials the thermal stability is sufficiently high for use at SOFC operating temperatures, however for some metallic compounds a reduction is operating temperature is required to allow for their utilisation.

Both melting and vaporisation of materials can also occur at high temperatures and this can cause significant problems with additional chemical reactions with other fuel cell components and degradation of material properties. Neither melting nor vaporisation of fuel cell components is usual within the operating temperature range,

although agglomeration of metal particles [64] and vaporisation of chromates [65] have both been observed under SOFC operating conditions. Additionally, fuel cell preparation is conducted at higher temperatures than SOFC operating temperatures and melting of some materials, such as copper in Cu cermets, can occur [66].

Structural phases occur over certain temperature ranges, with significant changes in material properties occurring with phase transitions. Shifting of the stable temperature range of desirable phases can be achieved through alternation of material composition, although this may also have a considerable effect on the material properties. Significant changes in the size and mechanical properties of materials can also occur upon phase transitions, where significant volume changes may cause considerable mechanical stresses to form, resulting in fuel cell degradation.

Due to the highly reducing atmosphere found at the SOFC anode under operating conditions, these materials must be stable in both oxidising and reducing environments. Reduction of many ceramic oxides has been observed to cause material degradation or phase transitions, both of which can be detrimental to anode performance [67-69]. Whilst many of the problems associated with redox cycling occur upon reduction, re-oxidation of compounds can also have a significant effect on materials properties. Some SOFC anode materials are pre-reduced at high temperatures to improve conductivity, therefore re-oxidation of these compounds will cause a significant degradation of anode performance [70]. Other materials advanced as SOFC anode materials are formed under reducing atmosphere and are unstable to oxidation, which considerable reduces their applicability [71].

A recent concept for SOFCs involves the use of redox reversible materials, which exhibit reversible phase transformations upon redox cycling [72]. These materials usually display a significant improvement of material properties upon reduction, although this is often accompanied by detrimental volume changes [73]. The applicability of these materials is questionable when compared to fully redox stable materials.

1.2.5. *Microstructure and Mechanical Properties*

Gas flow both toward and away from the three phase boundary at SOFC electrodes is essential to minimise the concentration polarisation and thus increase fuel cell performance. To this end the porosity of SOFC electrodes must be efficiently controlled to provide effective gas transport whilst maintaining sufficient electronic and ionic conductivity. Modification of electrode porosity is usually achieved through the use of pore forming materials. These materials are generally removed during electrode synthesis, thus compounds which either vaporise at low temperatures, such as starch [74], graphite [75] and PMMA [76], or can be removed after pellet sintering, such as MgO [77], are required. Effective control of the electrode microstructure can have a considerable effect on fuel cell efficiency, with significant improvements in fuel cell performance noted with microstructural modification [78, 79].

Whilst the formation of pores throughout the electrode structure is required for high fuel cell performance, the distribution and interconnectedness of these pores will also have a significant effect on the electrode performance. This is taken into consideration through the separation of material porosity into closed and open porosity. Closed porosity refers to those pores which are isolated within the materials and therefore are not used in gas transport through the materials, whilst open (or effective) porosity encapsulates those pores which form an interconnected network. The material properties of pore formers are known to alter the ratio of closed to open porosity, with particle size, shape, size distribution and removal temperature of the pore former effecting the effective porosity [80].

Pore formers can also have a significant effect on the sintering properties of electrode materials. The use of graphite as a pore former is known to cause a significant increase in pellet shrinkage, although this can be mitigated through the formation of a composite pore former [81]. Modification of the shrinkage of an electrode can be important when attempting to minimise strain between electrode and electrolyte materials, as close matching of the shrinkage and TEC of these contacting components will significantly reduce interfacial stresses [82].

Whilst reduction of concentration polarisation is necessary to provide efficient fuel cell performance, sufficient mechanical strength is also required to prevent electrodic disintegration. The porosity of a material is known to be inversely proportional to the mechanical strength [83], although significant reduction of the electrode performance is expected to occur prior to the point at which mechanical failure is likely. Varying fuel cell configurations will require differing mechanical properties of various fuel cell components, for example the mechanical strength of the anode in an anode supported planar SOFC will be required to be higher than for that of the anode in a tubular SOFC.

Mechanical failure of a fuel cell is not restricted to poor mechanical strength of the fuel cell components, as stresses are expected to form during cell preparation, thermal cycling and redox cycling. Interfacial stresses between electrolyte and electrode components during fuel cell preparation will form if the shrinkage of the contacting components is mismatched [84]. This can result in electrode/electrolyte deformation, delamination and possible electrolyte cracking. Mitigation of these interfacial stresses can be achieved through effective use of pore formers, sintering aids or graded electrodes [81, 85, 86].

Thermal cycling of fuel cells results in less acute stresses, usually a result of thermal expansion coefficient mismatch, than observed for shrinkage mismatch, although the cumulative effect over numerous cycles may have similar effects to those noted for shrinkage mismatch [87]. Most materials exhibit a gradual expansion in their volume upon heating due to thermally activated displacement of atoms off their sites in the crystal lattice. The fractional volume change with temperature is known as the thermal expansion coefficient (TEC). The thermal expansion coefficient is an intrinsic material property, which is dependent on material composition, structure and powder properties. Mismatch of the thermal expansion coefficient of contacting components causes the formation of interfacial stresses and leads to delamination or electrode/electrolyte cracking [87, 88]. Generally, a TEC mismatch of $4\text{-}5 \times 10^{-6}\,K^{-1}$ will require additional electrode processing to reduce interfacial stresses and prevent performance degradation.

Cycling between reducing and oxidising atmospheres is known to cause volume changes in SOFC anode materials, which can cause the formation of both interfacial stresses at the anode-electrolyte boundary and inter-anodic stresses [89, 90]. Redox cycling of ceramic oxide materials, without the presence of phase transitions or compound degradation, is known to cause small volume changes, usually < 1 % [91]. Larger volume changes are observed for redox cycling of metallic materials, with the asymmetrical volume change associated with the redox cycling of nickel the focus of substantial investigation [89]. For most SOFC anode materials compound degradation upon reduction is significantly more likely than considerable changes to mechanical stability with redox cycling.

Electrode functional layers, thin material layers $2 - 20$ μm thick at electrode-electrolyte interfaces, can be utilised to improve fuel cell performance [35, 92] and to prevent interfacial reactions with electrolyte materials [93, 94]. Improvements in fuel cell performance can be due to microstructural improvements, increasing gas flow to the catalytically active electrode sites, or through increases in the three phase boundary [35]. The prevention of interfacial reactions between electrolyte and electrode materials can be of interest as some effective electrode materials react with common electrolyte materials, restricting their applicability without the use of functional layers [95]. Functional layers can also be applied to the outer layer of the electrode to aid fuel processing and to remove harmful impurities [96].

Graded electrode materials have also been utilised to improve the performance of fuel cells [97] and reduce mechanical stresses at the electrode-electrolyte interface [98], although this does further increase the complexity of the electrode processing. Compositionally graded electrodes are used to improve abrupt transitions between material properties at interfaces [98], whilst porosity graded electrodes are used to improve gas transport while improving the length of the three phase boundary [82]. Combination of a composition and porosity gradient in electrode materials has also been shown to significantly reduce interfacial resistance [99]. Particle size grading has also been posited to have an effect on electrode performance through improvements in gas transport and reactive surface area close to the electrode-electrolyte interface [100],

although modelling suggested that this would have little overall effect on the ohmic and activation overpotentials [101].

The use of advanced processing methods, such as tape casting, screen printing and various deposition techniques [102], allows precise control of the thickness and composition of these additional layers, intimating that the use of functional layers and graded electrodes are viable techniques for improvement of mechanical and catalytic electrode properties.

1.3. SOFC Materials

The first solid oxide fuel cell was developed by E. Baur and H. Preis in 1937 [103] and consisted of a yttrium stabilized zirconia (YSZ) electrolyte separating iron or carbon electrodes. Since the discovery of the solid oxide fuel cell a significant amount of research has been dedicated to the development of these materials.

A variety of reviews have been published on all aspects of SOFC materials, design and implementation and much of the information in the following sections on electrolyte materials [28, 104-106], interconnect materials [65, 107-109], cathode materials [110-112] and anode materials [113-116] is based on reviews of these components.

1.3.1. Electrolytes

For an electrolyte materials to function efficiently the membrane must be an effective electronic insulator and ionic conductor (with a minimum ionic conductivity of 1×10^{-2} Scm^{-1}), without chemical reactions with anode, cathode and interconnect materials, thermally stable at the operating temperature and be impermeable to the fuel gas. Much of the research into these materials has focused on improvement of the ionic conductivity, whilst maintaining the electronic insulating properties.

The original fuel cell electrolyte was yttrium stabilised zirconia (YSZ), which meets all the criteria for a high temperature fuel cell electrolyte. As the low temperature phase of pure zirconia does not exhibit high ionic conductivity, acceptor doping is necessary to form the conductive cubic fluorite phase [28]. As with many ionic

31

conductors, the optimum doping level is the lower stability limit of the highly conducting phase, with both Y and Sc doping producing good electrolytes materials [117, 118]. In addition to high ionic conductivity, the electrolytic domain, conditions under which the electronic contribution to total conduction is minimal, of YSZ covers the temperature and pO_2 range for SOFC operation [28]. Whilst doped zirconates exhibit many of the desirable properties for intermediates temperature SOFC electrolytes, the conductivity of YSZ is too low for effective use below 800 °C [104] without significant materials processing. As YSZ is unsuitable for use at intermediate temperatures, a significant amount of research has focused on the development of alternative electrolyte materials for use at < 800 °C, with a selection of the most effective YSZ alternatives exhibited in Figure 1.6 [28].
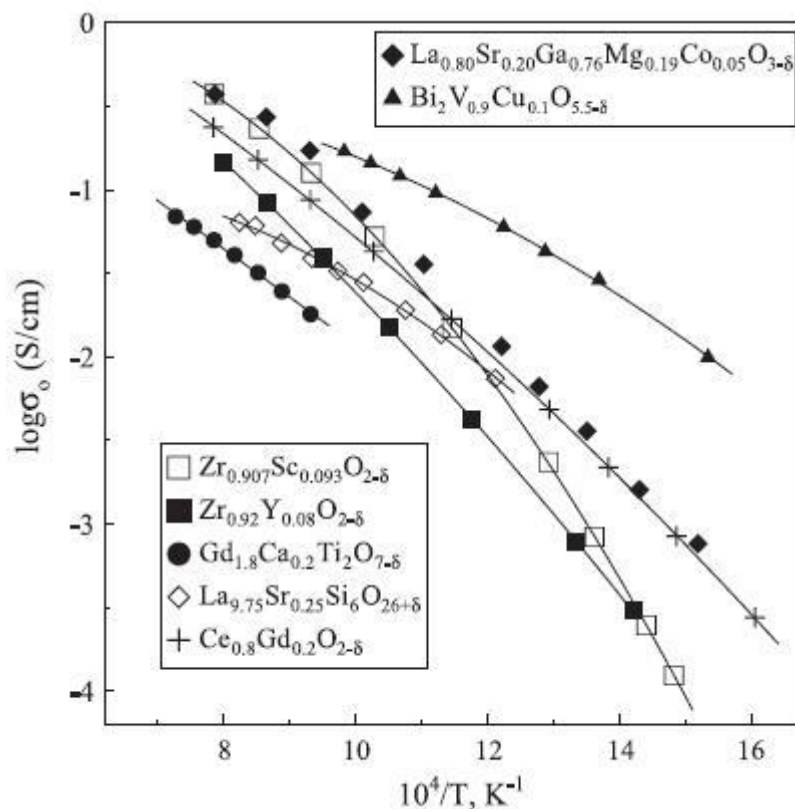
Figure 1.6: Comparison of the ionic conductivities of various oxide ion conducting electrolytes [28]

Rare earth-doped cerates exhibit higher ionic conductivity than doped zirconates at intermediate temperatures, with gadolinium doped ceria (GDC) and

samarium doped ceria (SDC) exhibiting conductivities of > 0.01 Scm^{-1} at 500 °C [28, 119, 120]. The use of cerates does present problems upon exposure of the electrolyte to reducing atmospheres, as partial reduction of cerium, from Ce^{4+} to Ce^{3+}, will occur [121]. Cerium reduction induces n-type electronic conduction in the sample, with a larger electronic contribution to total conductivity at temperatures greater than 550 °C noted for $Gd_{0.1}Ce_{0.9}O_{2-\delta}$ [122]. Simulations of SOFC operation with a doped ceria electrolyte did prove that anodic polarisation can suppress cerium reduction, allowing effective operation at temperatures below 600 °C [28]. An alternative technique to mitigate electronic conductivity in doped cerates introduces an electron blocking layer at the anode-electrolyte interface, which has been shown to improve the open circuit voltage with a subsequent improvement in fuel cell performance at intermediate temperatures [123]. Whilst the electronic conductivity of doped cerates in reducing atmospheres does limit their application, the high ionic conductivity, chemical stability and TEC match with other SOFC materials maintains interest in these materials as SOFC electrolytes.

Lanthanum strontium gallium magnesium oxide (LSGM) exhibits both higher ionic conductivity than YSZ and an electrolytic domain that extends to lower pO_2 than that of GDC [124, 125]. Unlike for the fluorite electrolytes, these materials do not require stabilisation of a high temperature, conductive phase as the low temperature $LaGaO_3$ perovskites exhibits reasonable ionic conductivity prior to dopant introduction [126]. Doping with aliovalent ions with the aim of increasing the number of oxygen vacancies functions optimally when lattice distortion is minimised, achieved through substitution with similar sized atoms, hence the effectiveness of dual La and Mg doping [29, 124]. Unlike both YSZ and GDC, chemical reactions between LSGM and other fuel cell components are not uncommon, with the formation of resistive La-Sr-Ga phases at electrolyte-electrode interfaces [58, 127]. Additional problems with gallium use include the volatisation of gallium during high temperature synthesis and sintering [127] and the high cost of gallium reactants. The use of LSGM as an IT-SOFC electrolyte is not undesirable, however the drawbacks associated with high temperature firing and durability limit the commercial applicability.

Bismuth oxide-based materials [128,129] and metal doped bismuth vanadium oxides [130, 131] exhibit the highest oxygen-ion conductivities at intermediate temperatures, although have a number of problems with their implementation . Pure δ–phase Bi_2O_3 exhibits ionic conductivities of ~ 1 Scm^{-1} around 825 °C, however the conductive polymorph has a narrow temperature range of formation and exhibits a large volume change on transformation from the low temperature (α) phase [132]. Stabilisation of the high temperature conductive Bi_2O_3 phase with various dopants is possible, although a slow transformation to the low temperature (α) phase at intermediate temperatures is still observed [132]. Doped γ-phase $Bi_4V_2O_{11}$ compounds exhibit greater phase stability than doped Bi_2O_3 at intermediate temperatures alongside improved conductivity at low temperatures, < 400 °C [28]. Despite the high ionic conductivities, Bi_2O_3 and BIMEVOX materials both suffer from high chemical reactivity, low mechanical strength and instability in reducing environments, rendering them unsuitable for use in solid oxide fuel cells [133,134,135].

The ionic conductivity of other electrolyte materials is dependent on the amount of Schöttky defects in the structure, due to conduction between anion lattice sites, however apatite materials can make use of an interstitial conduction mechanism [136-138]. Apatite materials, with the general formula $A_{10}(MO_4)_6O_2$ (A = alkali earth metal, rare earth metal, M = Si, Ge), have exhibited high ionic conductivities at intermediate temperatures with little electronic contribution to total conductivity [105]. The interstitial conduction mechanism is dominant at high pO_2, however in reducing atmospheres a vacancy conduction mechanism can occur, with a corresponding decrease in conductivity [28]. The volatility and reactivity of the silicon in apatites has been identified as a potential problem with their application, with silicon migration into electrodes causing significant increases in area specific resistances [139, 140]. Whilst the ionic conductivity of apatites is sufficiently high for IT-SOFCs, problems with silicon volatility and densification of these materials have, thus far, limited their use.

Other alternative materials have also been briefly investigated, such as $Ba_2In_2O_5$-based materials [141], other perovskites [142], pyrochlores [143] and $La_2Mo_2O_9$-based compounds [144], although none have exhibited either sufficiently high

conductivity or stability to be seriously considered as intermediate temperature replacements for YSZ. Barium indium oxides are unsuitable as IT-SOFC electrolytes due to redox instability and reactivity with water and carbon monoxide, despite reasonable ionic conductivity and low electronic conductivity at intermediate temperatures [141, 145, 146]. Lanthanum aluminates were of interest due to low cost and good stability but low ionic conductivity and relatively high electronic conductivity at intermediate temperatures rendered these compounds unsatisfactory as SOFC electrolytes [142, 147]. Gadolinium titanates were originally considered as electrolyte materials, however the electronic conductivity of these compounds was high enough for possible consideration as anode materials and therefore unsuitable for use as an electrolyte [143, 148, 149]. High thermal expansion coefficients and a lack of redox stability of $La_2Mo_2O_9$ (LAMOX) materials curtailed further development of these materials as IT-SOFC electrolytes [150].

Whilst it was stated previously that YSZ was not suitable as an SOFC electrolyte material below 800 °C, modern processing methods can mitigate the problems associated with intermediate temperature operation [151-153]. As electrolyte thickness is fundamental to fuel cell performance, reducing the thickness of the electrolyte has been shown to significantly improve fuel cell performance [152, 153]. A large variety of techniques, such as spray coating [154], screen printing [155] and electrophoretic deposition [156], have been used to achieve this goal, although some of these methods can result in non-dense membranes [102]. Despite the possibility of use of YSZ at intermediate temperatures, further improvements in performance are noted for fuel cells using either GDC or LSGM electrolytes using the same processing techniques [152, 157-160].

For intermediate temperature fuel cells, doped cerates and LSGM exhibit many of the desirable properties for electrolytes and, as such, are the most applicable electrolyte materials despite their drawbacks. Yttrium stabilised zirconia, the lower ionic conductivity notwithstanding, can still be an appropriate electrolyte at intermediate temperatures due to greater material stability compared to doped cerates and LSGM.

1.3.2. Interconnects

Interconnect materials are used to conduct electrons from one electrode to another, whilst maintaining gas separation of the electrodes, therefore these materials must be redox stable and maintain high electronic conductivity, and preferable negligible ionic conductivity, in both oxidizing and reducing atmospheres. A low permeability for both oxygen and the fuel gas is also necessary to prevent fuel crossover, which can significantly reduce fuel cell performance. As with all SOFC materials, chemical, thermal and mechanical stability, with respect to other fuel cell materials, is necessary to form an efficient interconnect.

High temperature SOFC operation favours the use of metal oxide interconnect materials as oxidation of metallic interconnects between 800 °C and 1000 °C causes substantial material degradation. Doped lanthanum chromites are of interest as high temperature interconnect materials due to their electronic conductivity in oxidizing and reducing environments, redox stability and similar thermal expansion to other fuel cell components [65, 161]. As undoped lanthanum chromite (LCrO) is a p-type semiconductor, the conductivity reduces substantially under reducing conditions. Introduction of alkaline earth dopants increases the conductivity in both oxidizing and reducing atmospheres, however this can also cause a significant increase in the thermal expansion coefficient [109].   Reduction of the temperature below 800 °C reduces the electronic conductivity of doped LCrO in reducing atmospheres to below the threshold conductivity for efficient operation, ~ 1 Scm^{-1} [109]. The chemical stability of strontium and calcium doped lanthanum chromite varies with differing electrolyte materials, with Ca-doped LCrO exhibiting interfacial reactivity with YSZ electrolytes while Sr-doped LCrO forms $SrCrO_4$ at the interface with ceria based electrolytes [65]. Doped lanthanum chromites are useful materials for high temperature SOFCs, however reduction of the operation temperature below 800 °C has reduced the utility of these compounds.

Reduction of the operating temperature to below 800 °C alleviates many of the problems associated with the use of metallic interconnect materials. Iron, nickel and

chromium [107] based alloys have all been investigated as possible interconnect materials due to their high electronic conductivity. The use of metallic materials has posed some additional problems, especially with oxidation, leading to the formation of poorly conductive surface oxide scales [107]. Most effective non-coated alloys contain a minimum of 10% chromium to provide an oxidation resistive coating, preventing the formation of surface insulating layers. Despite the desirability of formation of chromium oxide scales at the interconnect surface, chromium oxides and hydroxides are vaporized at SOFC operating temperatures. Chromium scale vapourisation leads to the formation of various chromites at the cathode, inhibiting the cathodic catalytic activity and degrading fuel cell performance [162]. Chromium volatisation can be partially alleviated by the use of alloying agents, such as Y, Ce and Zr, which form a coating on the chromium scale reducing chromium vapourisation [109]. An alternative technique is the coating of the interconnect surface with various metal oxides, such as reactive element oxides [163], rare earth perovskites [164] and spinels [165]. The most promising of these coatings are spinels as they have been shown to exhibit high electronic conductivity, similar TEC to other SOFC components and can easily incorporate Cr into the structure, inhibiting chromium migration, although some spinels are known to suffer from carburization [108].

Figure 1.7. The effect or carburization on various metal alloys of interest as SOFC interconnect materials [166]

Carburization, the absorption of carbon into the structure, is a particular problem for metallic interconnect materials, especially with the pressure to use alternative fuels such as biogas and various hydrocarbons for SOFCs. Formation of carbides on the surface of the interconnect can cause significant corrosion, with further degradation of the carbide causing 'metal dusting' [166], as exhibited in Figure 1.7. Carburization can be significantly reduced by the formation of chromium-rich scales, although some spinels also show reasonable carburization resistance [167].

Formation of an efficient interconnect materials consists of striking an effective balance between oxidation/carburization resistance and coating/scale volatility by variation of the chromium content of the compound and the coating. Coated metallic interconnect materials appear to be efficient under current operating conditions, with further improvements in stability likely with the expected reductions in SOFC operating temperature.

1.3.3. Cathodes

As cathode materials are only exposed to air, or oxygen, redox stability is not required, thus simplifying material design. High electronic conductivity, preferably over 100 Scm^{-1}, is essential for cathode materials, ideally with sufficient ionic conductivity to maximise the three phase boundary. Control of cathodic microstructure is also desirable, as sufficient porosity to minimise concentration polarisation is required for efficient fuel cell operation. The reaction at the cathode of oxygen ion conducting SOFCs is the oxygen reduction reaction, therefore sufficient catalytic activity for the ORR is necessary for efficient cathode operation.

Undoped lanthanum manganates exhibit high electronic conductivity and good thermal stability, although improvement of material properties for cathode applications is noted upon strontium doping [110, 168, 169]. Unusually, strontium doping increases the electronic conductivity without increasing oxygen vacancy concentration through charge compensation mechanisms, via oxidation of manganese in the structure [170]. Use of an undoped $LaMnO_3$ cathode with a YSZ electrolyte leads to the formation

of an insulating $La_2Zr_2O_7$ phase at the cathode-electrolyte interface, increasing cathodic resistance [171]. A careful balance of strontium doping levels is required to reduce $La_2Zr_2O_7$ formation whilst minimising formation of the $SrZrO_3$ phase which forms for strontium rich (x > 0.3) $La_{1-x}Sr_xMnO_3$ (LSM) samples [172]. The reactivity [172] and low ionic conductivity [173] suggest that solitary use of LSM as a cathode material is not ideal for efficient fuel cell operation, although this can be mitigated through the formation of composite cathodes.

Replacement of lanthanum in LSM with other lanthanides, such as neodymium, samarium and praseodymium, was found to improve both the stability range whilst maintaining high electronic conductivity [174, 175]. Additionally, the thermal expansion coefficients of the $Ln_{0.7}Sr_{0.3}MnO_3$ compounds, for Ln = Sm, Nd and Pr, all exhibited a close match with the TEC of YSZ electrolytes [175]. Praseodymium analogues have been found to exhibit the lowest ASR of any of the $Ln_{1-x}Sr_xMnO_3$ compounds [174], likely due improvements in the electrocatalytic activity of the cathode, as exhibited for other praseodymium containing materials [176, 177]. As with LSM, these materials exhibit negligible ionic conductivity and therefore have to be utilised in a composite materials, however improvement in stability and catalytic activity indicates that these materials may be of use in IT-SOFCs.

Cobalt analogues of LSM, $La_{1-x}Sr_xCoO_3$ (LSC), exhibit higher electronic and ionic conductivities combined with an improvement in catalytic activity and, as such, are of substantial interest as cathode materials [110, 178]. Compared to typical thermal expansion coefficients of electrolyte materials, the TECs of LSC-based compounds are high (~ 20×10^{-6} K^{-1} [179]), which can produce stresses at the interface resulting in possible electrolyte cracking and cathode delamination, severely limiting their use. High temperature firing with YSZ has been found to form insulating phases at the cathode-electrolyte interface, which, unlike LSM, cannot be mitigated through variation of the strontium content [180]. Doping with various transition metals has been utilised to improve material properties although, despite a reduction in chemical reactivity for Mn and Fe doping, a significant level of doping is required to reduce the TEC to acceptable levels [181-183]. As for LSM, Pr substitution corresponded with an improvement in cathode properties, although the TEC remained too high for effective use [184]. The high electronic and ionic conductivities of LSC-based compounds is

undermined by the high TEC and reactivity to other fuel cell components, with cobalt poor structures more likely to form efficient cathode materials.

Lanthanum strontium ferrites (LSF) are more stable than their cobalt analogues, albeit with lower electronic conductivities, similar to those of LSM (> 100 Scm^{-1} at 750 °C) [1, 180]. The electrochemical activity of LSF is also lower than is found for LSC, although the thermal expansion coefficient is closer to that of electrolyte materials [2, 182]. The oxygen ion conductivity of LSF is similar, or marginally less, to that of LSC, up to 0.15 Scm^{-1} at 750 °C, which is high enough for use as a non-composite cathode [1]. Copper doping has been found to significantly improve the cathodic performance of LSF, which could be due to improved sintering characteristics and increased catalytic activity [185, 186]. Additionally a reduction in the TEC of LSF was noted with the introduction of lanthanum deficiency, forming $La_{0.7}Sr_{0.25}FeO_3$, with a significant reduction in ASR over other ferrite cathodes [187]. The formation of additional phases or incorporation of yttrium into ferrite perovskites at high temperatures [188] requires the use of a cerate barrier layer between LSF and YSZ electrolytes. Considering the conductivity and thermal expansion coefficients of lanthanum strontium ferrites, they may find use as an intermediate temperature cathode with doped ceria electrolytes.

Various combinations of these three main perovskite cathodes have come under investigation, however $La_{1-x}Sr_xFe_{1-y}Co_yO_3$ (LSCF) has found extensive use in IT-SOFCs [189-191]. The conductivity of LSCF increases with increasing strontium and cobalt content, however this is also associated with increasing thermal expansion coefficients [2, 192]. One balanced LSCF composition is $La_{0.6}Sr_{0.4}Co_{0.2}Fe_{0.8}O_3$, which combines high electronic conductivity, reasonable ionic conductivity, good electrocatalytic activity and a TEC closer to that of SOFC electrolytes [2, 190]. Interfacial reaction with YSZ [2], as was observed for LSF, limits the use of this cathode to fuel cells utilising doped ceria electrolytes. As with LSM and LSC replacement of the lanthanum with praseodymium improved the cathodic performance, however the resultant increase in the thermal expansion requires a reduction in strontium content to ensure a TEC match with electrolyte materials [110, 193].

Barium strontium cobalt ferrites (BSCF) demonstrate high ionic conductivity, high catalytic activity for oxygen reduction and reasonable electronic conductivity [62].

These materials exhibit excellent performance as a cathode material at intermediate temperatures, with a maximum power density of 1.01 Wcm^{-2} observed at 600 °C for a BSCF/SDC/Ni-SDC cell [194]. Despite the good performance, the thermal expansion coefficient is higher than is found for lanthanum doped samples (19.2-22.9 $\times 10^{-6}$ K^{-1} between 25 °C and 850 °C) and reactions with both YSZ and GDC were observed at T > 800 °C [195]. Additionally, BSCF is known to form carbonates upon exposure to CO_2, decreasing cathodic performance and precluding the use of air at the cathode [196]. Despite the impressive performance of BSCF, LSCF is a more suitable material for use as an SOFC cathode due to lower TEC and lack of chemical reactivity to cerates and CO_2.

Perovskite-based lanthanum nickelates, cuprates, colbaltates and manganates with the K_2NiF_4-structure have recently come of interest as cathode materials due to high electronic conductivities and high oxygen diffusivity [197-200]. The thermal expansion coefficients of the K_2NiF_4-structured compounds are lower than for the respective perovskite compounds, which increases the utility of cobalt containing compounds [201]. Similar trends to those noted for the perovskite compounds are observed, with strontium doping improving the conductivity but increasing the TEC [202]. Lanthanum strontium nickelate (LSN) cathodes have exhibited high oxygen diffusivity, high electronic conductivities, thermal expansion coefficients close to electrolyte materials and high thermal stability [202, 203]. Doping of La_2NiO_4 with copper increases the conductivity and reduces the thermal expansion coefficient closer to that of SOFC electrolytes [204]. Substitution with cobalt increases both the oxygen ion diffusivity and the surface exchange coefficient, which suggests that the catalytic activity of the cobalt analogue should be higher than that of the nickel compound [205]. The thermal expansion coefficients of these compounds were also close to the TEC of SOFC electrolytes, which allows for use of cobalt rich compounds unlike for perovskite structured materials [201]. Despite promising characteristics the performance of cobalt doped LSN (LSCN) was less than noted for alternative perovskite cathode materials, with polarisation resistances of 1.36 Ωcm^{-2} and 5.15 Ωcm^{-2} at 600 °C and 850°C respectively [206, 207]. Substitution of nickel with manganese resulted in a

significant reduction in electronic conductivity accompanied by an increase in TEC, reducing the applicability of the material [199].

As with previous cathode materials, praseodymium doping was found to increase the electronic conductivity, oxygen mobility and the thermal expansion coefficient, with careful manipulation of the composition required to reduce the TEC to close to that of SOFC electrolytes [208, 209]. Replacement of praseodymium by samarium results in a reduction of the thermal expansion coefficient whilst maintaining high conductivities, with the highest noted for $SmSrCoO_4$, ~ 290 Scm^{-1} at 800 °C [210]. As with praseodymium compounds the TEC is still high, > 15×10^{-6} K^{-1}, thus nickel doping may be required for effective cathode use [211]. Neodymium based cathodes exhibited improved performance when compared to lanthanum analogues, exhibiting reduced area specific resistances combined with a lower TEC [212]. As for all cathode materials a careful balance between conductivity and thermal expansion must be maintained, with increasing strontium content in Nd_2CoO_4 increasing both the electrical conductivity and the TEC [213].

The stability of the pure lanthanide nickelates has been called into question, with Pr_2NiO_4 found to decompose after 24 hours at 700 °C and chemical reactions with YSZ and GDC exhibited for La_2NiO_4 and Nd_2NiO_4 [214]. No reaction was noted between LSN and LSGM, suggesting that the formation of LSGM based fuel cells may be required for the use of K_2NiF_4 cathodes [215]. Replacement of lanthanides with barium was suggested to improve cathodic polarisation resistance, however it is expected that similar problems with $BaCO_3$ formation will occur [216]. Further development of the Ruddlesden-Popper series for lanthanum nickelates, $La_{n+1}Ni_nO_{3n+1}$ (n = 1, 2, 3), determined that the electronic conductivity improved with increasing n, causing a subsequent reduction in polarisation resistance and therefore a marked increase in fuel cell performance [217].

A large proportion of recent research into SOFC cathode materials is devoted to determining the optimal composition of these materials and, despite promising results, further research is still required.

For many cathode materials used with YSZ a careful balance between stability and performance has to be attained, with electronic conductivity and catalytic activity

sacrificed for reduced chemical reactivity [171, 172, 187]. For many of these compounds formation of insulating secondary phases with YSZ has limited their effectiveness, however no reaction is observed for many of these compounds with doped cerate electrolytes [187]. The use of ceria electrolytes allows the use of more efficient compositions that were previously unavailable due to the formation of $SrZrO_3$ at high temperatures and thus the use of these electrolytes is desirable when constructing IT-SOFCs.

Of the current cathode materials, LSCF appears to exhibit most of the desired properties for an effective SOFC cathode, however improved material properties are noted for other materials, especially BSCF and the K_2NiF_4 structured cathodes, and therefore further research is required to develop these materials.

1.3.4. Anodes

As anode and cathode materials share many of the same functions, many of the required properties for cathodes, high electronic conductivity, ionic conductivity, thermal and chemical stability and TEC match with electrolyte and interconnect materials, are also desirable for efficient anode materials. The difference between cathodic and anodic requirements is in the catalytic activity and redox stability of the materials. As the anodic reaction, fuel oxidation, differs from the cathodic reaction, oxygen reduction, different catalysts are required, although high catalytic activity for the reaction is still desirable. Additionally, as the anode is exposed to a reducing atmosphere under SOFC operating conditions, stability under both oxidising and reducing environments is essential. Desirable electronic conductivity for an SOFC anode materials would be ~ 100 Scm^{-1}, although this can be as low as 10 Scm^{-1} depending on the fuel cell geometry, whilst area specific resistances of 0.1 Ωcm^{-2} to 1 Ωcm^{-2} are generally considered to be acceptable for fuel cell operation.

43

1.3.4.1. *Previous Research*

There have been a number of substantial reviews published in this area over the last decade, notably those by Atkinson et al (2004) [113], Tao and Irvine (2004) [114], Sun and Stimming (2007) [115] and Cowin *et al.*(2011) [116], and much of the information found in following section is a collation of these works. The most widely used of all the anode materials are metal-ceramic composites (cermets), of which nickel-yttrium doped zirconia is the most common. In this work referencing of alternative anode materials mostly refers to non-cermet materials.

1.3.4.1.1. Fluorites

Primarily, in SOFCs, metals were used as both anode and cathode, however as these materials were optimised, the use of a support was introduced, generally a metal oxide. As discussed in the preceding section, the introduction of an ionically conductive phase can be used to propagate the TPB and increase anode efficiency, whilst alleviating other numerous problems associated with pure metal anodes. Much of the research into fluorite structured materials has focused on the development of cermets, ceramic-metallic composite, anodes, especially transition metal-ceria/zirconia composites [218,219].

Cermets consisting of nickel and yttrium stabilised zirconia have been the state-of-the-art anode materials for a significant proportion of SOFC history. Ni-YSZ has high electronic conductivity, acceptable ionic conductivity, TEC match to the electrolyte and high catalytic activity for hydrogen oxidation, meeting a substantial portion of anode requirements. There are, however, a number of problems associated with the use of Ni-YSZ anodes. Nickel is prone to carbon deposition, or coking, when using hydrocarbon fuels [23], sulphur poisoning [220], agglomeration upon prolonged usage[221] and is not redox stable [222].

Whilst complete anodic exposure to oxidising conditions at the high temperatures required for nickel re-oxidation is improbable, partial oxidation of the anode can occur through accidental exposure to air upon start up/shut down, cross-seal

leakage of air or limited fuel supply to the anode. The reasons behind the lack of redox stability of nickel is found in the asymmetric volume change upon cycling between oxidising and reducing atmospheres, with a ~ 40 % decrease in volume observed upon NiO reduction but a ~ 70 % volume increase upon re-oxidation due to morphological changes [223,224]. A considerable amount of research on the redox stability of Ni-YSZ have been conducted [89, 225], with various methods of microstructural modification shown to reduce the detrimental effect of this redox instability on anode performance [226,227].

The use of Ni-YSZ with hydrocarbon fuels has been extensively investigated, with fuel oxidation of most hydrocarbons exhibiting substantial coking, causing a considerable reduction in fuel cell performance [23, 228]. Humidification of the fuel can partially alleviate the effect of coking through promotion of internal reforming of the fuel, but this reduces the electrical potential of the cell [47]. Addition of air to the fuel gas stream has been shown to have a similar effect on anodic coking, although again with a reduction in the fuel cell performance [229]. Application of high current densities, which increase the oxygen flow across the electrolyte, also reduce coking, although a substantial increase in current is required with increasing temperature [230, 231]. External anode fuel reforming layers have also successfully been utilised to reduce the effect of coking on Ni/YSZ anodes with hydrocarbon fuels through internal reforming of the fuel prior to anode exposure [54].

Alternative fuels which do not contain carbon do not exhibit those problems associated with the use of hydrocarbon fuels on Ni-YSZ anodes. Similar fuel cell performance was observed for an SOFC with a Ni-YSZ anode utilising humidified hydrogen or ammonia fuel, although the ammonia fuelled cell exhibited significantly interfacial polarisation from ammonia cracking and oxidation [232]. Whilst alteration of anodic conditions can markedly reduce coking many of these modifications also reduce fuel cell performance, thus alternative materials are required to provide the fuel flexibility desired for effective SOFC utilisation.

Many materials based on CeO_2 demonstrate mixed ionic and electronic conductivity in reducing atmospheres due to the mixed valence of cerium, Ce^{3+} and Ce^{4+} under these conditions. The use of doped ceria in cermets does provide a

significant advantage in terms of higher catalytic activity with hydrocarbon fuels and lower temperature conductivity over typical YSZ cermets [233]. Pure and doped ceria have also been found to promote catalytic activity for hydrocarbon oxidation reactions without coking [234]. The use of either GDC and SDC in place of YSZ in nickel cermets does not prevent coking with direct hydrocarbon utilisation [235], although, as for YSZ cermets, humidification is effective for coke reduction for some hydrocarbon fuels [236]. Replacement of YSZ with GDC has also been shown to considerably reduce, although not completely arrest, the effects of H_2S poisoning [237]. Further improvement of the catalytic activity for hydrocarbon reforming at the anode has been demonstrated through introduction of noble metals into a transition metal/doped ceria cermets [219]. Doped or undoped ceria, while improving the catalytic activity and coking resistance of nickel cermets, still suffer from nickel agglomeration and redox instability.

The use of mixed oxygen-ion and proton conducting cermets at the anode has been reported to reduce both coking and H_2S poisoning of nickel at the anode in proton conducting SOFCs [238], although the viability of this approach in oxygen ion-conducting SOFCs has yet to be proven.

Reactions between nickel and LSGM [239] and the other problems associated with use of LSGM in fuel cells have suppressed research into LSGM cermets as anode materials, thus alternative metal phases have been developed to mitigate the associated problems with the use of nickel at the anode.

Complete substitution of the nickel at the anode with copper was investigated by Gorte *et. al.* with regards to improving the coking and sulphur tolerance of the anode [240, 241]. Whilst copper exhibited improved performance over nickel with hydrocarbon fuels, the electrochemical performance of these anodes is substantially lower when operated in hydrogen [242]. The addition of ceria to the copper anode was found to substantially improve the electrocatalytic activity of the anode, however this is to the detriment of sulphur tolerance with CeO_2S formed upon exposure to H_2S [243, 244].

The relatively low melting temperature of both copper and copper oxide, 1085 °C and 1235 °C or 1326 °C respectively, prevent one-step production of anodes due to the high sintering temperatures of electrolyte materials. Impregnation of a copper

nitrate solution into a porous electrolyte matrix is an effective method for formation of copper-based anodes, however alloying of copper with other transition metals can both increase the melting temperature and improve the catalytic properties.

Further improvement of copper catalytic activity was attempted by alloying with nickel, however with the introduction of 10 % nickel into the alloy coking was observed on the anode [245]. Interestingly, the formation of carbon deposits over copper rich Ni-Cu alloys does not appear to be detrimental to fuel cell performance, with a significant increase in maximum power density observed over 500 hours of operation in dry methane [245]. Kim *et. al.* [245] posit that the observed increase in performance is linked to the formation of electronically conductive carbon 'bridges' between isolated areas of copper which could increase the three phase boundary.

Copper electroplating of Ni-YSZ anodes also exhibited an improved tolerance to coking, albeit with a gradual reduction in fuel cell performance noted over 200 hours in humidified CH_4 [246]. This drop is suggested to be due to the formation of an equilibrium between carbon deposition and oxidative removal, not observed with the copper-rich alloys. Wang *et. al* [247] also observed this gradual decrease in fuel cell performance over 12 hours in dry CH_4 with $Ni_{0.95}Cu_{0.05}$ alloys, although the SDC support in this study would likely have a suppressive effect towards coking, improving cell stability to direct utilisation. Nickel alloying certainly improves the catalytic activity of the anode, however only copper rich compositions have the potential for use with dry hydrocarbon fuels.

As copper and cobalt are immiscible, unlike copper and nickel, production of bi-metallic copper-cobalt anodes should theoretically form Cu-coated Co particles [248]. Lee *et. al.* [249] reported that the proportion of cobalt in Cu-Co alloys impregnated into a porous YSZ matrix did not significantly affect the fuel cell performance in either hydrogen or *n*-butane, however addition of cobalt to the Cu-CeO2-YSZ anode did improve fuel cell performance in both atmospheres. Exposure of various Cu-Co alloys to dry CH_4 for 2 hours demonstrated that carbon deposition did not vary considerably with composition, with 5 wt% and 0.1 wt% of carbon deposition observed for the Co(90):Cu(10) anode and pure Cu anode respectively, although > 200 wt% of carbon deposition was noted for the pure cobalt anode [250].

A bimetallic system incorporating copper and iron combined with various ceria electrolytes exhibited reasonable conductivities, however did not appear to have an appreciable effect on carbon deposition [251]. TPR of ($Cu_{0.5}$, $Fe_{0.5}$) on ceria, Gd-doped ceria or Tb-doped ceria exhibited catalytic activity for methane cracking at high temperatures, with the proportion of carbon deposition through these mechanisms related to the composition of the ceria support. As with both Cu-Co and Cu-Ni anodes, it is expected that copper rich anode compositions will be necessary to effectively suppress carbon deposition.

The improved coking tolerance of the copper-based anodes is somewhat diminished by the consistently lower performance of these anodes compared to pure nickel. Despite the various improvements with copper alloys, the catalytic activity of these anodes remains too low to produce the high power densities required for efficient SOFCs.

Comparison of various dopants, 10 % of iron, cobalt, platinum, iridium, rhenium, silver or manganese, into nickel in Ni-SDC cermets concluded that iron substitution would elucidate the greatest improvement in fuel cell performance [252]. The reduction in anodic overpotential is either due to intrinsic alloying effects or due to possible short term ordering effects affecting surface formation of Fe_3Ni phases, which are usually unstable at SOFC operating temperatures [253, 254]. The optimum alloy composition was determined to be either $Ni_{0.8}Fe_{0.2}$ [253] or $Ni_{0.75}Fe_{0.25}$ [254]. Testing of a $Ni_{0.75}Fe_{0.25}$-GDC anodes exhibited high fuel cell performances at intermediate temperatures, reaching 835 $mWcm^{-2}$ at 600 °C [255]. Further improvements in performance were noted by Ishihara *et. al.* [252], with a maximum power density of 2 Wcm^{-2} at 600 °C attained using a $Ni_{0.9}Fe_{0.1}$-SDC/LSGM/$Sm_{0.5}Sr_{0.5}CoO_3$ fuel cell with a 5 μm electrolyte. A similar reduction in anodic polarisation was noted with increasing iron content, from x = 0 to x = 0.15, for an $Ni_{1-x}Fe_x$-GDC anode in methane, with a subsequent improvement in fuel cell performance over pure nickel anodes [256].

Wu *et al.* [257] found that the extent of carbon deposition in dry methane over $Ni_{0.75}Fe_{0.25}$-GDC anodes to be highly dependent on the preparation method for the anode, although deposition was still observed for all anodes. TPO of anodes after treatment in dry CH_4 demonstrated that physical mixing of the powders results in the

lowest carbon deposition, lower than for combination of combustion powders which was again lower than for simultaneous combustion synthesis. It may be that the anode synthesis method will have a significant effect on the alloying effect of Fe on Ni. This would explain the reduction in anodic polarisation, noted by Cho *et. al.* [256], with increasing Fe content in $Ni_{1-x}Fe_x$-GDC anodes in hydrogen, which could be due to the use of simultaneous combustion for anode synthesis.

Ethanol steam reforming over a $Ni_{0.5}Fe_{0.5}$-ScSZ anode exhibited carbon deposition over 48 hours, although, as was observed for Cu-Ni anodes, this deposition was not detrimental to anodic performance, with the same explanation given [258]. A broader study of catalytic activity of $Ni_{1-x}Fe_x$-GDC powders for ethanol steam reforming by Paz Fiuza *et. al.* [259] demonstrated a significant reduction, although not complete absence, of carbon deposition with increasing iron content. Contrary to previous reports, Kan and Lee [260] observed that introduction of iron into Ni-GDC successfully suppressed carbon formation when using dry methane, with stable operation noted for all compositions containing iron. An absence of carbon deposition was also noted by Shi-Zhong and Jie [261] for composite $Ni_{1-x}Fe_x$ – cobalt doped LSGM anodes operating with dimethylether (DME) fuel.

The carbon deposition over Ni-Fe anodes remains unclear, with results varying dramatically depending on the electrolyte and the synthesis method. Whilst the reduction in anodic overpotential is desirable, there is no definitive evidence that these materials can provide stable operation for direct hydrocarbon oxidation.

Cobalt-YSZ anodes have not come under much scrutiny as SOFC cermet materials due to their high cost, however the conductivity of Co-YSZ cermets is equivalent to that of Ni-YSZ [262]. The sulphur tolerance of cobalt is of interest to fuel cell chemists, as for Co-YSZ the introduction of 10 vol% H_2S into hydrogen fuel gas results in an initial performance degradation, however subsequent improvements in fuel cell performance were exhibited over the following 2 hours [263]. The improved anodic performance was attributed to alteration of the H_2 oxidation kinetics, due to metal sulphide formation. As with previous studies, exposure to 10 vol% H_2S elucidated an immediate decrease in anode performance with a subsequent rapid performance increase, although a steady decrease of current density after 3 hours in 10

vol% H_2S/H_2 was observed, attributed to phase segregation of the cobalt sulphide phase toward the electrolyte [264]. Substitution of dry methane for hydrogen caused no significant variation in the current density, although coking-initiated delamination of the anode at the anode-electrolyte interface was observed [264]. Addition of 10 vol% H_2S to methane exhibited similar behaviour as that noted for H_2S in hydrogen, albeit without the gradual decrease in performance over time. Analysis of the exhaust gas determined that insignificant amounts of SO_2 were produced, suggesting that oxidation of the H_2S was not prominent, with the presence of CS_2 in the exhaust gas suggesting that, in these atmospheres, reactions between methane and H_2S, as per Equation 20, are promoted over cobalt sulphide.

$$CH_4 + 2H_2S \rightarrow CS_2 + 4H_2 \qquad (1.35)$$
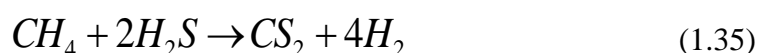
Reaction between methane and hydrogen sulphide posited to occur over SOFC anodes

Partial substitution of nickel with cobalt exhibits similar improvements in anodic polarisation as observed for iron substitution, although pure cobalt anodes exhibit considerably higher polarisation resistances [265]. Unsurprisingly, as coking is observed on pure cobalt and pure nickel anodes, the cobalt-nickel alloys tested by Grgicak *et. al.*[266] all exhibited detrimental amounts of carbon deposition under dry methane. Hydrogen sulphide introduction to methane elucidates a significant increase in the exchange current density for cobalt rich alloys, with alloy sulphides observed to form without segregation to form single metal sulphides [266]. A similar reaction mechanism to that for Co-YSZ anodes, Equation 1.35, was proposed to explain the lack of carbon deposition for Co-Ni alloys, with CS_2 again observed in the exhaust gas. The performance of a $Ni_{0.7}Co_{0.3}$-YSZ anode operating under varying compositions of carbon monoxide and hydrogen decreased with increasing CO content of the fuel, with substantial carbon deposition found to completely inhibit fuel cell operation after 6 days in a 25/75 CO/H_2 atmosphere [267].

Co-Fe-SDC cermets have exhibited maximum power densities in hydrogen comparable to that of nickel cermets [268], although their catalytic activity has not been fully elucidated. Whilst no catalytic studies have directly addressed Co-Fe alloys, production of a Co-Fe nanoparticles alloy upon reduction of a praseodymium strontium cobalt iron niobate was demonstrated to significantly improve fuel cell performance in hydrogen, methane and propane, with no observed coking with hydrocarbon fuels and minimal reduction in performance with exposure to 100ppm H_2S [72]. Whilst the hydrogen sulphide tolerance is not unexpected due to the formation of alloy sulphides at high H_2S concentrations, the stability to coking of a Co-Fe alloy is unusual as neither pure metal exhibits proven coking tolerance in dry methane.

As both cobalt and iron exhibited an alloying effect on nickel cermets, Xie *et. al.*[269] posited that further improvements could be made with co-substitution of cobalt and iron in a $Fe_{0.5-x}Co_xNi_{0.5}$-SDC cermet. The lowest interfacial polarisation and the highest maximum power density, of ~ 750 $mWcm^{-2}$ at 600 °C, was found for $Fe_{0.25}Co_{0.25}Ni_{0.5}$-SDC, exhibiting improved performance over pure nickel cermets which achieved ~ 540 $mWcm^{-2}$ at 600 °C in hydrogen.

Cobalt-based anodes do not improve coking resistance to dry hydrocarbon fuels over nickel based anodes, however the presence of hydrogen sulphide in the fuel can significantly improve the performance and durability of these anodes. Whilst the formation of nickel-cobalt sulphide anodes does improve fuel cell performance, the redox stability of these materials is questionable. The use of cobalt-iron alloys appears to have some promise, although there is a current dearth of research on these materials.

Modelling of nickel surfaces using density functional theory determined that alloying with tin could significantly reduce the deposition of carbon during hydrocarbon steam reforming [270]. Nikolla *et. al.* [271] confirmed that tin alloying resulted in the reduction of detrimental carbon deposition under isooctane steam reforming conditions, although similar results were also achieved for oxidation of humidified methane [272] and direct oxidation of methane [273]. Reduction of carbon deposition by tin alloying was attributed to the formation of surface Sn-Ni sites, which are thought to preferentially oxidise carbon deposits [274]. Introduction of either tin or antimony to Ni-YSZ anodes was found to increase the anodic tolerance to hydrogen

sulphide, which was ascribed to the weaker sulphur absorption on the surface alloys [275]. As the proportion of tin, or antimony, required to improve the coking or H_2S tolerance is minimal, 0.5-1 wt%, the effect on the overall properties of the nickel anodes is negligible, rendering this an effective technique at mitigating, but not completely eliminating, anodic degradation by coking or H_2S poisoning.

Introduction of calcium or magnesium oxide to nickel cermets has been found to increase anode durability, improving the redox kinetics and partially alleviating problems caused by redox cycling of the cermet [276]. Both magnesium and dual magnesium-aluminium doped Ni-ScSZ cermets exhibited reduction in the anodic overpotential compared to the undoped sample in both humidified hydrogen and simulated biogas, with the difference more pronounced under the biogas atmosphere [277]. The improvement in anodic overpotential is implied to be due to enhancement of the catalytic activity through modification of the electronic state of the nickel by the basic support. This technique has also previously been shown to suppress carbon deposition on Ni exposed to methane [278]. A similar effect was observed over a MgO doped $Ni_{0.75}Fe_{0.25}$-YSZ anode with 5 % substitution improving the fuel cell performance in humidified methane whilst also improving the anodic tolerance to coking, [279]. The introduction of these basic oxides are proven to improve both the redox and coking tolerance of nickel based cermets and are, as such, a viable option for further improvement of cermet anodes.

Many noble metals have exhibited high electrocatalytic activity for hydrocarbon oxidation [280, 281], although the cost of using most of these materials as the electronic conducting component in cermets is prohibitive. Some studies into noble metal cermets have still been conducted, with pure Ru/YSZ anodes exhibiting reasonable fuel cell performance in hydrogen, reaching 1.5 Wcm^{-2} at 1000 °C with stable operation with little degradation observed after operation for 1 week [282].

Whilst the use of a large proportion of noble metal in anode cermets is economically unfeasible, Wanatabe *et. al.* [283] proposed that infiltration of a small amount of noble metal was sufficient to promote electrocatalytic activity on the anode. A comparison of various noble metals, 1 wt% of either Ru, Rh, Pd or Pt infiltrated into

Ni/YSZ, demonstrated that rhodium and palladium did not significantly improve the electrocatalytic activity of the anode for methane steam reforming, although a significant reduction in the carbon deposition rate was observed for Ru, Pd and Pt infiltrated anodes at 1000 °C in dry CH_4/N_2 [284]. This is in contrast to results by McIntosh, Vohs and Gorte [285] who determined that fuel cell testing of Cu/GDC cells infiltrated with 1 wt% palladium, platinum or rhodium all exhibited similar improvements in fuel cell performance over the undoped anode, with significant increase in the maximum power density in both dry methane and dry *n*-butane.

Electrode resistance for a Ni-GDC anode in a hydrogen atmosphere reduced with increasing Ru content up to 3 wt%, with no observable increase with further infiltration, confirming that small amounts of noble metals are sufficient for maximal improvements in fuel cell performance [219]. The fuel cell performance of 3 wt% Ru infiltrated Ni-GDC anodes in dry hydrocarbon fuels reduced with increasing carbon content, although the carbon balance of inlet and exhaust gas suggests that negligible carbon deposition occurred.

Infiltration of a pure SDC anode with infiltrated nickel and palladium found that the catalytic activity in hydrogen was independent of the catalyst loading for loadings over 3 wt% Pd and 1.5 wt% Ni [286]. The catalytic activity of the same anode in dry methane increased with increasing catalyst content up to a maximum of 18 wt% Pd and 10 wt% Ni, with sole palladium infiltration exhibiting higher catalytic activity than nickel but lower than that of the duel Pd-Ni infiltrated anode. Addition of Pd to a Ni-GDC anode does improve the H_2S tolerance of the anode, demonstrating lower polarisation resistances at all H_2S concentrations from 5 ppm to 700 ppm, but does exhibit gradual degradation in 100 ppm H_2S/H_2, attributed to grain growth and segregation of Pd particles [287]. A fuel cell consisting of a 1 wt% Pd infiltrated SDC-YSZ anode, YSZ electrolyte and LSCF-YSZ cathode exhibited reasonable performance in humidified hydrogen, reaching 733 mWcm^{-2} at 750 °C, intimating that a high electronic conductive element is not required for fuel cell operation [288].

Carbon dioxide reforming of methane over noble metal catalysts supported on alumina demonstrates that ruthenium, rhodium and iridium exhibit high conversion of methane with negligible coking at 777 °C, although both palladium and nickel are reported to exhibit significant coking after 2 hours [289]. Despite previous suggestions

that ruthenium does not improve the anodic catalytic activity [284], introduction of 10 wt% of Rh into a CeO_2 anode was found to cause a significant increase in fuel cell performance in dry methane [290]. An anode consisting of 5 wt% Rh in Ni-GDC exhibited deactivation due to coking under propane steam reforming conditions at temperatures below 800 °C, although minimal coking was observed under autothermal reforming conditions [291]. The introduction of rhodium to nickel-based anodes does not appear to increase the tolerance of the anode to carbon deposition, however previous studies have suggested that rhodium has the highest catalytic activity for steam reforming of hydrocarbons [292].

The use of noble metals in indirect internal reforming layers has also been proven viable, with an anodic outer layer, consisting of 1 wt% Ir-GDC, protecting a Ni-YSZ anode operating in ethanol from coking over 150 hours [293]. Even smaller amounts of iridium have also been shown to influence methane oxidation, with 0.1 wt% Ir on GDC causing an approximate one hundred and fifty-fold increase in methane conversion over pure GDC [294]. The stability of iridium to H_2S is uncertain, with catalytic studies suggesting partial deactivation may occur upon exposure to 50 ppm H_2S [295], however minimal carbon deposition is observed over 0.1 wt% Ir-GDC under both humidified or dry methane, confirming that iridium has a high tolerance to coking.

Infiltration of small amounts of noble metals have been shown to significantly improve anodic catalytic activity, with subsequent improvements in fuel cell performance, and thus, due to the small amounts used, nobles metals are certainly feasible for use in SOFCs. The use of these materials with alternative cermet materials has a high probability of producing highly conductive and catalytically active anodes.

Development of the electronic conductivity of electrolytes materials is expected to improve the anodic performance through extension of the length of the three phase boundary. The electronic conductivity of YSZ is known to be much lower than that of ceria based materials upon reduction due to partial reduction of cerium, however titanium doping of YSZ has been found to increase the electronic conductivity [296]. At 930 °C, maximal electronic (0.2 Scm^{-1}) and ionic (0.01 Scm^{-1}) conductivity was achieved at the solubility limit of titanium, forming

$Y_{0.15}Zr_{0.67}Ti_{0.18}O_{2-\delta}$, with an increase in electronic conductivity and reduction in ionic conductivity noted with increasing yttrium content [297]. The use of Ti-doped YSZ with low Ti contents, < 10 wt%, was found to slightly reduce fuel cell performance for humidified hydrogen and methane, likely due to a reduction in the ionic conductivity without a significant increase in electronic conductivity [298]. Partial substitution of yttrium for scandium was observed to increase both the ionic and electronic conductivity, with both $Sc_{0.1}Y_{0.1}Zr_{0.62}Ti_{0.18}O_{2-\delta}$ and $Sc_{0.15}Y_{0.05}Zr_{0.62}Ti_{0.18}O_{2-\delta}$ reaching 0.14 Scm^{-1} and 0.14 Scm^{-1} respectively at 900 °C [296].

As doped cerates already exhibit some electronic conductivity upon reduction, whilst maintaining reasonable ionic conductivity, much of the research into ceria dopants concentrates on extending the electrolytic domain to lower oxygen partial pressures, which is not required at the anode []. Substitution of gadolinium in GDC with various trivalent dopants, up to 5 %, results in little variation of the electronic conductivity, with the exception of samarium which exhibits an increase in conductivity up to 3 % doping [299].

Whilst modification of electrolyte materials to further extend the three phase boundary may be necessary for YSZ based SOFCS, it appears to be unnecessary for ceria based cermets and the additional improvement in catalytic activity with ceria cermets would suggest that these materials are more suitable for use at SOFC anodes.

Accurate modelling of electrochemical reactions requires detailed knowledge of the reaction mechanism, which, as has been stated previously, is still unproven [40]. Comparison of these theoretical models to experimental data can result in additional problems, as the variety in experimental conditions, synthesis methods and impurity phases affects the comparability of the data. Despite these problems some studies have been conducted to attempt to elucidate reaction mechanisms and catalytic efficiency of various cermet materials. Rossmeisl and Bessler [41] concluded that the oxygen adsorption energy was closely related to the catalytic activity for hydrogen oxidation over metal-YSZ cermets, suggesting that the oxygen spillover is the dominant reaction mechanism over these materials. First principles modelling of the electrochemical oxidation of hydrogen and steam reforming of methane by Ingram and Linic [300] determined that nickel, cobalt, rhodium, ruthenium and iridium exhibited the most

promising electrocatalytic activity for both anodic reactions. Iron is also posited to have reasonable activity for hydrogen and carbon monoxide electro-oxidation, although the activity for methane steam reforming was noticeably lower. Platinum and palladium exhibited high activity for steam reforming but not for hydrogen or carbon monoxide electro-oxidation with the oxygen spillover mechanism.

Whilst these studies confirm experimental results, more complex modelling of surface perovskite oxides could be utilised to determine the catalytic efficiency of various alternative anode materials and electrolyte materials for use in SOFC anodes. It should also be noted that these studies do not take into account the effect of the support on the metal efficacy, which has been proven, in some cases, to have a promotional effect on metal catalysts [277].

The use of nickel cermets, whilst still making up a considerable proportion of current research into solid oxide fuel cells, has a number of obvious drawbacks, which are, thus far, only partially alleviated by alloying with other transition metals. The introduction of noble metals into the cermet anode, modification of the anode support and modification of the nickel surface have all proven efficacious in improving anode properties, although no definitive anode composition combines tolerance to both coking and H_2S, redox stability and high fuel cell performance. Whilst it has been proven that manipulation of the anodic conditions can also mitigate may of the drawbacks associated with nickel cermets, this also has a detrimental effect on the anodic performance and, if possible, other alternatives to the use of nickel cermets should be utilised.

1.3.4.1.2. Perovskites

Much of the research into cermet-alternatives for both anodic and cathodic application has focused on the production of perovskite-type compounds [301,302,4]. The perovskite structure consists of a network of corner-sharing BO_6 octahedra with a larger A-site atom in the resultant 12-coordinate position. Perovskites have been widely researched for a variety of applications due to their ease of production,

flexibility and sheer variety of properties. Two main series of perovskite-based anode compounds, LSCM and LST/YST, have been developed and have spawned subsequent lines of research.

Pure strontium titanium oxide, $SrTiO_3$ (STO), has exhibited a high sulphur tolerance, resistance to coking and good chemical and redox stability [303], however the electronic conductivity in a reducing atmosphere is poor [304]. A-site doping of either yttrium or lanthanum has been determined to significantly increase the electronic conductivity without adversely affecting the compound stability [305, 301]. Lanthanum doped STO, LST, has a higher conductivity but is coupled with negligible catalytic activity for hydrogen oxidation [306], whilst doping with yttrium, forming YST, provides both reasonable electronic conductivity and catalytic activity [307, 308]. It should be noted that high temperature reduction of either of these materials elicits significant higher electronic conductivities, with in-situ reduction of these compound likely to produce lower conductivities [306, 309], although the intrinsically higher conductivity of LST allows for lower reduction temperature to achieve acceptable conductivities [310]. Whilst barium titanate has been shown to exhibit significantly high catalytic activity than pure strontium titanate [311], recent studies demonstrated that strontium substitution with barium elicits poor fuel cell performances in both hydrogen and methane, although addition of H_2S to both fuels does significantly improve performance [312]. Périllat-Merceroz *et. al.* [313] found that cerium doping of LST elicited an improvement of the catalytic activity, however this was coupled with partial degradation upon oxidation and a phase transition upon heating in reducing atmosphere. As these compounds also have little to no ionic conductivity [314] they must be either modified or utilized as part of a composite anode.

Improvement of anode performance through promotion of catalytic activity and thus reduction of the activation polarisation has primarily involved the incorporation of various noble and transition metals, as well as ceria, to porous ceramic anodes. The use of a small amount, typically < 5 - 10 %, of nickel as an anode catalyst has been found to significantly increase fuel cell performance, with a five times increase in the maximum power density observed with a LST-GDC anode [315]. The method of catalyst incorporation into an anode can also have a significant effect on the

fuel cell performance. Infiltration of the metal into a porous framework was found to be more effective than mixing into the ceramic during synthesis, reducing the polarisation resistance by an order of magnitude for a Ni-YST-YSZ composite [316]. Without additional impregnation of catalyst, the fuel cell performance of both a SDC coated YST anode and pure YST anode is poor, although stable performance in dry methane is observed for both anodes for 900 hours [317].

Ma *et. al.* [318] demonstrated stable performance over 200 redox cycles with a 3 wt% Ni-YST-YSZ anode, with various cells reaching between 0.7 Wcm^{-2} and 1 Wcm^{-2} at 800 °C. The same anodes were found to exhibit little change in fuel cell performance operating in humidified methane with varying steam to carbon ratios, suggesting that these anodes are coking tolerant [319]. Exposure of a LST-yttrium doped ceria anode to 0.5 % H_2S in syn-gas for 48 hours demonstrated no degradation of the LST in the composite, although the presence of Ce_2O_2S was observed, suggesting that direct use of natural gas or biogas may be possible with composite anodes containing doped strontium titanates [320].

Increasing the catalytic activity will not, however, cover for other deficiencies, as formation of anodes comprised of LST or YST and ceria in a 1:1 ratio demonstrated [321,322]. Despite an improvement of the anodic microstructure, universally poor performance of these materials was observed, < 200mWcm^{-2} at 900 °C, which can be attributed to the low ionic conductivity of the anodes. Manipulation of the LST:YSZ ratio was found to be effective to increasing anode performance which, alongside incorporation of palladium and ceria, caused a threefold increase the fuel cell performance [323].

While nickel has been found to have the highest activity for hydrogen oxidation, thought to be due to the ideal strength of the oxygen-metal bond [324], other metals have been found to exhibit sufficient catalytic activity, without coking or sulphur poisoning, to supplant nickel in cermets. The use of palladium as an anode catalyst has met with definitive success, doubling the fuel cell performance of a LST-$La_{0.4}Ce_{0.6}O_2$ composite, reaching over 1 Wcm^{-2} at 850 °C with no observed degradation upon exposure to H_2S [325]. Ruthenium has also been found to be an effective replacement for nickel, causing a reduction in polarisation resistance from

2.6 Ωcm^{-2} to 0.8 Ωcm^{-2} at 800 °C for a YST-YSZ composite, further reduced to 0.5 Ωcm^{-2} with addition of ceria [56].

The effect of catalyst addition to fuel cell performance cannot be overstated, as aptly demonstrated by Lee *et al.* [326] who increased the fuel cell performance of a LST infiltrated YSZ anode from less than 20 $mWcm^{-2}$ to 780 $mWcm^{-2}$ through the addition of palladium and ceria. This study also ably demonstrated the effect that anodic microstructure has on the fuel cell performance as an increase of the sintering temperature caused a significant drop in fuel cell performance, due to an increase in the anode porosity and sintering of the LST in the YSZ pores.

The fuel cell performance of both LST and YST composites suggests that these anodes could find use in intermediate temperature SOFCs, although the infiltration of electrocatalysts is essential in achieving high performance.

Li *et al.* [327] used DFT to determine the optimum B-site dopant to increase ionic conductivity, through modelling of the oxygen migration energy in various $Sr(TM)O_3$ compounds, where TM is a transition metal. As scandium was determined to have the lowest oxygen migration energy, $La_{0.3}Sr_{0.7}Sc_{0.1}Ti_{0.9}O_3$ was synthesised and exhibited a good balance of electronic and ionic conductivities, 49 Scm^{-1} and 0.01 Scm^{-1} respectively at 800 °C. These results were confirmed in a blanket study of B-site doped LST, with the Sc-doped compound exhibiting the highest conductivity and lowest anodic overpotential [328]. Previous research by Marina *et. al.* [329] suggested that cerium doping elicits the greatest reduction in polarisation resistance whilst maintaining resistance to oxidation, coking and sulphur poisoning.

Doping with cobalt met with similar success, with a small decrease in electronic conductivity and a corresponding increase in ionic conductivity compared to the scandium doped analogue [330]. Infiltration of 19 wt% of nickel into a 30 % $La_{0.6}Sr_{0.4}Co_{0.2}Ti_{0.8}O_{3-\delta}$ - 70 % GDC porous matrix demonstrated an improvement in fuel cell density (638 $mWcm^{-2}$ to 924 $mWcm^{-2}$) after 30 hours in humidified hydrogen, with a reduction in performance under the same conditions observed for a 60 wt% Ni – 40 % GDC cermet (800 $mWcm^{-2}$ to 700 $mWcm^{-2}$) [331]. Exposure of the same anodes to dry methane exhibited the expected reduction in performance for the Ni-GDC cermet, however the Co-doped LST operated without coking for 30 hours with the

reduction in fuel cell performance attributed to nickel agglomeration. The corresponding Co-doped YST material exhibited comparatively lower electronic and ionic conductivities, likely owing to the reduced conductivity of the parent compound [332].

B-site substitution with iron into LST increases the p-type electronic conductivity, with modification of the lanthanum content found to limit the chemical reactivity to YSZ and improve the TEC match to electrolyte materials [69, 333]. Fagg *et. al.* [69] found that a slight A-site deficiency produced higher conductivities in reducing atmospheres with further reductions in the thermal expansion coefficient. The redox stability of Fe-doped YST was found to be poor, with iron exsolution upon reduction at 900 °C, although low polarisation resistances were still noted for these anodes, 0.7 Ωcm^{-1} and 1.8 Ωcm^{-1} at 800 °C and 700 °C respectively [334].

Doping with reducible metals which will precipitate upon reduction is a recently developed method for production of metal nanoparticles on the surface of anode materials, with nickel substitution for titanium in LST producing surface nanoparticles of nickel [335]. The high dependence of the conductivity of LST on reduction temperature also applies for $La_{0.5}Sr_{0.5}Ti_{0.75}Ni_{0.25}O_{3-\delta}$, with conductivities below 0.01 Scm^{-1} observed for reduction below 1200 °C.

B-site substitution, especially with scandium and cobalt, appears to significantly improve both LST and YST for use as pure SOFC anode materials, although no such studies have yet been conducted.

Creation of oxygen vacancies can also be achieved through charge balance compensation from the introduction of cation deficiencies, as demonstrated previously on doped STO [336]. Introduction of A-site deficiency (ASD) for both LST [337] and YST [338] was discovered to be more efficient at retaining the electronic conductivity than introduction of B-site deficiency (BSD) [339]. Li *et al.* [337] found that ASD-LST retained an electronic conductivity of 145 Scm^{-1} at 800 °C while improving the ionic conductivity to 0.01 Scm^{-1}, significantly higher electronic conductivity than was observed for ASD-YST [338], likely due to the higher initial electronic conductivity of LST. Li *et. al.* [337] also observed a reduction in anode porosity and increase in grain size with increasing a-site deficiency, suggesting that the sinterability of these

compounds improves with increasing a-site deficiency. Work on the stability of the deficient YST materials determined that sintering temperature or reduction has limited effects on the conductivity of the ASD compound, however the conductivity of the BSD compound is dictated by those same factors [340]. Neagu and Irvine [341] originally found that a highly deficient LST, $La_{0.4}Sr_{0.4}TiO_{3-\delta}$ exhibited similarly high conductivities to those observed by Lei *et. al.* [337], whilst noting a strong dependence of the conductivity upon the reduction temperature, with the conductivity decreasing from 96 Scm^{-1} to 17 Scm^{-1} at 880 °C with a reduction in the reduction temperature from 1400 °C to 1100 °C. Gallium substitution into highly A-site deficient LST, $La_{0.4}Sr_{0.4}TiO_{3-\delta}$, improved the reducibility, allowing for reduction at 1000 °C whilst maintaining high conductivities, 50 Scm^{-1} at 880 °C [342]. Gallium loss from these materials was noted to occur upon reduction, although without a significant reduction in anode properties. Calcium doping of ASD-LST did not appear to improve material properties, with addition of ceria and nickel required to obtain reasonable area specific resistance [343], although use of this material in a composite anode with higher proportions of doped ceria is likely to produce similar performance to that of ASD-LST composites. Copper infiltrated into a composite anode comprising of ASD-LST and GDC demonstrated similar fuel cell performance at lower temperatures than was observed for LST-YSZ composites [344]. It must be noted that the catalytic activity of copper is less than is found for other metal catalysts, thus it is likely that this performance could be improved by replacement of the copper with other, more catalytically active, metals.

A-site deficient LST and YST have both been found to retain reasonable electronic conductivity whilst gaining similar ionic conductivities to the B-site doped compounds, without, as yet, any observed drawbacks, which would make these compounds ideal for SOFC anode applications.

Not all contemporary research into strontium titanates has been limited solely to improvement of the ionic conductivity and catalytic activity. Blennow *et al.* [345] determined that a combination of niobium doping of STO and sintering at high temperature in reducing atmosphere gave electronic conductivity similar to LST and YST, up to 200 Scm^{-1} at 800 °C. The increased conductivity was proven to be a

consequence of the sintering conditions and this was nullified after oxidation at 1200 °C [346]. A further increase in conductivity was observed to occur upon sintering in ammonia gas for dual yttrium and niobium doped STO, however the conductivity enhancement was negated at much lower temperatures, ~ 600 °C, reducing the applicability of the material [347]. Introduction of A-site deficiency slightly improves the conductivity of niobium doped strontium titanate, STN, although this also corresponds with the formation of TiO_2 and Sr_2NbO_4 secondary phases [348].

As with other doped titanates, the ionic conductivity and electrocatalytic activity of STN requires the formation of a composite anode. A composite Nb-doped STO – YSZ anode, infiltrated with both palladium and ceria, proved to be an efficient anode material when combined with a YSZ electrolyte, reaching 415 mWcm^{-2} at 700 °C in humidified hydrogen [346]. Mohammed Hussain *et. al.* [349] confirmed the viability of palladium and ceria co-infiltrated STN anodes, achieving low polarisation resistances of 0.35 Ωcm^2 at 600 °C. A comparison of nickel, palladium, platinum and ruthenium co-infiltrated with ceria into a porous STN matrix exhibited low polarisation resistances, with platinum and ceria infiltration reaching 0.16 Ωcm^2 at 600 °C [350]. Alloying of the metal nanoparticles infiltrates further improved the anode performance, with infiltration of ceria and a Ni-Pt alloy reaching 0.1 Ωcm^2 at 600 °C.

Replacement of niobium with tantalum reduced the electronic conductivity without any observable improvement in anode properties, although formation of a CeO_2, Pd impregnated composite anode with YSZ did give a low area specific resistance (ASR) of 0.4 Ωcm^{-2} at 700 °C [351]. Introduction of gallium was found to reduce both the sinterability and reduction temperature of STN, although the low catalytic activity and low conductivity without high temperature reduction were retained [352].

Niobium doped strontium titanates appear to have similar advantages and disadvantages to those of LST and YST, although no studies have addressed the stability of these compounds to coking or H_2S. Additional research into these compounds is required to determine their efficacy in alternative fuels and to affect a direct comparison to both YST and LST.

Doped strontium titanates appear to have many of the desirable properties required for SOFC anodes, however these compounds require the addition of ionically conductivity and catalytically active phases to form efficient anode. The composite anodes have been shown to achieve good fuel cell performances at intermediate temperatures, with stable operation in hydrocarbons both with and without H_2S, and further development of cells with optimised microstructure could produce efficient SOFCs for operation with hydrocarbon fuels.

The first example of an efficient and fully redox stable anode material, $La_{0.75}Sr_{0.25}Cr_{0.5}Mn_{0.5}O_3$ (LSCM), was developed in 2003 by Tao and Irvine [302], building on previous research into interconnect, $LaCrO_3$, and cathode, $La_{1-x}Sr_xMnO_3$, materials [353]. $La_{0.75}Sr_{0.25}Cr_{0.5}Mn_{0.5}O_3$ is a *p*-type semiconductor with a conductivity of ~ 38 S cm^{-1} in air and ~ 1.5 S cm^{-1} at 900 °C in 5 % H_2/Ar [354]. A measured phase transition from rhombohedral perovskite, *R-3c*, to cubic perovskite, *Pm-3m*, occurs for LSCM from 500 °C to 1100 °C in air, albeit with minimal dimensional changes due to the gradual nature of the transition [355]. The transformation to the cubic phase is thought to minimise the dimensional change upon reduction, due to similarities between the oxidised phase and reduced cubic phase. Whilst lanthanum chromites exhibit little catalytic activity for methane oxidation, doping with manganese does improve the methane conversion, albeit only to the same extent as strontium doping [356]. LSCM also shows a high resistance to coking when using hydrocarbon fuels, with no coking observed after 4 hours exposure to humidified methane [354, 356]. The sulphur tolerance of LSCM is dictated by the manganese content of the material, with little poisoning observed for lanthanum chromites [303] and MnS, La_2O_2S and α-MnOS observed upon exposure of LSCM to 10% H_2S [357]. Whilst the coking stability and TEC of LSCM are ideal for use in SOFCs, both the electronic conductivity and catalytic activity is insufficient for sole use of LSCM as a SOFC anode.

The polarisation resistance of pure LSCM anodes in humidified hydrogen was much lower than that of the same anode in humidified methane, 0.26 Ωcm^2 and 0.87Ωcm^2 respectively at 900 °C, with reasonable fuel cell performances observed in hydrogen, 0.47 Wcm^{-2} at 900 °C, but low power density noted in humidified methane, 0.2 Wcm^{-2} at 950 °C [358]. Introduction of 4 wt% Ni into a LSCM-GDC composite

anode elicited similar power density as a Ni/GDC anode in hydrogen at 750 °C, with improved fuel cell performance noted in dry propane [359]. The introduction of nickel into the composite anode appears to be essential in producing high performances, although the amount is small enough so that operation in dry methane, propane and butane does not induce significant carbon deposition at the anode. Without infiltration of additional catalyst a LSCM-lanthanum doped ceria anode exhibits low polarisation resistances inn hydrogen and methane, 0.081 Ωcm^2 and 0.13 Ωcm^2 respectively at 800 °C, although the fuel cell performance was still low, reaching a maximum of 220 $mWcm^{-2}$ at 800 °C in humidified hydrogen for a 50:50 LSCM-LDC anode [360].

The use of noble metal catalysts at the anode is well documented and a substantial increase in fuel cell performance upon impregnation with palladium, with further increases noted upon ceria infiltration [361]. Substitution of 0.5 % rhodium or 1 % nickel in place of 0.5 % of palladium gave similar fuel cell performances, suggesting that the electrocatalytic activity and mechanism of reaction of these metals is not dissimilar. When using methane as a fuel, impregnation of palladium into the anode causes a significant increase in power density, not observed when hydrogen is utilised as the fuel, confirming the higher catalytic activity of palladium for hydrocarbon oxidation [362]. A reduction in the electrode polarisation resistance is also noted for palladium impregnated anodes when using methane or ethanol as the fuel, enhancing the performance of a LSCM/YSZ composite [363]. Without ceria co-impregnation palladium or nickel impregnated LSCM-YSZ anodes exhibited carbon deposition upon exposure to dry methane, although this was not observed for platinum impregnated anodes [25].

Despite previous research suggesting that addition of catalysts to LSCM anodes was required to achieve reasonable fuel cell performances, impregnation of 33 wt% of LSCM into a porous YSZ matrix formed catalytically active and stable anodes, with little difference in fuel cell performance between hydrogen and methane fuels, reaching 567 $mWcm^{-2}$ and 561 $mWcm^{-2}$ respectively at 850 °C [364]. Additional impregnation of nickel and silver doubled fuel cell performance in hydrogen and caused a 50 % increase in performance in methane with no observable anode degradation. Despite the increased catalytic activity of GDC compared to that of YSZ, impregnation of GDC into a porous LSCM matrix yielded poorer fuel cell

performances in humidified methane than in humidified hydrogen, 221 mWcm^{-2} compared to 628 mWcm^{-2} at 850 °C [365]. Co-impregnation of nickel and ceria to an LSCM support increased the fuel cell performance six-fold, reaching 948 mWcm^{-2} at 800 °C [366]. Similar performance was observed in a LSCM anode infiltrated with high levels of copper and palladium, 20 wt% and 1.5 wt% respectively, although a lanthanum-doped ceria interlayer was required to prevent interfacial reactions between LSGM and LSCM [367].

The method of impregnation has been found to have an effect on the anode performance, with co-impregnation of LSCM and nickel proving more effective than sequential impregnation of LSCM then nickel, likely due to microstructural and distributional differences [368]. Despite the high loading of the LSCM-nickel composite onto YSZ, stable operation was observed for 6 hours without coking or noticeable performance degradation and acceptable fuel cell performance was noted in both hydrogen and methane.

Other microstructural modification of LSCM anodes have been attempted, as a composite of copper, LSCM and YSZ, utilised as part of a graded anode with two anode functional layers Ni/YSZ and Ni/ScSZ, was found to treble fuel cell power density over the parent Cu/LSCM/ScSZ anodes [369]. While graded anodes do have the capacity to increase fuel cell performance, the practicality of these materials undermines their usage and comparable performances can be achieved using alternative, more efficient methods.

The fuel cell performances obtained with infiltrated LSCM composite anodes intimates that the current composite anodes have promise for use in intermediate temperature SOFCs.

As with LST and YST, introduction of A-site deficiency to LSCM causes a predictable increase in the ionic conductivity and a resultant decrease in electronic conductivity, however the conductivity changes are not as dramatic as found for the doped strontium titanates, with ionic conductivity peaking at $\sim 3 \times 10^{-4}$ Scm^{-1} at 950 °C [370]. Partial substitution of lanthanum with cerium did not significantly affect the thermal expansion coefficient or the conductivity in humidified hydrogen [371] whilst successfully increasing the catalytic activity of the anode, reducing the polarisation

resistance by one order of magnitude, from 2.3 Ωcm^{-2} to 0.2 Ωcm^{-2} at 800 °C [372]. The R_p of Ce-substituted LSCM was similar to that found for electrolyte-graded LSCM anodes [358] but less than for praseodymium substituted LSCM, which is more suited for cathodic applications [373]. Partial barium substitution for strontium in LSCM reduces the electronic conductivity of the material in humidified hydrogen, although this corresponds to a reduction in the polarisation resistance, suggesting that the barium analogues have higher electrocatalytic activity [374]. This is in contrast to the earlier results by Zhang *et. al.* [375], who suggest that the catalytic activity of LSCM is improved by calcium doping and degraded by barium doping, although these variations may be due to complete substitution of strontium in this study and a different A-site ratio.

Danilovic *et. al.* [376] investigated B-site substitution of manganese in LSCM with , with cobalt eliciting the highest conductivity of the tested transition metals. The catalytic activity of the compounds was determined by temperature programmed reduction (TPR) and was a reasonable indicator of fuel cell performance, with the iron analogue exhibiting the highest performance. The high catalytic activity of the iron-substituted compound was echoed in the results of fuel cell operation in CO/CO_2 mixtures [377]. The iron doped sample was observed to partially degrade into the spinel phase upon exposure to a highly reducing atmosphere at 900 °C, although this was reversible upon re-oxidation [378]. Similar performance in both hydrogen and methane was noted for a nickel, SDC and $La_{0.75}Sr_{0.25}Cr_{0.5}Fe_{0.5}O_3$ impregnated YSZ anode, with reasonable performance in ethanol also observed at 800 °C [379].

As for strontium titanates, the introduction of reducible cations, such as nickel or ruthenium forming LSCRu and LSCNi, is likely to form catalyst surface nanoparticles and therefore increase the catalytic activity of the anode [380]. The formation of nickel and ruthenium nanoparticles has previously been found to reduce anode polarisation resistance, albeit with greater efficacy for ruthenium [381,382]. The resultant fuel cell performance of both of these anodes was < 300 $mWcm^{-2}$ at 800 °C and both anodes required > 96 h before stable operation at these outputs was observed. A solid state combination of LSCRu with GDC was found to give steady fuel cell performances between 400 and 500 $mWcm^{-2}$ at 800 °C without noticeable ruthenium

nanoparticles coarsening over 1000 h of operation [381,382]. Despite the reasonable performance of LSCRu, wet chemical infiltration of the respective metals into a LSCM-electrolyte composite may be a more effective, and controllable, method for increasing the catalytic activity of these anodes.

The nickel substituted material, LSCNi, was additionally considered for symmetrical fuel cells as a result of high conversion of CH_4 at 800 °C and slightly improved conductivity over LSCM [383,384]. Despite an observed ASR of 1.3 Ωcm^{-2} at 800 °C the long term stability of these materials is in doubt over observed coarsening of the surface nickel nanoparticles upon extended use [380]. Building on the work by Lay *et al.* [372] and Kobsiriphat *et al.* [380], Bao *et al.* [385] formed $(La_{0.7}Sr_{0.3})_{0.4}Ce_{0.6}Cr_{0.4}Ni_{0.6}O_3$ which increased the conductivity upon reduction but degraded into CeO_2, Ni and LSCNi and thus exhibited poor fuel cell performance.

One main problem with the use of LSCM is the lack of stability to sulphurous impurities, which will significant limit the use of these anodes with alternative fuels, although infiltration with both ruthenium and ceria may suppress the degradation. Despite the mixed conductivity exhibited by LSCM, neither the electronic conductivity nor the ionic conductivity is sufficient for sole use as an SOFC anode and the use of this material in an anode composite is less advantageous than the use of other, more conductive materials.

Double perovskite materials [4] were first of interest due to reasonable ionic conductivity but early materials such as $SrFeNbO_{6-\delta}$ and $Sr_2MnNbO_{6-\delta}$ mostly had negligible electronic conductivity [386, 387,388]. Both Sr_2MgMoO_6 and Sr_2MnMoO_6 came of interest upon exhibition of electronic conductivity of ~ 10 Scm^{-1} at 800 °C in addition to redox stability and stability to sulphurous impurities [4,389]. Acceptable fuel cell performance was found for fuel cells with Sr_2MgMoO_6 or Sr_2MnMoO_6 anodes, albeit whilst using platinum as an anode current collector [4]. Further research into Sr_2MgMoO_6 determined that degradation of the compound occurred at 900 °C in a reducing atmosphere [388]. Doping with La was found to improve the fuel cell performance, although subsequent research noted compound degradation upon reoxidation [390,391].

The chemical and redox stability of SMMO has been questioned recently with reports of interfacial reactions with YSZ and LSGM electrolytes [392] and the formation of Ruddlesden-Poppler phases upon reduction at 900 °C [305]. The reported redox instability was successfully refuted by Marrero-López *et al.* [393, 141], being ascribed to the high temperature synthesis method, however interfacial reactivity with common electrolytes does occur and requires the use of either a GDC electrolyte or interlayer for long term stability.

Magnesium substitution in SMMO was found to increase the total conductivity, in the order Mg < Co < Ni, yet fuel cell performance for the cobalt analogue was determined to be superior to that of the nickel, likely due to higher catalytic activity for fuel oxidation [394, 142]. Increased conductivity over SMMO was further compounded by high temperature annealing in a reducing atmosphere, increasing the conductivity of Sr_2NiMoO_6 from ~ 5 Scm^{-1} to 50 Scm^{-1} at 800 °C [395]. Increased catalytic performance for methane combustion was also noted with partial substitution of manganese, although with a subsequent reduction in the compound stability [396]. Introduction of iron for magnesium achieved a slight increase in fuel cell performance compared to the nickel analogue, with no improvement observed upon increased iron doping [397.398]. Stable operation of the iron substituted SMMO in city gas was observed over 20 h with a reduction of ~ 100 $mWcm^{-2}$ at 850 °C compared with pure hydrogen, also hinting that these compounds may be stable to detrimental impurities such as H_2S, ammonia and naphthalene. The stability of the series of transition metal doped SMMO compounds was called into question by Vasala *et al.* [399] who concluded that only the Mg analogue was redox stable with the cobalt, nickel and zinc containing compounds unstable to reduction while the iron and manganese analogues unstable to oxidation. This corroborates previous reports that the cobalt and nickel analogues partially degrade upon reduction, forming small amounts of metallic nickel and cobalt alongside SrO and $SrMoO_4$ [394]. Reduction of the proportion of the molybdenum for the iron containing sample has, however, been show to improve the redox stability of the compound while retaining reasonable conductivity [400].

Much of the research into SOFC anode materials is a delicate balance between performance and stability. Substitution of calcium for strontium in Sr_2FeMoO_6 significantly increased the conductivity but was then observed to degrade at ~ 400 °C

in nitrogen, with the opposite effect noted for the barium analogue [397]. A similar effect was noted in SMMO, with niobium and tungsten substitution for molybdenum increasing the stability of the compound to reduction whilst reducing the electronic conductivity [401]. As SMMO has been found to be redox stable, the advantages of niobium doping are minimal, as a small increase in the ionic conductivity should occur upon increasing substitution, however doping of niobium into the transition metal doped analogues would be of interest to observe if this causes an increase in the redox stability of the compounds.

Substitution of potassium for strontium should maximise the ionic conductivity of these compounds, with minimal disruption to the material structure due to the similar atomic radii of the cations. An anode of $Sr_{1.6}K_{0.4}FeMoO_{6-\delta}$ and a cathode of $Sr_{0.9}K_{0.1}FeO_{3-\delta}$ were combined with LSGM to produce an efficient SOFC, with a maximum power density of 766 mWcm^{-2} with H_2 fuel at 800 °C [68]. The anode was later determined to be a dual phase composite of highly conductive $SrMoO_3$ phase and a MIEC $SrFe_{0.6}Mo_{0.4}O_{2.7}$ phase, with the potassium thought to have sublimed from the structure during high temperature synthesis. The effect of re-oxidation on the anode has yet to be investigated, however, due to the nature of the anode, problems associated with non-homogenous volume expansion are to be expected.

The double perovskite materials, as with doped strontium titanates, appear to require high temperature reduction to achieve maximum conductivities, with some compounds requiring reduction to form the perovskite structure and some exhibiting redox instability, which could limit utilisation. Whilst the catalytic activity of these compounds has not been sufficiently elucidated, the conductivity of these compounds is significantly high to warrant further research

Through their use as high temperature interconnect materials, lanthanum chromates are known to exhibit good stability to the anodic environment, although the electronic conductivity of these compounds is generally low under anodic conditions. Calcium doping was originally utilised to improve the sinterability of lanthanum chromite compounds, with the formation of calcium rich secondary phases encouraging liquid phase sintering [402]. These materials retain the p-type semiconductivity of $LaCrO_3$, although the conductivity of $La_{0.7}Ca_{0.3}CrO_{3-\delta}$ (LCC) was

still above that of LSCM, reaching 3.36 Scm^{-1} at 1000 °C [403]. Cobalt doping for chromium was found to further increase the conductivity of LCC, reaching 21.7 Scm^{-1} at 1000 °C in 20% H$_2$/Ar, whilst aluminium substitution significantly increased sinterability albeit with a subsequent decrease in conductivity [404]. Vashook *et. al.* [405-407] extensively investigated the titanium doped LCC, concluding that conductivity in reducing atmospheres increased with increasing calcium and titanium content. Propane conversion over the titanium doped LCC did not vary significantly with changes in the calcium content for the La$_{1-x}$Ca$_x$Ti$_{0.5}$Cr$_{0.5}$O$_3$ series, although CaCr$_{0.2}$Ti$_{0.8}$O$_{3-\delta}$ exhibited the highest conversion of any of the tested compounds therefore little conclusions can be drawn from the available data [406, 407]. Partial substitution of cerium for calcium, forming La$_{0.3}$Ca$_{0.6}$Ce$_{0.1}$CrO$_{3-\delta}$, elicited reasonable fuel cell performances in hydrogen, however the compound exhibits multiple phases both upon sintering and after reduction, with surface cerium oxide likely significantly improving the fuel cell performance [408]. Lanthanum chromates have been found to be stable under anodic conditions and exhibit acceptable electronic conductivities, however the conductivity of these compounds does not compare to that of the strontium titanates and the ionic conductivity of these compounds is unknown thus further research is required to determine the suitability of these compounds for anodic applications.

The appropriation of cathode materials for anode applications is not unknown but the most of existing cathode are expected to be unstable under anodic operating conditions [409]. As La$_{0.6}$Sr$_{0.4}$Co$_{0.2}$Fe$_{0.8}$O$_3$ (LSCF) was found to have reasonable catalytic activity for methane [410], propane and syn-gas [411] oxidation, it was investigated as a component in an anode composite with GDC. Reasonable fuel cell performance was noted with hydrogen fuel [410] and, after nickel impregnation, similar performance was noted with propane fuel [412]. No anodic degradation was observed upon operation for 50 hours for the LSCF-GDC composite, although after 100 hours partial degradation into La$_2$NiO$_4$ and SrCo$_{1-x}$Fe$_x$O$_3$ was seen for the nickel impregnated LSCF-GDC anode [413].

The activity of lanthanide ferrites for methane combustion is indeterminate with Ciambelli *et. al.* [414] stating that the order of activity was La > Nd > Sm, whilst Stathopoulos *et. al.*[415] found that SmFeO$_3$ exhibited higher activity than LaFeO$_3$.

Further work by Ciambelli *et. al.* [416] found that the reducibility of the same series observed the same order they found for the activity for methane combustion, leading credibility to their earlier findings. The higher redox stability of samarium ferrite leads to the conclusion that the compound may be stable under SOFC anode conditions. Despite the poor conductivity of $Sm_{1-x}Ce_xFeO_{3-\delta}$, > 0.3 Scm^{-1} between 0 °C and 1000 °C [417], Bukhari *et. al.* [418] tested $Sm_{1-x}Ce_xFeO_{3-\delta}$ anodes under dry hydrogen and methane achieving maximum power densities of 7 mWcm^{-2} and 0.45 mWcm^{-2} respectively at 600 °C ,with no coking observed in dry methane after 23 hours. The poor performance can, in part, be ascribed to the thick, 2mm SDC, electrolyte and the poor catalytic activity of the anode. Whilst the conductivity and fuel cell performance for samarium ferrite are poor, the stability of the anode leads to further consideration of ferrite anodes, especially with further reductions in SOFC operating temperatures allowing for use of additional materials.

Research into oxidation catalysts of hydrocarbons is a viable field in its own right, however it can also be a fruitful area for SOFC anode researchers to utilise. Vanadium oxides have been previously investigated for their catalytic activity for hydrocarbon and hydrogen sulphide oxidation [419,420]. A composite anode of vanadium oxide, YSZ and LaCrO$_3$ was expected to provide the necessary anode properties, however carbon deposition was observed upon extended use with syn-gas [421].

Lanthanum strontium vanadates (LSV) have been extensive investigated as anodes for H$_2$S containing atmospheres due to their high conductivity in reducing atmospheres, reaching 50 Scm^{-1} at 800 °C [422], and stability to sulphur poisoning, although oxidation of these compounds produces a secondary strontium vanadate phase [71]. LSV anodes exhibit little electrocatalytic activity for hydrogen oxidation, however the activity for hydrogen sulphide oxidation allows for direct oxidation of H$_2$S [423, 424]. Operation of a pure LSV anode in syn-gas containing H$_2$S demonstrated reasonable performance without poisoning or coking, although anode coarsening caused performance degradation upon extended use [425]. Operation in both humidified methane, in the presence of Pd and CeO$_2$ catalysts, and dry methane with 5% H$_2$S exhibited no coking, suggesting that these materials are unlikely to promote carbon deposition [426, 427]. An additional complication with the use of vanadate anodes is the

high chemical reactivity of these compounds, with poisoning of the palladium catalyst observed after heating in air at 700 °C [426].

Replacement of the lanthanum in LSV with cerium exhibited little change in the catalytic properties, with low catalytic activity for methane oxidation and high catalytic activity for sulphur oxidation observed, exhibited as lower fuel cell performances in 0.5% H_2S/CH_4 than in 0.5% H_2S/N_2 at 800 °C [428]. Replacement of vanadium with chromium in $Ce_{0.9}Sr_{0.1}VO_3$ increased both the conductivity in reducing atmospheres and the redox stability of the compound, but despite the formation of a composite anode with nickel and YSZ the fuel cell performance was still predominantly related to the H_2S reaction for 0.5 % H_2S/CH_4 fuel [429]. Petit *et. al.* [73, 430] observed that calcium and strontium doped cerium vanadates exhibited a reversible phase transition, between the oxidised $ReVO_4$ and reduced $ReVO_3$ phases, without formation of secondary phases, although a significant volume change is observed upon transition between the oxidised and reduced phases. Introduction of cobalt, nickel or copper into the orthovanadates causes exsolution of the transition metals upon reduction to the perovskite phase, forming surface metal nanoparticles [431]. Fuel cell testing with the transition metal doped $CeVO_3$ anodes exhibited reasonable performance, although this is mainly a result of the catalytic activity of the surface nanoparticles, with the $CeVO_3$ providing negligible improvement over other anode supports.

Formation of a mixed vanadate-molybdate oxide, $CaV_{0.5}Mo_{0.5}O_3$, exhibited high electronic conductivity, ~ 525 Scm^{-1} at 800 °C, although degradation of the compound was observed above 600 °C in argon [432], which precludes the use of the compound as an anode material.

The poor fuel cell performance, lack of redox stability and coking upon use with hydrocarbon fuels observed for most vanadates reduces their applicability as SOFC anodes, however as part of a composite the introduction of a small percentage of some of these materials may simultaneously prevent H_2S poisoning and increase anode performance.

1.3.4.1.3. Other Materials

Tungsten bronze structured compounds were first investigated as SOFC anode materials in 1999 with limited success, producing electronic conducting materials of the order of ~ 5 Scm^{-1} at 930 °C [433,434]. Tungsten bronze structured samarium molybdate, doped and undoped, was not found to react with a YSZ electrolyte yet exhibited conductivities uniformly less than 0.2 Scm^{-1} [435]. While the recently developed pyrochlore may have some promise, the low electronic conductivity of the tungsten bronze compounds likely excludes them from application as SOFC anode materials.

Gadolinium titanate-based pyrochlores were first of interest as electrolyte materials but were further developed into mixed electronic-ionic conductor materials through B-site doping [436,437]. Despite initial promising results, further investigation uncovered various deficiencies, such as interfacial reactivity with YSZ for the most promising tungsten bronze, $Sr_{0.2}Ba_{0.4}Ti_{0.2}Nb_{0.8}O_3$ [438], and low electronic conductivity and redox instability for pyrochlores such as $Pr_2Sn_2O_7$ [439]. A redox stable pyrochlore $Yb_{0.96}Ca_{1.04}TiNbO_{6.98}$ exhibited a conductivity of 9 Scm^{-1} at 800 °C, although high temperature firing in reducing atmosphere was required, with conductivity of 0.07 Scm^{-1} at 800 °C observed after low temperature reduction [440].

Rutile structured compound have previously come under consideration as SOFC anode materials due to their short M-M distances, which promotes electronic conductivity [441,442]. Building on previous work on rutile niobium titanates, Lashtabeg *et al*. [443] attempted to form a compound with a rutile structure under oxidising and reducing atmospheres, by co-doping rutile TiO_2 with niobium and chromium. While a significant increase in conductivity was observed, the reduction kinetics of the compound were slow, with equilibrium not reached after 50 h at 900 °C in 5% H_2/Ar. Similarly structured chromium niobate was not observed to suffer similarly slow kinetics, although exhibited lesser conductivity, of ~ 3.7 Scm^{-1}, than was observed for $Ti_{1-2x}Cr_xNb_xO_2$ at 800 °C [444]. Degradation of the chromium niobate upon high

temperature reduction prevented attempts to increase the conductivity through further formation of oxygen vacancies.

Whilst K_2NiF_4-structured compounds have become of significant interest for cathodic purposes, the utilisation of these compounds as anode materials is significantly hindered by the expected lack of redox stability. A praseodymium strontium cobalt iron niobate (PSCFN), $Pr_{0.8}Sr_{1.2}(Co, Fe)_{0.8}Nb_{0.2}O_4$, with the K_2NiF_4 structure was formed through reduction of the perovskite analogue, $Pr_{0.4}Sr_{0.6}Co_{0.2}Fe_{0.7}Nb_{0.1}O_3$, at 900 °C, with no additional phases observed upon redox cycling of the compound [72]. Whilst PSFCN exhibited high fuel cell performances in hydrogen, methane and propane, reaching 0.96 mWcm^{-2}, 0.6 mWcm^{-2} and 0.94 mWcm^{-2} at 850 °C respectively, the high performances are likely to be mainly due to the exsolution of a Co-Fe nanoparticle alloy on the surface, with the pure anode exhibiting significantly lower power densities [72].

1.3.4.1.4. Symmetrical Electrodes

The use of symmetrical electrodes in fuel cells, the same material for both anode and cathode, would simultaneously simplify fuel cell manufacture and reduce fuel cell costs [445]. While both anode and cathode share various requirements, the problem lies in achieving sufficient catalytic activity for both oxygen reduction and hydrogen oxidation and the retention of conductivity and stability in both oxidising and reducing environments. A review in 2011 by J.C. Ruiz-Morales *et. al.* [446] covers many of the main points and also notes the potential application of symmetric fuel cells as reversible SOFCs, which can operate under both fuel cell and electrolyser modes.

Bastidas *et. al.* [447] produced the first symmetrical SOFC in 2006, utilising a LSCM-YSZ electrode, although the performance was not high, ~ 300 mWcm^{-2} at 900 °C. Similar performance of LSCM-YSZ symmetrical fuel cells was attained by Ruiz-Morales *et. al.* [448], reaching 546 mWcm^{-2} in hydrogen and 347 mWcm^{-2} in methane at 950 °C. As for LSCM, the double perovskite $Sr_2Fe_{1.5}Mo_{0.5}O_{6-\delta}$ exhibits redox

stability and reasonable conductivity in both air and hydrogen, which supports its use as a symmetrical electrode [400]. Fuel cell testing with a LSGM electrolyte in hydrogen demonstrated fuel cell performances higher than those achieved using LSCM, ~ 650 mWcm^{-2} at 850 °C, however the performance in humidified methane was poor, only reaching ~ 100 mWcm^{-2} at the same temperature.

Building on research into cathodic materials [449], $La_{0.8}Sr_{0.2}Sc_{0.2}Mn_{0.8}O_3$ (LSSM) was investigated as an anode material for symmetric SOFCs [409]. Scandium was previously calculated to be the most effective dopant to increase the oxygen ion conductivity in strontium based perovskites [327], albeit for LSSM an improvement in total conductivity in reducing atmospheres was observed. Despite the improvement in conductivity, symmetrical fuel cell performance was not an improvement on that found for symmetrical LSCM-based FCs, achieving a power density of 310 mWcm^{-2} at 900 °C in hydrogen [447]. A composite electrode based upon another cathode material, $La_{0.7}Ca_{0.3}CrO_3$, impregnated with GDC nanoparticles exhibited acceptable conductivity and TEC values in both oxidising and reducing atmospheres, achieving similar performance to symmetrical LSCM electrodes at high temperatures, 521 mWcm^{-2} at 850 °C [450].

Whilst these materials cannot currently obtain the power densities of fuel cells which utilise specialised anode and cathode materials, the additional flexibility that these materials provide has a significant advantage for future applications. The use of these materials as reversible SOFCs could provide a medium for energy storage and utilisation to sufficiently supplement renewable energy utilisation.

1.3.4.1.5. Operation with alternative fuels

One of the main advantages to the use of SOFCs is the sheer variety of different fuels that can be utilised. Alongside hydrogen, methane [46], ethane [451], propane [413], butane [452], ethanol [47], methanol [47], dimethyl ether [453] and ammonia [48] have all been investigated as to their efficacy as SOFC fuels. Theoretically the fuel cell performance for many of these fuels is higher than that achievable for pure hydrogen, however currently many of these show reduced performance when compared to pure hydrogen. The use of these fuels in SOFCS is preferable over the use of hydrogen due

the higher energy storage density and lesser associated problems concerning storage and transportation. Whilst many alternative fuels currently undergo pre-reforming prior to anode exposure, direct utilisation of these fuels would further improve the utilisabilty and potential fuel cell performance.

While the use of these fuels and other similar fuel mixtures, such as coal derived syngas, is eminently desirable, it does present further problems to anode development, as these gases contain sulphurous impurities which are known to have a detrimental effect on some SOFC anodes [63,454]. Sulphurous impurities can be found in various hydrocarbon gases, and in un-processed hydrogen fuels, and a substantial amount of research has been conducted on the deleterious effect of these compound on fuel cell anode performance [22].

The presence of sulphurous impurities is not always detrimental to fuel cell performance as addition of significant proportions of H_2S to a methane fuel gas has exhibited considerable improvements in fuel cell performance for some anodes [455]. Introduction of hydrogen sulphide to dry syn-gas on an LST-YDC anode elicited an improvement in fuel cell performance, despite an increase in the polarisation resistance [320]. Whilst minimal fuel cell performance is elicited in 0.5 % H_2S/Ar over these anodes, the lack of SO_2 production in the sulphided syn-gas suggests that oxidation of H_2S is not the cause of the enhanced performance. Roushanafshar *et. al.* [320] observed that partial sulphidation of carbon monoxide, forming COS, was observed to occur, although no definitive mechanism was proposed to explain the promotional effect of H_2S. Additional work by Vincent *et. al.* [455] utilised a LST-YSZ anode, which is expected to have poor catalytic activity, to determine the effect of H_2S addition to CH_4. The fuel cell performance increased from 2 mWcm^{-2} to 400 mWcm^{-2} as the H_2S content in the methane fuel increased from 0 % to 10 %, with only incremental improvements noted from 10 % to 40 % H_2S. Further investigation of this effect over H_2S tolerant anodes with high catalytic activity for hydrocarbon oxidation could further elucidate the effectiveness of H_2S promotion in SOFCs.

Alternatively, improvement of the fuel cell performance can be achieved by use of sulphurous impurities as an alternative fuel, through promotion of hydrogen sulphide oxidation. LSV has been shown to be active for hydrogen sulphide oxidation, operating as a fuel cell anode in both H_2S containing fuels and weak H_2S gas mixtures [424]. Other vanadates have also exhibited this propensity for H_2S catalysis, although to a lesser degree [456]. Generally, the performances obtained for these fuel cells are low, < 300 mWcm^{-2} at C [423, 424], however use of these materials in a conventional fuel cell could prove beneficial.

Whilst the formation of metal sulphides at the anode is generally detrimental to fuel cell performance, some researchers have attempted to utilise these materials as anode components. Molybdenum sulphides were primarily investigated as an anode catalyst for the hydrodesulphurisation of natural gas [457]. A MoS_2 framework was impregnated with gold nanoparticles to prevent CO poisoning when using syn-gas [458]. Despite this, fuel cell performance was observed to degrade over time which was attributed to sintering of the gold nanoparticles. Addition of $Ni_{3\pm x}S_2$ was used to reduce the volatility of MoS_2 in air by preventing MoO_3 formation, however, despite promising fuel cell performance, significant reductions in performance were noted, ascribed to nickel sulphide agglomeration [459]. Further investigation into transition metal sulphides found that MoV_2S_4 demonstrated low polarisation resistance of 1.5 Ωcm^2 at 800 °C in a H_2S stream with stable operation observed over 3 days [460]. The utilisation of these materials as H_2S catalysts in conventional fuel cells might be viable, although it would be more practical to use these systems, when efficient, as to remove the H_2S from the fuel prior to use in a conventional SOFC. This could be applied in the same way as an internal reforming layer, such as $Cu_{1.3}Mn_{1.7}O_4$ which improved both stability and performance of a Ni/SDC anode operating with methane fuel [461].

The use of these H_2S catalysts in concert with alternative, H_2S tolerant, anode materials is expected to enhance fuel cell performance, with impregnation of a small amount of H_2S catalyst identified as the optimal route for anodic improvement. Further investigation of the use of these H_2S catalysts in concert with hydrocarbon fuels may be of interest to determine the effect on the observed promotion of hydrocarbon oxidation by H_2S.

Whilst the presence of hydrogen sulphide has been shown to have a promotional effect of fuel cell performance of certain anode materials, other impurities, such as chlorides, arsenides and phosphides which have all been detected in coal-derived syngas, are solely detrimental to fuel cell performance. There are various fuel contaminants, the concentration of which is dependent on the fuel type and feedstock, which are found to poison current Ni/YSZ anodes through formation of Ni-impurity compounds [63]. Previous results were found to conflict on the effect of HCl on fuel cell performance [462], although recent research by Marina *et al.* [463] convincingly demonstrated that fuel cell performance at intermediate temperatures showed reversible degradation up to 100 ppm HCl, with no further effect on fuel cell performance observed with increasing HCl concentrations. The presence of a lesser concentration of arsenic impurities was found to cause observable anode degradation, with 10 ppm of AsH_3 causing a 10 % drop in fuel cell performance at 750 °C [464] and even lower concentrations of 1 ppm and 0.1 ppm show gradual degradation over 600 h [465]. Irreversible degradation is observed upon exposure to PH_3, through microstructural changes caused by the formation of both $Ni_3(PO)_4$ and $Zr_2P_2O_7$ [466].

Degradation of anode materials by syn-gas impurities is not limited to nickel-based cermets, as irreversible degradation of a LSCF-GDC composite at 800 °C was found for phosphine levels as low as ~ 1 ppm [467]. The surface formation of both $LaPO_4$ and FeP_x suggests that further investigation into the effect of phosphine impurities will be necessary before syngas is considered for long term use with current alternative SOFC anode materials.

These additional impurities are usually present at ppm levels in various fuels and, as such, may not cause significant anode degradation, although, with the promotion of direct use of biogas and other alternative fuels, the detrimental effects of these compounds are likely to come under increased scrutiny.

The effects and causes of coking have been dealt with extensively previously and, whilst coking has been shown to cause significant degradation to the performance of various anode materials [23], the sheer variety of methods to prevent carbon formation intimates that coking is no longer a pressing issue with the use of hydrocarbon fuels. Whilst, the use of traditional nickel-based cermets still suffers from

problems with coking, the use of alternative materials, catalyst infiltration and fuel reforming can achieve high fuel cell performances at intermediate temperatures with hydrocarbon fuels. The use of ammonia fuels can allow for effective use of nickel based anodes without coking, although currently the fuel cell performance is less than that achieved in pure hydrogen, reaching 1190 mWcm^{-2} at 650 °C [48].

1.4. Objectives

Due to the material benefits in the reduction of the operating temperatures of SOFCs, development of novel electrolyte and electrode materials is deemed to be essential for SOFC performance optimisation at intermediate temperatures. Iron-based perovskites were previously overlooked as anode materials due to their instability in reducing atmospheres at SOFC operating temperatures, although substantial research has been conducted into the use of these materials as SOFC cathodes [1,2]. The reduction in operating temperature allows for use of materials, such as iron-based perovskites, which lack the requisite thermal or redox stability for high temperature operation.

The overall aim of this work was to elucidate the suitability of ferrites as anode materials for intermediate temperature solid oxide fuel cells and to synthesise novel ferrite materials which meet that criteria. The suitability criteria chosen for these materials was the electronic conductivity in reducing atmospheres and the redox stability at 700 °C.

The initial research aim was to modify the composition of a previously investigated series of iron-based perovskites to determine the effect of reduction on both the structure and electronic conductivity. Following on from the initial research, a study on the redox stability and conductivity of B-site doped and undoped strontium ferrite was conducted to determine the optimal dopant levels. Further elucidation of the effect of doping on strontium ferrite materials was undertaken using A-site dopants and an optimal composition from each chapter of research chosen for fuel cell testing.

Due to the performance of these materials in both reducing atmospheres and air, fuel cell testing was completed in symmetrical fuel cell configurations. The performance of the symmetrical fuel cells was compared to that of symmetrical fuel cell performance from the literature and conclusions drawn over the suitability of these materials for use in intermediate temperature SOFCs.

1.5. References

1. M. V. Patrakeev, J. A. Bahteeva, E. B. Mitberg, I. A. Leonidov, V. L. Kozhevnikov and K. R. Poeppelmeier, *Journal of Solid State Chemistry*, 2003, **172**, 219-231.

2. A. Mai, V. A. C. Haanappel, S. Uhlenbruck, F. Tietz and D. Stöver, *Solid State Ionics*, 2005, **176**, 1341-1350.

3. S. E. Dann, D. B. Currie, M. T. Weller, M. F. Thomas and A. D. Al-Rawwas, *Journal of Solid State Chemistry*, 1994, **109**, 134-144.

4. Y.-H. Huang, R. I. Dass, Z.-L. Xing and J. B. Goodenough, *Science*, 2006, **312**, 254-257.

5. L. Zhang, Q. Zhou, Q. He and T. He, *Journal of Power Sources*, 2010, **195**, 6356-6366.

6. P. Zhang, Y.-H. Huang, J.-G. Cheng, Z.-Q. Mao and J. B. Goodenough, *Journal of Power Sources*, **196**, 1738-1743.

7. A. Kirubakaran, S. Jain and R. K. Nema, *Renewable and Sustainable Energy Reviews*, 2009, **13**, 2430-2440.

8. S. K. Kamarudin, F. Achmad and W. R. W. Daud, *International Journal of Hydrogen Energy*, 2009, **34**, 6902-6916.

9. A. Serov and C. Kwak, *Applied Catalysis B: Environmental*, 2010, **98**, 1-9.

10. D. D. Burnette, G. G. Kremer and D. J. Bayless, *Journal of Power Sources*, 2008, **182**, 329-333.

11. J. M. Andújar and F. Segura, *Renewable and Sustainable Energy Reviews*, 2009, **13**, 2309-2322.

12. Z. Du, H. Li and T. Gu, *Biotechnology Advances*, 2007, **25**, 464-482.

13. X. Cheng, Z. Shi, N. Glass, L. Zhang, J. Zhang, D. Song, Z.-S. Liu, H. Wang and J. Shen, *Journal of Power Sources*, 2007, **165**, 739-756.

14. Y. Wang, K. S. Chen, J. Mishler, S. C. Cho and X. C. Adroher, *Applied Energy*, 2011, **88**, 981-1007.

15. G. Merle, M. Wessling and K. Nijmeijer, *Journal of Membrane Science*, 2011, **377**, 1-35.

16. R. Lan, S. Tao and J. T. S. Irvine, *Energy & Environmental Science*, 2010, **3**, 438-441.

17. N. Sammes, R. Bove and K. Stahl, *Current Opinion in Solid State and Materials Science*, 2004, **8**, 372-378.

18. J. P. P. Huijsmans, G. J. Kraaij, R. C. Makkus, G. Rietveld, E. F. Sitters and H. T. J. Reijers, *Journal of Power Sources*, 2000, **86**, 117-121.

19. R. Ciccoli, V. Cigolotti, R. Lo Presti, E. Massi, S. J. McPhail, G. Monteleone, A. Moreno, V. Naticchioni, C. Paoletti, E. Simonetti and F. Zaza, *Waste Management*, 2010, **30**, 1018-1024.

20. L. G. J. De Haart and I. C. Vinke, *ECS Transactions*, 2011, **35**, 187-194.

21. S. Mekhilef, R. Saidur and A. Safari, *Renewable and Sustainable Energy Reviews*, 2012, **16**, 981-989.

22. M. Gong, X. Liu, J. Trembly and C. Johnson, *Journal of Power Sources*, 2007, **168**, 289-298.

23. K. Nikooyeh, R. Clemmer, V. Alzate-Restrepo and J. M. Hill, *Applied Catalysis A: General*, 2008, **347**, 106-111.

24. T. Kharlamova, S. Pavlova, V. Sadykov, T. Krieger, G. Alikina and C. Argirusis, *Catalysis Today*, 2009, **146**, 141-147.

25. J.-S. Kim, V. V. Nair, J. M. Vohs and R. J. Gorte, *Scripta Materialia*, 2011, **65**, 90-95.

26. *Fuel Cell Handbook, US Department of Energy, Morgantown, WV*, 2004, http://netl.doe.gov.

27. H. Inaba and H. Tagawa, *Solid State Ionics*, 1996, **83**, 1-16.

28. V. V. Kharton, F. M. B. Marques and A. Atkinson, *Solid State Ionics*, 2004, **174**, 135-149.

29. H. Hayashi, H. Inaba, M. Matsuyama, N. G. Lan, M. Dokiya and H. Tagawa, *Solid State Ionics*, 1999, **122**, 1-15.

30. J. R. Tolchard, M. S. Islam and P. R. Slater, *Journal of Materials Chemistry*, 2003, **13**, 1956-1961.

31. A. Chroneos, D. Parfitt, J. A. Kilner and R. W. Grimes, *Journal of Materials Chemistry*, 2010, **20**, 266-270.

32. E. Fabbri, D. Pergolesi and E. Traversa, *Chemical Society Reviews*, 2010, **39**, 4355-4369.

33. R. J. G. S. McIntosh, *Chemical Reviews*, 2004, **104**, 4845-4865.

34. V. M. Janardhanan, V. Heuveline and O. Deutschmann, *Journal of Power Sources*, 2008, **178**, 368-372.

35. J. S. Ahn, H. Yoon, K. T. Lee, M. A. Camaratta and E. D. Wachsman, *Fuel Cells*, 2009, **9**, 643-649.

36. M. Mogensen, K. V. Jensen, M. J. Jørgensen and S. Primdahl, *Solid State Ionics*, 2002, **150**, 123-129.

37. S. B. Adler, *Chemical Reviews*, 2004, **104**, 4791-4844.

38. S. H. Chan, X. J. Chen and K. A. Khor *Journal of The Electrochemical Society*, 2004, **151**, A164-A172.

39. W. G. Bessler, M. Vogler, H. Stormer, D. Gerthsen, A. Utz, A. Weber and E. Ivers-Tiffee, *Physical Chemistry Chemical Physics*, 2010, **12**, 13888-13903.

40. W. G. Bessler, J. Warnatz and D. G. Goodwin, *Solid State Ionics*, 2007, **177**, 3371-3383.

41. J. Rossmeisl and W. G. Bessler, *Solid State Ionics*, 2008, **178**, 1694-1700.

42. M. Vogler, A. Bieberle-Hütter, L. Gauckler, J. Warnatz and W. G. Bessler, *Journal of The Electrochemical Society*, 2009, **156**, B663-B672.

43. P. Holtappels, I. C. Vinke, L. G. J. de Haart and U. Stimming, *Journal of The Electrochemical Society*, 1999, **146**, 2976-2982.

44. M. Vogler and W. G. Bessler, *ECS Transactions*, 2009, **25**, 1957-1966.

45. A. Gorski, V. Yurkiv, D. Starukhin and H.-R. Volpp, *Journal of Power Sources*, 2011, **196**, 7188-7194.

46. B. Huang, X. F. Ye, S. R. Wang, H. W. Nie, J. Shi, Q. Hu, J. Q. Qian, X. F. Sun and T. L. Wen, *Journal of Power Sources*, 2006, **162**, 1172-1181.

47. N. Laosiripojana and S. Assabumrungrat, *Journal of Power Sources*, 2007, **163**, 943-951.

48. G. Meng, C. Jiang, J. Ma, Q. Ma and X. Liu, *Journal of Power Sources*, 2007, **173**, 189-193.

49. S. McIntosh and R. J. Gorte, *Chemical Reviews*, 2004, **104**, 4845-4866.

50. P. Aguiar, D. Chadwick and L. Kershenbaum, *Chemical Engineering Science*, 2002, **57**, 1665-1677.

51. M. Cimenti and J. M. Hill, *Journal of Power Sources*, 2009, **186**, 377-384.

52. H. Sumi, Y.-H. Lee, H. Muroyama, T. Matsui and K. Eguchi, *Journal of The Electrochemical Society*, 2010, **157**, B1118-B1125.

53. L. T. Lim, D. Chadwick and L. Kershenbaum, *Industrial & Engineering Chemistry Research*, 2005, **44**, 9609-9618.

54. Z. Zhan and S. A. Barnett, *Science*, 2005, **308**, 844-847.

55. D. J. Bayless and J. P. Trembly, *United States Patent Application*, 2008, **US 2008/0138669 A1**.

56. H. Kurokawa, L. Yang, C. P. Jacobson, L. C. De Jonghe and S. J. Visco, *Journal of Power Sources*, 2007, **164**, 510-518.

57. J.-H. Lee, K. Kim, J.-W. Kim, B.-K. Kim, H.-W. Lee and J. Moon, *Journal of Materials Science*, 2007, **42**, 1866-1871.

58. K. N. Kim, B. K. Kim, J. W. Son, J. Kim, H. W. Lee, J. H. Lee and J. Moon, *Solid State Ionics*, 2006, **177**, 2155-2158.

59. S. P. S. Badwal, *Solid State Ionics*, 2001, **143**, 39-46.

60. G. C. Kostogloudis, C. Ftikos, A. Ahmad-Khanlou, A. Naoumidis and D. Stöver, *Solid State Ionics*, 2000, **134**, 127-138.

61. R. Knibbe, J. Hjelm, M. Menon, N. Pryds, M. Søgaard, H. J. Wang and K. Neufeld, *Journal of the American Ceramic Society*, 2010, **93**, 2877-2883.

62. W. Zhou, R. Ran and Z. Shao, *Journal of Power Sources*, 2009, **192**, 231-246.

63. F. N. Cayan, M. Zhi, S. R. Pakalapati, I. Celik, N. Wu and R. Gemmen, *Journal of Power Sources*, 2008, **185**, 595-602.

64. B. Iwanschitz, L. Holzer, A. Mai and M. Schütze, *Solid State Ionics*, 2012, **211**, 69-73.

65. J. W. Fergus, *Solid State Ionics*, 2004, **171**, 1-15.

66. R. J. Gorte, S. Park, J. M. Vohs and C. Wang, *Advanced Materials*, 2000, **12**, 1465-1469.

67. S. Vasala, M. Lehtimäki, Y. H. Huang, H. Yamauchi, J. B. Goodenough and M. Karppinen, *Journal of Solid State Chemistry*, 2010, **183**, 1007-1012.

68. S.-e. Hou, A. Aguadero, J. A. Alonso and J. B. Goodenough, *Journal of Power Sources*, 2011, **196**, 5478-5484.

69. D. P. Fagg, V. V. Kharton, J. R. Frade and A. A. L. Ferreira, *Solid State Ionics*, 2003, **156**, 45-57.

70. M. D. Gross, K. M. Carver, M. A. Deighan, A. Schenkel, B. M. Smith and A. Z. Yee, *Journal of The Electrochemical Society*, 2009, **156**, B540-B545.

71. J.-S. Park, J. Luo, L. Adijanto, J. M. Vohs and R. J. Gorte, *Journal of Power Sources*, 2013, **222**, 123-128.

72. C. Yang, Z. Yang, C. Jin, G. Xiao, F. Chen and M. Han, *Advanced Materials*, 2012, **24**, 1439-1443.

73. C. T. G. Petit, R. Lan, P. I. Cowin, J. T. S. Irvine and S. Tao, *Journal of Materials Chemistry*, 2011, **21**, 8854-8861.

74. L. Mingyi, Y. Bo, X. Jingming and C. Jing, *International Journal of Hydrogen Energy*, 2010, **35**, 2670-2674.

75. R. M. C. Clemmer and S. F. Corbin, *Solid State Ionics*, 2004, **166**, 251-259.

76. D. Marrero-López, J. C. Ruiz-Morales, J. Peña-Martínez, J. Canales-Vázquez and P. Núñez, *Journal of Solid State Chemistry*, 2008, **181**, 685-692.

77. F.-Y. Wang, S. Cheng, B.-Z. Wan, C.-H. Chung and M.-J. Chen, *Ceramics International*, 2008, **34**, 1989-1992.

78. A. Sarikaya, V. Petrovsky and F. Dogan, *International Journal of Hydrogen Energy*, 2012, **37**, 11370-11377.

79. L. Nie, J. Liu, Y. Zhang and M. Liu, *Journal of Power Sources*, 2011, **196**, 9975-9979.

80. A. Sarikaya and F. Dogan, *Ceramics International*.

81. J. Hu, Z. Lü, K. Chen, X. Huang, N. Ai, X. Du, C. Fu, J. Wang and W. Su, *Journal of Membrane Science*, 2008, **318**, 445-451.

82. P. Holtappels, C. Sorof, M. C. Verbraeken, S. Rambert and U. Vogt, *Fuel Cells*, 2006, **6**, 113-116.

83. H. L. Frandsen, T. Ramos, A. Faes, M. Pihlatie and K. Brodersen, *Journal of the European Ceramic Society*, 2012, **32**, 1041-1052.

84. W. Bao, Q. Chang and G. Meng, *Journal of Membrane Science*, 2005, **259**, 103-109.

85. D. Montinaro, V. M. Sglavo, M. Bertoldi, T. Zandonella, A. Aricò, M. Lo Faro and V. Antonucci, *Solid State Ionics*, 2006, **177**, 2093-2097.

86. S. Le, S. Zhu, X. Zhu and K. Sun, *Journal of Power Sources*, 2013, **222**, 367-372.

87. K. Park, S. Yu, J. Bae, H. Kim and Y. Ko, *International Journal of Hydrogen Energy*, 2010, **35**, 8670-8677.

88. L. Liu, G.-Y. Kim and A. Chandra, *Journal of Power Sources*, 2010, **195**, 2310-2318.

89. D. Sarantaridis and A. Atkinson, *Fuel Cells*, 2007, **7**, 246-258.

90. T. Klemensø, C. Chung, P. H. Larsen and M. Mogensen, *Journal of The Electrochemical Society*, 2005, **152**, A2186-A2192.

91. Q. X. Fu and F. Tietz, *Fuel Cells*, 2008, **8**, 283-293.

92. H. Moon, S. D. Kim, E. W. Park, S. H. Hyun and H. S. Kim, *International Journal of Hydrogen Energy*, 2008, **33**, 2826-2833.

93. H.-G. Jung, Y.-K. Sun, H. Y. Jung, J. S. Park, H.-R. Kim, G.-H. Kim, H.-W. Lee and J.-H. Lee, *Solid State Ionics*, 2008, **179**, 1535-1539.

94. S. Uhlenbruck, N. Jordan, D. Sebold, H. P. Buchkremer, V. A. C. Haanappel and D. Stöver, *Thin Solid Films*, 2007, **515**, 4053-4060.

95. F. P. Van Berkel, Y. Zhang-Steenwinkel, G. Schoemakers, M. Van Tuel and B. G. Rietveld, *ECS Transactions*, 2009, **25**, 2717-2726.

96. P. K. Cheekatamarla, C. M. Finnerty and J. Cai, *International Journal of Hydrogen Energy*, 2008, **33**, 1853-1858.

97. Z. Wang, N. Zhang, J. Qiao, K. Sun and P. Xu, *Electrochemistry Communications*, 2009, **11**, 1120-1123.

98. G. Anandakumar, N. Li, A. Verma, P. Singh and J.-H. Kim, *Journal of Power Sources*, 2010, **195**, 6659-6670.

99. Y. Liu, C. Compson and M. Liu, *Journal of Power Sources*, 2004, **138**, 194-198.

100. M. Ni, M. K. H. Leung and D. Y. C. Leung, *Chemical Engineering & Technology*, 2007, **30**, 587-592.

101. M. Ni, M. K. H. Leung and D. Y. C. Leung, *Journal of Power Sources*, 2007, **168**, 369-378.

102. J. Will, A. Mitterdorfer, C. Kleinlogel, D. Perednis and L. J. Gauckler, *Solid State Ionics*, 2000, **131**, 79-96.

103. E. Baur. and H. Preis, *Z. Elektrochem*, 1937, **43**, 727.

104. N. Sammes and Y. Du, eds. N. Sammes, A. Smirnova and O. Vasylyev, Springer Netherlands, 2005, pp. 19-34.

105. P. R. Slater, J. E. H. Sansom and J. R. Tolchard, *The Chemical Record*, 2004, **4**, 373-384.

106. V. Thangadurai and W. Weppner, *Ionics*, 2006, **12**, 81-92.

107. J. W. Fergus, *Materials Science and Engineering: A*, 2005, **397**, 271-283.

108. N. Shaigan, W. Qu, D. G. Ivey and W. Chen, *Journal of Power Sources*, 2010, **195**, 1529-1542.

109. W. Z. Zhu and S. C. Deevi, *Materials Science and Engineering: A*, 2003, **348**, 227-243.

110. C. Sun, R. Hui and J. Roller, *Journal of Solid State Electrochemistry*, 2010, **14**, 1125-1144.

111. E. Tsipis and V. Kharton, *Journal of Solid State Electrochemistry*, 2011, **15**, 1007-1040.

112. S. J. Skinner, *Fuel Cells Bulletin*, 2001, **4**, 6-12.

113. A. Atkinson, S. Barnett, R. J. Gorte, J. T. S. Irvine, A. J. McEvoy, M. Mogensen, S. C. Singhal and J. Vohs, *Nat Mater*, 2004, **3**, 17-27.

114. S. Tao and J. T. S. Irvine, *The Chemical Record*, 2004, **4**, 83-95.

115. C. Sun and U. Stimming, *Journal of Power Sources*, 2007, **171**, 247-260.

116. P. I. Cowin, C. T. G. Petit, R. Lan, J. T. S. Irvine and S. Tao, *Advanced Energy Materials*, 2011, **1**, 314-332.

117. S. P. S. Badwal, *Solid State Ionics*, 1992, **52**, 23-32.

118. S. P. S. Badwal, F. T. Ciacchi and D. Milosevic, *Solid State Ionics*, 2000, **136–137**, 91-99.

119. V. V. Kharton, F. M. Figueiredo, L. Navarro, E. N. Naumovich, A. V. Kovalevsky, A. A. Yaremchenko, A. P. Viskup, A. Carneiro, F. M. B. Marques and J. R. Frade, *Journal of Materials Science*, 2001, **36**, 1105-1117.

120. H. Yahiro, K. Eguchi and H. Arai, *Solid State Ionics*, 1989, **36**, 71-75.

121. A. Atkinson, *Solid State Ionics*, 1997, **95**, 249-258.

122. B. C. H. Steele, *Solid State Ionics*, 2000, **129**, 95-110.

123. W. Sun and W. Liu, *Journal of Power Sources*, 2012, **217**, 114-119.

124. T. Ishihara, H. Matsuda and Y. Takita, *Journal of the American Chemical Society*, 1994, **116**, 3801-3803.

125. J.-H. Kim and H.-I. Yoo, *Solid State Ionics*, 2001, **140**, 105-113.

126. T. Ishihara, H. Matsuda, M. Azmi bin Bustam and Y. Takita, *Solid State Ionics*, 1996, **86–88**, 197-201.

127. K. Yamaji, T. Horita, M. Ishikawa, N. Sakai and H. Yokokawa, *Solid State Ionics*, 1999, **121**, 217-224.

128. M. J. Verkerk, K. Keizer and A. J. Burggraaf, *Journal of Applied Electrochemistry*, 1980, **10**, 81-90.

129. N. Jiang, E. D. Wachsman and S.-H. Jung, *Solid State Ionics*, 2002, **150**, 347-353.

130. F. Krok, I. Abrahams, D. Bangobango, W. Bogusz and J. A. G. Nelstrop, *Solid State Ionics*, 1998, **111**, 37-43.

131. S. P. Simner, D. Suarez-Sandoval, J. D. Mackenzie and B. Dunn, *Journal of the American Ceramic Society*, 1997, **80**, 2563-2568.

132. A. M. Azad, S. Larose and S. A. Akbar, *Journal of Materials Science*, 1994, **29**, 4135-4151.

133. A. A. Yaremchenko, V. V. Kharton, E. N. Naumovich, A. A. Tonoyan and V. V. Samokhval, *Journal of Solid State Electrochemistry*, 1998, **2**, 308-314.

134. J. C. B. G. Mairesse, G. Lagrange, P. Cocolios, *International Patent Application*, 1994, **94**, 06544.

135. J. C. B. G. Mairesse, G. Lagrange, P. Cocolios, *International Patent Application*, 1994, **94**, 06545.

136. L. Leon-Reina, E. R. Losilla, M. Martinez-Lara, S. Bruque and M. A. G. Aranda, *Journal of Materials Chemistry*, 2004, **14**, 1142-1149.

137. S. S. Pramana, W. T. Klooster and T. J. White, *Acta Crystallographica Section B*, 2007, **63**, 597-602.

138. E. Kendrick, M. S. Islam and P. R. Slater, *Chemical Communications*, 2008, 715-717.

139.   E. V. Tsipis, V. V. Kharton and J. R. Frade, *Electrochimica Acta*, 2007, **52**, 4428-4435.

140.   D. Marrero-López, M. C. Martín-Sedeño, J. Peña-Martínez, J. C. Ruiz-Morales, P. Núñez, M. A. G. Aranda and J. R. Ramos-Barrado, *Journal of Power Sources*, 2010, **195**, 2496-2506.

141.   T. Yao, Y. Uchimoto, M. Kinuhata, T. Inagaki and H. Yoshida, *Solid State Ionics*, 2000, **132**, 189-198.

142.   K. Nomura and S. Tanase, *Solid State Ionics*, 1997, **98**, 229-236.

143.   M. Mori, G. M. Tompsett, N. M. Sammes, E. Suda and Y. Takeda, *Solid State Ionics*, 2003, **158**, 79-90.

144.   P. Lacorre, F. Goutenoire, O. Bohnke, R. Retoux and Y. Laligant, *Nature*, 2000, **404**, 856-858.

145.   T. Schober, J. Friedrich and F. Krug, *Solid State Ionics*, 1997, **99**, 9-13.

146.   T. Hashimoto, Y. Inagaki, A. Kishi and M. Dokiya, *Solid State Ionics*, 2000, **128**, 227-231.

147.   D. Lybye, F. W. Poulsen and M. Mogensen, *Solid State Ionics*, 2000, **128**, 91-103.

148.   V. Kharton, E. Tsipis, A. Yaremchenko, N. Vyshatko, A. Shaula, E. Naumovich and J. Frade, *Journal of Solid State Electrochemistry*, 2003, **7**, 468-476.

149.   J. J. Sprague and H. L. Tuller, *Journal of the European Ceramic Society*, 1999, **19**, 803-806.

150.   I. P. Marozau, A. L. Shaula, V. V. Kharton, N. P. Vyshatko, A. P. Viskup, J. R. Frade and F. M. B. Marques, *Materials Research Bulletin*, 2005, **40**, 361-371.

151.   H. Huang, M. Nakamura, P. Su, R. Fasching, Y. Saito and F. B. Prinz, *Journal of The Electrochemical Society*, 2007, **154**, B20-B24.

152.   T. Hibino, A. Hashimoto, T. Inoue, J.-i. Tokuno, S.-i. Yoshida and M. Sano, *Science*, 2000, **288**, 2031-2033.

153.   T. Tsai, E. Perry and S. Barnett, *Journal of The Electrochemical Society*, 1997, **144**, L130-L132.

154. R. Yan, D. Ding, B. Lin, M. Liu, G. Meng and X. Liu, *Journal of Power Sources*, 2007, **164**, 567-571.

155. X. Ge, X. Huang, Y. Zhang, Z. Lu, J. Xu, K. Chen, D. Dong, Z. Liu, J. Miao and W. Su, *Journal of Power Sources*, 2006, **159**, 1048-1050.

156. T. Ishihara, K. Sato and Y. Takita, *Journal of the American Ceramic Society*, 1996, **79**, 913-919.

157. D. Beckel, A. Bieberle-Hütter, A. Harvey, A. Infortuna, U. P. Muecke, M. Prestat, J. L. M. Rupp and L. J. Gauckler, *Journal of Power Sources*, 2007, **173**, 325-345.

158. C. Xia, F. Chen and M. Liu, *Electrochemical and Solid-State Letters*, 2001, **4**, A52-A54.

159. J. Yan, H. Matsumoto, M. Enoki and T. Ishihara, *Electrochemical and Solid-State Letters*, 2005, **8**, A389-A391.

160. M. Matsuda, O. Ohara, K. Murata, S. Ohara, T. Fukui and M. Miyake, *Electrochemical and Solid-State Letters*, 2003, **6**, A140-A143.

161. S. W. Paulik, S. Baskaran and T. R. Armstrong, *Journal of Materials Science*, 1998, **33**, 2397-2404.

162. H. Yokokawa, T. Horita, N. Sakai, K. Yamaji, M. E. Brito, Y. P. Xiong and H. Kishimoto, *Solid State Ionics*, 2006, **177**, 3193-3198.

163. K. Huang, P. Y. Hou and J. B. Goodenough, *Materials Research Bulletin*, 2001, **36**, 81-95.

164. I. Belogolovsky, X.-D. Zhou, H. Kurokawa, P. Y. Hou, S. Visco and H. U. Anderson, *Journal of The Electrochemical Society*, 2007, **154**, B976-B980.

165. J.-J. Choi, J. Ryu, B.-D. Hahn, W.-H. Yoon, B.-K. Lee and D.-S. Park, *Journal of Materials Science*, 2009, **44**, 843-848.

166. Z. Zeng and K. Natesan, *Solid State Ionics*, 2004, **167**, 9-16.

167. H. Li, Y. Zheng, L. W. Benum, M. Oballa and W. Chen, *Corrosion Science*, 2009, **51**, 2336-2341.

168. J. Mizusaki, Y. Yonemura, H. Kamata, K. Ohyama, N. Mori, H. Takai, H. Tagawa, M. Dokiya, K. Naraya, T. Sasamoto, H. Inaba and T. Hashimoto, *Solid State Ionics*, 2000, **132**, 167-180.

169. S. Jiang, *Journal of Materials Science*, 2008, **43**, 6799-6833.

170. J. Nowotny and M. Rekas, *Journal of the American Ceramic Society*, 1998, **81**, 67-80.

171. C. Clausen, C. Bagger, J. B. Bilde-Sørensen and A. Horsewell, *Solid State Ionics*, 1994, **70–71, Part 1**, 59-64.

172. G. Stochniol, E. Syskakis and A. Naoumidis, *Journal of the American Ceramic Society*, 1995, **78**, 929-932.

173. I. Yasuda, K. Ogasawara, M. Hishinuma, T. Kawada and M. Dokiya, *Solid State Ionics*, 1996, **86–88, Part 2**, 1197-1201.

174. T. Ishiham, T. Kudo, H. Matsuda and Y. Takita, *Journal of the American Ceramic Society*, 1994, **77**, 1682-1684.

175. Y. Sakaki, Y. Takeda, A. Kato, N. Imanishi, O. Yamamoto, M. Hattori, M. Iio and Y. Esaki, *Solid State Ionics*, 1999, **118**, 187-194.

176. V. N. Tikhonovich, V. V. Kharton, E. N. Naumovich and A. A. Savitsky, *Solid State Ionics*, 1998, **106**, 197-206.

177. J. M. Serra, V. B. Vert, M. Betz, V. A. C. Haanappel, W. A. Meulenberg and F. Tietz, *Journal of The Electrochemical Society*, 2008, **155**, B207-B214.

178. M. Søgaard, P. V. Hendriksen, M. Mogensen, F. W. Poulsen and E. Skou, *Solid State Ionics*, 2006, **177**, 3285-3296.

179. A. V. Kovalevsky, V. V. Kharton, V. N. Tikhonovich, E. N. Naumovich, A. A. Tonoyan, O. P. Reut and L. S. Boginsky, *Materials Science and Engineering: B*, 1998, **52**, 105-116.

180. O. Yamamoto, Y. Takeda, R. Kanno and M. Noda, *Solid State Ionics*, 1987, **22**, 241-246.

181. R. V. Wandekar, B. N. Wani and S. R. Bharadwaj, *Solid State Sciences*, 2009, **11**, 240-250.

182. H. Ullmann, N. Trofimenko, F. Tietz, D. Stöver and A. Ahmad-Khanlou, *Solid State Ionics*, 2000, **138**, 79-90.

183. A. Petrov, V. Cherepanov and A. Zuev, *Journal of Solid State Electrochemistry*, 2006, **10**, 517-537.

184. G. C. Kostgloudis, N. Vasilakos and C. Ftikos, *Solid State Ionics*, 1998, **106**, 207-218.

185. S. Simner, M. Anderson, J. Bonnett and J. Stevenson, *Solid State Ionics*, 2004, **175**, 79-81.

186. G. Coffey, J. Hardy, O. Marina, L. Pederson, P. Rieke and E. Thomsen, *Solid State Ionics*, 2004, **175**, 73-78.

187. J. M. Ralph, C. Rossignol and R. Kumar *Journal of The Electrochemical Society*, 2003, **150**, A1518-A1522.

188. M. D. Anderson, J. W. Stevenson and S. P. Simner, *Journal of Power Sources*, 2004, **129**, 188-192.

189. C. Fu, K. Sun, N. Zhang, X. Chen and D. Zhou, *Electrochimica Acta*, 2007, **52**, 4589-4594.

190. E. Perry Murray, M. J. Sever and S. A. Barnett, *Solid State Ionics*, 2002, **148**, 27-34.

191. Y. Leng, S. H. Chan and Q. Liu, *International Journal of Hydrogen Energy*, 2008, **33**, 3808-3817.

192. J. W. Stevenson, T. R. Armstrong, R. D. Carneim, L. R. Pederson and W. J. Weber, *Journal of The Electrochemical Society*, 1996, **143**, 2722-2729.

193. X. Meng, S. Lü, Y. Ji, T. Wei and Y. Zhang, *Journal of Power Sources*, 2008, **183**, 581-585.

194. Z. Shao and S. M. Haile, *Nature*, 2004, **431**, 170 - 173.

195. Z. Qingshan, J. Tongan and W. Yong, *Solid State Ionics*, 2006, **177**, 1199-1204.

196. M. Arnold, H. Wang and A. Feldhoff, *Journal of Membrane Science*, 2007, **293**, 44-52.

197. D.-P. Huang, Q. Xu, W. Chen, F. Zhang and H.-X. Liu, *Ceramics International*, 2008, **34**, 651-655.

198. Q. Li, H. Zhao, L. Huo, L. Sun, X. Cheng and J.-C. Grenier, *Electrochemistry Communications*, 2007, **9**, 1508-1512.

199. C. N. Munnings, S. J. Skinner, G. Amow, P. S. Whitfield and I. J. Davidson, *Solid State Ionics*, 2006, **177**, 1849-1853.

200. F. Riza and C. Ftikos, *Journal of the European Ceramic Society*, 2007, **27**, 571-573.

201. M. Al Daroukh, V. V. Vashook, H. Ullmann, F. Tietz and I. Arual Raj, *Solid State Ionics*, 2003, **158**, 141-150.

202. A. Aguadero, M. J. Escudero, M. Perez, J. A. Alonso, V. Pomjakushin and L. Daza, *Dalton Transactions*, 2006, 4377-4383.

203. S. J. Skinner and J. A. Kilner, *Solid State Ionics*, 2000, **135**, 709-712.

204. A. Aguadero, J. A. Alonso, M. J. Escudero and L. Daza, *Solid State Ionics*, 2008, **179**, 393-400.

205. C. N. Munnings, S. J. Skinner, G. Amow, P. S. Whitfield and I. J. Davidson, *Solid State Ionics*, 2005, **176**, 1895-1901.

206. F. Zhao, X. Wang, Z. Wang, R. Peng and C. Xia, *Solid State Ionics*, 2008, **179**, 1450-1453.

207. M. A. Laguna-Bercero, N. Kinadjan, R. Sayers, H. El Shinawi, C. Greaves and S. J. Skinner, *Fuel Cells*, 2011, **11**, 102-107.

208. K. Zheng, A. Gorzkowska-Sobaś and K. Świerczek, *Materials Research Bulletin*.

209. V. Vashook, J. Zosel, T.-L. Wen and U. Guth, *Solid State Ionics*, 2006, **177**, 1827-1830.

210. Y. Wang, H. Nie, S. Wang, T.-L. Wen, U. Guth and V. Valshook, *Materials Letters*, 2006, **60**, 1174-1178.

211. H. W. Nie, T. L. Wen, S. R. Wang, Y. S. Wang, U. Guth and V. Vashook, *Solid State Ionics*, 2006, **177**, 1929-1932.

212. X. Ding, X. Kong, X. Wang, J. Jiang and C. Cui, *Journal of Alloys and Compounds*, 2010, **502**, 472-476.

213. Y. Cao, H. Gu, H. Chen, Y. Zheng, M. Zhou and L. Guo, *International Journal of Hydrogen Energy*, 2010, **35**, 5594-5600.

214. A. Montenegro-Hernández, J. Vega-Castillo, L. Mogni and A. Caneiro, *International Journal of Hydrogen Energy*, 2011, **36**, 15704-15714.

215. R. Sayers, J. Liu, B. Rustumji and S. J. Skinner, *Fuel Cells*, 2008, **8**, 338-343.

216. C. Jin, J. Liu, Y. Zhang, J. Sui and W. Guo, *Journal of Power Sources*, 2008, **182**, 482-488.

217. S. Choi, S. Yoo, J.-Y. Shin and G. Kim, *Journal of The Electrochemical Society*, 2011, **158**, B995-B999.

218. J. B. Wang, J.-C. Jang and T.-J. Huang, *Journal of Power Sources*, 2003, **122**, 122-131.

219. T. Hibino, A. Hashimoto, M. Yano, M. Suzuki and M. Sano, *Electrochimica Acta*, 2003, **48**, 2531-2537.

220. J. F. B. Rasmussen and A. Hagen, *Journal of Power Sources*, 2009, **191**, 534-541.

221. T. Iwata, *Journal of The Electrochemical Society*, 1996, **143**, 1521-1525.

222. M. Cassidy, G. Lindsay and K. Kendall, *Journal of Power Sources*, **61**, 189-192.

223. A. Faes, A. Nakajo, A. Hessler-Wyser, D. Dubois, A. Brisse, S. Modena and J. Van herle, *Journal of Power Sources*, 2009, **193**, 55-64.

224. J. Laurencin, G. Delette, B. Morel, F. Lefebvre-Joud and M. Dupeux, *Journal of Power Sources*, 2009, **192**, 344-352.

225. T. Klemensø and M. Mogensen, *Journal of the American Ceramic Society*, 2007, **90**, 3582-3588.

226. S.-D. Kim, H. Moon, S.-H. Hyun, J. Moon, J. Kim and H.-W. Lee, *Solid State Ionics*, 2006, **177**, 931-938.

227. D. Waldbillig, A. Wood and D. G. Ivey, *Solid State Ionics*, 2005, **176**, 847-859.

228. C. M. Finnerty, N. J. Coe, R. H. Cunningham and R. M. Ormerod, *Catalysis Today*, 1998, **46**, 137-145.

229. Z. Zhan, J. Liu and S. A. Barnett, *Applied Catalysis A: General*, 2004, **262**, 255-259.

230. V. Alzate-Restrepo and J. M. Hill, *Applied Catalysis A: General*, 2008, **342**, 49-55.

231. Y. Lin, Z. Zhan, J. Liu and S. A. Barnett, *Solid State Ionics*, 2005, **176**, 1827-1835.

232. Q. Ma, J. Ma, S. Zhou, R. Yan, J. Gao and G. Meng, *Journal of Power Sources*, 2007, **164**, 86-89.

233. T.-J. Huang and C.-H. Wang, *Chemical Engineering Journal*, 2007, **132**, 97-103.

234. S. Xu and X. Wang, *Fuel*, 2005, **84**, 563-567.

235. W. Zhu, C. Xia, J. Fan, R. Peng and G. Meng, *Journal of Power Sources*, 2006, **160**, 897-902.

236. S. Zha, A. Moore, H. Abernathy and M. Liu, *Journal of The Electrochemical Society*, 2004, **151**, A1128-A1133.

237. L. Zhang, S. P. Jiang, H. Q. He, X. Chen, J. Ma and X. C. Song, *International Journal of Hydrogen Energy*, 2010, **35**, 12359-12368.

238. L. Yang, S. Wang, K. Blinn, M. Liu, Z. Liu, Z. Cheng and M. Liu, *Science*, 2009, **326**, 126-129.

239. K. Huang, M. Feng, J. B. Goodenough and C. Milliken, *Journal of The Electrochemical Society*, 1997, **144**, 3620-3624.

240. S. Park, R. Craciun, J. M. Vohs and R. J. Gorte, *Journal of The Electrochemical Society*, 1999, **146**, 3603-3605.

241. S. Park, J. M. Vohs and R. J. Gorte, *Nature*, 2000, **404**, 265-267.

242. R. J. Gorte, H. Kim and J. M. Vohs, *Journal of Power Sources*, 2002, **106**, 10-15.

243. R. J. Gorte and J. M. Vohs, *Journal of Catalysis*, 2003, **216**, 477-486.

244. H. Kim, J. M. Vohs and R. J. Gorte, *Chemical Communications*, 2001, 2334-2335.

245. H. Kim, C. Lu, W. L. Worrell, J. M. Vohs and R. J. Gorte, *Journal of The Electrochemical Society*, 2002, **149**, A247-A250.

246. E. W. Park, H. Moon, M.-s. Park and S. H. Hyun, *International Journal of Hydrogen Energy*, 2009, **34**, 5537-5545.

247. Z. Wang, W. Weng, K. Cheng, P. Du, G. Shen and G. Han, *Journal of Power Sources*, 2008, **179**, 541-546.

248. J. Llorca, N. s. Homs, O. Rossell, M. Seco, J.-L. G. Fierro and P. Ramírez de la Piscina, *Journal of Molecular Catalysis A: Chemical*, 1999, **149**, 225-232.

249. S.-I. Lee, J. M. Vohs and R. J. Gorte, *Journal of The Electrochemical Society*, 2004, **151**, A1319-A1323.

250. S.-I. Lee, K. Ahn, J. M. Vohs and R. J. Gorte, *Electrochemical and Solid-State Letters*, 2005, **8**, A48-A51.

251. A. Hornés, G. Munuera, A. Fuerte, M. J. Escudero, L. Daza and A. Martínez-Arias, *Journal of Power Sources*, 2011, **196**, 4218-4225.

252. T. Ishihara, J. Yan, M. Shinagawa and H. Matsumoto, *Electrochimica Acta*, 2006, **52**, 1645-1650.

253. X. C. Lu and J. H. Zhu, *Journal of Power Sources*, 2007, **165**, 678-684.

254. X. C. Lu, J. H. Zhu and Z. H. Bi, *Solid State Ionics*, 2009, **180**, 265-270.

255. C. J. Fu, S. H. Chan, X. M. Ge, Q. L. Liu and G. Pasciak, *International Journal of Hydrogen Energy*, 2011, **36**, 13727-13734.

256. C.-K. Cho, B.-H. Choi and K.-T. Lee, *Ceramics International*.

257. Y. Wu, C. Su, W. Wang, H. Wang and Z. Shao, *International Journal of Hydrogen Energy*, 2012, **37**, 9287-9297.

258. B. Huang, S. R. Wang, R. Z. Liu and T. L. Wen, *Journal of Power Sources*, 2007, **167**, 288-294.

259. R. da Paz Fiuza, M. Aurélio da Silva and J. S. Boaventura, *International Journal of Hydrogen Energy*, 2010, **35**, 11216-11228.

260. H. Kan and H. Lee, *Catalysis Communications*, 2010, **12**, 36-39.

261. W. Shi-zhong and G. Jie, *Electrochemical and Solid-State Letters*, 2006, **9**, A395-A398.

262. L. Ortega-San-Martín, V. Gil, J. I. Peña, Á. Larrea and V. M. Orera, *Solid State Ionics*, 2012, **226**, 30-36.

263. C. M. Grgicak and J. B. Giorgi, *The Journal of Physical Chemistry C*, 2007, **111**, 15446-15455.

264. C. M. Grgicak, R. G. Green and J. B. Giorgi, *Journal of Power Sources*, 2008, **179**, 317-328.

265. A. Ringuedé, D. Bronine and J. R. Frade, *Electrochimica Acta*, 2002, **48**, 437-442.

266. C. M. Grgicak, M. M. Pakulska, J. S. O'Brien and J. B. Giorgi, *Journal of Power Sources*, 2008, **183**, 26-33.

267. J. S. O'Brien and J. B. Giorgi, *Journal of Power Sources*, 2012, **200**, 14-20.

268. Z. G. Lu, J. H. Zhu, Z. H. Bi and X. C. Lu, *Journal of Power Sources*, 2008, **180**, 172-175.

269. Z. Xie, W. Zhu, B. Zhu and C. Xia, *Electrochimica Acta*, 2006, **51**, 3052-3057.

270. E. Nikolla, A. Holewinski, J. Schwank and S. Linic, *Journal of the American Chemical Society*, 2006, **128**, 11354-11355.

271. E. Nikolla, J. W. Schwank and S. Linic, *Catalysis Today*, 2008, **136**, 243-248.

272. H. Kan and H. Lee, *Applied Catalysis B: Environmental*, 2010, **97**, 108-114.

273. H. Kan, S. H. Hyun, Y.-G. Shul and H. Lee, *Catalysis Communications*, 2009, **11**, 180-183.

274. E. Nikolla, J. Schwank and S. Linic, *Journal of The Electrochemical Society*, 2009, **156**, B1312-B1316.

275. O. A. Marina, C. A. Coyle, M. H. Engelhard and L. R. Pederson, *Journal of The Electrochemical Society*, 2011, **158**, B424-B429.

276. N. M. Tikekar, T. J. Armstrong and A. V. Virkar, *Journal of The Electrochemical Society*, 2006, **153**, A654-A663.

277. Y. Shiratori, Y. Teraoka and K. Sasaki, *Solid State Ionics*, 2006, **177**, 1371-1380.

278. T. Horiuchi, K. Sakuma, T. Fukui, Y. Kubo, T. Osaki and T. Mori, *Applied Catalysis A: General*, 1996, **144**, 111-120.

279. Y. Liu, Y. Bai and J. Liu, *Journal of Power Sources*, 2011, **196**, 9965-9969.

280. P. Gélin and M. Primet, *Applied Catalysis B: Environmental*, 2002, **39**, 1-37.

281. M. Huff, P. M. Torniainen and L. D. Schmidt, *Catalysis Today*, 1994, **21**, 113-128.

282. M. Suzuki, H. Sasaki, S. Otoshi, A. Kajimura and M. Ippommatsu, *Solid State Ionics*, 1993, **62**, 125-130.

283. M. Watanabe, H. Uchida, M. Shibata, N. Mochizuki and K. Amikura, *Journal of The Electrochemical Society*, 1994, **141**, 342-346.

284. T. Takeguchi, R. Kikuchi, T. Yano, K. Eguchi and K. Murata, *Catalysis Today*, 2003, **84**, 217-222.

285. S. McIntosh, J. M. Vohs and R. J. Gorte, *Electrochemical and Solid-State Letters*, 2003, **6**, A240-A243.

286. Y. Nabae, I. Yamanaka, M. Hatano and K. Otsuka, *Journal of The Electrochemical Society*, 2006, **153**, A140-A145.

287. L. L. Zheng, X. Wang, L. Zhang, J.-Y. Wang and S. P. Jiang, *International Journal of Hydrogen Energy*, 2012, **37**, 10299-10310.

288. Z. Liu, Z.-w. Zheng, M.-f. Han and M.-l. Liu, *Journal of Power Sources*, 2010, **195**, 7230-7233.

289. A. T. Ashcroft, A. K. Cheetham, M. L. H. Green and P. D. F. Vernon, *Nature*, 1991, **352**, 225-226.

290. E. S. Putna, J. Stubenrauch, J. M. Vohs and R. J. Gorte, *Langmuir*, 1995, **11**, 4832-4837.

291. M. Boaro, V. Modafferi, A. Pappacena, J. Llorca, V. Baglio, F. Frusteri, P. Frontera, A. Trovarelli and P. L. Antonucci, *Journal of Power Sources*, 2010, **195**, 649-661.

292. J. P. Breen, R. Burch and H. M. Coleman, *Applied Catalysis B: Environmental*, 2002, **39**, 65-74.

293. S. D. Nobrega, M. V. Galesco, K. Girona, D. Z. de Florio, M. C. Steil, S. Georges and F. C. Fonseca, *Journal of Power Sources*, 2012, **213**, 156-159.

294. J. Toyir, P. Gélin, H. Belatel and A. Kaddouri, *Catalysis Today*, 2010, **157**, 451-455.

295. G. Postole, K. Girona, J. Toyir, A. Kaddouri and P. Gélin, *Fuel Cells*, 2012, **12**, 275-287.

296. S. Tao and J. T. S. Irvine, *Journal of Solid State Chemistry*, 2002, **165**, 12-18.

297. A. Kaiser, A. Feighery, D. Fagg and J. Irvine, *Ionics*, 1998, **4**, 215-219.

298. X. Mantzouris, N. Zouvelou, V. Haanappel, F. Tietz and P. Nikolopoulos, *Journal of Materials Science*, 2007, **42**, 10152-10159.

299. N. Kim, B.-H. Kim and D. Lee, *Journal of Power Sources*, 2000, **90**, 139-143.

300. D. B. Ingram and S. Linic, *Journal of The Electrochemical Society*, 2009, **156**, B1457-B1465.

301. O. A. Marina, N. L. Canfield and J. W. Stevenson, *Solid State Ionics*, 2002, **149**, 21-28.

302. S. Tao and J. T. S. Irvine, *Nat Mater*, 2003, **2**, 320-323.

303. R. Mukundan, E. L. Brosha and F. H. Garzon, *Electrochemical and Solid-State Letters*, 2004, **7**, A5-A7.

304. U. Balachandran and N. G. Eror, *Journal of Solid State Chemistry*, 1981, **39**, 351-359.

305. X. Li, H. Zhao, W. Shen, F. Gao, X. Huang, Y. Li and Z. Zhu, *Journal of Power Sources*, 2007, **166**, 47-52.

306. O. A. Marina, N. L. Canfield and J. W. Stevenson, *Solid State Ionics*, 2002, **149**, 21-28.

307. S. Koutcheiko, Y. Yoo, A. Petric and I. Davidson, *Ceramics International*, 2006, **32**, 67-72.

308. S. Hui and A. Petric, *Journal of The Electrochemical Society*, 2002, **149**, J1-J10.

309. Q. X. Fu, S. B. Mi, E. Wessel and F. Tietz, *Journal of the European Ceramic Society*, 2008, **28**, 811-820.

310. Q. Ma and F. Tietz, *Solid State Ionics*, 2012, **225**, 108-112.

311. J.-H. Li, X.-Z. Fu, J.-L. Luo, K. T. Chuang and A. R. Sanger, *Journal of Power Sources*, 2012, **213**, 69-77.

312. A. Vincent, J.-L. Luo, K. T. Chuang and A. R. Sanger, *Journal of Power Sources*, 2010, **195**, 769-774.

313. C. d. Périllat-Merceroz, G. Gauthier, P. Roussel, M. Huvé, P. Gélin and R.-N. l. Vannier, *Chemistry of Materials*, 2011, **23**, 1539-1550.

314. P. R. Slater, D. P. Fagg and J. T. S. Irvine, *Journal of Materials Chemistry*, 1997, **7**, 2495-2498.

315. K. B. Yoo and G. M. Choi, *Solid State Ionics*, 2009, **180**, 867-871.

316. Q. Fu, F. Tietz, D. Sebold, S. Tao and J. T. S. Irvine, *Journal of Power Sources*, 2007, **171**, 663-669.

317. H. S. Kim, S. P. Yoon, J. W. Yun, S. A. Song, S.-C. Jang, S. W. Nam and Y.-G. Shul, *International Journal of Hydrogen Energy*, 2012, **37**, 16130-16139.

318. Q. Ma, F. Tietz, A. Leonide and E. Ivers-Tiffée, *Electrochemistry Communications*, 2010, **12**, 1326-1328.

319. Q. Ma, F. Tietz, A. Leonide and E. Ivers-Tiffée, *Journal of Power Sources*, 2011, **196**, 7308-7312.

320. M. Roushanafshar, J.-L. Luo, A. L. Vincent, K. T. Chuang and A. R. Sanger, *International Journal of Hydrogen Energy*, 2012, **37**, 7762-7770.

321. X. Sun, S. Wang, Z. Wang, X. Ye, T. Wen and F. Huang, *Journal of Power Sources*, 2008, **183**, 114-117.

322. X. Sun, S. Wang, Z. Wang, J. Qian, T. Wen and F. Huang, *Journal of Power Sources*, 2009, **187**, 85-89.

323. G. Kim, M. D. Gross, W. Wang, J. M. Vohs and R. J. Gorte, *Journal of The Electrochemical Society*, 2008, **155**, B360-B366.

324. J. Rossmeisl and W. G. Bessler, *Solid State Ionics*, 2008, **178**, 1694-1700.

325. X. C. Lu, J. H. Zhu, Z. Yang, G. Xia and J. W. Stevenson, *Journal of Power Sources*, 2009, **192**, 381-384.

326. S. Lee, G. Kim, J. M. Vohs and R. J. Gorte, *Journal of The Electrochemical Society*, 2008, **155**, B1179-B1183.

327. X. Li, H. Zhao, F. Gao, N. Chen and N. Xu, *Electrochemistry Communications*, 2008, **10**, 1567-1570.

328. D. N. Miller and J. T. S. Irvine, *Journal of Power Sources*, 2011, **196**, 7323-7327.

329. O. A. Marina and L. R. Pederson, *Fifth European Solid Oxide Fuel Cell Forum, European Fuel Cell Forum, Oberrohfdorf, Switzerland,*, 2002, 481-489.

330. X. Li, H. Zhao, N. Xu, X. Zhou, C. Zhang and N. Chen, *International Journal of Hydrogen Energy*, 2009, **34**, 6407-6414.

331. K. B. Yoo, B. H. Park and G. M. Choi, *Solid State Ionics*, 2012, **225**, 104-107.

332. X. Li, H. Zhao, F. Gao, Z. Zhu, N. Chen and W. Shen, *Solid State Ionics*, 2008, **179**, 1588-1592.

333. D. P. Fagg, V. V. Kharton, A. V. Kovalevsky, A. P. Viskup, E. N. Naumovich and J. R. Frade, *Journal of the European Ceramic Society*, 2001, **21**, 1831-1835.

334. J. S. Yoon, M. Y. Yoon, C. Kwak, H. J. Park, S. M. Lee, K. H. Lee and H. J. Hwang, *Materials Science and Engineering: B*, 2012, **177**, 151-156.

335. C. Arrivé, T. Delahaye, O. Joubert and G. Gauthier, *Journal of Power Sources*, 2013, **223**, 341-348.

336. T. Kolodiazhnyi and A. Petric, *Journal of Electroceramics*, 2005, **15**, 5-11.

337. X. Li, H. Zhao, X. Zhou, N. Xu, Z. Xie and N. Chen, *International Journal of Hydrogen Energy*, 2010, **35**, 7913-7918.

338. H. Zhao, F. Gao, X. Li, C. Zhang and Y. Zhao, *Solid State Ionics*, 2009, **180**, 193-197.

339. F. Gao, H. Zhao, X. Li, Y. Cheng, X. Zhou and F. Cui, *Journal of Power Sources*, 2008, **185**, 26-31.

340.   Q. Ma, F. Tietz and D. Stöver, *Solid State Ionics*, 2011, **192**, 535-539.

341.   D. Neagu and J. T. S. Irvine, *Chemistry of Materials*, 2010, **22**, 5042-5053.

342.   D. Neagu and J. T. S. Irvine, *Chemistry of Materials*, 2011, **23**, 1607-1617.

343.   M. C. Verbraeken, B. Iwanschitz, A. Mai and J. T. S. Irvine, *Journal of The Electrochemical Society*, 2012, **159**, F757-F762.

344.   C. D. Savaniu and J. T. S. Irvine, *Solid State Ionics*, 2011, **192**, 491-493.

345.   P. Blennow, A. Hagen, K. K. Hansen, L. R. Wallenberg and M. Mogensen, *Solid State Ionics*, 2008, **179**, 2047-2058.

346.   M. D. Gross, K. M. Carver, M. A. Deighan, A. Schenkel, B. M. Smith and A. Z. Yee, *Journal of The Electrochemical Society*, 2009, **156**, B540-B545.

347.   J. Karczewski, B. Riegel, S. Molin, A. Winiarski, M. Gazda, P. Jasinski, L. Murawski and B. Kusz, *Journal of Alloys and Compounds*, 2009, **473**, 496-499.

348.   B. Bochentyn, J. Karczewski, T. Miruszewski, A. Krupa, M. Gazda, P. Jasinski and B. Kusz, *Solid State Ionics*, 2012, **225**, 118-123.

349.   A. M. Hussain, J. V. T. Høgh, W. Zhang, E. Stamate, K. T. S. Thydén and N. Bonanos, *Journal of Power Sources*, 2012, **212**, 247-253.

350.   A. M. Hussain, J. V. T. Høgh, W. Zhang and N. Bonanos, *Journal of Power Sources*, 2012, **216**, 308-313.

351.   B. H. Smith, W. C. Holler and M. D. Gross, *Solid State Ionics*, 2011, **192**, 383-386.

352.   G. Xiao, X. Dong, K. Huang and F. Chen, *Materials Research Bulletin*, 2011, **46**, 57-61.

353.   N. Q. Minh, *Journal of the American Ceramic Society*, 1993, **76**, 563-588.

354.   S. Tao and J. T. S. Irvine, *Journal of The Electrochemical Society*, 2004, **151**, A252-A259.

355.   S. Tao and J. T. S. Irvine, *Chemistry of Materials*, 2006, **18**, 5453-5460.

356.   J. Sfeir, P. A. Buffat, P. Möckli, N. Xanthopoulos, R. Vasquez, H. Joerg Mathieu, J. Van herle and K. Ravindranathan Thampi, *Journal of Catalysis*, 2001, **202**, 229-244.

357.   S. Zha, P. Tsang, Z. Cheng and M. Liu, *Journal of Solid State Chemistry*, 2005, **178**, 1844-1850.

358. S. Tao and J. T. S. Irvine, *Journal of The Electrochemical Society*, 2004, **151**, A252-A259.

359. J. Liu, B. D. Madsen, Z. Ji and S. A. Barnett, *Electrochemical and Solid-State Letters*, 2002, **5**, A122-A124.

360. M. K. Rath, B.-H. Choi and K.-T. Lee, *Journal of Power Sources*, 2012, **213**, 55-62.

361. G. Kim, S. Lee, J. Y. Shin, G. Corre, J. T. S. Irvine, J. M. Vohs and R. J. Gorte, *Electrochemical and Solid-State Letters*, 2009, **12**, B48-B52.

362. M. v. d. Bossche, R. Matthews, A. Lichtenberger and S. McIntosh, *Journal of The Electrochemical Society*, 2010, **157**, B392-B399.

363. S. P. Jiang, Y. Ye, T. He and S. B. Ho, *Journal of Power Sources*, 2008, **185**, 179-182.

364. X. Zhu, Z. Lü, B. Wei, K. Chen, M. Liu, X. Huang and W. Su, *Journal of Power Sources*, 2010, **195**, 1793-1798.

365. X. J. Chen, Q. L. Liu, S. H. Chan, N. P. Brandon and K. A. Khor, *Electrochemistry Communications*, 2007, **9**, 767-772.

366. X. Zhu, Z. Lü, B. Wei, K. Chen, M. Liu, X. Huang and W. Su, *Journal of Power Sources*, 2009, **190**, 326-330.

367. X. C. Lu and J. H. Zhu, *Solid State Ionics*, 2007, **178**, 1467-1475.

368. X. Zhu, Z. Lü, B. Wei, M. Liu, X. Huang and W. Su, *Electrochimica Acta*, 2010, **55**, 3932-3938.

369. X.-F. Ye, S. R. Wang, Z. R. Wang, Q. Hu, X. F. Sun, T. L. Wen and Z. Y. Wen, *Journal of Power Sources*, 2008, **183**, 512-517.

370. V. V. Kharton, E. V. Tsipis, I. P. Marozau, A. P. Viskup, J. R. Frade and J. T. S. Irvine, *Solid State Ionics*, 2007, **178**, 101-113.

371. E. Lay, G. Gauthier and L. Dessemond, *Solid State Ionics*, 2011, **189**, 91-99.

372. E. Lay, G. Gauthier, S. Rosini, C. Savaniu and J. T. S. Irvine, *Solid State Ionics*, 2008, **179**, 1562-1566.

373. E. S. Raj and J. T. S. Irvine, *Solid State Ionics*, 2010, **180**, 1683-1689.

374. E. Lay, L. Dessemond and G. Gauthier, *Journal of Power Sources*, 2013, **221**, 149-156.

375. L. Zhang, X. Chen, S. P. Jiang, H. Q. He and Y. Xiang, *Solid State Ionics*, 2009, **180**, 1076-1082.

376. N. Danilovic, A. Vincent, J.-L. Luo, K. T. Chuang, R. Hui and A. R. Sanger, *Chemistry of Materials*, 2009, **22**, 957-965.

377. K. Papazisi, S. Balomenou and D. Tsiplakides, *Journal of Applied Electrochemistry*, 2010, **40**, 1875-1881.

378. J. M. Haag, S. A. Barnett, J. W. Richardson and K. R. Poeppelmeier, *Chemistry of Materials*, 2010, **22**, 3283-3289.

379. X. Zhu, Z. Lu, B. Wei, Y. Zhang, X. Huang and W. Su, *Electrochemical and Solid-State Letters*, 2010, **13**, B91-B94.

380. W. Kobsiriphat, B. D. Madsen, Y. Wang, M. Shah, L. D. Marks and S. A. Barnett, *Journal of The Electrochemical Society*, 2010, **157**, B279-B284.

381. W. Kobsiriphat, B. D. Madsen, Y. Wang, L. D. Marks and S. A. Barnett, *Solid State Ionics*, 2009, **180**, 257-264.

382. W. K. B.D. Madsen, L.D. Marks, Y. Wang, S.A. Barnett, *10th International Symposium on Solid Oxide Fuel Cells, ECS Proc. Series, Pennington, NJ*, 2007.

383. T. Jardiel, M. T. Caldes, F. Moser, J. Hamon, G. Gauthier and O. Joubert, *Solid State Ionics*, 2010, **181**, 894-901.

384. T. Delahaye, T. Jardiel, O. Joubert, R. Laucournet, G. Gauthier and M. T. Caldes, *Solid State Ionics*, 2011, **184**, 39-41.

385. W. Bao, H. Guan and J. Cheng, *Journal of Power Sources*, 2008, **175**, 232-237.

386. S. W. Tao and J. T. S. Irvine, *J. Mater. Chem.*, 2002, **12**, 2356-2360.

387. Tao, J. Canales-Vázquez and J. T. S. Irvine, *Chemistry of Materials*, 2004, **16**, 2309-2316.

388. C. Bernuy-Lopez, M. Allix, C. A. Bridges, J. B. Claridge and M. J. Rosseinsky, *Chemistry of Materials*, 2007, **19**, 1035-1043.

389. Y.-H. Huang, R. I. Dass, J. C. Denyszyn and J. B. Goodenough, *Journal of The Electrochemical Society*, 2006, **153**, A1266-A1272.

390. Y. Ji, Y.-H. Huang, J.-R. Ying and J. B. Goodenough, *Electrochemistry Communications*, 2007, **9**, 1881-1885.

391. D. Marrero-López, J. Peña-Martínez, J. C. Ruiz-Morales, M. C. Martín-Sedeño and P. Núñez, *Journal of Solid State Chemistry*, 2009, **182**, 1027-1034.

392. D. Marrero-López, J. Peña-Martínez, J. C. Ruiz-Morales, D. Pérez-Coll, M. C. Martín-Sedeño and P. Núñez, *Solid State Ionics*, 2007, **178**, 1366-1378.

393. D. Marrero-López, J. Peña-Martínez, J. C. Ruiz-Morales, D. Pérez-Coll, M. A. G. Aranda and P. Núñez, *Materials Research Bulletin*, 2008, **43**, 2441-2450.

394. P. Zhang, Y.-H. Huang, J.-G. Cheng, Z.-Q. Mao and J. B. Goodenough, *Journal of Power Sources*, 2011, **196**, 1738-1743.

395. T. Wei, Y. Ji, X. Meng and Y. Zhang, *Electrochemistry Communications*, 2008, **10**, 1369-1372.

396. C. Li, W. Wang, N. Zhao, Y. Liu, B. He, F. Hu and C. Chen, *Applied Catalysis B: Environmental*, 2011, **102**, 78-84.

397. L. Zhang, Q. Zhou, Q. He and T. He, *Journal of Power Sources*, 2010, **195**, 6356-6366.

398. G. Xiao, Q. Liu, X. Dong, K. Huang and F. Chen, *Journal of Power Sources*, 2010, **195**, 8071-8074.

399. S. Vasala, M. Lehtimäki, Y. H. Huang, H. Yamauchi, J. B. Goodenough and M. Karppinen, *Journal of Solid State Chemistry*, 2010, **183**, 1007-1012.

400. Q. Liu, X. Dong, G. Xiao, F. Zhao and F. Chen, *Advanced Materials*, 2010, **22**, 5478-5482.

401. S. Vasala, M. Lehtimäki, S. C. Haw, J. M. Chen, R. S. Liu, H. Yamauchi and M. Karppinen, *Solid State Ionics*, 2010, **181**, 754-759.

402. L. A. Chick, J. Liu, J. W. Stevenson, T. R. Armstrong, D. E. McCready, G. D. Maupin, G. W. Coffey and C. A. Coyle, *Journal of the American Ceramic Society*, 1997, **80**, 2109-2120.

403. A. Kumar, P. S. Devi and H. S. Maiti, *Chemistry of Materials*, 2004, **16**, 5562-5563.

404. S. Ghosh, A. D. Sharma, R. N. Basu and H. S. Maiti, *Journal of the American Ceramic Society*, 2007, **90**, 3741-3747.

405. V. Vashook, L. Vasylechko, J. Zosel, W. Gruner, H. Ullmann and U. Guth, *Journal of Solid State Chemistry*, 2004, **177**, 3784-3794.

406. V. Vashook, L. Vasylechko, J. Zosel and U. Guth, *Solid State Ionics*, 2003, **159**, 279-292.

407. V. Vashook, L. Vasylechko, J. Zosel, R. Müller, E. Ahlborn and U. Guth, *Solid State Ionics*, 2004, **175**, 151-155.

408. X. Dong, S. Ma, K. Huang and F. Chen, *International Journal of Hydrogen Energy*, 2012, **37**, 10866-10873.

409. Y. Zheng, C. Zhang, R. Ran, R. Cai, Z. Shao and D. Farrusseng, *Acta Materialia*, 2009, **57**, 1165-1175.

410. J. C. Fisher Ii and S. S. C. Chuang, *Catalysis Communications*, 2009, **10**, 772-776.

411. M. Lo Faro, D. La Rosa, I. Nicotera, V. Antonucci and A. S. Aricò, *Electrochimica Acta*, 2009, **54**, 5280-5285.

412. T.-J. Huang, C.-L. Chou, W.-J. Chen and M.-C. Huang, *Electrochemistry Communications*, 2009, **11**, 294-297.

413. M. Lo Faro, D. La Rosa, I. Nicotera, V. Antonucci and A. S. Aricò, *Applied Catalysis B: Environmental*, 2009, **89**, 49-57.

414. P. Ciambelli, S. Cimino, S. De Rossi, L. Lisi, G. Minelli, P. Porta and G. Russo, *Applied Catalysis B: Environmental*, 2001, **29**, 239-250.

415. V. Stathopoulos, V. Belessi and A. Ladavos, *Reaction Kinetics and Catalysis Letters*, 2001, **72**, 49-55.

416. P. Porta, S. Cimino, S. De Rossi, M. Faticanti, G. Minelli and I. Pettiti, *Materials Chemistry and Physics*, 2001, **71**, 165-173.

417. S. M. Bukhari and J. B. Giorgi, *Solid State Ionics*, 2009, **180**, 198-204.

418. S. M. Bukhari and J. B. Giorgi, *Journal of Power Sources*, 2012, **198**, 51-58.

419. L. J. Csányi and K. Jáky, *Journal of Molecular Catalysis A: Chemical*, 1999, **145**, 229-235.

420. M. Y. Shin, D. W. Park and J. S. Chung, *Applied Catalysis B: Environmental*, 2001, **30**, 409-419.

421. Z. Xu, J.-L. Luo, K. T. Chuang and A. R. Sanger, *The Journal of Physical Chemistry C*, 2007, **111**, 16679-16685.

422. S. Hui and A. Petric, *Solid State Ionics*, 2001, **143**, 275-283.

423.   L. Aguilar, S. Zha, S. Li, J. Winnick and M. Liu, *Electrochemical and Solid-State Letters*, 2004, **7**, A324-A326.

424.   L. Aguilar, S. Zha, Z. Cheng, J. Winnick and M. Liu, *Journal of Power Sources*, 2004, **135**, 17-24.

425.   C. Peng, J. Luo, A. R. Sanger and K. T. Chuang, *Chemistry of Materials*, 2009, **22**, 1032-1037.

426.   J.-S. Park, I. D. Hasson, M. D. Gross, C. Chen, J. M. Vohs and R. J. Gorte, *Journal of Power Sources*, 2011, **196**, 7488-7494.

427.   Z. Cheng, S. Zha, L. Aguilar, D. Wang, J. Winnick and M. Liu, *Electrochemical and Solid-State Letters*, 2006, **9**, A31-A33.

428.   N. Danilovic, J.-L. Luo, K. T. Chuang and A. R. Sanger, *Journal of Power Sources*, 2009, **192**, 247-257.

429.   N. Danilovic, J.-L. Luo, K. T. Chuang and A. R. Sanger, *Journal of Power Sources*, 2009, **194**, 252-262.

430.   C. T. G. Petit, R. Lan, P. I. Cowin, J. T. S. Irvine and S. Tao, *Journal of Materials Chemistry*, 2011, **21**, 525-531.

431.   L. Adijanto, V. Balaji Padmanabhan, R. Kungas, R. J. Gorte and J. M. Vohs, *Journal of Materials Chemistry*, 2012, **22**, 11396-11402.

432.   A. Aguadero, C. de la Calle, J. A. Alonso, D. Pérez-Coll, M. J. Escudero and L. Daza, *Journal of Power Sources*, 2009, **192**, 78-83.

433.   P. R. Slater and J. T. S. Irvine, *Solid State Ionics*, 1999, **120**, 125-134.

434.   P. R. Slater and J. T. S. Irvine, *Solid State Ionics*, 1999, **124**, 61-72.

435.   Q. Li and V. Thangadurai, *Journal of Power Sources*, 2011, **196**, 169-178.

436.   O. Porat, C. Heremans and H. L. Tuller, *Solid State Ionics*, 1997, **94**, 75-83.

437.   J. J. Sprague and H. L. Tuller, *Journal of the European Ceramic Society*, 1999, **19**, 803-806.

438.   A. Kaiser, J. L. Bradley, P. R. Slater and J. T. S. Irvine, *Solid State Ionics*, 2000, **135**, 519-524.

439.   P. Holtappels, F. W. Poulsen and M. Mogensen, *Solid State Ionics*, 2000, **135**, 675-679.

440.   Z. Q. Deng, H. J. Niu, X. J. Kuang, M. Allix, J. B. Claridge and M. J. Rosseinsky, *Chemistry of Materials*, 2008, **20**, 6911-6916.

441. A. Lashtabeg, J. Irvine and A. Feighery, *Ionics*, 2003, **9**, 220-226.

442. C. M. Reich, A. Kaiser and J. T. S. Irvine, *Fuel Cells*, 2001, **1**, 249-255.

443. A. Lashtabeg, J. Canales-Vazquez, J. T. S. Irvine and J. L. Bradley, *Chemistry of Materials*, 2009, **21**, 3549-3561.

444. J. C. Pérez Flores and F. García-Alvarado, *Solid State Sciences*, 2009, **11**, 207-213.

445. J. C. Ruiz-Morales, J. Canales-Vázquez, B. Ballesteros-Pérez, J. Peña-Martínez, D. Marrero-López, J. T. S. Irvine and P. Núñez, *Journal of the European Ceramic Society*, 2007, **27**, 4223-4227.

446. J. C. Ruiz-Morales, D. Marrero-Lopez, J. Canales-Vazquez and J. T. S. Irvine, *RSC Advances*, 2011, **1**, 1403-1414.

447. D. M. Bastidas, S. Tao and J. T. S. Irvine, *Journal of Materials Chemistry*, 2006, **16**, 1603-1605.

448. J. C. Ruiz-Morales, J. Canales-Vázquez, J. Peña-Martínez, D. M. López and P. Núñez, *Electrochimica Acta*, 2006, **52**, 278-284.

449. H. Gu, Y. Zheng, R. Ran, Z. Shao, W. Jin, N. Xu and J. Ahn, *Journal of Power Sources*, 2008, **183**, 471-478.

450. Y. Zhang, Q. Zhou and T. He, *Journal of Power Sources*, 2011, **196**, 76-83.

451. K. Yamaji, H. Kishimoto, Y. Xiong, T. Horita, N. Sakai, M. E. Brito and H. Yokokawa, *Journal of Power Sources*, 2006, **159**, 885-890.

452. Z. Zhan and S. A. Barnett, *Science*, 2005, **308**, 844.

453. C. Su, R. Ran, W. Wang and Z. Shao, *Journal of Power Sources*, 2011, **196**, 1967-1974.

454. H. Yokokawa, K. Yamaji, M. E. Brito, H. Kishimoto and T. Horita, *Journal of Power Sources*, 2011, **196**, 7070-7075.

455. A. L. Vincent, J.-L. Luo, K. T. Chuang and A. R. Sanger, *Applied Catalysis B: Environmental*, 2011, **106**, 114-122.

456. N. Danilovic, J.-L. Luo, K. T. Chuang and A. R. Sanger, *Journal of Power Sources*, 2009, **192**, 247-257.

457. R. Prins, V. H. J. De Beer and G. A. Somorjai, *Catalysis Reviews: Science and Engineering*, 1989, **31**, 1 - 41.

458. Z.-R. Xu, J.-L. Luo and K. T. Chuang, *Journal of Power Sources*, 2009, **188**, 458-462.

459. V. Vorontsov, W. An, J. L. Luo, A. R. Sanger and K. T. Chuang, *Journal of Power Sources*, 2008, **179**, 9-16.

460. V. Vorontsov, J. L. Luo, A. R. Sanger and K. T. Chuang, *Journal of Power Sources*, 2008, **183**, 76-83.

461. C. Jin, C. Yang, F. Zhao, A. Coffin and F. Chen, *Electrochemistry Communications*, 2010, **12**, 1450-1452.

462. J. P. Trembly, R. S. Gemmen and D. J. Bayless, *Journal of Power Sources*, 2007, **169**, 347-354.

463. O. A. Marina, L. R. Pederson, E. C. Thomsen, C. A. Coyle and K. J. Yoon, *Journal of Power Sources*, 2010, **195**, 7033-7037.

464. G. Krishnan, *Proceedings of the 8th Annual SECA Review Workshop. San Antonio, TX*, 2007.

465. J. P. Trembly, R. S. Gemmen and D. J. Bayless, *Journal of Power Sources*, 2007, **171**, 818-825.

466. H. F. M. Zhi, N. Madhiri, I. Celik, B. Kang, X. Liu, N.Q. Wu, *Proceedings of the 212th ECS Meeting, Washington, DC*, 2007.

467. M. Gong, D. Bierschenk, J. Haag, K. R. Poeppelmeier, S. A. Barnett, C. Xu, J. W. Zondlo and X. Liu, *Journal of Power Sources*, 2010, **195**, 4013-4021.

2. Experimental Techniques

This chapter begins by explaining the background of the main characterisation techniques used in this thesis and how these techniques are applied to SOFC electrode materials. Fuel cell testing through electrochemical impedance spectroscopy and DC techniques is explained. This is followed by a description of the approach to different synthesis methods and the respective benefits of each procedure.

2.1. Characterisation

2.1.1. X-Ray Diffraction

X-ray diffraction (XRD) is a characterisation technique used to determine the bulk crystal structure of a solid material. This technique exposes a sample to a monochromatic x-ray beam and records the intensity of the scattered radiation whilst varying the angle of reflection. Scattering of x-rays from the sample can occur either elastically, changing direction whilst maintaining the beam energy, or inelastically, a change in direction with a variation in the energy of the beam, with XRD measuring the intensity of the elastic scatterers. The resultant pattern of intensities at each angle is determined by the periodic arrangement of atoms in the bulk material. The x-ray diffraction pattern can be used to determine the structure of the compound by either indexing the pattern to an identical or similar pattern using a structural database or by judgement of the crystal system and determination of the potential lattice parameters. The technique can also be used to determine various crystalline structures in a mixture of phases and even, with further analysis, determine the relative proportion of the phases within the mixture.

Atoms occupying the same crystallographic positions occur periodically in three dimensions throughout the bulk material. Considering an atom on a single crystallographic position and disregarding all others, the atoms would appear to form distinct planes throughout the sample. Diffraction of x-rays in solids occurs due to the

reflection of the x-rays from the electron cloud surrounding the atomic nucleus. Diffraction from atoms occupying the same crystallographic position will diffract at the same angle, with the resultant waves interacting constructively to strengthen the output signal. Constructive interference occurs when interacting waves, which share the same wavelength, are in phase with each other, i.e. are shifted by a multiple of 2π. Destructive interference, complete negation of the output signal, will occur when the interacting waves are out of phase, i.e. shifted by half a wavelength. The interaction between the waves, with a changing angle of incidence, results in a variation in intensity of the output signal, dependent on the relative positions of the atoms in the periodic structure. Diffraction from a three dimensional periodic structure is known as Bragg diffraction, with constructive interference between crystal 'planes' demonstrated by the Bragg equation, as shown in Figure 2.1 and Equations 2.1 to 2.4, where d is the distance between the 'planes', λ is the wavelength and n is a positive integer.
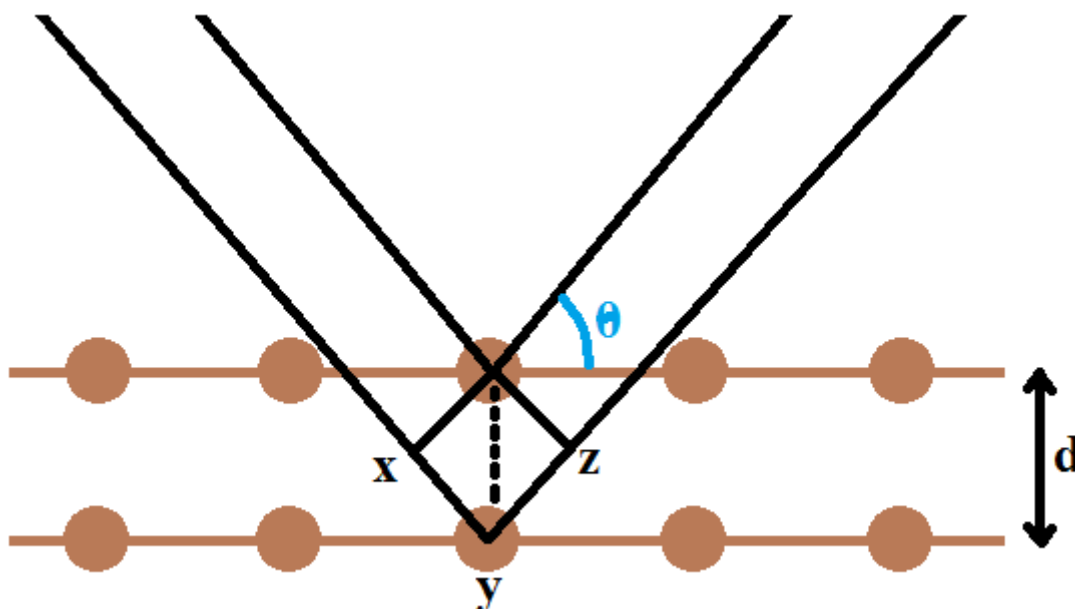
Figure 2.1. Scattering from parallel 'planes' of atoms in a compound

$$xy = yz = d \sin \theta \qquad (2.1)$$
$$xyz = 2d \sin \theta \qquad (2.2)$$
$$xyz = n\lambda \qquad (2.3)$$
$$n\lambda = 2d \sin \theta \qquad (2.4)$$

The Bragg Equation

The angle at which the peaks occur is indicative of atomic positions within the structure, whilst peak intensity can be influenced by a wide range of instrumental and powder properties. The integrated intensity of a peak is mainly governed by the structure factor, the multiplicity, the Lorenz and polarisation factors and the temperature factor, although additional factors such as absorption, preferred orientation and extinction may also influence the peak intensity. The structure factor incorporates the interference of other atoms in the unit cell on the intensity of a peak. This is achieved through summation of the elements in the unit cell for the hkl values of each peak, multiplied by their atomic scattering factors (the measure of the scattering amplitude of a wave by an isolated atom). The multiplicity of the peak is given by the number of equivalent hkl 'planes', with the intensity of the peak proportional to its multiplicity. The Lorenz factor takes into account the dependence of the intensity on the angle of the incident beam, which reduces with an increase in the angle, whilst the polarisation factor accounts for the effect of the angular difference between the scattered beam and the electric field gradient. Increasing atomic vibration leads to a reduction in the scattering factor of the atom, reducing peak intensity. As atomic vibration is temperature dependent, the temperature factor is used to account for the thermal displacement effects.

For particles smaller than 0.1-0.2 μm, the particle size of the powder can be calculated from the broadness of the peak using the Scherrer equation, Equation 2.5, where τ is the mean size of the ordered domains, K is the shape factor, (usually ~ 0.9) λ is the x-ray wavelength, β is the line broadening at half maximum intensity and θ is the Bragg angle.

$$\tau = \frac{K\lambda}{\beta cos\theta} \qquad (2.5)$$

The Scherrer equation

Additional information on the crystal structure can also be attained through the use of neutron diffraction, which uses a neutron beam in the place of an x-ray beam to probe the bulk structure. As x-ray scattering occurs from interaction with the electron cloud and neutron scattering occurs from the atomic nucleus, the intensity of x-ray scattering is significantly larger for atoms with a higher atomic number, whilst neutron diffraction is highly dependent on the isotope of the element. Scattering of x-rays from an electron cloud is dependent on the scattering power of the atom, which decreases as the angle of incidence increases, therefore at high angles the intensity of the peaks for x-ray diffraction reduces significantly. As neutrons interact with the nucleus, the scattering does not exhibit this angle dependency and therefore additional detail is exhibited at high angles.

Analysis of the observed diffraction pattern is usually achieved through comparison to a database of diffraction patterns, such as the Inorganic Crystal Structure Database (ICSD), which can be used to match the experimental and database structures according to their peak positions. Complex mixture of compounds can be differentiated with knowledge of the elemental composition of the material, however this becomes more complex with increases in the number of compounds and elements. This is simplified by the use of computer programs, such as Bruker's EVA and Crystal Impact's Match!, which allow comparison of the experimental data with multiple standard diffractions patterns simultaneously. These programs can also aid in identifying the structure of novel materials through comparison to previous materials with a similar elemental composition.

If the material has not previously been synthesised or characterised then determination of the crystal structure is possible through judgement of the potential crystal system and calculation of the potential lattice parameters. This approach uses the relationship between the diffraction angle, Miller indices and lattice parameters for

the proposed crystal system to construct a plot which incorporates all Miller indices for a range of lattice parameters. This plot is then compared to the experimental pattern to derive potential lattice parameters for the compound. This approach is rarely utilised nowadays due to the rise of computational programs tailored for this purpose.

The use of computational refinement programs, such as TOPAS and GSAS [1], can be used to for further elucidation of the crystal structure of the materials. These programs utilise a Least Squares refinement of a theoretical crystal structure, the parameters for which must be manually input, through determination of the x-ray diffraction pattern and comparison to the experimental data. The 'goodness of fit' is then determined and used to assess the suitability of the theoretical model. Refinement of various instrument and atomic parameters can be used to further improve the fit of theoretical model.

One of the drawbacks to the use of XRD for the determination of phase purity is that resolution of impurity phases is limited to ~ 1wt%, which means that the presence of secondary phases below this limit cannot be discounted. Identification of secondary phases with a <1% weight fraction have to be determined through alternative techniques such as scanning electron microscopy (SEM) or transmission electron microscopy (TEM).

2.1.2. Simultaneous Thermal Analysis

Simultaneous thermal analysis (STA) combines thermogravimetric analysis (TGA) and differential scanning calorimetry (DSC) to determine the physical and chemical changes to a compound over a temperature range under a controlled atmosphere. STA utilises a microbalance to accurately measure the weight of the sample whilst a thermocouple measures the furnace temperature and separate thermocouples attached to the crucibles monitor the temperature difference between the sample and reference. The sample is mounted in a platinum or alumina crucible, accurately weighed and placed in a furnace alongside an empty crucible, which acts as a reference. As the sample is heated and cooled, as dictated by the temperature profile, the sample weight and heat flow are observed and correlated to the temperature plot.

Thermogravimetric analysis measures the weight change of the sample with changes in temperature. For most SOFC materials the processes which elicit changes in weight are usually simple to interpret, such as losses in weight due to either compound degradation or loss of oxygen due to cationic reduction in reducing atmospheres. The use of both oxidising and reducing conditions allows comparison of the relative stability of these materials in these environments and conclusions as to the material stability to be drawn.

Heat flow differential scanning calorimetry measures the difference in the temperature between a sample and a reference over an identical temperature program. This differs from differential thermal analysis (DTA) in that a thermally conductive connector links the sample and reference, ensuring that any change in the temperature of the sample results in a heat flow between the sample and reference. The increase in the accuracy and resolution of the heat flow DSC system provides an advantage over DTA systems. Power controlled differential scanning calorimetry uses separate furnaces for the sample and reference and maintain a negligible temperature difference by modifying the power input to each furnace. As chemical processes are either endothermic or exothermic, an absorption or emission of energy from the sample will register as an increase or decrease in the heat flow or sample temperature, respectively. This can be correlated with TGA data to further elucidate the physical or chemical processes under the desired conditions.

2.1.3. Conductivity and Fuel Cell Testing

Alternating current (A.C.) and direct current (D.C.) conductivity measurement techniques determine the electrical conductivity of samples through application of a current between two electrodes and measurement of the resulting potential difference (voltage), utilising a measurement jig such as that exhibited in Figure 2.2 (a). Electrical conductivity does not distinguish between charge carriers, thus both electronic and ionic conductivity are observed. Separation of the electronic and ionic segments of the total conductivity can be achieved through the use of blocking electrodes, which are ionic, but not electronic conductors.

Measurement of the electrical conductivity of highly conductive materials is generally achieved using direct current methods, as A.C. techniques are limited by the resistance of the instrument ($\sim 0.01\ \Omega$). Additionally, the sample collection time is also significantly lower for D.C. techniques, in the order of s^{-1} compared to min^{-1} for A.C methods, which allows for a higher resolution of the changes in the response of a system over time. Despite the limitations of A.C. techniques, the oscillation of the frequency of the current imparts additional information on the electrochemical processes, such as separation of bulk and grain boundary contributions to the total conductivity.

Throughout this body of work the majority of conductivity measurements are taken using D.C. techniques due to the resistance of the samples, which were on the scale of $0.01\ \Omega$ – $0.0001\ \Omega$ for pellets of ~12mm diameter and 1mm thickness. The testing was also completed using a 2-probe technique, which has a single point of contact for the current and voltage probe, rather than a 4-probe technique, which has two separate voltage probes bounded by two current probes. Separation of the current and voltage probes ensures that the voltage drop in the current wires does not contribute to the voltage measurement, reducing the error in the measurement.

As the 4-probe method requires larger pellets, to incorporate the separation of the voltage and current probes, the known difficulty in preparation of small dense test pellets, and the volume of samples, meant that the time constraints during the body of

work favoured the use of the 2-probe technique. Additionally, the increased resistance of the larger pellets for the 4-probe technique would require the use of AC impedance measurements, which further increases the time required for each measurement. Whilst the 4-probe technique is accepted to be the preferable technique for accurately determining the conductivity of a sample, the additional demands on experimental requirements must also be considered when starting a series of measurements.

The pellets testing in this study were not of optimal density for conductivity measurements, between 80 and 90% of the theoretical density, due to difficulties in obtaining dense pellets during sintering. Density corrections for conductivity measurements are not possible due to the number of variables to be taken into account, and potentially a non-linear relationship may be observed. An assumption was made that the termination ink used as a current collector had a negligible contribution to the observed resistance. At room temperature, the resistance across the surface of a pellet coated with dried ink could not be observed using a multimeter and literature values of the electronic conductivity of silver suggests that the magnitude of the resistance is an order of magnitude below those observed in this study [2].
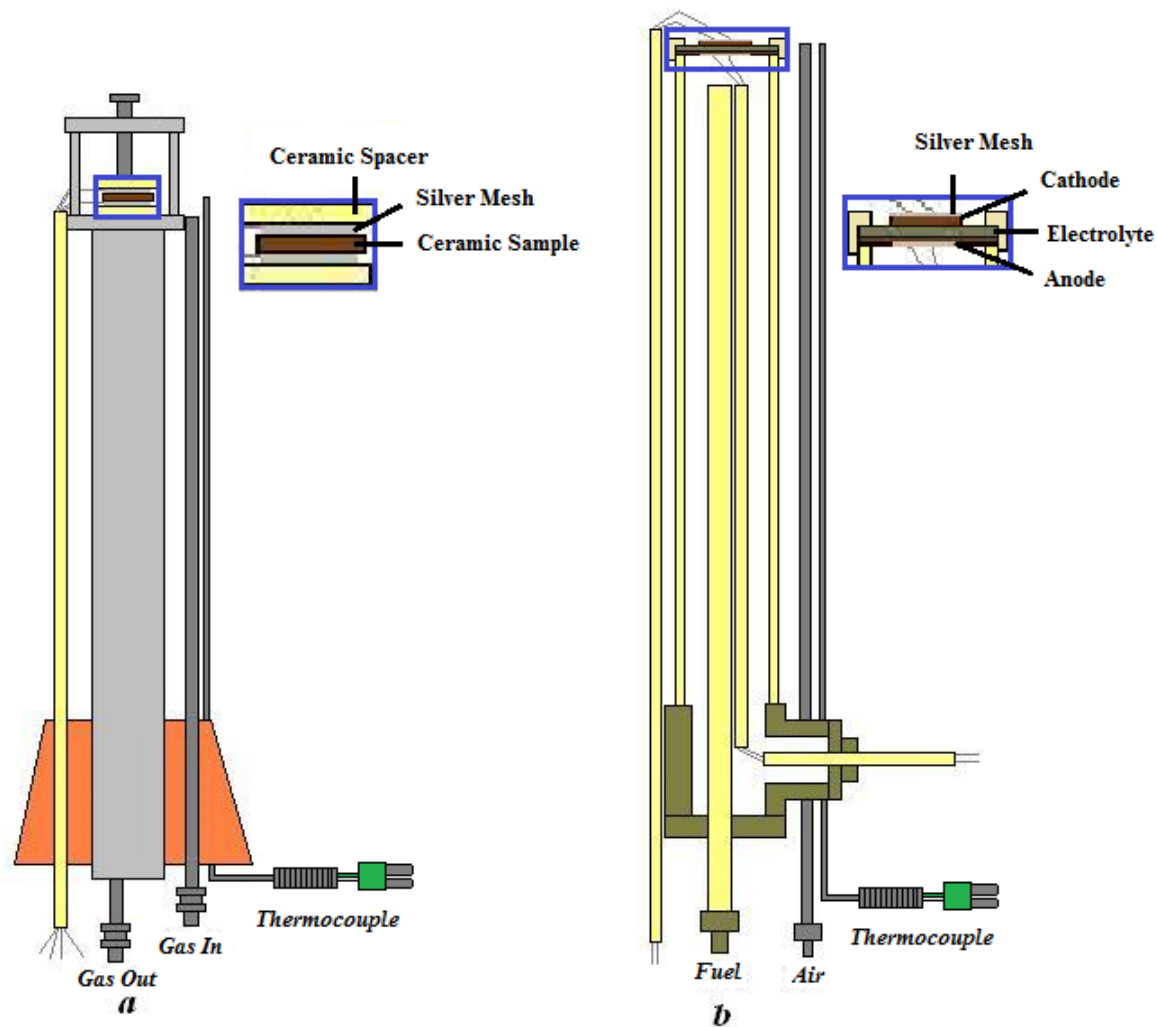
Figure 2.2. Schematic of a jig for conductivity testing (a) and fuel cell testing (b)

The difference in the analysis of alternating and direct current can be observed in the mathematical response to the current, with direct current eliciting a linear response to the stimuli whilst alternating current results in a complex response with both real and imaginary components. The measurement of the conductivity using direct current techniques involves application of a constant current, usually ~ 1 A, and measurement of the resultant voltage. The resistance is determined through use of Ohm's law, Equation 2.6, in which V is the voltage, I is the current and R is the resistance.

$$V = IR \tag{2.6}$$

Ohm's Law

From the resistance of the sample (R), the conductivity of the sample (σ) can be calculated given its length (l) and area (A), as shown in Equation 2.7.

$$\sigma = \frac{1}{R} \times \frac{l}{A} \tag{2.7}$$

Conductivity of a sample of length l and area A

Alternating current techniques utilise an alternating potential difference, oscillating with frequency (f) and angular frequency (ω, ω = 2πf), resulting in an oscillating current output, with a phase shift (φ). The phase shift of the output current occurs due to the delay between the input and output signals. The impedance (Z), or resistance, of the system is given by applying Ohm's law to the signals, as demonstrated in Equations 2.8 to 2.13, and can be further simplified, using Euler's relationship (exp(iφ) = cos(φ) + $i$sin(φ)), to be expressed as a complex number.

$$V_t = V_0 \sin(\omega t), \tag{2.8}$$

$$I_t = I_0 \sin(\omega t + \varphi) \tag{2.9}$$

$$Z(\omega) = \frac{V(\omega)}{I(\omega)} = \frac{V_0 \sin(\omega t)}{I_0 \sin(\omega t + \varphi)} = Z_0 \frac{\sin(\omega t)}{\sin(\omega t + \varphi)} \tag{2.10}$$

$$\text{As } e^{i\varphi} = cos\varphi + isin\varphi, \tag{2.11}$$

$$\text{thus } V_t = V_0 e^{i\omega t}, \ I_t = I_0 e^{i\omega t + \varphi} \tag{2.12}$$

$$Z(\omega) = \frac{V_0 e^{i\omega t}}{I_0 e^{i(\omega t + \varphi)}} = Z_0 (cos\varphi - isin\varphi) \tag{2.13}$$

Derivation of the expression of impedance as a complex number

Plotting of impedance data involves splitting of the impedance of the system into real (Z') and imaginary terms (Z''), forming respectively the x-axis and y-axis of an Nyquist plot, Figure 2.3 Whilst the resistance of the system is solely associated with the real impedance term, other processes, such as inductance and capacitance may impact on the imaginary component. For conductivity and fuel cell measurements, inductance, the formation of an electromotive force in an electrical circuit as a result of changes in the current, is generally associated with interference from the measuring instrument or the connections to the equipment.

During electrochemical processes some of the charge may be retained, or stored, within the conducting material, according to the capacitance of the sample. As most experimental electrochemical processes result in the storage of some charge, a combination of a resistance and capacitance is often observed. Derivation of the impedance of these processes, as shown in Equations 2.13 to 2.21 results in formation of a semicircle on the Nquist plot, Figure 2.3.

The charge stored (Q) is dependent on the potential difference (V) and the capacitance (C),

$$Q = CV \tag{2.14}$$

A change in the voltage results in a current (I),

$$I = \frac{dQ}{dt} = C\frac{dV}{dt} \tag{2.15}$$

For an alternating voltage,

$$I(t) = C\frac{V_0 e^{i\omega t}}{dt} = iCV_0 e^{i\omega t} \tag{2.16}$$

Which results in an admittance (Y, Y=1/Z),

$$Y_c(\omega) = \frac{I(\omega)}{V(\omega)} = i\omega C \tag{2.17}$$

Therefore the admittance of a combined resistance and capacitance gives,

$$Y(\omega) = \frac{1}{R} + i\omega C \tag{2.18}$$

$$Z(\omega) = \frac{1}{Y(\omega)} = \frac{1}{\frac{1}{R}+i\omega C} \cdot \frac{\frac{1}{R}-i\omega C}{\frac{1}{R}-i\omega C} = \frac{R-i\omega R^2 C}{1+\omega^2 R^2 C^2} \tag{2.19}$$

$$\tau = RC \qquad (2.20)$$

$$Z(\omega) = R \frac{1 - i\omega\tau}{1 + \omega^2\tau^2} \qquad (2.21)$$

Impedance of a resistance and a capacitance

As Electrical Impedance Spectroscopy (EIS) utilises an alternating current to probe electrochemical phenomena, variation of the frequency of the oscillation of the current provides a differing timeframe of measurement at each frequency, separating various electrochemical processes. Different electrochemical processes have different capacitances due to the varying duration of the process, with representative figures given in Table 2.1, which allows for identification and separation of each process from the impedance data.

Capacitance (F)	Related Process
10^{-12}	Bulk
10^{-11}	Minor Second Phase
10^{-11}-10^{-8}	Grain Boundary
10^{-10}-10^{-9}	Bulk Ferroelectric
10^{-9}-10^{-5}	Surface Layer
10^{-7}-10^{-5}	Sample Electrode Interface
10^{-4}	Electrochemical Reaction

Table 2.1. The capacitance of various electrochemical processes from EIS[3]

Equivalent circuit diagrams utilise electrical symbols, such as those listed in Table 2.2, to construct a theoretical model of a physical circuit, such as those measured using EIS. The theoretical model can then be fitted to the experimental data to elucidate further information about the system. These circuits can also be translated into circuit description code (CDC), Table 2.2, which is a format suitable for computer processing.

Symbol	Circuits Description Code	Element
▭	R	Resistor
‖	C	Capacitor
⟿	I	Inductor
W	W	Warburg (diffusion) Impedance
≫	Q	Constant Phase Element

Table 2.2. Electrical symbols and the corresponding electrochemical processes

Modelling an ideal equivalent circuit can utilise RC elements, however this assumes a perfect capacitance, therefore constant phase elements (Q) are generally used to account for non-ideal capacitance. Diffusion of reactants to the interface can also result in an impedance, known as a Warburg impedance, although this is mainly observed for low temperature systems. Assuming an infinite potential diffusion length, the impedance will increase linearly with reducing frequency due to the longer diffusion length for the reactants, which is observed on an Nyquist plot, Figure 2.3, as a 45° line at low frequencies. For instances in which the diffusion length is limited, a bounded Warburg is observed, which is initially observed as a 45° line transforming to a resistive semicircle upon reducing frequency. Various simple circuits, exhibited as a circuit diagram, in CDC and as would be observed through EIS, are demonstrated in Figure 2.3.
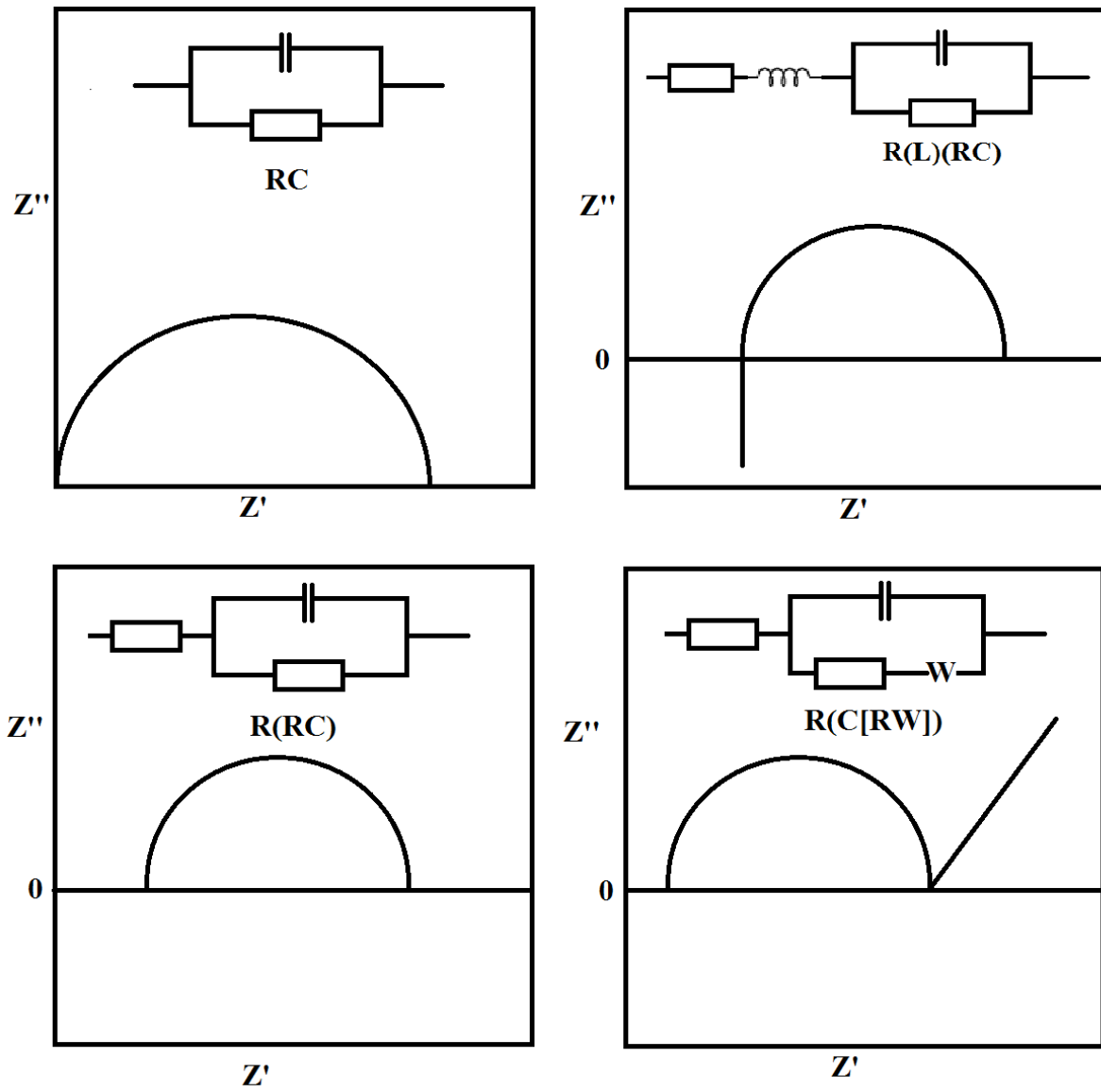
Figure 2.3. Nyquist plots of simple circuits

Analysis of fuel cell performance utilises both A.C. and D.C. techniques to characterise the losses observed during fuel cell operation, using the jig detailed in Figure 2.1 (b).

Open circuit voltage (OCV) measurements, as shown in Figure 2.4, determine the potential difference between the anode and cathode under no applied current. The actual OCV of the cell can be compared to the theoretical OCV, calculated from the Gibbs free energy of the reactants, and a measure of the efficiency of the cell can be determined. The difference between the theoretical and observed OCV is mainly due to incomplete fuel oxidation.
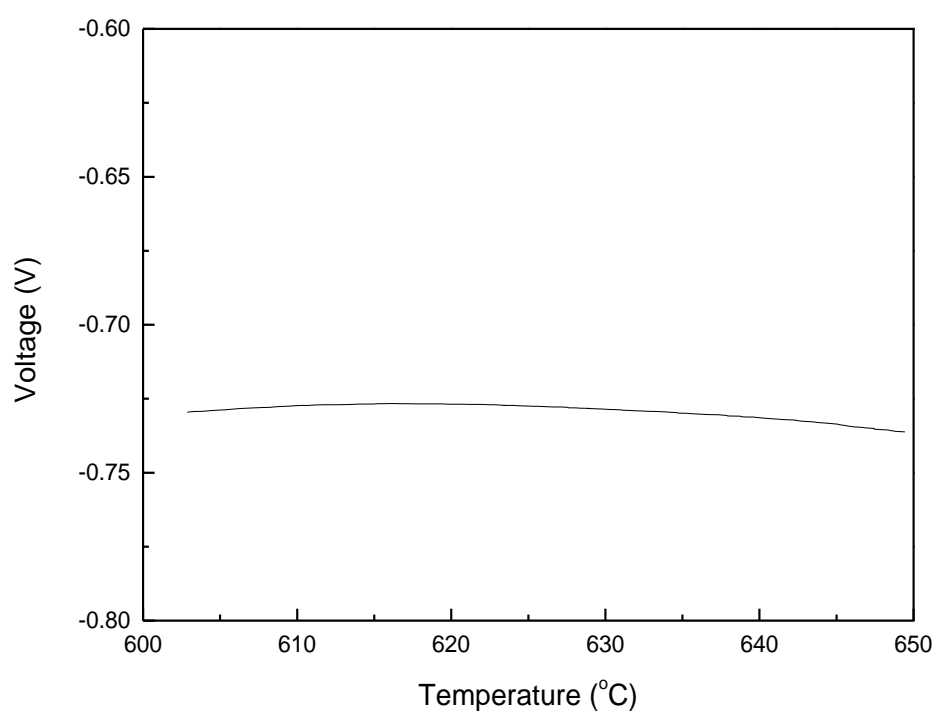
Figure 2.4. Sample fuel cell operation from 600 °C to 650 °C under open circuit voltage

These losses can be further elucidated through analysis of current voltage (I-V) curves, which incrementally reduce the voltage from the open circuit voltage to zero whilst measuring the resultant current, as exhibited in Figure 1.2. Observation of the current-voltage curves elucidates the contributions to losses during fuel cell

operation from the anodic/cathodic reactions (activation polarisation), the electrical resistance (ohmic polarisation) and the mass transport resistance (concentration polarisation).

Determination of the power density of the fuel cell can be achieved through manipulation of the data from the I-V curve using Equation 2.22, in which P is the power density, V is the applied voltage and J is the current density.

$$P \ (Wm^{-3}) = JV \qquad (2.22)$$

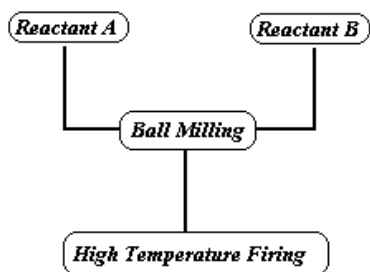Calculation of the power density of a fuel cell

Maximum power density, the highest observed power density achieved during the measurement, is a general parameter used to easily compare the performance of fuel cells configurations and composition.

EIS is also used extensively in fuel cell analysis to determine the various resistances which exist during fuel cell operation. Fuel cell impedance is comprised of contributions from anodic, cathodic and electrolytic sources, although, due to the similar time constants of both anodic and cathodic processes, the charge transfer resistance of the electrodes often overlaps. Actual electrodic resistance can be determined through EIS of a fuel cell using identical electrodes and gas feeds.
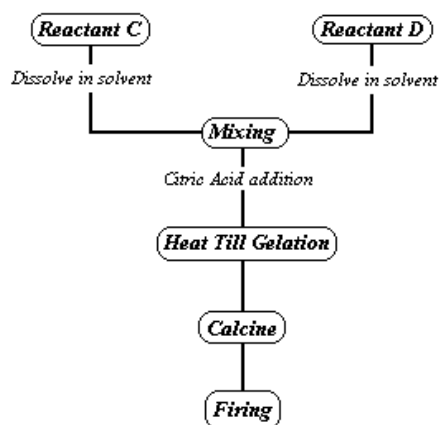
2.2. Synthesis Methods

Variation of powder synthesis methods can have a profound effect on the product, with significant changes in grain size, sinterability and material properties. The use of solid state synthesis techniques is prevalent in the development of novel materials due to both the simplicity of the method and the low manufacturing cost. Solid state synthesis involves the homogenisation of reactants prior to high temperature firing, usually utilising mechanical grinding and mixing techniques. This process is slow as powder homogenisation occurs on the particulate level, but not the atomic level. Contacting grains of different reactants will form the product at the interface, with further reaction only possible through reactant diffusion through the product layer. Solid state diffusion is limited by the diffusivity of both the reacting ions in the product, although this process can be accelerated by frequent regrinding of the sample between firing steps, reducing the boundaries between reactant grains, or by liquid phase assisted transport, which uses a liquid as a transport medium for reactant particles reducing the need for solid state diffusion. The particle size of the reactants will also affect the synthesis temperature and duration, with milling generally utilised to both reduce particle size and homogenise the powders.

The high temperatures reached during solid state synthesis can also prove problematic for some reactants, as volatisation of various materials can occur below the synthesis temperature. Wet chemical, or 'Chimie Douce, techniques for synthesising ceramic powders can be used to significantly reduce the synthesis temperatures, as these techniques achieve atomic scale mixing of the reactants. The three main wet chemical techniques; solution-gelation, combustion and co-precipitation, as exhibited in Figure 2.6, utilise solubilisation of the reactants to produce a homogenous mixture prior to reaction.
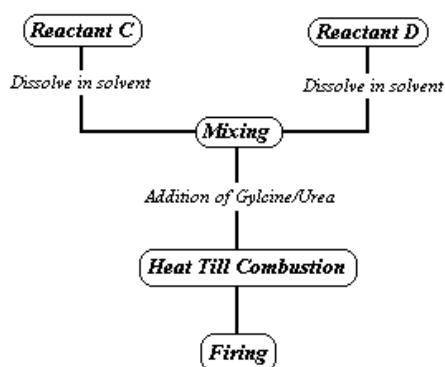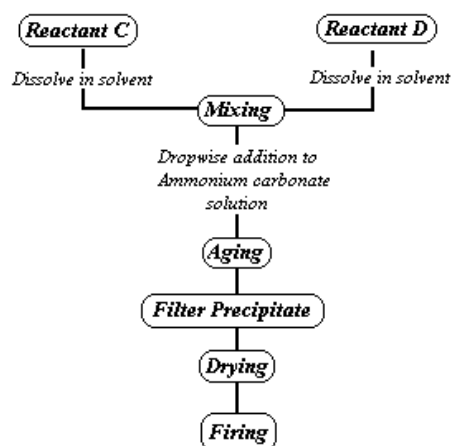
Figure 2.6. Basic Synthesis Routes for solid state (a), sol-gel (b), combustion (c) and co-precipitation (d) methods.

The basic sol-gel technique involves dissolving the requisite metal salts in a suitable solvent, usually water, adding a complexing agent, such as citric acid, and then heating the solution till gelation. The gel is then decomposed and the powder calcined to form the desired material, although a further firing step may be required for some materials.

Both urea and glycine, utilised as the fuel in combustion based synthesis techniques, form stable complexes with metal ions in solution, which, as with sol-gel

techniques, increases solubility of the reactants and prevents precipitation during solvent evaporation. Combustion techniques also form a gel after removal of a significant amount of the solvent, however this gel then auto-ignites in an exothermic, self sustaining reaction after reaching between 300 °C and 400 °C. The reactants in combustion synthesis are required to be oxidisers, such as metal nitrates, to initiate the reaction with the urea or glycine fuels. The desired product may form after combustion or may require a further firing step to form the single phase material.

Co-precipitation methods utilise variations in pH to induce precipitation of nano-size particles of metal salts from a homogenous solution of metal ions. The reactant solutions, formed from the metal hydroxides or nitrates, are added dropwise into the basic ammonium carbonate solution, resulting in precipitation of the pre-cursor powder. This powder is then washed to remove the ammonium salt and dried, prior to firing to produce the desired material.

Whilst all of these wet chemical techniques are viable for ceramic synthesis, however each method will produce slight differences in powder properties. Despite significant advantages over solid state synthesis techniques, the use of these wet-chemical techniques is not always desirable. Optimisation of 'Chimie Douce' techniques is time consuming as there are a considerable number of variables inherent in these methods. Additionally, the reactants used in these methods are frequently more expensive than the oxide analogues utilised in solid state synthesis and the solubility of some elements can be low in many solvents, limiting their usability for wet-chemical synthesis. In general solid state synthesis is primarily used to synthesise novel compounds due to the simplicity of the technique, whilst wet-chemical techniques are more prevalent when tailoring of material properties is desired or where solid state synthesis will not be successful.

Other synthesis methods for ceramic powder preparation, such as hydrothermal, molten salt and spray pyrolysis, are available but are used infrequently as many of these techniques are unsuitable for larger scale powder synthesis.

Determination of the most suitable synthesis method for each series in this thesis was partially dependent on the observed methods used in the literature and

partially on the materials available for use. For the $Sr_2FeMoO_{6-\delta}$ based materials, a traditional solid state synthesis method was utilised, due to the availability of the raw materials. Synthesis of $SrFe_{1-x}Ti_xO_{3-\delta}$ materials using sol-gel methods was a composite method based upon wet chemical synthesis of $SrFeO_{3-\delta}$ [4] and $BaTiO_{3-\delta}$ [5]. $SrBi_2Nb_2O_{9-\delta}$ synthesis using a citrate based sol-gel method [6] was used as the basis for the wet chemical synthesis of $SrFe_{1-x}Nb_xO_{3-\delta}$ materials. For dopant additions to the $SrFe_{1-x}Ti_xO_{3-\delta}$ and $SrFe_{1-x}Nb_xO_{3-\delta}$ systems, the previous synthesis method for that series was utilised with the addition of a suitable water soluble salt for the dopant. Wet chemical synthesis of both $La_xSr_{1-x}FeO_{3-\delta}$ and $Y_xSr_{1-x}FeO_{3-\delta}$ materials was based on the previous synthesis method utilised for the $SrFeO_{3-\delta}$ based compounds, substituting in the appropriate metal nitrates.

The focus on wet chemical synthesis for these materials was partially due to the improved powder properties explained previously, but also due to the available equipment, as the lowering of synthesis temperatures favoured the equipment in the laboratory. Optimisation of each synthesis method involves the calcination of the powder at a series of temperatures to determine the lowest synthesis temperature. Multiple firings at each temperature was complete until a single phase powder was obtained, where possible. Initial optimisation of the wet chemical technique used in this thesis was completed for $SrFe_{0.9}Ti_{0.1}O_{3-\delta}$ and $SrFe_{0.9}Nb_{0.1}O_{3-\delta}$, through modification of the metal ions:citric acid ratio, calcination temperatures and, for $SrFe_{0.9}Ti_{0.1}O_{3-\delta}$, variation of the ethanol:water ratio.

2.3. References

1. A. C. Larson and R. B. V. Dreele, *"General Structural Analysis System" Los Alamos National Laboratory Report LAUR*, 1994, 86.

2. C. R. Hammond, *Handbook of Chemistry and Physics, 81st Edition*, 2000, **CRC Press**.

3. J. T. Irvine, D. C. Sinclair and A. R. West, *Adv. Mater.*, 1990, **2**, 132-138.

4. H. FalcÃ³n, J. A. Barbero, J. A. Alonso, M. J. MartÃnez-Lope and J. L. G. Fierro, *Chemistry of Materials*, 2002, **14**, 2325-2333.

5. G. A. Hutchins, G. H. Maher and S. D. Ross, *American Ceramics Society Bulletin*, 1967, **66**.

6. D. Nelis, D. Mondelaers, G. Vanhoyland, A. Hardy, K. V. Werde, H. V. d. Rul, M. K. V. Bael, J. Mullens, L. C. V. Poucke and J. Dâ€™Haen, *Thermochimica Acta*, 2005, **426**, 39-48.

3. Redox stability of the electronic conductivity of molybdenum doped alkaline earth ferrites

This chapter continues investigations into strontium iron molybdenum double perovskite materials, which have previously been investigated as SOFC anode materials. The effect of calcium doping and variation of the iron-molybdenum ratio on the formability of these materials is elucidated. The effect of high temperature reduction on the properties of $Ca_2Fe_{1+x}Mo_{1-x}O_{6-\delta}$ is investigated and the stability of these properties over a single redox cycle is determined. A similar investigation is also conducted on $Sr_{1.6}K_{0.4}Fe_{1+x}Mo_{1-x}O_{6-\delta}$. The practicality of high temperature reduction for anode materials is also considered.

3.1. $Ca_2Fe_{1+x}Mo_{1-x}O_{6-\delta}$ and $CaSrFe_{1+x}Mo_{1-x}O_{6-\delta}$

3.1.1. Introduction

Development of $Sr_2(TM)MoO_{6-\delta}$ (TM = Mn, Mg, Fe, Co, Ni, Cu, Zn) as potential anode materials has already been covered in detail in Section 1.6.4.1.2. Whilst reasonable fuel cell performance has been achieved using $Sr_2MgMoO_{6-\delta}$ (642 mWcm^{-2} at 750 °C in pure H$_2$) [1], $Sr_2MnMoO_{6-\delta}$ (467 mWcm^{-2} at 750 °C in pure H$_2$) [1], $Sr_2CoMoO_{6-\delta}$ (1017 mWcm^{-2} at 800 °C in pure H$_2$) [2] and $Sr_2FeMoO_{6-\delta}$ (412 mWcm^{-2} at 750 °C in pure H$_2$) [3] anodes, of these compounds only $Sr_2MgMoO_{6-\delta}$ (SMMO) has been proven to be redox stable [4]. Despite achieving redox stability, the chemical reactivity of SMMO with common electrolytes, such as LSGM and YSZ, limits its utility [5].

Substitution of magnesium with iron has previously been shown to improve the conductivity, albeit with a reduction in the redox stability [4]. Xiao *et. al.* [6] improved both the formability and stability of $Sr_2FeMoO_{6-\delta}$ through an increase in the iron content of the sample, with $Sr_2Fe_{1.33}Mo_{0.66}O_{6-\delta}$ formed in at 800 °C in H$_2$, 300 °C below the synthesis temperature of $Sr_2FeMoO_{6-\delta}$ in 5% H$_2$/Ar [7]. The conductivity of $Sr_2Fe_{1.33}Mo_{0.66}O_{6-\delta}$ in 5% H$_2$/Ar ranges between 15 Scm^{-1} and 30 Scm^{-1} from 700 °C

to 300 °C, sufficient for an IT-SOFC anode material, although the fuel cell performance only reached 268 mWcm^{-2} at 700 °C in pure H_2. Further development of this series by Liu *et. al.* [8] formed $Sr_2Fe_{1.5}Mo_{0.5}O_{6-\delta}$ in air at 1000 °C and demonstrated high conductivity in both oxidising and reducing atmospheres. Good performance of $Sr_2Fe_{1.5}Mo_{0.5}O_{6-\delta}$ as a symmetrical electrode was achieved, attaining ~ 500 mWcm^{-2} at 800 °C in humidified H_2 with good stability over successive redox cycles.

A-site substitution of alkaline earth metals was determined to cause a significant alteration of material properties, with a reduction in cation size (from Ba to Sr to Ca) causing an increase in the conductivity and a reduction in the material stability [7]. The increase in conductivity achieved through calcium substitution would be expected to improve anodic performance, although a significant improvement in the stability of the compound is required for use in IT-SOFCs. To this end a series of compounds of iron rich calcium iron molybdates, $Ca_2Fe_{1+x}Mo_{1-x}O_{6-\delta}$ (x = 0.2, 0.4, 0.6), were synthesised to determine whether a simultaneous improvement of the conductivity and stability of these compounds was attainable.

3.1.2. Experimental

3.1.2.1. Synthesis

$Ca_2Fe_{1+x}Mo_{1-x}O_{6-\delta}$ (x = 0.2, 0.4, 0.6) were produced by solid state synthesis technique. Stoichiometric amounts of $CaCO_3$ (99 % min, Alfa Aesar), Fe_2O_3 (99.5%, Alfa Aesar) and MoO_3 (99.5 %, Alfa Aesar) were weighed and mixed in a planetary ball mill for 2 hours prior to firing at 900 °C for 10 hours. A second firing at 1200 °C for 50 hours was then performed. A final firing at 1000 °C for 10 hours in 5% H_2/Ar was completed.

$SrCaFe_{1+x}Mo_{1-x}O_{6-\delta}$ (x = 0.2, 0.4, 0.6) were produced by solid state synthesis technique. Stoichiometric amounts of $CaCO_3$ (99 % min, Alfa Aesar), $SrCO_3$ (> 99.9 %, Sigma Aldrich), Fe_2O_3 (99.5%, Alfa Aesar) and MoO_3 (99.5 %, Alfa Aesar) were weighed and mixed in a planetary ball mill for 2 hours prior to firing at 900 °C for 10 hours. Pellets of all the samples (ø ≈ 13 mm × 2 mm) were uniaxially pressed at 221 MPa and sintered in air at 1300°C for 5 hours.

3.1.2.2. Analytical Procedures

Phase purity and crystal parameters of the samples were examined by X-ray diffraction (XRD) analysis using a PANalytical X'Pert PRO MPD Multipurpose diffractometer (Cu $K_{\alpha 1}$ radiation, λ = 1.5405Å). GSAS [9] software was used to perform a least squares refinement of the lattice parameters of all suitable samples.

The densities of the pellets were determined from the measured mass and volume. Theoretical densities were calculated using experimental lattice parameters and the chemical formula of the sample. The relative densities were calculated from the actual and theoretical density values. The density of the pellets was 65-80 % for $Ca_2Fe_{1+x}Mo_{1-x}O_{6-\delta}$ (x = 0.2, 0.4, 0.6) and 80 % for $SrCaFe_{1+x}Mo_{1-x}O_{6-\delta}$ (x = 0.2, 0.4, 0.6).

Thermal analysis was conducted on a 10 ± 0.5 mg sample using a Stanton Redcroft STA 1500 Thermal Analyser on heating from room temperature to 800 °C and on cooling from 800 °C to room temperature in air, with a heating/cooling rate of 10 °C/min, and in 5% H_2/Ar, again with a heating/cooling rate of 10 °Cmin^{-1}, and with a flow rate of 5% H_2/Ar of 50 mLmin^{-1}.

3.1.2.1. Conductivity Testing

Pellets for $SrCaFe_{1+x}Mo_{1-x}O_{6-\delta}$ (x = 0.2, 0.4, 0.6) were coated on opposing sides using silver paste after firing at 1200 °C for 8 hours in 5% H_2/Ar. The conductivity of the samples was measured in primarily in 5% H_2/Ar between 300 °C to 700 °C. Secondary measurements over the same temperature range were conducted in air following an equilibration step of 12 hours at 700 °C in air. Final measurements over the same temperature range were conducted after an equilibration step of 12 hours at 700 °C in 5% H_2/Ar. Measurements were conducted using either an A.C. method utilising a Solartron 1455A frequency response analyser coupled to a Solartron 1470E potentiostat/galvanostat controlled by CoreWare software over the frequency range 1 MHz to 100 mHz or a DC method using a Solartron 1470E potentiostat/galvanostat controlled by CoreWare software with an applied current of 1 - 0.1 A.

3.1.1.   Results and Discussion

Synthesis of single phase $Ca_2Fe_{1+x}Mo_{1-x}O_{6-\delta}$ (x = 0.2, 0.4, 0.6) compounds in air was unsuccessful, with the formation of both $CaMoO_4$ (PDF: 01-077-2238, 29-351) $Ca_2Fe_2O_5$ (PDF: 01-071-2108, 38-408) phases observed, Figure 3.1 (a). Previous research by Zhang *et. al.* [7] indicated that formation of the calcium based compounds would require firing in reducing atmospheres, therefore it is somewhat unsurprising that synthesis of pure calcium materials in air was unsuccessful. Formation of a single phase perovskite after firing at 700 °C in 5% H_2/Ar was also found to be unsuccessful, with the presence of calcium oxide and pure iron phases observed for all compounds, Figure 3.1 (b). Comparison to the unreduced samples, Fig. 3.1 (a), demonstrates that reduction causes degradation of the phases formed in air, likely due to reduction of the iron and molybdenum in the samples. This corresponds to previous reports which suggest that extended reduction of calcium iron molybdates at high temperatures will cause the exsolution of iron and molybdenum from the structure [10]. The differing phase fractions observed for this series could be related to the stability of the $Ca_2Fe_{1+x}Mo_{1-x}O_{6-\delta}$ phase, with increasing proportions of the desired phase evident with increasing iron content.
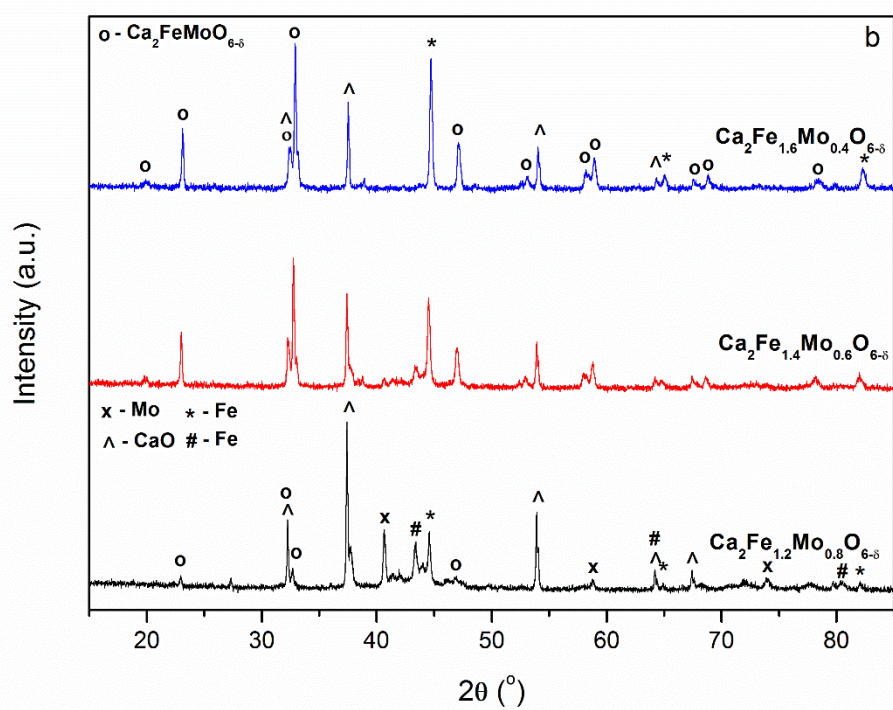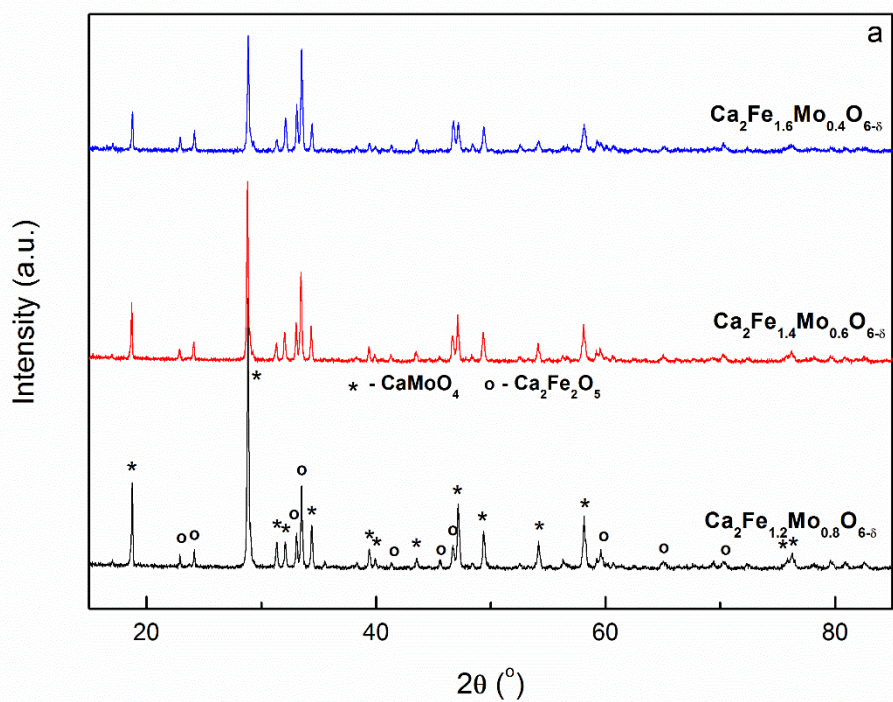
Figure 3.1. XRD patterns of $Ca_2Fe_{1+x}Mo_{1-x}O_{6-\delta}$ (x = 0.2, 0.4 and 0.6) synthesised in air (a) and 5%H_2/Ar (b)

As the formation of pure strontium iron molybdates in air has already been demonstrated [8], the formation of a mixed strontium calcium iron molybdate, $SrCaFe_{1+x}Mo_{1-x}O_{6-\delta}$ (x = 0.2, 0.4, 0.6), was posited to possibly improve the formability and conductivity of the pure calcium and strontium analogues respectively.
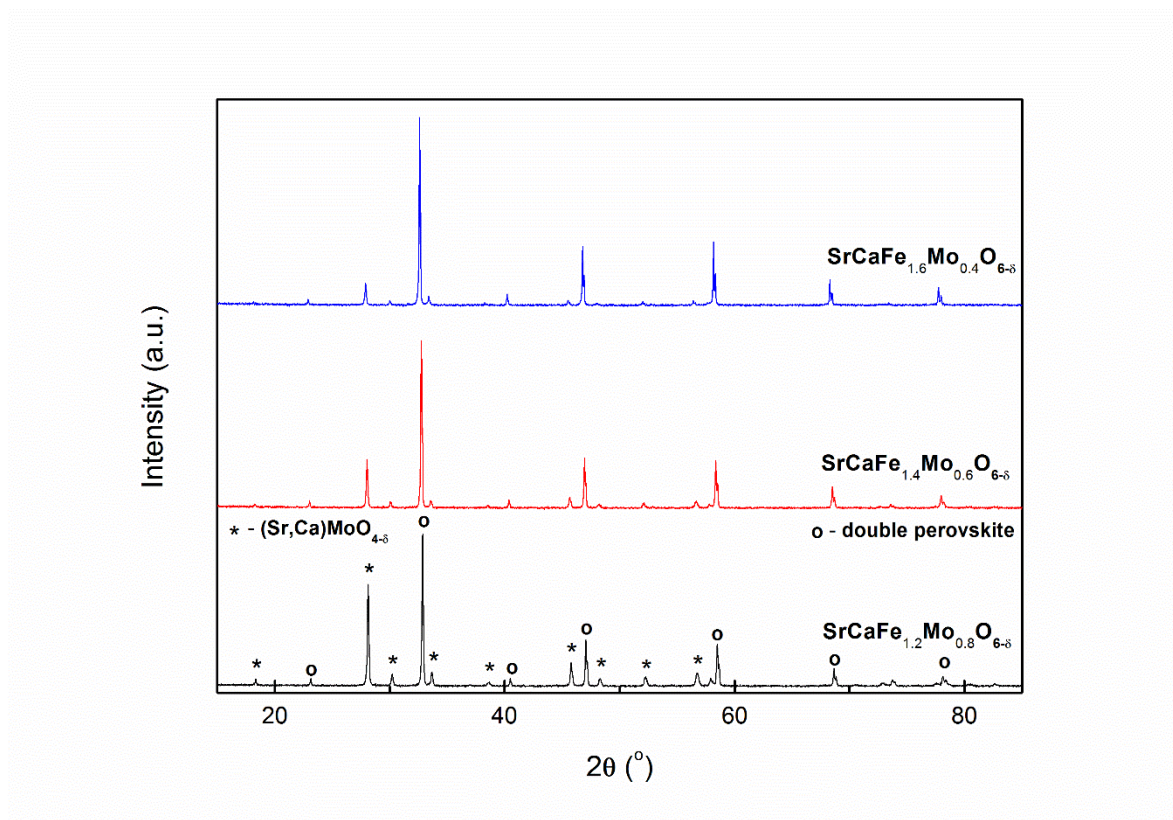
Figure 3.2. XRD patterns of SrCaFe$_{1+x}$Mo$_{1-x}$O$_{6-\delta}$ (x = 0.2, 0.4 and 0.6) synthesised in air

Synthesis of $SrCaFe_{1+x}Mo_{1-x}O_{6-\delta}$ (x = 0.2, 0.4, 0.6) in air was found to form a two phase mixture, with a primary double perovskite phase (Space Group (SG): *Fm-3m*) and a secondary SrMoO$_{4-\delta}$–based phase (PDF: 01-085-0809, SG: *I4/mmm*) observed for all compounds, Figure 3.2. The formation of materials with the *Fm-3m* space group correlates with the observed structure of the iron rich strontium analogues previously synthesised by Liu *et. al.* [11]. Due to the formation of the desired phase, comparison of these compounds to $Ca_2Fe_{1+x}Mo_{1-x}O_{6-\delta}$ (x = 0.2, 0.4, 0.6) demonstrates a significant improvement in the formability in air with increased strontium content.

136
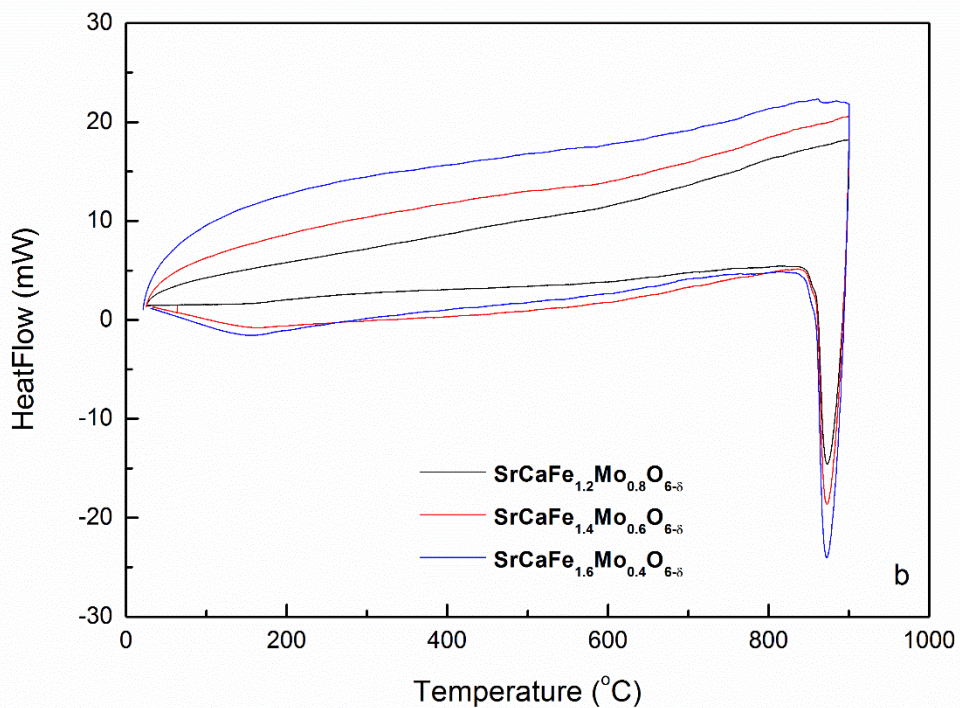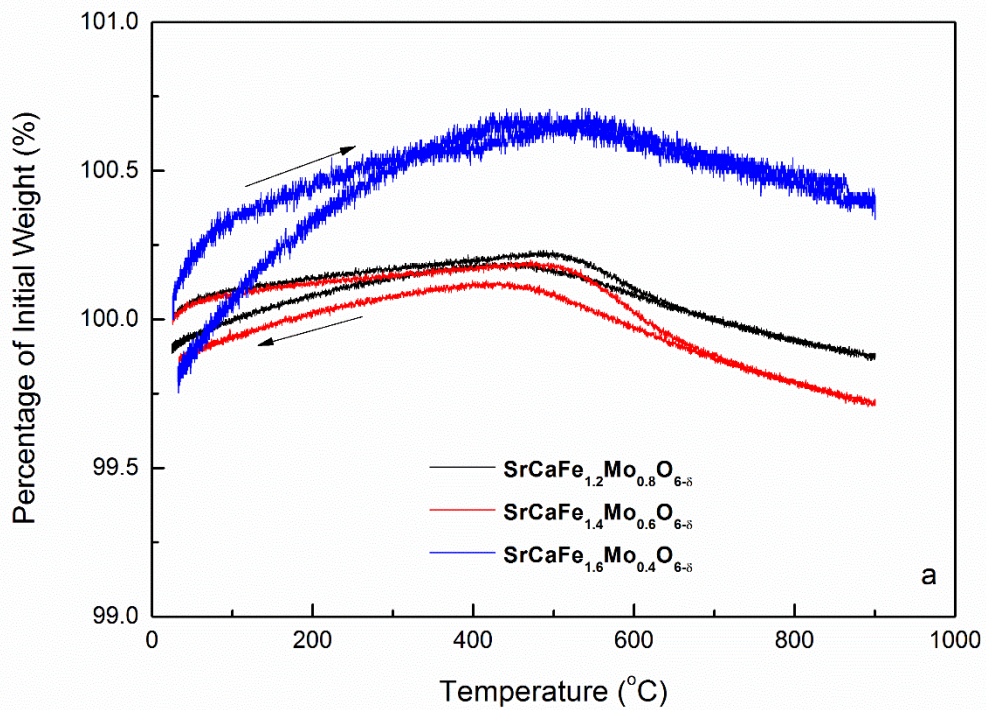
Figure 3.3. Thermogravimetric analysis (a) and differential scanning calorimetry (b) of SrCaFe$_{1+x}$Mo$_{1-x}$O$_{6-\delta}$ (x = 0.2, 0.4 and 0.6) in 5% H$_2$/Ar

Simultaneous thermal analysis in 5% H_2/Ar of the samples formed in air, Figure 3.3 (a), exhibited a weight loss proportional to the iron content of the samples. This suggests that the primary element reduced during exposure to 5% H_2/Ar at this temperature is iron, from Fe^{4+} to Fe^{3+}, and that reduction at higher temperatures, > 800 °C, is required for significant reduction of the molybdenum and subsequent formation of single phase perovskites. A small deviation in the DSC, Figure 3.3 (b), was observed for all compound between 550 °C and 750 °C, correlating with the induction of weight loss observed on the TGA.
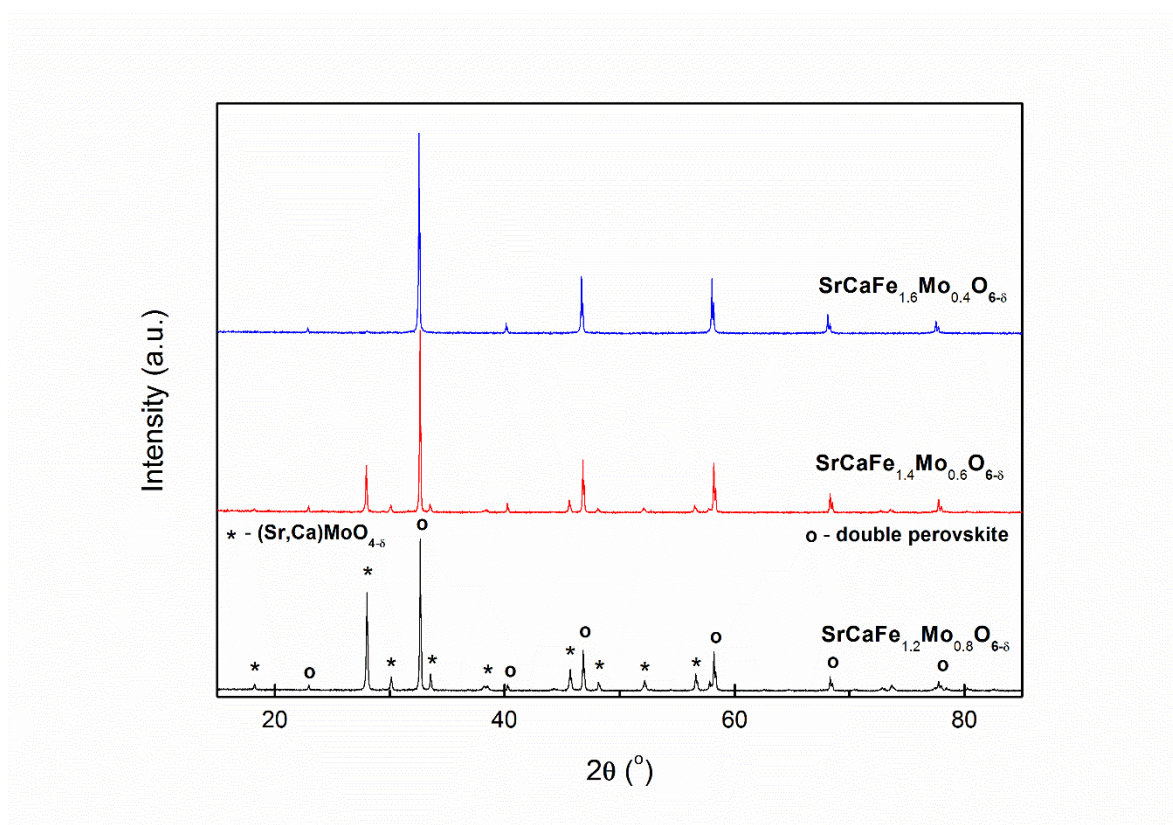
Figure 3.4. XRD patterns of SrCaFe$_{1+x}$Mo$_{1-x}$O$_{6-δ}$ (x = 0.2, 0.4 and 0.6) after reduction in 5% H$_2$/Ar at 700 °C

Reduction of the samples at 700 °C in 5% H_2/Ar formed a single phase double perovskite for the iron rich $SrCaFe_{1.6}Mo_{0.4}O_{6-δ}$ sample (PDF: *Fm-3m*), Figure 3.4, although both $SrCaFe_{1.2}Mo_{0.8}O_{6-δ}$ and $SrCaFe_{1.4}Mo_{0.6}O_{6-δ}$ continued to exhibit the secondary $SrMoO_{4-δ}$–based phase (PDF: 01-085-0809), with little change in the phase fraction. The formation of a single phase double perovskite for $SrCaFe_{1.6}Mo_{0.4}O_{6-δ}$ at

700 °C in 5% H_2/Ar demonstrates an improvement in the formability over the pure calcium analogue.
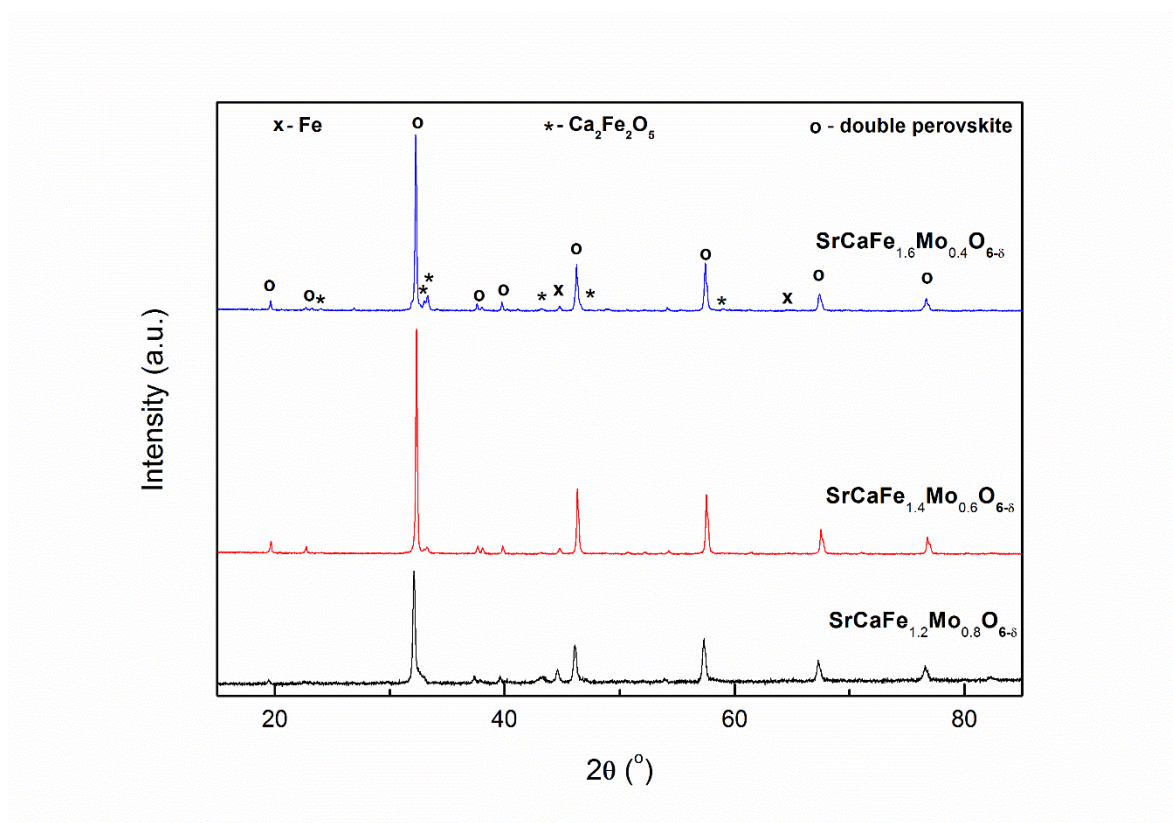

Figure 3.5. XRD patterns of SrCaFe$_{1+x}$Mo$_{1-x}$O$_{6-\delta}$ (x = 0.2, 0.4 and 0.6) after reduction in 5% H_2/Ar at 1200 °C

Formation of mainly single phase double perovskites (SG: *Fm-3m*) was achieved for all compounds after further reduction at 1200 °C in 5% H_2/Ar, Figure 3.5. The formation of the double perovskite phase at 1200 °C in 5% H_2/Ar was predicted to occur, as previous reports suggested that the formation of the less stable $Ca_2FeMoO_{6-\delta}$ phase was achieved at 1100 °C in 5% H_2/Ar [7]. As with reduction of the pure calcium analogue at 700 °C in 5% H_2/Ar, exsolution of elemental iron (PDF: 6-696) was observed for all compounds, reducing with increasing iron content in the primary phase. A proportion of $Ca_2Fe_2O_5$ (PDF: 01-071-2108, 38-408) was also observed for SrCaFe$_{1.6}$Mo$_{0.4}$O$_{6-\delta}$. The proportion of the secondary phase in the synthesised materials was calculated as 2 - 8 wt% for iron and 24 wt% for $Ca_2Fe_2O_5$ through GSAS refinement of the phase fractions. Due to the proportion of these phases, elemental iron in the samples is considered to have a minimal effect on the preceding

measurements, however the sizeable presence of $Ca_2Fe_2O_5$ in $SrCaFe_{1.6}Mo_{0.4}O_{6-\delta}$ must be considered in the analysis of the material properties.

|		SrCaFe$_{1.2}$Mo$_{0.8}$O$_{6-\delta}$	SrCaFe$_{1.4}$Mo$_{0.6}$O$_{6-\delta}$	SrCaFe$_{1.6}$Mo$_{0.4}$O$_{6-\delta}$
χ^2		1.924	5.111	3.851
Rp (%)		8.24	7.82	6.75
wRp (%)		6.27	5.38	4.89
Space Group		*Fm-3m*	*Fm-3m*	*Fm-3m*
		7.850(2)	7.849(1)	7.863(1)
V (Å^3)		483.8(5)	483.6(2)	486.1(2)
Fe (%)		7.8	2.4	1.7
Space Group		*Im-3m*	*Im-3m*	*Im-3m*
a (Å)		2.864(1)	2.866(1)	2.866(1)
Ca$_2$Fe$_2$O$_5$ (%)		-	-	24
Space Group		-	-	*Pcmn*
a (Å)		-	-	5.618(1)
b (Å)		-	-	14.905(3)
c (Å)		-	-	5.437(1)
Sr/Ca	x	0.5	0.5	0.25
	y	0.5	0.5	0.25
	z	0.5	0.5	0.25
	U$_{iso}$	0.007(2)	0.005(1)	0.002(1)
Fe	x	0	0	0
	y	0	0	0
	z	0	0	0
	U$_{iso}$	0.029(5)	0.034(2)	0.049(3)
Fe/Mo	x	0.5	0.5	0.5
	y	0.5	0.5	0.5
	z	0.5	0.5	0.5
	U$_{iso}$	0.038(3)	0.003(1)	0.002(1)
O	x	0.243(2)	0.257(1)	0.266(1)
	y	0	0	0
	z	0.5	0.5	0
	U$_{iso}$	0.068(4)	0.062(2)	0.077(2)

Table 3.1. Rietveld refinement and lattice parameters from GSAS refinement of SrCaFe$_{1+x}$Mo$_{1-x}$O$_{6-\delta}$ (x = 0.2, 0.4, 0.6) after reduction at 1200 °C in 5% H$_2$/Ar
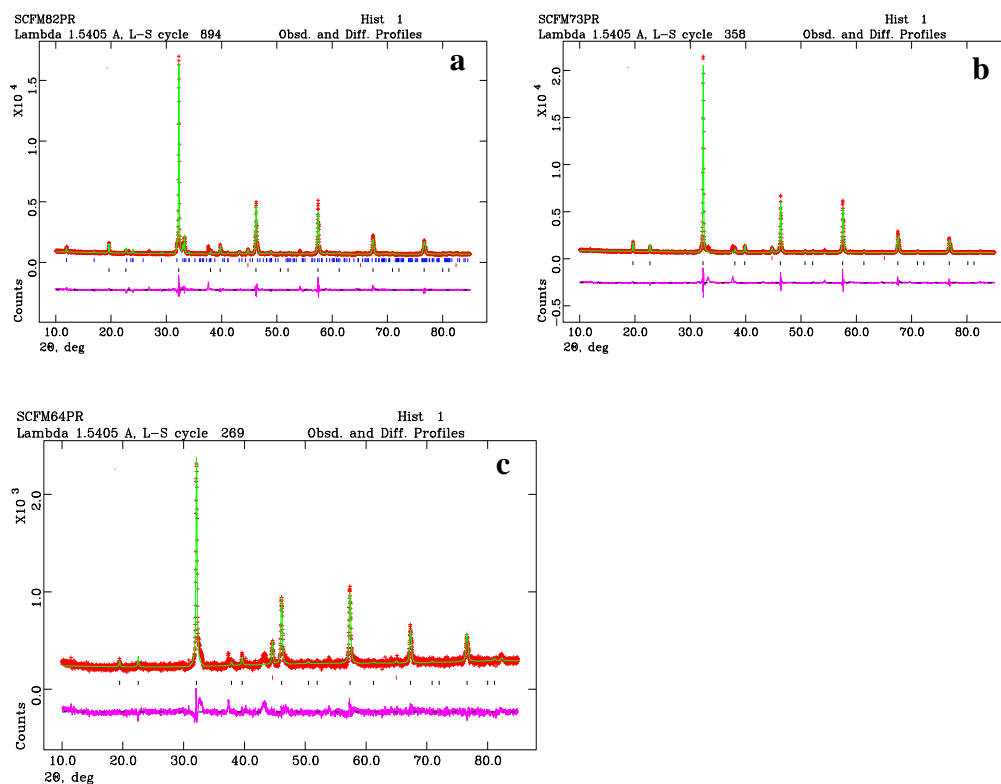
Figure 3.6. GSAS plots of SrCaFe$_{1+x}$Mo$_{1-x}$O$_{6-\delta}$, x = 0.2 (a), x = 0.4 (b) and x = 0.6 (c) after reduction in 5% H$_2$/Ar at 1200 °C

GSAS refinement of the structure of these compounds, Table 3.1 and Figure 3.6, demonstrated a non-linear increase in lattice parameters with increasing iron content. Both SrCaFe$_{1.2}$Mo$_{0.8}$O$_{6-\delta}$ and SrCaFe$_{1.4}$Mo$_{0.6}$O$_{6-\delta}$ exhibit similar lattice parameters with SrCaFe$_{1.6}$Mo$_{0.4}$O$_{6-\delta}$ exhibiting significantly higher lattice parameters. The higher lattice parameter noted for SrCaFe$_{1.6}$Mo$_{0.4}$O$_{6-\delta}$ may be due to the large proportion of the secondary phase and the corresponding inaccuracy associated with three phase.

142
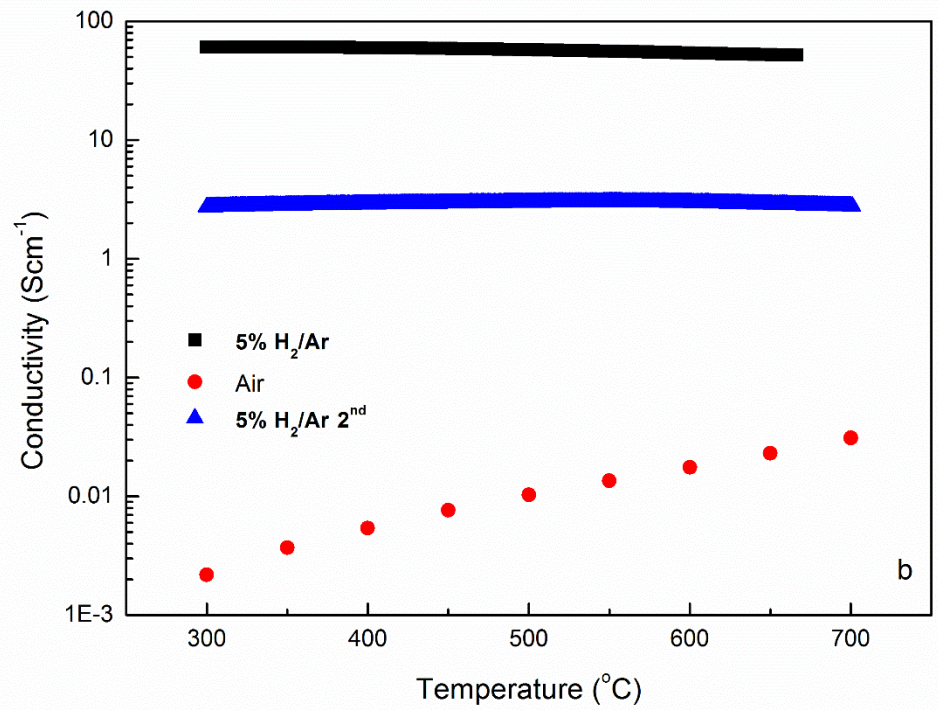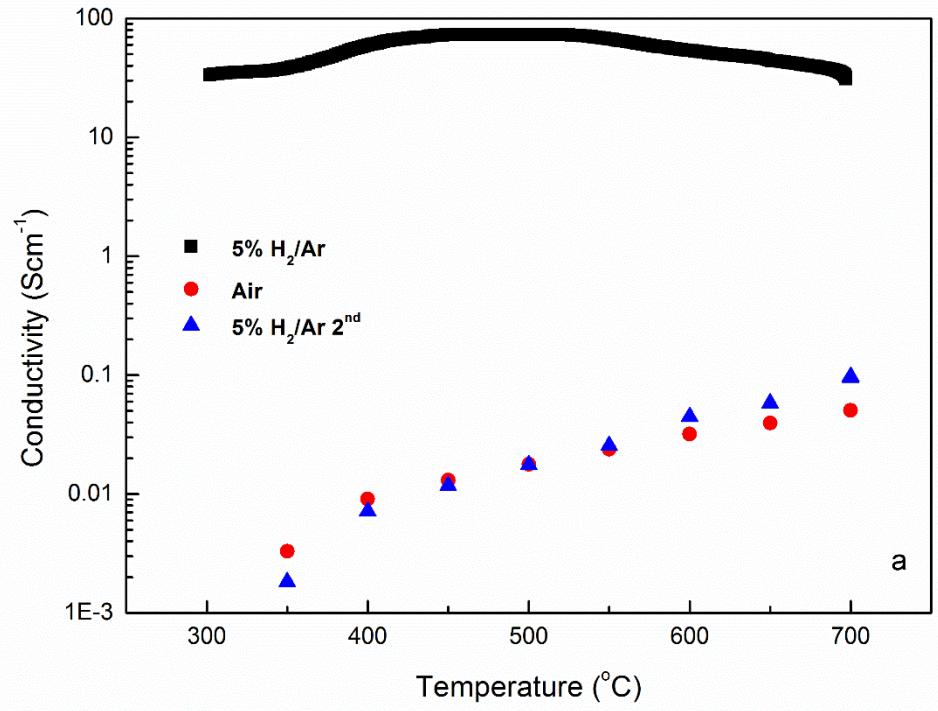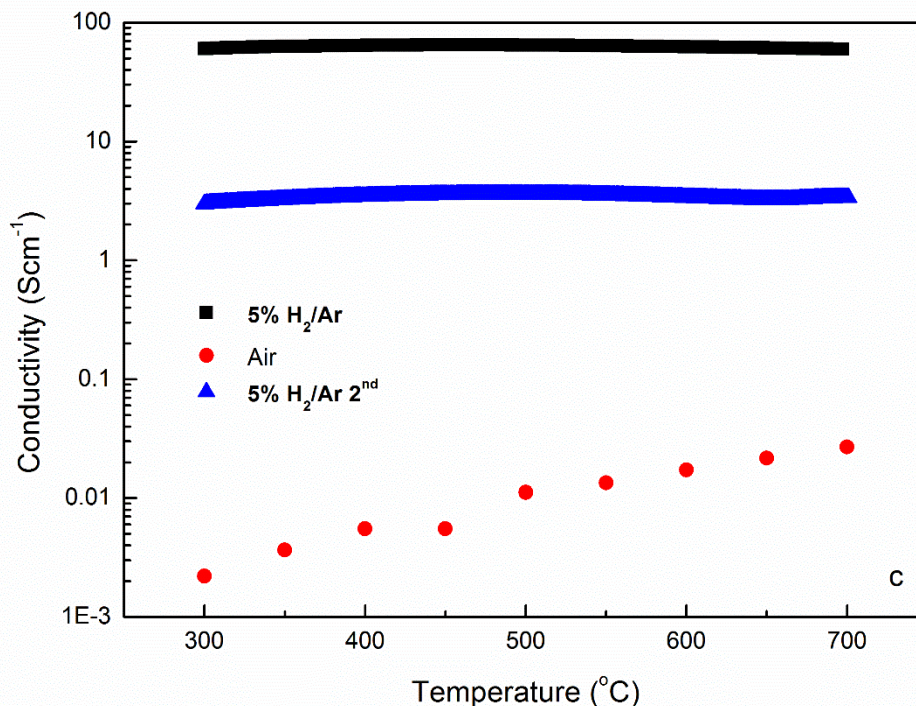
Figure 3.7. Conductivity of SrCaFe$_{1+x}$Mo$_{1-x}$O$_{6-\delta}$, x = 0.2 (a), x = 0.4 (b) and x = 0.6 (c), in 5% H$_2$/Ar after reduction at 1200 °C in 5% H$_2$ Ar (black), in air after re-oxidation of the sample reduced at 1200 °C in 5% H$_2$ Ar (red) and in 5% H$_2$/Ar using the re-oxidised sample (blue).

DC conductivity measurements of each of the SrCaFe$_{1+x}$Mo$_{1-x}$O$_{6-\delta}$ (x = 0.2, 0.4, 0.6) compounds exhibited high electronic conductivity, > 30 Scm^{-1}, between 300 °C and 700 °C in 5% H$_2$/Ar immediately after reduction at 1200 °C in 5% H$_2$/Ar, Figure 3.7 (a-c). Initial semiconducting behaviour was observed for SrCaFe$_{1.6}$Mo$_{0.4}$O$_{6-\delta}$ between 300 °C and 450 °C, SrCaFe$_{1.4}$Mo$_{0.6}$O$_{6-\delta}$ between 300 °C and 350 °C and SrCaFe$_{1.2}$Mo$_{0.8}$O$_{6-\delta}$ between 300 °C and 500 °C, exhibiting maximum conductivities of 64.8 Scm^{-1}, 60.6 Scm^{-1} and 73.5 Scm^{-1} respectively, with metallic conductivity was observed for all compounds above 500 °C. The conductivity of these compounds is significantly reduced from those observed for Sr$_2$Fe$_{1.5}$Mo$_{0.5}$O$_{6-\delta}$ by Liu *et. al.* [8], although similar values was noted to those achieved later by the same authors for the same compound [12] and achieved by Xiao *et. al.* [6] for Sr$_2$Fe$_{1.33}$Mo$_{0.66}$O$_{6-\delta}$.

The metallic conductivity observed for all compounds above 500 °C is also found for $Ca_2FeMoO_{6-\delta}$ [10] and $Sr_2FeMoO_{6-\delta}$ [13] as a result of the delocalisation of electrons in the spin down band at the Fermi level. Band structure calculations of $Ca_{2-x}Sr_xFeMoO_{6-\delta}$ [14] exhibit a gap at the Fermi level between Fe 3d and Mo 4d states for the spin up structure, however the spin down structure exhibits a mixing of the Fe 3d, Mo 4d and O 2p bands at the Fermi level. Spin down electrons from either the Mo 4d or Fe 3d states are delocalised at the Fermi level, arising from Mo^{5+} ($4d^1$) and Fe^{3+} ($3d^5$), accounting for the observed metallic conductivity [7, 10, 13].

The high conductivity of $SrCaFe_{1.2}Mo_{0.8}O_{6-\delta}$, $SrCaFe_{1.4}Mo_{0.6}O_{6-\delta}$ and $SrCaFe_{1.6}Mo_{0.4}O_{6-\delta}$ after reduction in 5% H_2/Ar at 1200 °C suggests that delocalised electrons from Mo^{5+} are unlikely to be the sole source of the metallic conductivity, as minimal variation in the electronic conductivity was observed despite significant variation in the molybdenum content.

The observed conductivity of $A_2FeMoO_{6-\delta}$ (A = Ca, Sr, Ba) [7] was linked to a potential double exchange mechanism, with conduction between Fe^{3+}-O-Mo-O-Fe^{2+}. Double-exchange mechanisms, as proposed by Zener [15], posit that electron transfer between ions in different oxidation states may be facilitated if the electron does not have to alter its spin state. Replacement of Mo with Fe in this mechanism would be expected to result in a reduction of the conductivity through reduction of the available percolation pathways, unless delocalisation of Fe electrons through Fe^{2+}-O-Fe^{3+} exchange could also occur. Double exchange mechanisms have been observed previously for mixed valent iron in iron oxides [16], and, as iron is known to exist in a mixed valent state for $Ca_{2-x}Sr_xFeMoO_{6-\delta}$ [17], this provides a plausible explanation for the observed metallic conductivity. Band structure calculations and Mossbauer spectroscopy could be utilised to further elucidate the conduction mechanism for these compounds, however this is outside the scope of this enquiry.

Whilst metallic conductivity is observed for pure calcium molybdenum ferrites over the entire temperature range, a region of semiconductivity, as was observed for $SrCaFe_{1+x}Mo_{1-x}O_{6-\delta}$ (x = 0.2, 0.4, 0.6), has been observed previously for barium and strontium molybdenum ferrites [7]. Previous reports have attributed the initial region of semiconductivity observed for all compounds to either disorder of the iron and molybdenum or the presence of oxygen vacancies, causing Anderson localisation [13,

[18, 19]. Anderson localisation is used to account for the absence of wave diffusion in a disordered medium and can account for electron localisation in materials when lattice disorder is sufficiently large. Under these conditions the mobility edge, the highest energy at which states are localised, occurs at a higher energy than the Fermi level, resulting in electron localisation. The transition to metallic conductivity could then be rationalised through a gradual increase of the Fermi level to a higher energy than the mobility edge, due to a reduction in the lattice disorder with increasing temperature [13].

Oxidation of these compounds at 700 °C significantly reduced the conductivity, to < 0.1 Scm^{-1}, for all compounds, Figure 3.7 (a-c). Compound oxidation of these materials favours the formation of Fe^{3+} and Mo^{6+}, which reduces double exchange conduction through the reduction in mixed valence cations. The transition to semiconducting behaviour upon oxidation observed for these materials has been previously exhibited in $Sr_2FeMoO_{6-\delta}$ [13].

Reduction of the previously oxidised compounds at 700 °C in 5% H_2/Ar did not attain the high conductivity observed after reduction at 1200 °C, with both $SrCaFe_{1.6}Mo_{0.4}O_{6-\delta}$ and $SrCaFe_{1.4}Mo_{0.6}O_{6-\delta}$ retaining ~ 5 % of the initial conductivity, whilst $SrCaFe_{1.2}Mo_{0.8}O_{6-\delta}$ only retained 0.3%. Although the conductivity exhibited after re-reduction at 700 °C is lower than previously observed, the initial semiconduction with a higher temperature transition to metallic conduction is still observed for both $SrCaFe_{1.6}Mo_{0.4}O_{6-\delta}$ and $SrCaFe_{1.4}Mo_{0.6}O_{6-\delta}$. This suggests that the same conduction mechanism occurs, however the magnitude of the conduction is reduced. As the ratio of both Fe^{3+}/Fe^{2+} and Mo^{6+}/Mo^{5+} is known to be highly dependent on the reducing atmosphere and temperature [10,13], it is expected that the reduction in the conductivity is a result of a lower degree of mixed valency due to the lower reduction temperature.
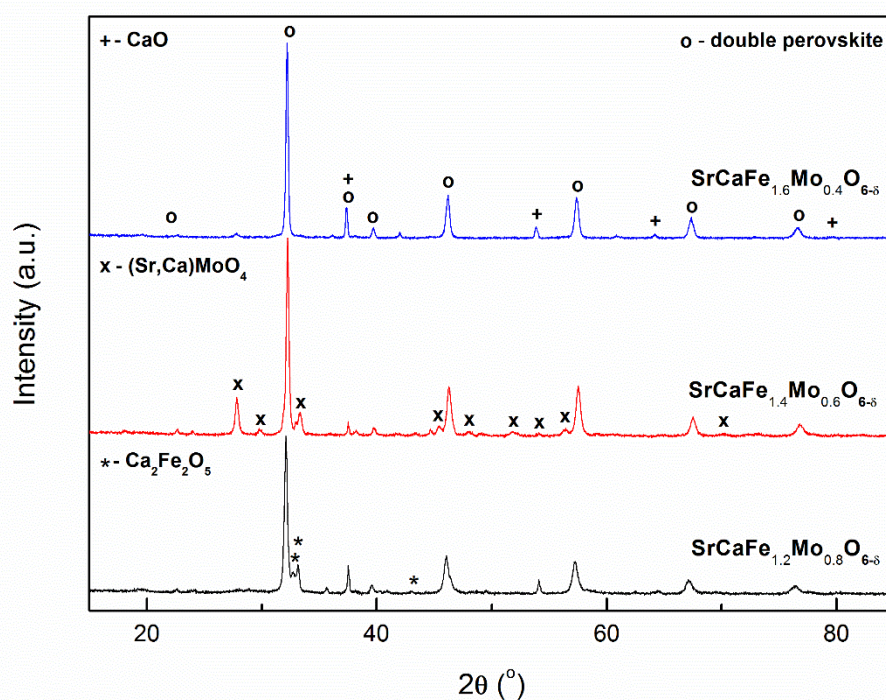
Figure 3.8. XRD patterns of SrCaFe$_{1+x}$Mo$_{1-x}$O$_{6-\delta}$ (x = 0.2, 0.4 and 0.6) after re-oxidation and re-reduction of the samples reduced in 5% H$_2$/Ar at 1200 °C

XRD of SrCaFe$_{1+x}$Mo$_{1-x}$O$_{6-\delta}$ (x = 0.2, 0.4, 0.6) after redox cycling, Figure 3.8, exhibited differing impurity phases and phase fractions for all compounds. The SrMoO$_4$–based impurity phase (PDF: 01-085-0809) was noted for SrCaFe$_{1.4}$Mo$_{0.6}$O$_{6-\delta}$, CaO (PDF: 01-075-0264, 43-1001) was observed for SrCaFe$_{1.6}$Mo$_{0.4}$O$_{6-\delta}$, whilst SrCaFe$_{1.2}$Mo$_{0.8}$O$_{6-\delta}$ exhibited a Ca$_2$Fe$_2$O$_5$ (PDF: 01-071-2108, 38-408) impurity phase. GSAS analysis, Table 3.2 and Figure 3.9, demonstrated a non-linear variation in lattice parameters likely due to the formation of the various secondary phases. The lack of redox stability of these materials further reduces any potential application of these materials for SOFC utilisation.

147
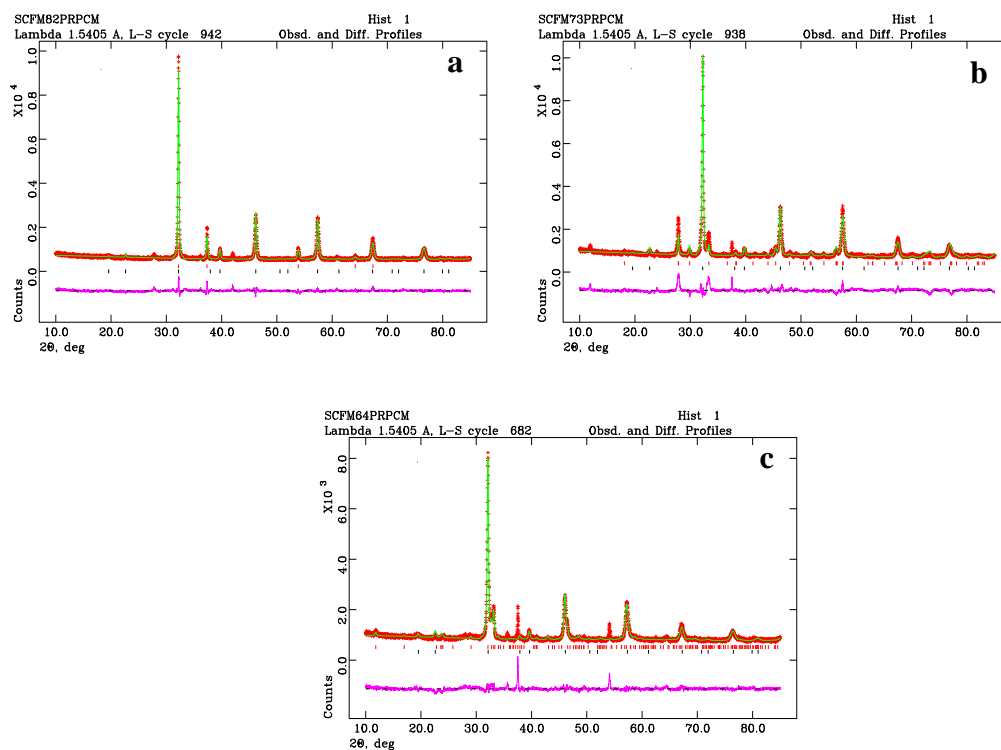
Figure 3.9. GSAS plots of SrCaFe$_{1+x}$Mo$_{1-x}$O$_{6-\delta}$, x = 0.2 (a), x = 0.4 (b) and x = 0.6 (c) after re-oxidation and re-reduction of the samples reduced in 5% H$_2$/Ar at 1200 °C

		$SrCaFe_{1.2}Mo_{0.8}O_{6-\delta}$	$SrCaFe_{1.4}Mo_{0.6}O_{6-\delta}$	$SrCaFe_{1.6}Mo_{0.4}O_{6-\delta}$
χ^2		4.466	6.432	2.565
Rp (%)		6.84	8.41	6.17
wRp (%)		4.46	5.83	4.70
Space Group		*Fm-3m*	*Fm-3m*	*Fm-3m*
a (Å)		7.867(5)	7.836(1)	7.862(2)
V (Å^3)		487.0(1)	481.2(1)	485.9(4)
Secondary Phase		$Ca_2Fe_2O_5$	$SrMoO_4$	CaO
Space Group		*Pcmn*	*I4$_1$/a*	*Fm-3m*
Second Phase (%)		32	7.5	17
a (Å)		5.568(4)	5.359(1)	4.810(1)
b (Å)		14.947(1)	5.359(1)	4.810(1)
c (Å)		5.458(4)	11.93(1)	4.810(1)
Sr/Ca	x	0.5	0.5	0.25
	y	0.5	0.5	0.25
	z	0.5	0.5	0.25
	U_{iso}	0.001(2)	0.016(2)	0.019(1)
Fe	x	0	0	0
	y	0	0	0
	z	0	0	0
	U_{iso}	0.053(5)	0.013(6)	0.008(2)
Fe/Mo	x	0.5	0.5	0.5
	y	0.5	0.5	0.5
	z	0.5	0.5	0.5
	U_{iso}	0.065(3)	0.065(5)	0.010(4)
O	x	0.237(2)	0.248(3)	0.250(2)
	y	0	0	0
	z	0.5	0.5	0
	U_{iso}	0.081(4)	0.081(4)	0.018(2)

Table 3.2 Rietveld refinement and lattice parameters from GSAS refinement of $SrCaFe_{1+x}Mo_{1-x}O_{6-\delta}$ (x = 0.2, 0.4, 0.6) after re-oxidation and re-reduction at 700 °C in 5% H$_2$/Ar of the compounds previously reduced at 1200 °C in 5% H$_2$/Ar

3.1.2. Conclusions

The reliance upon high temperature reduction to maximise the electronic conductivity in $SrCaFe_{1+x}Mo_{1-x}O_{6-\delta}$ (x = 0.2, 0.4, 0.6) is expected to limit the utility of these materials as SOFC anode materials. As is discussed in Section 1.3.4, redox stability of anodic compounds is required so that fuel shortages do not cause inadvertent oxidation of the material, which, for these materials, could result in deactivation of the fuel cell without subsequent high temperature reduction. Whilst prior reduction of these materials at high temperatures could allow for use in IT-SOFCs, this would further complicate the preparation of fuel cell assemblies and would likely limit the commercial viability of fuel cells utilising these materials.

3.2. $Sr_{1.6}K_{0.4}Fe_{1+x}Mo_{1-x}O_{6-\delta}$

3.2.1. Introduction

Whilst the redox stability of the $SrCaFe_{1+x}Mo_{1-x}O_{6-\delta}$ (x = 0.2, 0.4, 0.6) series was insufficient for use as an SOFC anode material, the technique of utilising increases in the iron content to improve the formability and redox stability of these materials was proven to be successful. Further investigation was deemed to be necessary to determine the influence of high temperature reduction on the conductivity of similar compounds and to determine whether the formation of a conductive mixed molybdenum ferrite material could be synthesised in air or in mildly reducing conditions.

Hou *et. al.* [20] posited that potassium doping of $Sr_2FeMoO_{6-\delta}$ could improve the ionic conductivity of the parent material with minimal disruption to the compound structure, due to the similar ionic size of the potassium and strontium cations [21]. Synthesis of the potassium doped strontium molybdenum ferrite was noted to improve the formability of these compounds, with the formation of single phase $Sr_{1.6}K_{0.4}FeMoO_{6-\delta}$ observed after reduction at 850 °C in H_2., 250 °C lower than is required for the pure strontium analogue in 5% H_2/Ar [7]. The conductivity of these compounds was comparable to that of the pure strontium iron molybdate, despite the lower synthesis temperature. Acceptable fuel cell performance, 766 mWcm^{-2} at 800 °C in H_2, was also observed for a $Sr_{1.6}K_{0.4}FeMoO_{6-\delta}/LSGM/Sr_{0.9}K_{0.1}FeO_{3-\delta}$ cell [20], although the anodic composition was later determined to exhibit a mixture of $SrMoO_3$ and $SrFe_{0.6}Mo_{0.4}O_{2.7}$ phases. As the introduction of potassium had exhibited an improvement in the compound formability, it was posited that a further increase could be elicited through an increase in the iron content, as for the pure strontium analogue [6, 8, 12]. To this end the formability and redox stability of a series of materials of the composition $Sr_{1.6}K_{0.4}Fe_{1+x}Mo_{1-x}O_{6-\delta}$ (x = 0.2, 0.4, 0.6) was determined and conclusions as to the suitability of these compounds for use as IT-SOFC anode materials were drawn.

151

3.2.2. Experimental

3.2.2.1. Synthesis

$Sr_{1.6}K_{0.4}Fe_{1+x}Mo_{1-x}O_{6-\delta}$ (x = 0.2, 0.4, 0.6) were produced by solid state synthesis technique. Stoichiometric amounts of $SrCO_3$ (> 99.9 %, Sigma Aldrich), $KHCO_3$ (99%, Alfa Aesar), Fe_2O_3 (99.5%, Alfa Aesar) and MoO_3 (99.5 %, Alfa Aesar) were weighed and mixed in a planetary ball mill for 2 hours prior to firing at 900 °C for 5 hours. A second firing at 1100 °C for 2 hours was then performed. Pellets of all the samples (ø ≈ 13 mm × 2 mm) were uniaxially pressed at 221 MPa and sintered in air at 1200°C for 2 hours.

3.2.2.2. Analytical Procedures

Phase purity and crystal parameters of the samples were examined by X-ray diffraction (XRD) analysis using a PANalytical X'Pert PRO MPD Multipurpose diffractometer (Cu $K_{\alpha1}$ radiation, λ = 1.5405Å). GSAS [9] software was used to perform a least squares refinement of the lattice parameters of all suitable samples.

The densities of the pellets were determined from the measured mass and volume. Theoretical densities were calculated using experimental lattice parameters and the chemical formula of the sample. The relative densities were calculated from the actual and theoretical density values. The density of the pellets was 90 % for $Sr_{1.6}K_{0.4}Fe_{1+x}Mo_{1-x}O_{6-\delta}$ (x = 0.2, 0.4, 0.6).

Thermal analysis was conducted on a 10 ± 0.5 mg sample using a Stanton Redcroft STA 1500 Thermal Analyser on heating from room temperature to 800 °C and on cooling from 800 °C to room temperature in air, with a heating/cooling rate of 10 °C/min, and in 5% H_2/Ar, again with a heating/cooling rate of 10 °Cmin^{-1}, and with a flow rate of 5% H_2/Ar of 50 mLmin^{-1}.

3.2.2.3. Conductivity Testing

Pellets for $Sr_{1.6}K_{0.4}Fe_{1+x}Mo_{1-x}O_{6-\delta}$ (x = 0.2, 0.4, 0.6) were coated on opposing sides using silver paste after firing at 1200 °C for 8 hours in 5% H_2/Ar. The conductivity of the samples was measured in primarily in 5% H_2/Ar between 300 °C to 700 °C. Secondary measurements over the same temperature range were conducted in air

following an equilibration step of 12 hours at 700 °C in air. Final measurements over the same temperature range were conducted after an equilibration step of 12 hours at 700 °C in 5% H_2/Ar. Measurements were conducted using either an A.C. method utilising a Solartron 1455A frequency response analyser coupled to a Solartron 1470E potentiostat/galvanostat controlled by CoreWare software over the frequency range 1 MHz to 100 mHz or a DC method using a Solartron 1470E potentiostat/galvanostat controlled by CoreWare software with an applied current of 1 - 0.1 A.

3.2.3. Results and Discussion
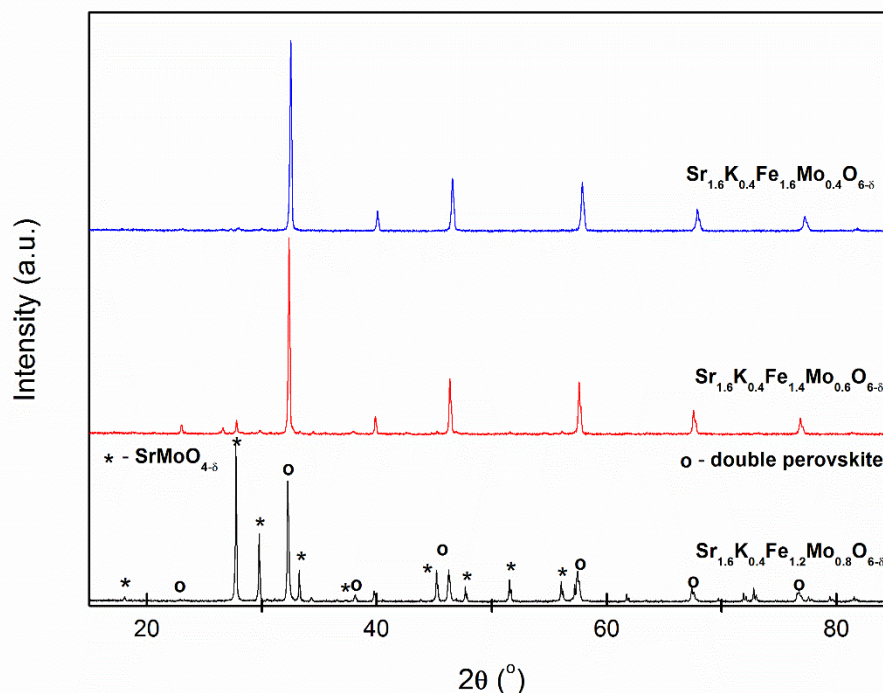
Figure 3.10. XRD patterns of $Sr_{1.6}K_{0.4}Fe_{1+x}Mo_{1-x}O_{6-\delta}$ (x = 0.2, 0.4 and 0.6) synthesised in air

XRD of $Sr_{1.6}K_{0.4}Fe_{1+x}Mo_{1-x}O_{6-\delta}$ (x = 0.2, 0.4, 0.6) after synthesis in air exhibited a single phase double perovskite structure for $Sr_{1.6}K_{0.4}Fe_{1.6}Mo_{0.4}O_{6-\delta}$ (SG: *Fm-3m*), Figure 3.10, however an additional $SrMoO_{4-\delta}$ phase (PDF: 01-085-0809) was observed for both $Sr_{1.6}K_{0.4}Fe_{1.4}Mo_{0.6}O_{6-\delta}$ and $Sr_{1.6}K_{0.4}Fe_{1.2}Mo_{0.8}O_{6-\delta}$. The formation of a single phase double perovskite structure for $Sr_{1.6}K_{0.4}Fe_{1.6}Mo_{0.4}O_{6-\delta}$ correlates with previous research into iron rich strontium iron ferrites, which suggests that the formability limit in air for $Sr_{1.6}K_{0.4}Fe_{1+x}Mo_{1-x}O_{6-\delta}$ lies between x = 0.4 and x = 0.5 [6, 12].

154
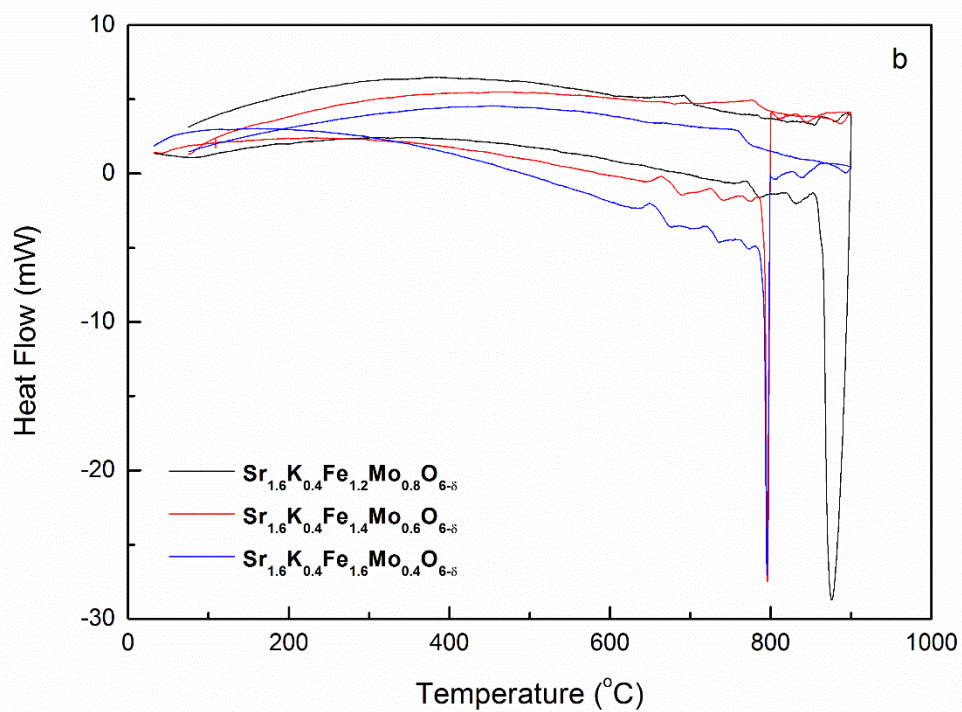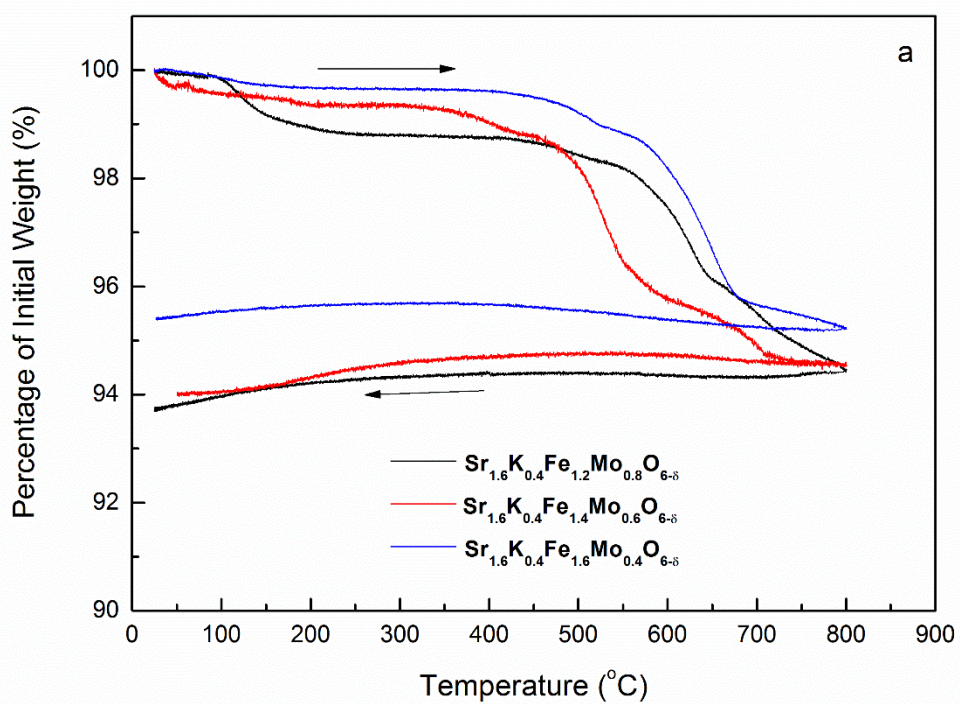
Figure 3.11. Thermogravimetric analysis (a) and differential scanning calorimetry (b) of Sr$_{1.6}$K$_{0.4}$Fe$_{1+x}$Mo$_{1-x}$O$_{6-\delta}$ (x = 0.2, 0.4 and 0.6) in 5% H$_2$/Ar

Thermogravimetric analysis in 5% H_2/Ar of the $Sr_{1.6}K_{0.4}Fe_{1+x}Mo_{1-x}O_{6-\delta}$ (x = 0.2, 0.4, 0.6) samples synthesised in air, Figure 3.11 (a), exhibits a minor increase in the percentage weight loss with increasing molybdenum content. This behaviour is in contrast to that observed for $SrCaFe_{1+x}Mo_{1-x}O_{6-\delta}$ (x = 0.2, 0.4, 0.6) upon reduction at 700 °C, Figure 3.3 (a), and implies that the primary cation reduced at this temperature is molybdenum, from Mo^{6+} to Mo^{5+}. Differential scanning calorimetry, Figure 3.11 (b) of all compounds exhibits two main peaks upon heating between 400 °C and 550 °C and between 650 °C and 750 °C, with an additional peak observed on cooling between 650 °C and 750 °C.
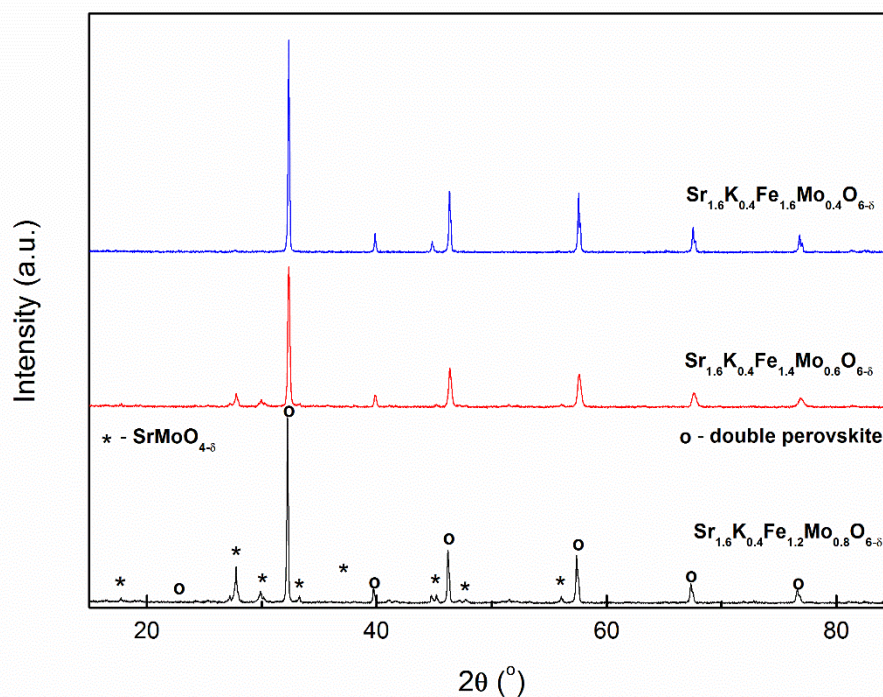
Figure 3.12. XRD patterns of $Sr_{1.6}K_{0.4}Fe_{1+x}Mo_{1-x}O_{6-\delta}$ (x = 0.2, 0.4 and 0.6) after reduction in 5% H_2/Ar at 700 °C

Reduction of $Sr_{1.6}K_{0.4}Fe_{1.2}Mo_{0.8}O_{6-\delta}$ in 5% H_2/Ar at 700 °C elicits a significant reduction in the proportion of the secondary $SrMoO_4$ phase (PDF: 01-085-0809) in the XRD pattern, Figure 3.12. A similar reduction in the secondary phase is not observed for $Sr_{1.6}K_{0.4}Fe_{1.4}Mo_{0.6}O_{6-\delta}$, whilst $Sr_{1.6}K_{0.4}Fe_{1.6}Mo_{0.4}O_{6-\delta}$ was observed to retain the

single phase double perovskite structure. Although the proportion of the secondary phase is significantly smaller than is observed for the calcium doped analogues, the formability of these materials does not appear to be significantly improved by potassium doping. Whilst potassium doping appears to elicit a slight increase in the formability of these compounds, as observed by Hou *et. al.* [20], the iron content of the sample exhibits a significantly larger influence over the formation of single phase double perovskites.
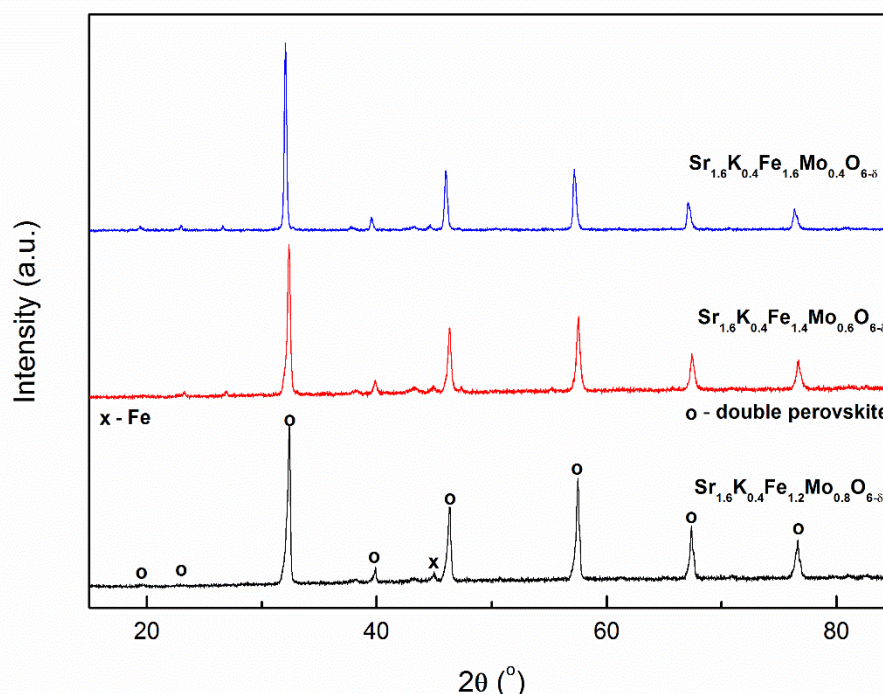
Figure 3.13. XRD patterns of $Sr_{1.6}K_{0.4}Fe_{1+x}Mo_{1-x}O_{6-\delta}$ (x = 0.2, 0.4 and 0.6) after reduction in 5% H_2/Ar at 1200 °C

$Sr_{1.6}K_{0.4}Fe_{1+x}Mo_{1-x}O_{6-\delta}$ (x = 0.2, 0.4, 0.6) exhibited a double perovskite structure (SG: *Fm-3m*) after reduction in 5% H_2/Ar at 1200 °C, Figure 3.13, albeit with a small proportion of a secondary Fe phase (PDF: 6-696) also observed. The structure of these materials differs from that observed by Hou *et. al.* [20] for $Sr_{1.6}K_{0.4}FeMoO_{6-\delta}$, which was refined as a mixture of two perovskite structures (SG: *Pm-3m*) with similar lattice parameters. GSAS analysis, Table 3.3 and Figure 3.14, demonstrates a linear reduction in the lattice parameter with reducing molybdenum content. The size of the

molybdenum cation ($Mo^{6+} = 0.59$ Å, $Mo^{5+} = 0.61$ Å) is generally smaller than that of iron in the *Fm-3m* structure ($Fe^{2+}_{LS} = 0.61$ Å, $Fe^{2+}_{HS} = 0.78$ Å, $Fe^{3+}_{LS} = 0.55$ Å, $Fe^{3+}_{HS} = 0.645$ Å) [21] which would intimate that a reduction in the lattice should occur with increasing molybdenum content. As the valency of these cations is known to alter with compositional modifications [17], it may be possible that the reduction in the molybdenum content could result in a modification of the valency of the B-site cations in $Sr_{1.6}K_{0.4}Fe_{1+x}Mo_{1-x}O_{6-\delta}$ (x = 0.2, 0.4, 0.6), resulting in the observed increase in the lattice parameter. Further investigation using Mössbauer spectroscopy could determine the feasibility of this supposition. The proportion of the secondary iron phase increased with increasing iron content, although the minimal secondary phase fraction observed, 2 − 3 %, expected to have a negligible effect on the preceding measurements.
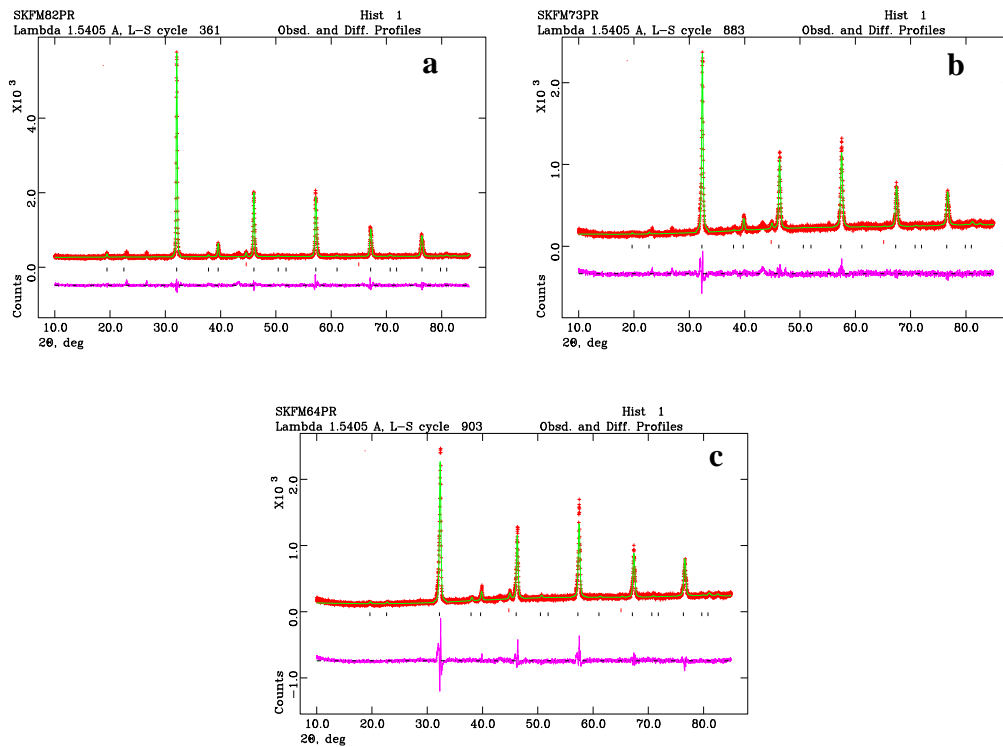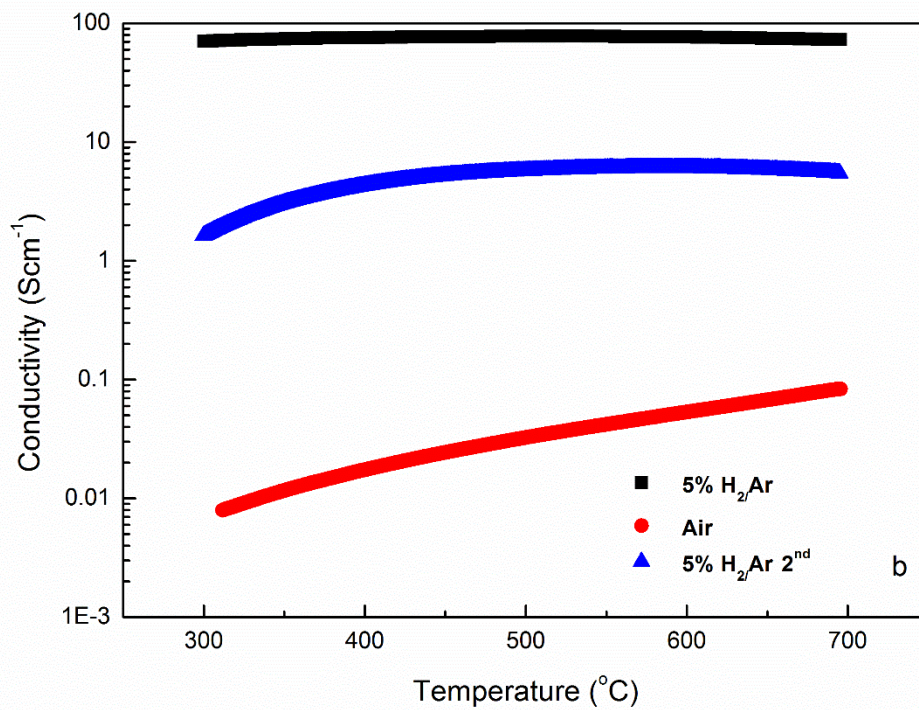

Figure 3.14. GSAS plots of $Sr_{1.6}K_{0.4}Fe_{1+x}Mo_{1-x}O_{6-\delta}$ x = 0.2 (a), x = 0.4 (b) and x = 0.6 (c) after reduction in 5% H$_2$/Ar at 1200 °C

		$Sr_{1.6}K_{0.4}Fe_{1.2}Mo_{0.8}O_{6-\delta}$	$Sr_{1.6}K_{0.4}Fe_{1.4}Mo_{0.6}O_{6-\delta}$	$Sr_{1.6}K_{0.4}Fe_{1.6}Mo_{0.4}O_{6-\delta}$
χ^2		2.941	1.868	1.758
Rp (%)		11.45	8.82	7.23
wRp (%)		8.60	6.70	5.57
Space Group		*Fm-3m*	*Fm-3m*	*Fm-3m*
a (Å)		7.898(2)	7.881(2)	7.869(1)
V (Å^3)		492.7(4)	489.6(4)	487.4(3)
Fe (%)		3.3	2.4	2.1
Space Group		*Im-3m*	*Im-3m*	*Im-3m*
a (Å)		2.871(1)	2.869(1)	2.864(1)
Sr/K	x	0.5	0.5	0.25
	y	0.5	0.5	0.25
	z	0.5	0.5	0.25
	U_{iso}	0.007(1)	0.014(1)	0.001(1)
Fe	x	0	0	0
	y	0	0	0
	z	0	0	0
	U_{iso}	0.005(3)	0.015(3)	0.005(2)
Fe/Mo	x	0.5	0.5	0.5
	y	0.5	0.5	0.5
	z	0.5	0.5	0.5
	U_{iso}	0.009(2)	0.061(4)	0.016(1)
O	x	0.237(2)	0.244(2)	0.252(1)
	y	0	0	0
	z	0.5	0.5	0
	U_{iso}	0.017(3)	0.032(2)	0.027(2)

Table 3.3. Rietveld refinement and lattice parameters from GSAS refinement of

$Sr_{1.6}K_{0.4}Fe_{1+x}Mo_{1-x}O_{6-\delta}$ (x = 0.2, 0.4, 0.6) after reduction at 1200 °C in 5% H_2/Ar
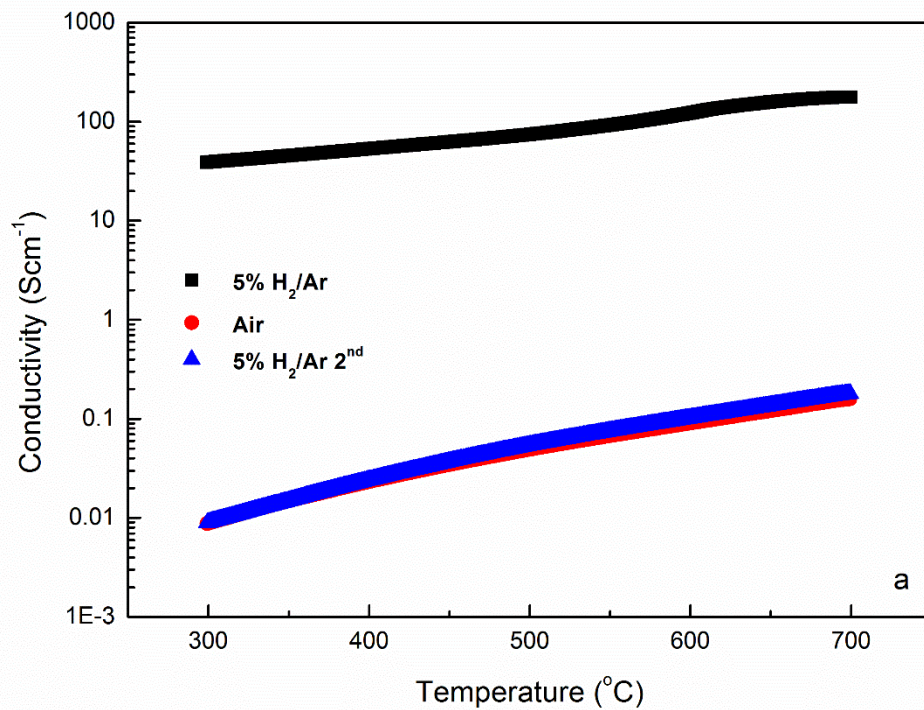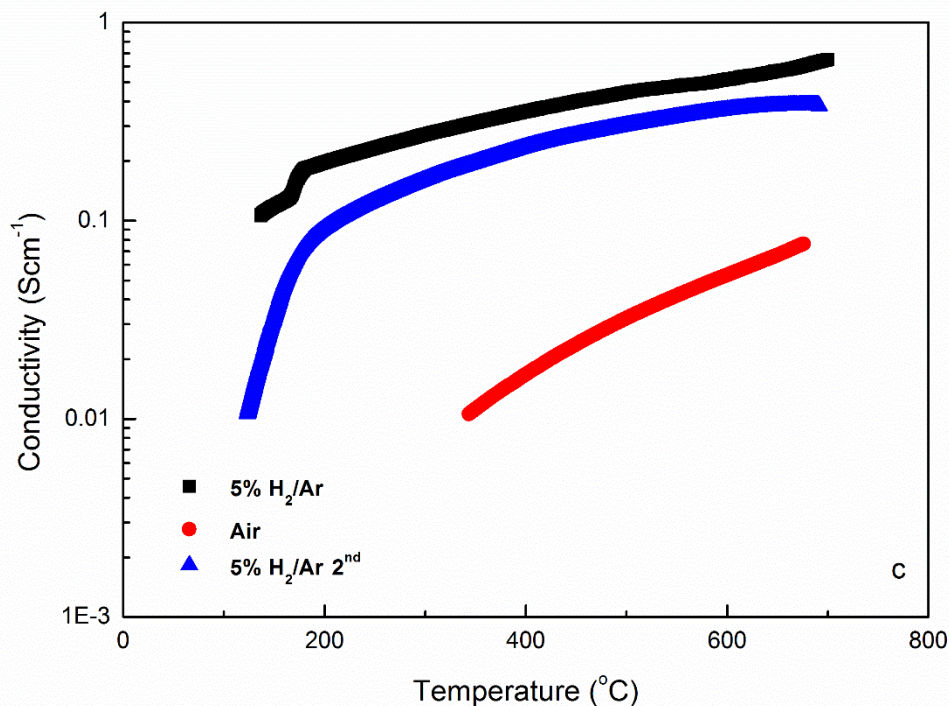
Figure 3.15. Conductivity of $Sr_{1.6}K_{0.4}Fe_{1+x}Mo_{1-x}O_{6-\delta}$, x = 0.2 (a), x = 0.4 (b) and x = 0.6 (c), in 5% H_2/Ar after reduction in 5% H_2/Ar at 1200 °C (black), in air after re-oxidation of the sample reduced in 5% H_2/Ar at 1200 °C (red) and in 5% H_2/Ar using the re-oxidised sample (blue).

$Sr_{1.6}K_{0.4}Fe_{1.4}Mo_{0.6}O_{6-\delta}$ and $Sr_{1.6}K_{0.4}Fe_{1.2}Mo_{0.8}O_{6-\delta}$ after reduction at 1200 °C in 5% H_2/Ar exhibited high electronic conductivity, > 40 Scm^{-1}, over the entire temperature range, Figure 3.15. The conductivity of $Sr_{1.6}K_{0.4}Fe_{1.6}Mo_{0.4}O_{6-\delta}$ was significantly lower after the same treatment, < 1 Scm^{-1} over the same temperature range, although a significant reduction in the initial conductivity was observed at 700 °C in 5% H_2/Ar. Semiconductivity was observed for both $Sr_{1.6}K_{0.4}Fe_{1.2}Mo_{0.8}O_{6-\delta}$ and $Sr_{1.6}K_{0.4}Fe_{1.6}Mo_{0.4}O_{6-\delta}$ over the entire measurement range, however a metal-insulator transition was observed for $Sr_{1.6}K_{0.4}Fe_{1.4}Mo_{0.6}O_{6-\delta}$ at 530 °C. The conduction mechanism is expected to be similar to that observed for $SrCaFe_{1+x}Mo_{1-x}O_{6-\delta}$ (x = 0.2, 0.4, 0.6), however the difference in the conduction behaviour suggests the potassium doping may affect the iron or molybdenum valency. X-ray photoelectron spectroscopy (XPS) could be utilised to determine the effect of potassium doping on iron and

161

molybdenum valence and to further elucidate the conduction mechanism, although this is outside the scope of this enquiry.
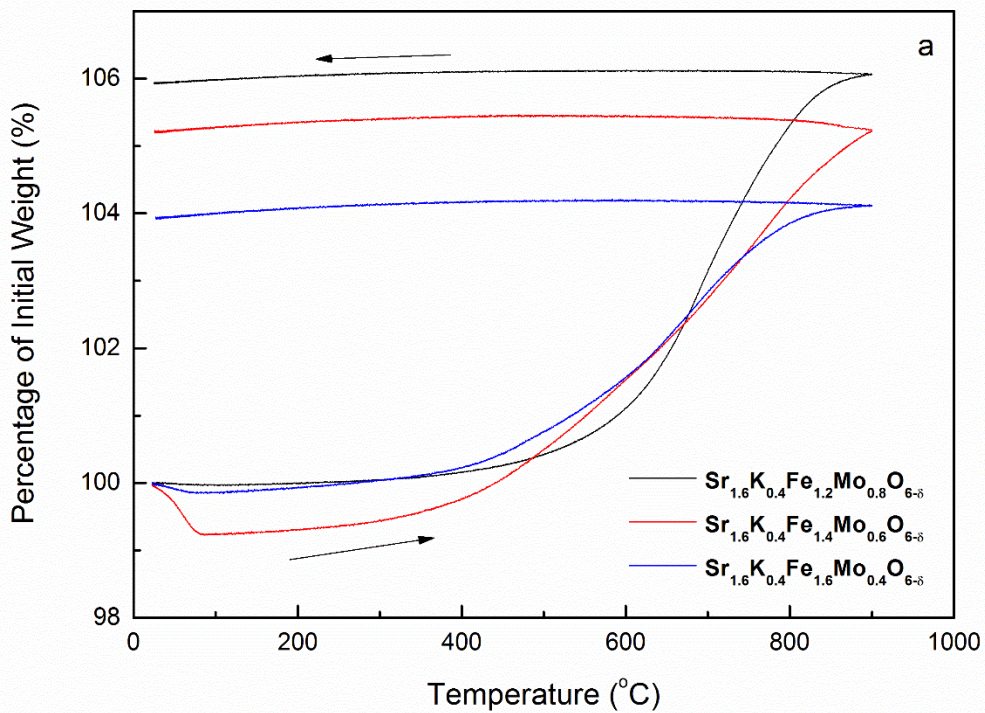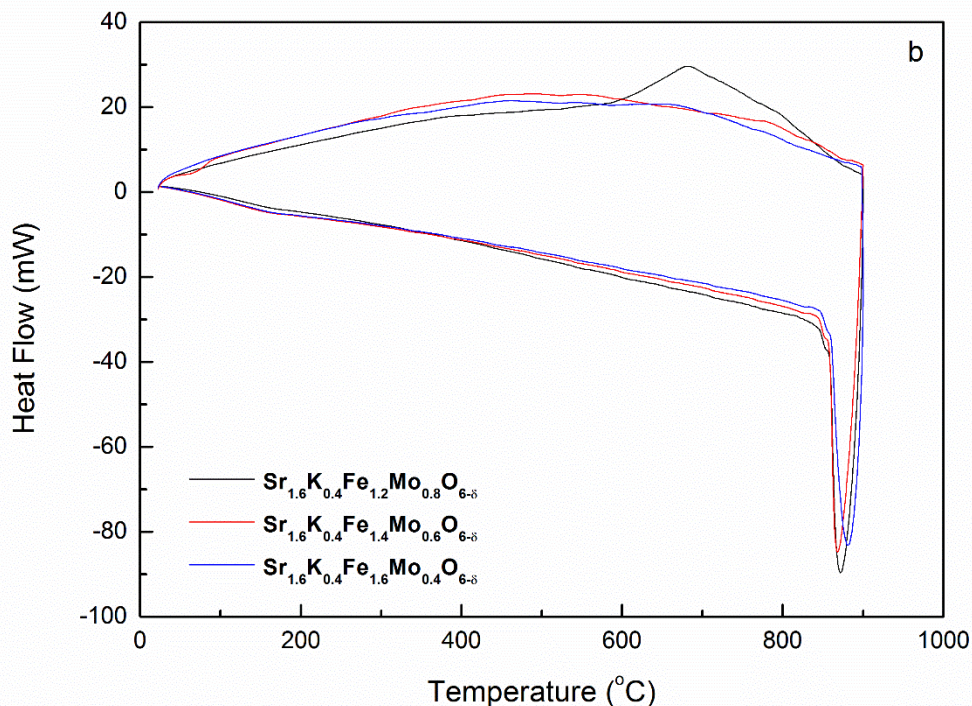
Figure 3.16. Thermogravimetric analysis (a) and differential scanning calorimetry (b) of $Sr_{1.6}K_{0.4}Fe_{1+x}Mo_{1-x}O_{6-\delta}$ (x = 0.2, 0.4 and 0.6) in air after reduction in 5% H_2/Ar at 1200 °C

Re-oxidation of $Sr_{1.6}K_{0.4}Fe_{1+x}Mo_{1-x}O_{6-\delta}$ (x = 0.2, 0.4, 0.6) after reduction in 5% H_2/Ar at 1200 °C caused an increase in weight proportional to the molybdenum content, as exhibited in Figure 3.16 (a). Re-oxidation was observed to begin between 400 °C and 600 °C, lower than the current operating temperature of SOFCs. Re-oxidation of these materials occurs at a similar temperature to that of $Sr_2FeMoO_{6-\delta}$ [4], suggesting a minimal modification of the material redox stability. A significant deviation was observed between 600 °C and 800 °C by differential scanning calorimetry, Figure 3.16 (b), for $Sr_{1.6}K_{0.4}Fe_{1.2}Mo_{0.8}O_{6-\delta}$, which can be attributed to formation of the secondary $SrMoO_4$ phase observed in the XRD pattern after redox cycling, Figure 3.17.

A significant reduction in the conductivity was observed for $Sr_{1.6}K_{0.4}Fe_{1+x}Mo_{1-x}O_{6-\delta}$ (x = 0.2, 0.4, 0.6) after re-oxidation at 700 °C, Figure 3.15. As was observed for

SrCaFe$_{1+x}$Mo$_{1-x}$O$_{6-\delta}$ (x = 0.2, 0.4, 0.6), oxidation of these materials will likely form Fe^{3+} and Mo^{6+}, reducing conduction through double exchange mechanisms.

Re-reduction of Sr$_{1.6}$K$_{0.4}$Fe$_{1+x}$Mo$_{1-x}$O$_{6-\delta}$ (x = 0.2, 0.4, 0.6) at 700 °C in 5% H$_2$/Ar elicited an increase in the conductivity, as was observed previously for SrCaFe$_{1+x}$Mo$_{1-x}$O$_{6-\delta}$ (x = 0.2, 0.4, 0.6), Figure 3.7 (a-c). The compounds did not attain similar conductivities as those observed after reduction at 1200 °C in 5% H$_2$/Ar, with the percentage retained increasing with iron content, 0.1 % for Sr$_{1.6}$K$_{0.4}$Fe$_{1.2}$Mo$_{0.8}$O$_{6-\delta}$, 7.5 % for Sr$_{1.6}$K$_{0.4}$Fe$_{1.4}$Mo$_{0.6}$O$_{6-\delta}$ and 58.4 % for Sr$_{1.6}$K$_{0.4}$Fe$_{1.6}$Mo$_{0.4}$O$_{6-\delta}$. Similar conduction behaviour is also observed for all compounds, with the metal insulator transition shifted to 580 °C for Sr$_{1.6}$K$_{0.4}$Fe$_{1.4}$Mo$_{0.6}$O$_{6-\delta}$. As the ratio of both Fe^{3+}/Fe^{2+} and Mo^{6+}/Mo^{5+} is known to be highly dependent on the reducing atmosphere and temperature [10, 13], it is expected that the reduction in the conductivity is a result of a lower degree of mixed valency due to the lower reduction temperature. The minimal increase in the conductivity of upon re-reduction of Sr$_{1.6}$K$_{0.4}$Fe$_{1.2}$Mo$_{0.8}$O$_{6-\delta}$ was also observed for SrCaFe$_{1.2}$Mo$_{0.8}$O$_{6-\delta}$. As minimal reduction of molybdenum is expected to occur after reduction at 700 °C, the mixed valence on the Fe/Mo site will be lower than for either of Sr$_{1.6}$K$_{0.4}$Fe$_{1.4}$Mo$_{0.6}$O$_{6-\delta}$ or Sr$_{1.6}$K$_{0.4}$Fe$_{1.6}$Mo$_{0.4}$O$_{6-\delta}$, thus a similar proportional increase in the conductivity does not occur.
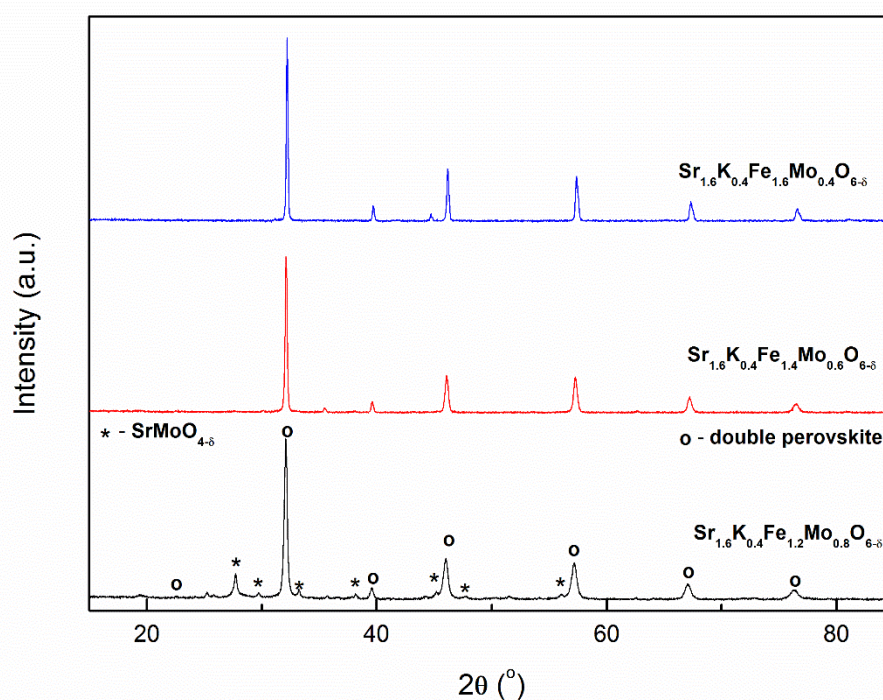
Figure 3.17. XRD patterns of $Sr_{1.6}K_{0.4}Fe_{1+x}Mo_{1-x}O_{6-\delta}$ (x = 0.2, 0.4 and 0.6) after re-oxidation and re-reduction of the samples reduced in 5% H_2/Ar at 1200 °C

XRD of $Sr_{1.6}K_{0.4}Fe_{1+x}Mo_{1-x}O_{6-\delta}$ (x = 0.2, 0.4, 0.6) after redox cycling, Figure 3.17, exhibited an observed change in the secondary phase fractions with minimal observable change in the primary phase. The Fe (PDF: 6-696) phase was observed for $Sr_{1.6}K_{0.4}Fe_{1.6}Mo_{0.4}O_{6-\delta}$ after redox cycling, with a 1 % increase in the phase fraction, whilst a $SrMoO_4$ phase (PDF: 01-085-0809) was observed for $Sr_{1.6}K_{0.4}Fe_{1.2}Mo_{0.8}O_{6-\delta}$. $Sr_{1.6}K_{0.4}Fe_{1.4}Mo_{0.6}O_{6-\delta}$ exhibited a single phase double perovskite structure (SG: *Fm-3m*) with no observable secondary phases. GSAS analysis, Table 3.4 and Figure 3.18, demonstrated a reduction in the lattice parameters after redox cycling, Table 3.3, although the lattice parameters of $Sr_{1.6}K_{0.4}Fe_{1+x}Mo_{1-x}O_{6-\delta}$ (x = 0.2, 0.4, 0.6) exhibit no observable trend. The formation of the $SrMoO_{4-\delta}$ phase for $Sr_{1.6}K_{0.4}Fe_{1.2}Mo_{0.8}O_{6-\delta}$ suggests that the redox stability of these compounds reduces with increasing molybdenum content, with the redox stability limit falling between x = 0.2 and x = 0.4.

		$Sr_{1.6}K_{0.4}Fe_{1.2}Mo_{0.8}O_{6-\delta}$	$Sr_{1.6}K_{0.4}Fe_{1.4}Mo_{0.6}O_{6-\delta}$	$Sr_{1.6}K_{0.4}Fe_{1.6}Mo_{0.4}O_{6-\delta}$
χ^2		4.541	1.714	1.547
Rp (%)		10.44	6.41	5.95
wRp (%)		7.59	4.92	4.72
Space Group		*Fm-3m*	*Fm-3m*	*Fm-3m*
a (Å)		7.862(2)	7.872(1)	7.861(1)
V (Å^3)		486.0(3)	487.9(5)	485.8(2)
Secondary Phase		$SrMoO_4$	-	Fe
Space Group		*I4$_1$/m*	-	*Im-3m*
Second Phase (%)		13	-	3.2
a (Å)		5.394(1)	-	2.864(5)
b (Å)		5.394(1)	-	2.864(5)
c (Å)		12.013(3)	-	2.864(5)
Sr/K	x	0.25	0.25	0.25
	y	0.25	0.25	0.25
	z	0.25	0.25	0.25
	U_{iso}	0.026(1)	0.003(1)	0.005(1)
Fe	x	0	0	0
	y	0	0	0
	z	0	0	0
	U_{iso}	0.010(3)	0.019(3)	0.001(3)
Fe/Mo	x	0.5	0.5	0.5
	y	0.5	0.5	0.5
	z	0.5	0.5	0.5
	U_{iso}	0.031(5)	0.041(3)	0.028(4)
O	x	0.231(2)	0.238(1)	0.248(2)
	y	0	0	0
	z	0.5	0.5	0
	U_{iso}	0.061(4)	0.032(4)	0.033(2)

Table 3.4. Rietveld refinement and lattice parameters from GSAS refinement of $Sr_{1.6}K_{0.4}Fe_{1+x}Mo_{1-x}O_{6-\delta}$ (x = 0.2, 0.4, 0.6) after re-oxidation and re-reduction at 700 °C in 5% H_2/Ar of the compounds previously reduced at 1200 °C in 5% H_2/Ar
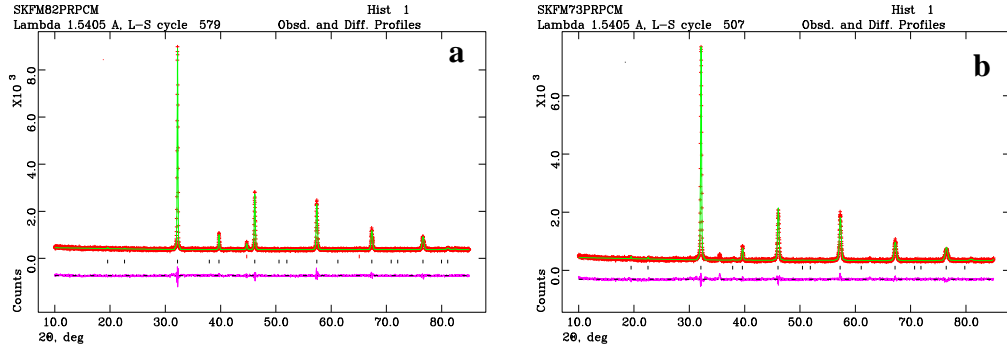
Figure 3.18. GSAS plots of $Sr_{1.6}K_{0.4}Fe_{1+x}Mo_{1-x}O_{6-\delta}$ x = 0.2 (a), x = 0.4 (b) and x = 0.6 (c) after re-oxidation and re-reduction of the samples reduced in 5% H_2/Ar at 1200 °C

3.2.4. Conclusion

Introduction of potassium into $Sr_2Fe_{1+x}Mo_{1-x}O_{6-\delta}$ (x = 0.2, 0.4, 0.6) appears to have a negligible effect on the formability of these compounds, with the variation of the iron content exhibiting greater influence on material formability. As for $SrCaFe_{1+x}Mo_{1-x}O_{6-\delta}$ (x = 0.2, 0.4, 0.6), the dependence of the conductivity of $Sr_{1.6}K_{0.4}Fe_{1+x}Mo_{1-x}O_{6-\delta}$ (x = 0.2, 0.4, 0.6) on high temperature reduction, suggests that these compounds may have reduced utility as IT-SOFC anode materials, due to the associated problems with fuel cell durability.

3.3. Conclusion

Introduction of calcium to $Sr_2Fe_{1+x}Mo_{1-x}O_{6-\delta}$ (x = 0.2, 0.4, 0.6) was not successful in simultaneously improving the conductivity and stability of these compounds, with a significant reduction in the formability observed with increasing calcium content. Potassium substitution into $Sr_2Fe_{1+x}Mo_{1-x}O_{6-\delta}$ (x = 0.2, 0.4, 0.6) with the intention of increasing the formability and ionic conductivity was also unsuccessful, with no notable formability improvements observed. Synthesis of both $SrCaFe_{1+x}Mo_{1-x}O_{6-\delta}$ (x = 0.2, 0.4, 0.6) and $Sr_{1.6}K_{0.4}Fe_{1+x}Mo_{1-x}O_{6-\delta}$ (x = 0.2, 0.4, 0.6) were achieved above 700 °C in 5% H_2/Ar, albeit with the formation of some impurity phases. Phase stability upon redox cycling was not observed for $SrCaFe_{1+x}Mo_{1-x}O_{6-\delta}$ (x = 0.2, 0.4, 0.6) and $Sr_{1.6}K_{0.4}Fe_{1.2}Mo_{0.8}O_{6-\delta}$, however both $Sr_{1.6}K_{0.4}Fe_{1.4}Mo_{0.6}O_{6-\delta}$ and $Sr_{1.6}K_{0.4}Fe_{1.6}Mo_{0.4}O_{6-\delta}$ exhibited sufficient redox stability.

Redox cycling of $SrCaFe_{1+x}Mo_{1-x}O_{6-\delta}$ (x = 0.2, 0.4, 0.6) and $Sr_{1.6}K_{0.4}Fe_{1+x}Mo_{1-x}O_{6-\delta}$ (x = 0.2, 0.4, 0.6) demonstrates a strong dependence on high temperature reduction to achieve high conductivities, with re-reduction at lower temperatures attaining between 0.1 % and 58.4 % of the initial conductivity observed after high temperature reduction. The reliance of these compounds on high temperature reduction is expected to limit their utility as SOFC anode materials, as the vulnerability to oxidation can have disastrous consequence for fuel cell durability. As the redox stability of these materials was observed to increase with increasing iron content, further investigation into strontium ferrite materials was deemed to be a suitable avenue for further investigations.

3.4. References

1. Y.-H. Huang, R. I. Dass, Z.-L. Xing and J. B. Goodenough, *Science*, 2006, **312**, 254-257.

2. P. Zhang, Y.-H. Huang, J.-G. Cheng, Z.-Q. Mao and J. B. Goodenough, *Journal of Power Sources*, 2011, **196**, 1738-1743.

3. L. Zhang, Q. Zhou, Q. He and T. He, *Journal of Power Sources*, **195**, 6356-6366.

4. S. Vasala, M. Lehtimäki, Y. H. Huang, H. Yamauchi, J. B. Goodenough and M. Karppinen, *Journal of Solid State Chemistry*, 2010, **183**, 1007-1012.

5. A. Atkinson, S. Barnett, R. J. Gorte, J. T. S. Irvine, A. M. McEvoy, M. Mogensen, S. C. Singhal and J. Vohs, *Nature Materials*, 2004, **3**, 17-27.

6. G. Xiao, Q. Liu, X. Dong, K. Huang and F. Chen, *Journal of Power Sources*, 2010, **195**, 8071-8074.

7. L. Zhang, Q. Zhou, Q. He and T. He, *Journal of Power Sources*, 2010, **195**, 6356-6366.

8. Q. Liu, X. Dong, G. Xiao, F. Zhao and F. Chen, *Advanced Materials*, 2010, **22**, 5478-5482.

9. A. C. Larson and R. B. V. Dreele, *"General Structural Analysis System" Los Alamos National Laboratory Report LAUR*, 1994, 86.

10. J. A. Alonso, M. T. Casais, M. J. Martà-nez-Lope, J. L. Martà-nez, P. Velasco, A. Muñoz and M. T. Fernández-Dà-az, *Chemistry of Materials*, 1999, **12**, 161-168.

11. G. Y. Liu, G. H. Rao, X. M. Feng, H. F. Yang, Z. W. Ouyang, W. F. Liu and J. K. Liang, *Journal of Alloys and Compounds*, 2003, **353**, 42-47.

12. Q. Liu, G. Xiao, T. Howell, T. L. Reitz and F. Chen, *ECS Transactions*, 2011, **35**, 1357-1366.

13. D. Niebieskikwiat, R. D. Sánchez, A. Caneiro, L. Morales, M. Vásquez-Mansilla, F. Rivadulla and L. E. Hueso, *Physical Review B*, 2000, **62**, 3340-3345.

14. R. S. Liu, T. S. Chan, S. Mylswamy, G. Y. Guo, J. M. Chen and J. P. Attfield, *Current Applied Physics*, 2008, **8**, 110-113.

15. C. Zener, *Physical Review*, 1951, **82**, 403-405.

16. A. Rosencwaig, *Physical Review*, 1969, **181**, 946-948.

17. Y. Yasukawa, J. Lindén, T. S. Chan, R. S. Liu, H. Yamauchi and M. Karppinen, *Journal of Solid State Chemistry*, 2004, **177**, 2655-2662.

18. P. W. Anderson, *Physical Review*, 1958, **109**, 1492-1505.

19. R. Allub and B. Alascio, *Physical Review B*, 1997, **55**, 14113-14116.

20. S.-e. Hou, A. Aguadero, J. A. Alonso and J. B. Goodenough, *Journal of Power Sources*, 2011, **196**, 5478-5484.

21. R. D. Shannon, *Acta Crystallographia Section A*, 1976, **A32**, 751.

4. Suitability of B-site doped Strontium Ferrite for Application as a Symmetrical SOFC Electrode

The initial investigations in this chapter focus on the applicability of iron rich $SrFe_{1-x}Ti_xO_{3-\delta}$ as SOFC electrode materials, through determination of the electronic conductivity and redox stability. A single material was chosen to take through for fuel cell testing, to determine a baseline fuel cell performance. Doping of the chosen material with transition metal dopants was investigated and the properties of these materials used to determine the suitability of the series for use as SOFC electrode materials.

4.1. $SrFe_{1-x}Ti_xO_{3-\delta}$ $(0 - 0.3)$

4.1.1. Introduction

The development of high performance novel ferrite based materials for SOFCs has thus far been mainly limited to cathodic applications, with LSF [1], LSCF [2] and BSCF [3] all exhibiting considerable performance as SOFC cathode materials. Many of the properties required for cathodic application, high electronic conductivity, ionic conductivity, thermal stability, compatibility with SOFC electrolyte and interconnect materials et cetera, are equally as desirable for anode materials. The limiting factor for use of these materials as symmetrical electrodes tends to be the redox stability and the catalytic activity of these compounds [4].

The structure of $SrFeO_{3-\delta}$ (SFO) at room temperature is highly dependent on the oxygen stoichiometry, with the cubic perovskite structure (SG: *Pm-3m* (221), a = 3.851) forming for $\delta = 0$, the tetragonal phase (SG: *I4/mmm* (139), a = 10.929, c = 7.698) forming for $\delta = 0.125$, the orthorhombic phase (SG: *Cmmm* (65), a = 10.974, b = 7.702, c = 5.473) forming for $\delta = 0.27$ and the brownmillerite phase occurring for δ = 0.5 (SG: *Icmm* (74), a = 5.672, b = 15.59, c = 5.527) [5, 6]. The relationship between the oxygen stoichiometry and the structure mean that the material properties change

significantly with variations in the synthesis and testing conditions [7]. Upon heating, however, the tetragonal, orthorhombic and brownmillerite phases all exhibit reversible phase transitions to the cubic perovskite phase [5, 8].

One example of this stoichiometry dependence is the electronic conductivity of $SrFeO_{3-\delta}$, which is known to transition from metallic to p-type semiconducting behaviour with an increase in the oxygen vacancy concentration between $0 \leq \delta \leq 0.5$ [9, 10]. Hombo *et. al.* [11] determined that the carrier mobility decreased with increasing oxygen vacancy concentration, concluding that the carrier mobility, along with the Fe-O-Fe bond length, were the major factors in dictating the electronic conductivity. The ionic conductivity of SFO also exhibits a strong correlation with the oxygen vacancy concentration, with the activation energy for ionic conduction reducing significantly with a transition from the brownmillerite phase to the cubic perovskite phase [10].

The observed catalytic activity of SFO exhibited for various reactions, such as toluene oxidation [12], methane oxidation [13] and oxidative dehydration of ethane [14], is again intrinsically linked to the availability of lattice oxygen, and therefore to the oxygen stoichiometry of SFO [9, 15]. As the structure and properties of strontium ferrite are highly dependent on the oxygen vacancy concentration, this allows controlled manipulation of the desired material properties through control of the composition and synthesis conditions.

B-site doping of strontium ferrites has been generally pursued with one aim in mind, stabilisation of the cubic perovskite structure to improve the mixed electronic-ionic conductivity. As was noted previously, the cubic perovskite structure of $SrFeO_3$ exhibits the maximal ionic and electronic conductivity of this series [9, 10]. As the cubic perovskite structure is known to form for those compounds with lower oxygen vacancy concentrations ($\delta < 0.125$), formation of this phase in air has been attempted through doping of cations with a higher oxidation state. Various dopants have been utilised to achieve this aim, with varying proportions of Ti [16], Mo [17], Nb [18], Re [19] and Sn [20] all producing the desired perovskite structure.

A cubic perovskite structure was observed for 25% rhenium doping, forming $Sr_4Fe_3ReO_{12-\delta}$ [19], close to the maximal doping level observed for molybdenum [17]. Despite the smaller cation sizes of both Re^{7+}/Re^{6+} (0.53 Å and 0.55 Å) and Mo^{6+} (0.59 Å), an increase in the lattice parameter was noted with increasing dopant levels,

attributed to the corresponding increase in Fe^{3+}, confirmed by Xiao *et. al.* [17]. The reduction in Fe^{4+} with increasing dopant levels results in a reduction in the electronic conductivity, due to the effective reduction of charge carriers.

Beurmann *et. al.* [20] found that the cubic perovskite structure was also formed for $SrFe_{1-x}Sn_xO_{3-\delta}$ (x = 0.1-0.6). The oxygen content of these samples was noted to primarily decrease between $SrFeO_{2.74}$ and $SrFe_{0.9}Sn_{0.1}O_{2.70}$, with minimal increases in the oxygen content upon additional tin doping. The Fe^{4+}/Fe^{tot} ratio was observed to decrease with increasing tin content, with the minimal variation in oxygen content suggesting that the increased charge from Sn^{4+} was balanced by the increase in Fe^{3+}.

A similar decrease in the Fe^{4+} content was observed for increasing titanium doping, even with synthesis of cubic perovskite samples in a highly oxidising atmosphere, 60 MPa O_2 [16]. Whilst $SrFeO_3$ synthesised in oxygen exhibits metallic behaviour, increasing the titanium content results in electron localisation despite the synthesis conditions, with sufficient oxygen vacancy concentration to imply mixed electronic-ionic conduction. Both electronic and ionic conduction was confirmed in air for $Sr_{0.97}Fe_{0.8}Ti_{0.2}O_{3-\delta}$ and $Sr_{0.97}Fe_{0.6}Ti_{0.4}O_{3-\delta}$ by Kharton *et. al.* [21], albeit exhibiting lower conductivities than the cobalt analogue.

Titanium rich strontium ferrites have previously come under scrutiny as cathode materials due to the mixed electronic-ionic conductivity [22, 23] and the observed activity for the oxygen reduction reaction [24]. The introduction of iron into strontium titanate was posited to improve the ionic conductivity and, possibly, the catalytic activity of these compounds through the introduction of oxygen vacancies. Additional improvement of the electronic conductivity of strontium titanate at 850 °C between $10^{-15} \leq pO_2 \leq 10^5$ was observed with increasing levels of iron doping, between [22]. As predicted, the ionic conductivity exhibited a similar trend with an increase observed with increasing iron content between $0.05 \leq x \leq 0.5$ at 800 °C in air [23]. Whilst the oxygen exchange kinetic for $SrTi_{1-x}Fe_xO_{3-\delta}$ (x = 0.35, 0.5) were not dissimilar to those observed for known cathode materials, LSCF, testing of SFT electrodes exhibited significantly higher area specific resistance, likely due to the lower conductivity of the compounds investigated [22]. Although lanthanum doping of

SFT was noted to reduce the thermal expansion coefficient, a subsequent reduction in both the electronic and ionic conductivity was observed [25].

Whilst there is a reasonable amount of research into strontium titanium ferrites, much of the research has focused on titanium rich materials, despite reports suggesting that increased iron doping improves material properties for application in SOFCs. A series of titanium doped strontium ferrites, $SrFe_{1-x}Ti_xO_{3-\delta}$ (x = 0 − 0.3), were synthesised to determine the temperature range for redox stability and to elucidate the suitability of these compounds for use as intermediate temperature SOFC electrode materials.

4.1.2. Experimental

4.1.2.1. Synthesis

$SrFe_{1-x}Ti_xO_{3-\delta}$ (x = 0 – 0.3) were produced by sol-gel synthesis technique. Stoichiometric amounts of $Sr(NO_3)_2$ (98%, Alfa Aesar) and $Fe(NO_3)_3 \cdot 9\ H_2O$ (98%, Alfa Aesar) were dissolved in distilled water. A stoichiometric amount of $C_{12}H_{28}O_4Ti$ (97%, Alfa Aesar) was dissolved in ethanol and the solutions were combined, whilst maintaining a 2:1 ratio of ethanol to distilled water. Citric acid (99+%, Alfa Aesar) was added in a 2:1 ratio to metal ions and the solution was heated until gelation. The resultant gel was fired at 600 °C for 2 hours. A second firing at 1100 °C for 24 hours was then performed, followed by a subsequent firing at 1300 °C for 12 hours. Pellets of all the samples (ø ≈ 13 mm × 2 mm) were uniaxially pressed at 221 MPa and sintered in air at 1300°C for 5 hours.

4.1.2.2. Analytical Procedures

Phase purity and crystal parameters of the samples were examined by X-ray diffraction (XRD) analysis using a Bruker D8 Advance diffractometer (Cu $K_{\alpha 1}$ radiation, λ = 1.5405Å). GSAS [26] software was used to perform a least squares refinement of the lattice parameters of all the samples.

The densities of the pellets were determined from the measured mass and volume. Theoretical densities were calculated using experimental lattice parameters and the chemical formula $SrFe_{1-x}Ti_xO_{3-\delta}$ (x = 0 – 0.3). The relative densities were calculated from the actual and theoretical density values. The density of the pellets was 75-85 % for all compounds.

Thermal analysis was conducted on a 10 ± 0.5 mg sample using a Stanton Redcroft STA 1500 Thermal Analyser on heating from room temperature to 800 °C and on cooling from 800 °C to room temperature in air, with a heating/cooling rate of 10 °C/min, and in 5% H_2/Ar, again with a heating/cooling rate of 10 °Cmin⁻¹, and with a flow rate of 5% H_2/Ar of 50 mLmin⁻¹.

4.1.2.3. Conductivity Testing

The pellets (ø ≈ 13 mm × 2 mm) were coated on opposing sides using silver paste. The conductivity of the samples was measured in the range 300 °C to 700 °C, with the exception of $SrFe_{1-x}Ti_xO_{3-\delta}$ ($x = 0 - 0.3$) in 5% H_2/Ar which measured in the range 300 °C to 600 °C. Measurements in air were conducted using an A.C. method using a Solartron 1287 electrochemical interface controlled by ZPlot software over the frequency range 65 kHz to 100 mHz. Measurements in dry 5% H_2/Ar, dried by passing the gas through 98% H_2SO_4, were conducted using the above A.C method and a D.C. method using a Solartron1250 Frequency Response Analyser coupled to a 1287 Electrochemical Interface controlled by CorrWare software with a constant current of 0.01 - 0.1 A, after reduction in the same atmosphere at 700 °C for 600 minutes.

4.1.2.4. Fuel Cell Testing

$Gd_{0.2}Ce_{0.8}O_{2-\delta}$ was prepared by a co-precipitation technique. Gd_2O_3 (99.9 %, Alfa Aesar) was dissolved in dilute nitric acid. $Ce(NO_3)_3 \cdot 6 H_2O$ (99%, Sigma Aldrich) was added to the Gd solution and diluted further. A 0.1M solution of $(NH_4)_2CO_3$ (NH_3 ca 30%, Alfa Aesar) was produced and the Gd-Ce solution was added dropwise to the solution. The resultant suspension was aged prior to filtration. The precipitate was dried, ground and fired at 600 °C for 2 hours. Pellets (ø ≈ 22 mm × 0.5 mm) were prepared and fired at 1500 °C for 5 hours.

A symmetrical fuel cell utilising a dense thick electrolyte, ~ 300 μm, and a porous electrode was tested between 600 °C and 800 °C, with flowing humidified H_2 , at $100mLmin^{-1}$ and flowing humidified air at the anode and cathode respectively. A paste containing $SrFe_{0.9}Ti_{0.1}O_{3-\delta}$, $Gd_{0.2}Ce_{0.8}O_{2-\delta}$ and α-Terpineol (96%, Alfa Aesar) was painted separately on each side of the previously prepared dense pellets and fired at 1200 °C for 2 hours. The impedance of the cell was measured at each temperature using a Solartron 1455A frequency response analyser coupled to a Solartron 1470E potentiostat/galvanostat controlled by CoreWare software over the frequency range 1 MHz to 100 mHz. Voltage-current curves were produced using Solartron 1470E potentiostat/galvanostat controlled by CoreWare software, with a ramp from OCV to 0 V and step time of 0.1s.

4.1.3. Results and Discussion
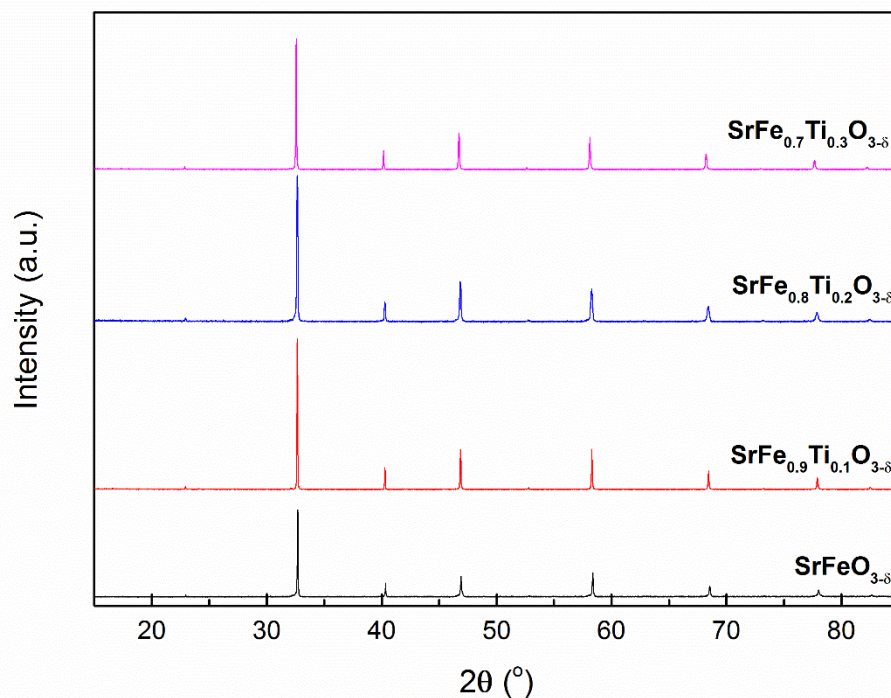
Figure 4.1. X-ray diffraction pattern for SrFe$_{1-x}$Ti$_x$O$_{3-\delta}$ (x = 0 - 0.3)

X-ray diffraction of SrFe$_{1-x}$Ti$_x$O$_{3-\delta}$ (x = 0 − 0.3) after synthesis in air at exhibited a single phase cubic perovskite structure, with the space group *Pm-3m* (No. 221), for all compounds, Figure 4.1. As the undoped strontium iron oxide appears to form a cubic perovskite structure (PDF: 01-070-5775) rather than the tetragonal (PDF: 01-070-5776), orthorhombic (PDF: 01-070-5777) or brownmillerite (PDF: 01-070-5778) structures, the oxygen vacancy concentration of the compound would be expected to be between $0 \leq \delta \leq 0.125$. Previous reports suggest that synthesis of the cubic perovskite phase of SrFeO$_{3-\delta}$ at room temperature requires cooling in flowing O$_2$/Ar [6], with cooling in air resulting in δ values of 0.16-0.18, forming a mixture of the cubic and tetragonal phases [6, 27].
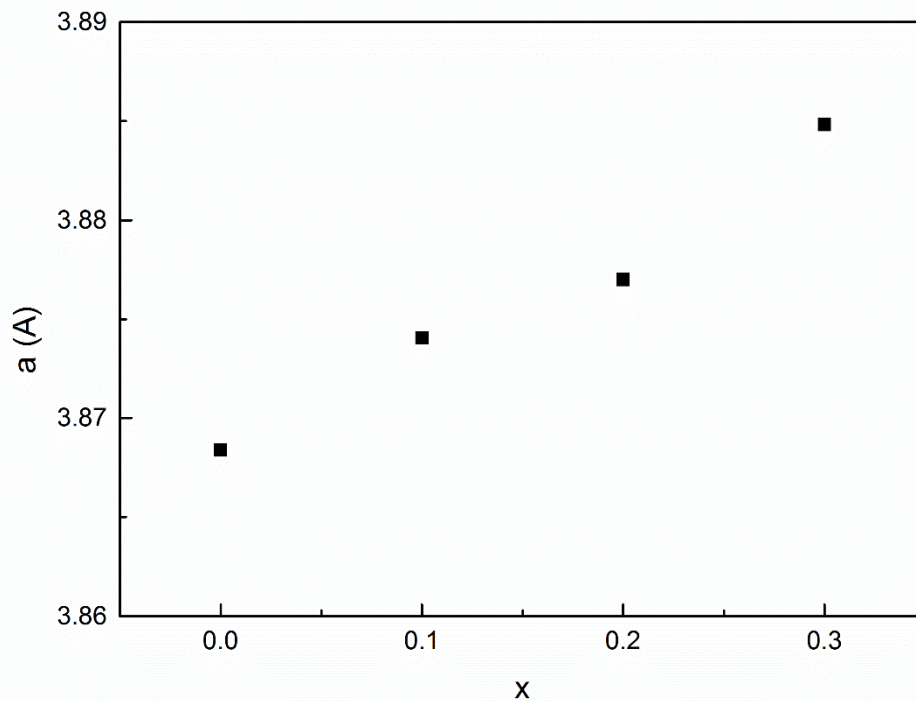
Figure 4.2. Variation of lattice parameters with increasing dopant concentration for SrFe$_{1-x}$Ti$_x$O$_{3-\delta}$ (x = 0 - 0.3)
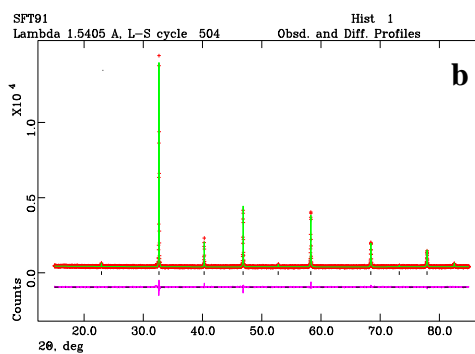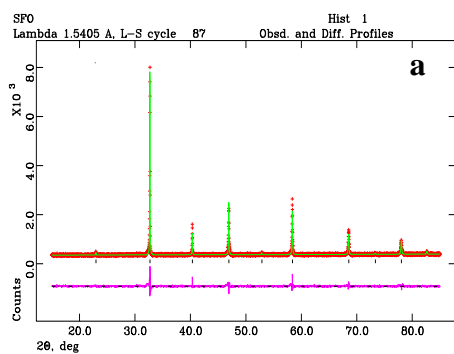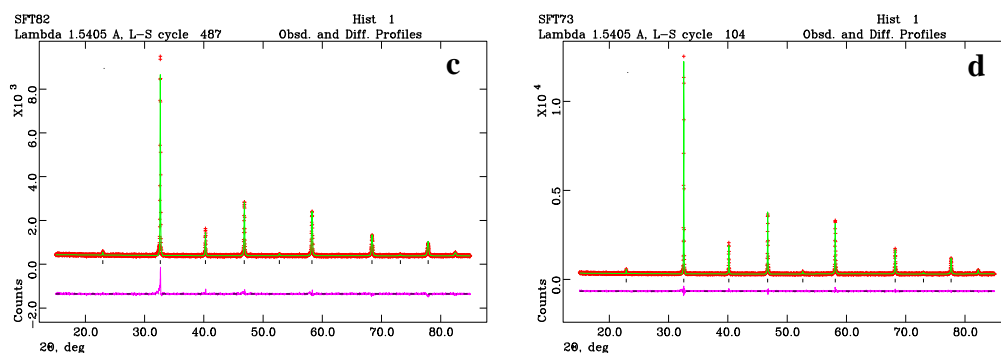
Figure 4.3. GSAS plots for SrFe$_{1-x}$Ti$_x$O$_{3-\delta}$, x = 0 (a), x = 0.1 (b), x = 0.2 (c) and x = 0 0.3 (d) after synthesis in air

GSAS [26] analysis of SrFeO$_{3-\delta}$ suggests that a single phase cubic perovskite is formed, Table 4.1, although, due to the similarity in the XRD patterns of the cubic and tetragonal phases and the resolution of the scan, the presence of the tetragonal phase cannot be discounted. Rietveld refinement of SrFe$_{1-x}$Ti$_x$O$_{3-\delta}$ (x = 0 − 0.3) demonstrated a linear increase in lattice parameters with increasing titanium content, Figure 4.2, 4.3 and Table 4.1. This is consistent with previous reports which suggest that a pseudo-linear increase in the lattice parameter occurs upon doping of SrFeO$_{3-\delta}$, as a result of either larger dopant cation radius or increasing proportions of Fe^{3+} [16, 20].

179

		SrFeO$_{3-\delta}$	SrFe$_{0.9}$Ti$_{0.1}$O$_{3-\delta}$	SrFe$_{0.8}$Ti$_{0.2}$O$_{3-\delta}$	SrFe$_{0.7}$Ti$_{0.3}$O$_{3-\delta}$
χ^2		1.760	1.193	1.386	1.179
Rp (%)		6.67	5.21	5.60	5.76
wRp (%)		4.96	4.11	4.31	4.52
Space Group		*Pm-3m*	*Pm-3m*	*Pm-3m*	*Pm-3m*
a (Å)		3.8683(3)	3.8740(2)	3.8775(3)	3.8848(3)
V (Å^3)		57.88(1)	58.14(1)	58.29(1)	58.62(1)
Sr	x	0	0	0	0
	y	0	0	0	0
	z	0	0	0	0
	U$_{iso}$	0.001(8)	0.004(3)	0.008(1)	0.004(4)
Fe/Ti	x	0.5	0.5	0.5	0.5
	y	0.5	0.5	0.5	0.5
	z	0.5	0.5	0.5	0.5
	U$_{iso}$	0.002(1)	0.006(6)	0.004(1)	0.005(6)
O	x	0	0	0	0
	y	0.5	0.5	0.5	0.5
	z	0.5	0.5	0.5	0.5
	U$_{iso}$	0.014(4)	0.022(1)	0.016(1)	0.017(1)

Table 4.1. 'Goodness of fit' parameters, lattice parameters and atomic parameters from GSAS refinement of SrFe$_{1-x}$Ti$_x$O$_{3-\delta}$ (x = 0 - 0.5) after synthesis in air
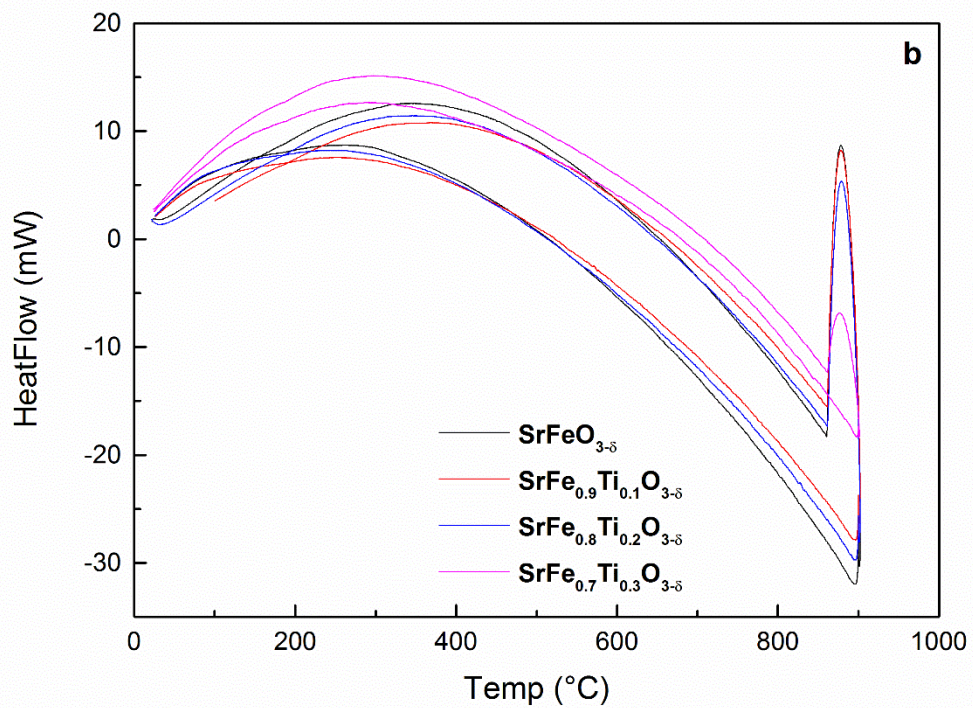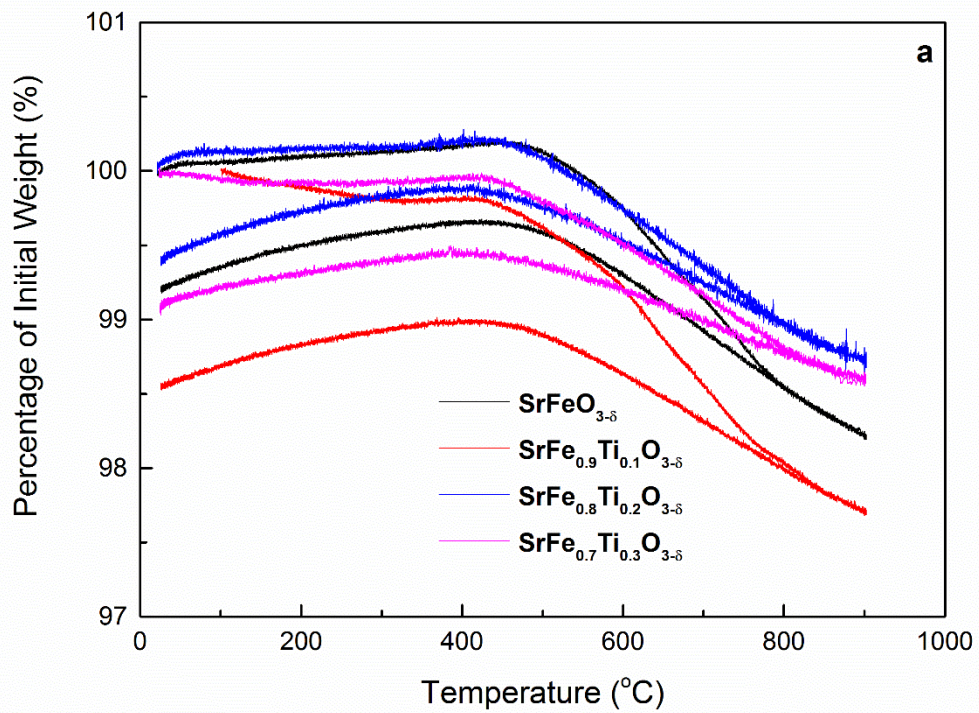
Figure 4.4. Thermogravimetric analysis (a) and differential scanning calorimetry (b) of SrFe$_{1-x}$Ti$_x$O$_{3-\delta}$ (x = 0 - 0.3) in air

Thermogravimetric analysis of these compounds in air, Figure 4.4 (a), exhibited a negligible reduction in weight, with variation in weight loss between the compounds showing no observable trend. Differential scanning calorimetry of $SrFe_{1-x}Ti_xO_{3-\delta}$ (x = 0 − 0.3) in air, Figure 4.4 (b), exhibited no significant deviations associated with phase transitions or compound decomposition, suggesting that these compounds are thermally stable over this temperature range. As the non-cubic phases of $SrFeO_{3-\delta}$ all exhibit a high temperature transition to the cubic perovskite phase within the temperature range of the STA [5, 8], the lack of inflections in the DSC trace for $SrFeO_{3-\delta}$ also imply the formation of the single phase cubic perovskite.
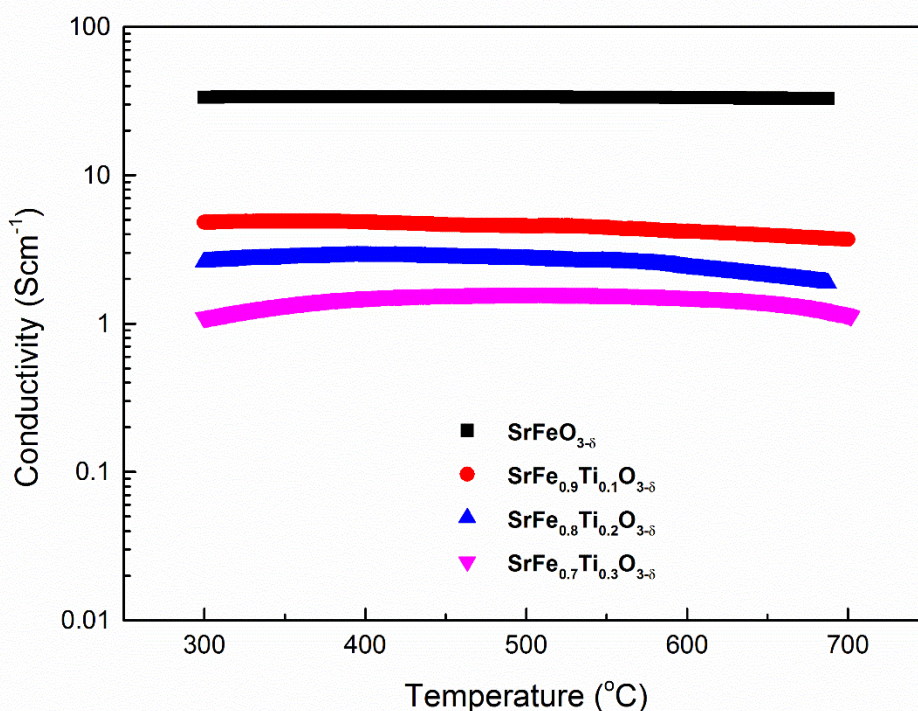
Figure 4.5. Conductivity of $SrFe_{1-x}Ti_xO_{3-\delta}$ (x = 0 - 0.3) in air

Conductivity of $SrFe_{1-x}Ti_xO_{3-\delta}$ (x = 0 − 0.3) in air was observed to reduce with increasing levels of titanium doping, Figure 4.5, with a semiconductor-metal transition noted for all compounds. The reduction in conductivity with increasing titanium

content is consistent with previous reports investigating the effect of iron doping on strontium titanates [22, 23], which noted that an increase in the iron content of $SrTi_{1-x}Fe_xO_{3-\delta}$ improved both the electronic and ionic conductivities.

The reduction in the conductivity between $SrFeO_{3-\delta}$ and $SrTi_{0.5}Fe_{0.5}O_{3-\delta}$ can be attributed to a reduction in the number of charge carriers, due to the expected reduction in the Fe^{4+}/Fe_{tot} ratio with increasing titanium doping. Whilst the reduction in the Fe^{4+}/Fe_{tot} ratio cannot be proven using the techniques utilised in this study, previous research overwhelmingly suggests that for most B-site dopants a reduction in the Fe^{4+}/Fe_{tot} ratio is observed with increasing dopant concentration [17, 20, 28].

The activation energy for conduction between 300 °C and 450 °C exhibits a small increase with increasing titanium content, from 0.07(1) eV for $SrFe_{0.9}Ti_{0.1}O_{3-\delta}$ to 0.17(1) eV for $SrFe_{07}Ti_{0.3}O_{3-\delta}$. Titanium is proposed to mainly occur in the Ti^{4+} state and is predicted to elicit little direct effect on conduction through the Fe-O-Fe pathway, as demonstrated by comparison of the predicted DOS of $SrFeO_3$ and $SrFe_{0.5}Ti_{0.5}O_3$ [29]. The oxygen content of these materials is expected to either not change or decrease slightly with increasing dopant levels, as was found for Sn^{4+} [20]. Variation of the carrier concentration in strontium ferrites is observed to cause variations in the average Fe-O bond length, as the average length of Fe^{3+}-O bonds is larger than that of Fe^{4+}-O bonds [10]. Bond lengthening is known to have a detrimental effect on the carrier mobility, thus an increase in the activation energy should be observed with a reduction in the carrier concentration. As a reduction in the charge carrier concentration is proposed with increasing titanium doping, the observed increase in activation energy is likely the result of lengthening of the Fe-O bonds. Only for dopants with a higher oxidation state, such as Mo^{6+} [17], does the increase in carrier mobility from an increased percolation pathway, due to increasing oxygen content, negate the reduction from bond shortening, due to Fe^{4+}-Fe^{3+} charge compensation.

The temperature of the transition between semiconducting behaviour and metallic behaviour was observed to increase with increasing titanium content, from 350°C for $SrFe_{0.9}Ti_{0.1}O_{3-\delta}$ to 480 °C for $SrFe_{0.7}Ti_{0.3}O_{3-\delta}$. Poulsen *et.* al [30] posited that the transition was due to compound reduction at high temperature, resulting in a reduction in the charge carriers. Previous research [27] demonstrated a pseudo-linear

reduction in the oxygen content of strontium ferrite in air above 400 °C with increasing temperature, which would appear to corroborate this conclusion.

The effect of high temperature compound reduction was further elucidated by Patrakeev *et. al.* [31] who demonstrated that the increase in the conductivity with increasing temperature, associated with E_a, was offset by the reduction in charge carrier concentration, causing an overall reduction in the electronic conductivity with increasing temperature, resulting in the pseudo-metallic behaviour. The temperature of the transition between semiconducting and pseudo-metallic behaviour occurs when the reduction in the conductivity through loss of charge carriers is balanced by the increase in conductivity through temperature activated conduction.

Whilst the reduction in the charge carriers with increasing temperature does explain the observed semiconductor-metal transition, the association with dopant concentration is less clear. Interrogation of the relevant literature demonstrates a significant reduction in the transition temperature with reduction of the dopant oxidation state, 600 °C for $SrFe_{0.9}Mo^{6+}_{0.1}O_{3-\delta}$ [17], 350 °C for $SrFe_{0.9}Ti^{4+}_{0.1}O_{3-\delta}$ and 320 °C for $SrFe_{0.9}Al^{3+}_{0.1}O_{3-\delta}$ [28]. Additionally, an increase in the temperature of the semiconductor-metal transition is observed with increasing dopant concentration for Mo^{6+} doped [17], Ti^{4+} and Al^{3+} doped [28] $SrFeO_{3-\delta}$.

Xiao *et. al.* [17] attributed the increase in the transition temperature with increasing dopant concentration for $SrFe_{1-x}Mo_xO_{3-\delta}$ to an increasing tolerance to reduction, however a similar increase in the transition temperature is also observed for increasing dopant concentration in $SrFe_{1-x}Al_xO_{3-\delta}$, which would not be expected to exhibit a similarly increasing tolerance to reduction. Thus the reducibility of the compound, whilst likely to affect the rate of reduction of the charge carriers, is unlikely to be the sole cause of increasing transition temperature with increasing dopant concentration.
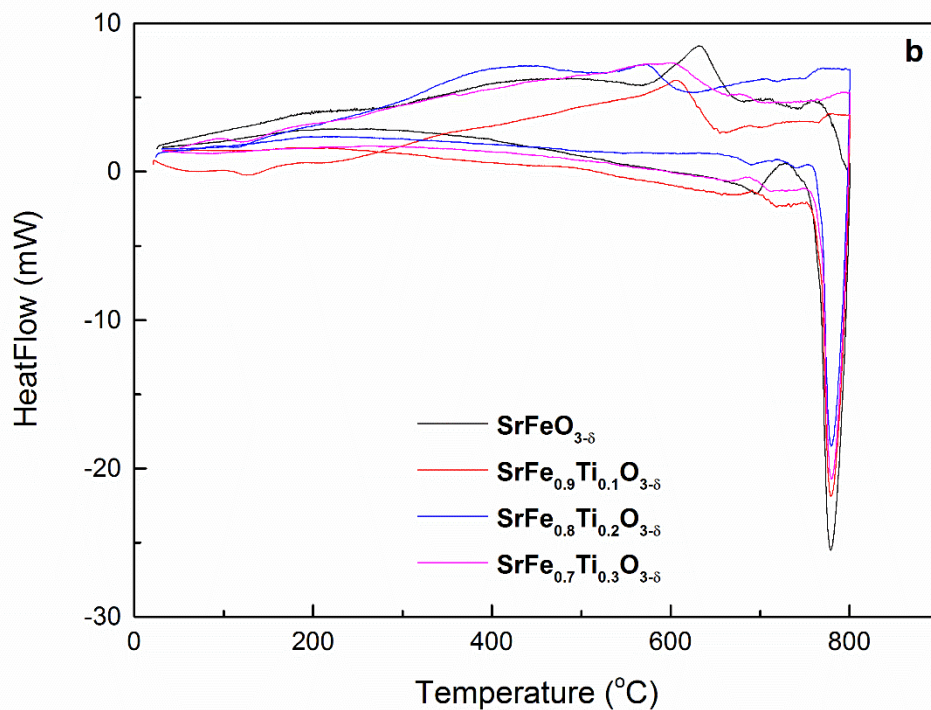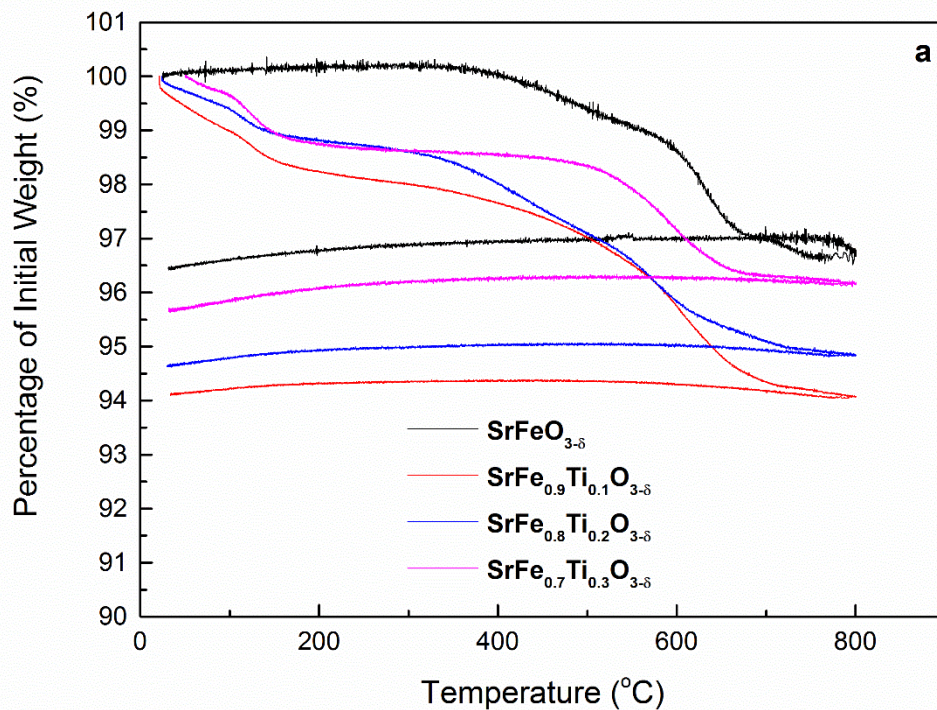
Figure 4.6. Thermogravimetric analysis (a) and differential scanning calorimetry (b) of SrFe$_{1-x}$Ti$_x$O$_{3-\delta}$ (x = 0 - 0.3) in 5% H$_2$/Ar

Thermogravimetric analysis of $SrFe_{1-x}Ti_xO_{3-\delta}$ (x = 0 − 0.3) in 5% H_2/Ar demonstrated a significant reduction in weight for all compounds, Figure 4.6 (a), with an reduction in weight loss with increasing titanium content observed from $SrFe_{0.9}Ti_{0.1}O_{3-\delta}$ to $SrFe_{0.7}Ti_{0.3}O_{3-\delta}$. Two separate weight loss regions occur on the TGA plot, with $SrFe_{1-x}Ti_xO_{3-\delta}$ (x = 0.1 − 0.3) exhibiting an initial loss of 0.5 − 2 % between 50 °C and 150 °C and all compounds exhibiting the second region, observed between 500 °C and 700 °C. The observed reduction in weight loss with increasing titanium content could either be attributed to differences in the initial oxygen content or to preferential reduction of the titanium in the sample. Differential scanning calorimetry of all compounds, Figure 4.6 (b), exhibited a reversible transition between 500 °C to 650 °C upon heating and between 750 °C to 650 °C on cooling.
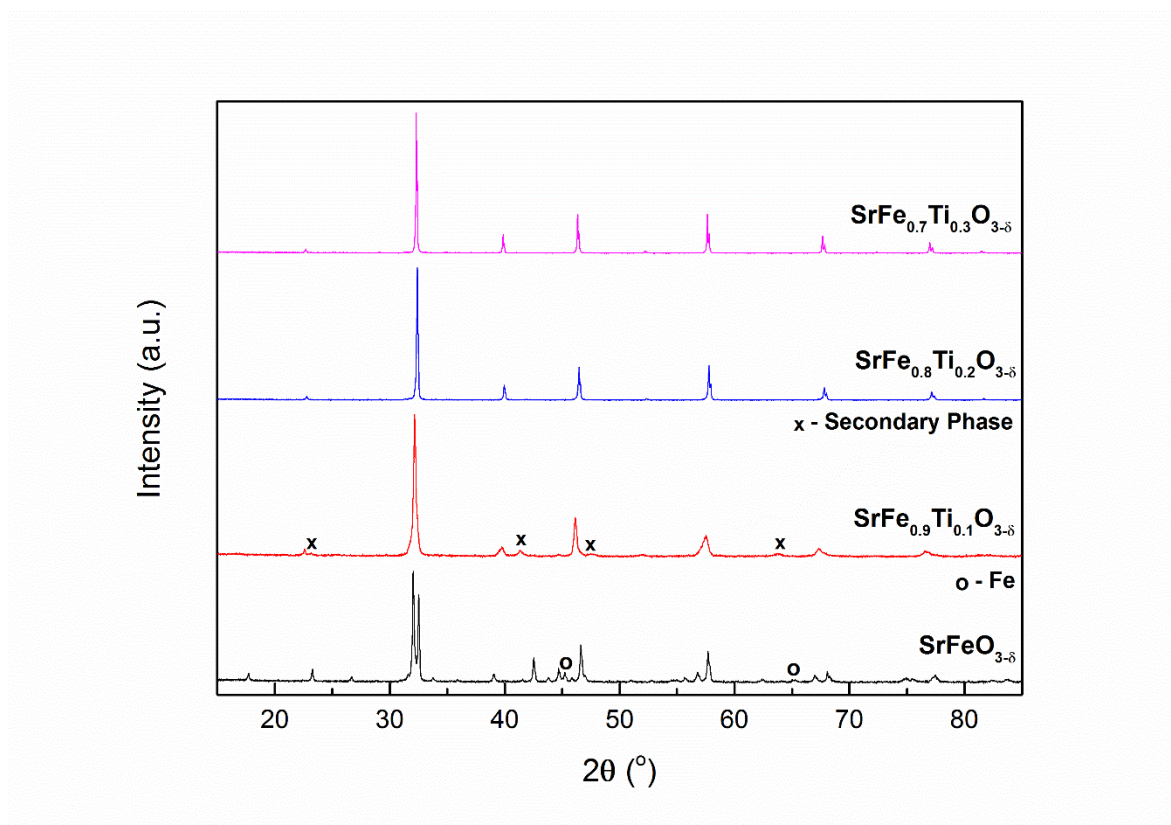
Figure 4.7. X-ray diffraction pattern of $SrFe_{1-x}Ti_xO_{3-\delta}$ (x = 0 - 0.3) after reduction in 5% H_2/Ar at 700 °C

Reduction of $SrFe_{1-x}Ti_xO_{3-\delta}$ (x = 0 − 0.3) at 700 °C in 5% H_2/Ar exhibited little change in the structure for titanium dopant levels > 0.1, Figure 4.7, with $SrFeO_{3-\delta}$

observed to degrade into $Sr_3Fe_2O_6$ (CDS collection code: 420235) and Fe (PDF: 6-696). Previous research into strontium ferrite suggested that exposure of the cubic strontium ferrite to a reducing atmosphere would result in Fe^{4+} reduction to Fe^{3+} and the formation of the highly oxygen deficient $Sr_2Fe_2O_5$ structure [10]. The structure of $SrFe_{0.9}Ti_{0.1}O_{3-\delta}$ mostly corresponded to the cubic perovskite structure, although minor additional peaks at 2θ = 23.2, 41.4, 47.6 and 63.8 were attributed to an unidentified secondary phase.
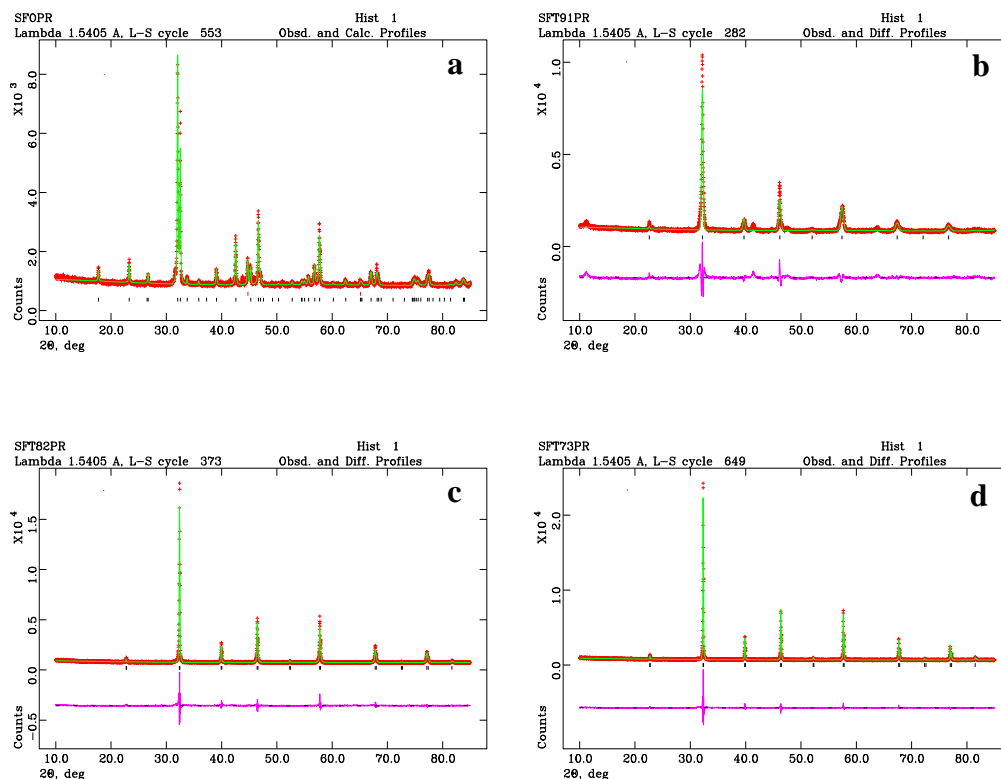
Figure 4.8. GSAS plots for $SrFe_{1-x}Ti_xO_{3-\delta}$, x = 0 (a), x = 0.1 (b), x = 0.2 (c) and x = 0 0.3 (d) after reduction in 5%H_2/Ar at 700 °C

Structural comparison of the cubic perovskite $SrFe_{1-x}Ti_xO_{3-\delta}$ (x = 0.1 − 0.3) after reduction at 700 °C in 5% H_2/Ar using GSAS [26] refinement demonstrated a pseudo-linear increase in lattice parameters, Table 4.2 and Figure 4.8, with increasing titanium content. Comparison of the oxidised and reduced compounds, Table 4.1 and 4.2, demonstrated an increase in the lattice parameters for all compounds upon

reduction, due to the increased atomic size of both Fe^{3+} (0.645 Å) and Ti^{3+} (0.67 Å) compared to Fe^{4+} (0.585 Å) and Ti^{4+} (0.605 Å) [32].

As the primary focus of the study was to determine the stability limits for use of these compounds at intermediate temperatures, conductivity measurements for all compounds were conducted at 600 °C, after additional stability testing demonstrated redox stability in both $SrFeO_{3-\delta}$ and $SrFe_{0.9}Ti_{0.1}O_{3-\delta}$ at that temperature.

		SrFeO$_{3-\delta}$		SrFe$_{0.9}$Ti$_{0.1}$O$_{3-\delta}$	SrFe$_{0.8}$Ti$_{0.2}$O$_{3-\delta}$	SrFe$_{0.7}$Ti$_{0.3}$O$_{3-\delta}$
χ^2		2.692		5.853	3.541	3.296
Rp (%)		5.17		7.74	6.42	6.31
wRp (%)		3.83		5.39	4.55	4.51
Primary Phase Fraction		93%		100%	100%	100%
Space Group		Immm		Pm-3m	Pm-3m	Pm-3m
a (Å)		3.890(1)		3.924(1)	3.906(1)	3.912(1)
c (Å)		20.014(5)		-	-	-
V (Å^3)		302.8(2)		60.437	59.7(1)	59.9(1)
Secondary Phase Fraction		7%		-	-	
Space Group		(Fe) Im-3m		-	-	
a (Å)		2.862(1)		-	-	
V (Å^3)		23.4(1)		-	-	
Sr	x	0	0	0	0	0
	y	0	0	0	0	0
	z	0.5	0.318(1)	0	0	0
P1	U$_{iso}$	0.012(2)	0.014(1)	0.042(2)	0.017(1)	0.024(1)
P2	U$_{iso}$	-		-	-	-
Fe/Ti	x	0		0.5	0.5	0.5
	y	0		0.5	0.5	0.5
	z	0.102(3)		0.5	0.5	0.5
P1	U$_{iso}$	0.007(1)		0.022(2)	0.013(1)	0.028(1)
P2	U$_{iso}$	-		-	-	-
O	x	0	0	0	0	0
	y	0.5	0	0.5	0.5	0.5
	z	0.082(7)	0.198(8)	0.5	0.5	0.5
P1	U$_{iso}$	0.014(3)	0.008(5)	0.088(4)	0.061(2)	0.057(3)
P2	U$_{iso}$	-		-	-	-

Table 4.2. 'Goodness of fit' parameters, lattice parameters and atomic parameters from GSAS refinement of SrFe$_{1-x}$Ti$_x$O$_{3-\delta}$ (x = 0 - 0.5) after reduction at 700 °C in 5% H$_2$/Ar
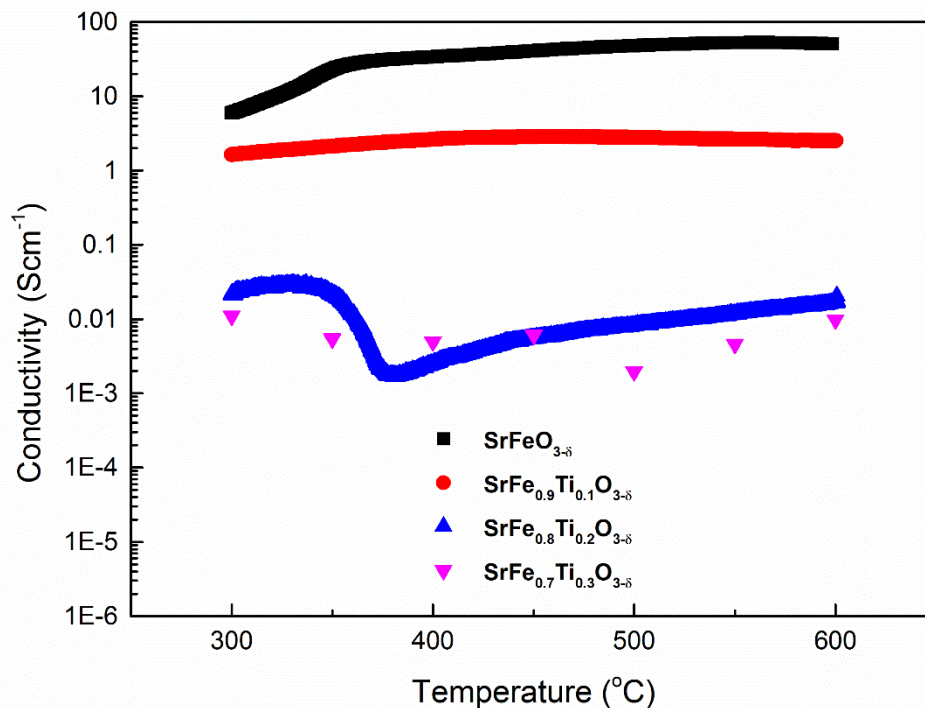
Figure 4.9. Conductivity of SrFe$_{1-x}$Ti$_x$O$_{3-\delta}$ (x = 0 - 0.3) in 5% H$_2$/Ar

Conductivity measurements of SrFe$_{1-x}$Ti$_x$O$_{3-\delta}$ (x = 0 – 0.3) from 600 °C to 300 °C in 5% H$_2$/Ar, Figure 4.9, exhibited a significant decrease in conductivity with increasing titanium content, as was observed in air, Figure 4.5. SrFeO$_{3-\delta}$ exhibited little change in the conductivity after exposure to 5% H$_2$/Ar whilst SrFe$_{0.9}$Ti$_{0.1}$O$_{3-\delta}$ exhibited a slight decrease in the conductivity upon reduction, from 4.191 Scm^{-1} to 2.527 Scm^{-1} at 600 °C. Minimal reduction of the conductivity of both SrFeO$_{3-\delta}$ and SrFe$_{0.9}$Ti$_{0.1}$O$_{3-\delta}$ is suggestive of partial reduction at these temperatures.

A more significant decrease in conductivity upon reduction was observed for both SrFe$_{0.8}$Ti$_{0.2}$O$_{3-\delta}$ and SrFe$_{0.7}$Ti$_{0.3}$O$_{3-\delta}$, which can be attributed to the lower initial charge carrier concentration with increasing dopant levels. Consequently a uniform reduction in the charge carrier concentration, as likely occurs for all compounds, disproportionally affects compounds with lower initial charge carrier concentrations, causing a larger reduction in the conductivity. In addition to the reduction in the conductivity, the behaviour of the conductivity of both SrFe$_{0.8}$Ti$_{0.2}$O$_{3-\delta}$ and

SrFe$_{0.7}$Ti$_{0.3}$O$_{3-\delta}$ exhibits an unusual temperature dependence, although currently the cause of this behaviour is unknown.
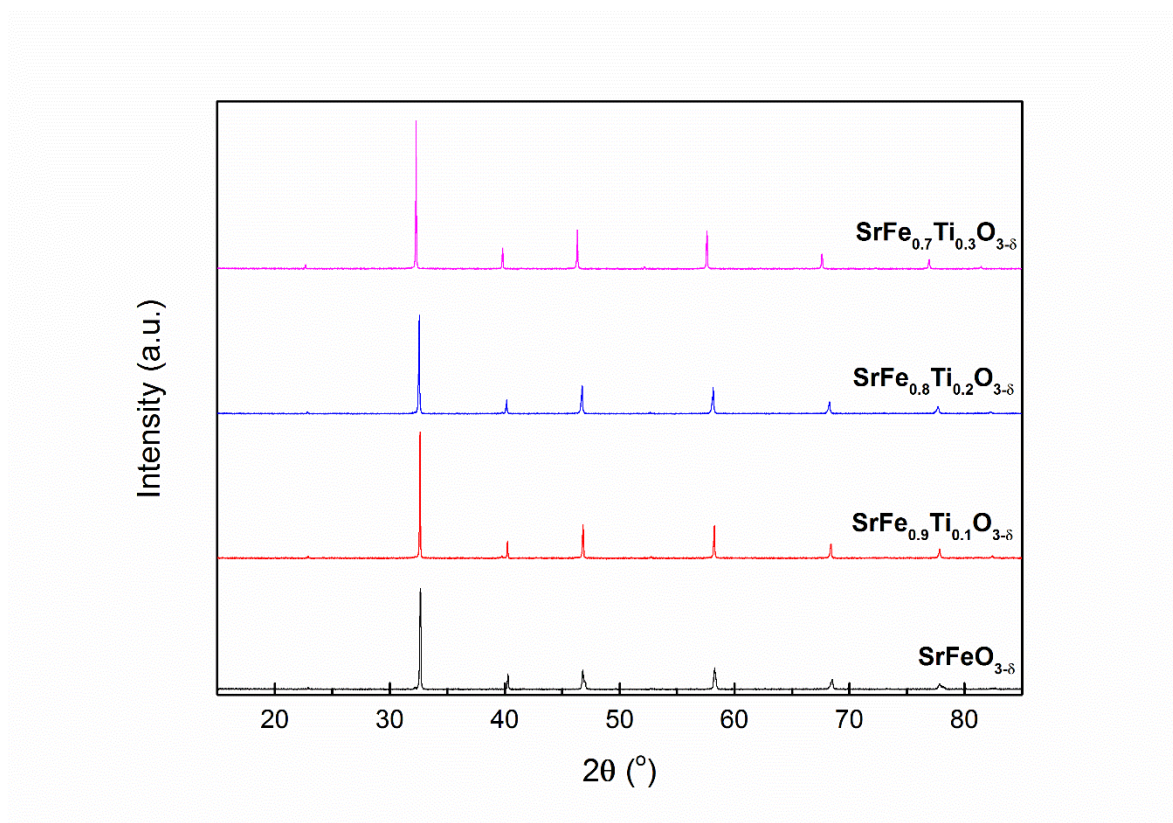
Figure 4.10. X-ray diffraction pattern of SrFe$_{1-x}$Ti$_x$O$_{3-\delta}$ (x = 0 - 0.3) after reduction in 5% H$_2$/Ar at 600 °C

Retention of the cubic perovskite structure was observed for all compounds after reduction at 600 °C in 5% H$_2$/Ar, Figure 4.10 and Table 4.3. GSAS [26] analysis demonstrated a pseudo-linear increase in the lattice parameter with increasing titanium content, Figure 4.11 and Figure 4.12. Comparison to the lattice parameters obtained after synthesis in air, Figure 4.2 and Table 4.1, demonstrates an increase in the lattice parameters upon reduction, with the increase proportional to the dopant concentration. This suggests that titanium is preferentially reduced at 600 °C, with the increase in the lattice parameter a result of the transition between Ti^{4+} (0.605 Å) and Ti^{3+} (0.67 Å) [32].
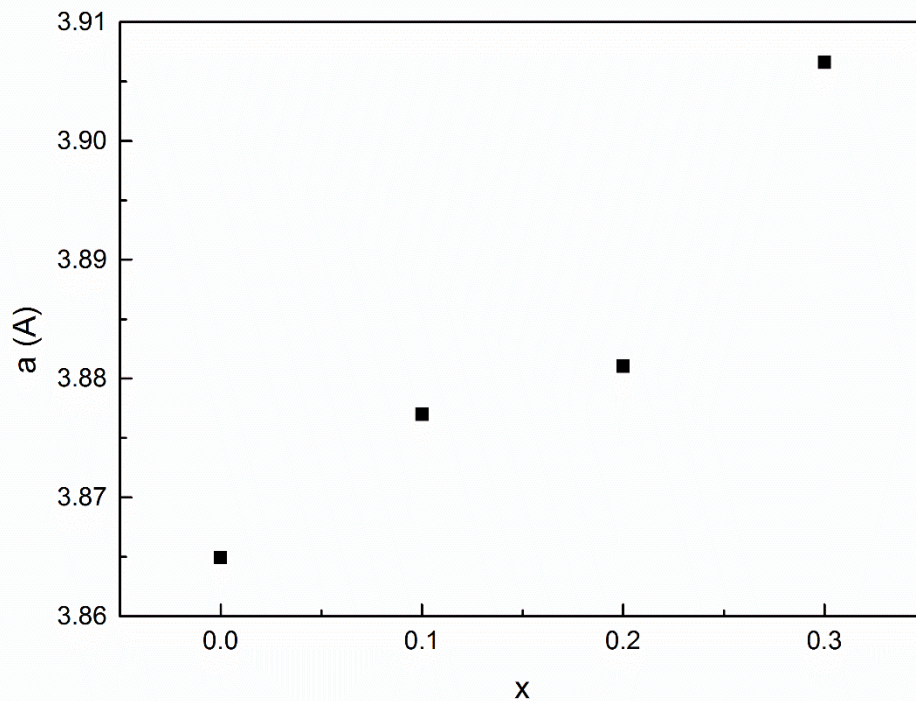
Figure 4.11. Variation of lattice parameters with increasing dopant concentration for SrFe$_{1-x}$Ti$_x$O$_{3-\delta}$ (x = 0 - 0.3) after reduction in 5% H$_2$/Ar at 600 °C
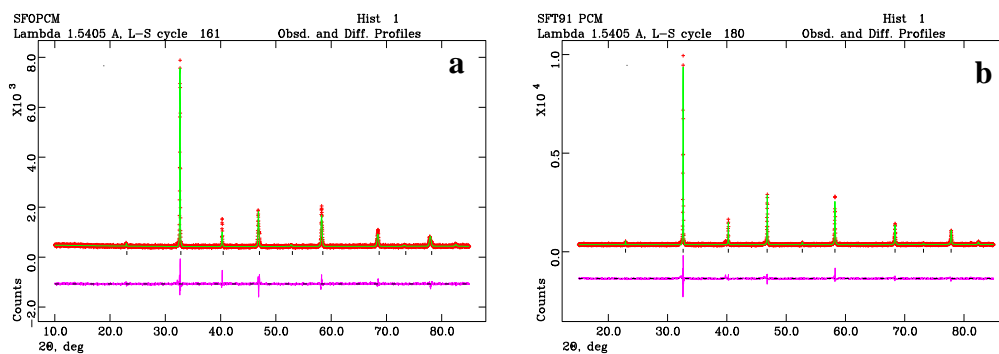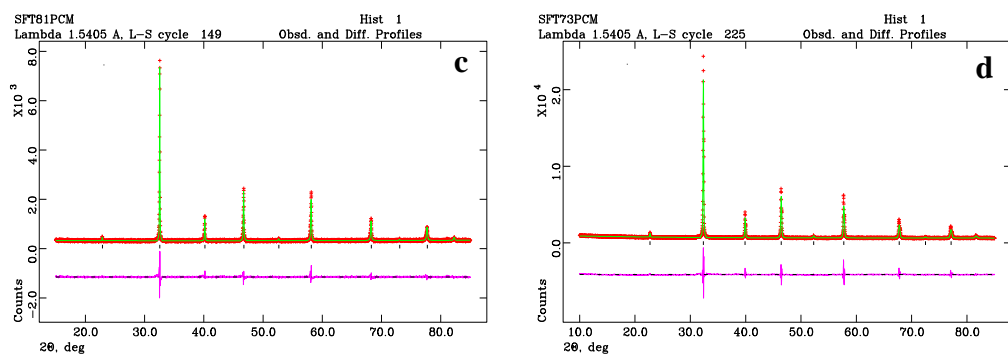
Figure 4.12. GSAS plots for SrFe$_{1-x}$Ti$_x$O$_{3-\delta}$, x = 0 (a), x = 0.1 (b), x = 0.2 (c) and x = 0 0.3 (d) after reduction in 5%H$_2$/Ar at 600 °C

		SrFeO$_{3-\delta}$	SrFe$_{0.9}$Ti$_{0.1}$O$_{3-\delta}$	SrFe$_{0.8}$T$_{0.2}$O$_{3-\delta}$	SrFe$_{0.7}$Ti$_{0.3}$O$_{3-\delta}$
χ^2		2.202	1.657	1.394	4.939
Rp (%)		6.88	6.44	5.63	7.84
wRp (%)		4.82	4.91	4.34	5.46
Space Group		*Pm-3m*	*Pm-3m*	*Pm-3m*	*Pm-3m*
a (Å)		3.8649(7)	3.8769(2)	3.8774(3)	3.9066(7)
V (Å^3)		57.73(3)	58.27(1)	58.29(1)	59.62(3)
Sr	x	0	0	0	0
	y	0	0	0	0
	z	0	0	0	0
	U$_{iso}$	0.001(9)	0.005(1)	0.007(6)	0.018(1)
Fe/Ti	x	0.5	0.5	0.5	0.5
	y	0.5	0.5	0.5	0.5
	z	0.5	0.5	0.5	0.5
	U$_{iso}$	0.004(1)	0.007(9)	0.003(7)	0.022(1)
O	x	0	0	0	0
	y	0.5	0.5	0.5	0.5
	z	0.5	0.5	0.5	0.5
	U$_{iso}$	0.052(2)	0.028(1)	0.015(1)	0.041(1)

Table 4.3. 'Goodness of fit' parameters, lattice parameters and atomic parameters from GSAS refinement of SrFe$_{1-x}$Ti$_x$O$_{3-\delta}$ (x = 0 - 0.3) after reduction at 600 °C in 5% H$_2$/Ar

Despite retaining the cubic perovskite structure at 700 °C the conductivities of $SrFe_{1-x}Ti_xO_{3-\delta}$ (x = 0.2 − 0.3) were significantly lower in 5% H_2/Ar. Whilst the conductivity of $SrFe_{0.9}Ti_{0.1}O_{3-\delta}$ exhibited comparatively low conductivity in reducing atmospheres, the redox stability of this compound allows for further modification to improve the material properties for potential use as an SOFC symmetrical electrode material.

Preparation of symmetrical fuel cells with pure $SrFe_{0.9}Ti_{0.1}O_{3-\delta}$ electrodes resulted in significant degradation of the mechanical stability of the anode, with cracking and delamination observed during fuel cell production. The mechanical instability of the fuel cell during synthesis is most likely the result of the difference in the thermal expansion coefficient between $SrFe_{0.9}Ti_{0.1}O_{3-\delta}$ [21] and $Gd_{0.2}Ce_{0.8}O_{2-\delta}$ [33]. Reduction of the mismatch between $SrFe_{0.9}Ti_{0.1}O_{3-\delta}$ and $Gd_{0.2}Ce_{0.8}O_{2-\delta}$ was achieved through the use of composite $SrFe_{0.9}Ti_{0.1}O_{3-\delta}$-$Gd_{0.2}Ce_{0.8}O_{2-\delta}$ electrodes.

Fuel cell performance of a (60:40 $SrFe_{0.9}Ti_{0.1}O_{3-\delta}$-$Gd_{0.2}Ce_{0.8}O_{2-\delta}$) - $Gd_{0.2}Ce_{0.8}O_{2-\delta}$ - (60:40 $SrFe_{0.9}Ti_{0.1}O_{3-\delta}$-$Gd_{0.2}Ce_{0.8}O_{2-\delta}$) symmetrical SOFC, Figure 4.13, exhibited a maximum power density of 22 $mWcm^{-2}$ at 700 °C, 15 $mWcm^{-2}$ at 650 °C and 9 $mWcm^{-2}$ at 600 °C. The maximum power densities were obtained at 0.33 V over the entire temperature range. The low operating voltage observed suggests that the operating efficiency of these cells is also low, as the fuel cell operating voltage is directly related to the efficiency of the fuel cell [34]. The low operating voltage is also a direct result of the low open circuit voltage of the fuel cell.
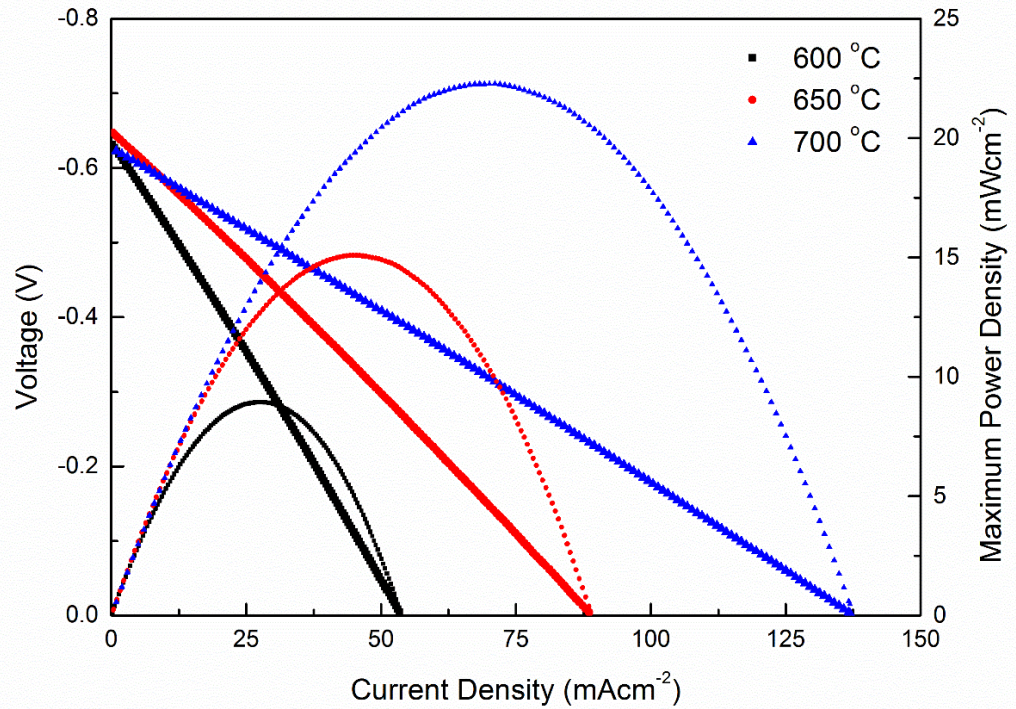
Figure 4.13. Fuel cell performance of a (60:40 SrFe$_{0.9}$Ti$_{0.1}$O$_{3-\delta}$-Gd$_{0.2}$Ce$_{0.8}$O$_{2-\delta}$) - Gd$_{0.2}$Ce$_{0.8}$O$_{2-\delta}$ - (60:40 SrFe$_{0.9}$Ti$_{0.1}$O$_{3-\delta}$-Gd$_{0.2}$Ce$_{0.8}$O$_{2-\delta}$) symmetrical SOFC, with flowing humidified H$_2$ and flowing humidified air at the anode and cathode respectively

The open circuit voltage, 0.63-0.64 V, of these fuel cells is significantly lower than the theoretical open circuit voltage, Equation 4. Reduction of the OCV could be a result of a lack of gas tightness of the electrolyte or the sealant, which could result in gas crossover and a subsequent reduction of the open circuit voltage [34]. Equally this drop in OCV can be a result of cerium reduction, which results in an increase in the electronic conductivity of the electrolyte [35, 36], reducing the electrons transferred round the external circuit, reducing the efficiency of the fuel cell and reducing the OCV.
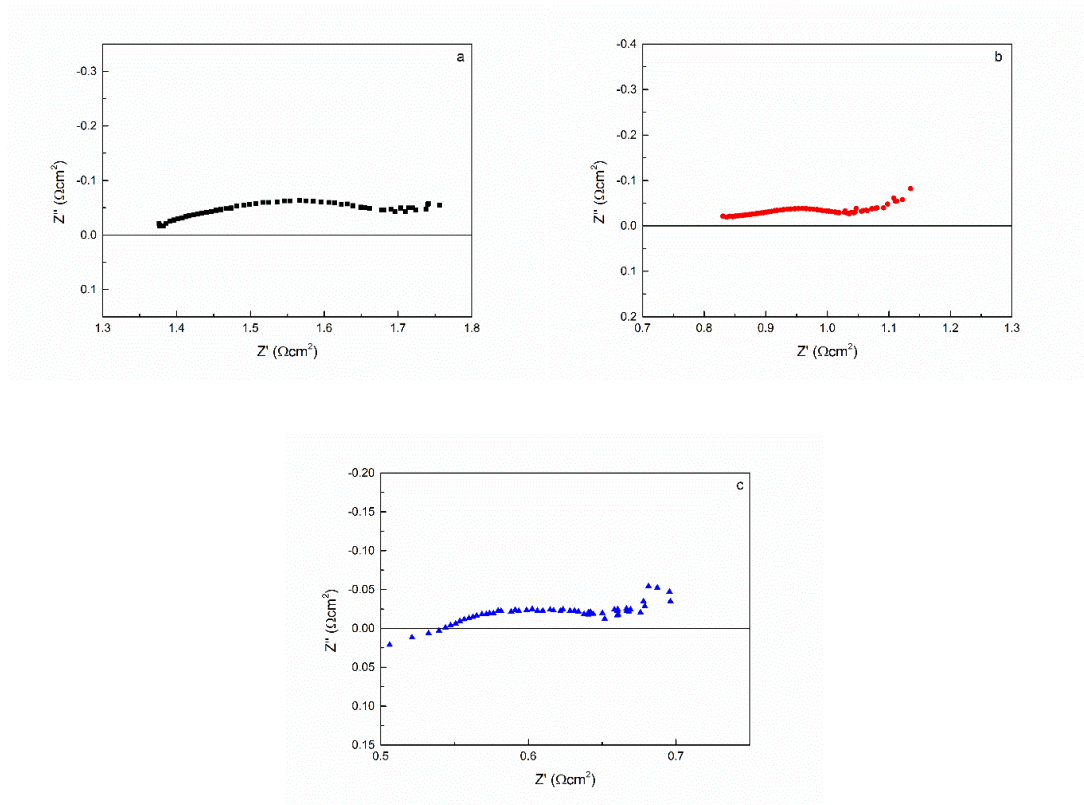
Figure 4.14. Impedance of a (60:40 SrFe$_{0.9}$Ti$_{0.1}$O$_{3-\delta}$-Gd$_{0.2}$Ce$_{0.8}$O$_{2-\delta}$) - Gd$_{0.2}$Ce$_{0.8}$O$_{2-\delta}$ - (60:40 SrFe$_{0.9}$Ti$_{0.1}$O$_{3-\delta}$-Gd$_{0.2}$Ce$_{0.8}$O$_{2-\delta}$) symmetrical SOFC over the frequency range 1 MHz to 100 mHz at 600°C (a), 650°C (b) and 700°C (c), with flowing humidified H$_2$ and flowing humidified air at the anode and cathode respectively

A reduction of the series resistance, Figure 4.14, (R$_s$) (from 1.376 Ωcm^2 to 0.544 Ωcm^2), total resistance (R$_t$) (from 1.75 Ωcm^2 to 0.65 Ωcm^2) and the polarisation resistance (R$_p$) (from 0.374 Ωcm^2 to 0.106 Ωcm^2) is observed with reducing temperature, a result of improving electrode and electrolyte conductivity and reaction kinetics. Determination of the fuel cell resistances was achieved through fitting of a theoretical circuit to the experimental data, using ZView software. This uses the circuits description code (CDC), as explained in Section 2.1.3, to create a theoretical circuit, which is then modelled, and the fit of the model is compared to the experimental data. The initial values given for the theoretical circuit are then refined until the fit to the experimental data is maximised. Determination of the polarisation resistance from this method was achieved through fitting of the main peak observed in the impedance plots,

197

Comparison of the experimental data, Figure 4.14, to model circuits, Figure 2.3, demonstrates a flattening of the ideal resistance-capacitance semicircle, which is indicative of non-ideal capacitance and was modelled using a constant phase element. Constant phase elements are commonly used in modelling of fuel cell resistances and it has been suggested that this is the result of capacitance from double layer charging being distributed along the pores in the electrode [37, 38].

Values of the ASR from the fuel cell impedance and from the voltage-current curves do not tally, with values of 0.65 Ωcm^{-1} and 0.80 Ωcm^{-1} at 700 °C and values of 1.75 Ωcm^{-1} and 2.083 Ωcm^{-1} at 600 °C, calculated from impedance and voltage-current curves respectively. Research by Atkinson *et. al.* [39] found that the observed impedance response of a GDC electrolyte can demonstrate a reduction in the various observed AC resistances, due to a partial short circuit of the ionic current as a result of the additional conduction contribution from the electronic carriers. This is due to the induction of mixed electronic-ionic conductivity in GDC upon material reduction. This mixed electronic-ionic conduction has been well documented over the fuel cell temperature range with an electronic conductivity between $3x10^{-2}$ Scm^{-1} and $5x10^{-2}$ Scm^{-1} observed between 500 °C ($pO_2 = 10^{-27}$) and 700 °C ($pO_2 = 10^{-20}$) respectively [36]. Upon exposure to the anodic operating conditions, reduction of the ceria in the electrolyte, from Ce^{4+} to Ce^{3+}, induces n-type semiconduction in the electrolyte material. As the resistance from electronic conduction is parallel to the resistance from ionic conduction, the total resistance will be equal to the reciprocal of the sum of the reciprocal of the resistances, resulting in a reduction of the total resistance. Additionally, a 'chemical' capacitance, resulting in a large low frequency response, is observed, due to the deviation from oxygen stoichiometry. This is intrinsically linked to the increase in the electronic conductivity, as reduction of the ceria results in both charge carrier formation and an increase in oxygen vacancy concentration.

Mitigation of the electronic conductivity of the electrolyte could be achieved through the replacement of GDC with an alternative electrolyte material, such as scandium doped zirconia (ScSZ) or LSGM [40]. As has been covered in Section 1.3.1, replacement of GDC with alternative electrolyte materials merely causes separate issues with compound reactivity or low ionic conductivity. An alternative method to

reduce the impact of electronic conductivity from GDC uses a barium based electron blocking layer, as was demonstrated by Sun *et. al.* [41]. One disadvantage to the use of an electron blocking layer is that the thickness of the layer will have a significant effect on the fuel cell performance. Minimisation of the thickness of the electron blocking layer is required to minimise the detrimental reduction in the ionic conductivity, although this can be achieved through the use of modern manufacturing techniques.

It should be noted that the production methods for the fuel cell electrodes are not optimal, with the electrodes painted, not printed, onto the electrolyte. The limitations of this production method mean that there is little control over electrode physical properties, such as thickness, open porosity and mechanical strength. Additionally, due to the unknown effect of the electrode paste and pore former on the sintering of the electrode material, the density of the as fired electrode may be lower than was previously observed and therefore may have a detrimental effect on anode performance. The lack of control over the porosity of the electrode could also result in poor open porosity of the electrode, which would limit the gas flow to and from the electrodes and cause a reduction of the three phase boundary, limiting electrode performance. Determination of the electrode porosity and thickness could be achieved using scanning electron microscopy and the data from this could be fed into electrode microstructure optimisation studies

4.1.4. Conclusion

The formation of redox stable materials for $SrFe_{1-x}Ti_xO_{3-\delta}$ ($x = 0 - 0.3$) was observed between room temperature and 600 °C, albeit with relatively low conductivity Whilst the conductivity of $SrFe_{0.9}Ti_{0.1}O_{3-\delta}$ was not sufficiently high to recommend for use as an SOFC electrode material, the redox stability of this compound allows for further modification to improve the material properties for potential use as an SOFC symmetrical electrode material.

For the (60:40 $SrFe_{0.9}Ti_{0.1}O_{3-\delta}$-$Gd_{0.2}Ce_{0.8}O_{2-\delta}$) - $Gd_{0.2}Ce_{0.8}O_{2-\delta}$ - (60:40 $SrFe_{0.9}Ti_{0.1}O_{3-\delta}$-$Gd_{0.2}Ce_{0.8}O_{2-\delta}$) fuel cell, both the impedance and the I-V data

demonstrate overall poor fuel cell performance, with high resistances and low open circuit voltage contributing to low maximum power densities. The conclusion that can be drawn from these fuel cells is that, despite the poor performance, production of a working symmetrical fuel cell at intermediate temperatures using strontium ferrite materials is possible. This demonstrates potential for these compounds as symmetrical electrode materials, although further optimisation of both the fuel cell processing and material properties of the strontium ferrites is required to produce an efficient symmetrical SOFC at these temperatures.

4.2. SrFe$_{0.7}$TM$_{0.2}$Ti$_{0.1}$O$_{3-\delta}$ (TM = Mn, Fe, Co, Ni, Cu)

4.2.1. Introduction

B-site substitution with transition metal dopants has also been utilised extensively to modify material properties of anode materials, with modification to SrTiO$_{3-\delta}$ and (La,Sr)CrO$_{3-\delta}$ producing effective anode materials [42, 43]. The majority of preceding research into B-site doped strontium ferrites has concentrated on stabilisation of the cubic perovskite structure. Doping with cations with a similar oxidation state has also been shown to result in the formation of the cubic perovskite phase for SrFeO$_{3-\delta}$ through suppression of oxygen vacancy ordering [28, 44, 45]. Suppression of oxygen vacancy ordering can be achieved through random distribution of dopant cations which either preferentially associate with oxygen vacancies [44] or which repel oxygen vacancies [45].

Stabilisation of the cubic perovskite structure through oxygen vacancy repulsion can be demonstrated through comparison of the gallium and scandium doped SrFeO$_{3-\delta}$ [45, 44]. Gallium (Ga^{3+}- 3d^{10}) and scandium (Sc^{3+} - 3p^6) both exhibit stable oxidation states, although there is a significant cation size difference in the SrFeO$_{3-\delta}$ structure, for Ga^{3+} and for Sc^{3+} [32]. Both dopants form the cubic perovskite structure in air for dopant levels up to 20 % for gallium and 30 % for scandium. Reduction of the gallium analogues results in the formation of the brownmillerite phase under mild reducing conditions [44], whilst the scandium analogues retain the cubic perovskite structure even under highly reducing conditions [45]. The authors posit that the increased stability of these phases over the gallium analogues is likely to be the result of gallium not inhibiting the ordering of oxygen vacancies with increasing vacancy content, as, whilst it is known to be energetically unfavourable in air [44], gallium can assume tetrahedral coordination. Despite the observed redox stability, Patrakeev *et. al.* [45] concluded that utilisation of scandium doped materials was impractical due to the high cost of the raw material and the presence of other, more suitable, dopants.

SrFe$_{1-x}$Al$_x$O$_{3-\delta}$ (x = 0.1-0.3) exhibits the cubic perovskite structure in air [28, 44], although, in contrast to the Ga and Sc dopants, aluminium doped into the SrFeO$_{3-\delta}$

structure associates with oxygen vacancies in the form of the energetically favourable tetrahedral coordinated Al^{3+} [44]. As aluminium can accommodate oxygen vacancies, reduction of these compounds results in the formation of co-existing domains of the cubic perovskite and brownmillerite structures, with modelling suggesting that aluminium is predominantly concentrated in the brownmillerite phase [44, 46]. The strong association of oxygen vacancies with randomly distributed aluminium in the structure minimises the Fe-associated oxygen vacancies. The resultant increase in the Fe-O-Fe bonds, is reflected in the increase of the hole mobility with increasing aluminium doping. This is in stark contrast to the variation in hole mobility observed with increasing scandium and gallium doping, which exhibits a reduction in the hole mobility due to an increase in Fe-associated oxygen vacancies due to the preferential octahedral coordination of both dopants in air.

Previous dopants exhibited a reduction in the electronic conductivity with increasing dopant concentration, attributed to the reduction in charge carriers due to the induced Fe^{4+}-Fe^{3+} transition [17, 18, 44]. Variation in the Fe^{4+}/Fe_{tot} ratio is thought to be partially dependent on the synthesis conditions and on the charge and co-ordination environment of the dopant cation, albeit for all B^{3+}, B^{4+}, B^{5+} and B^{7+} dopants a reduction in the total conductivity, due to a reduction in the Fe^{4+}/Fe_{tot} ratio, is noted upon increased doping levels.

Our previous research into titanium doped strontium ferrites, section 4.2, indicated that the minimal dopant level to stabilise the cubic perovskite structure, x = 0.1, was also required to achieve redox stability at 600 °C, albeit to the detriment of the electronic conductivity. It was posited that minimal doping of $SrFe_{0.9}Ti_{0.1}O_{3-\delta}$ with cations with a lower oxidation state could be utilised to improve the conductivity whilst retaining the redox stability. To this end a series of transition metal doped strontium titanium ferrites, $SrFe_{0.7}TM_{0.2}Ti_{0.1}O_{3-\delta}$ (TM = Mn, Fe, Co, Ni, Cu), were synthesised and their stability and conductivity in oxidising and reducing atmospheres elucidated.

4.2.2. Experimental

4.2.2.1.   Synthesis

$SrFe_{0.7}TM_{0.2}Ti_{0.1}O_{3-\delta}$ (TM = Co, Cu, Fe, Mn, Ni) were produced by sol-gel synthesis technique. Stoichiometric amounts of $Sr(NO_3)_2$ (98%, Alfa Aesar) and $Fe(NO_3)_3 \cdot 9\,H_2O$ (98%, Alfa Aesar) with either $Co(NO_3)_2 \cdot 6\,H_2O$ (98^+%, Alfa Aesar), $Cu(NO_3)_2 \cdot 2.5\,H_2O$ (ACS grade 98-102%, Alfa Aesar), $MnC_4H_6O_4 \cdot 4\,H_2O$ (>99%, Sigma Aldrich) or $Ni(NO_3)_2 \cdot 6\,H_2O$ (98%, Alfa Aesar) were dissolved in distilled water. A stoichiometric amount of $C_{12}H_{28}O_4Ti$ (97%, Alfa Aesar) was dissolved in ethanol and the solutions were combined, whilst maintaining a 2:1 ratio of ethanol to distilled water. Citric acid (99^+%, Alfa Aesar) was added in a 2:1 ratio to metal ions and the solution was heated until gelation. The resultant gel was fired at 600 °C for 2 hours. A second firing at 1300 °C for 3 hours was then performed. Pellets of all the samples (ø ≈ 13 mm × 2 mm) were uniaxially pressed at 221 MPa and sintered in air at 1300°C for 2 hours.

4.2.2.2.   Analytical Procedures

Phase purity and crystal parameters of the samples were examined by X-ray diffraction (XRD) analysis using a Bruker D8 Advance diffractometer (Cu $K_{\alpha 1}$ radiation, λ = 1.5405Å). GSAS [26] software was used to perform a least squares refinement of the lattice parameters of all the samples.

The densities of the pellets were determined from the measured mass and volume. Theoretical densities were calculated using experimental lattice parameters and the chemical formula $SrFe_{1-x}Ti_xO_{3-\delta}$ (x = 0 – 0.3) and $SrFe_{0.7}TM_{0.2}Ti_{0.1}O_{3-\delta}$ (TM = Co, Cu, Mn, Ni). The relative densities were calculated from the actual and theoretical density values. The density of the pellets was 75-85 % for all compounds.

Thermal analysis was conducted on a 10 ± 0.5 mg sample using a Stanton Redcroft STA 1500 Thermal Analyser on heating from room temperature to 800 °C and on cooling from 800 °C to room temperature in air, with a heating/cooling rate of 10

°C/min, and in 5% H₂/Ar, again with a heating/cooling rate of 10 °Cmin^{-1}, and with a flow rate of 5% H₂/Ar of 50 mLmin^{-1}.

4.2.2.3.   Conductivity Testing

The pellets (ø ≈ 13 mm × 2 mm) were coated on opposing sides using silver paste. The conductivity of the samples was measured in the range 300 °C to 700 °C, with the exception of $SrFe_{1-x}Ti_xO_{3-\delta}$ (x = 0 – 0.3) in 5% H₂/Ar which measured in the range 300 °C to 600 °C. Measurements in air were conducted using an A.C. method using a Solartron 1287 electrochemical interface controlled by ZPlot software over the frequency range 65 kHz to 100 mHz. Measurements in dry 5% H₂/Ar, dried by passing the gas through 98% H_2SO_4, were conducted using the above A.C method and a D.C. method using a Solartron1250 Frequency Response Analyser coupled to a 1287 Electrochemical Interface controlled by CorrWare software with a constant current of 0.01 - 0.1 A, after reduction in the same atmosphere at 700 °C for 600 minutes.

4.2.3. Results and Discussion
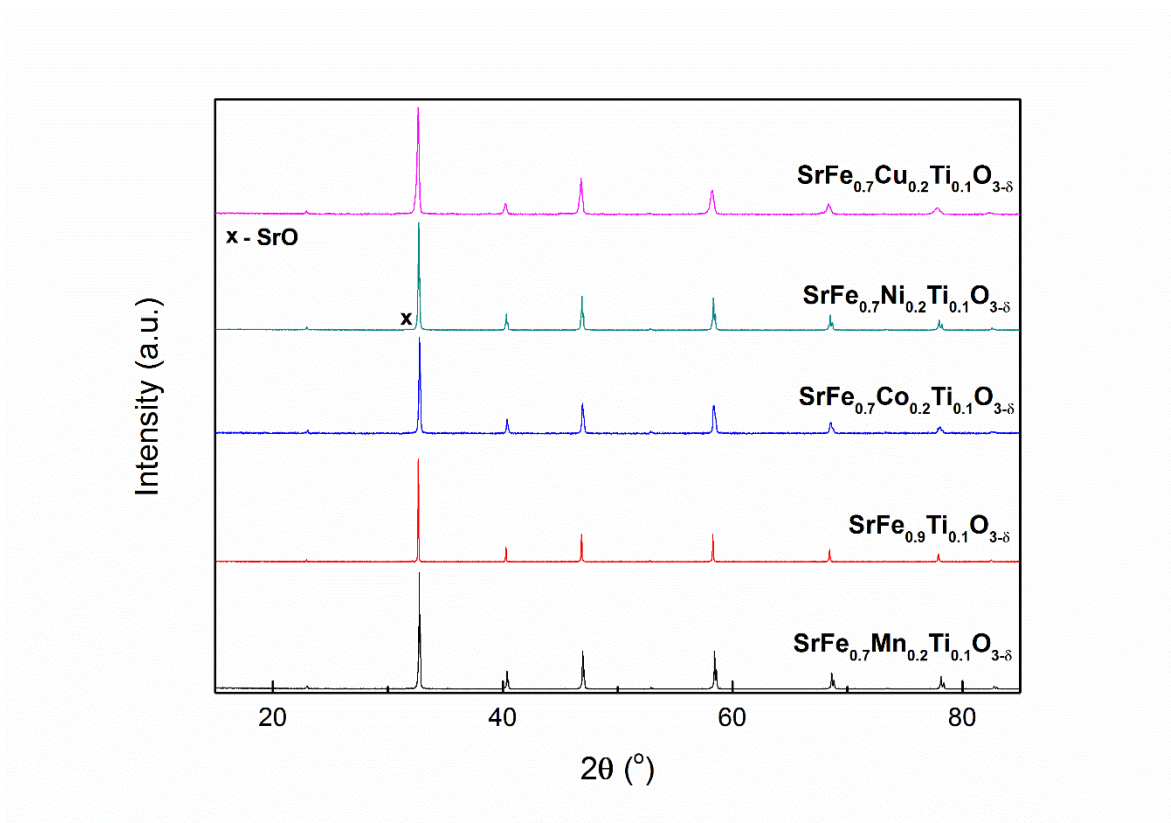
Figure 4.15. X-ray diffraction pattern for SrFe$_{0.7}$TM$_{0.2}$Ti$_{0.1}$O$_{3-\delta}$ (TM = Mn, Fe, Co, Ni, Cu)

X-ray diffraction of SrFe$_{0.7}$TM$_{0.2}$Ti$_{0.1}$O$_{3-\delta}$ (TM = Mn, Fe, Ni, Cu) after synthesis in air exhibited a cubic perovskite structure, space group *Pm-3m* (No. 221), for all compounds, Figure 4.15, albeit with a small amount, 3.5 % phase fraction, of an SrO impurity phase (PDF: 6-520) observed for SrFe$_{0.7}$Ni$_{0.2}$Ti$_{0.1}$O$_{3-\delta}$ [32].
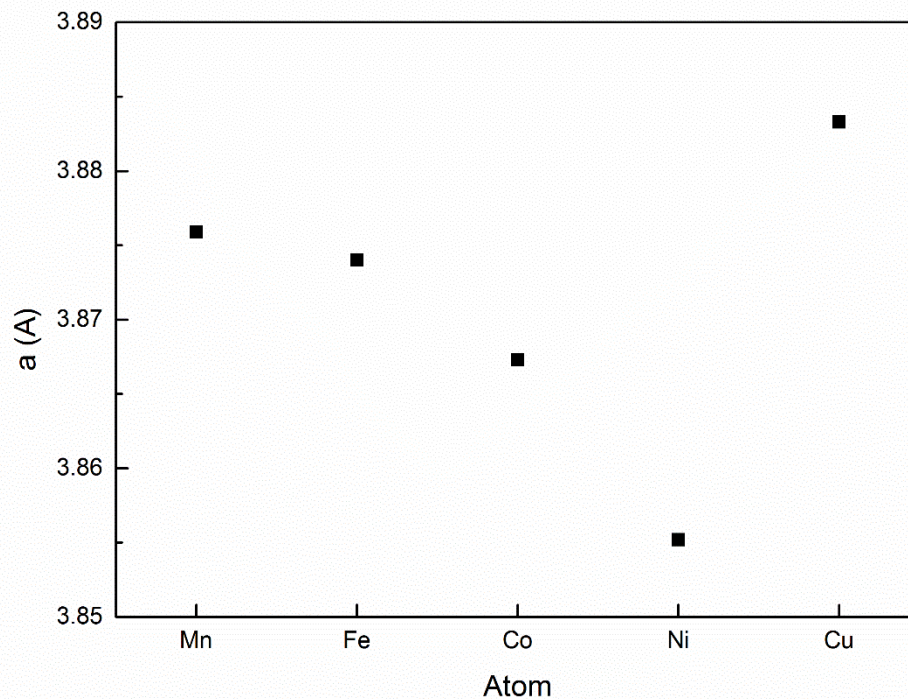
Figure 4.16. Variation of lattice parameters for SrFe$_{0.7}$TM$_{0.2}$Ti$_{0.1}$O$_{3-\delta}$ (TM = Mn, Fe, Co, Ni, Cu)

GSAS [26] analysis of the compounds, Figure 4.16, Figure 4.17 and Table 4.3, exhibited a variation in the lattice parameters which does not directly correlate with the variation in the average size of the dopant cation, with the lattice parameters reducing in the order Cu>Mn>Fe>Co>Ni [32].
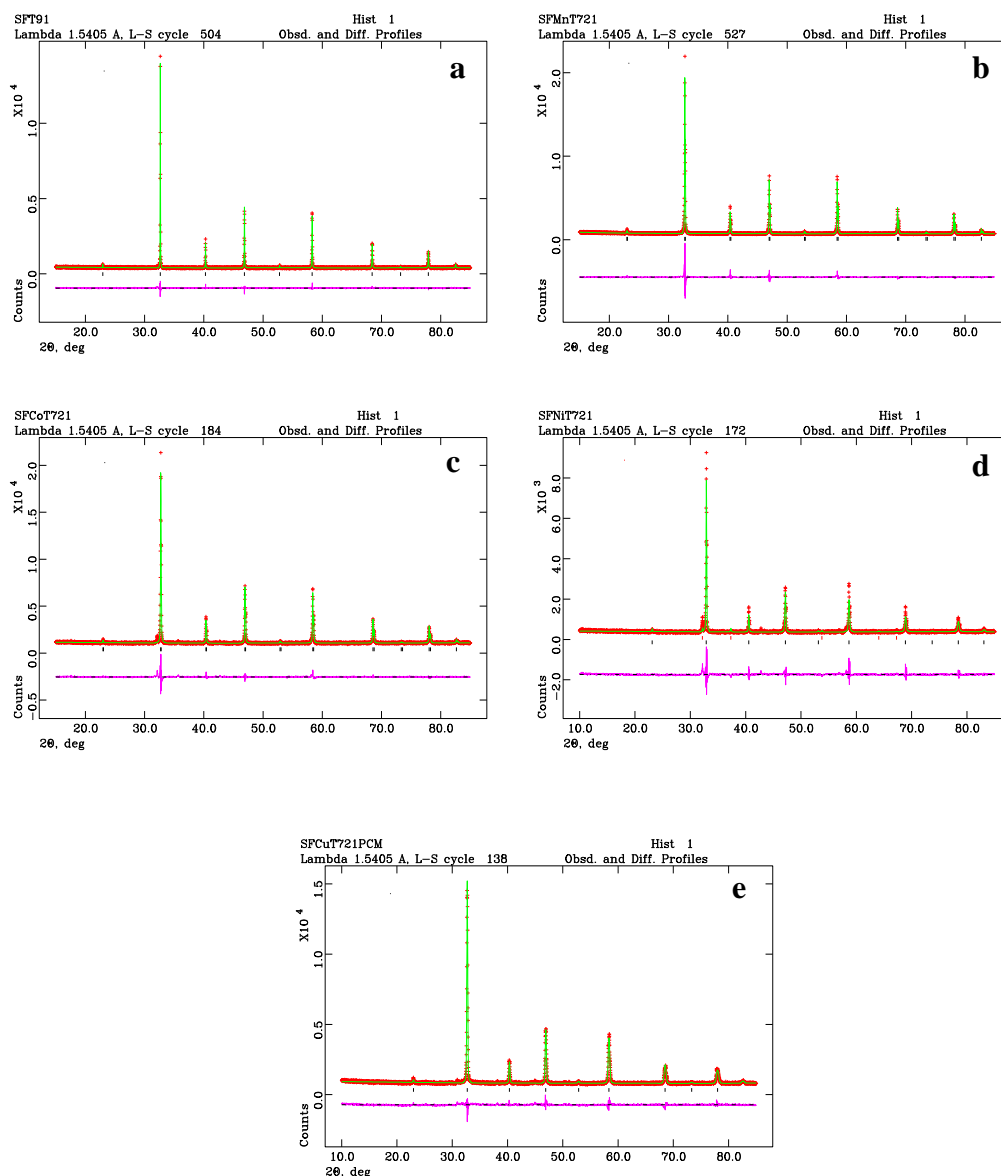
Figure 4.17. GSAS plots for SrFe$_{0.7}$TM$_{0.2}$Ti$_{0.1}$O$_{3-\delta}$ (TM = Mn (a), Fe (b), Co (c), Ni (d), Cu(e))

All previous dopants exhibited an reduction of the average oxidation state of iron in SrFeO$_{3-\delta}$ with increasing dopant concentration, with the larger cation size of Fe^{3+} over Fe^{4+} or the increase in the oxygen content resulting in an increase in the lattice parameters [17, 20, 44]. Due to the lower oxidation state of the dopants, it would be expected that a reduction in the lattice parameters, from Fe^{3+}-Fe^{4+} transitions and the reduction in oxygen content, would be observed with B^{2+} doping. This is true for both cobalt and nickel, which, due to the dopant sizes (0.745 Å for Co$^{2+}_{oct}$, 0.58 Å for Co$^{2+}_{tet}$

207

and 0.69 Å for Ni^{2+}_{oct}, 0.55 Å for Ni^{2+}_{tet}), is indicative of Fe^{4+} formation. An increase in the lattice parameter with doping of copper (Cu^{2+}_{oct}, 0.73 Å) was observed, suggesting that the expansion resulting from Cu doping is higher than the lattice shrinkage from the Fe^{3+}-Fe^{4+} transition and the loss of oxygen from the structure. Doping of manganese elicits a minimal increase in the lattice parameter, 0.0019 Å, over $SrFe_{0.9}Ti_{0.1}O_{3-\delta}$, which, due to the size of the Mn^{2+} cation (0.83 Å for Mn^{2+}_{oct} or 0.66 Å for Mn^{2+}_{tet}), is either suggestive of Mn^{3+} formation (0.645 Å for Mn^{3+}_{oct} or 0.58 Å for Mn^{3+}_{tet}) or of preferential tetrahedral coordination, balancing the reduction from the Fe^{3+}-Fe^{4+} transition and the loss of oxygen from the structure. Further information on the oxidation state and coordination of the dopant cations or iron can only be obtained through additional analysis techniques, such as Mössbauer Spectroscopy or X-ray Photoelectron Spectroscopy (XPS).

		$SrFe_{0.7}Mn_{0.2}Ti_{0.1}O_{3-\delta}$	$SrFe_{0.9}Ti_{0.1}O_{3-\delta}$	$SrFe_{0.7}Co_{0.2}Ti_{0.1}O_{3-\delta}$	$SrFe_{0.7}Ni_{0.2}Ti_{0.1}O_{3-\delta}$	$SrFe_{0.7}Cu_{0.2}Ti_{0.1}O_{3-\delta}$
χ^2		3.795	1.193	6.098	3.639	3.038
Rp (%)		6.40	5.21	7.15	9.20	5.64
wRp (%)		4.56	4.11	4.41	6.50	4.11
Space Group		Pm-$3m$	Pm-$3m$	Pm-$3m$	Pm-$3m$	Pm-$3m$
a (Å)		3.8759(2)	3.8740(2)	3.8673(1)	3.8551(10)	3.8833(1)
V (Å^3)		58.22(1)	58.14(1)	57.84(1)	57.29(4)	58.56(3)
Sr	x	0	0	0	0	0
	y	0	0	0	0	0
	z	0	0	0	0	0
	U_{iso}	0.009(7)	0.004(3)	0.007(1)	0.007(1)	0.012(1)
Fe/TM/Ti	x	0.5	0.5	0.5	0.5	0.5
	y	0.5	0.5	0.5	0.5	0.5
	z	0.5	0.5	0.5	0.5	0.5
	U_{iso}	0.013(1)	0.006(6)	0.007(1)	0.001(1)	0.002(1)
O	x	0	0	0	0	0
	y	0.5	0.5	0.5	0.5	0.5
	z	0.5	0.5	0.5	0.5	0.5
	U_{iso}	0.032(1)	0.022(1)	0.027(5)	0.023(3)	0.025(1)

Table 4.4. 'Goodness of fit' parameters, lattice parameters and atomic parameters from GSAS refinement of $SrFe_{0.7}TM_{0.2}Ti_{0.1}O_{3-\delta}$ (TM = Mn, Fe, Co, Ni, Cu) after synthesis in air
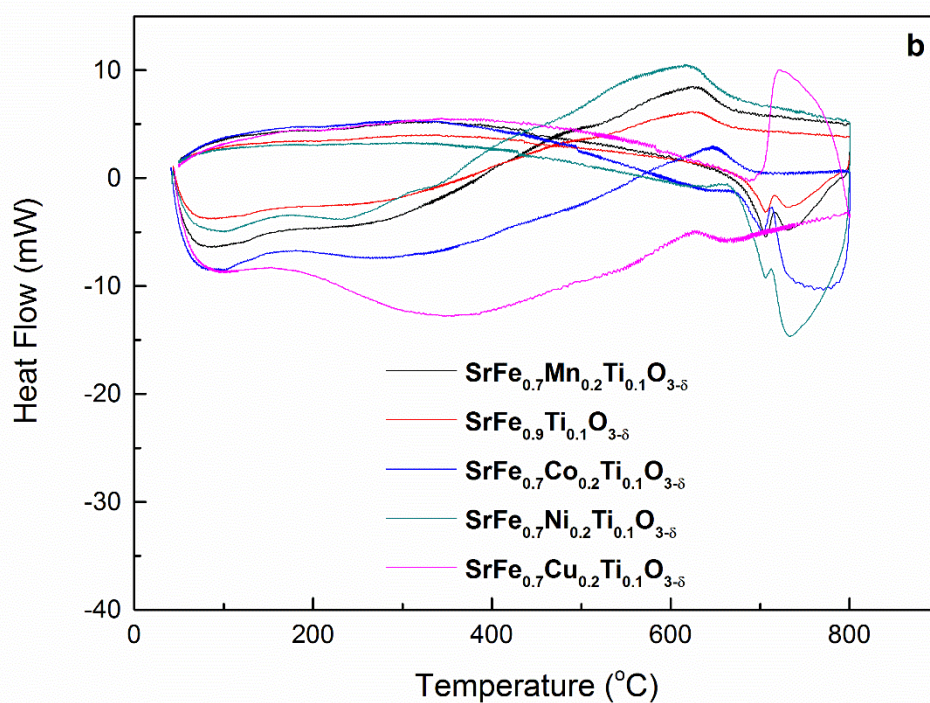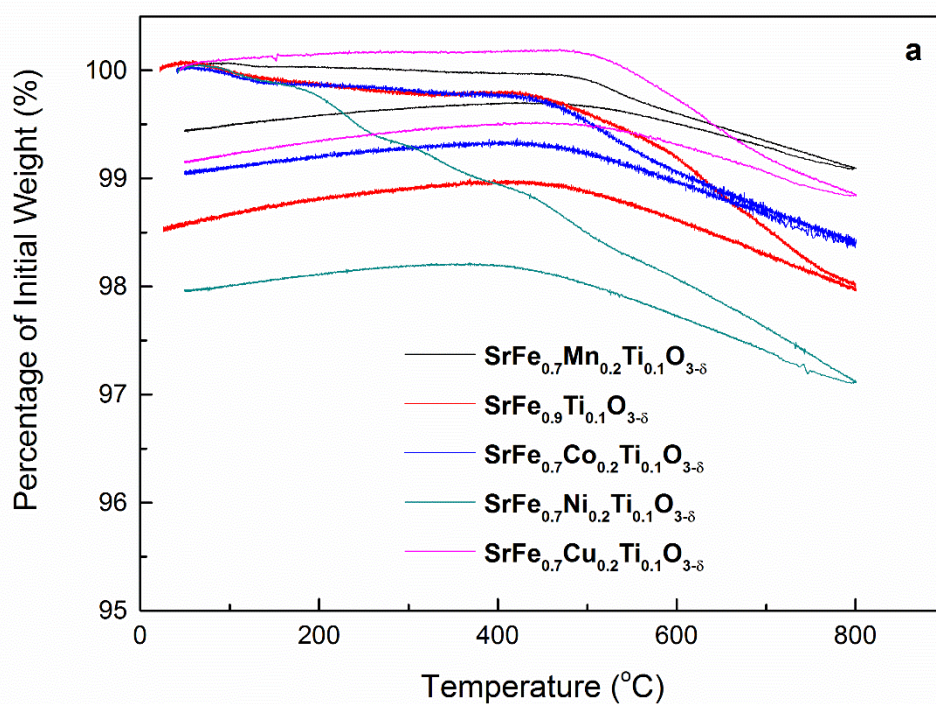
Figure 4.18. Thermogravimetric analysis (a) and differential scanning calorimetry (b) of SrFe$_{0.7}$TM$_{0.2}$Ti$_{0.1}$O$_{3-\delta}$ (TM = Mn, Fe, Co, Ni, Cu) in air

Thermogravimetric analysis of $SrFe_{0.7}TM_{0.2}Ti_{0.1}O_{3-\delta}$ (TM = Mn, Fe, Co, Ni, Cu) in air, Figure 4.18 (a), exhibits a minimal weight reduction, between 0.5 % and 2 %, for all compounds upon heating in air. Differential scanning calorimetry, Figure 4.18 (b), reveals a reversible transition for all compounds, observed between 600 °C and 700 °C on heating and between 750 °C and 700 °C on cooling.
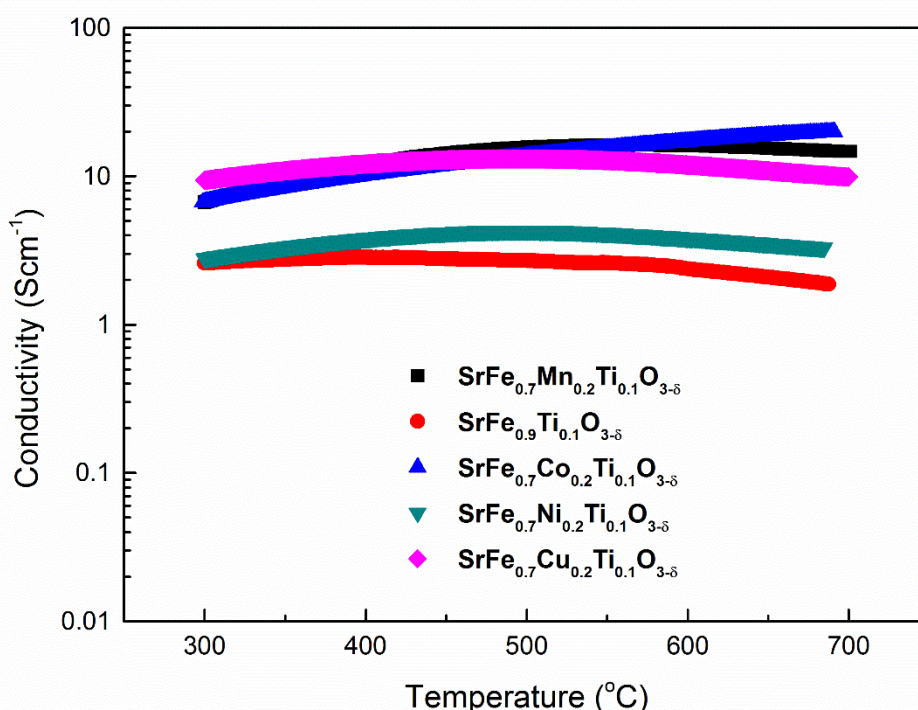
Figure 4.19. Conductivity of $SrFe_{0.7}TM_{0.2}Ti_{0.1}O_{3-\delta}$ (TM = Mn, Fe, Co, Ni, Cu) in air

The conductivity of $SrFe_{0.7}TM_{0.2}Ti_{0.1}O_{3-\delta}$ (TM = Mn, Co, Ni, Cu) in air, Figure 4.19, exhibited an increase for all transition metal dopants over that of $SrFe_{0.9}Ti_{0.1}O_{3-\delta}$, with all compounds, excluding $SrFe_{0.7}Co_{0.2}Ti_{0.1}O_{3-\delta}$, exhibiting a semiconductor-metal transition between 400 °C and 550 °C. The conductivity of $SrFe_{0.7}Mn_{0.2}Ti_{0.1}O_{3-\delta}$, $SrFe_{0.7}Co_{0.2}Ti_{0.1}O_{3-\delta}$ and $SrFe_{0.7}Cu_{0.2}Ti_{0.1}O_{3-\delta}$ remained between 5 Scm^{-1} and 20 Scm^{-1} over the measured temperature range, thus exhibiting potential for use as SOFC

cathode materials. The increase in conductivity for all compounds over $SrFe_{0.9}Ti_{0.1}O_{3-\delta}$ can be attributed to an increase in the carrier concentration, as a result of charge compensation mechanisms.

A reduction in the charge carrier concentration can also be affected by the preferred environment of the dopant cation. As it is not energetically favourable for Fe^{4+} to adopt a 5-coordinate state, incorporating an oxygen vacancy, a dopant which localises oxygen vacancies on the iron sites will cause a further reduction in the charge carrier concentration. This is found for Ga doped $SrFeO_{3-\delta}$ [44], which exhibits a reduction in the average iron valence despite the similar charge of Ga^{3+}. As it is not energetically favourable for Ga^{3+} to accommodate oxygen vacancies in air, gallium doping increases the proportion of oxygen vacancies at the Fe sites. The reduction in the number of Fe-O bonds results in an increase in the activation energy, which, when combined with replacement of some of the iron cations with the dopant, results in an overall reduction in the compound conductivity. The variation in the coordination wnvironment of the dopants could explain some of the observed variations in the conductivity.

As for $SrFe_{1-x}Ti_xO_{3-\delta}$, the observed semiconductor-metal transition for $SrFe_{0.7}TM_{0.2}Ti_{0.1}O_{3-\delta}$ (TM = Mn, Fe, Ni, Cu) is the result of reduction of the number of charge carriers at high temperature reducing the conductivity at a greater rate than the conductivity increase from E_a. The transition temperature for nickel and copper doped $SrFe_{0.9}Ti_{0.1}O_{3-\delta}$, 495 °C, is similar to that of $SrFe_{0.9}Ti_{0.1}O_{3-\delta}$, with manganese doping eliciting a significantly higher transition temperature, 560 °C.

Despite exhibiting an activation energy for conduction similar to that of $SrFe_{0.7}TM_{0.2}Ti_{0.1}O_{3-\delta}$ (TM = Mn, Fe, Ni, Cu), semiconducting behaviour was observed for $SrFe_{0.7}Co_{0.2}Ti_{0.1}O_{3-\delta}$ over the entire temperature range. Previous research into $La_{0.8}Sr_{0.2}Co_{1-y}Fe_yO_{3-\delta}$ [47] suggests that the transition between semiconducting and metallic behaviour should still be observed for cobalt doped strontium ferrites. As the transition for $La_{0.8}Sr_{0.2}Co_{1-y}Fe_yO_{3-\delta}$ occurs at temperatures in excess of 700 °C, potentially the transition temperature for the cobalt analogue is outside the measurement range of this study.
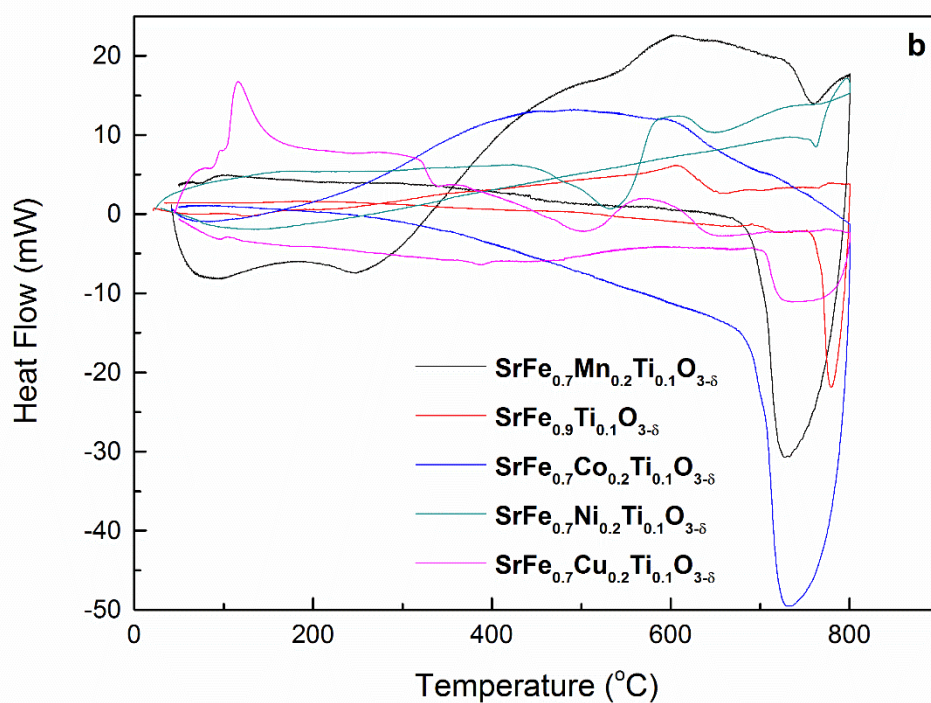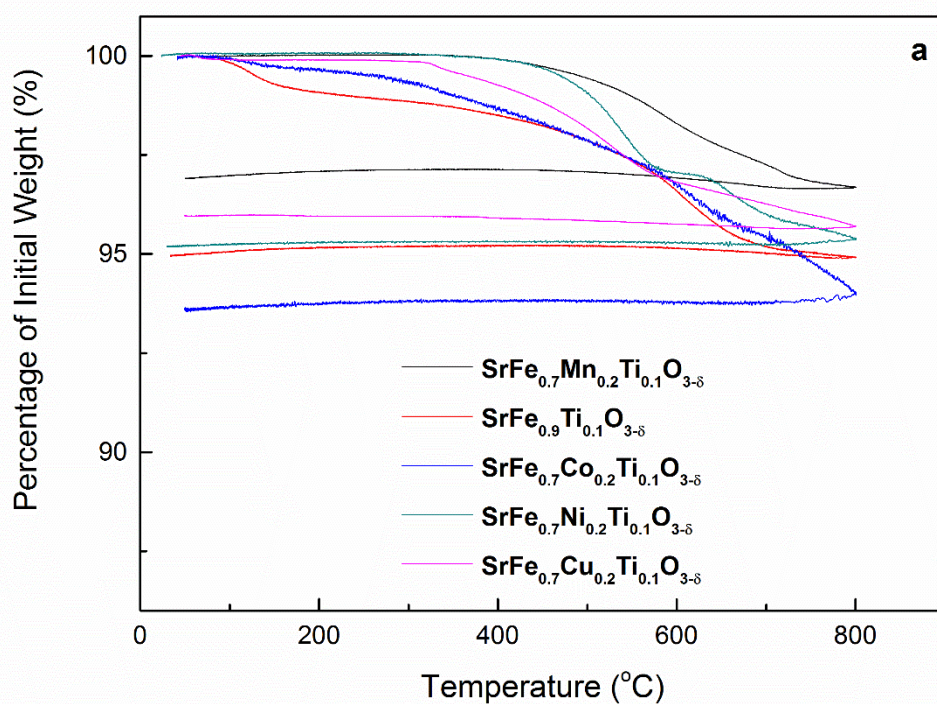
Figure 4.20. Thermogravimetric analysis (a) and differential scanning calorimetry (b) of SrFe$_{0.7}$TM$_{0.2}$Ti$_{0.1}$O$_{3-\delta}$ (TM = Mn, Fe, Co, Ni, Cu) in 5% H$_2$/Ar

Reduction of $SrFe_{0.7}TM_{0.2}Ti_{0.1}O_{3-\delta}$ (TM = Mn Ni, Cu) at 700 °C in 5% H_2/Ar, Figure 4.20 (a) exhibited a lower weight loss than was observed for $SrFe_{0.9}Ti_{0.1}O_{3-\delta}$. In contrast to the other doped compounds, $SrFe_{0.7}Co_{0.2}Ti_{0.1}O_{3-\delta}$ exhibited an increase in weight loss, 6.4 %, compared to $SrFe_{0.9}Ti_{0.1}O_{3-\delta}$, 5.05 %. The increased weight loss is likely indicative of cobalt reduction at these temperatures. Differential scanning calorimetry of all compounds, Figure 4.20 (b), exhibited a similar transition upon heating to that observed in air, between 550 °C and 650 °C, however the transition was not reversible. As for the transition in air, this can be attributed to structural alterations as a result of cation reduction and oxygen loss.
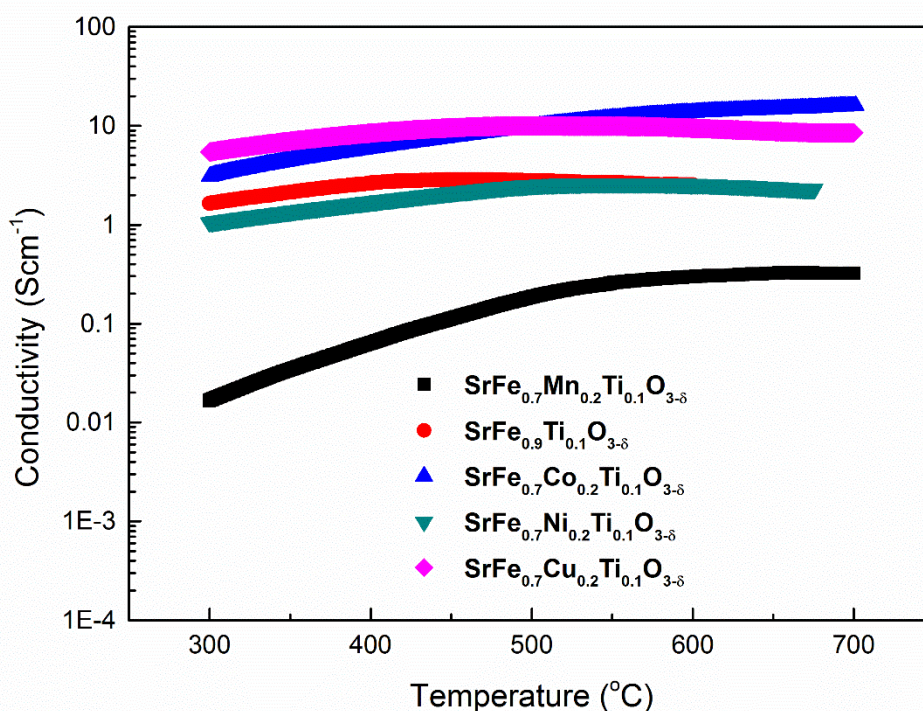
Figure 4.21. Conductivity of $SrFe_{0.7}TM_{0.2}Ti_{0.1}O_{3-\delta}$ (TM = Mn, Fe, Co, Ni, Cu) in 5% H_2/Ar

The conductivity of the transition metal doped samples reduced at 700 °C in 5% H_2/Ar, Figure 4.21, exhibited minor reductions in the conductivity, with the

exception of the manganese doped sample. Minimal reduction of the conductivity of $SrFe_{0.7}Co_{0.2}Ti_{0.1}O_{3-\delta}$, $SrFe_{0.7}Ni_{0.2}Ti_{0.1}O_{3-\delta}$ and $SrFe_{0.7}Cu_{0.2}Ti_{0.1}O_{3-\delta}$ is suggestive of minor decreases in the charge carrier concentration at these temperatures. This correlates with the minor decrease in the activation energy, between 0.02(1) eV and 0.07(1) eV, noted for the cobalt, nickel and copper doped compounds upon reduction.

The conductivity of the Mn doped sample demonstrated a reduction of several orders of magnitude, 14.69 Scm^{-1} in air to 0.323 Scm^{-1} in 5% H_2/Ar at 700 °C. This was also demonstrated in the increase in the activation energy upon reduction, from 0.22(1) eV to 0.51(4) eV. The semiconductor-metal transition observed in air is also observed, albeit at higher temperature, from 560 °C to 660 °C upon reduction, suggesting that the conduction mechanism does not change. The reduction in conductivity is likely associated with a significant decrease in the charge carrier concentration, as a result of cationic reduction.

This may intimate that manganese dopes as Mn^{3+}, directly contributing to the charge carrier concentration in air, and not altering the charge carrier concentration through charge compensation mechanisms. Reduction of Mn^{3+} to Mn^{2+} upon exposure to 5% H_2/Ar would reduce the charge carrier concentration, similar to the Fe^{4+}-Fe^{3+} transition. Significant reductions in the electronic conductivity is also observed for manganite perovskites, as a result of Mn^{3+}-Mn^{2+} transitions [48].
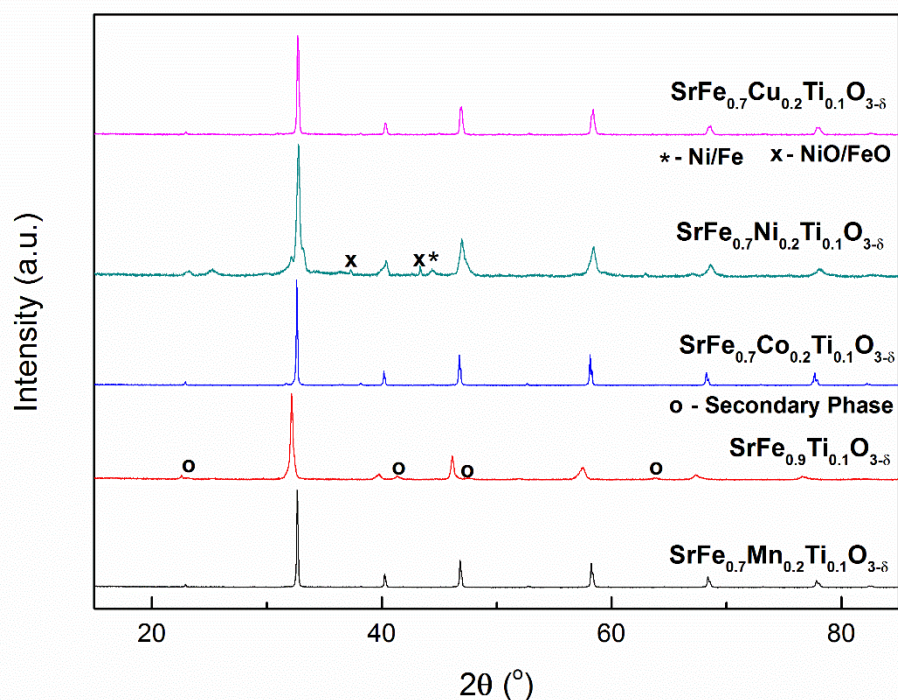
Figure 4.22. X-ray diffraction pattern of SrFe$_{0.7}$TM$_{0.2}$Ti$_{0.1}$O$_{3-\delta}$ (TM = Mn, Fe, Co, Ni, Cu) after reduction in 5% H$_2$/Ar at 700 °C

X-ray diffraction of SrFe$_{0.7}$TM$_{0.2}$Ti$_{0.1}$O$_{3-\delta}$ (TM = Mn, Fe, Co, Ni, Cu), Figure 4.22, after reduction at 700 °C in 5% H$_2$/Ar demonstrates little change in the material structure, with the exception of SrFe$_{0.7}$Ni$_{0.2}$Ti$_{0.1}$O$_{3-\delta}$ which exhibits a 5.6 % phase fraction of NiO (PDF: 4-835) and a 4.4 % phase fraction of Ni (PDF: 6-696) and SrFe$_{0.9}$Ti$_{0.1}$O$_{3-\delta}$ which exhibits an unidentified impurity phase. The redox instability observed for the nickel doped phase is likely due to the reducibility of the nickel within the structure, further implied by exsolution of nickel metal. This has also been observed for other nickel doped perovskite materials [49, 50], although redox reversibility may be observed upon re-oxidation.

The introduction of dopants of lower valence, copper, cobalt and manganese, which might be expected to reduce the redox stability of the compound through an

increase in the oxygen vacancy concentration, were noted to cause an increase in the compound redox stability at 700 °C. As was posited for scandium [45] and gallium [44] dopants, if the incorporation of oxygen vacancies at randomly situated dopant sites is energetically unfavourable, oxygen vacancy ordering can be prevented even for high concentrations of oxygen vacancies.
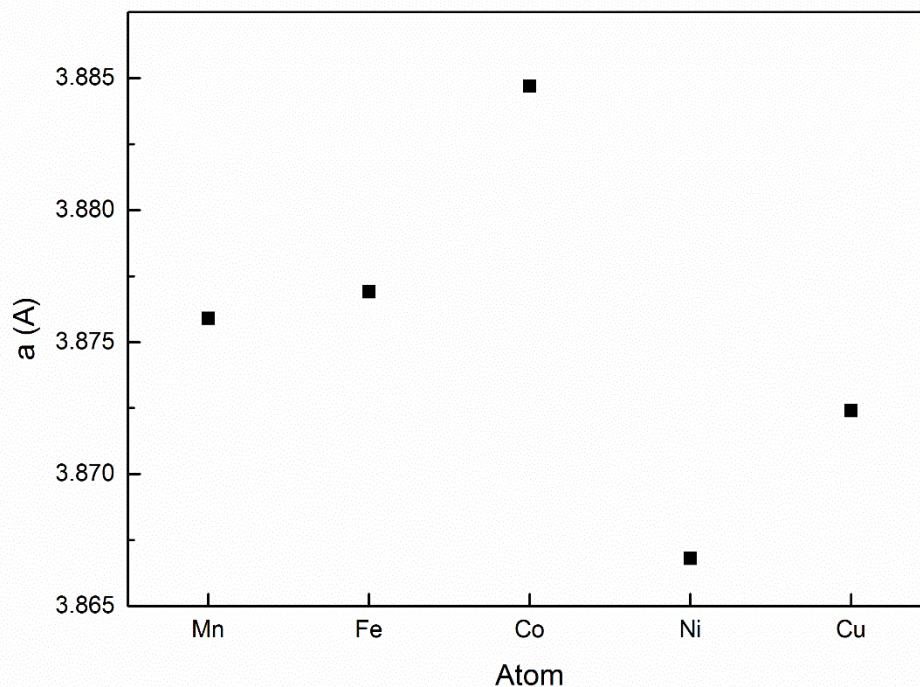
Figure 4.23. Variation of lattice parameters for SrFe$_{0.7}$TM$_{0.2}$Ti$_{0.1}$O$_{3-\delta}$ (TM = Mn, Fe, Co, Ni, Cu) after reduction in 5% H$_2$/Ar at 700 °C

217
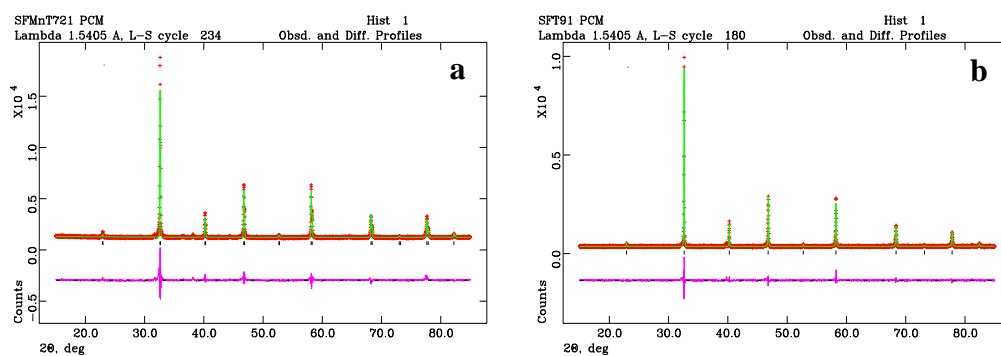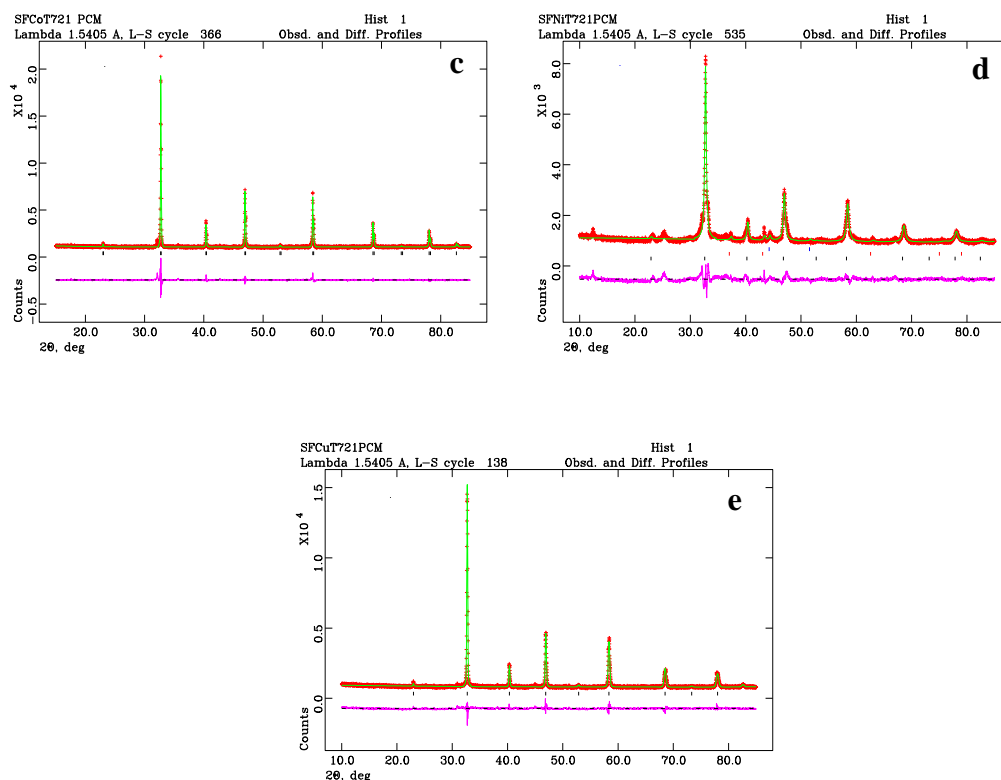
Figure 4.24. GSAS plots for SrFe$_{0.7}$TM$_{0.2}$Ti$_{0.1}$O$_{3-\delta}$ (TM = Mn (a), Fe (b), Co (c), Ni (d), Cu(e)) after reduction in 5%H$_2$/Ar at 700 °C

GSAS [26] analysis, Figure 4.23, Figure 4.24 and Table 4.5, of these compounds exhibits an increase in the lattice parameters for SrFe$_{0.9}$Ti$_{0.1}$O$_{3-\delta}$, SrFe$_{0.7}$Co$_{0.2}$Ti$_{0.1}$O$_{3-\delta}$ and SrFe$_{0.7}$Ni$_{0.2}$Ti$_{0.1}$O$_{3-\delta}$ upon reduction, Table 4.4 and 4.5, which is indicative of partial reduction of the B-site cation. Whilst reduction would be expected to result in an increase in the lattice parameter, a minor reduction in the lattice parameter of SrFe$_{0.7}$Cu$_{0.2}$Ti$_{0.1}$O$_{3-\delta}$ was observed. This is likely a result of the lattice shrinkage from oxygen loss and possible changes in the cationic coordination environment, overcoming the lattice expansion from cationic reduction.

In contrast to other dopants, SrFe$_{0.7}$Mn$_{0.2}$Ti$_{0.1}$O$_{3-\delta}$ exhibits no change in the lattice parameters after reduction at 700 °C. Whilst this would normally suggest minimal variation in the material properties, a significant variation in the conductivity is observed upon reduction, cationic reduction is known to occur and therefore would be expected to induce lattice expansion. In this case a balance between lattice

shrinkage and lattice expansion is posited to occur, resulting in the stability of the lattice parameter upon reduction.

		SrFe$_{0.7}$Mn$_{0.2}$Ti$_{0.1}$O$_{3-\delta}$	SrFe$_{0.9}$Ti$_{0.1}$O$_{3-\delta}$	SrFe$_{0.7}$Co$_{0.2}$Ti$_{0.1}$O$_{3-\delta}$	SrFe$_{0.7}$Ni$_{0.2}$Ti$_{0.1}$O$_{3-\delta}$	SrFe$_{0.7}$Cu$_{0.2}$Ti$_{0.1}$O$_{3-\delta}$
χ^2		3.795	1.657	4.896	4.665	2.490
Rp (%)		6.40	6.44	6.06	6.43	5.15
wRp (%)		4.56	4.91	3.73	4.85	3.94
Space Group		*Pm-3m*	*Pm-3m*	*Pm-3m*	*Pm-3m*	*Pm-3m*
a (Å)		3.8759(2)	3.8769(2)	3.8847(1)	3.8759(7)	3.8724(7)
V (Å^3)		58.22(1)	58.27(1)	58.62(1)	58.22(2)	58.07(3)
Sr	x	0	0	0	0	0
	y	0	0	0	0	0
	z	0	0	0	0	0
	U$_{iso}$	0.007(7)	0.005(1)	0.002(1)	0.020(1)	0.003(6)
Fe/TM/Ti	x	0.5	0.5	0.5	0.5	0.5
	y	0.5	0.5	0.5	0.5	0.5
	z	0.5	0.5	0.5	0.5	0.5
	U$_{iso}$	0.016(10)	0.007(9)	0.004(1)	0.004(2)	0.004(9)
O	x	0	0	0	0	0
	y	0.5	0.5	0.5	0.5	0.5
	z	0.5	0.5	0.5	0.5	0.5
	U$_{iso}$	0.027(1)	0.028(1)	0.026(2)	0.034(3)	0.036(1)

Table 4.5. 'Goodness of fit' parameters, lattice parameters and atomic parameters from GSAS refinement of SrFe$_{0.7}$TM$_{0.2}$Ti$_{0.1}$O$_{3-\delta}$ (TM = Mn, Fe, Co, Ni, Cu) after reduction at 700 °C in 5% H$_2$/Ar

4.2.4. Conclusion

An improvement in the stability and conductivity in air and 5% H_2/Ar of $SrFe_{0.9}Ti_{0.1}O_{3-\delta}$ was achieved through doping of copper and cobalt, forming $SrFe_{0.7}Cu_{0.2}Ti_{0.1}O_{3-\delta}$ and $SrFe_{0.7}Co_{0.2}Ti_{0.1}O_{3-\delta}$. The high conductivity and stability of these compounds demonstrates potential for use as electrode materials for IT-SOFCs. Whilst manganese doping improved the redox stability and conductivity in air, the reduction of the conductivity in 5% H_2/Ar renders this compound unsuitable for use as a SOFC anode material. Nickel doping achieved only a minimal increase in conductivity in both air and 5% H_2/Ar and did not exhibit redox stability and is therefore also unsuitable for use as a SOFC electrode material.

4.3. Conclusion

A solid solution with the cubic perovskite structure was observed for $SrFe_{1-x}Ti_xO_{3-\delta}$ (x = 0 – 0.3), with an increase in the lattice parameters noted upon increasing dopant concentration. Material stability in air was observed for all compounds, with a decrease in conductivity noted upon increasing dopant concentration attributed to a reduction in charge carrier concentration. A reduction in weight proportional to the titanium content was observed upon exposure to 5% H_2/Ar, although reduction at 700 °C was observed to elicit a structural transition and the formation of a secondary phase for $SrFeO_{3-\delta}$ and $SrFe_{0.9}Ti_{0.1}O_{3-\delta}$ respectively. Conductivity measurements at 600 °C demonstrated a larger decrease in the conductivity with increasing dopant concentration, with the cubic perovskite structure was observed for all compounds after reduction.

The cubic perovskite structure was observed for all dopants for $SrFe_{0.7}TM_{0.2}Ti_{0.1}O_{3-\delta}$ (TM = Mn, Fe, Co, Ni, Cu), with variation in the lattice parameters associated with differing dopant environments and charge compensation mechanisms. Improvement of the electronic conductivity over $SrFe_{0.9}Ti_{0.1}O_{3-\delta}$ was observed for all dopants in air, attributed to increasing charge carrier concentration. Reduction in 5% H_2/Ar exhibited minimal variation in material properties for $SrFe_{0.7}Co_{0.2}Ti_{0.1}O_{3-\delta}$ and $SrFe_{0.7}Cu_{0.2}Ti_{0.1}O_{3-\delta}$, with a significant reduction in conductivity was observed for $SrFe_{0.7}Mn_{0.2}Ti_{0.1}O_{3-\delta}$. All doped compounds exhibited a single phase cubic perovskite structure after reduction with the exception of $SrFe_{0.7}Ni_{0.2}Ti_{0.1}O_{3-\delta}$ which displays secondary nickel phases upon reduction. Both $SrFe_{0.7}Co_{0.2}Ti_{0.1}O_{3-\delta}$ and $SrFe_{0.7}Cu_{0.2}Ti_{0.1}O_{3-\delta}$ exhibit promising properties for use as symmetrical electrode materials, however the fuel cell performance should be elucidated before making further judgements.

The significant improvement in the conductivity and stability upon doping of $SrFe_{0.9}Ti_{0.1}O_{3-\delta}$ suggests that a more suitable parent compound may produce further improvements in material conductivity and stability. The initial properties of doped strontium ferrites exhibit potential for use as symmetrical SOFC electrode materials, however improvement of the conductivity of these compounds, whilst maintaining the redox stability, is desirable.

4.4. References

1. S. P. Simner, J. F. Bonnett, N. L. Canfield, K. D. Meinhardt, V. L. Sprenkle and J. W. Stevenson, *Electrochemical and Solid-State Letters*, 2002, **5**, A173-A175.

2. Y. Leng, S. H. Chan and Q. Liu, *International Journal of Hydrogen Energy*, 2008, **33**, 3808-3817.

3. S. Zongping and S. M. Haile, *Nature*, 2004, **431**, 170-173.

4. J. C. Ruiz-Morales, D. Marrero-Lopez, J. Canales-Vazquez and J. T. S. Irvine, *RSC Advances*, 2011, **1**, 1403-1414.

5. Y. Takeda, K. Kanno, T. Takada, O. Yamamoto, M. Takano, N. Nakayama and Y. Bando, *Journal of Solid State Chemistry*, 1986, **63**, 237-249.

6. J. P. Hodges, S. Short, J. D. Jorgensen, X. Xiong, B. Dabrowski, S. M. Mini and C. W. Kimball, *Journal of Solid State Chemistry*, 2000, **151**, 190-209.

7. M. Schmidt, *Journal of Physics and Chemistry of Solids*, 2000, **61**, 1363-1365.

8. J. Mizusaki, M. Okayasu, S. Yamauchi and K. Fueki, *Journal of Solid State Chemistry*, 1992, **99**, 166-172.

9. V. V. Vashuk, L. V. Kokhanovskii and I. I. Yushkevich, *Inorganic Materials*, 2000, **36**, 79-83.

10. M. V. Patrakeev, I. A. Leonidov, V. L. Kozhevnikov and V. V. Kharton, *Solid State Sciences*, 2004, **6**, 907-913.

11. J. Hombo, Y. Matsumoto and T. Kawano, *Journal of Solid State Chemistry*, 1990, **84**, 138-143.

12. K. Ji, H. Dai, J. Deng, L. Zhang, F. Wang, H. Jiang and C. T. Au, *Applied Catalysis A: General*, 2012, **425â€"426**, 153-160.

13. A. Evdou, V. Zaspalis and L. Nalbandian, *Fuel*, 2010, **89**, 1265-1273.

14. G. Yi, T. Hayakawa, A. Andersen, K. Suzuki, S. Hamakawa, A. E. York, M. Shimizu and K. Takehira, *Catalysis Letters*, 1996, **38**, 189-195.

15. Y. Wang, J. Chen and X. Wu, *Materials Letters*, 2001, **49**, 361-364.

16. P. Adler and S. Eriksson, *Zeitschrift für anorganische und allgemeine Chemie*, 2000, **626**, 118-124.

17. G. Xiao, Q. Liu, S. Wang, V. G. Komvokis, M. D. Amiridis, A. Heyden, S. Ma and F. Chen, *Journal of Power Sources*, 2012, **202**, 63-69.

18. P. V. Anikina, A. A. Markov, M. V. Patrakeev, I. A. Leonidov and V. L. Kozhevnikov, *Solid State Sciences*, 2009, **11**, 1156-1162.

19. A. Nag, J. Manjanna, R. M. Tiwari and J. Gopalakrishnan, *Chemistry of Materials*, 2008, **20**, 4420-4424.

20. P. S. Beurmann, V. Thangadurai and W. Weppner, *Journal of Solid State Chemistry*, 2003, **174**, 392-402.

21. V. V. Kharton, A. P. Viskup, A. V. Kovalevsky, J. R. Jurado, E. N. Naumovich, A. A. Vecher and J. R. Frade, *Solid State Ionics*, 2000, **133**, 57-65.

22. W. Jung and H. L. Tuller, *Journal of The Electrochemical Society*, 2008, **155**, B1194-B1201.

23. W. Jung and H. L. Tuller, *Solid State Ionics*, 2009, **180**, 843-847.

24. Y. Chen, W. Jung, Z. Cai, J. J. Kim, H. L. Tuller and B. Yildiz, *Energy & Environmental Science*, 2012, **5**, 7979-7988.

25. D. P. Fagg, V. V. Kharton, A. V. Kovalevsky, A. P. Viskup, E. N. Naumovich and J. R. Frade, *Journal of the European Ceramic Society*, 2001, **21**, 1831-1835.

26. A. C. Larson and R. B. V. Dreele, *"General Structural Analysis System" Los Alamos National Laboratory Report LAUR*, 1994, 86.

27. M. Schmidt and S. J. Campbell, *Journal of Physics and Chemistry of Solids*, 2002, **63**, 2085-2092.

28. J. C. Waerenborgh, D. P. Rojas, A. L. Shaula, G. C. Mather, M. V. Patrakeev, V. V. Kharton and J. R. Frade, *Materials Letters*, 2005, **59**, 1644-1648.

29. V. E. Alexandrov, J. Maier and R. A. Evarestov, *Physical Review B*, 2008, **77**, 075111.

30. F. W. Poulsen, G. Lauvstad and R. Tunold, *Solid State Ionics*, 1994, **72, Part 2**, 47-53.

31. M. V. Patrakeev, E. B. Mitberg, A. A. Lakhtin, I. A. Leonidov, V. L. Kozhevnikov, V. V. Kharton, M. Avdeev and F. M. B. Marques, *Journal of Solid State Chemistry*, 2002, **167**, 203-213.

32. R. D. Shannon, *Acta Crystallographia Section A*, 1976, **A32**, 751.

33.	H. Hayashi, M. Kanoh, C. J. Quan, H. Inaba, S. Wang, M. Dokiya and H. Tagawa, *Solid State Ionics*, 2000, **132**, 227-233.

34.	J. Larminie and A. Dicks, *Fuel Cell Systems Explained*, J. Wiley, 2003.

35.	A. Atkinson, *Solid State Ionics*, 1997, **95**, 249-258.

36.	B. C. H. Steele, *Solid State Ionics*, 2000, **129**, 95-110.

37.	X. Yuan, H. Wang, J. Colin Sun and J. Zhang, *International Journal of Hydrogen Energy*, 2007, **32**, 4365-4380.

38.	S. Ricciardi, J. C. Ruiz-Morales and P. NuÃ±ez, *Solid State Ionics*, 2009, **180**, 1083-1090.

39.	A. Atkinson, S. A. Baron and N. P. Brandon, *Journal of The Electrochemical Society*, 2004, **151**, E186-E193.

40.	V. V. Kharton, F. M. B. Marques and A. Atkinson, *Solid State Ionics*, 2004, **174**, 135-149.

41.	W. Sun and W. Liu, *Journal of Power Sources*, **217**, 114-119.

42.	K. B. Yoo, B. H. Park and G. M. Choi, *Solid State Ionics*, **225**, 104-107.

43.	K. M. Papazisi, S. Balomenou and D. Tsiplakides, *Journal of Applied Electrochemistry*, **40**, 1875-1881.

44.	M. V. Patrakeev, V. V. Kharton, Y. A. Bakhteeva, A. L. Shaula, I. A. Leonidov, V. L. Kozhevnikov, E. N. Naumovich, A. A. Yaremchenko and F. M. B. Marques, *Solid State Sciences*, 2006, **8**, 476-487.

45.	M. V. Patrakeev, A. A. Markov, I. A. Leonidov, V. L. Kozhevnikov and V. V. Kharton, *Solid State Ionics*, 2006, **177**, 1757-1760.

46.	V. V. Kharton, J. C. Waerenborgh, D. P. Rojas, A. A. Yaremchenko, A. A. Valente, A. L. Shaula, M. V. Patrakeev, F. M. B. Marques and J. Rocha, *Catalysis Letters*, 2005, **99**, 249-255.

47.	L. W. Tai, M. M. Nasrallah, H. U. Anderson, D. M. Sparlin and S. R. Sehlin, *Solid State Ionics*, 1995, **76**, 259-271.

48.	E. O. Ahlgren and F. W. Poulsen, *Solid State Ionics*, 1996, **86â€"88, Part 2**, 1173-1178.

49.	W. Kobsiriphat, B. D. Madsen, Y. Wang, M. Shah, L. D. Marks and S. A. Barnett, *Journal of The Electrochemical Society*, 2010, **157**, B279-B284.

50. W. Bao, H. Guan and J. Cheng, *Journal of Power Sources*, 2008, **175**, 232-237.

5. Development of the Material Properties of Niobium Doped Strontium Ferrite for Application as a Symmetrical SOFC Electrode

Based on the performance of the titanium doped strontium ferrite materials in Chapter 4 and on research from the literature, niobium doping of strontium ferrite was investigated as a new baseline material. The optimal material from the $SrFe_{1-x}Nb_xO_{3-\delta}$ series was chosen for transition metal doping trials, utilising copper, cobalt, manganese and nickel. Copper doping was determined to elicit the optimal balance between electronic conductivity and redox stability, thus the effect of additional copper doping is investigated. Fuel cell testing of the material which exhibited the best properties is conducted and the performance compared to that from Chapter 4 and from the literature.

5.1. $SrFe_{1-x}Nb_xO_{3-\delta}$ (x = 0, 0.1, 0.2, 0.3, 0.4)

5.1.1. Introduction

Stabilisation of the cubic perovskite structure for strontium ferrite materials through titanium doping was previously demonstrated to increase the redox stability, Section 4.1. Transition metal doping of the stabilised strontium titanium ferrite was observed to improve the material properties with various dopants without resulting in a detrimental effect on the redox stability. The conductivity and stability of these materials in both oxidising and reducing conditions leads to consideration of ferrite materials as symmetrical electrodes for IT-SOFCs, providing that materials with suitable conductivity can be synthesised.

B-site doping of strontium ferrite with cations of higher valency was previously shown to stabilise the cubic perovskite structure either through reduction of the oxygen vacancy concentration or interruption of oxygen vacancy ordering [1, 2]. Anikina *et. al.* [3] demonstrated that even minimal niobium doping of strontium ferrite, forming

SrFe$_{0.95}$Nb$_{0.05}$O$_{3-\delta}$, could stabilise the perovskite structure whilst maintaining the desirable electronic and ionic conductive properties. Maximisation of both the electronic and ionic conductivities of SrFe$_{1-x}$Nb$_x$O$_{3-\delta}$ was noted to occur for x = 0.1, as both the oxygen vacancy concentration and carrier concentration reduces with increased doping. Reduction of SrFe$_{0.95}$Nb$_{0.05}$O$_{3-\delta}$ and SrFe$_{0.9}$Nb$_{0.1}$O$_{3-\delta}$ at 700 C in humidified 5% H$_2$/He was noted to double the perovskite unit cell, which, according to Alario-Franco *et. al* [4] and Nakayama *et. al.* [5] intimates the formation of randomly distributed brownmillerite microdomains not observable using XRD.

Synthesis of the intermediate composition, SrFe$_{0.5}$Nb$_{0.5}$O$_{3-\delta}$ or Sr$_2$FeNbO$_{6-\delta}$, produces varying structures and properties depending on the synthesis conditions [6, 7, 8]. The double perovskite Sr$_2$FeNbO$_{6-\delta}$, space group *I4/m* (87), was previously investigated by Tao *et. al.* [8], although this compound exhibited low electronic conductivity in both oxidising, 0.0313 Scm^{-1}, and reducing atmospheres, 2.39 Scm^{-1}, at 900 °C. This further intimates that high niobium content is not desirable for the production of effective anode materials.

Demonstration of the high oxygen ion conductivity of the SrFe$_{1-x}$Nb$_x$O$_{3-\delta}$ series has also led to investigation of SrFe$_{0.8}$Nb$_{0.2}$O$_{3-\delta}$ as a potential oxygen separation membrane [9]. Potential use of SrFe$_{0.9}$Nb$_{0.1}$O$_{3-\delta}$ as an SOFC cathode material has been demonstrated by Zhou *et. al.* [10], reaching 407 mWcm^{-2} at 800 °C for a Ni-SDC/SDC/SFN fuel cell. The effective utilisation of SrFe$_{1-x}$Nb$_x$O$_{3-\delta}$ for these applications certainly demonstrates potential applicability of these compounds as either an anode material or a symmetrical electrode material.

Whilst Anikina *et. al.* [3] have previously elucidated the conductivity and stability of SrFe$_{1-x}$Nb$_x$O$_{3-\delta}$, the temperature range of their study, 650 °C to 950 °C, is slightly higher than that of interest for intermediate temperature SOFCs, 300 °C – 700 °C. To accurately evaluate these materials for use as symmetrical electrodes for IT-SOFCs further research into the properties of these compound at intermediate temperatures is required. To this end a series of niobium doped strontium ferrites SrFe$_{1-x}$Nb$_x$O$_{3-\delta}$ (x = 0, 0.1, 0.2, 0.3, 0.4) was synthesised to confirm the conductivity and redox stability at intermediate temperatures and asses the suitability of these materials as symmetrical electrodes for IT-SOFCs.

5.1.2. Experimental Information

5.1.2.1. Synthesis

$SrFe_{1-x}Nb_xO_{3-\delta}$ (x = 0 – 0.5) were produced by sol-gel synthesis technique. A stoichiometric amount of $C_4H_4NNbO_9 \cdot H_2O$ (99.9%, Sigma Aldrich) was dissolved in distilled water. H_2O_2 was added dropwise to the niobium solution until a colour change was produced. Citric acid (99+%, Alfa Aesar), in a 2:1 ratio to the metal ions in the final product, was added and heated till a solution was formed. Stoichiometric amounts of $Sr(NO_3)_2$ (98%, Alfa Aesar) and $Fe(NO_3)_3 \cdot 9\ H_2O$ (98%, Alfa Aesar) were dissolved in distilled water. The solutions were mixed and the solution was heated until gelation. The resultant gel was fired at 600 °C for 2 hours. Subsequent firings between 1300 °C and 1500 °C for 5-15 hours were performed, with intermediate grinding steps in between each firing. Pellets of all the samples (ø ≈ 13 mm × 2 mm and ø ≈ 10 mm × 5 mm) were uniaxially pressed at 221 MPa and sintered in air between 1450 °C and 1500 °C for 5 hours.

5.1.2.2. Analytical Procedures

Phase purity and crystal parameters of the samples were examined by X-ray diffraction (XRD) analysis using a PANalytical X'Pert PRO MPD Multipurpose diffractometer (Cu $K_{\alpha1}$ radiation, λ = 1.5405Å). GSAS [11] software was used to perform a least squares refinement of the lattice parameters of all suitable samples.

The densities of the pellets were determined from the measured mass and volume. Theoretical densities were calculated using experimental lattice parameters and the chemical formula of the sample. The relative densities were calculated from the actual and theoretical density values. The density of the pellets was ~ 75 % for all compounds.

Thermal analysis was conducted on a 10 ± 0.5 mg sample using a Stanton Redcroft STA 1500 Thermal Analyser on heating from room temperature to 800 °C and on cooling from 800 °C to room temperature in air, with a heating/cooling rate of

10 °C/min, and in 5% H$_2$/Ar, again with a heating/cooling rate of 10 °Cmin^{-1}, and with a flow rate of 5% H$_2$/Ar of 50 mLmin^{-1}.

5.1.2.3.   Conductivity Testing

Pellets for all samples were coated on opposing sides using silver paste. The conductivity of the samples was measured in primarily in air between 300 °C to 700 °C. Secondary measurements over the same temperature range were conducted in 5% H$_2$/Ar following an equilibration step of 10 hours at 700 °C in 5% H$_2$/Ar. Measurements were conducted using either an A.C. method utilising a Solartron 1455A frequency response analyser coupled to a Solartron 1470E potentiostat/galvanostat controlled by CoreWare software over the frequency range 1 MHz to 100 mHz or a DC method using a Solartron 1470E potentiostat/galvanostat controlled by CoreWare software with an applied current of 1 - 0.1 A.

5.1.3. Results and Discussion
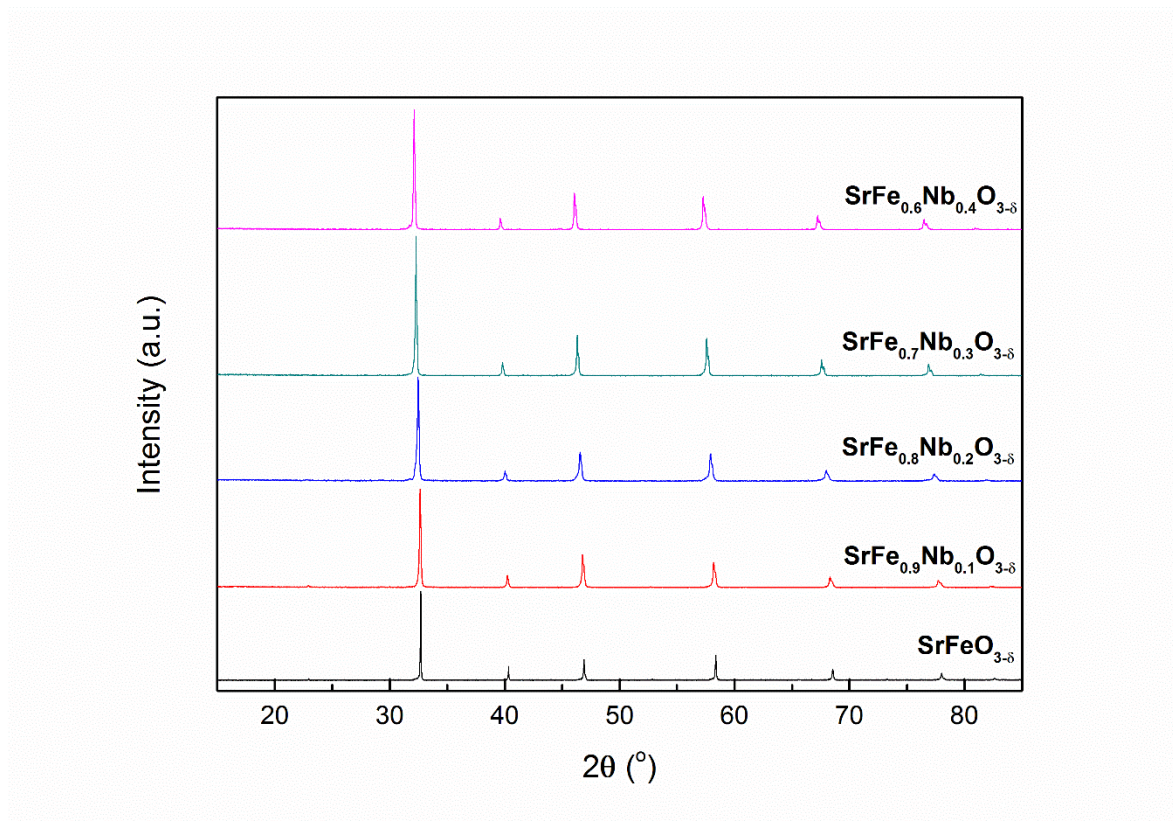
Figure 5.1. X-ray diffraction patterns of SrFe$_{1-x}$Nb$_x$O$_{3-\delta}$ (x = 0-0.4)

SrFe$_{1-x}$Nb$_x$O$_{3-\delta}$ (x = 0, 0.1, 0.2, 0.3, 0.4) was found to form a solid solution with the cubic perovskite structure (SG: *Pm-3m*), Figure 5.1. An increase in the synthesis time and/or temperature was required to form the single phase cubic perovskite structure with increasing niobium content, intimating that niobium doping decreases compound sinterability.
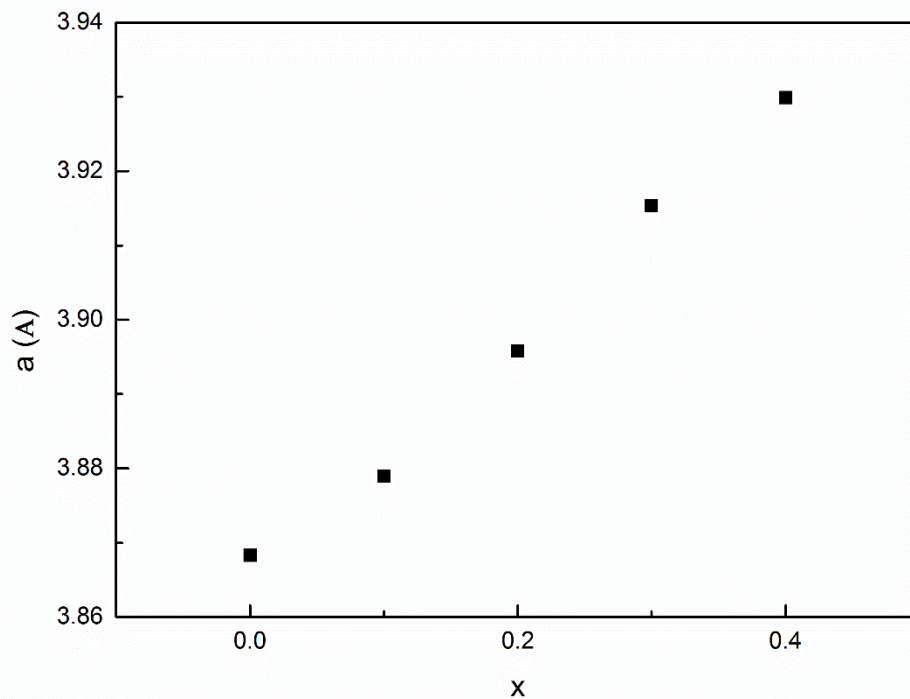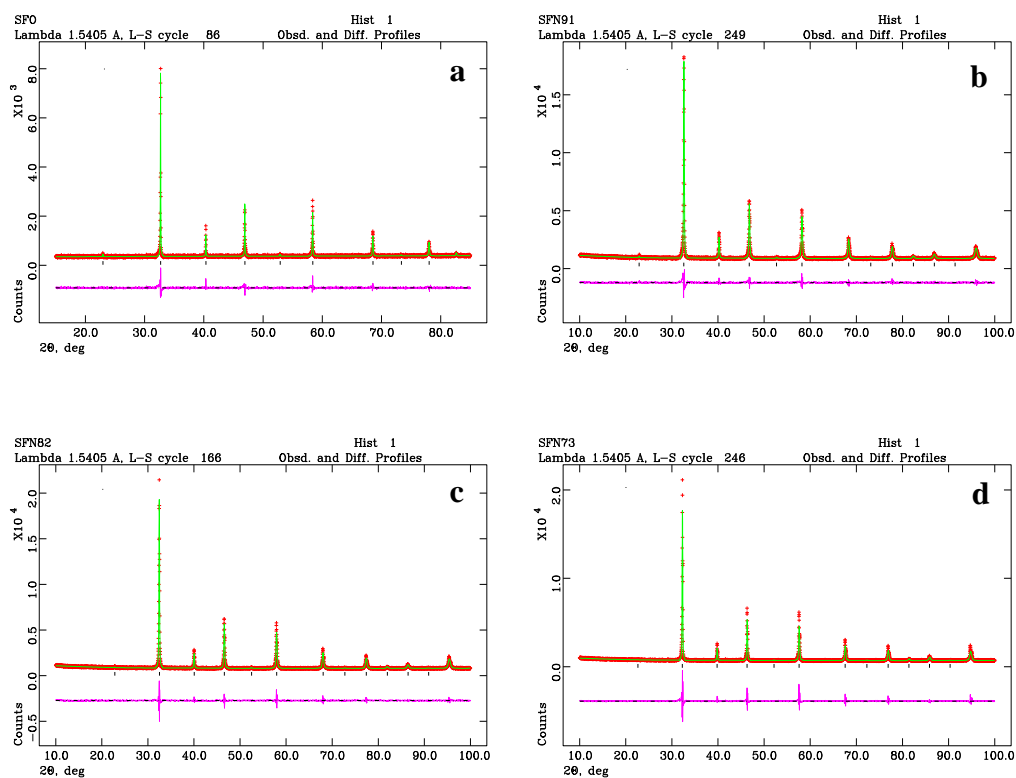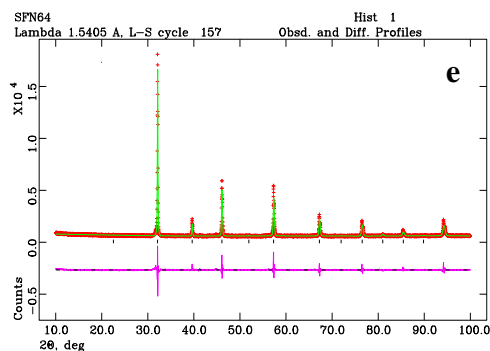
Figure 5.2. Variation of lattice parameters for SrFe$_{1-x}$Nb$_x$O$_{3-\delta}$ (x = 0-0.4)

Figure 5.3. GSAS plots for SrFe$_{1-x}$Nb$_x$O$_{3-\delta}$, x = 0 (a), x = 0.1 (b), x = 0.2 (c), x = 0.3 (d), x = 0.4(e))

GSAS refinement [12] of the SrFe$_{1-x}$Nb$_x$O$_{3-\delta}$ (x = 0, 0.1, 0.2, 0.3, 0.4) exhibits an increase in lattice parameters with increasing niobium content, Figure 5.2, 5.3 and Table 5.1. The increase in lattice parameters can be attributed to the greater cationic size of Nb^{5+} (0.64 Å) over that of Fe^{4+} (0.605 Å) [13]. As with other SrFeO$_{3-\delta}$ dopants [2, 14], the expected increase in Fe^{3+} content with increasing dopant content may also contribute to lattice expansion. The observed structure and lattice parameters correlates with those observed previously by Anikina *et. al.* [3], with the slight reduction in the lattice parameters for all samples attributed to differing synthesis methods.

|		$SrFeO_{3-\delta}$	$SrFe_{0.9}Nb_{0.1}O_{3-\delta}$	$SrFe_{0.8}Nb_{0.2}O_{3-\delta}$	$SrFe_{0.7}Nb_{0.3}O_{3-\delta}$	$SrFe_{0.6}Nb_{0.4}O_{3-\delta}$
χ^2		1.760	2.775	2.515	4.874	4.081
Rp (%)		6.67	5.21	5.15	7.67	7.51
wRp (%)		4.96	3.76	3.78	5.13	5.30
Space		*Pm-3m*	*Pm-3m*	*Pm-3m*	*Pm-3m*	*Pm-3m*
a (Å)		3.8683(3)	3.8789(3)	3.8958(2)	3.9153(3)	3.9299(3)
V (Å^3)		57.88(1)	58.36(1)	59.13(1)	60.02(1)	60.69(1)
Sr	x	0	0	0	0	0
	y	0	0	0	0	0
	z	0	0	0	0	0
	U_{iso}	0.001(8)	0.006(1)	0.006(1)	0.001(1)	0.014(8)
Fe/Nb	x	0.5	0.5	0.5	0.5	0.5
	y	0.5	0.5	0.5	0.5	0.5
	z	0.5	0.5	0.5	0.5	0.5
	U_{iso}	0.002(1)	0.008(1)	0.010(1)	0.011(1)	0.012(1)
O	x	0	0	0	0	0
	y	0.5	0.5	0.5	0.5	0.5
	z	0.5	0.5	0.5	0.5	0.5
	U_{iso}	0.014(4)	0.011(1)	0.022(1)	0.019(2)	0.008(1)

Table 5.1. Rietveld refinement and lattice parameters from GSAS refinement of $SrFe_{1-x}Nb_xO_{3-\delta}$ (x = 0 - 0.4) after synthesis in air
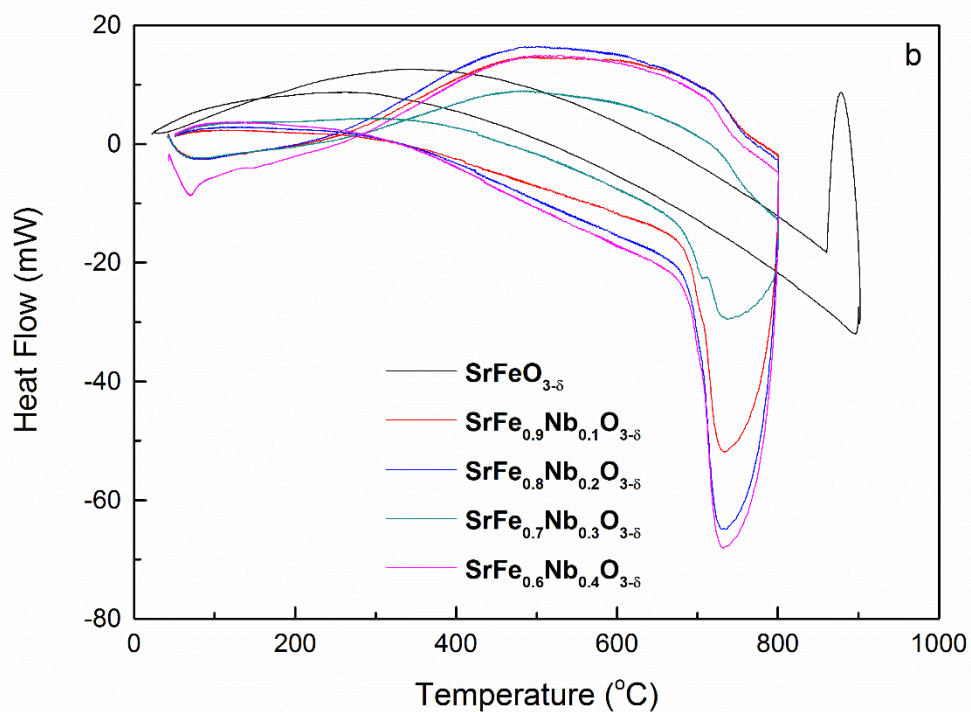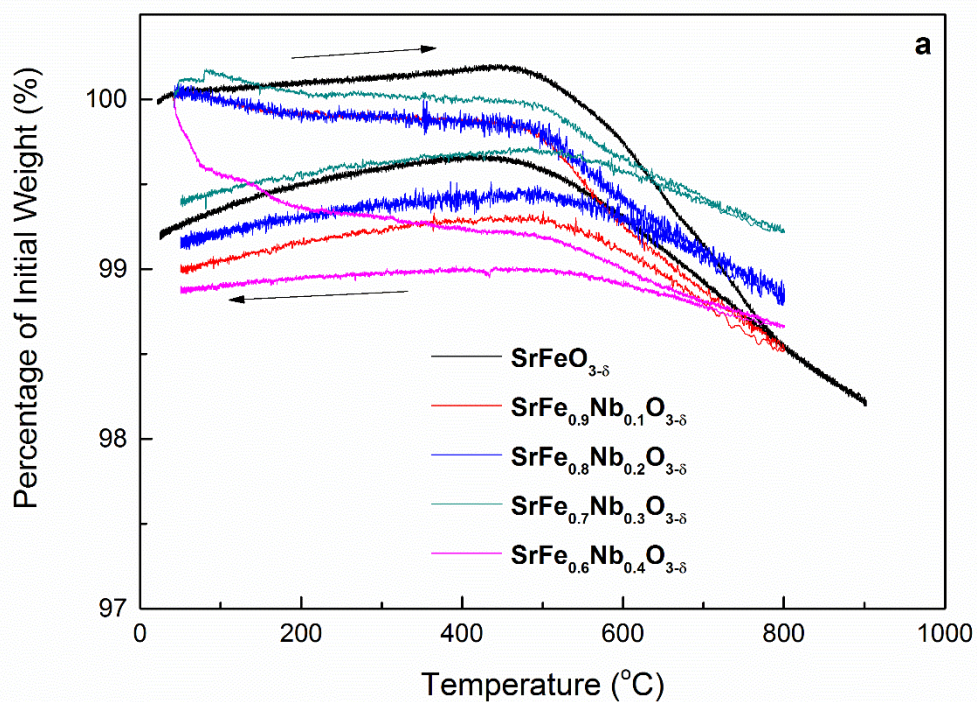
Figure 5.4. Thermogravimetric analysis (a) and differential scanning calorimetry (b) of SrFe$_{1-x}$Nb$_x$O$_{3-\delta}$ (x = 0-0.4) in air

Thermogravimetric analysis of $SrFe_{1-x}Nb_xO_{3-\delta}$ (x = 0, 0.1, 0.2, 0.3, 0.4) in air, Figure 5.4 (a), demonstrated a partially reversible reduction in weight beginning between 450 °C and 550 °C. The overall weight loss was negligible, between 0.6 % and 1.2 %, with no observable trend with increasing dopant concentration. Differential scanning calorimetry, Figure 5.4 (b), exhibited no significant transitions over the temperature range, intimating that the materials are thermally stable over this temperature range.
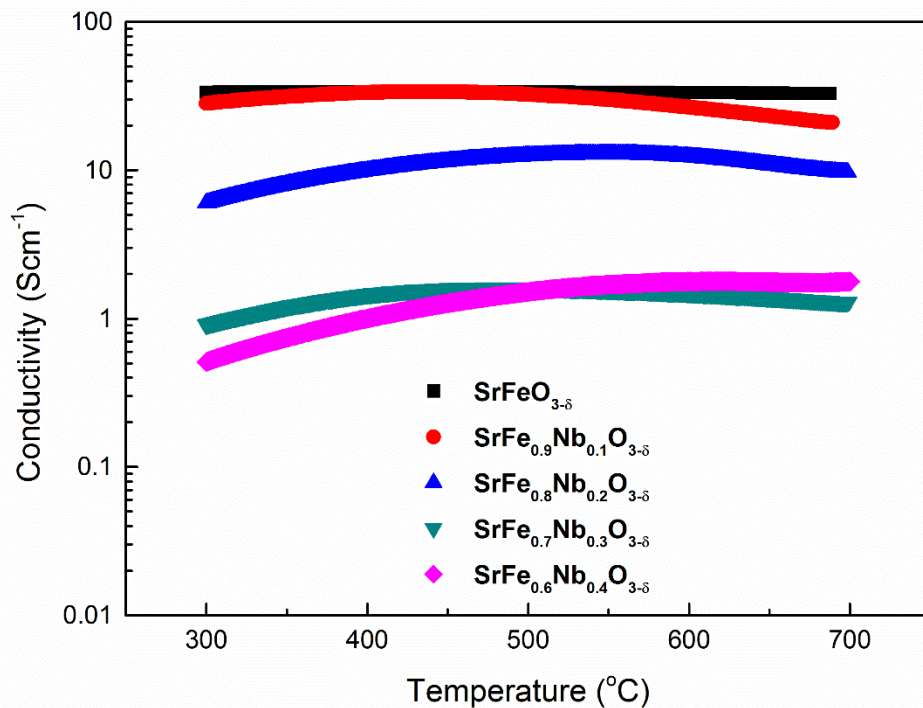
Figure 5.5. Conductivity of $SrFe_{1-x}Nb_xO_{3-\delta}$ (x = 0-0.4) in air

The conductivity of $SrFe_{1-x}Nb_xO_{3-\delta}$ (x = 0, 0.1, 0.2, 0.3, 0.4) reduces with increasing niobium content, Figure 5.5, as was observed by Anikina *et. al.* [3]. Semiconductor-metal transitions were observed for all compounds between 400 °C and 600 °C, increasing with increasing dopant concentration. Poulsen *et.* al [15] posited that the transition was due to compound reduction at high temperature, resulting in a

reduction in the charge carriers. Previous research [16] demonstrated a pseudo-linear reduction in the oxygen content of strontium ferrite in air above 400 °C with increasing temperature, which would appear to confirm compound reduction at these temperatures. Patrakeev $et.$ $al.$ [17] concluded from the evidence that the increase in the conductivity with increasing temperature, associated with E_a, was offset by the reduction in charge carrier concentration, causing an overall reduction in the electronic conductivity with increasing temperature, resulting in the pseudo-metallic behaviour.

The observed increase in the activation energy with increasing niobium content, from 0.19(2) eV for $SrFe_{0.9}Nb_{0.1}O_{3-\delta}$ to 0.27(1) eV for $SrFe_{0.6}Nb_{0.4}O_{3-\delta}$, can be attributed to the increase in bond length with reducing charge carrier concentration. Variation in the activation energy for conduction in doped strontium ferrites is largely determined by the charge carrier mobility. An increase in charge carrier mobility can be achieved through an increase in the percolation pathway, as is observed for $SrFe_{1-x}Mo_xO_{3-\delta}$, where the additional Fe-O-Fe bonds cause a reduction in the activation energy for conduction with increasing molybdenum content [2]. A reduction in the charge carrier mobility is also observed with a reduction in the charge carrier, Fe^{4+}, concentration, as this corresponds in an increase in the Fe-O bond length, as is observed for $SrFe_{1-x}Ti_xO_{3-\delta}$. In contrast to $SrFe_{1-x}Mo_xO_{3-\delta}$, for $SrFe_{1-x}Nb_xO_{3-\delta}$ (x = 0, 0.1, 0.2, 0.3, 0.4) the increase in charge carrier mobility with increasing dopant concentration from the increase in the percolation pathway is not sufficient to outweigh the reduction in mobility with increasing dopant concentration from the reduction in the charge carrier concentration.

Anikina $et.$ al [3] also attributed the reduction in the conductivity with increasing niobium content to the reduction of electron holes, as a result of charge compensation mechanisms. Akhtar $et.$ $al.$ [6] observed that the Fe-O bond lengths in $SrFe_{1-x}Nb_xO_{3-\delta}$ (x = 0, 0.25, 0.5) increase with increasing niobium content, whilst the niobium environment remains unchanged. This is suggestive of the Fe^{4+}-Fe^{3+} transition upon increasing dopant concentration, further confirming that the reduction in conductivity is associated with the reduction in charge carriers.
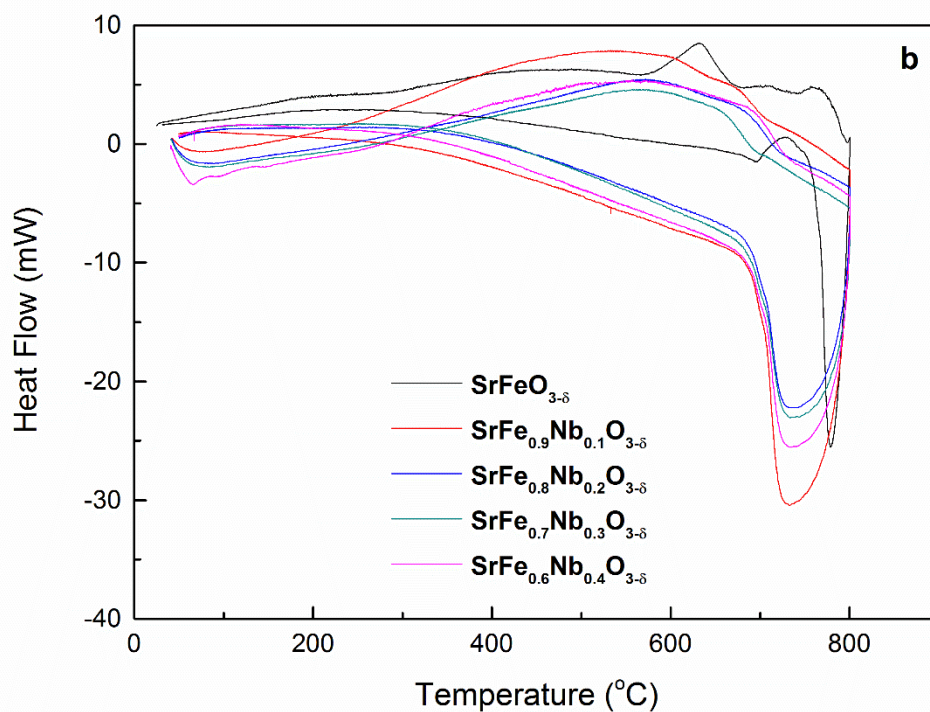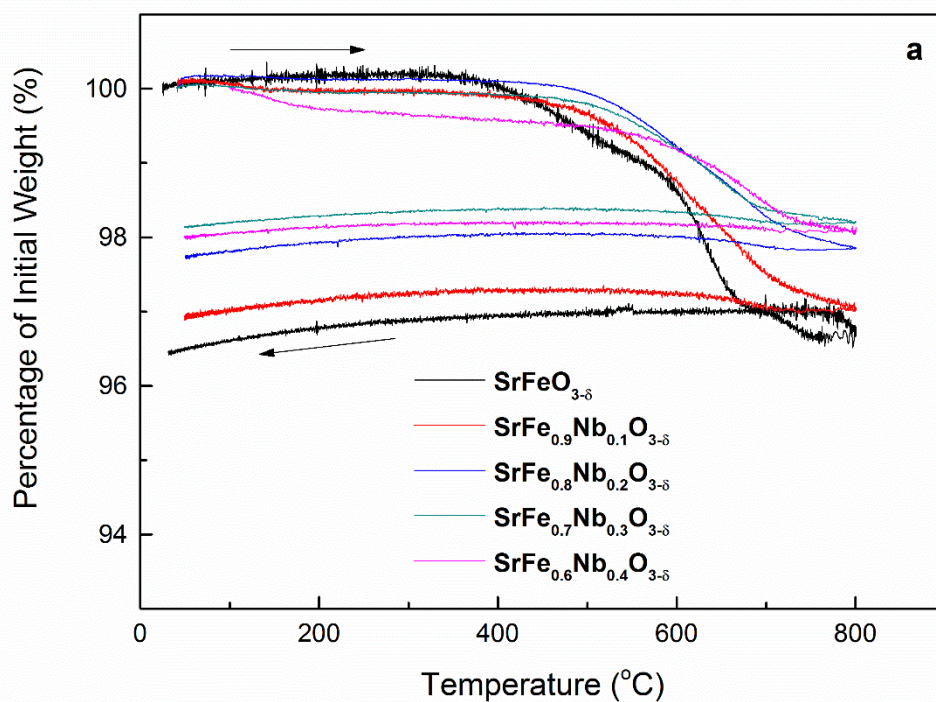
Figure 5.6. Thermogravimetric analysis (a) and differential scanning calorimetry (b) of SrFe₁₋ₓNbₓO₃₋δ (x = 0-0.4) in 5% H₂/Ar

Thermogravimetric analysis of $SrFe_{1-x}Nb_xO_{3-\delta}$ (x = 0, 0.1, 0.2, 0.3, 0.4) in 5% H_2/Ar, Figure 5.6 (a), demonstrated a reduction in weight inversely proportional to the dopant concentration, excluding $SrFe_{0.6}Nb_{0.4}O_{3-\delta}$. The lesser loss in weight with increasing dopant concentration is likely due to the reduction in the proportion of reducible cations with increasing dopant concentration. The reduction in weight was initiated between 400 °C and 600 °C for all compounds, suggesting that compound reduction will occur under fuel cell operating conditions. The reversible DSC transition previously observed for $SrFe_{1-x}Ti_xO_{3-\delta}$ (x = 0.1 – 0.3) was not exhibited by $SrFe_{1-x}Nb_xO_{3-\delta}$ (x = 0.1, 0.2, 0.3, 0.4), Figure 5.6 (b), with only a minor peak on heating in 5% H_2/Ar observed between 400 °C and 700 °C and attributed to cationic reduction.
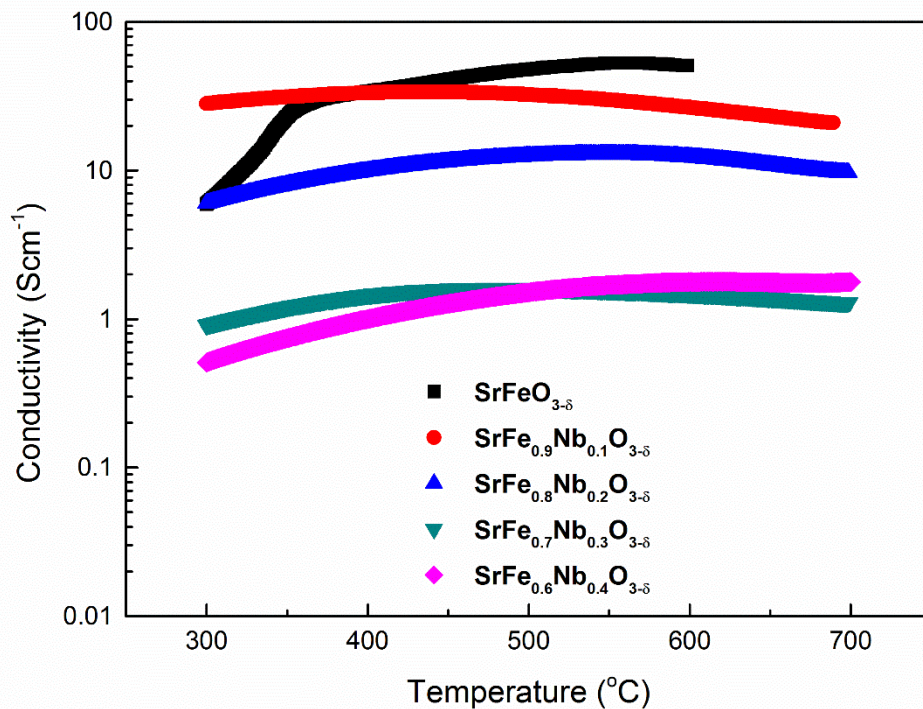
Figure 5.7. Conductivity of $SrFe_{1-x}Nb_xO_{3-\delta}$ (x = 0-0.4) in 5% H_2/Ar

Minimal reduction in the electronic conductivity of $SrFe_{1-x}Nb_xO_{3-\delta}$ (x = 0, 0.1, 0.2, 0.3, 0.4) was observed upon reduction at 700 °C in 5% H_2/Ar, Figure 5.7. The minimal reduction in the electronic conductivity can be attributed to minimal reduction

of the charge carriers at these temperatures. A similar semiconductor-metal transition to that in air was observed for all compounds, albeit with a small increase in the transition temperature upon reduction for lower dopant levels. As these transitions are evident in both oxidising and reducing atmosphere, this indicates that the conduction mechanism likely does not change upon reduction. The activation energy for conduction was observed to increase for all compounds upon reduction, with an increase in activation energy with increasing dopant concentration. A reduction in the average iron charge is known to increase the average bond length, reducing the charge carrier mobility and thus increasing the activation energy for conduction. Thus this increase in the activation energy upon reduction may confirm partial reduction of the charge carrier concentration.
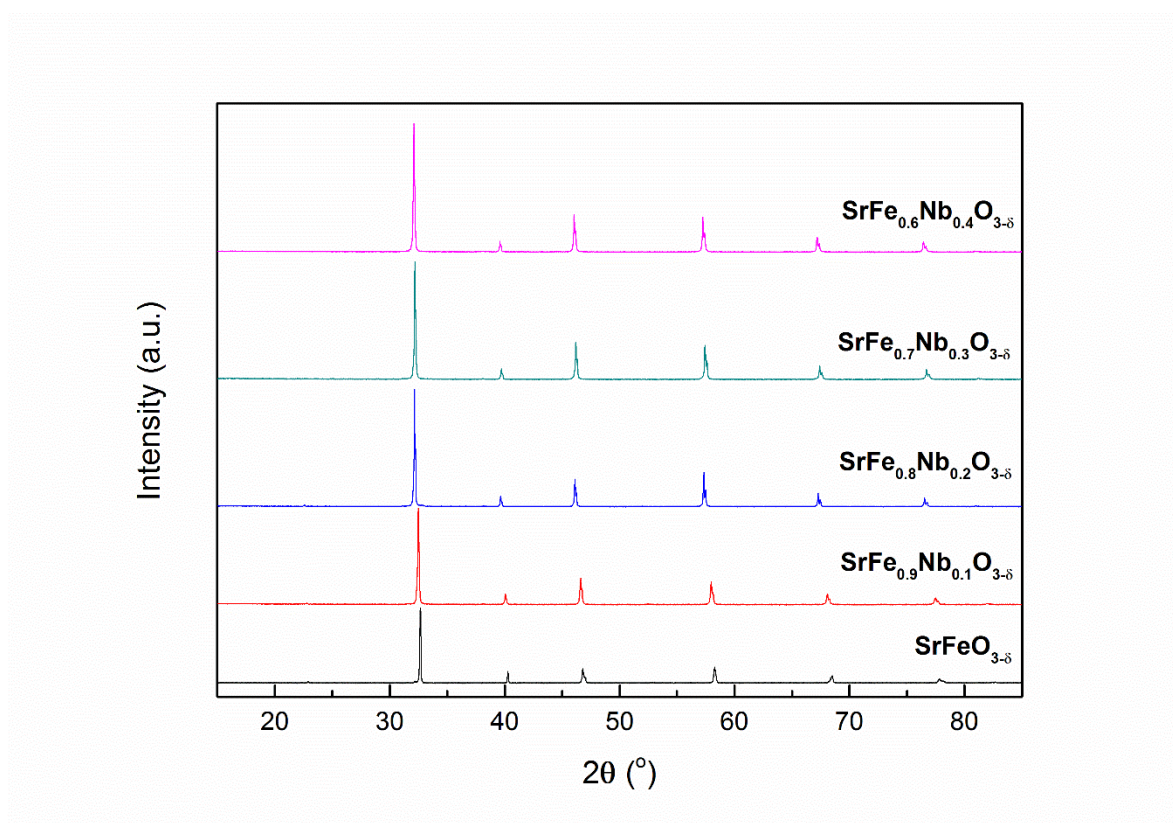
Figure 5.8. X-ray diffraction patterns of $SrFe_{1-x}Nb_xO_{3-\delta}$ (x = 0-0.4) after reduction at 700 °C in 5% H_2/Ar

Structural redox stability was observed for $SrFe_{1-x}Nb_xO_{3-\delta}$ (x = 0, 0.1, 0.2, 0.3, 0.4) after reduction at 700 °C in 5% H_2/Ar, Figure 5.8 and Figure 5.10, with all compounds retaining the cubic perovskite (SG: *Pm-3m*). A linear increase in the lattice parameters with increasing niobium content, as per Vegard's Law, was observed, Figure 5.9 and Table 5.2.
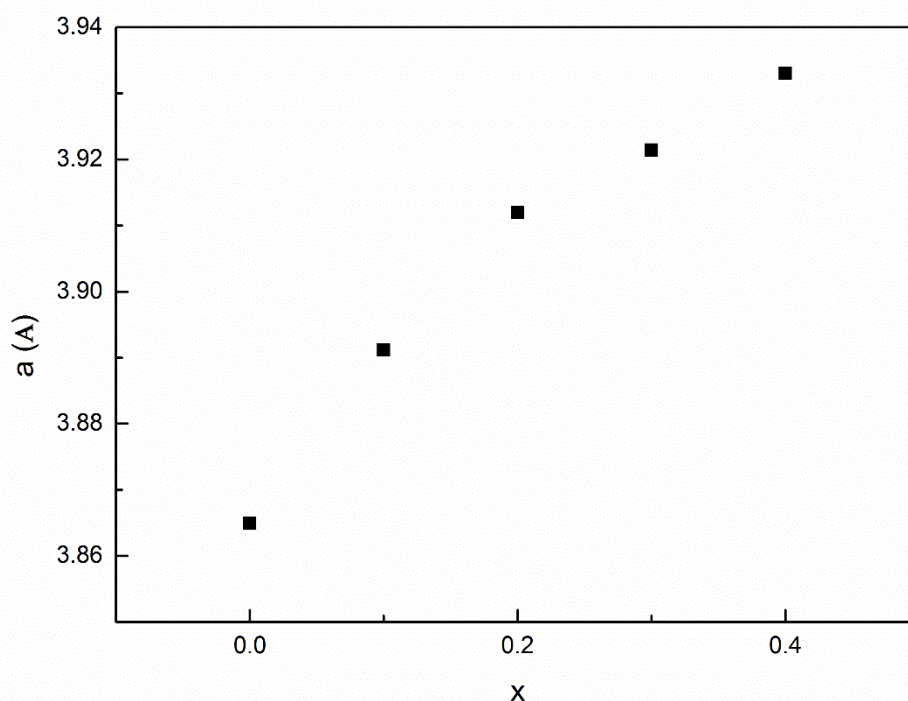
Figure 5.9. Variation of lattice parameters for SrFe$_{1-x}$Nb$_x$O$_{3-\delta}$ (x = 0-0.4) after reduction at 700 °C in 5% H$_2$/Ar and SrFeO$_{3-\delta}$ after reduction in 5%H$_2$/Ar at 600 °C
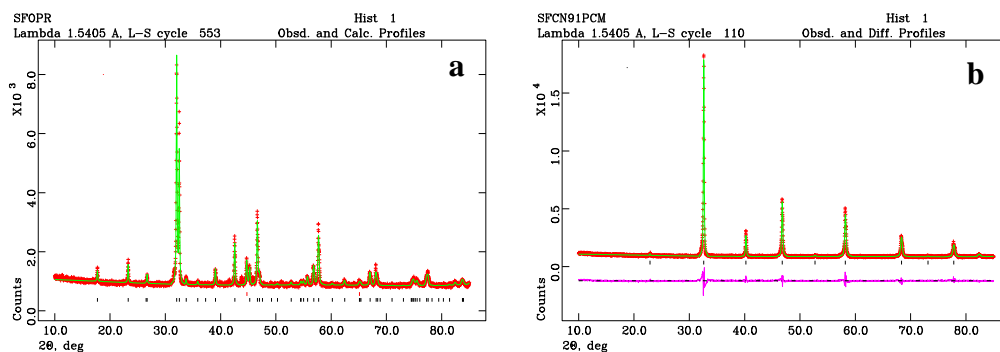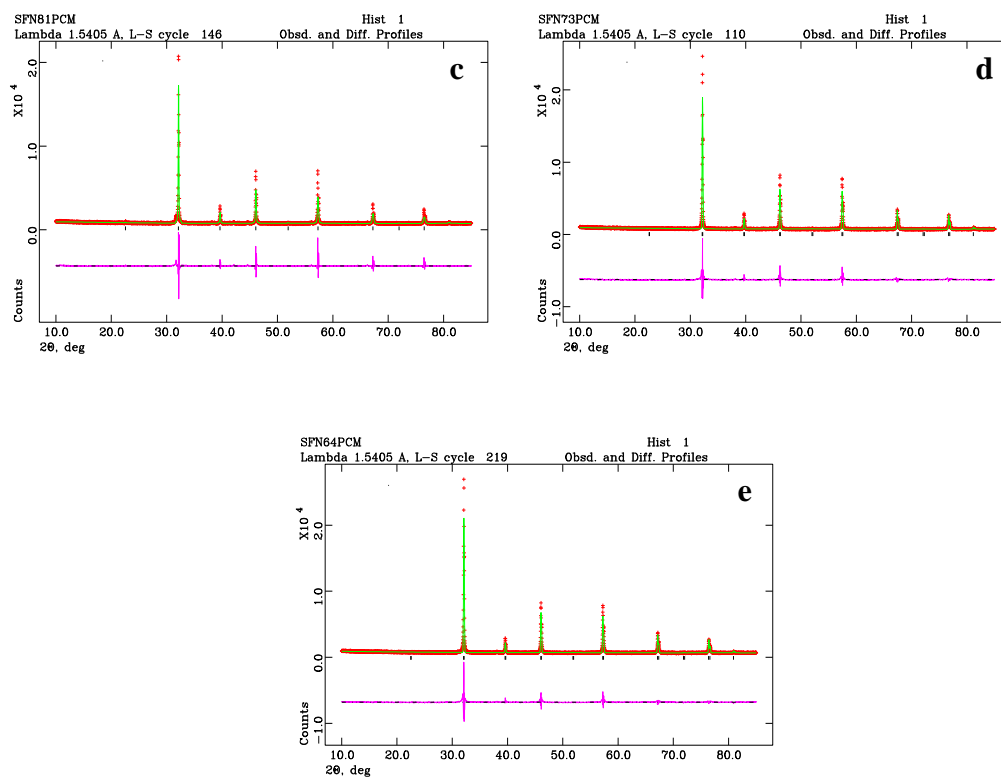
Figure 5.10. GSAS plots for SrFe$_{1-x}$Nb$_x$O$_{3-\delta}$, x = 0 (a), x = 0.1 (b), x = 0.2 (c), x = 0.3 (d), x = 0.4(e)) after reduction at 700 °C in 5% H$_2$/Ar and SrFeO$_{3-\delta}$ after reduction in 5%H$_2$/Ar at 600 °C

Comparison to the oxidised samples, Figure 5.1, indicates that a minimal increase in lattice parameters occurs with compound reduction. This is suggestive of minimal reduction of the iron and niobium at these temperatures, with niobium increasing the redox stability of the parent compound. This is in contrast to the non-uniform increase in lattice parameters upon reduction of SrFe$_{1-x}$Nb$_x$O$_{3-\delta}$ observed by Anikina *et. al.* [3]. This may be a result of the differing synthesis methods of the compounds, as the reduction conditions only differ in the humidity of the dilute hydrogen gas.

		$SrFeO_{3-\delta}$	$SrFe_{0.9}Nb_{0.1}O_{3-\delta}$	$SrFe_{0.8}Nb_{0.2}O_{3-\delta}$	$SrFe_{0.7}Nb_{0.3}O_{3-\delta}$	$SrFe_{0.6}Nb_{0.4}O_{3-\delta}$
χ^2		2.202	3.572	7.805	5.907	6.920
Rp (%)		6.88	6.10	9.14	8.13	9.01
wRp (%)		4.82	4.39	5.51	5.34	5.99
Space		*Pm-3m*	*Pm-3m*	*Pm-3m*	*Pm-3m*	*Pm-3m*
a (Å)		3.8649(7)	3.8912(6)	3.9120(10)	3.9241(8)	3.9362(4)
V (Å^3)		57.73(3)	58.92(3)	60.75(5)	60.43(3)	60.99(2)
Sr	x	0	0	0	0	0
	y	0	0	0	0	0
	z	0	0	0	0	0
	U_{iso}	0.001(9)	0.011(1)	0.017(1)	0.007(1)	0.010(1)
Fe/Nb	x	0.5	0.5	0.5	0.5	0.5
	y	0.5	0.5	0.5	0.5	0.5
	z	0.5	0.5	0.5	0.5	0.5
	U_{iso}	0.004(1)	0.013(1)	0.028(1)	0.014(1)	0.020(1)
O	x	0	0	0	0	0
	y	0.5	0.5	0.5	0.5	0.5
	z	0.5	0.5	0.5	0.5	0.5
	U_{iso}	0.052(2)	0.021(1)	0.070(4)	0.022(2)	0.021(2)

Table 5.2. Rietveld refinement and lattice parameters from GSAS refinement of $SrFe_{1-x}Nb_xO_{3-\delta}$ (x = 0.1 - 0.4) after reduction in 5%H_2/Ar at 700 °C and $SrFeO_{3-\delta}$ after reduction in 5%H_2/Ar at 600 °C

Anikina *et. al.* [3] also observed that $SrFe_{0.95}Nb_{0.05}O_{3-\delta}$ and $SrFe_{0.9}Nb_{0.1}O_{3-\delta}$ exhibited a comparatively higher increase in the lattice parameter after reduction than $SrFe_{1-x}Nb_xO_{3-\delta}$ (x = 0.2 - 0.5), attributed to the formation of brownmillerite-like domains for x = 0.1. A similar lattice contraction is not observed for our series, suggesting that brownmillerite phases are not present for the reduced compounds in this study.

5.1.3.1. *Conclusion*

As was predicted from previous research [3], $SrFe_{0.9}Nb_{0.1}O_{3-\delta}$ exhibited the highest electronic conductivity in both oxidising and reducing conditions. The observed redox stability of $SrFe_{0.9}Nb_{0.1}O_{3-\delta}$, despite the inconsistencies between the two studies, demonstrates the suitability of this material for use as an intermediate temperature SOFC anode material.

5.2. SrFe$_{0.8}$TM$_{0.1}$Nb$_{0.1}$O$_{3-\delta}$ (TM = Cr, Mn, Fe, Co, Ni, Cu)

5.2.1. Introduction

Doping of various transition metals into a titanium stabilised strontium ferrite, Section 4.2, demonstrated an improvement in the electronic conductivity without a reduction of the redox stability of the compound. Whilst the suitability of the properties of SrFe$_{0.9}$Nb$_{0.1}$O$_{3-\delta}$ for use as an IT-SOFC electrode material was demonstrated in Section 5.1, further improvement in the electronic conductivity would further improve the applicability of the material to IT-SOFCs. To this end, a series of transition metal doped strontium niobium ferrites SrFe$_{0.8}$TM$_{0.1}$Nb$_{0.1}$O$_{3-\delta}$ (TM = Cr, Mn, Fe, Co, Ni, Cu) was synthesised to determine the effect of aliovalent doping on the conductivity and stability of strontium niobium ferrite and to assess the suitability of these materials for use as symmetrical electrodes for IT-SOFCs.

5.2.2. Experimental Information

5.2.2.1. Synthesis

SrFe$_{0.8}$TM$_{0.1}$Nb$_{0.1}$O$_{3-\delta}$ (TM = Co, Cr, Cu, Mn, Ni) were produced by sol-gel synthesis technique. A stoichiometric amount of C$_4$H$_4$NNbO$_9$·H$_2$O (99.9%, Sigma Aldrich) was dissolved in distilled water. H$_2$O$_2$ was added dropwise to the niobium solution until a colour change was produced. Citric acid (99$^+$%, Alfa Aesar), in a 2:1 ratio to the metal ions in the final product, was added and heated till a solution was formed. Stoichiometric amounts of Sr(NO$_3$)$_2$ (98%, Alfa Aesar), Fe(NO$_3$)$_3$·9 H$_2$O (98%, Alfa Aesar) and either Co(NO$_3$)$_2$·6 H$_2$O (98$^+$%, Alfa Aesar), Cr(NO$_3$)$_2$·9 H$_2$O (99%, Sigma Aldrich), Cu(NO$_3$)$_2$·2.5 H$_2$O (ACS grade, Alfa Aesar), MnC$_4$H$_6$O$_4$·4 H$_2$O (>99%, Sigma Aldrich) or Ni(NO$_3$)$_2$·6 H$_2$O (98%, Alfa Aesar) were dissolved in distilled water. The solutions were mixed and the solution was heated until gelation.

The resultant gel was fired at 600 °C for 2 hours. A subsequent firing at 1300 °C for 5 hours was performed. Pellets of all the samples (ø ≈ 13 mm × 2 mm and ø ≈ 10 mm × 5 mm) were uniaxially pressed at 221 MPa and sintered in air at 1350°C for 5 hours.

5.2.2.2. Analytical Procedures

Phase purity and crystal parameters of the samples were examined by X-ray diffraction (XRD) analysis using a PANalytical X'Pert PRO MPD Multipurpose diffractometer (Cu $K_{\alpha1}$ radiation, λ = 1.5405Å). GSAS [11] software was used to perform a least squares refinement of the lattice parameters of all suitable samples.

The densities of the pellets were determined from the measured mass and volume. Theoretical densities were calculated using experimental lattice parameters and the chemical formula of the sample. The relative densities were calculated from the actual and theoretical density values. The density of the pellets was ~ 75 % for all compounds.

Thermal analysis was conducted on a 10 ± 0.5 mg sample using a Stanton Redcroft STA 1500 Thermal Analyser on heating from room temperature to 800 °C and on cooling from 800 °C to room temperature in air, with a heating/cooling rate of 10 °C/min, and in 5% H_2/Ar, again with a heating/cooling rate of 10 °Cmin^{-1}, and with a flow rate of 5% H_2/Ar of 50 mLmin^{-1}.

5.2.2.3. Conductivity Testing

Pellets for all samples were coated on opposing sides using silver paste. The conductivity of the samples was measured in primarily in air between 300 °C to 700 °C. Secondary measurements over the same temperature range were conducted in 5% H_2/Ar following an equilibration step of 10 hours at 700 °C in 5% H_2/Ar. Measurements were conducted using either an A.C. method utilising a Solartron 1455A frequency response analyser coupled to a Solartron 1470E

potentiostat/galvanostat controlled by CoreWare software over the frequency range 1 MHz to 100 mHz or a DC method using a Solartron 1470E potentiostat/galvanostat controlled by CoreWare software with an applied current of 1 - 0.1 A.

5.2.3. Results and Discussion
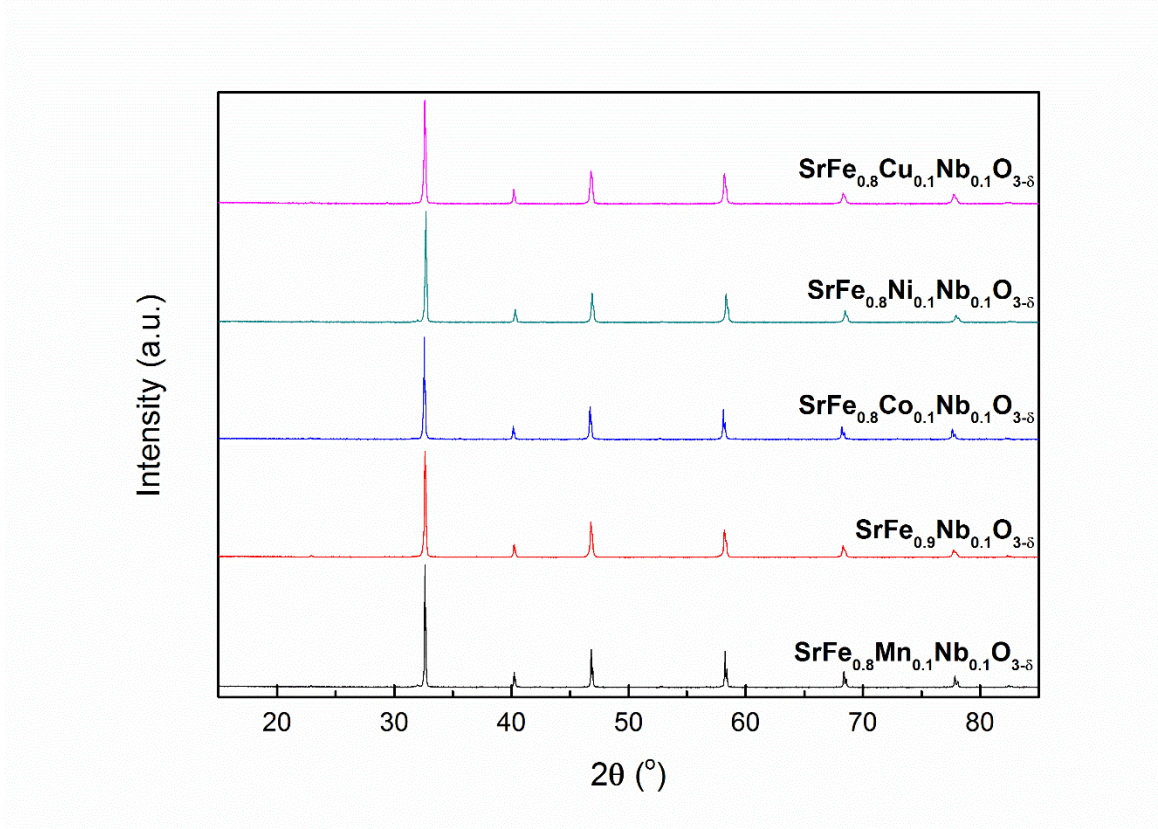
Figure 5.11. X-ray diffraction patterns of SrFe$_{0.8}$TM$_{0.1}$Nb$_{0.1}$O$_{3-\delta}$ (TM = Mn, Fe, Co, Ni, Cu)

X-ray diffraction of SrFe$_{0.8}$TM$_{0.1}$Nb$_{0.1}$O$_{3-\delta}$ (TM = Mn, Fe, Co, Ni, Cu) demonstrated the formation of single phase cubic perovskites for all compounds, Figure 5.11. As for SrFe$_{0.7}$TM$_{0.2}$Ti$_{0.1}$O$_{3-\delta}$ (TM = Mn, Fe, Co, Ni, Cu), doping of B^{2+} would be expected to cause a reduction in the lattice parameters, as a result of the subsequent Fe^{3+}-Fe^{4+} transitions and the reduction in oxygen content.
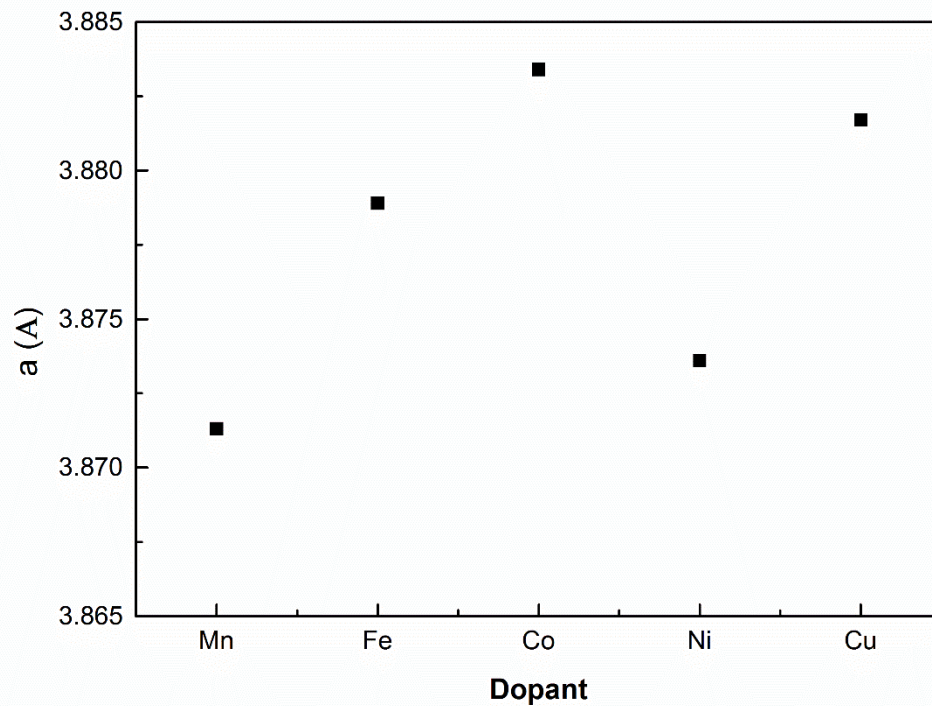
Figure 5.12. Variation of lattice parameters for SrFe$_{0.8}$TM$_{0.1}$Nb$_{0.1}$O$_{3-\delta}$ (TM = Mn, Fe, Co, Ni, Cu)
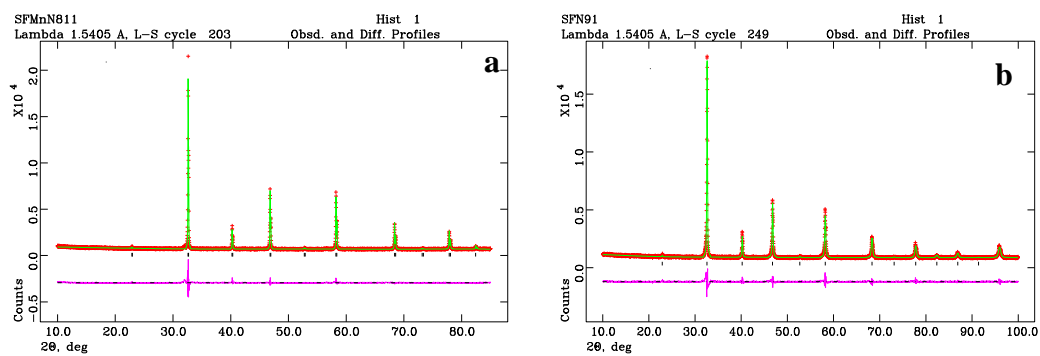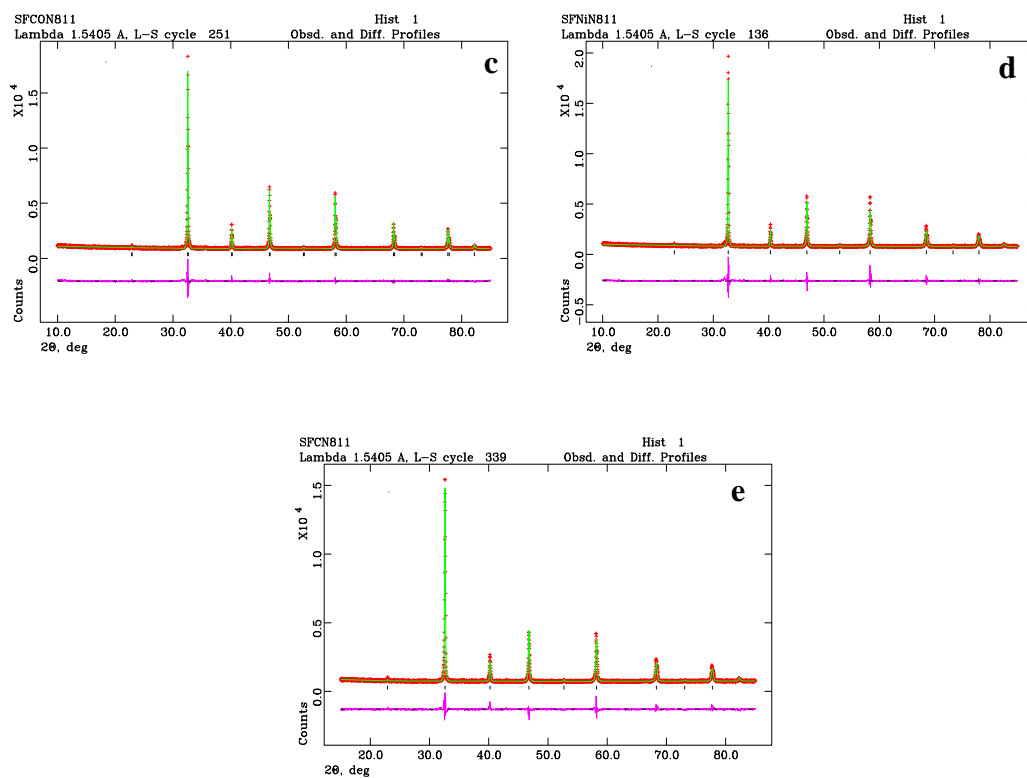
Figure 5.13. GSAS plots for SrFe$_{0.8}$TM$_{0.1}$Nb$_{0.1}$O$_{3-\delta}$ (TM = Mn (a), Fe (b), Co (c), Ni (d), Cu (e))

GSAS [12] analysis of the structures of both SrFe$_{0.8}$Ni$_{0.1}$Nb$_{0.1}$O$_{3-\delta}$ and SrFe$_{0.8}$Mn$_{0.1}$Nb$_{0.1}$O$_{3-\delta}$ demonstrated the anticipated reduction in lattice parameters, Figure 5.12, Figure 5.13 and Table 5.3. The reduction in the lattice parameter from Fe^{3+}-Fe^{4+} transitions and oxygen loss is only partially balanced by the expansion from manganese and nickel doping, a result of the larger atomic size of the dopants (0.83 Å for Mn$^{2+}_{oct}$ or 0.66 Å for Mn$^{2+}_{tet}$ and 0.69 Å for Ni$^{2+}_{oct}$, 0.55 Å for Ni$^{2+}_{tet}$). An increase in the lattice parameter was observed for both SrFe$_{0.8}$Co$_{0.1}$Nb$_{0.1}$O$_{3-\delta}$ and SrFe$_{0.8}$Cu$_{0.1}$Nb$_{0.1}$O$_{3-\delta}$ due to the larger atomic size of the dopants (0.745 Å for Co$^{2+}_{oct}$, 0.58 Å for Co$^{2+}_{tet}$ and Cu$^{2+}_{oct}$, 0.73 Å). As the cationic size of Mn^{2+} is larger than that of cobalt or copper, this is suggestive of either Mn^{3+} formation (0.645 Å for Mn$^{3+}_{oct}$ or 0.58 Å for Mn$^{3+}_{tet}$) or of preferential tetrahedral coordination. The differing trends observed for the titanium doped and niobium doped compounds can be partially attributed to the varying dopant levels, x = 0.2 and x = 0.1, of the respective series.

		$SrFe_{0.8}Mn_{0.1}Nb_{0.1}$	$SrFe_{0.9}Nb_{0.1}O_{3-\delta}$	$SrFe_{0.8}Co_{0.1}Nb_{0.1}O_{3-\delta}$	$SrFe_{0.8}Ni_{0.1}Nb_{0.1}O_{3-\delta}$	$SrFe_{0.8}Cu_{0.1}Nb_{0.1}O_{3-\delta}$
χ^2		8.098	2.775	4.666	3.479	2.607
Rp (%)		9.92	5.21	6.75	6.07	5.553
wRp (%)		5.81	3.76	4.33	4.26	4.00
Space		*Pm-3m*	*Pm-3m*	*Pm-3m*	*Pm-3m*	*Pm-3m*
a (Å)		3.8736(10)	3.8789(3)	3.8834(8)	3.8713(7)	3.8817(1)
V (Å^3)		58.12(4)	58.36(1)	58.56(4)	58.02(3)	58.49(1)
Sr	x	0	0	0	0	0
	y	0	0	0	0	0
	z	0	0	0	0	0
	U_{iso}	0.008(1)	0.006(1)	0.008(1)	0.003(1)	0.001(1)
Fe/TM/Nb	X	0.5	0.5	0.5	0.5	0.5
	Y	0.5	0.5	0.5	0.5	0.5
	Z	0.5	0.5	0.5	0.5	0.5
	U_{iso}	0.013(1)	0.008(1)	0.009(1)	0.007(1)	0.015(1)
O	x	0	0	0	0	0
	y	0.5	0.5	0.5	0.5	0.5
	z	0.5	0.5	0.5	0.5	0.5
	U_{iso}	0.019(3)	0.011(1)	0.015(2)	0.022(2)	0.022(1)

Table 5.3. Rietveld refinement and lattice parameters from GSAS refinement of $SrFe_{0.8}TM_{0.1}Nb_{0.1}O_{3-\delta}$ (TM = Mn, Fe, Co, Ni, Cu) after synthesis in air
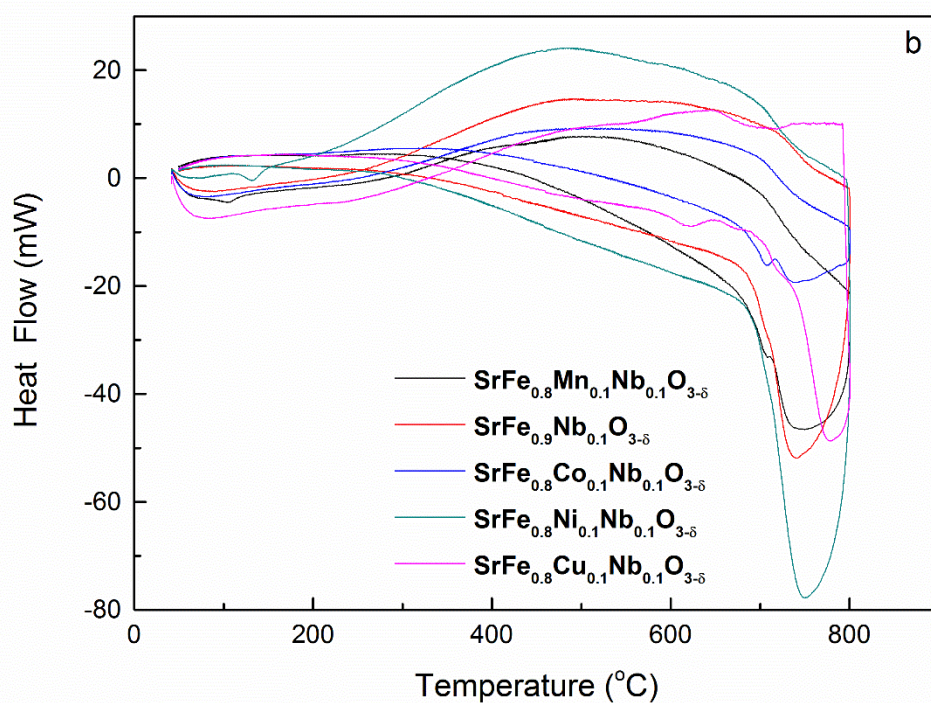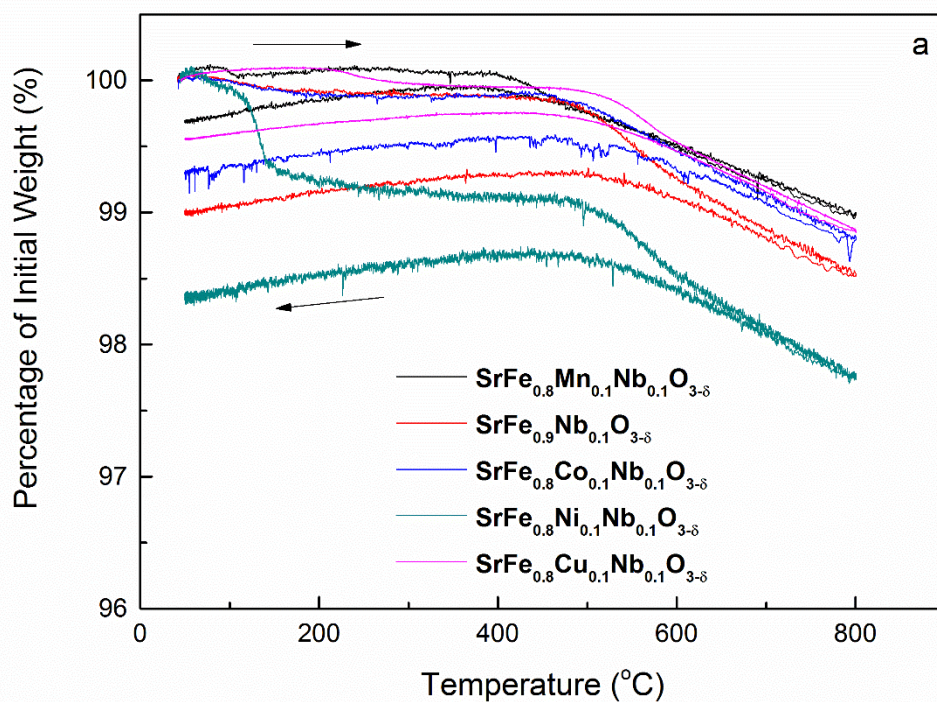
Figure 5.14. Thermogravimetric analysis (a) and differential scanning calorimetry (b) of SrFe$_{0.8}$TM$_{0.1}$Nb$_{0.1}$O$_{3-\delta}$ (TM = Mn, Fe, Co, Ni, Cu) in air

Thermogravimetric analysis of $SrFe_{0.8}TM_{0.1}Nb_{0.1}O_{3-\delta}$ (TM = Mn, Fe, Co, Ni, Cu) in air demonstrated minimal weight loss, between 0.3 % and 1.6 %, for all compounds, Figure 5.14 (a). A partially reversible reduction in weight was observed, beginning between 400 °C and 550 °C, attributed to high temperature cationic reduction. Differential scanning calorimetry over the same range, Figure 5.14 (b), exhibited no significant transitions over the temperature range, intimating thermal stability over this temperature range.
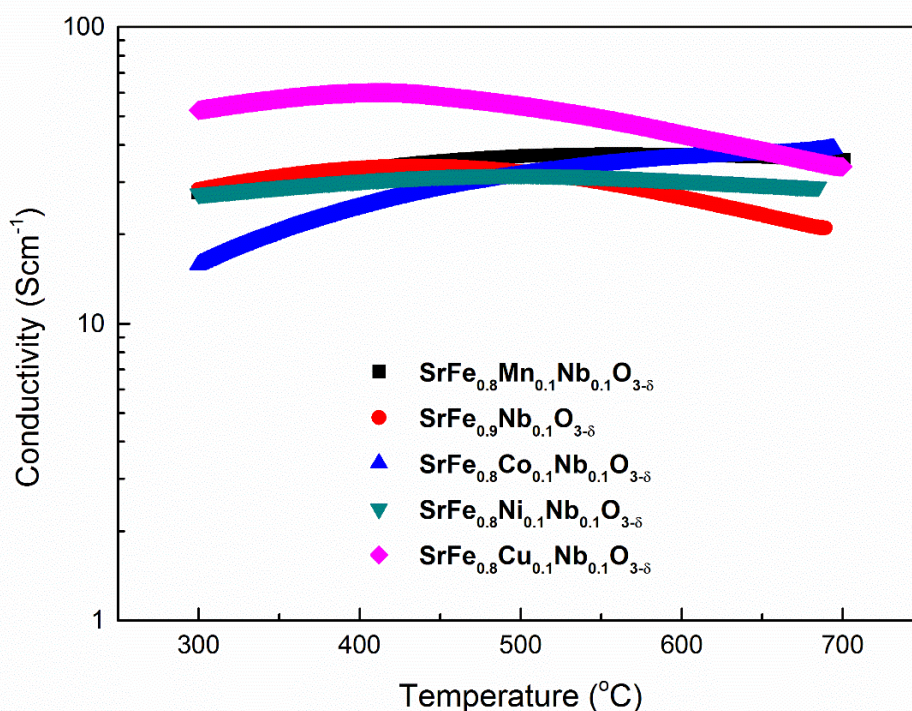
Figure 5.15. Conductivity of $SrFe_{0.8}TM_{0.1}Nb_{0.1}O_{3-\delta}$ (TM = Mn, Fe, Co, Ni, Cu) in air

Unlike for $SrFe_{0.9}Ti_{0.1}O_{3-\delta}$, transition metal doping of $SrFe_{0.9}Nb_{0.1}O_{3-\delta}$ did not result in a unilateral increase in the conductivity, Figure 5.15, with only $SrFe_{0.8}Cu_{0.1}Nb_{0.1}O_{3-\delta}$ maintaining a higher conductivity over the measured temperature range. Despite the lack of significant improvement over $SrFe_{0.9}Nb_{0.1}O_{3-\delta}$, the conductivity of all $SrFe_{0.8}TM_{0.1}Nb_{0.1}O_{3-\delta}$ (TM = Mn, Fe, Co, Ni, Cu) compounds

remained between 10 Scm^{-1} and 70 Scm^{-1}, demonstrating potential for use as SOFC electrode materials.

A transition between semiconducting and metallic behaviour is observed for all compounds, with the exception of SrFe$_{0.8}$Co$_{0.1}$Nb$_{0.1}$O$_{3-\delta}$. As was previously noted for SrFe$_{1-x}$Nb$_x$O$_{3-\delta}$, the transition between semiconducting and metallic behaviour is a result of the balance between the reduction in electronic conductivity, due to the reduction of charge carriers, with high temperature reduction and the increase in the electronic conductivity, due to increasing temperature, as given by the activation energy for conduction [17]. Previous research into lanthanum strontium cobalt ferrite [18] demonstrated a semiconductor-metal transition, albeit at above 700 °C, thus it is posited that the absence of a transition for SrFe$_{0.8}$Co$_{0.1}$Nb$_{0.1}$O$_{3-\delta}$ is due to the transition temperature occurring at a higher temperature than the measurement range in this study.
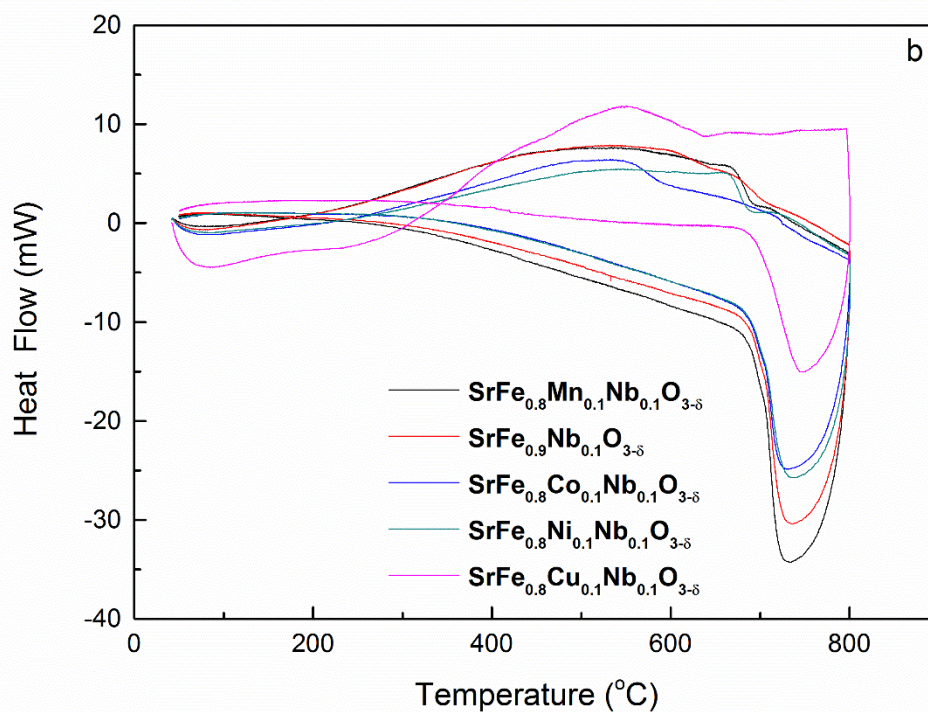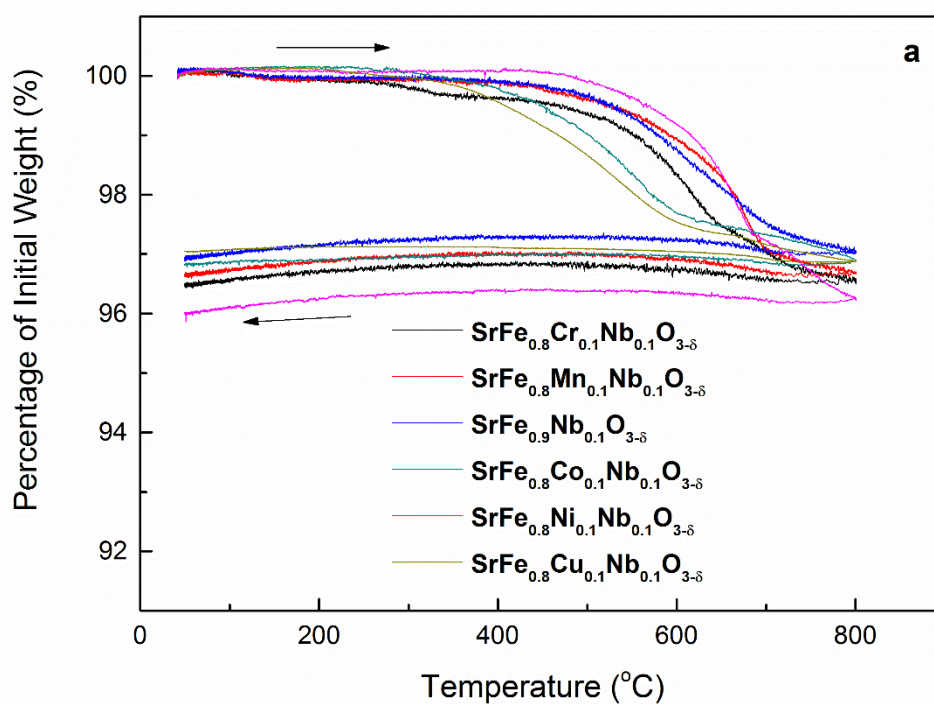
Figure 5.16. Thermogravimetric analysis (a) and differential scanning calorimetry (b) of SrFe$_{0.8}$TM$_{0.1}$Nb$_{0.1}$O$_{3-\delta}$ (TM = Mn, Fe, Co, Ni, Cu) in 5% H$_2$/Ar

Weight loss upon reduction of $SrFe_{0.8}TM_{0.1}Nb_{0.1}O_{3-\delta}$ (TM = Mn, Fe, Co, Ni, Cu), Figure 5.16 (a), exhibited minimal variation between dopants, between 2.95 % and 3.35 %. Only $SrFe_{0.8}Ni_{0.1}Nb_{0.1}O_{3-\delta}$ exhibited a slightly higher weight loss, of 3.99 %. This could be indicative of preferential iron and nickel reduction at these temperatures. Differential scanning calorimetry, Figure 5.16 (b), exhibited an irreversible transition upon heating for all compounds, between 500 °C and 600 °C for $SrFe_{0.8}Co_{0.1}Nb_{0.1}O_{3-\delta}$ and $SrFe_{0.8}Cu_{0.1}Nb_{0.1}O_{3-\delta}$ and between 600 °C and 700 °C for $SrFe_{0.9}Nb_{0.1}O_{3-\delta}$, $SrFe_{0.8}Mn_{0.1}Nb_{0.1}O_{3-\delta}$ and $SrFe_{0.8}Ni_{0.1}Nb_{0.1}O_{3-\delta}$. The observed inflection in the DSC trace is likely a result of cationic reduction.
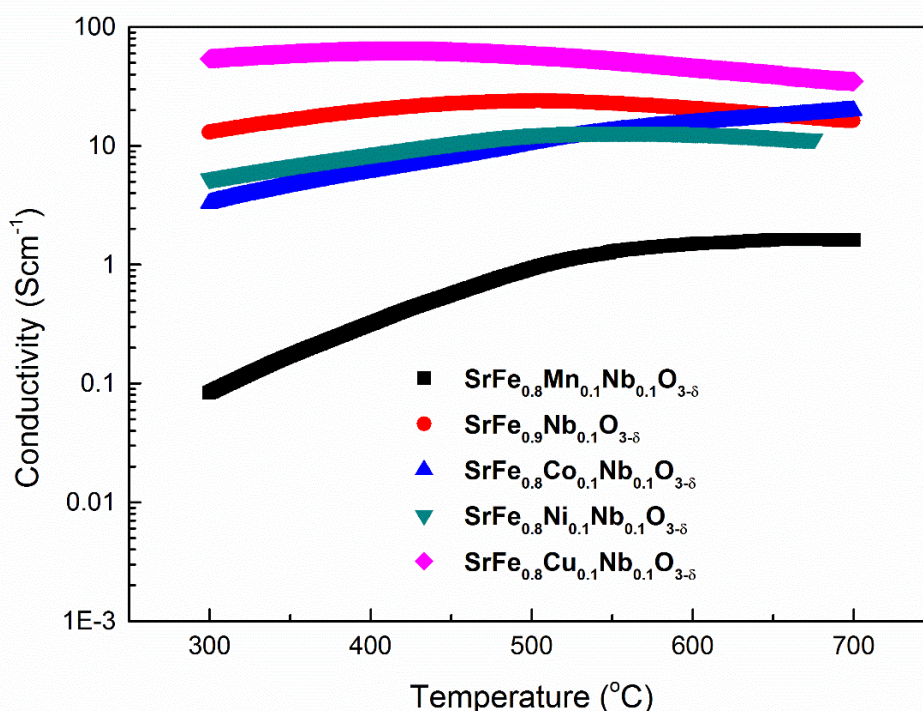
Figure 5.17. Conductivity of $SrFe_{0.8}TM_{0.1}Nb_{0.1}O_{3-\delta}$ (TM = Mn, Fe, Co, Ni, Cu) in 5% H_2/Ar

A minor reduction in the electronic conductivity of $SrFe_{0.8}TM_{0.1}Nb_{0.1}O_{3-\delta}$ (TM = Fe, Co, Ni, Cu) was observed upon reduction at 700 °C in 5% H_2/Ar, Figure 5.17. The minimal reduction in the conductivity, as was observed for $SrFe_{1-x}Nb_xO_{3-\delta}$, is likely the result of partial cationic reduction. An increase in the activation energy for

conduction was observed upon reduction of $SrFe_{0.8}TM_{0.1}Nb_{0.1}O_{3-\delta}$ (TM = Fe, Co, Ni, Cu), a result of the Fe^{4+}-Fe^{3+} transition, increasing the Fe-O bond length and thus reducing the charge carrier mobility. The semiconductor-metal transition is observed for both $SrFe_{0.8}Cu_{0.1}Nb_{0.1}O_{3-\delta}$ and $SrFe_{0.9}Nb_{0.1}O_{3-\delta}$ upon reduction, suggesting the conduction mechanism does not vary upon reduction, despite the reduction in conductivity.

In contrast to the other compounds, the conductivity of $SrFe_{0.8}Mn_{0.1}Nb_{0.1}O_{3-\delta}$ exhibits a significant decrease upon reduction, Figure 5.17. A similarly significant decrease in conductivity was observed for $SrFe_{0.7}Mn_{0.2}Ti_{0.1}O_{3-\delta}$ upon reduction, which was attributed to manganese doping as Mn^{3+}, directly contributing to the charge carrier concentration in air, and not significantly altering the charge carrier concentration through charge compensation mechanisms. Reduction of Mn^{3+} to Mn^{2+} upon exposure to 5% H_2/Ar would result in a reduction in the charge carrier concentration, similar to the Fe^{4+}-Fe^{3+} transition.
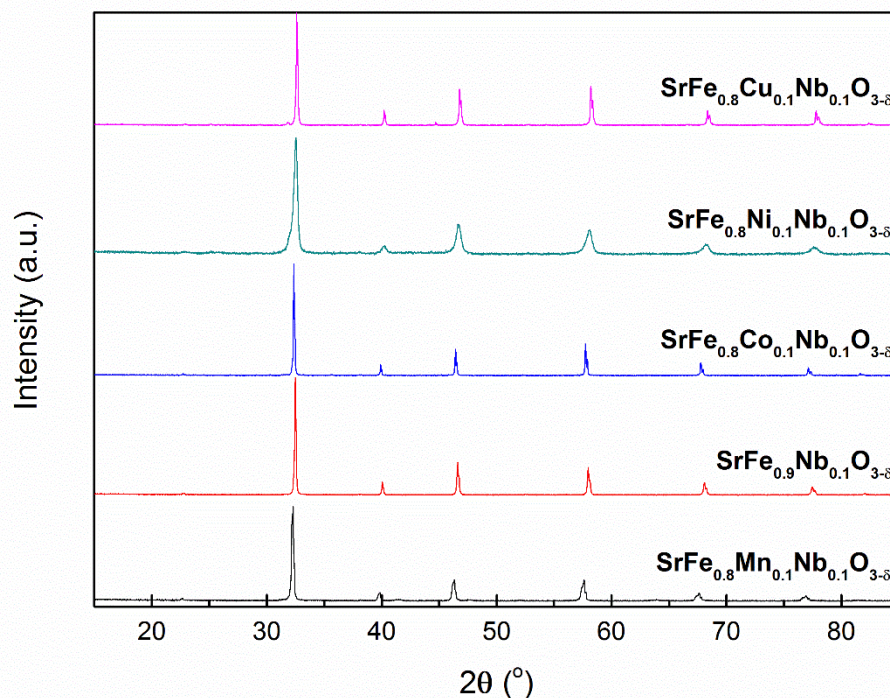
Figure 5.18. XRD patterns of $SrFe_{0.8}TM_{0.1}Nb_{0.1}O_{3-\delta}$ (TM = Mn, Fe, Co, Ni, Cu) after reduction at 700 °C in 5% H_2/Ar

All compounds exhibited the cubic perovskite structure after reduction at 700 °C in 5% H_2/Ar, Figure 5.18, albeit with significant peak broadening observed for $SrFe_{0.8}Ni_{0.1}Nb_{0.1}O_{3-\delta}$.
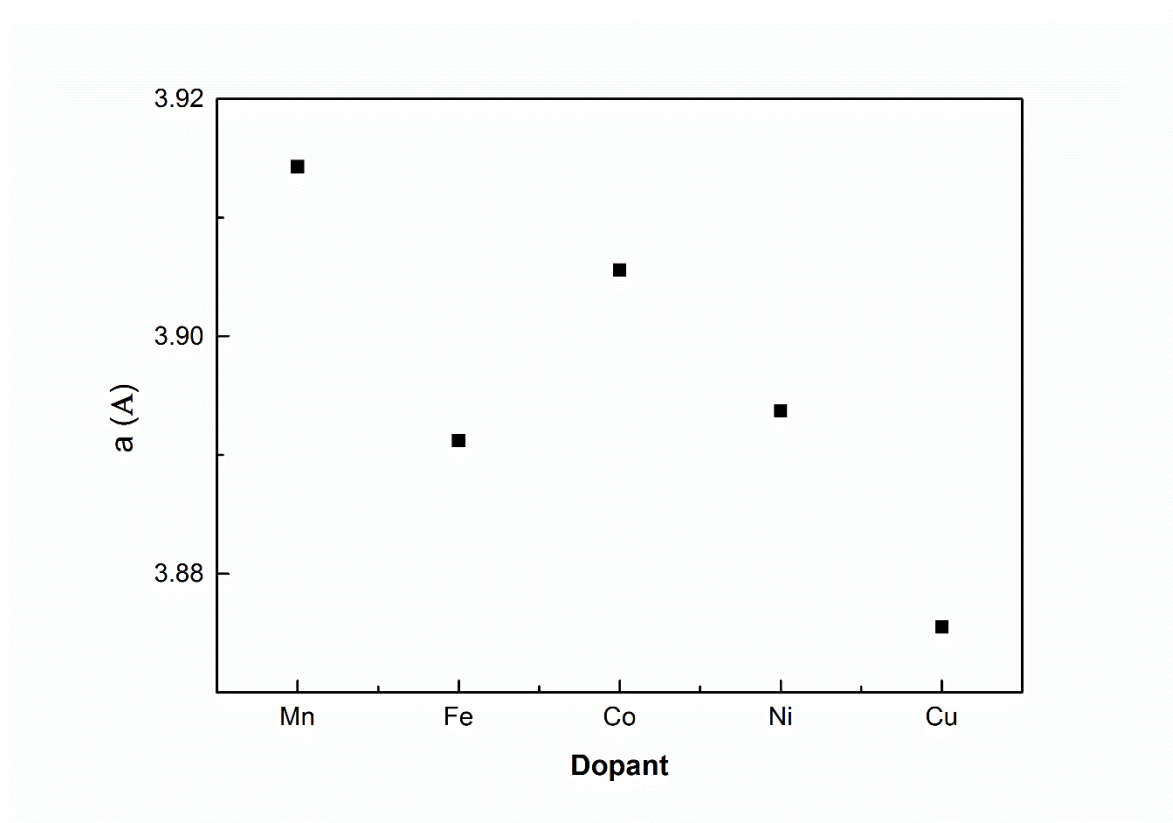
Figure 5.19. Variation of lattice parameters for $SrFe_{0.8}TM_{0.1}Nb_{0.1}O_{3-\delta}$ (TM = Mn, Fe, Co, Ni, Cu) after reduction at 700 °C in 5% H_2/Ar
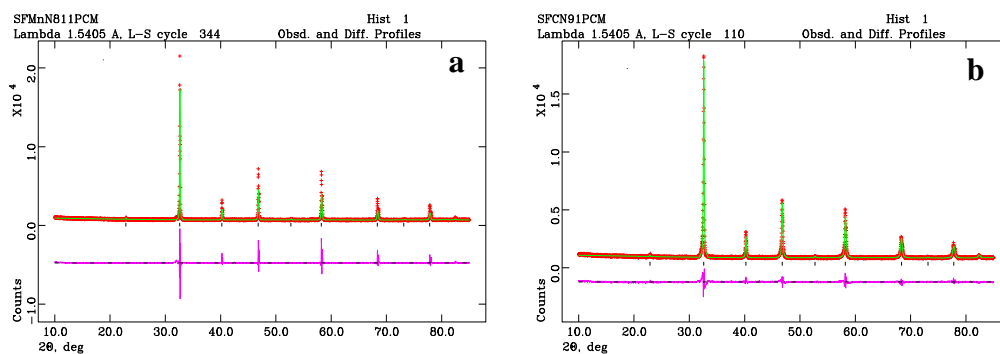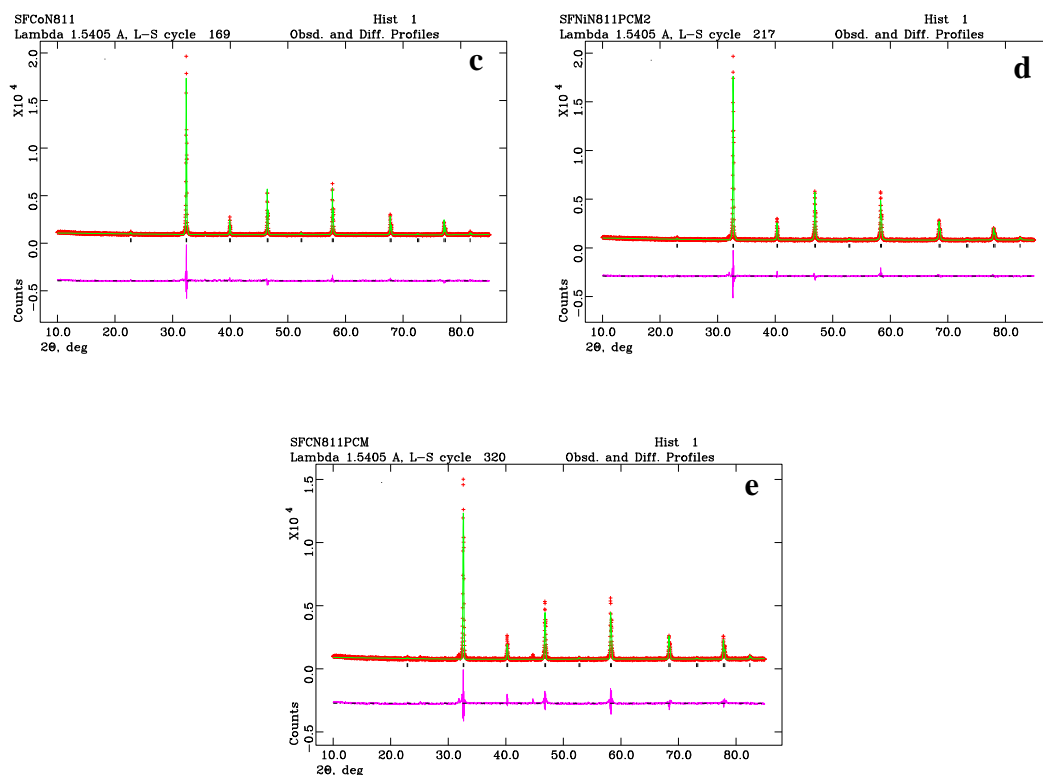
Figure 5.20. GSAS plots for SrFe$_{0.8}$TM$_{0.1}$Nb$_{0.1}$O$_{3-\delta}$ (TM = Mn (a), Fe (b), Co (c), Ni (d), Cu (e)) after reduction at 700 °C in 5% H$_2$/Ar

GSAS [12] analysis, Figure 5.20, demonstrates an increase in the lattice parameters of SrFe$_{0.8}$TM$_{0.1}$Nb$_{0.1}$O$_{3-\delta}$ (TM = Mn, Fe, Ni, Co) upon reduction, Table 5.3 and Table 5.4, attributable to the increase in the cationic radius upon reduction. The lattice parameters of SrFe$_{0.8}$TM$_{0.1}$Nb$_{0.1}$O$_{3-\delta}$ (TM = Mn, Ni, Co) exhibit an increase over the undoped compound, Figure 5.16, intimating partial dopant reduction. Reduction of SrFe$_{0.8}$Cu$_{0.1}$Nb$_{0.1}$O$_{3-\delta}$ exhibits a decrease in the lattice parameter, likely a result of the lattice shrinkage from oxygen loss and possible changes in the cationic coordination environment, overcoming the lattice expansion from cationic reduction.

		SrFe$_{0.8}$Mn$_{0.1}$Nb$_{0.1}$	SrFe$_{0.9}$Nb$_{0.1}$O$_{3-\delta}$	SrFe$_{0.8}$Co$_{0.1}$Nb$_{0.1}$O$_{3-\delta}$	SrFe$_{0.8}$Ni$_{0.1}$Nb$_{0.1}$O$_{3-\delta}$	SrFe$_{0.8}$Cu$_{0.1}$Nb$_{0.1}$O$_{3-\delta}$
χ^2		2.627	3.572	3.006	3.027	4.790
Rp (%)		5.46	6.10	5.46	5.60	7.41
wRp (%)		4.21	4.39	3.90	4.12	5.04
Space		*Pm-3m*	*Pm-3m*	*Pm-3m*	*Pm-3m*	*Pm-3m*
a (Å)		3.9143(12)	3.8912(6)	3.9056(10)	3.8937(24)	3.8755(8)
V (Å^3)		59.97(5)	58.92(3)	59.57(5)	59.04(11)	58.21(4)
Sr	x	0	0	0	0	0
	y	0	0	0	0	0
	z	0	0	0	0	0
	U$_{iso}$	0.025(1)	0.011(1)	0.014(1)	0.050(2)	0.001(1)
Fe/TM/Nb	x	0.5	0.5	0.5	0.5	0.5
	y	0.5	0.5	0.5	0.5	0.5
	z	0.5	0.5	0.5	0.5	0.5
	U$_{iso}$	0.026(1)	0.013(1)	0.022(2)	0.006(2)	0.006(1)
O	x	0	0	0	0	0
	y	0.5	0.5	0.5	0.5	0.5
	z	0.5	0.5	0.5	0.5	0.5
	U$_{iso}$	0.075(2)	0.021(1)	0.069(4)	0.051(2)	0.026(2)

Table 5.4. Rietveld refinement and lattice parameters from GSAS refinement of SrFe$_{0.8}$TM$_{0.1}$Nb$_{0.1}$O$_{3-\delta}$ (TM = Mn, Fe, Co, Ni, Cu) after reduction at 700 °C in 5% H$_2$/Ar

5.2.4. Conclusion

As for the manganese doped strontium iron titanate, manganese doped $SrFe_{0.9}Nb_{0.1}O_{3-\delta}$ exhibits a significant decrease in the conductivity upon reduction, which reduces the utility of the material. Cobalt doping is known to significantly increase the thermal expansion coefficient of strontium based perovskites [18, 19, 20], and therefore potential problems may occur during fuel cell processing. Both $SrFe_{0.8}Ni_{0.1}Nb_{0.1}O_{3-\delta}$ and $SrFe_{0.8}Cu_{0.1}Nb_{0.1}O_{3-\delta}$ exhibit redox stability and high electronic conductivity in air and 5% H_2/Ar, however the higher electronic conductivity of $SrFe_{0.8}Cu_{0.1}Nb_{0.1}O_{3-\delta}$ increases the suitability for utilisation as an SOFC anode material.

5.3. $SrFe_{0.9-x}Cu_xNb_{0.1}O_{3-\delta}$ (x = 0, 0.1, 0.2, 0.3, 0.4)

5.3.1. Introduction

Transition metal doping of $SrFe_{0.9}Nb_{0.1}O_{3-\delta}$ exhibited a significant improvement in the electronic conductivity with the introduction of copper, forming $SrFe_{0.8}Cu_{0.1}Nb_{0.1}O_{3-\delta}$, Section 5.2. To determine the specific effect of copper doping on the properties of $SrFe_{0.9}Nb_{0.1}O_{3-\delta}$, the series $SrFe_{0.9-x}Cu_xNb_{0.1}O_{3-\delta}$ (x = 0, 0.1, 0.2, 0.3, 0.4) was synthesised.

5.3.2. Experimental Information

5.3.2.1. Synthesis

$SrFe_{0.9-x}Cu_xNb_{0.1}O_{3-\delta}$ (x = 0.1 − 0.4) were produced by sol-gel synthesis technique. A stoichiometric amount of $C_4H_4NNbO_9 \cdot H_2O$ (99.9%, Sigma Aldrich) was dissolved in distilled water. H_2O_2 was added to the niobium solution until a colour change was produced. Citric acid (99+%, Alfa Aesar), in a 2:1 ratio to the metal ions in the final product, was added and heated till a solution was formed. Stoichiometric amounts of $Sr(NO_3)_2$ (98%, Alfa Aesar), $Fe(NO_3)_3 \cdot 9 \ H_2O$ (98%, Alfa Aesar) and $Cu(NO_3)_2 \cdot 2.5 \ H_2O$ (ACS grade, Alfa Aesar) were dissolved in distilled water. The solutions were mixed and the solution was heated until gelation. The resultant gel was fired at 600 °C for 2 hours. Subsequent firings at 1200 °C - 1300 °C were performed, as detailed in Table 5.1. Pellets of all the samples (ø ≈ 13 mm × 2 mm and ø ≈ 10 mm × 5 mm) were uniaxially pressed at 221 MPa and sintered as detailed in Table 5.9.

Compound	Firing conditions	Sintering conditions
$SrFe_{0.8}Cu_{0.1}Nb_{0.1}O_{3-\delta}$	1300 °C, 5 hours	1300 °C, 5 hours
$SrFe_{0.7}Cu_{0.2}Nb_{0.1}O_{3-\delta}$	1300 °C, 10 hours	1300 °C, 5 hours
$SrFe_{0.6}Cu_{0.3}Nb_{0.1}O_{3-\delta}$	1300 °C, 10 hours	1300 °C, 5 hours

$SrFe_{0.5}Cu_{0.4}Nb_{0.1}O_{3-\delta}$	1200 °C, 12 hours	1200 C, 12 hours

Table 5.9. Firing and sintering conditions for $SrFe_{0.9-x}Cu_xNb_{0.1}O_{3-\delta}$ (x = 0.1 – 0.4)

5.3.2.2. Analytical Procedures

Phase purity and crystal parameters of the samples were examined by X-ray diffraction (XRD) analysis using a PANalytical X'Pert PRO MPD Multipurpose diffractometer (Cu $K_{\alpha 1}$ radiation, λ = 1.5405Å). GSAS [11] software was used to perform a least squares refinement of the lattice parameters of all suitable samples.

The densities of the pellets were determined from the measured mass and volume. Theoretical densities were calculated using experimental lattice parameters and the chemical formula of the sample. The relative densities were calculated from the actual and theoretical density values. The density of the pellets was ~ 75 % for all compounds.

Thermal analysis was conducted on a 10 ± 0.5 mg sample using a Stanton Redcroft STA 1500 Thermal Analyser on heating from room temperature to 800 °C and on cooling from 800 °C to room temperature in air, with a heating/cooling rate of 10 °C/min, and in 5% H_2/Ar, again with a heating/cooling rate of 10 °Cmin^{-1}, and with a flow rate of 5% H_2/Ar of 50 mLmin^{-1}.

5.3.2.3. Conductivity Testing

Pellets for all samples were coated on opposing sides using silver paste. The conductivity of the samples was measured in primarily in air between 300 °C to 700 °C. Secondary measurements over the same temperature range were conducted in 5% H_2/Ar following an equilibration step of 10 hours at 700 °C in 5% H_2/Ar. Measurements were conducted using either an A.C. method utilising a Solartron 1455A frequency response analyser coupled to a Solartron 1470E

potentiostat/galvanostat controlled by CoreWare software over the frequency range 1 MHz to 100 mHz or a DC method using a Solartron 1470E potentiostat/galvanostat controlled by CoreWare software with an applied current of 1 - 0.1 A.

5.3.2.4. Fuel Cell Testing

$Gd_{0.2}Ce_{0.8}O_{2-\delta}$ was prepared by a co-precipitation technique. Gd_2O_3 (99.9 %, Alfa Aesar) was dissolved in dilute nitric acid. $Ce(NO_3)_3 \cdot 6 H_2O$ (99%, Sigma Aldrich) was added to the Gd solution and diluted further. A 0.1M solution of $(NH_4)_2CO_3$ (NH_3 ca 30%, Alfa Aesar) was produced and the Gd-Ce solution was added dropwise to the solution. The resultant suspension was aged prior to filtration. The precipitate was dried, ground and fired at 600 °C for 2 hours. Pellets (ø ≈ 22 mm × 0.5 mm) were prepared and fired at 1500 °C for 5 hours.

A symmetrical fuel cell utilising a dense thick electrolyte, ~ 300 μm, and a porous electrode was tested between 600 °C and 800 °C, with flowing humidified H_2 and flowing humidified air at the anode and cathode respectively. A paste containing $SrFe_{0.8}Cu_{0.1}Nb_{0.1}O_{3-\delta}$ and α-Terpineol (96%, Alfa Aesar) was printed separately on each side of the previously prepared dense pellets and fired at 1200 °C for 2 hours. The impedance of the cell was measured at each temperature using a Solartron 1455A frequency response analyser coupled to a Solartron 1470E potentiostat/galvanostat controlled by CoreWare software over the frequency range 1 MHz to 100 mHz. Voltage-current curves were produced using Solartron 1470E potentiostat/galvanostat controlled by CoreWare software, with a ramp from OCV to 0 V and step time of 0.1s.

5.3.3. *Results and Discussion*
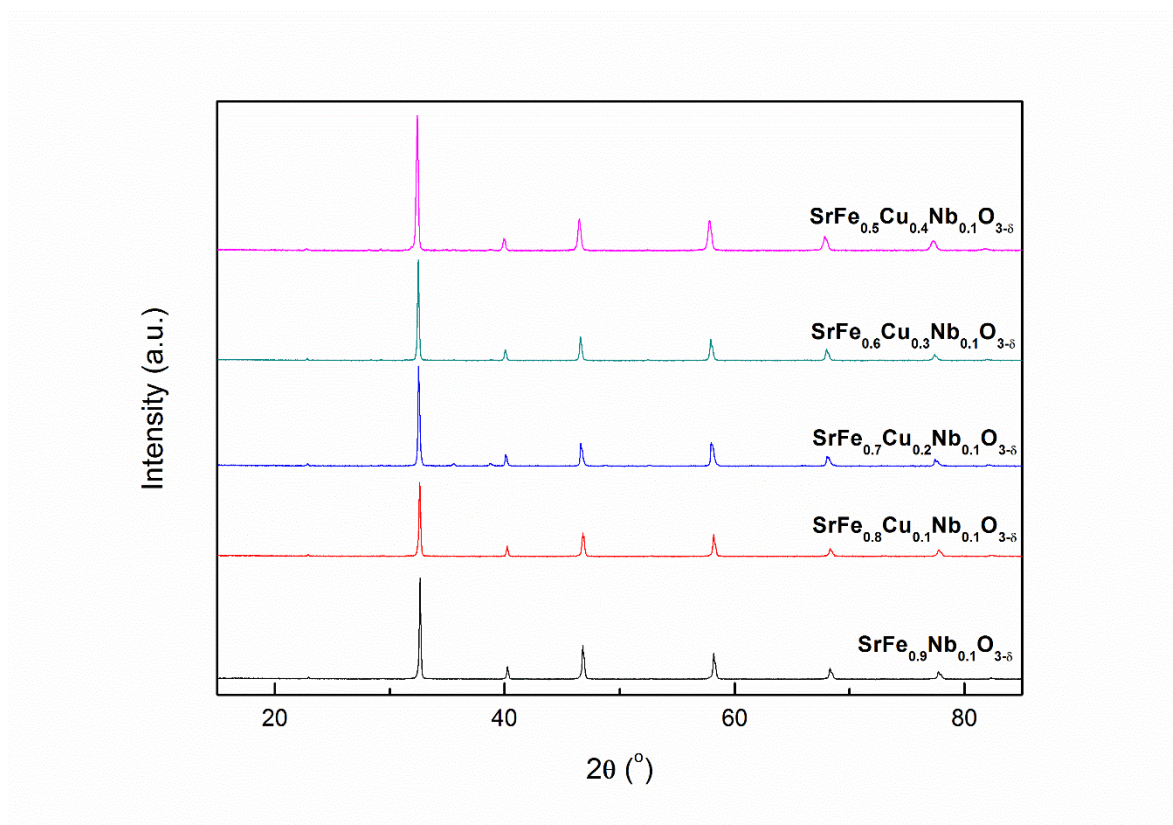
Figure 5.21. X-ray diffraction patterns of SrFe$_{1-x}$Cu$_x$Nb$_{0.1}$O$_{3-\delta}$ (x = 0 - 0.4)

X-ray diffraction of SrFe$_{0.9-x}$Cu$_x$Nb$_{0.1}$O$_{3-\delta}$ (x = 0, 0.1, 0.2, 0.3, 0.4) exhibited a single phase cubic perovskite structure (SG: *Pm-3m*) for all compounds, Figure 5.21. The increase in the copper content significantly reduced the sintering temperature of the material, although further doping did not result in the formation of single phase perovskite material for SrFe$_{0.4}$Cu$_{0.5}$Nb$_{0.1}$O$_{3-\delta}$.
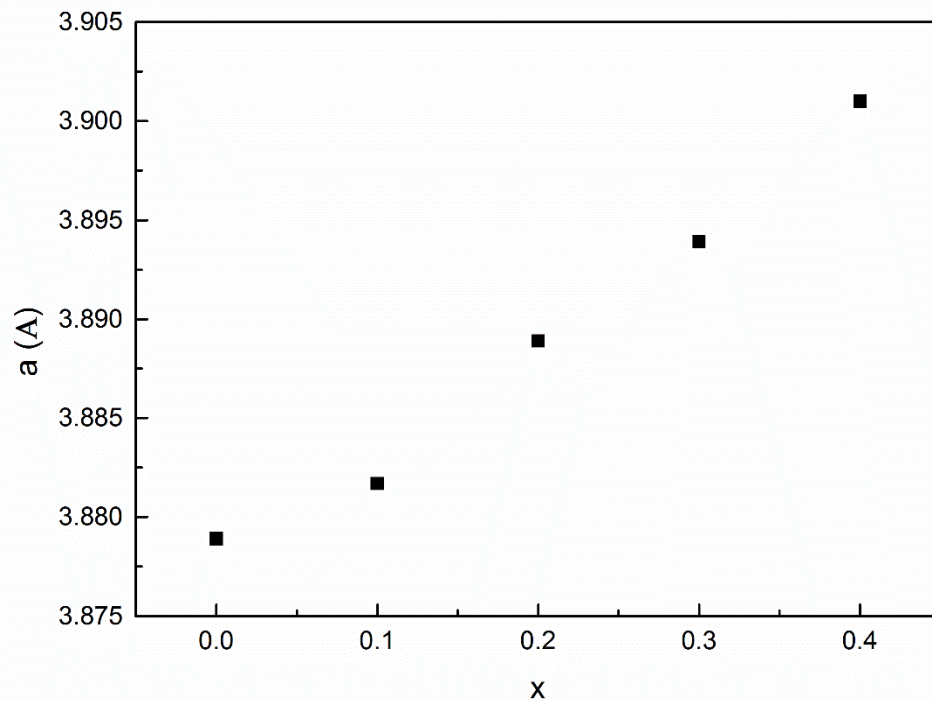
Figure 5.22. Variation of lattice parameters for SrFe$_{1-x}$Cu$_x$Nb$_{0.1}$O$_{3-\delta}$ (x = 0-0.4)
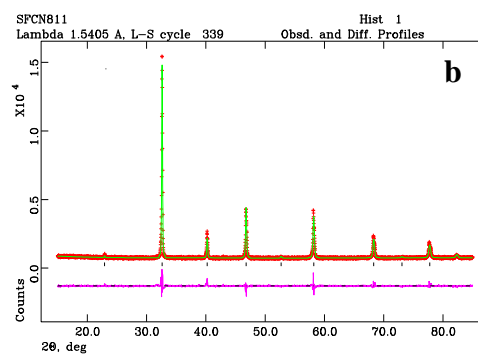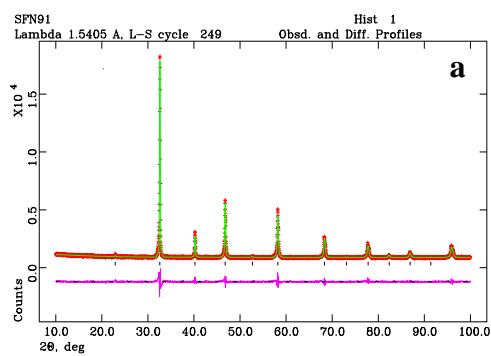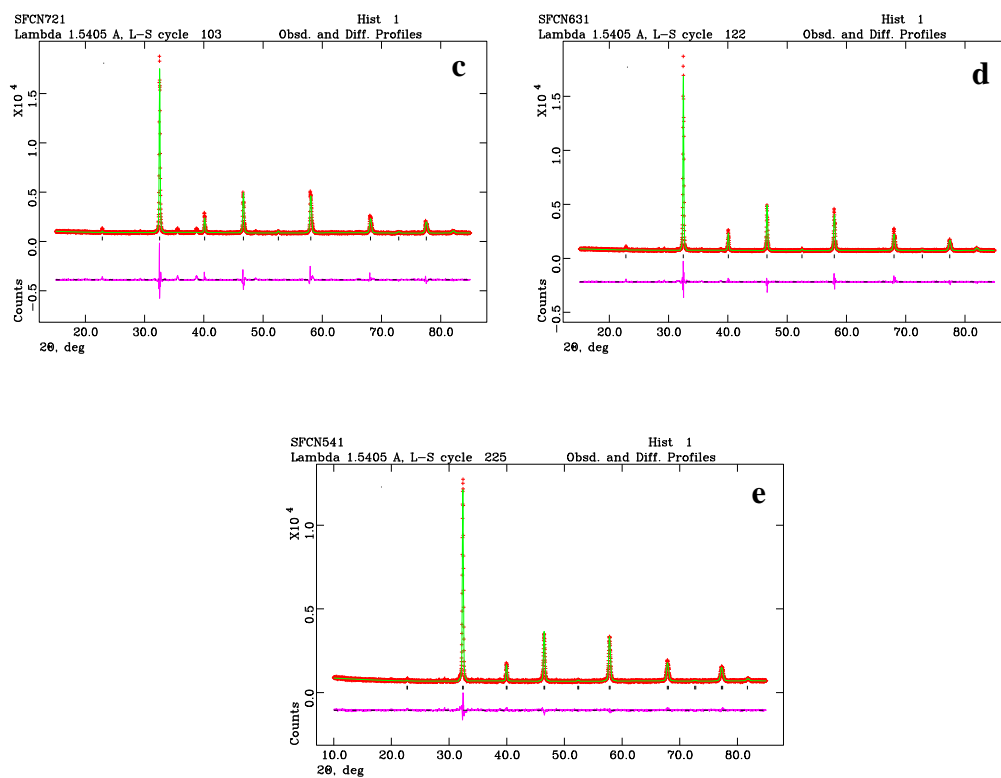
Figure 5.23. GSAS plots for SrFe$_{1-x}$Cu$_x$Nb$_{0.1}$O$_{3-\delta}$, x = 0 (a), x = 0.1 (b), x = 0.2 (c), x = 0.3 (d), x = 0.4 (e).

Rietveld refinement of the structure using GSAS [11] demonstrated a pseudo-linear increase in the lattice parameters with increased doping up to SrFe$_{0.6}$Cu$_{0.3}$Nb$_{0.1}$O$_{3-\delta}$, Figure 5.22, Figure 5.23 and Table 5.5. The increase in lattice parameter with increasing copper content can be attributed to be the larger ionic radius of copper compared to iron (Cu^{2+} 0.73 Å, Fe^{3+} 0.645 Å, Fe^{4+} 0.585 Å) [12], with the increase in the lattice parameter limited by the expected reduction through Fe^{3+}-Fe^{4+} charge compensation and reduction in oxygen content.

		SrFe$_{0.9}$Nb$_{0.1}$O$_{3-\delta}$	SrFe$_{0.8}$Cu$_{0.1}$Nb$_{0.1}$O$_{3-\delta}$	SrFe$_{0.7}$Cu$_{0.2}$Nb$_{0.1}$O$_{3-\delta}$	SrFe$_{0.6}$Cu$_{0.3}$Nb$_{0.1}$O$_{3-\delta}$	SrFe$_{0.5}$Cu$_{0.4}$Nb$_{0.1}$O$_{3-\delta}$
χ^2		2.775	2.607	5.116	2.541	1.701
Rp (%)		5.21	5.553	7.09	5.44	4.63
wRp (%)		3.76	4.00	4.82	4.05	3.65
Space		*Pm-3m*	*Pm-3m*	*Pm-3m*	*Pm-3m*	*Pm-3m*
a (Å)		3.8789(3)	3.8817(1)	3.8889(9)	3.8939(1)	3.9019(1)
V (Å^3)		58.36(1)	58.49(1)	58.81(4)	59.04(1)	59.41(1)
Sr	x	0	0	0	0	0
	y	0	0	0	0	0
	z	0	0	0	0	0
	U$_{iso}$	0.006(1)	0.001(1)	0.001(1)	0.005(1)	0.001(1)
Fe/Cu/Nb	x	0.5	0.5	0.5	0.5	0.5
	y	0.5	0.5	0.5	0.5	0.5
	z	0.5	0.5	0.5	0.5	0.5
	U$_{iso}$	0.008(1)	0.015(1)	0.017(1)	0.019(1)	0.008(1)
O	x	0	0	0	0	0
	y	0.5	0.5	0.5	0.5	0.5
	z	0.5	0.5	0.5	0.5	0.5
	U$_{iso}$	0.011(1)	0.022(1)	0.055(2)	0.020(1)	0.032(1)

Table 5.5. 'Goodness of fit' parameters, lattice parameters and atomic parameters from GSAS refinement of SrFe$_{1-x}$Cu$_x$Nb$_{0.1}$O$_{3-\delta}$ (x = 0 - 0.5) after synthesis in air
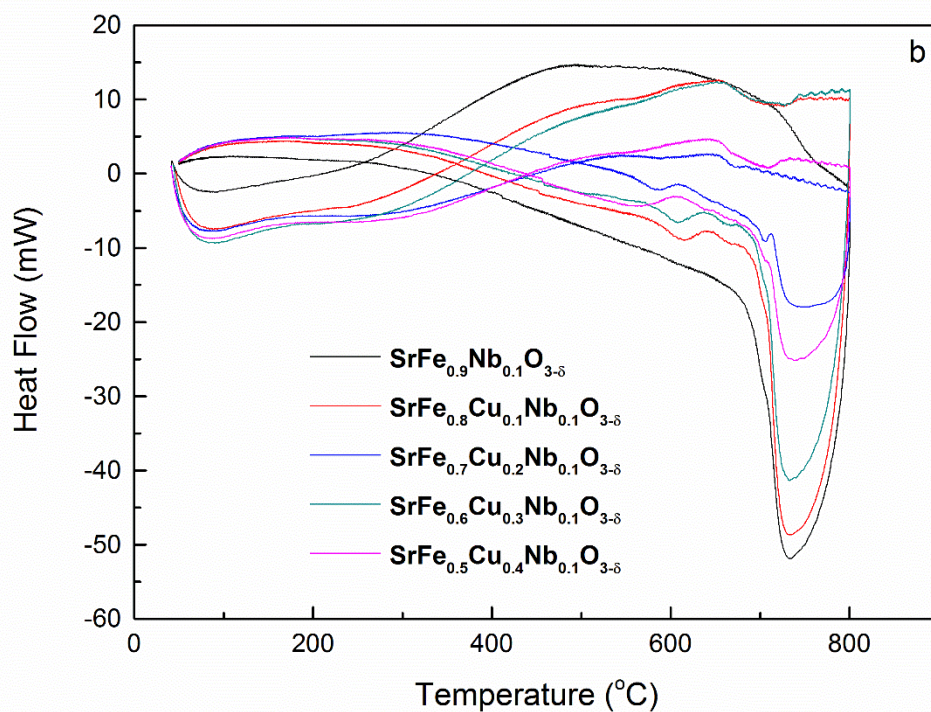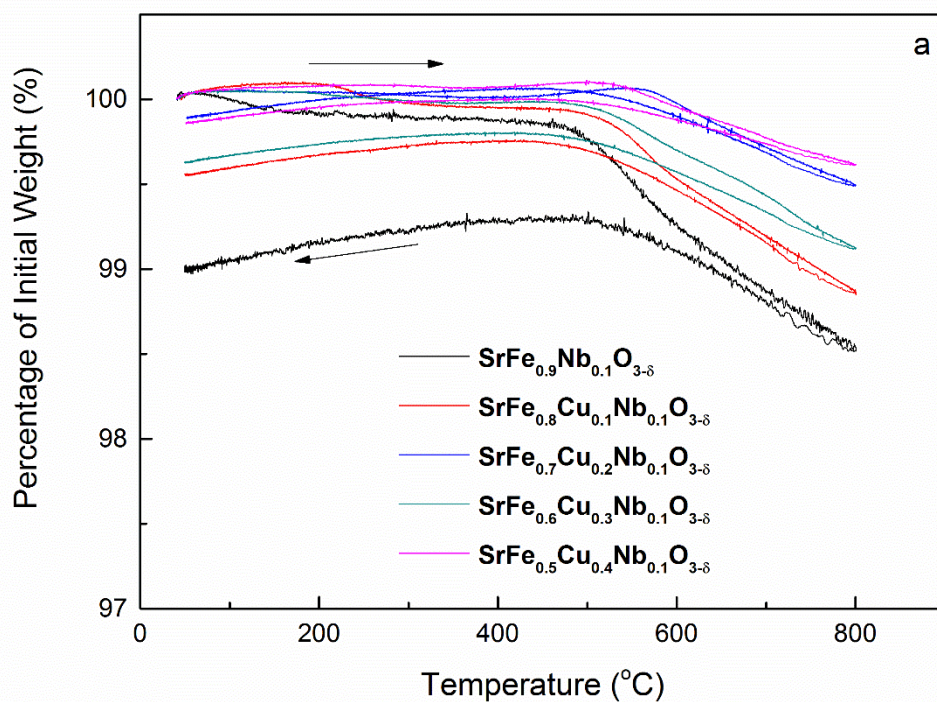
Figure 5.24. Thermogravimetric analysis (a) and differential scanning calorimetry (b) of SrFe$_{1-x}$Cu$_x$Nb$_{0.1}$O$_{3-\delta}$ (x = 0-0.4) in air

Thermogravimetric analysis of $SrFe_{0.9-x}Cu_xNb_{0.1}O_{3-\delta}$ (x = 0 - 0.4) in air exhibited a minor total loss in weight for all compounds, between 0.2 % and 1 %, with no observable trend on increasing dopant level, Figure 5.24 (a). Accelerated weight loss was observed for all compounds on heating between 500 °C and 800 °C, with the weight loss noted to be reversible upon cooling. This acceleration in weight loss is likely to be the result of oxygen loss through high temperature reduction. Differential scanning calorimetry, Figure 5.24 (b), exhibits a reversible transition for all copper doped compounds, between 600 °C and 670 °C on heating and between 670 °C and 590 °C on cooling. The DSC transition is likely a result of partial cationic reduction at high temperatures.
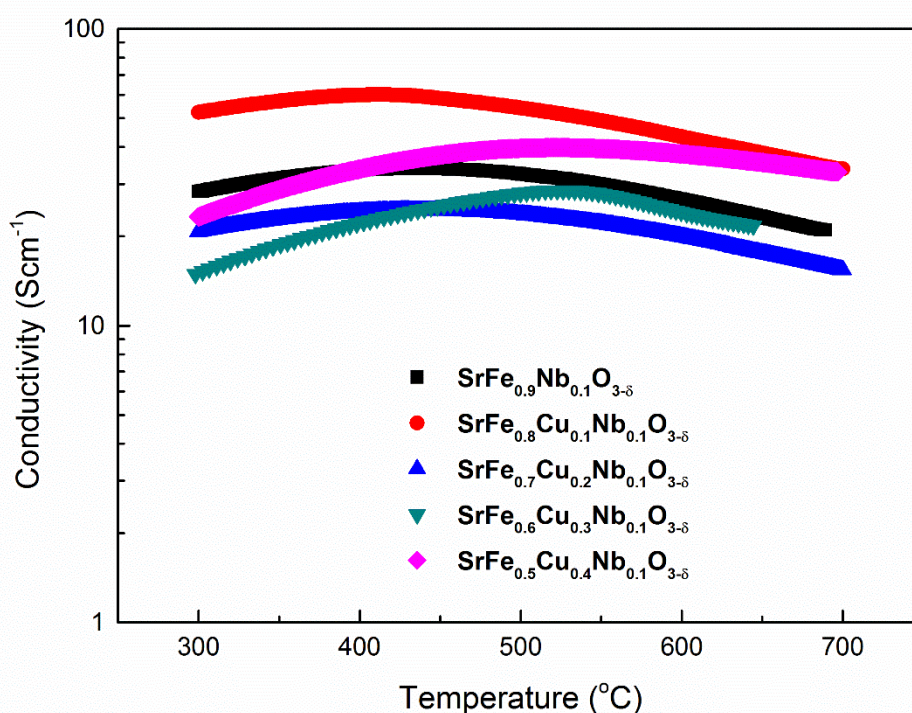
Figure 5.25. Conductivity of $SrFe_{1-x}Cu_xNb_{0.1}O_{3-\delta}$ (x = 0-0.4) in air

Whilst minimal copper doping, forming $SrFe_{0.8}Cu_{0.1}Nb_{0.1}O_{3-\delta}$, elicits a significant increase in conductivity in air over $SrFe_{0.9}Nb_{0.1}O_{3-\delta}$, additional copper doping is observed to reduce the conductivity of the materials, although increasing dopant levels do not elicit a linear response, Figure 5.25. As was stated previously, the

introduction of B^{2+} dopant is expected to increase the average charge of iron in the sample, increasing the number of charge carriers and thus, in theory, increasing the conductivity. Assuming that the copper dopant does not directly contribute to electronic conduction, the increase in the charge carrier concentration is only proportional to the iron content of the compound, which reduces with increasing dopant concentration. Thus at higher dopant concentrations the increase in charge carriers through increase of the average charge of iron is outweighed by the reduction in charge carriers through reduction of the iron content through dopant introduction.

The activation energy for conduction was noted to increase with increasing copper content, from 0.10(1) eV for $SrFe_{0.8}Cu_{0.1}Nb_{0.1}O_3$ to 0.17(1) eV for $SrFe_{0.5}Cu_{0.4}Nb_{0.1}O_3$. The increase in the activation energy for conductivity can be attributed to the reduction in the percolation pathway, due to reduction of the oxygen content.

A semiconductor-metal transition was observed for all compounds, with an increase in the transition temperature noted with increasing dopant levels. This transition has been observed previously for strontium ferrites, with Poulsen *et.* al [15] suggesting that compound reduction at high temperature, resulting in a reduction in the charge carriers, was the cause of the transition. A pseudo-linear reduction in the oxygen content of strontium ferrite in air above 400 °C with increasing temperature, which would appear to confirm compound reduction at these temperatures, was observed previously [16]. The increase in the conductivity with increasing temperature, associated with E_a, was determined by Patrakeev *et. al.* [17] to be offset by the reduction in charge carrier concentration, causing an overall reduction in the electronic conductivity with increasing temperature, resulting in the pseudo-metallic behaviour.
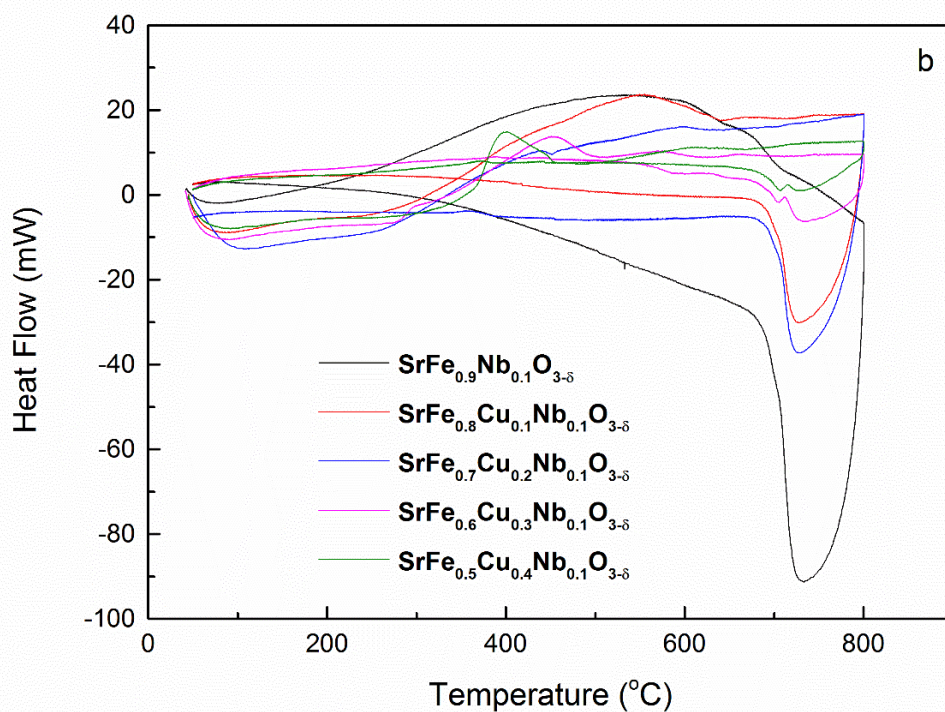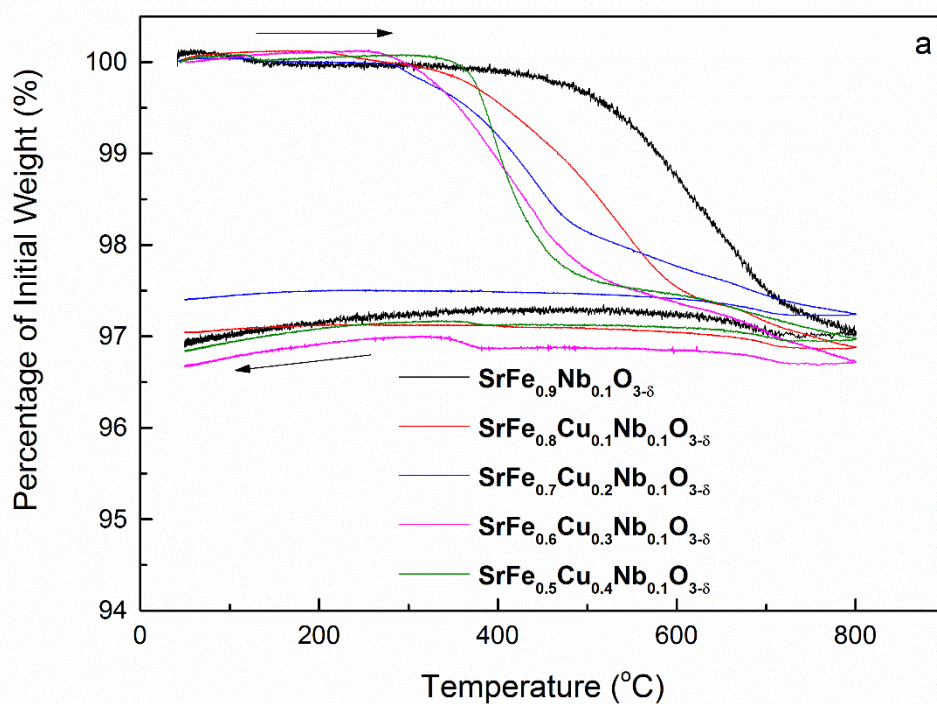
Figure 5.26. Thermogravimetric analysis (a) and differential scanning calorimetry (b) of SrFe$_{1-x}$Cu$_x$Nb$_{0.1}$O$_{3-\delta}$ (x = 0-0.4) in 5% H$_2$/Ar

The observed weight loss upon reduction of $SrFe_{0.9-x}Cu_xNb_{0.1}O_{3-\delta}$ (x = 0 - 0.4) varies between 2.6 % and 3.3 %, Figure 5.26 (a), with no observed trend with increasing dopant concentration. Differential scanning calorimetry, Figure 5.26 (b), exhibits non-reversible transitions on heating for all compounds between 600 °C and 670 °C, associated with cationic reduction. Both $SrFe_{0.6}Cu_{0.3}Nb_{0.1}O_{3-\delta}$ and $SrFe_{0.5}Cu_{0.4}Nb_{0.1}O_{3-\delta}$ exhibit a significant non-reversible transition on heating between 400 °C and 500 °C, attributed to a structural transition.
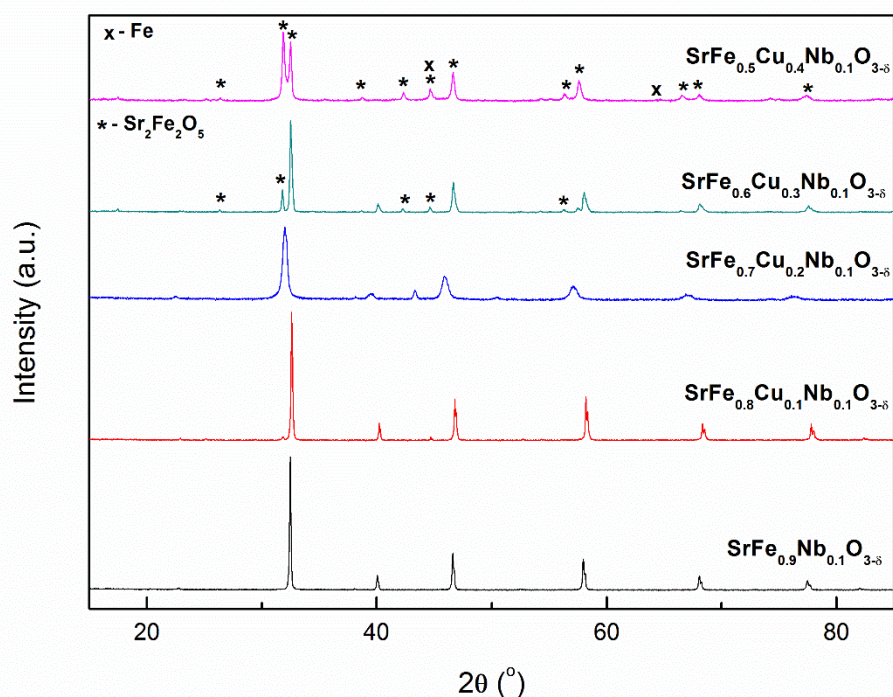
Figure 5.27. X-ray diffraction patterns of $SrFe_{1-x}Cu_xNb_{0.1}O_{3-\delta}$ (x = 0-0.4) after reduction at 700 °C in 5% H_2/Ar

Retention of the single phase perovskite structure was observed for lower levels of copper doping however increasing copper content from $SrFe_{0.7}Cu_{0.2}Nb_{0.1}O_{3-\delta}$ results in a subsequent increase in the phase fraction of an $I4/mmm$ $Sr_3Fe_2O_{6+\delta}$ phase [21], Figure 5.27, Figure 5.28 and Table 5.6. Complete compound degradation upon reduction was observed for $SrFe_{0.5}Cu_{0.4}Nb_{0.1}O_{3-\delta}$, which exhibits a pure iron or copper phase in addition to the $I4/mmm$ phase. The formation of the $Sr_3Fe_2O_{6+\delta}$ Ruddlesden-

Popper phase is likely due to cationic reduction resulting in exsolution of a pure metal phase, either Fe or Cu. Reduction of pure strontium ferrite forms the various oxygen vacancy ordered phases $Sr_nFe_nO_{3n-1}$ (n = 2, 4, 8) [22, 23], however introduction of the niobium and copper dopants leads to compound degradation rather than the phase transition. As $SrFe_{0.7}Cu_{0.2}Nb_{0.1}O_{3-\delta}$ retains the cubic perovskite structure upon reduction, the redox stability limit must lie between x = 0.3 and x = 0.4. Comparison of the lattice parameters of the oxidised and reduced samples, Table 5.5 and 5.6, demonstrates that partial cationic reduction occurs for both $SrFe_{0.9}Nb_{0.1}O_{3-\delta}$ and $SrFe_{0.7}Cu_{0.2}Nb_{0.1}O_{3-\delta}$, however the lattice parameter of $SrFe_{0.8}Cu_{0.1}Nb_{0.1}O_{3-\delta}$ decreases upon reduction. This was previously attributed to lattice shrinkage from oxygen loss and possible changes in the cationic coordination environment, overcoming the lattice expansion from cationic reduction.

		$SrFe_{0.9}Nb_{0.1}O_{3-\delta}$	$SrFe_{0.8}Cu_{0.1}Nb_{0.1}O_{3-\delta}$	$SrFe_{0.7}Cu_{0.2}Nb_{0.1}O_{3-\delta}$	$SrFe_{0.6}Cu_{0.3}Nb_{0.1}O_{3-\delta}$	$SrFe_{0.5}Cu_{0.4}Nb_{0.1}O_{3-\delta}$	
χ^2		3.572	4.790	4.002	4.710	3.388	
Rp (%)		6.10	7.41	6.14	6.97	6.52	
wRp (%)		4.39	5.04	4.40	4.87	5.02	
Primary Phase Fraction		*100%*	*100%*	*100%*	*74%*	*94%*	
Space Group		*Pm-3m*	*Pm-3m*	*Pm-3m*	*Pm-3m*	*I4/mmm*	
a (Å)		3.8912(6)	3.8755(8)	3.9279(43)	3.876(1)	3.894(1)	
c (Å)		3.8912(6)	3.8755(8)	3.9279(43)	3.876(1)	20.225(2)	
V (Å³)		58.92(3)	58.21(4)	60.60(19)	58.2(1)	306.7(1)	
Secondary Phase Fraction		-	-	-	*22%*	*6%*	
Space Group		-	-	-	*I4/mmm*	*(Fe) Im-3m*	
a (Å)		-	-	-	3.859(1)	2.869(1)	
c (Å)		-	-	-	20.374(7)	2.869(1)	
V (Å³)		-	-	-	303.5(3)	23.6(1)	
Primary Phase							
Sr	x	0	0	0	0	0	0
	y	0	0	0	0	0	0
	z	0	0	0	0	0.5	0.317(1)
	U_{iso}	0.011(1)	0.001(1)	0.552(11)	0.020(1)	0.046(3)	0.004(1)
Fe/Cu/Nb	x	0.5	0.5	0.5	0.5	0	
	y	0.5	0.5	0.5	0.5	0	
	z	0.5	0.5	0.5	0.5	0.100(1)	
	U_{iso}	0.013(1)	0.006(1)	0.003(2)	0.005(1)	0.011(1)	
O	x	0	0	0	0	0	0
	y	0.5	0.5	0.5	0.5	0.5	0
	z	0.5	0.5	0.5	0.5	0.078(1)	0.202(1)
	U_{iso}	0.021(1)	0.026(2)	0.084(3)	0.002(2)	0.017(1)	0.034(4)

Table 5.6. 'Goodness of fit' parameters, lattice parameters and atomic parameters from GSAS refinement of $SrFe_{1-x}Cu_xNb_{0.1}O_{3-\delta}$ (x = 0 - 0.5) after reduction at 700 °C in 5%H_2/Ar
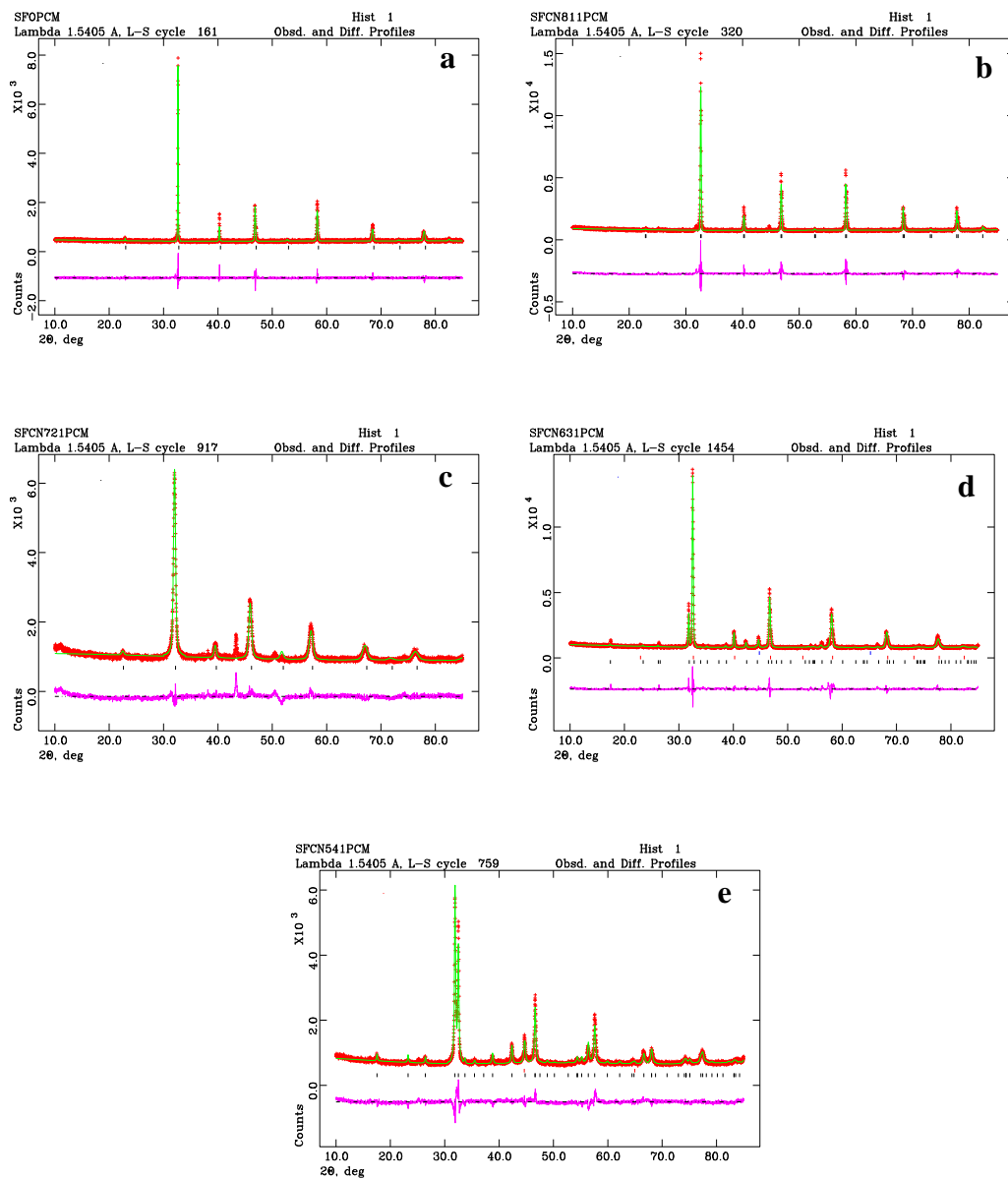
Figure 5.28. GSAS plots for SrFe$_{1-x}$Cu$_x$Nb$_{0.1}$O$_{3-\delta}$, x = 0 (a), x = 0.1 (b), x = 0.2 (c), x = 0.3 (d), x = 0.4 (e) after reduction at 700 °C in 5%H$_2$/Ar
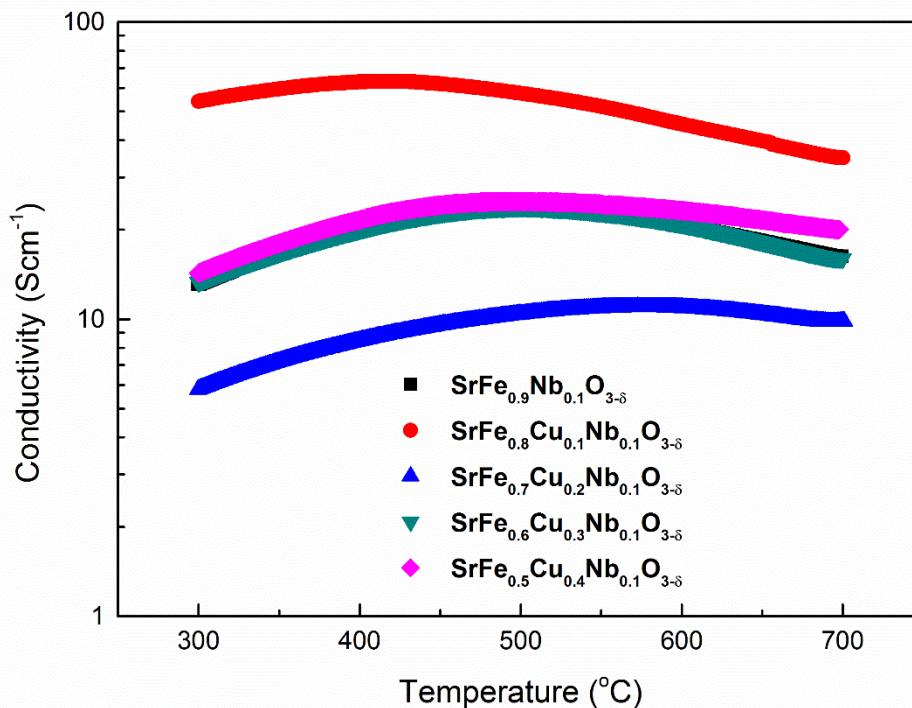
Figure 5.29. Conductivity of SrFe$_{1-x}$Cu$_x$Nb$_{0.1}$O$_{3-\delta}$ (x = 0-0.4) in 5% H$_2$/Ar

Reduction of SrFe$_{0.9-x}$Cu$_x$Nb$_{0.1}$O$_{3-\delta}$ (x = 0, 0.1, 0.3, 0.4) at 700 °C in 5% H$_2$/Ar elicits a minimal reduction in the electronic conductivity, Figure 5.29. For SrFe$_{0.9}$Nb$_{0.1}$O$_{3-\delta}$, SrFe$_{0.8}$Cu$_{0.1}$Nb$_{0.1}$O$_{3-\delta}$ and SrFe$_{0.7}$Cu$_{0.2}$Nb$_{0.1}$O$_{3-\delta}$ the reduction in the conductivity can be attributed to partial reduction of the charge carrier concentration. As both SrFe$_{0.6}$Cu$_{0.3}$Nb$_{0.1}$O$_{3-\delta}$ and SrFe$_{0.5}$Cu$_{0.4}$Nb$_{0.1}$O$_{3-\delta}$ exhibit a significant phase fraction of a Sr$_3$Fe$_2$O$_{6+\delta}$ phase (SG: *I4/mmm*), the minor reduction in the conductivity can be attributed to the lower electronic conductivity of the Sr$_3$Fe$_2$O$_{6+\delta}$ phase [21]. The activation energy for conduction exhibits a minor increase upon reduction for SrFe$_{0.9-x}$Cu$_x$Nb$_{0.1}$O$_{3-\delta}$ (x = 0, 0.1, 0.3, 0.4), 0.01-0.02 eV, confirming partial cationic reduction. The conductivity of SrFe$_{0.7}$Cu$_{0.2}$Nb$_{0.1}$O$_{3-\delta}$ exhibits a more significant decrease upon reduction than other copper doped compounds. This is likely a result of the larger increase in the lattice parameter of SrFe$_{0.7}$Cu$_{0.2}$Nb$_{0.1}$O$_{3-\delta}$ upon reduction, which would reduce the percolation pathway and thus the charge carrier mobility. This correlates with the larger increase in the activation energy upon reduction, 0.07 eV, observed for SrFe$_{0.7}$Cu$_{0.2}$Nb$_{0.1}$O$_{3-\delta}$. A similar semiconductor-metal transition to that observed in air,

Figure 5.25, was noted for all compounds, albeit with a significant increase in the transition temperature exhibited for $SrFe_{0.9-x}Cu_xNb_{0.1}O_{3-\delta}$ (x = 0.2 - 0.4).

5.3.4. Conclusion

Increasing the copper content of $SrFe_{0.9-x}Cu_xNb_{0.1}O_{3-\delta}$ from $SrFe_{0.8}Cu_{0.1}Nb_{0.1}O_{3-\delta}$ both reduced the redox stability and the conductivity. The reduction in desirable material properties with increasing copper content subsequently reduces the suitability of these materials for use as an SOFC electrode material. This does suggest that minimisation of the dopant levels is required to optimise the material properties and promotes the use of $SrFe_{0.8}Cu_{0.1}Nb_{0.1}O_{3-\delta}$ as a symmetrical electrode material.

5.4. Fuel Cell Testing of SrFe$_{0.8}$Cu$_{0.1}$Nb$_{0.1}$O$_{3-\delta}$

Of all the materials under investigation in this study, SrFe$_{0.8}$Cu$_{0.1}$Nb$_{0.1}$O$_{3-\delta}$ exhibited the optimal balance of conductivity and stability for potential use as a symmetrical electrode material for IT-SOFCs. Analysis of potential electrolyte materials for intermediate temperature SOFCs suggested that GDC would also exhibit the requisite properties for efficient operation at these temperatures, Section 1.4.1. Despite no dilatometry data existing for SrFe$_{0.8}$Cu$_{0.1}$Nb$_{0.1}$O$_{3-\delta}$, the thermal expansion coefficient is thought to be close to that of Gd$_{0.2}$Ce$_{0.8}$O$_{2-\delta}$, as synthesis of fuel cells with a pure SrFe$_{0.8}$Cu$_{0.1}$Nb$_{0.1}$O$_{3-\delta}$ anode did not exhibit electrode delamination, cracking or any other signs of significant TEC mismatch.
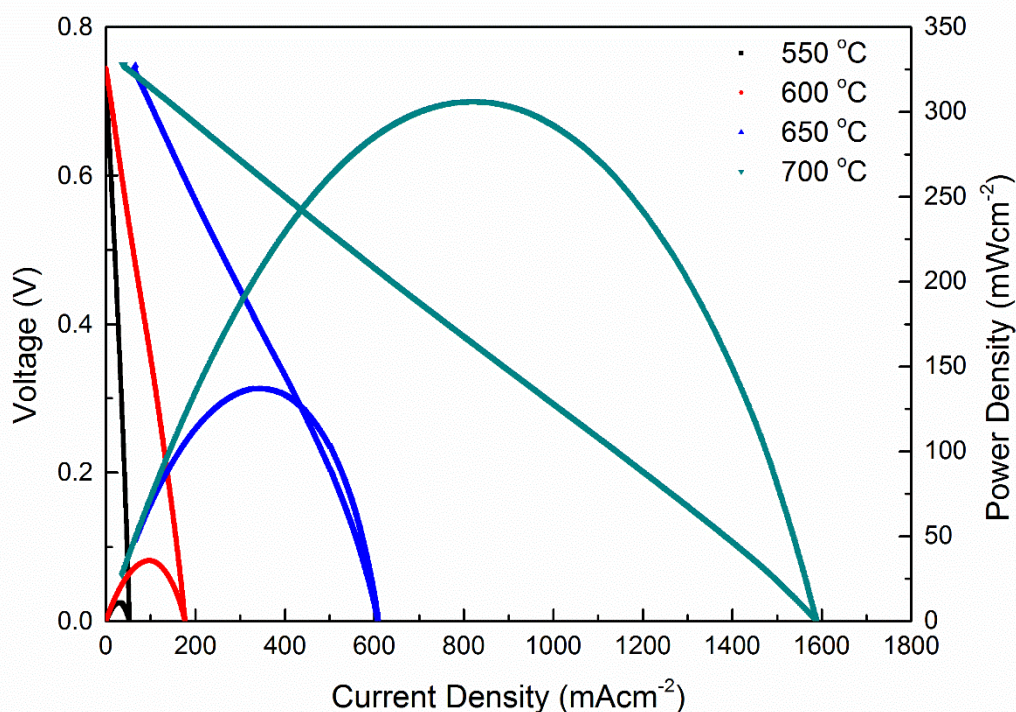
Figure 5.30. Current-voltage curves of a SrFe$_{0.8}$Cu$_{0.1}$Nb$_{0.1}$O$_{3-\delta}$ –Gd$_{0.2}$Ce$_{0.8}$O$_{2-\delta}$-SrFe$_{0.8}$Cu$_{0.1}$Nb$_{0.1}$O$_{3-\delta}$ symmetrical SOFC, with flowing humidified H$_2$ and flowing humidified air at the anode and cathode respectively

Fuel cell testing of a symmetrical $SrFe_{0.8}Cu_{0.1}Nb_{0.1}O_{3-\delta}$–$Gd_{0.2}Ce_{0.8}O_{2-\delta}$-$SrFe_{0.8}Cu_{0.1}Nb_{0.1}O_{3-\delta}$ fuel cell, Figure 5.30, demonstrated a maximum power density of 306 mWcm^{-2} at 700 °C. Significant reduction of the performance was observed with reducing temperature, 136 mWcm^{-2} at 650 °C, 35 mWcm^{-2} at 600 °C and 11 mWcm^{-2} at 550 °C. The operating voltage of the fuel cell was between 0.367 V and 0.397 V over the measured temperature range. As for the (60:40 $SrFe_{0.9}Ti_{0.1}O_{3-\delta}$-$Gd_{0.2}Ce_{0.8}O_{2-\delta}$) - $Gd_{0.2}Ce_{0.8}O_{2-\delta}$ - (60:40 $SrFe_{0.9}Ti_{0.1}O_{3-\delta}$-$Gd_{0.2}Ce_{0.8}O_{2-\delta}$) symmetrical SOFC in Chapter 4.1.3, the low operating voltages are considered to be a result of the low open circuit voltage. The OCV demonstrated values between 0.7 V and 0.815 V, lower than would be desirable for commercial use, with optimal values of 1 - 1.1 V attainable. The low OCV could be attributable to the use of a gadolinium doped ceria electrode, which has demonstrated partial n-type electronic conductivity upon exposure to reducing atmospheres [24,25]. Improvement of the OCV could be achieved through the use of a barium based electron blocking layer, which limits the impact of the induced electronic conductivity [26], or the use of alternative electrolyte materials [27]. Alternatively, reduction of the OCV could be a result of a lack of gas tightness of the electrolyte or the sealant, which could result in gas crossover and a subsequent reduction of the open circuit voltage [28].
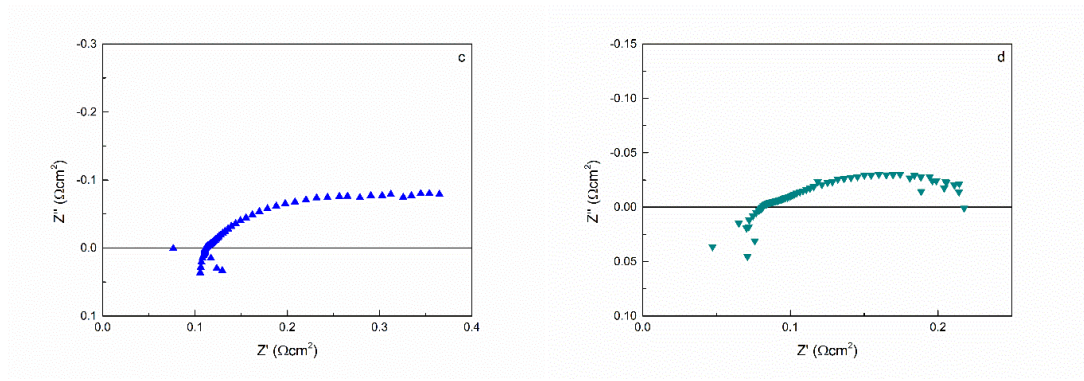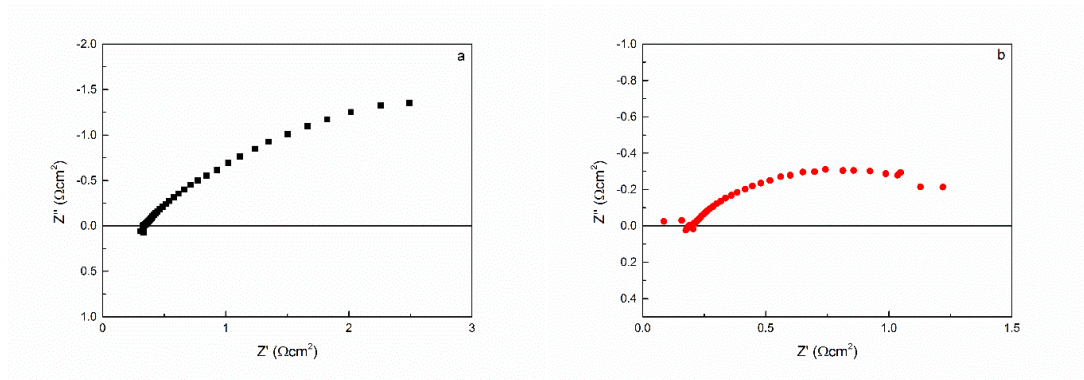
Figure 5.31. Electrochemical impedance spectroscopy of a SrFe$_{0.8}$Cu$_{0.1}$Nb$_{0.1}$O$_{3-\delta}$ –Gd$_{0.2}$Ce$_{0.8}$O$_{2-\delta}$- SrFe$_{0.8}$Cu$_{0.1}$Nb$_{0.1}$O$_{3-\delta}$ symmetrical SOFC over the frequency range 1 MHz to 100 mHz at 550°C (a), 600°C (b), 650°C (c) and 700°C (d), with flowing humidified H$_2$ and flowing humidified air at the anode and cathode respectively

A significant reduction in the series resistance (from 0.321 Ωcm^2 to 0.081 Ωcm^2), total resistance (from 4 Ωcm^2 to 0.25 Ωcm^2) and polarisation resistance (from 3.679 Ωcm^2 to 0.169 Ωcm^2) was observed upon heating, Figure 5.31a and Figure 5.31b. The reduction in the resistances is likely a result of improving electrode and electrolyte conductivity and reaction kinetics. Whilst the series and total resistances of SrFe$_{0.8}$Cu$_{0.1}$Nb$_{0.1}$O$_{3-\delta}$–Gd$_{0.2}$Ce$_{0.8}$O$_{2-\delta}$-SrFe$_{0.8}$Cu$_{0.1}$Nb$_{0.1}$O$_{3-\delta}$ fuel cells are lower than are observed for (60:40 SrFe$_{0.9}$Ti$_{0.1}$O$_{3-\delta}$-Gd$_{0.2}$Ce$_{0.8}$O$_{2-\delta}$) - Gd$_{0.2}$Ce$_{0.8}$O$_{2-\delta}$ - (60:40 SrFe$_{0.9}$Ti$_{0.1}$O$_{3-\delta}$-Gd$_{0.2}$Ce$_{0.8}$O$_{2-\delta}$) fuel cells at the same temperature, the polarisation resistance exhibits the opposite trend. This is indicative of a reduction in the ohmic

resistance of the cell, albeit with an increase in the polarisation resistance, which is likely a result of poor electrodic reaction kinetics.

Values of the ASR from the fuel cell impedance and from the voltage-current curves do not tally, with values of 0.25 Ωcm^{-1} and 0.13 Ωcm^{-1} at 700 °C and values of 4 Ωcm^{-1} and 3.39 Ωcm^{-1} at 550 °C, calculated from impedance and voltage-current curves respectively. As was found for the (60:40 $SrFe_{0.9}Ti_{0.1}O_{3-\delta}$-$Gd_{0.2}Ce_{0.8}O_{2-\delta}$)-$Gd_{0.2}Ce_{0.8}O_{2-\delta}$-(60:40 $SrFe_{0.9}Ti_{0.1}O_{3-\delta}$-$Gd_{0.2}Ce_{0.8}O_{2-\delta}$) symmetrical SOFC in Chapter 4.1.3, the observed impedance response of a GDC electrolyte can demonstrate a reduction in the various observed AC resistances, due to a partial short circuit of the ionic current as a result of the additional conduction contribution from the electronic carriers [29]. The lack of accuracy of the data from the A.C. impedance plots should be borne in mind when drawing conclusions from the experimental results.

Fuel cell performance of symmetrical fuel cells previously attained 521 $mWcm^{-2}$ for a $La_{0.7}Ca_{0.3}CrO_3$ electrode and 650 $mWcm^{-2}$ for a LSCM electrode, albeit at 850 °C [30, 31]. Thus the fuel cell performance of the $SrFe_{0.8}Cu_{0.1}Nb_{0.1}O_{3-\delta}$–$Gd_{0.2}Ce_{0.8}O_{2-\delta}$-$SrFe_{0.8}Cu_{0.1}Nb_{0.1}O_{3-\delta}$ cell is comparable or an improvement on previous symmetrical electrode materials. Further improvements to the fuel cell performance would be expected to be attained through optimisation of the electrodic microstructure [31, 32] and infiltration of anodic and cathodic catalysts [33, 34]. The performance of the non-optimised symmetrical cell demonstrates promise for further development of $SrFe_{0.8}Cu_{0.1}Nb_{0.1}O_{3-\delta}$ symmetrical fuel cells.

5.5. Conclusion

A solid solution with the cubic perovskite structure was formed for $SrFe_{1-x}Nb_xO_{3-\delta}$ (x = 0, 0.1, 0.2, 0.3, 0.4). The electronic conductivity in both air and 5% H_2/Ar reduced with increasing dopant concentration, with a minimal reduction in the electronic conductivity upon reduction. Redox stability was observed for all doped compounds after reduction at 700 °C in 5% H_2/Ar. Previous research by Anikina *et. al.* [3] had demonstrated promising material properties for this series, which was confirmed in this work.

Doping of B^{2+} was posited to increase the material properties of $SrFe_{0.9}Nb_{0.1}O_{3-\delta}$ for utilisation as a symmetrical IT-SOFC electrode. This was confirmed for both copper and cobalt doping which was observed to improve the electronic conductivity in both air and 5% H_2/Ar, whilst maintaining the inherent redox stability of the parent compound. Both manganese and nickel doping exhibited redox stability, albeit with significantly lower conductivities. Due to the known influence of cobalt doping on the thermal expansion coefficient of perovskite materials, it is suggested that $SrFe_{0.8}Cu_{0.1}Nb_{0.1}O_{3-\delta}$ may prove to be more compatible with current SOFC materials.

A solid solution with the cubic perovskite structure was formed for $SrFe_{0.9-x}Cu_xNb_{0.1}O_{3-\delta}$ (x = 0 - 0.4). An increase in the lattice parameter was observed with increasing dopant concentration up to x = 0.2, with the lack of variation between $SrFe_{0.6}Cu_{0.3}Nb_{0.1}O_{3-\delta}$ and $SrFe_{0.5}Cu_{0.4}Nb_{0.1}O_{3-\delta}$ attributed to microdomain formation. Maximal electronic conductivity was observed for in both air, 63 Scm^{-1} at 415 °C, and 5% H_2/Ar, 60 Scm^{-1} at 415 °C. Redox stability was observed for $SrFe_{0.9-x}Cu_xNb_{0.1}O_{3-\delta}$ (x = 0 - 0.2), with a secondary *I4/mmm* phase observed for both $SrFe_{0.6}Cu_{0.3}Nb_{0.1}O_{3-\delta}$ and $SrFe_{0.5}Cu_{0.4}Nb_{0.1}O_{3-\delta}$.

Fuel cell performance of a symmetrical $SrFe_{0.8}Cu_{0.1}Nb_{0.1}O_{3-\delta}$–$Gd_{0.2}Ce_{0.8}O_{2-\delta}$-$SrFe_{0.8}Cu_{0.1}Nb_{0.1}O_{3-\delta}$ fuel cell reached 306 mWcm^{-2} at 700 °C, comparable to prior symmetrical fuel cell performance. The fuel cell performance demonstrates that these symmetrical cells exhibit potential for further utilisation in symmetrical IT-SOFCs.

Further optimisation of the compositional and microstructural properties of the electrode could be utilised for further improvement in the performance.

5.6. References

1. M. V. Patrakeev, A. A. Markov, I. A. Leonidov, V. L. Kozhevnikov and V. V. Kharton, *Solid State Ionics*, 2006, **177**, 1757-1760.

2. G. Xiao, Q. Liu, S. Wang, V. G. Komvokis, M. D. Amiridis, A. Heyden, S. Ma and F. Chen, *Journal of Power Sources*, 2012, **202**, 63-69.

3. P. V. Anikina, A. A. Markov, M. V. Patrakeev, I. A. Leonidov and V. L. Kozhevnikov, *Solid State Sciences*, 2009, **11**, 1156-1162.

4. M. A. Alario-Franco, J.-C. Joubert and J.-P. LÃ©vy, *Materials Research Bulletin*, 1982, **17**, 733-740.

5. N. Nakayama, M. Takano, S. Inamura, N. Nakanishi and K. Kosuge, *Journal of Solid State Chemistry*, 1987, **71**, 403-417.

6. M. J. Akhtar, Z. N. Akhtar, J. P. Dragun and C. R. A. Catlow, *Solid State Ionics*, 1997, **104**, 147-158.

7. K. Tezuka, K. Henmi, Y. Hinatsu and N. M. Masaki, *Journal of Solid State Chemistry*, 2000, **154**, 591-597.

8. Tao, J. Canales-VÃ¡zquez and J. T. S. Irvine, *Chemistry of Materials*, 2004, **16**, 2309-2316.

9. J. Yi, M. Schroeder and M. Martin, *Chemistry of Materials*, 2013, **25**, 815-817.

10. Q. Zhou, L. Zhang and T. He, *Electrochemistry Communications*, 2010, **12**, 285-287.

11. A. C. Larson and R. B. V. Dreele, *"General Structure Analysis System (GSAS)", Los Alamos National Laboratory Report LAUR*, 1994, 86-748.

12. A. C. Larson and R. B. V. Dreele, *"General Structural Analysis System" Los Alamos National Laboratory Report LAUR*, 1994, 86.

13. R. D. Shannon, *Acta Crystallographia Section A*, 1976, **A32**, 751.

14. M. V. Patrakeev, V. V. Kharton, Y. A. Bakhteeva, A. L. Shaula, I. A. Leonidov, V. L. Kozhevnikov, E. N. Naumovich, A. A. Yaremchenko and F. M. B. Marques, *Solid State Sciences*, 2006, **8**, 476-487.

15. F. W. Poulsen, G. Lauvstad and R. Tunold, *Solid State Ionics*, 1994, **72, Part 2**, 47-53.

16. M. Schmidt and S. J. Campbell, *Journal of Physics and Chemistry of Solids*, 2002, **63**, 2085-2092.

17. M. V. Patrakeev, E. B. Mitberg, A. A. Lakhtin, I. A. Leonidov, V. L. Kozhevnikov, V. V. Kharton, M. Avdeev and F. M. B. Marques, *Journal of Solid State Chemistry*, 2002, **167**, 203-213.

18. L. W. Tai, M. M. Nasrallah, H. U. Anderson, D. M. Sparlin and S. R. Sehlin, *Solid State Ionics*, 1995, **76**, 259-271.

19. J. W. Stevenson, T. R. Armstrong, R. D. Carneim, L. R. Pederson and W. J. Weber, *Journal of The Electrochemical Society*, 1996, **143**, 2722-2729.

20. A. Mai, V. A. C. Haanappel, S. Uhlenbruck, F. Tietz and D. Stöver, *Solid State Ionics*, 2005, **176**, 1341-1350.

21. M. V. Patrakeev, I. A. Leonidov, V. L. Kozhevnikov and V. V. Kharton, *Solid State Sciences*, 2004, **6**, 907-913.

22. Y. Takeda, K. Kanno, T. Takada, O. Yamamoto, M. Takano, N. Nakayama and Y. Bando, *Journal of Solid State Chemistry*, 1986, **63**, 237-249.

23. J. P. Hodges, S. Short, J. D. Jorgensen, X. Xiong, B. Dabrowski, S. M. Mini and C. W. Kimball, *Journal of Solid State Chemistry*, 2000, **151**, 190-209.

24. A. Atkinson, *Solid State Ionics*, 1997, **95**, 249-258.

25. B. C. H. Steele, *Solid State Ionics*, 2000, **129**, 95-110.

26. W. Sun and W. Liu, *Journal of Power Sources*, 2012, **217**, 114-119.

27. V. V. Kharton, F. M. B. Marques and A. Atkinson, *Solid State Ionics*, 2004, **174**, 135-149.

28. J. Larminie and A. Dicks, *Fuel Cell Systems Explained*, J. Wiley, 2003.

29. A. Atkinson, S. A. Baron and N. P. Brandon, *Journal of The Electrochemical Society*, 2004, **151**, E186-E193.

30. Q. Liu, X. Dong, G. Xiao, F. Zhao and F. Chen, *Advanced Materials*, 2010, **22**, 5478-5482.

31. A. Sarikaya, V. Petrovsky and F. Dogan, *International Journal of Hydrogen Energy*, 2012, **37**, 11370-11377.

32. L. Nie, J. Liu, Y. Zhang and M. Liu, *Journal of Power Sources*, 2011, **196**, 9975-9979.

33. K. B. Yoo and G. M. Choi, *Solid State Ionics*, 2009, **180**, 867-871.

34.   J. Liu, B. D. Madsen, Z. Ji and S. A. Barnett, *Electrochemical and Solid-State Letters*, 2002, **5**, A122-A124.

6. Utilisation of Cathodic Ferrites as IT-SOFC Symmetrical Electrode Materials

This chapter considers the effect of A-site doping on the redox stability of strontium ferrites, initially based on well characterised cathode materials, $La_xSr_{1-x}FeO_{3-\delta}$. The collected fuel cell data is compared to the previous materials and conclusions drawn as to the suitability of these materials for use as SOFC electrode materials. The redox stability limits of a series of yttrium doped strontium ferrites are elucidated and these materials are considered as SOFC electrode materials.

6.1. $La_xSr_{1-x}FeO_{3-\delta}$ (x = 0.2, 0.4, 0.6, 0.8)

6.1.1. Introduction

Testing of previous SOFC single electrode materials as symmetrical electrodes has previously been applied to LSSM [1, 2], LSCM [3, 4] and LCC [5], as expanded upon in section 1.6.4.1.4. The use of ferrites as symmetrical electrodes, despite the proven performance as cathode materials, has been limited due to the expected instability under anodic conditions. As has been exhibited in the previous chapter, use of doped ferrite materials in anodic conditions at intermediate temperatures will not invariably result in compound degradation or deterioration of desirable material properties.

A-site doping of strontium ferrites has been utilised extensively in the development of SOFC cathode materials, with LSF [6], LSCF [7-9] and BSCF [10] all exhibiting good performance in intermediate temperature SOFCs. Comparison of the three main ferrite cathodes suggests that the utilisation of lanthanum strontium ferrite as a symmetrical electrode may show the greatest promise, as LSCF is known to exhibit compound degradation after long term operation in reducing conditions [11] and BSCF is known to degrade upon exposure to CO_2 [12], which could limit use for alternative fuels.

The structure of lanthanum strontium ferrite, $La_xSr_{1-x}FeO_{3-\delta}$, is known to vary with increasing lanthanum content: from cubic perovskite $0 \leq x \leq 0.3$, rhombohedral $0.4 \leq x \leq 0.7$ to orthorhombic $0.8 \leq x \leq 1$ [13]. Deviation from the cubic perovskite structure does not, however, limit the electronic conductivity of lanthanum doped strontium ferrite, which exhibits an increase with increasing lanthanum content up to $La_{0.5}Sr_{0.5}FeO_{3-\delta}$ [14], a result of the reduction in hole localisation and vacancy ordering. Further increases in the lanthanum content from $La_{0.5}Sr_{0.5}FeO_{3-\delta}$ results in a decrease in the electronic conductivity due to the reduction in p-type charge carriers and mobile oxygen vacancies.

Stabilisation of the cubic perovskite structure of strontium ferrites by B-site dopants has been achieved either through reduction of the oxygen vacancy concentration or interruption of oxygen vacancy ordering [15,16]. A-site dopants can improve the redox stability of strontium ferrites through reduction of the oxygen vacancy concentration so that exposure of the compound to reducing atmospheres does not lead to the formation of ordered oxygen vacancies. Patrakeev *et. al.* [14] demonstrated that the stability limit for $La_xSr_{1-x}FeO_{3-\delta}$ (x = 0, 0.1, 0.3, 0.5, 0.6, 0.8) in 5% H_2/He increased with increasing dopant concentration, although compounds with $x < 0.3$ exhibited a phase transition from a cubic perovskite structure to an orthorhombic triple perovskite structure.

Whilst current symmetrical fuel cells have not exhibited similarly high performance as has been noted for fuel cells with specialised anode and cathode materials, the additional flexibility and manufacturing simplification that these materials provide is sufficient incentive for further investigation. Lanthanum strontium ferrites appear to exhibit many of the desirable properties for use as symmetrical electrodes for IT-SOFCs, although further confirmation of their stability and conductivity under anodic conditions is necessary. To this end a series of lanthanum doped strontium ferrites, $La_xSr_{1-x}FeO_{3-\delta}$ (x = 0.2, 0.4, 0.6, 0.8), was synthesised to confirm the redox stability at intermediate temperatures and to assess their suitability for use as symmetrical electrodes for IT-SOFCs.

6.1.2. Experimental Information

6.1.2.1. Synthesis

$La_xSr_{1-x}FeO_{3-\delta}$ (x = 0.2, 0.4, 0.6, 0.8) were produced by sol-gel synthesis technique. . Stoichiometric amounts of $La(NO_3)_3 \cdot 6\ H_2O$ (99.9%, Alfa Aesar), $Sr(NO_3)_2$ (98%, Alfa Aesar) and $Fe(NO_3)_3 \cdot 9\ H_2O$ (98%, Alfa Aesar) were dissolved in distilled water. Citric acid (99+%, Alfa Aesar), in a 2:1 ratio to the metal ions and the solution was heated until gelation. The resultant gel was fired at 600 °C for 2 hours. A second firing at 1100 °C for 5 hours was then performed. Pellets of all the samples (ø ≈ 13 mm × 2 mm and ø ≈ 10 mm × 5 mm) were uniaxially pressed at 221 MPa and sintered in air at 1300°C for 2 hours.

6.1.2.2. Analytical Procedures

Phase purity and crystal parameters of the samples were examined by X-ray diffraction (XRD) analysis using a PANalytical X'Pert PRO MPD Multipurpose diffractometer (Cu $K_{\alpha 1}$ radiation, λ = 1.5405Å). GSAS [17] software was used to perform a least squares refinement of the lattice parameters of all suitable samples.

The densities of the pellets were determined from the measured mass and volume. Theoretical densities were calculated using experimental lattice parameters and the chemical formula of the sample. The relative densities were calculated from the actual and theoretical density values. The density of the pellets was 70 - 85 % for all compounds.

Thermal analysis was conducted on a 10 ± 0.5 mg sample using a Stanton Redcroft STA 1500 Thermal Analyser on heating from room temperature to 800 °C and on cooling from 800 °C to room temperature in air, with a heating/cooling rate of 10 °C/min, and in 5% H_2/Ar, again with a heating/cooling rate of 10 °Cmin^{-1}, and with a flow rate of 5% H_2/Ar of 50 mLmin^{-1}.

6.1.2.3. Conductivity Testing

Pellets for all samples were coated on opposing sides using silver paste. The conductivity of the samples was measured in primarily in air between 300 °C to 700 °C. Secondary measurements over the same temperature range were conducted in 5% H_2/Ar following an equilibration step of 10 hours at 700 °C in 5% H_2/Ar. Measurements were conducted using either an A.C. method utilising a Solartron 1455A frequency response analyser coupled to a Solartron 1470E potentiostat/galvanostat controlled by CoreWare software over the frequency range 1 MHz to 100 mHz or a DC method using a Solartron 1470E potentiostat/galvanostat controlled by CoreWare software with an applied current of 1 - 0.1 A.

6.1.2.4. Fuel Cell Testing

$Gd_{0.2}Ce_{0.8}O_{2-\delta}$ was prepared by a co-precipitation technique. Gd_2O_3 (99.9 %, Alfa Aesar) was dissolved in dilute nitric acid. $Ce(NO_3)_3 \cdot 6\,H_2O$ (99%, Sigma Aldrich) was added to the Gd solution and diluted further. A 0.1M solution of $(NH_4)_2CO_3$ (NH_3 ca 30%, Alfa Aesar) was produced and the Gd-Ce solution was added dropwise to the solution. The resultant suspension was aged prior to filtration. The precipitate was dried, ground and fired at 600 °C for 2 hours. Pellets (ø ≈ 22 mm × 0.5 mm) were prepared and fired at 1500 °C for 5 hours.

A symmetrical fuel cell utilising a dense thick electrolyte, ~ 300 μm, and a porous electrode was tested between 600 °C and 800 °C, with flowing humidified H_2 and flowing humidified air at the anode and cathode respectively. A paste containing $La_{0.6}Sr_{0.4}FeO_{3-\delta}$, $Gd_{0.2}Ce_{0.8}O_{2-\delta}$ and α-Terpineol (96%, Alfa Aesar) was printed separately on each side of the previously prepared dense pellets and fired at 1200 °C for 2 hours. The impedance of the cell was measured at each temperature using a Solartron 1455A frequency response analyser coupled to a Solartron 1470E potentiostat/galvanostat controlled by CoreWare software over the frequency range 1 MHz to 100 mHz. Voltage-current curves were produced using Solartron 1470E potentiostat/galvanostat controlled by CoreWare software, with a ramp from OCV to 0 V and step time of 0.1s.

6.1.3. Results and Discussion
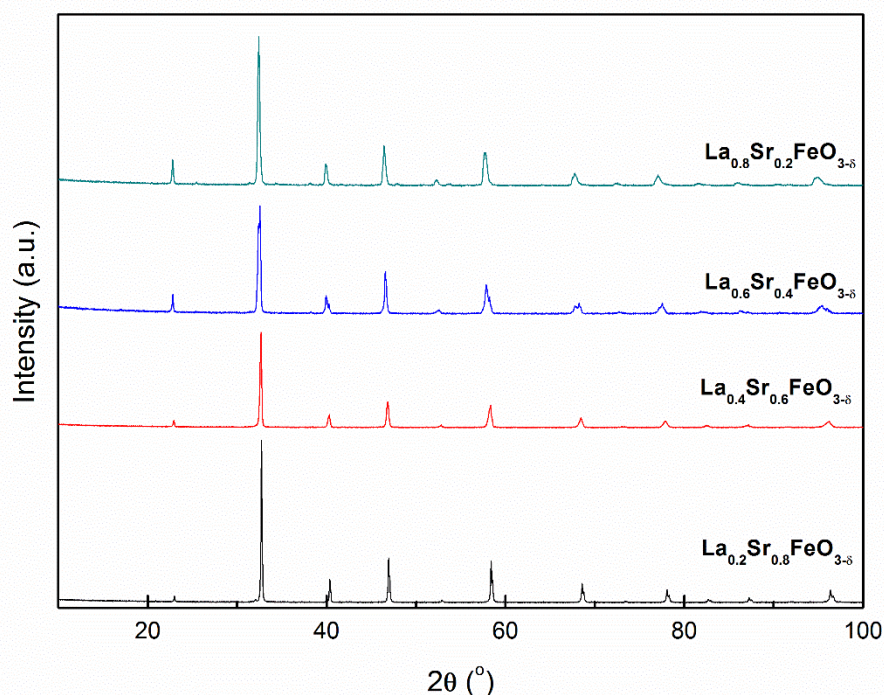
Figure 6.1. XRD patterns of La$_{1-x}$Sr$_x$FeO$_{3-\delta}$ (x = 0.2, 0.4, 0.6 and 0.8) synthesised in air

Sol-gel synthesis of La$_{0.2}$Sr$_{0.8}$FeO$_{3-\delta}$ and La$_{0.6}$Sr$_{0.4}$FeO$_{3-\delta}$ produced the predicted structures from the literature, cubic perovskite (SG: *Pm-3m*) for La$_{0.2}$Sr$_{0.8}$FeO$_{3-\delta}$ and rhombohedral (SG: *R-3cH*) for La$_{0.6}$Sr$_{0.4}$FeO$_{3-\delta}$ respectively [13, 14], which was confirmed by GSAS analysis [17], Figure 6.2 and Table 6.1. The lattice parameters for the compounds in this study and those from literature were closely correlated, deviating by no more than 0.02 Å [13, 14]. Neither La$_{0.4}$Sr$_{0.6}$FeO$_{3-\delta}$ nor La$_{0.8}$Sr$_{0.2}$FeO$_{3-\delta}$ exhibited the predicted structure from literature, with the cubic perovskite structure (SG: *Pm-3m*) noted for La$_{0.4}$Sr$_{0.6}$FeO$_{3-\delta}$ and the rhombohedral structure (SG: *R-3cH*) observed for La$_{0.8}$Sr$_{0.2}$FeO$_{3-\delta}$. As La$_{0.4}$Sr$_{0.6}$FeO$_{3-\delta}$ and La$_{0.8}$Sr$_{0.2}$FeO$_{3-\delta}$ are close to the cubic-rhombohedral and the rhombohedral-orthorhombic phase transitions, it is feasible that both phases are present in these compounds. The presence of both phases and the similarities in the diffraction patterns

292

could result in the resolution of the structural characterisation method not allowing for complete structural identification.

		$La_{0.2}Sr_{0.8}FeO_{3-\delta}$	$La_{0.4}Sr_{0.6}FeO_{3-\delta}$	$La_{0.6}Sr_{0.4}FeO_{3-\delta}$	$La_{0.8}Sr_{0.2}FeO_{3-\delta}$
χ^2		3.829	2.813	2.295	3.661
Rp (%)		6.80	6.70	6.98	8.82
wRp (%)		4.84	5.27	5.47	6.57
Space Group		*Pm-3m*	*Pm-3m*	*R-3cH*	*R-3cH*
a (Å)		3.864(1)	3.875(1)	5.523(1)	5.547(1)
c (Å)		3.864(1)	3.875(1)	13.415(1)	13.525(3)
V (Å^3)		57.7(1)	58.2(1)	354.4(2)	360.4(2)
La/Sr	x	0	0	0	0
	y	0	0	0	0
	z	0	0	0.25	0
	U_{iso}	0.007(1)	0.003(1)	0.019(1)	0.001(1)
Fe	x	0.5	0.5	0	0.5
	y	0.5	0.5	0	0.5
	z	0.5	0.5	0	0.5
	U_{iso}	0.005(2)	0.001(1)	0.015(1)	0.034(1)
O	x	0	0	0.450(3)	0
	y	0.5	0.5	0	0.5
	z	0.5	0.5	0.25	0.5
	U_{iso}	0.012(1)	0.011(1)	0.011(2)	0.028(2)

Table 6.1. Rietveld refinement and lattice parameters from GSAS refinement of

$La_xSr_{1-x}FeO_{3-\delta}$ (x = 0.2 - 0.8) after synthesis in air
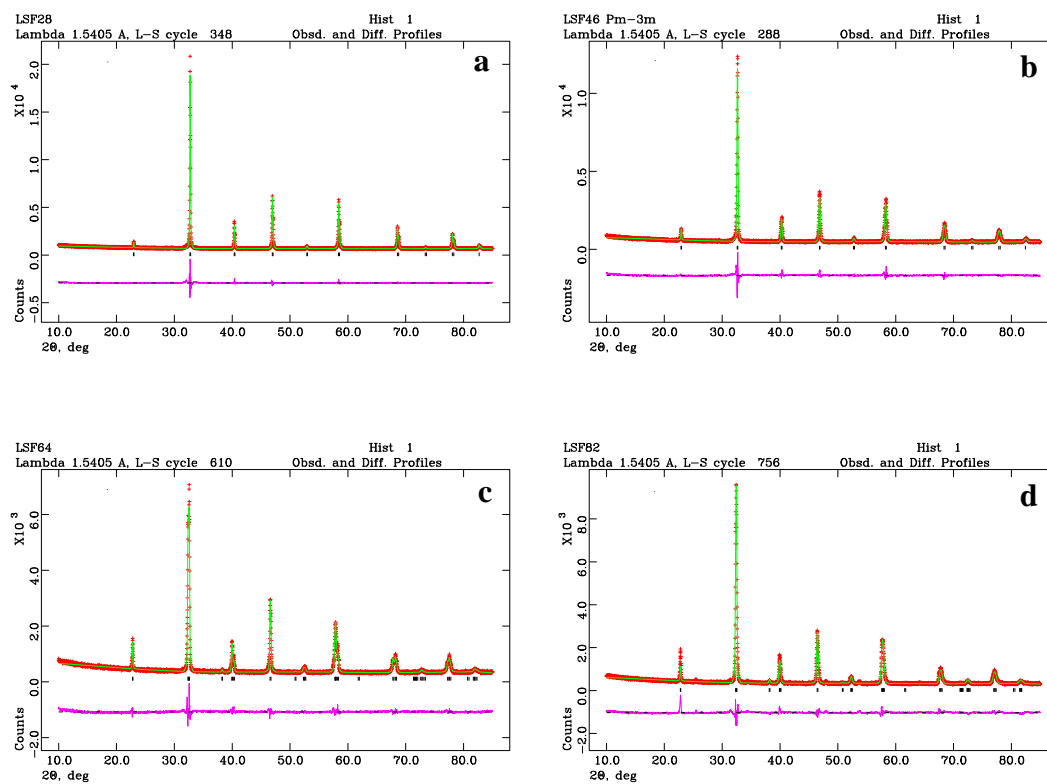
Figure 6.2. GSAS plots for La$_x$Sr$_{1-x}$FeO$_{3-\delta}$, x = 0.2 (a), x = 0.4 (b), x = 0.6 (c) and x = 0.8 (d)
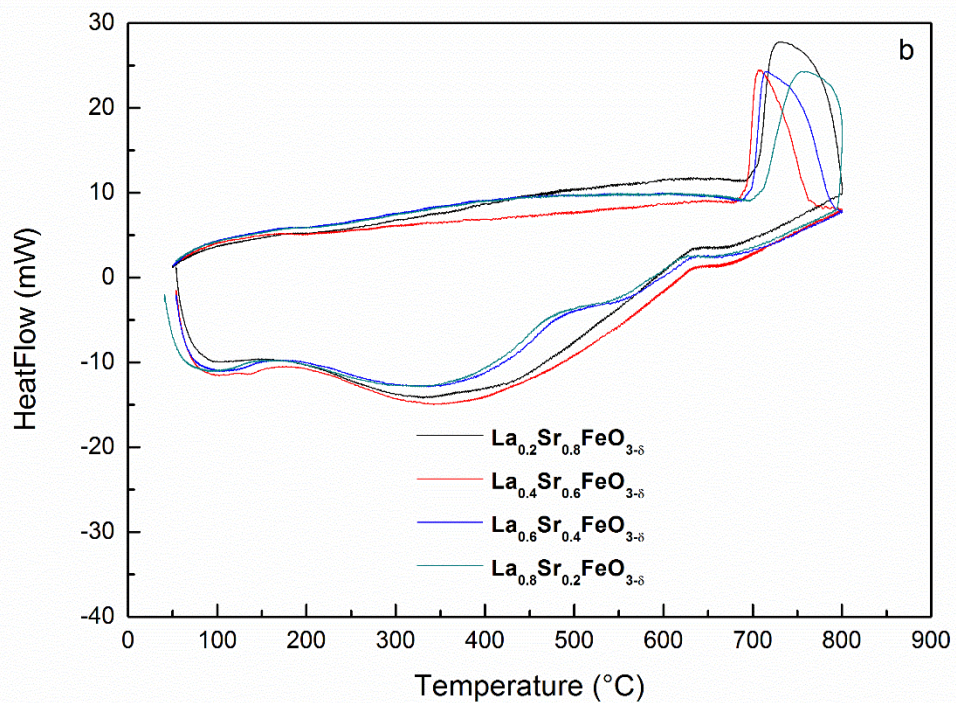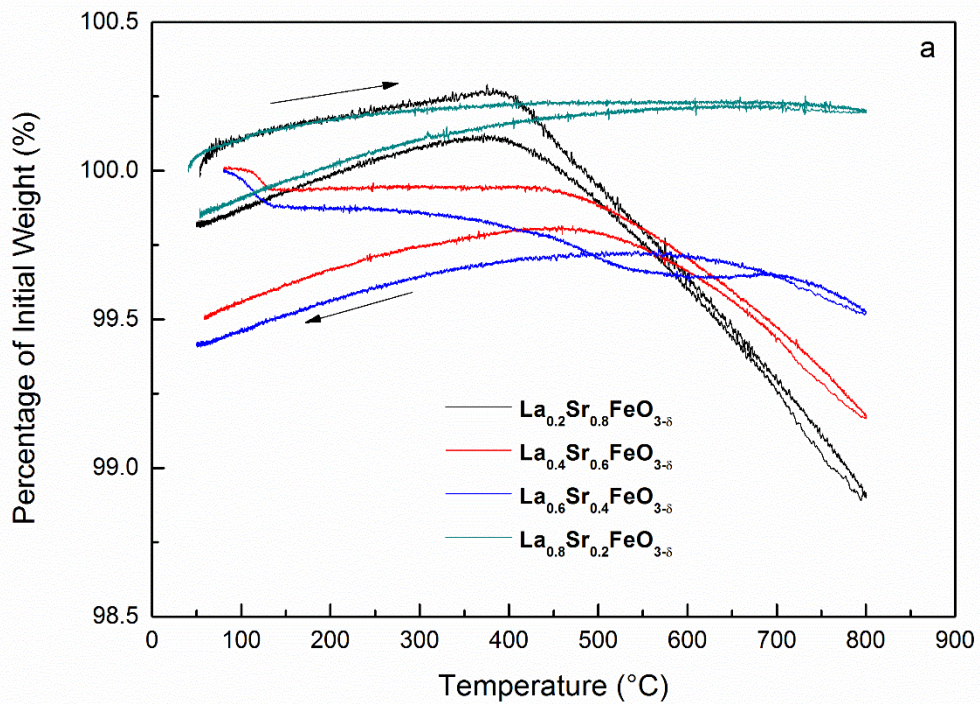
Figure 6.3. Thermogravimetric analysis (a) and differential scanning calorimetry (b) of $La_xSr_{1-x}FeO_{3-\delta}$ (x = 0.2, 0.4, 0.6 and 0.8) in air

296

Thermogravimetric analysis of $La_xSr_{1-x}FeO_{3-\delta}$ (x = 0.2, 0.4, 0.6, 0.8) in air demonstrates an overall weight loss of between 0.3% and 0.6%, without any observable correlation with the dopant content, Figure 6.3 (a). The weight loss at high temperature, previously attributed to oxygen loss from high temperature cationic reduction, is reduced with increasing dopant concentration. Differential scanning calorimetry, Figure 6.3 (b), exhibits no significant transitions over the experimental temperature range, implying thermal stability for all materials.
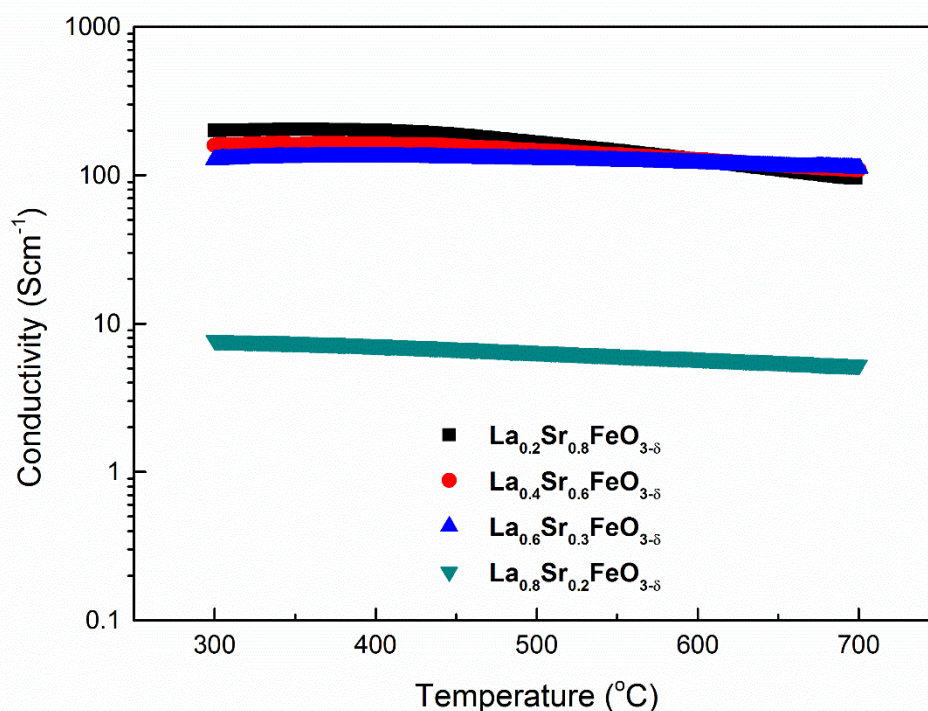
Figure 6.4. Conductivity of $La_xSr_{1-x}FeO_{3-\delta}$ (x = 0.2, 0.4, 0.6 and 0.8) in air

$La_xSr_{1-x}FeO_{3-\delta}$ (x = 0.2, 0.4, 0.6) exhibited high conductivity in air, > 100 Scm^{-1}, Figure 6.4, which generally correlates with previous research [14, 18], with minor discrepancies in the magnitude a result of differing synthesis and testing conditions. The increase in the electronic conductivity observed for $La_xSr_{1-x}FeO_{3-\delta}$ (x = 0.2, 0.4, 0.6) over that of $SrFeO_{3-\delta}$ is a result of an increase in the charge carrier mobility, as a result of the reduction in the oxygen vacancy concentration [18]. The marked reduction in the electronic conductivity for $La_{0.8}Sr_{0.2}FeO_{3-\delta}$ is a result of the reduction in the

charge carrier concentration with increasing dopant content [14]. As for previous strontium ferrites, Chapter 4 and 5, a semiconductor-metal transition was observed, between 300 °C and 400 °C for all compounds. The transition, as for all previous compounds, can be attributed to the reduction in the charge carrier concentration upon heating.
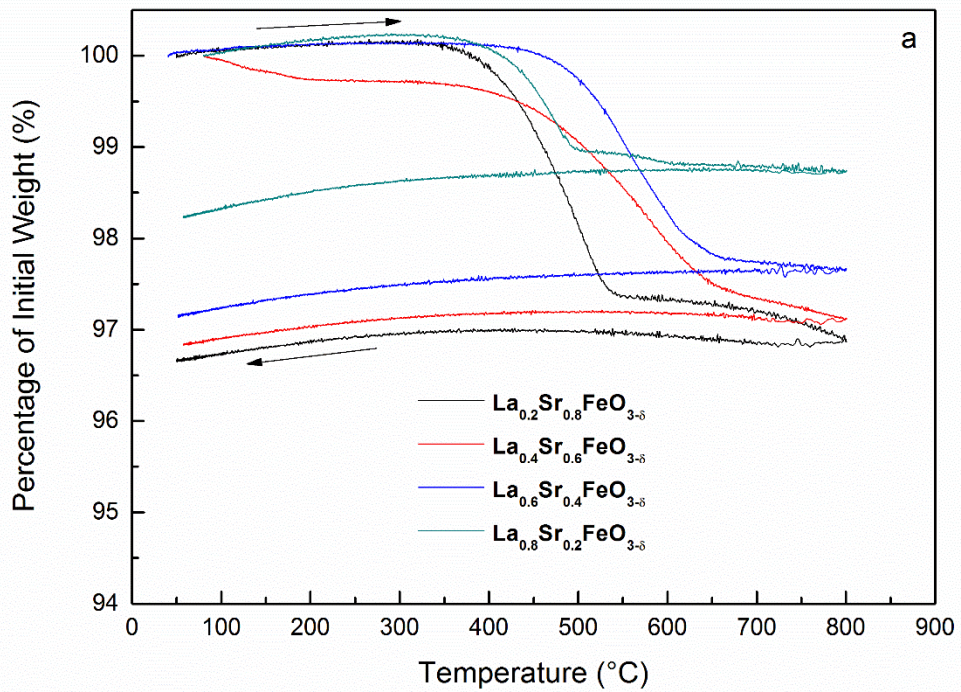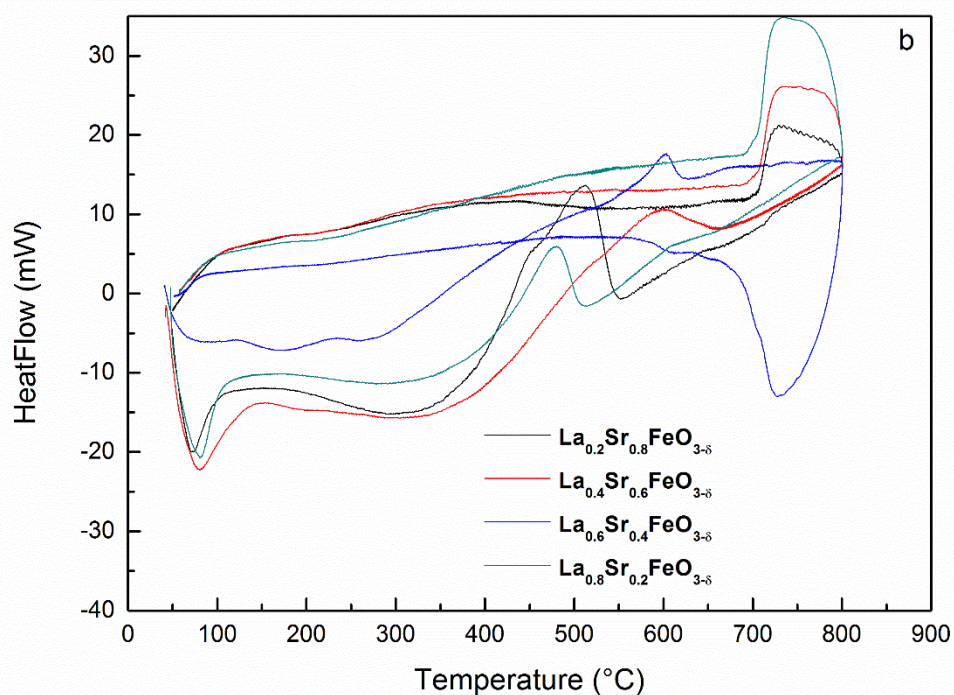
Figure 6.5. Thermogravimetric analysis (a) and differential scanning calorimetry (b) of $La_xSr_{1-x}FeO_{3-\delta}$ (x = 0.2, 0.4, 0.6 and 0.8) in 5%H_2/Ar

Weight loss upon reduction of $La_xSr_{1-x}FeO_{3-\delta}$ (x = 0.2, 0.4 0.8) in 5% H_2/Ar, Figure 6.5 (a), exhibited a linear dependence on the dopant concentration, from 3.33 % for $La_{0.2}Sr_{0.8}FeO_{3-\delta}$ to 1.77 % for $La_{0.8}Sr_{0.2}FeO_{3-\delta}$. Differential scanning calorimetry, Figure 6.5 (b), exhibited a non-reversible transition upon heating in 5% H_2/Ar for all compounds, between 400 °C and 650 °C. A similar transition was observed for previous ferrite materials on heating in reducing atmospheres, Chapter 4 and 5, attributed to cationic reduction.
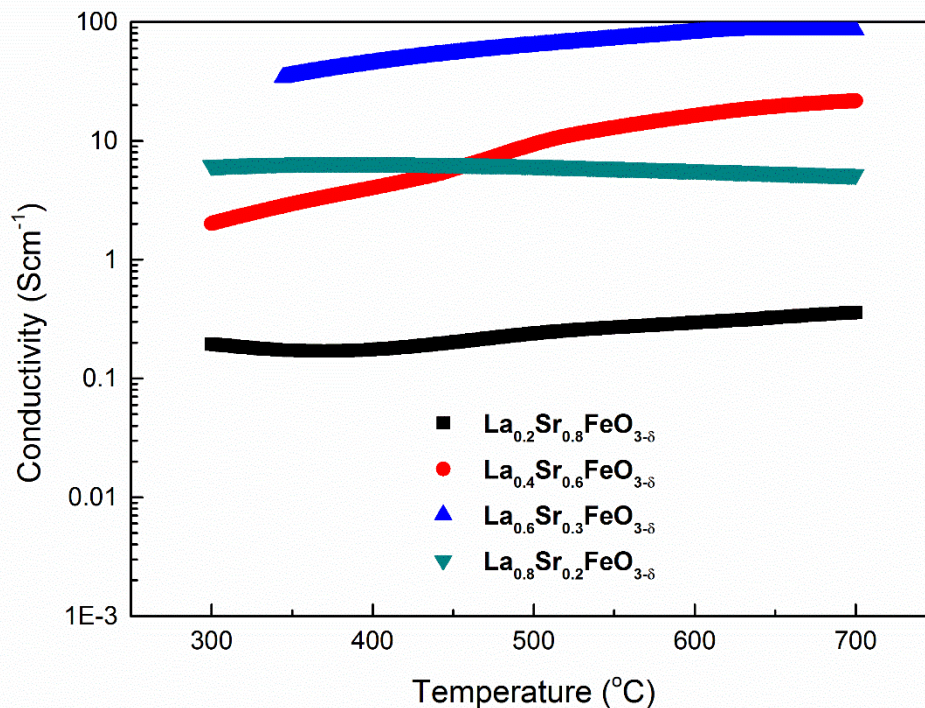
Figure 6.6. Conductivity of La$_x$Sr$_{1-x}$FeO$_{3-\delta}$ (x = 0.2, 0.4, 0.6 and 0.8) in 5% H$_2$/Ar

Reduction of both La$_{0.6}$Sr$_{0.4}$FeO$_{3-\delta}$ and La$_{0.8}$Sr$_{0.2}$FeO$_{3-\delta}$ results in a minor decrease in the electronic conductivity upon reduction, Figure 6.6. The temperature of the semiconductor-metal transition increases upon reduction, from 400 °C to 600 °C for La$_{0.6}$Sr$_{0.4}$FeO$_{3-\delta}$ and from 300 °C to 400 °C for La$_{0.8}$Sr$_{0.2}$FeO$_{3-\delta}$, with similar behaviour to that observed in air, Figure 6.4, suggesting that only partial reduction occurs for these compounds at 700 °C. In contrast to La$_{0.6}$Sr$_{0.4}$FeO$_{3-\delta}$ and La$_{0.8}$Sr$_{0.2}$FeO$_{3-\delta}$, semiconducting behaviour was observed between 300 °C and 700 °C for both La$_{0.2}$Sr$_{0.8}$FeO$_{3-\delta}$ and La$_{0.4}$Sr$_{0.6}$FeO$_{3-\delta}$ upon reduction, Figure 6.5, with a subsequent decrease in the conductivity. Patrakeev *et. al.* [14] noted that the oxygen content of La$_x$Sr$_{1-x}$FeO$_{3-\delta}$ on heating in 5% H$_2$/Ar tended towards 3 - x/2 after initial reduction, which was observed to plateau at ~ 500 °C. Research into pure strontium ferrites demonstrated that oxygen vacancy ordering could significantly reduce the electronic conductivity [19, 20], therefore it may be that the oxygen loss from reduction could cause oxygen vacancy ordering, thus reducing the conductivity of the strontium rich samples. The loss of conductivity upon reduction can be prevented upon B-site

doping due to interruption of the vacancy ordering by randomly distributed dopant cations, as demonstrated in Chapter 4 and 5.
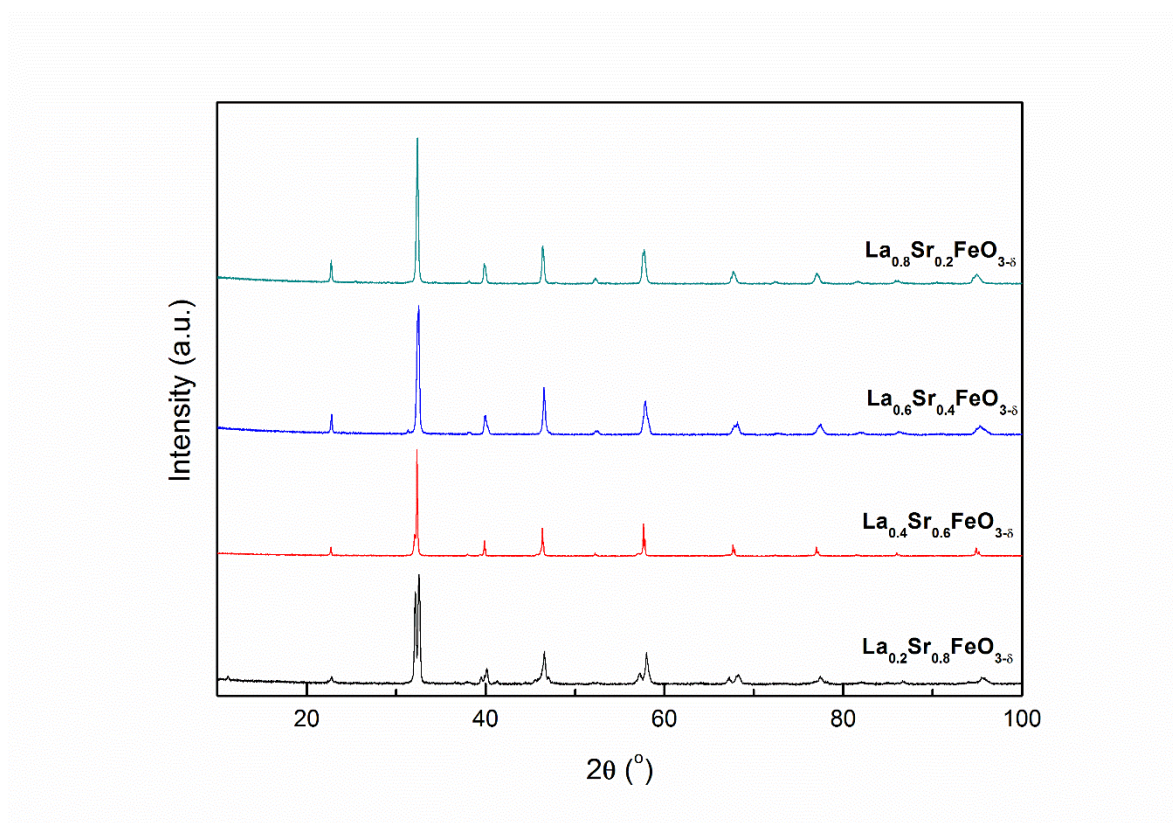
Figure 6.7. XRD patterns of La$_x$Sr$_{1-x}$FeO$_{3-\delta}$ (x = 0.2, 0.4, 0.6 and 0.8) after reduction at 700 °C in 5% H$_2$/Ar
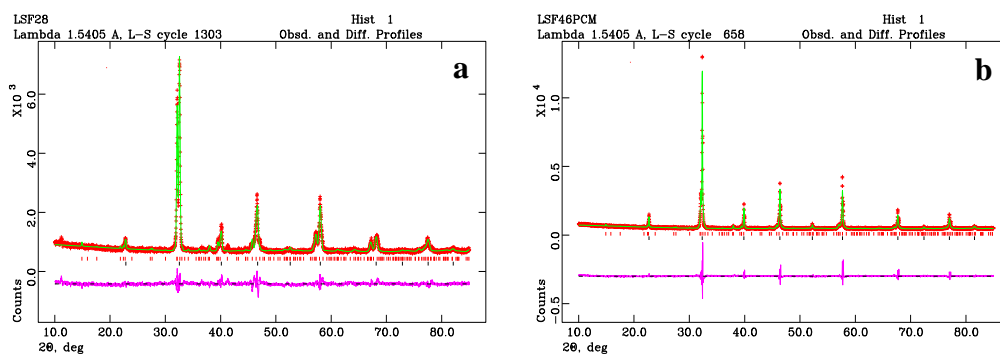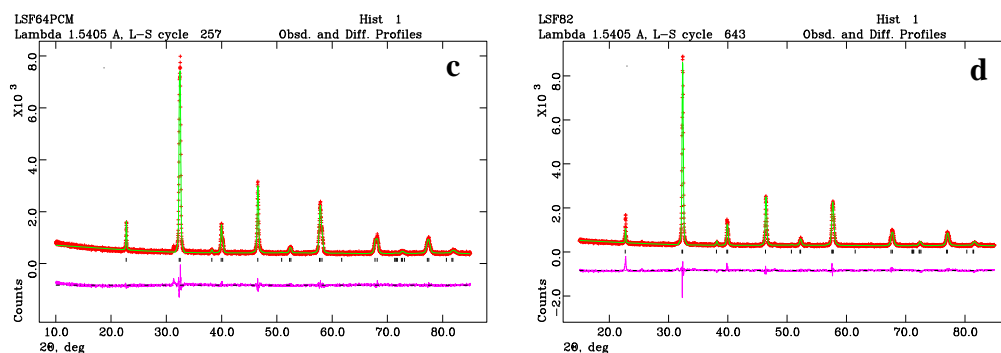
Figure 6.8. GSAS plots for La$_x$Sr$_{1-x}$FeO$_{3-\delta}$, x = 0.2 (a), x = 0.4 (b), x = 0.6 (c) and x = 0.8 (d) after reduction at 700 °C in 5% H$_2$/Ar

The formation of a secondary orthorhombic phase (SG: *Pmma*) was observed for both La$_{0.2}$Sr$_{0.8}$FeO$_{3-\delta}$ and La$_{0.4}$Sr$_{0.6}$FeO$_{3-\delta}$ upon reduction, Figure 6.7, Figure 6.8 and Table 6.2, as a result of the predicted oxygen vacancy ordering. The formation of the secondary phase correlates with the orthorhombic phase formed upon reduction of La$_{0.3}$Sr$_{0.7}$FeO$_{3-\delta}$ at 700 °C in 5% H$_2$/He, as reported by Patrakeev *et. al.* [14]. The rhombohedral phase observed for La$_{0.6}$Sr$_{0.4}$FeO$_{3-\delta}$ and La$_{0.8}$Sr$_{0.2}$FeO$_{3-\delta}$ exhibited only minor variation in the lattice parameter upon reduction, Table 6.1 and 6.2, demonstrating acceptable redox stability at these temperatures.

		$La_{0.2}Sr_{0.8}FeO_{3-\delta}$	$La_{0.4}Sr_{0.6}FeO_{3-\delta}$	$La_{0.6}Sr_{0.4}FeO_{3-\delta}$	$La_{0.8}Sr_{0.2}FeO_{3-\delta}$
χ^2		3.168	4.054	2.093	2.881
Rp (%)		6.18	8.23	6.20	8.11
wRp (%)		4.61	5.68	4.89	6.10
Primary Phase Fraction		*48.3 %*	*73.5 %*	*100 %*	*100 %*
Space Group		*Pm-3m*	*Pm-3m*	*R-3cH*	*R-3cH*
a (Å)		3.891(1)	3.912(1)	5.523(1)	5.542(1)
c (Å)		3.891(1)	3.912(1)	13.429(2)	13.518(1)
V (Å^3)		58.9(1)	59.9(1)	354.8(1)	359.6(1)
Secondary Phase Fraction		*51.6 %*	26.5 %	-	-
Space Group		*Pmma*	*Pmma*	-	-
a (Å)		5.489(1)	5.510(1)	-	-
b (Å)		11.905(1)	11.881(1)	-	-
c (Å)		5.575(1)	5.597(1)	-	-
V (Å^3)		364.4(1)	366.4(1)	-	-
La/Sr	x	0	0	0	0
	y	0	0	0	0
	z	0	0	0.25	0
	U_{iso}	0.016(1)	0.010(1)	0.012(1)	0.003(1)
Fe	x	0.5	0.5	0	0.5
	y	0.5	0.5	0	0.5
	z	0.5	0.5	0	0.5
	U_{iso}	0.016(2)	0.009(1)	0.007(1)	0.030(1)
O	x	0	0	0.446(1)	0
	y	0.5	0.5	0	0.5
	z	0.5	0.5	0.25	0.5
	U_{iso}	0.076(4)	0.044(3)	0.002(2)	0.026(2)

Table 6.2. Rietveld refinement and lattice parameters from GSAS refinement of

$La_xSr_{1-x}FeO_{3-\delta}$ (x = 0.2 - 0.8) after reduction at 700 °C in 5%H$_2$/Ar

303

The optimum combination of electronic conductivity and redox stability for $La_xSr_{1-x}FeO_{3-\delta}$ (x = 0.2, 0.4, 0.6, 0.8) was demonstrated by $La_{0.6}Sr_{0.4}FeO_{3-\delta}$, indicating potential for use as a symmetrical electrode for IT-SOFCs. As previous research indicated that a reaction may occur at high temperatures between LSF and YSZ, resulting in a reduction in the electrode performance [21], GDC was deemed more suitable for use as an electrolyte in LSF fuel cells. As for $Sr_{0.4}Fe_{0.9}Ti_{0.1}O_{3-\delta}$, a thermal mismatch between $La_{0.6}Sr_{0.4}FeO_{3-\delta}$, with a TEC of $(12.4-13.6)\times10^{-6}$ K^{-1} between 23 °C and 623 °C and a TEC of $(21.6-24.9)\times10^{-6}$ K^{-1} between 623 °C and 1023 °C [22], and $Gd_{0.2}Ce_{0.8}O_{2-\delta}$, TEC of ~ 12×10^{-6} K^{-1} [23], is known to occur at high temperature, therefore a composite anode is required for fuel cell synthesis.

The fuel cell performance, Figure 6.9, of a symmetrical cell with a 55 wt% $La_{0.6}Sr_{0.4}FeO_{3-\delta}$: 45 wt% $Gd_{0.2}Ce_{0.8}O_{2-\delta}$ electrode and a $Gd_{0.2}Ce_{0.8}O_{2-\delta}$ electrolyte was poor, reaching 116 mWcm^{-2} at 800 °C. The maximum power density for the LSF-GDC electrode at 800 °C is also significantly lower than was achieved for the pure $SrFe_{0.8}Cu_{0.1}Nb_{0.1}O_{3-\delta}$ electrode at 700 °C, 306 mWcm^{-2}. As good cathodic performance of LSF has been extensively demonstrated previously [6], it is suspected that the reduction in the fuel cell performance is due, in part, to the poorer anodic properties of $La_{0.6}Sr_{0.4}FeO_{3-\delta}$ compared to $SrFe_{0.8}Cu_{0.1}Nb_{0.1}O_{3-\delta}$.
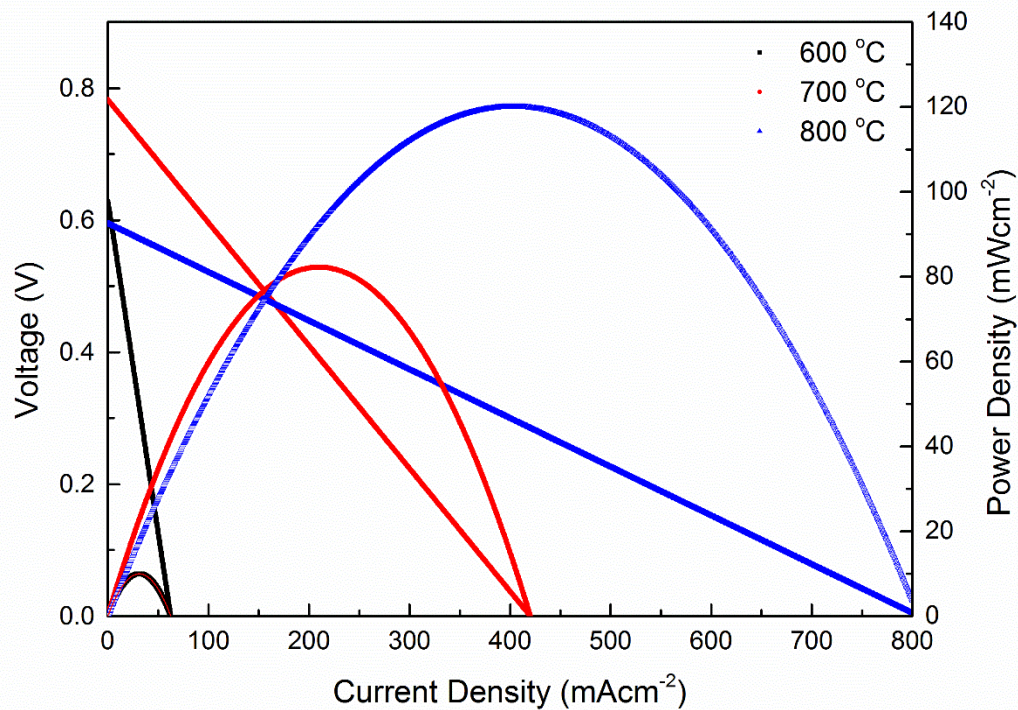
Figure 6.9. Fuel cell performance of a symmetrical (La$_{0.6}$Sr$_{0.4}$FeO$_{3-\delta}$-Gd$_{0.2}$Ce$_{0.8}$O$_{2-\delta}$)- Gd$_{0.2}$Ce$_{0.8}$O$_{2-\delta}$-(La$_{0.6}$Sr$_{0.4}$FeO$_{3-\delta}$-Gd$_{0.2}$Ce$_{0.8}$O$_{2-\delta}$) cell, with flowing humidified H$_2$ and flowing humidified air at the anode and cathode respectively
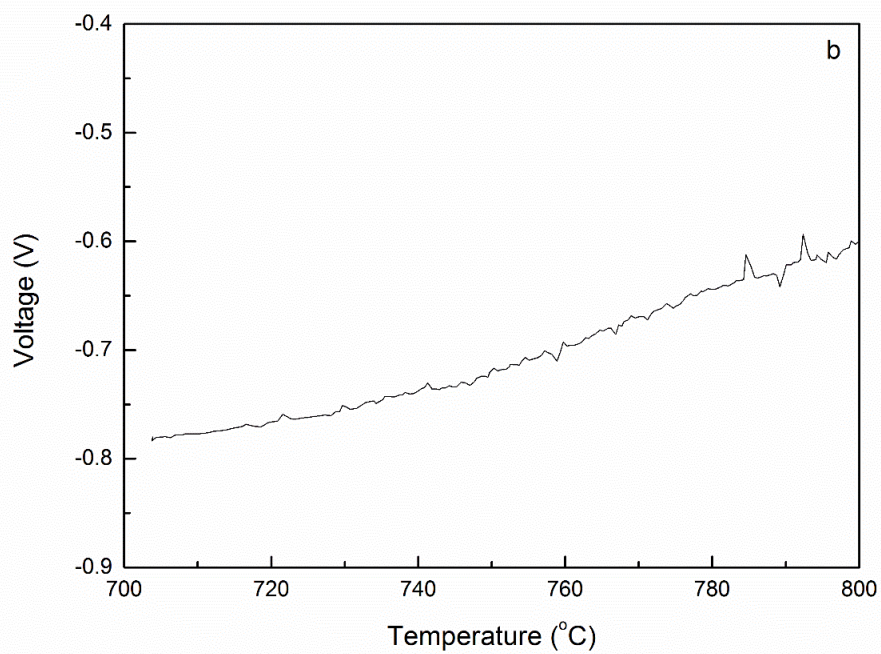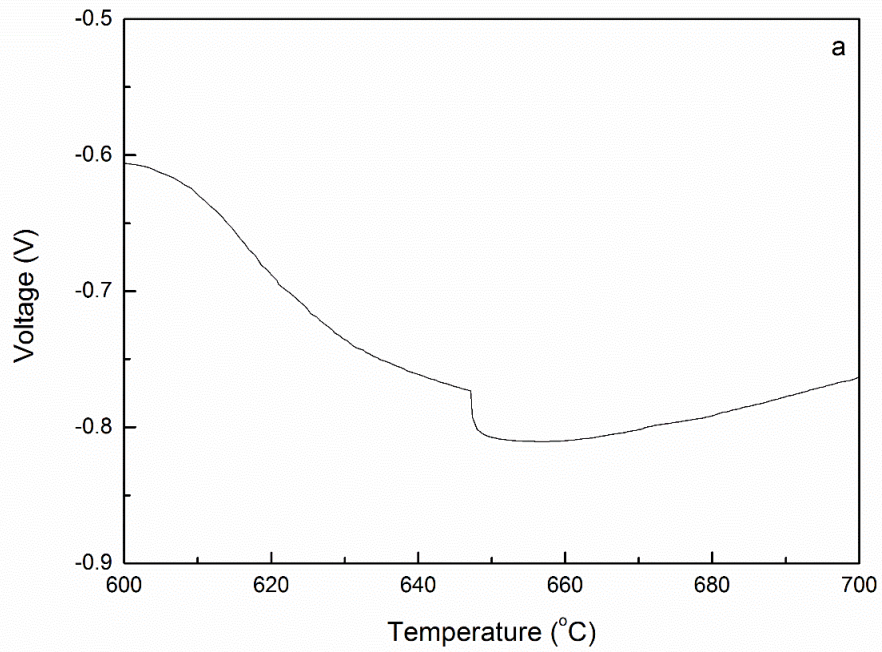
Figure 6.10. Open circuit voltage of a symmetrical ($La_{0.6}Sr_{0.4}FeO_{3-\delta}$-$Gd_{0.2}Ce_{0.8}O_{2-\delta}$)- $Gd_{0.2}Ce_{0.8}O_{2-\delta}$-($La_{0.6}Sr_{0.4}FeO_{3-\delta}$-$Gd_{0.2}Ce_{0.8}O_{2-\delta}$) cell between 600 °C and 700 °C (a) and 700 °C and 800 °C (b), with flowing humidified H_2 and flowing humidified air at the anode and cathode respectively

The operating voltage of the fuel cell was between 0.306 V and 0.40 V over the measured temperature range. As for the (60:40 $SrFe_{0.9}Ti_{0.1}O_{3-\delta}$-$Gd_{0.2}Ce_{0.8}O_{2-\delta}$) - $Gd_{0.2}Ce_{0.8}O_{2-\delta}$ - (60:40 $SrFe_{0.9}Ti_{0.1}O_{3-\delta}$-$Gd_{0.2}Ce_{0.8}O_{2-\delta}$) symmetrical SOFC in Chapter 4.1.3, the low operating voltages are considered to be a result of the low open circuit voltage. Low OCV was observed over the entire measurement temperature range, between 0.595 V and 0.782 V at 800 °C and 700 °C respectively. Previously, for symmetrical fuel cells with (60:40 $SrFe_{0.9}Ti_{0.1}O_{3-\delta}$-$Gd_{0.2}Ce_{0.8}O_{2-\delta}$) or $SrFe_{0.8}Cu_{0.1}Nb_{0.1}O_{3-\delta}$ electrodes, reduction of the OCV was deemed to either be a result of a lack of gas tightness of the electrolyte or the sealant, which could result in gas crossover and a subsequent reduction of the open circuit voltage [24], or the result of a lack of gas tightness of the electrolyte or the sealant, which could result in gas crossover and a subsequent reduction of the open circuit voltage.

An increase in the open circuit voltage is observed between 600 °C and 700 °C, Figure 6.10a, with a subsequent reduction between 700 °C and 800 °C, Figure 6.10b. Both the electronic conductivity of the electrolyte and the gas tightness of the fuel cell have been given as reasons for the reduction of the OCV from the theoretical maximum, however neither of these should exhibit a temperature dependence as is observed here. Whilst no significant change in the material properties upon reduction of $La_{0.6}Sr_{0.4}FeO_{3-\delta}$ is observed, Figure 6.6 and Figure 6.7, a reversible transition is observed by differential scanning calorimetry upon heating between 600 °C and 700 °C, Figure 6.5b. As this phenomenon is not observed for any other fuel cell tests conducted in this thesis, this suggests that this OCV variation is related to the electrode composition. The use of scanning electron microscopy could be essential in the determination of the origin of this phenomenon, although no further conclusions can be drawn from the current data.
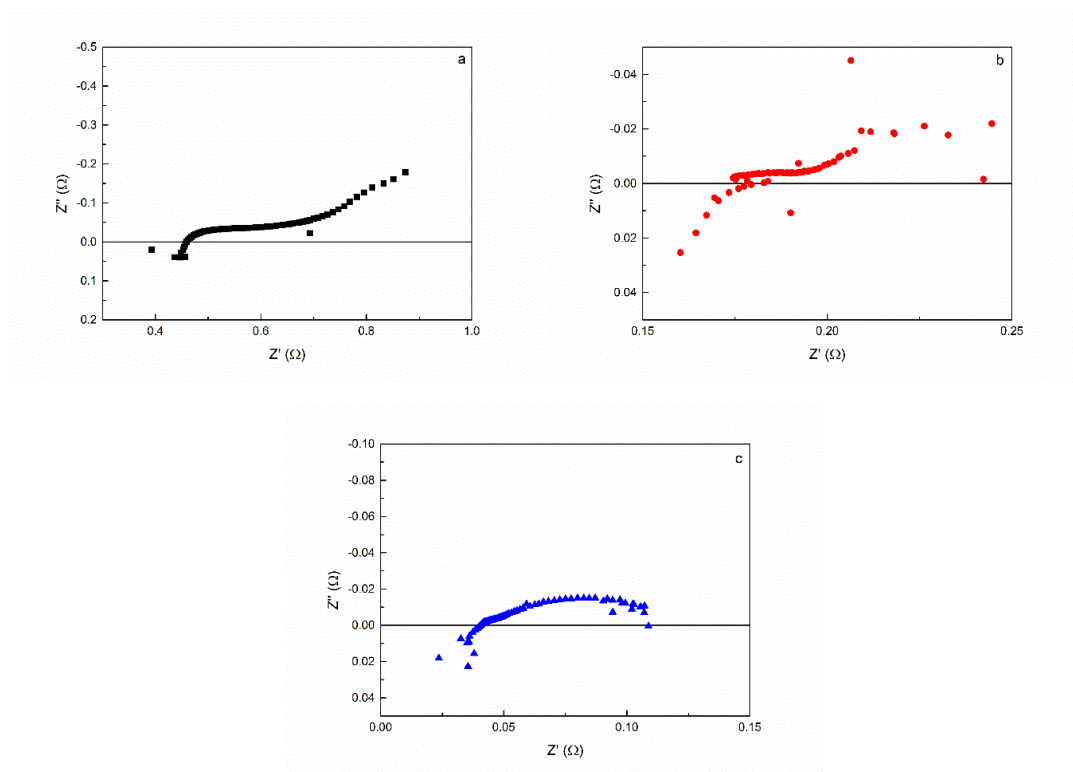
Figure 6.11. Impedance of a symmetrical (La$_{0.6}$Sr$_{0.4}$FeO$_{3-\delta}$-Gd$_{0.2}$Ce$_{0.8}$O$_{2-\delta}$)-Gd$_{0.2}$Ce$_{0.8}$O$_{2-\delta}$-(La$_{0.6}$Sr$_{0.4}$FeO$_{3-\delta}$-Gd$_{0.2}$Ce$_{0.8}$O$_{2-\delta}$) cell over the frequency range 1 MHz to 100 mHz at 600°C (a), 700°C (b) and 800°C (c), with flowing humidified H$_2$ and flowing humidified air at the anode and cathode respectively

A significant reduction in the series resistance (from 0.462 Ωcm^2 to 0.040 Ωcm^2), total resistance (from 1.5 Ωcm^2 to 0.102 Ωcm^2) and polarisation resistance (from 1.038 Ωcm^2 to 0.062 Ωcm^2), Figure 6.11 was observed with increasing temperature. Whilst the total resistance of both La$_{0.6}$Sr$_{0.4}$FeO$_{3-\delta}$-Gd$_{0.2}$Ce$_{0.8}$O$_{2-\delta}$ and SrFe$_{0.8}$Cu$_{0.1}$Nb$_{0.1}$O$_{3-\delta}$ symmetrical fuel cells are similar at both 600 °C and 700 °C, the series resistance of the SrFe$_{0.8}$Cu$_{0.1}$Nb$_{0.1}$O$_{3-\delta}$ symmetrical fuel cell is significantly lower. This is indicative of lower ohmic resistances for the SrFe$_{0.8}$Cu$_{0.1}$Nb$_{0.1}$O$_{3-\delta}$ symmetrical fuel cell, albeit coupled with poorer reaction kinetics, resulting in a higher polarisation resistance.

Values of the ASR from the fuel cell impedance and from the voltage-current curves do not tally, with values of 0.102 Ωcm^{-1} and 0.373 Ωcm^{-1} at 800 °C and values of 1.5 Ωcm^{-1} and 5.05 Ωcm^{-1} at 600 °C, calculated from impedance and voltage-current curves respectively. As was found for both the (60:40 SrFe$_{0.9}$Ti$_{0.1}$O$_{3-\delta}$-Gd$_{0.2}$Ce$_{0.8}$O$_{2-\delta}$)-

$Gd_{0.2}Ce_{0.8}O_{2-\delta}$-(60:40 $SrFe_{0.9}Ti_{0.1}O_{3-\delta}$-$Gd_{0.2}Ce_{0.8}O_{2-\delta}$) symmetrical SOFC in Chapter 4.1.3 and the $SrFe_{0.8}Cu_{0.1}Nb_{0.1}O_{3-\delta}$–$Gd_{0.2}Ce_{0.8}O_{2-\delta}$-$SrFe_{0.8}Cu_{0.1}Nb_{0.1}O_{3-\delta}$ symmetrical SOFC in Chapter 5.4, the observed impedance response of a GDC electrolyte can demonstrate a reduction in the various observed AC resistances, due to a partial short circuit of the ionic current as a result of the additional conduction contribution from the electronic carriers [25]. The lack of accuracy of the data from the A.C. impedance plots should be borne in mind when drawing conclusions from the experimental results.

Despite the proven performance of $La_{0.6}Sr_{0.4}FeO_{3-\delta}$ as an efficient cathode material [6], use of $La_{0.6}Sr_{0.4}FeO_{3-\delta}$ as a symmetrical electrode material was unsatisfactory. Comparison to the performance of the symmetrical $SrFe_{0.8}Cu_{0.1}Nb_{0.1}O_{3-\delta}$ fuel cells, suggests that these materials are better suited for use in asymmetrical fuel cells with specialised anode and cathode materials.

The potential for utilisation of lanthanum strontium ferrites as symmetrical electrodes for IT-SOFCs is exhibited in the material properties, however actual fuel cell performance at intermediate temperatures was noted to be poor. Further optimisation of the electrode composition and microstructure could result in further improvements in fuel cell performance and additional research into the catalytic activity of these materials could further elucidate the potential utility of these materials as symmetrical IT-SOFC electrodes.

6.2. $Y_xSr_{1-x}FeO_{3-\delta}$ (x = 0, 0.05, 0.1, 0.15, 0.2, 0.25, 0.3)

6.2.1. Introduction

Lanthanum doped strontium ferrites have previously been demonstrated to exhibit both high electronic conductivity and redox stability at intermediate temperatures and were considered suitable materials for use in symmetrical IT-SOFCs, Chapter 6.1. The fuel cell performance of these materials, however, was poor, either a result of negligible catalytic activity for the anodic reaction or insufficiently optimised electrodic microstructure. The advantages of A-site doping for alteration of the properties of strontium ferrites is evident from lanthanum doping and warrants further investigation.

Whilst both lanthanum and yttrium doping of strontium titanate elicit increases in the electronic conductivity without adversely affecting the desirable properties of the parent material [26, 27, 28]. Whilst lanthanum doping of strontium ferrite causes a larger increase in the electronic conductivity when compared to yttrium doping [27, 28], introduction of yttrium results in an improvement in the catalytic activity for hydrogen oxidation [29, 30]. Considering that the poor fuel cell performance of lanthanum strontium ferrite was posited to be a result of poor catalytic activity for the anodic reaction, yttrium doping could result in an improvement in both the electronic conductivity and the catalytic activity of strontium ferrite.

Yttrium doping of strontium ferrite has, to the best of our knowledge, not been investigated with a focus on the conductivity and redox stability of these materials. The solitary study on yttrium strontium ferrite was conducted by Azad *et. al.* [31] concentrating on the determination of the magnetic and structural properties at low temperatures. $YSr_2Fe_3O_{8-\delta}$ exhibited a tetragonal structure (SG: *P4/mmm*), intimating that formation of the cubic perovskite structure may only occur at lower doping levels. Considering the performance of the lanthanum doped strontium ferrite and the structure of $YSr_2Fe_3O_{8-\delta}$, a series of yttrium doped strontium ferrites, $Y_xSr_{1-x}FeO_{3-\delta}$ (x = 0, 0.05, 0.1, 0.15, 0.2, 0.25, 0.3), were synthesised and the suitability of these materials as symmetrical electrodes for IT-SOFCs ascertained.

6.2.2. Experimental Information

6.2.2.1. Synthesis

$Y_xSr_{1-x}FeO_{3-\delta}$ (x = 0.05, 0.1, 0.15, 0.2, 0.25, 0.3) were produced by sol-gel synthesis technique. A stoichiometric amount of Y_2O_3 (99.9%, Alfa Aesar) was dissolved in dilute nitric acid. Stoichiometric amounts of $Sr(NO_3)_2$ (98%, Alfa Aesar) and $Fe(NO_3)_3 \cdot 9\ H_2O$ (98%, Alfa Aesar) were dissolved in the solution. Citric acid (99+%, Alfa Aesar), in a 2:1 ratio to the metal ions and the solution was heated until gelation. The resultant gel was fired at 600 °C for 2 hours. A second firing at 1300 °C for 5 hours was then performed. Pellets of all the samples (ø ≈ 13 mm × 2 mm and ø ≈ 10 mm × 5 mm) were uniaxially pressed at 221 MPa and sintered in air at 1300°C for 5 hours.

6.2.2.2. Analytical Procedures

Phase purity and crystal parameters of the samples were examined by X-ray diffraction (XRD) analysis using a PANalytical X'Pert PRO MPD Multipurpose diffractometer (Cu $K_{\alpha 1}$ radiation, λ = 1.5405Å). GSAS [17] software was used to perform a least squares refinement of the lattice parameters of all suitable samples.

The densities of the pellets were determined from the measured mass and volume. Theoretical densities were calculated using experimental lattice parameters and the chemical formula of the sample. The relative densities were calculated from the actual and theoretical density values. The density of the pellets was 70 - 85 % for all compounds.

Thermal analysis was conducted on a 10 ± 0.5 mg sample using a Stanton Redcroft STA 1500 Thermal Analyser on heating from room temperature to 800 °C and on cooling from 800 °C to room temperature in air, with a heating/cooling rate of

10 °C/min, and in 5% H_2/Ar, again with a heating/cooling rate of 10 °Cmin^{-1}, and with a flow rate of 5% H_2/Ar of 50 mLmin^{-1}.

6.2.2.3. Conductivity Testing

Pellets for all samples were coated on opposing sides using silver paste. The conductivity of the samples was measured in primarily in air between 300 °C to 700 °C. Secondary measurements over the same temperature range were conducted in 5% H_2/Ar following an equilibration step of 10 hours at 700 °C in 5% H_2/Ar. Measurements were conducted using either an A.C. method utilising a Solartron 1455A frequency response analyser coupled to a Solartron 1470E potentiostat/galvanostat controlled by CoreWare software over the frequency range 1 MHz to 100 mHz or a DC method using a Solartron 1470E potentiostat/galvanostat controlled by CoreWare software with an applied current of 1 - 0.1 A.

6.2.3. Results and Discussion
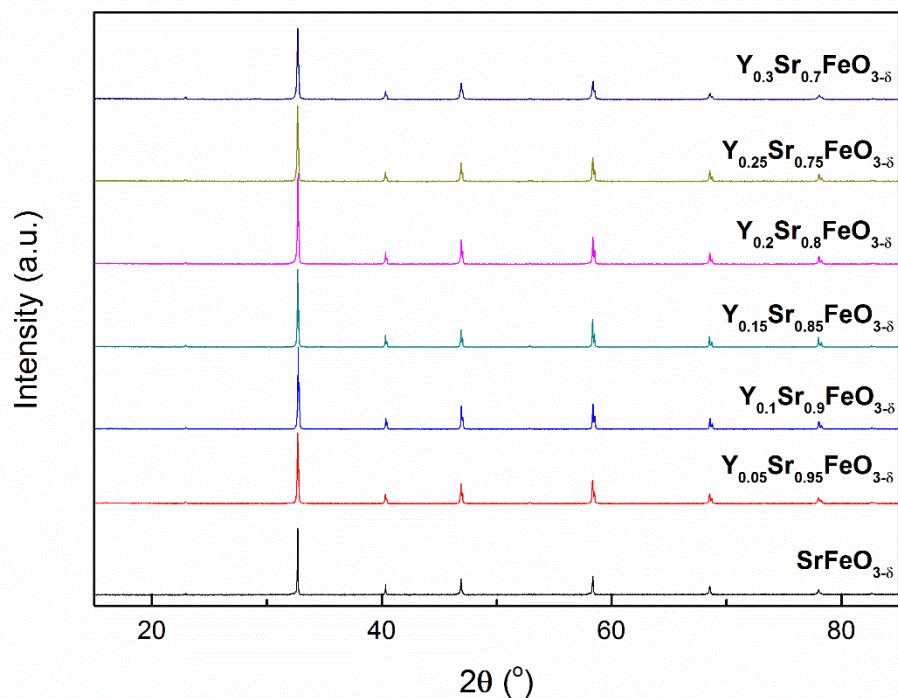
Figure 6.12. XRD pattern of $Y_xSr_{1-x}FeO_{3-\delta}$ (x = 0 – 0.3) synthesised in air

X-ray diffraction of $Y_xSr_{1-x}FeO_{3-\delta}$ (x = 0, 0.05, 0.1, 0.15, 0.2, 0.25, 0.3), Figure 6.12, exhibited the formation of cubic perovskite structures up to x = 0.3. Synthesis of $Y_{0.4}Sr_{0.6}FeO_{3-\delta}$ under the same conditions exhibited multiple unidentified secondary phases, thus the solid solution limit occurs in the doping region 0.3 < x < 0.4. Whilst lanthanum doping of strontium ferrite forms single phase structures over the entire dopant range, the lower cationic size of yttrium (Y^{3+} = 1.19 Å) compared to lanthanum (La^{3+} = 1.36 Å) [32] lowers the tolerance factor and thus destabilises the perovskite structure.

313
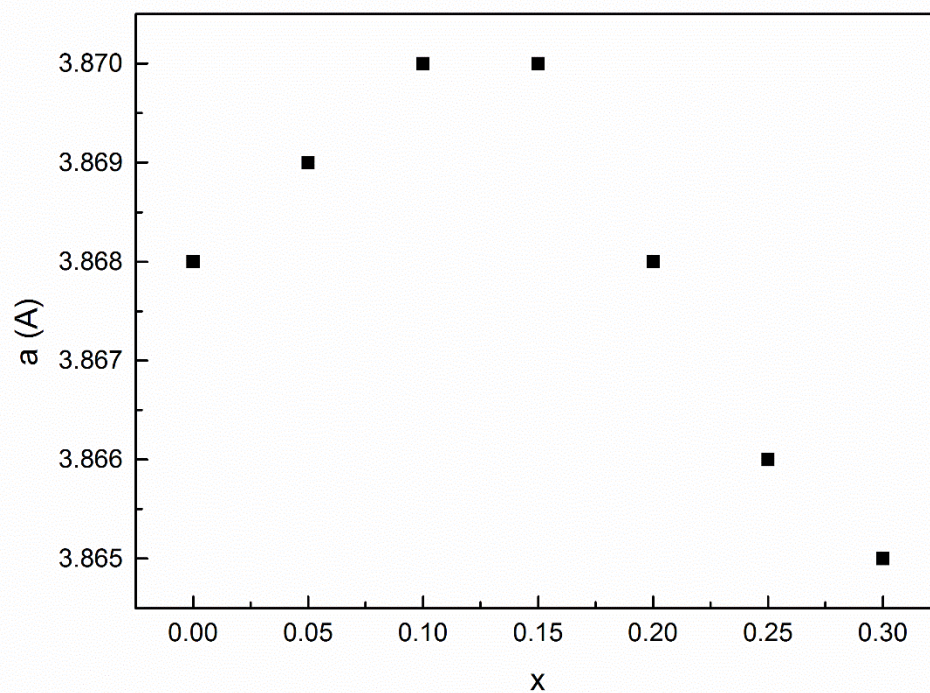
Figure 6.13. Variation of lattice parameters for $Y_xSr_{1-x}FeO_{3-\delta}$ (x = 0 − 0.3)
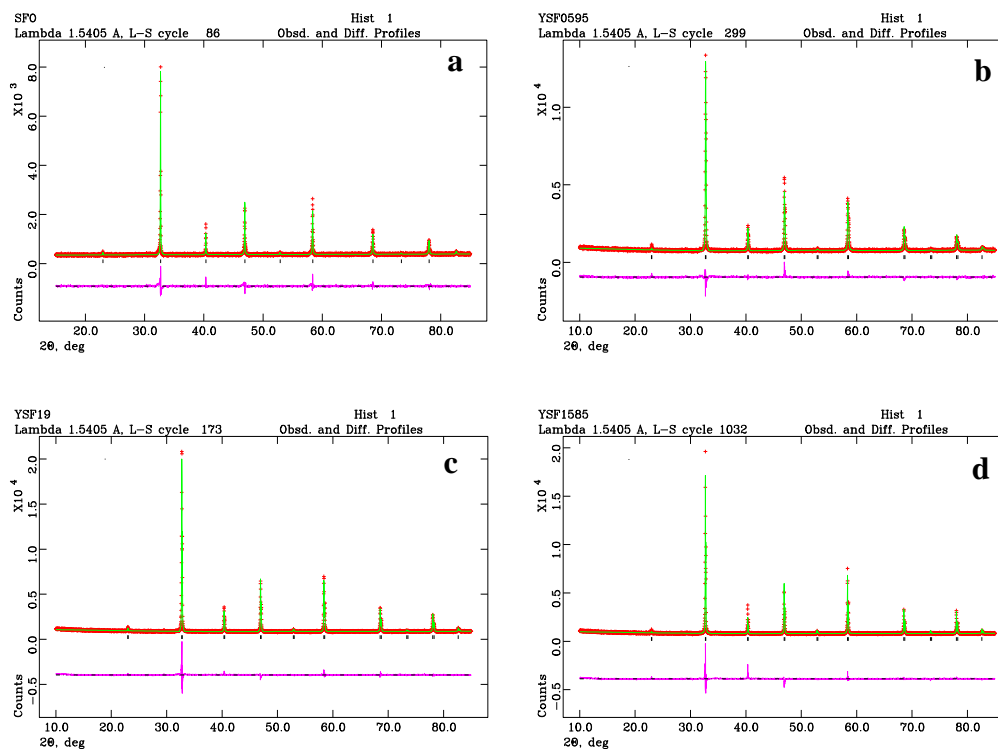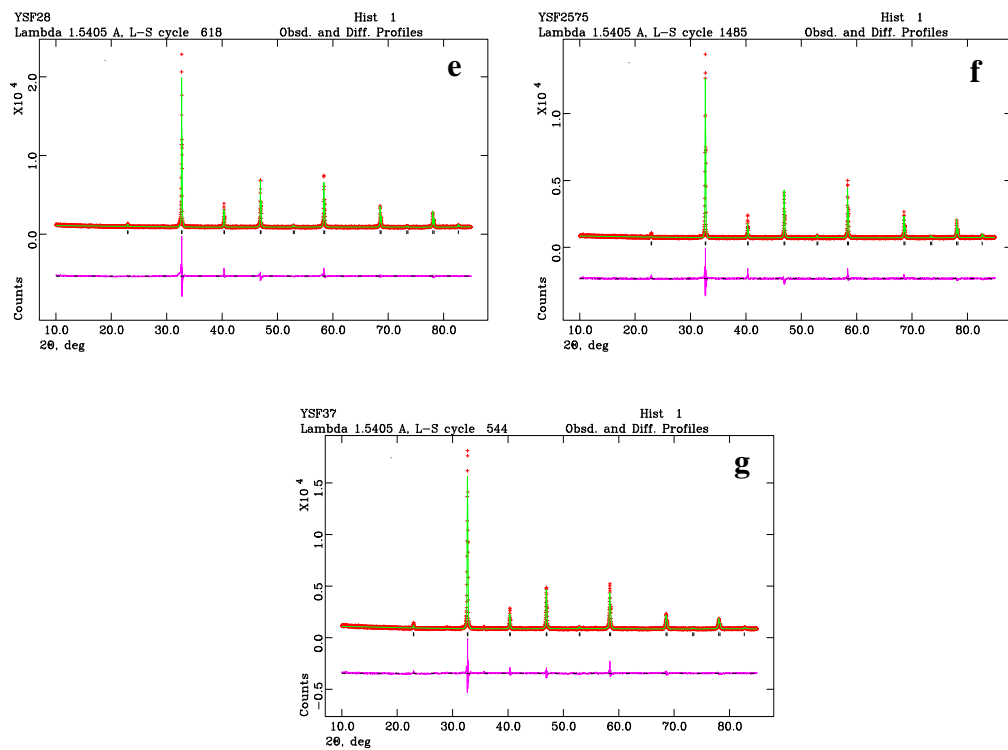
Figure 6.14. GSAS plots for $Y_xSr_{1-x}FeO_{3-\delta}$, x = 0 (a), x = 0.05 (b), x = 0.1 (c), x = 0.15 (d), x = 0.2 (e), x = 0.25 (f) and x = 0.3 (g)

(a)		$SrFeO_{3-\delta}$	$Y_{0.05}Sr_{0.95}FeO_{3-\delta}$	$Y_{0.1}Sr_{0.9}FeO_{3-\delta}$	$Y_{0.15}Sr_{0.85}FeO_{3-\delta}$
χ^2		1.760	1.984	2.523	3.163
Rp (%)		6.67	4.81	5.05	5.94
wRp (%)		4.96	3.67	3.81	4.10
Space Group		*Pm-3m*	*Pm-3m*	*Pm-3m*	*Pm-3m*
a (Å)		3.868(3)	3.869(1)	3.870(1)	3.870(1)
V (Å^3)		57.8(1)	57.9(1)	58.0(1)	58.0(1)
Y/Sr	x	0	0	0	0
	y	0	0	0	0
	z	0	0	0	0
P1	U_{iso}	0.001(8)	0.006(1)	0.021(1)	0.016(1)
Fe	x	0.5	0.5	0.5	0.5
	y	0.5	0.5	0.5	0.5
	z	0.5	0.5	0.5	0.5
P1	U_{iso}	0.002(1)	0.012(1)	0.028(1)	0.036(1)
O	x	0	0	0	0
	y	0.5	0.5	0.5	0.5
	z	0.5	0.5	0.5	0.5
P1	U_{iso}	0.014(4)	0.023(2)	0.063(2)	0.081(3)

(b)		$Y_{0.2}Sr_{0.8}FeO_{3-\delta}$	$Y_{0.25}Sr_{0.75}FeO_{3-\delta}$	$Y_{0.3}Sr_{0.7}FeO_{3-\delta}$
χ^2		4.493	2.397	3.179
Rp (%)		6.59	5.45	5.67
wRp (%)		4.26	3.94	4.11
Space Group		*Pm-3m*	*Pm-3m*	*Pm-3m*
a (Å)		3.868(1)	3.866(1)	3.865(1)
V (Å^3)		57.9(1)	57.8(1)	57.7(1)
Y/Sr	x	0	0	0
	y	0	0	0
	z	0	0	0
P1	U_{iso}	0.008(1)	0.003(1)	0.033(1)
Fe	x	0.5	0.5	0.5
	y	0.5	0.5	0.5
	z	0.5	0.5	0.5
P1	U_{iso}	0.007(1)	0.025(1)	0.033(1)
O	x	0	0	0
	y	0.5	0.5	0.5
	z	0.5	0.5	0.5
P1	U_{iso}	0.044(3)	0.045(2)	0.089(3)

Table 6.3. Rietveld refinement and lattice parameters from GSAS refinement of

$Y_xSr_{1-x}FeO_{3-\delta}$ (x = 0-0.15 (a), x = 0.2-0.3 (b)) after synthesis in air

GSAS [17] analysis, Figure 6.13, Figure 6.14 and Table 6.1, of the series exhibited a single phase cubic perovskite structure, with a maximum in the lattice parameter occurring between x = 0.1 and x = 0.15. Due to the smaller cationic size of the yttrium dopant, 1.19 Å for Y^{3+} compared to 1.44 Å for Sr^{2+}, a linear reduction in the lattice parameter might be expected to occur with increasing dopant concentration. Charge compensation upon yttrium doping of strontium ferrite can, however, result in a reduction in the average iron cation valence or a reduction in the oxygen vacancy concentration, both of which would result an expansion in the lattice parameter. Potentially, the subsequent decrease could be a result of the reduction in the A-site cation size, due to the smaller ionic radius of Y^{3+}, becoming more significant than the changes in the lattice through charge compensation. Alternatively, the reduction of the lattice parameters from $Y_{0.15}Sr_{0.85}FeO_{3-\delta}$ to $Y_{0.3}Sr_{0.7}FeO_{3-\delta}$ may be partially due to the effects of A-site cation disorder.

Previous research determined that increasing the A-site cation size disorder can result in a non-linear variation in the lattice parameters of doped lanthanide manganese oxides [33, 34]. The variance, or disorder, in the A-site cation sizes is given by Equation 6.1, where y is the fractional occupancy and r is the cationic radius.

$$\sigma^2 = \Sigma y_i r_i^2 - \langle r_A \rangle^2 \qquad (6.1)$$

<div align="center">Variance of the A-site cation radius distribution</div>

A-site cation disorder generally results in random displacement of oxygen anions from their average crystallographic positions, resulting in the non-linear effects on the lattice parameters. As the disorder is random, the displacement is not reflected by changes in the average structure of the crystallographic lattice and therefore is not observed by x-ray diffraction. The significant size difference between yttrium and strontium, 0.25 Å, will elicit a significantly larger cationic size disorder with increasing yttrium content, as exhibited in Table 6.4.

Composition	$\langle r_A \rangle$	A^{x+}	σ^2
$Y_{0.05}Sr_{0.95}FeO_{3-\delta}$	1.4275	2.05	0.00296875
$Y_{0.1}Sr_{0.99}FeO_{3-\delta}$	1.415	2.1	0.005625
$Y_{0.15}Sr_{0.85}FeO_{3-\delta}$	1.4025	2.15	0.00796875
$Y_{0.2}Sr_{0.8}FeO_{3-\delta}$	1.39	2.2	0.01
$Y_{0.25}Sr_{0.75}FeO_{3-\delta}$	1.3775	2.25	0.01171875
$Y_{0.3}Sr_{0.7}FeO_{3-\delta}$	1.365	2.3	0.013125

Table 6.4 A-site parameters for $Y_xSr_{1-x}FeO_{3-\delta}$ (x = 0, 0.05, 0.1, 0.15, 0.2, 0.25, 0.3)

It should be noted that most of the studies on the effects of A-site disorder constrain both the A-site cation size and charge, which also increase with increasing dopant concentration, Table 6.4, and these will likely have a further effect on the lattice parameters of these materials.
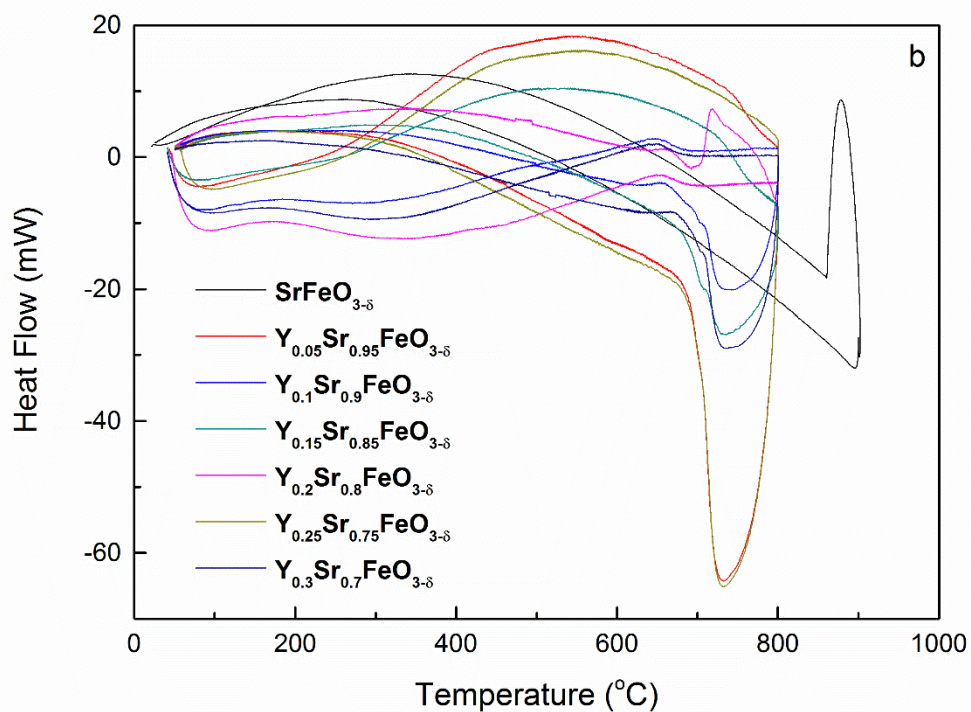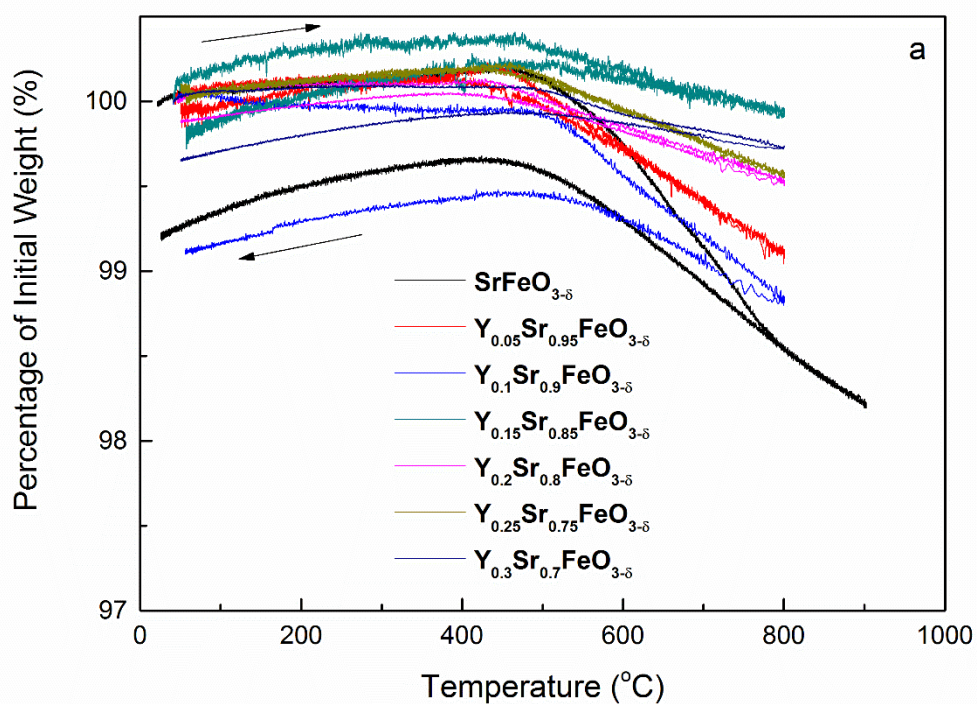
Figure 6.15. Thermogravimetric analysis (a) and differential scanning calorimetry (b) of $Y_xSr_{1-x}FeO_{3-\delta}$ (x = 0 − 0.3) in air

Thermogravimetric analysis of all compounds in air, Figure 6.15 (a), exhibited a partially reversible reduction in weight beginning at 450 °C, attributed to high temperature cationic reduction. The overall weight loss was negligible, between 0.1 % and 1 %, which in association with the lack of peaks or troughs from differential scanning calorimetry, Figure 6.15 (b), indicates a deficit of phase transitions or compound degradation, intimating thermal stability for all compounds in air.
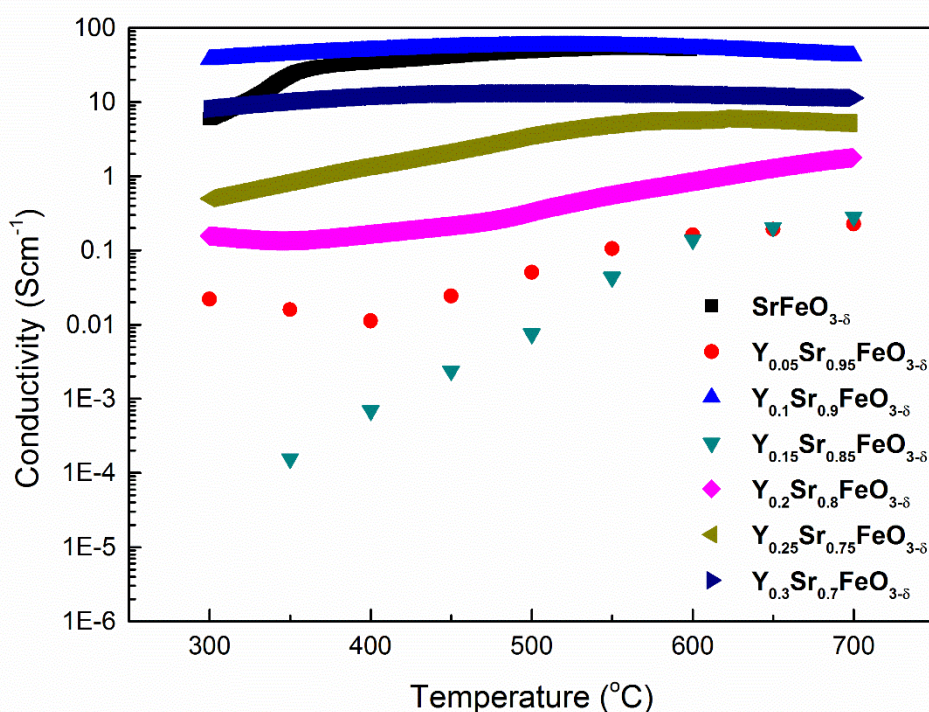
Figure 6.16. Conductivity of $Y_xSr_{1-x}FeO_{3-\delta}$ (x = 0 – 0.3) in air

An increase in the electronic conductivity of $Y_xSr_{1-x}FeO_{3-\delta}$ (x = 0, 0.05, 0.1, 0.15) in air, Figure 6.16, was observed with increasing yttrium content. As was predicted, the conductivity of $Y_xSr_{1-x}FeO_{3-\delta}$ (x = 0.05, 0.1, 0.15) was of a lower magnitude than was observed for $La_xSr_{1-x}FeO_{3-\delta}$ (x = 0.2, 0.4, 0.6), Chapter 6.1, however still of a magnitude of interest for SOFC electrode materials, > 10 Scm^{-1}. Whilst the A-site cation disorder can result in non-linear variations in the lattice parameters, previous research intimated that isolated variation of the A-site cation disorder would evoke a linear response in the electrical properties [33, 34]. The electronic

conductivity of these materials exhibits a minor correlation with the variation in the lattice parameters, with increasing conductivity observed with increasing lattice parameters, from $Y_{0.05}Sr_{0.95}FeO_{3-\delta}$ to $Y_{0.15}Sr_{0.85}FeO_{3-\delta}$ and increasing conductivity with reducing lattice parameters, from $Y_{0.15}Sr_{0.85}FeO_{3-\delta}$ to $Y_{0.3}Sr_{0.7}FeO_{3-\delta}$. This is suggesting that the mechanisms by which lattice variations occur is intrinsically linked to the magnitude of the electronic conductivity.

The activation energy for conduction consistently increased with increasing dopant concentration from $Y_{0.05}Sr_{0.95}FeO_{3-\delta}$, 0.09(2) eV, to $Y_{0.3}Sr_{0.7}FeO_{3-\delta}$, 0.15(2) eV. The increase in the activation energy can be mainly attributed to the reduction in the charge carrier concentration, however this is likely partially balanced by the increased percolation pathway due to increased oxygen content from charge compensation mechanisms.

As for other doped strontium ferrites, Chapter 4 and 5, a semiconductor-metal transition is observed to occur for $Y_xSr_{1-x}FeO_{3-\delta}$ (x = 0, 0.05, 0.1, 0.15, 0.2, 0.25, 0.3) between 400 °C and 500 °C, with an increase in the transition temperature observed with increasing dopant concentration. As for previous materials, the transition is a result of the increase in the conductivity with increasing temperature, associated with E_a, nullified by the reduction in charge carrier concentration, causing an overall reduction in the electronic conductivity with increasing temperature, resulting in the pseudo-metallic behaviour

As both the activation energy and the semiconductor metal transition do not appear to correlate with the variations in the lattice parameter, it would be expected that the magnitude of the conductivity would equally be independent of the observed variations in the structural lattice. Whilst it may be that the A-site disorder might affect the charge compensation mechanisms with increasing dopant concentration, this cannot be determined using the techniques in this study.
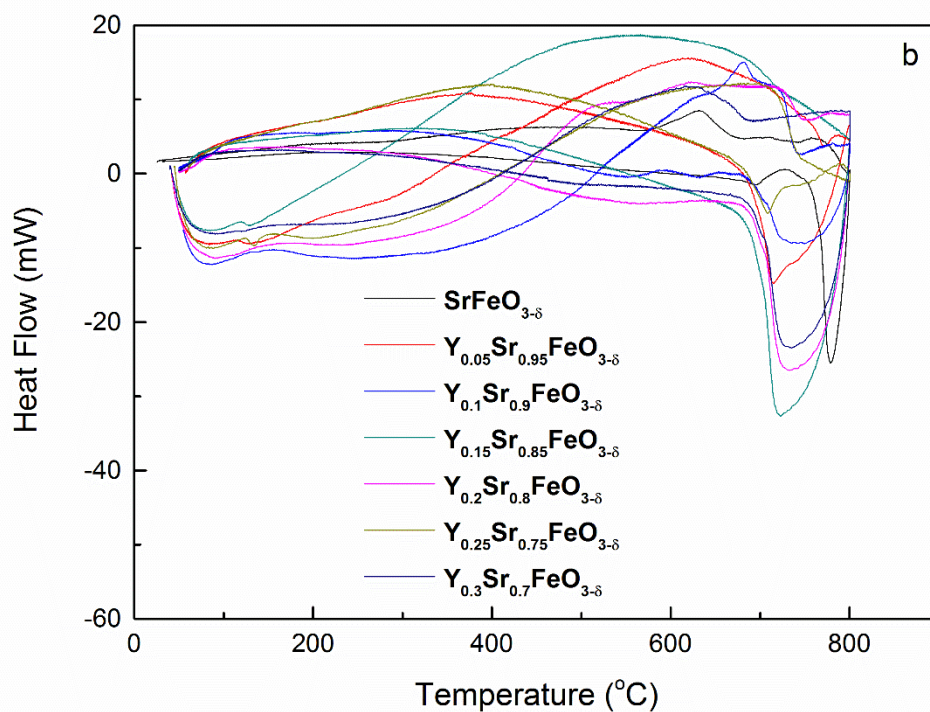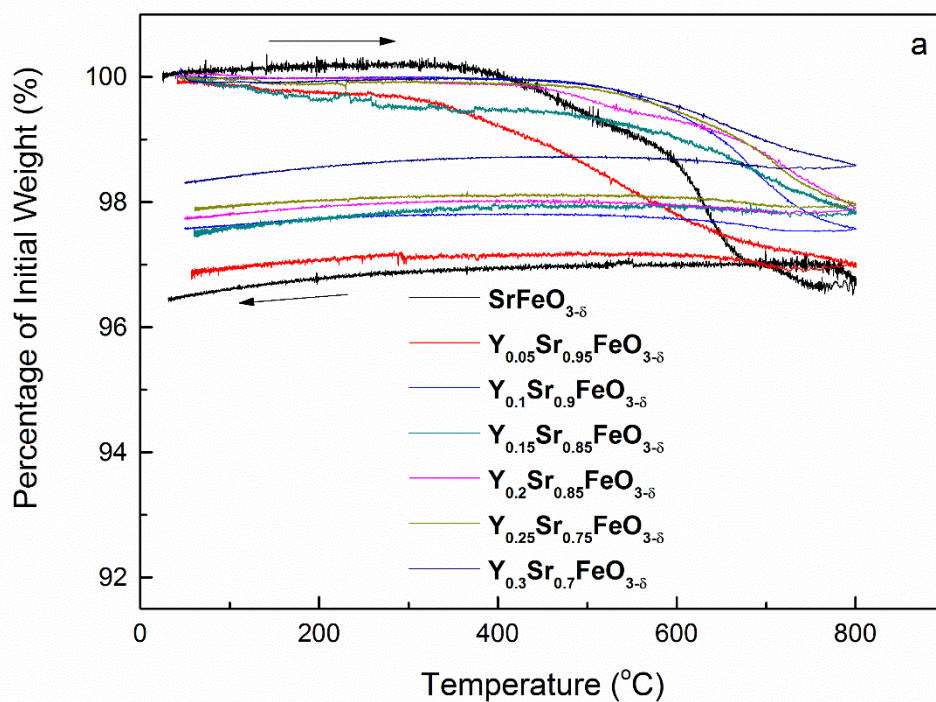
Figure 6.17. Thermogravimetric analysis (a) and differential scanning calorimetry (b) of $Y_xSr_{1-x}FeO_{3-\delta}$ (x = 0 – 0.3) in 5% H_2/Ar

Thermogravimetric analysis of $Y_xSr_{1-x}FeO_{3-\delta}$ (x = 0, 0.05, 0.1, 0.15, 0.2, 0.25, 0.3) in 5% H_2/Ar, Figure 6.17 (a), exhibited a broadly linear reduction in weight loss with increasing dopant concentration, from 3.6 % for $SrFeO_{3-\delta}$ to 1.7 % for $Y_{0.3}Sr_{0.7}FeO_{3-\delta}$, beginning between 300 °C and 400 °C. As for all previous strontium ferrites, differential scanning calorimetry exhibited a non-reversible transition on heating for all compounds between 400 °C and 650 °C, Figure 6.17 (b), attributed to cationic reduction.
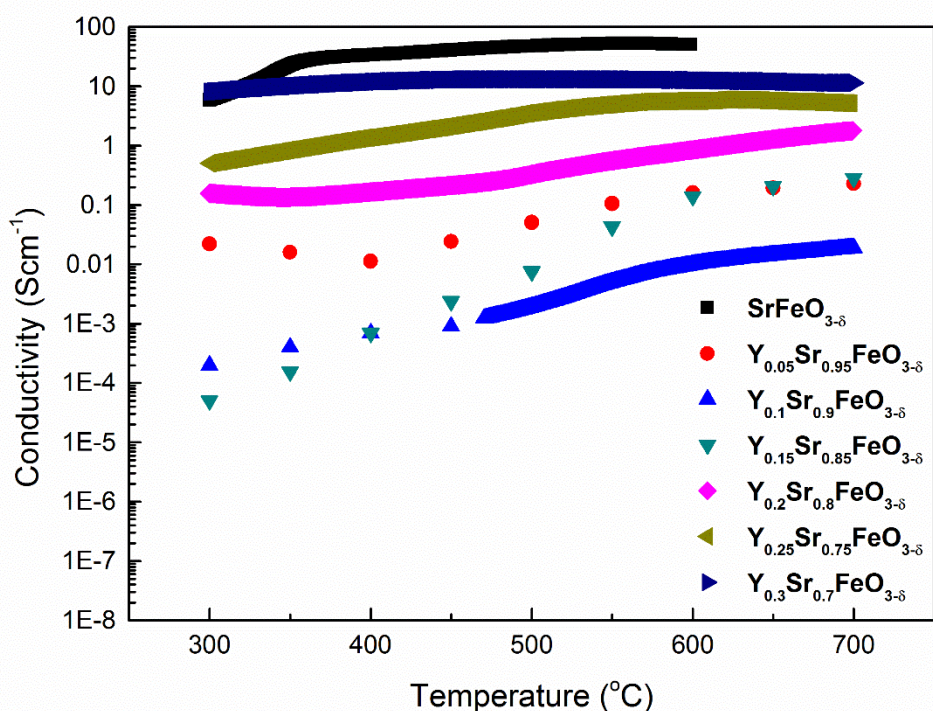
Figure 6.18. Conductivity of $Y_xSr_{1-x}FeO_{3-\delta}$ (x = 0 – 0.3) in 5% H_2/Ar

A significant decrease in the conductivity of $Y_xSr_{1-x}FeO_{3-\delta}$ (x = 0, 0.05, 0.1, 0.15, 0.2, 0.25, 0.3) is observed upon reduction, Figure 6.18. Semiconducting behaviour is observed for $Y_xSr_{1-x}FeO_{3-\delta}$ (x = 0, 0.05, 0.1, 0.15, 0.2) over the entire temperature range, which is indicative of a p-type to n-type transition as can be observed for reduction of other doped strontium ferrites [15, 35]. The *p-n* transition occurs when of Fe^{2+} is formed upon reduction, as in Equation 6.2.

$$2Fe'_{Fe} + O^x_O \leftrightarrow 2Fe''_{Fe} + V^{\cdot\cdot}_O + \frac{1}{2}O_2 \qquad\qquad (6.2)$$
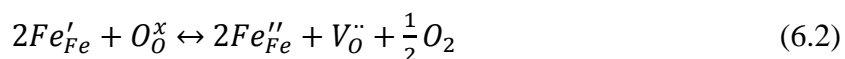
Formation of n-type charge carriers in ferrites

The formation of n-type charge carriers is characteristic of further reduction of ferrites, which generally exhibit significantly lower n-type conductivity than p-type conductivity [14, 35], hence the decrease in conductivity observed upon reduction. The semiconductor-metal transition was retained for $Y_{0.25}Sr_{0.75}FeO_{3-\delta}$ and $Y_{0.3}Sr_{0.7}FeO_{3-\delta}$, albeit at a higher temperature than was observed in air, correlating with previous redox stable ferrites, Chapter 5.3. The activation energy for conduction for $Y_{0.3}Sr_{0.7}FeO_{3-\delta}$ exhibits a slight increase upon reduction, from 0.15(2) eV to 0.18(1) eV, whilst a significant increase in the activation energy, from 0.14(1) eV to 0.39(4) eV, for was observed for $Y_{0.25}Sr_{0.75}FeO_{3-\delta}$. The differing effects of reduction on these compounds can be related to the reducibility of these materials, with increasing redox stability observed with increasing yttrium content, as evidenced by a lesser decrease in the conductivity upon reduction with increasing yttrium content.
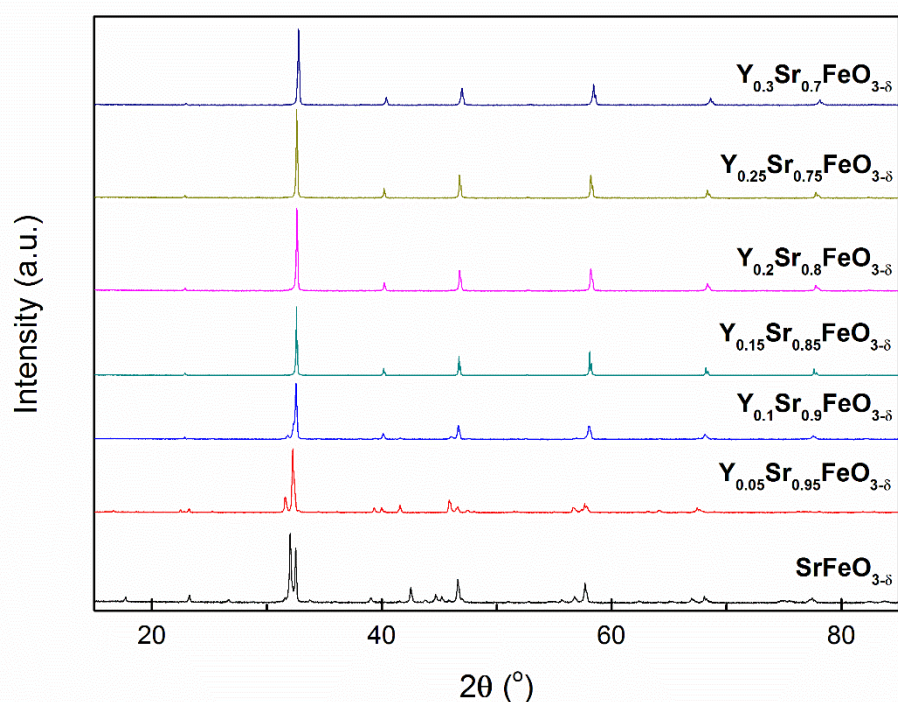
Figure 6.19. XRD patterns of $Y_xSr_{1-x}FeO_{3-\delta}$ (x = 0 – 0.3) after reduction at 700 °C in 5% H_2/Ar

Retention of the perovskite structure was observed for all compounds upon reduction at 700 °C in 5% H_2/Ar, Figure 6.19, with the exception of $SrFeO_{3-\delta}$ (SG: *Immm*) and $Y_{0.05}Sr_{0.95}FeO_{3-\delta}$ (SG: *Icmm*) and $Y_{0.1}Sr_{0.9}FeO_{3-\delta}$ (SG: *Icmm* and *Pm-3m*), Table 6.5 (a). The lower doping limit of redox stability occurs for $0.1 < x \leq 0.15$, significantly lower than was observed for $La_xSr_{1-x}FeO_{3-\delta}$ (x = 0.2, 0.4, 0.6), which occurred for $0.2 < x \leq 0.4$. The lower dopant concentration required to achieve redox stability for yttrium doped compounds is likely a result of the increasing A-site disorder, which displaces oxygen anions off lattice sites, causing localised structural distortions. These randomised structural distortions may prevent oxygen vacancy ordering, maintaining the observed cubic perovskite structure, although, again, this cannot be proven using the techniques in this study.
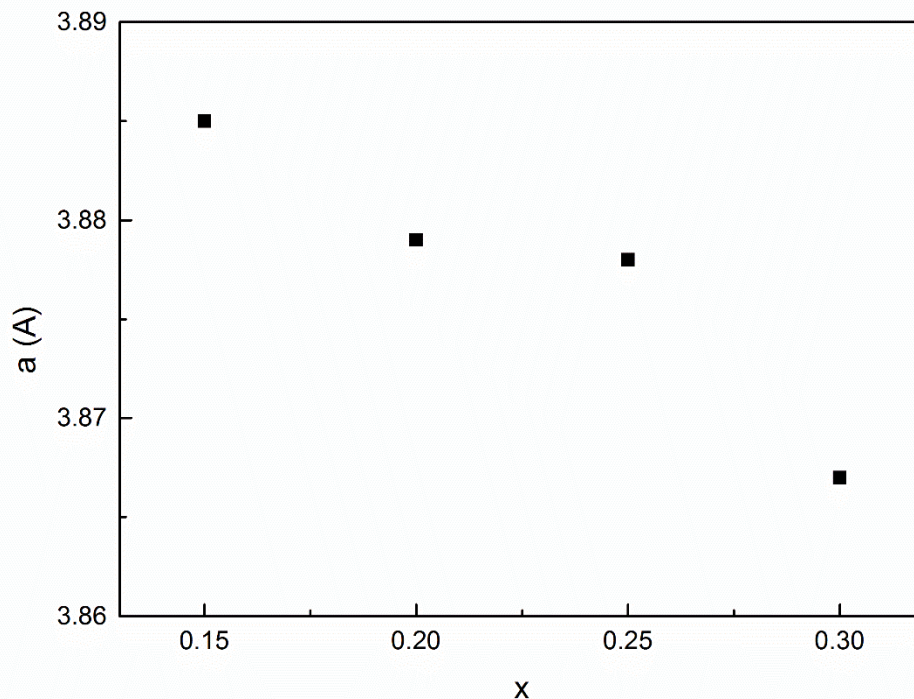
Figure 6.20. Variation of lattice parameters for $Y_xSr_{1-x}FeO_{3-\delta}$ (x = 0.15 – 0.3) after reduction at 700 °C in 5% H_2/Ar

GSAS [17] analysis of $Y_xSr_{1-x}FeO_{3-\delta}$ (x = 0.15, 0.2, 0.25, 0.3), Figure 6.20, Figure 6.21 and Table 6.5 (b), demonstrated retention of the cubic perovskite phase, albeit with an increase in the lattice parameters due to cationic reduction. In contrast to the compounds in air, a general decrease in the lattice parameters was observed with increasing dopant concentration, from $Y_{0.15}Sr_{0.85}FeO_{3-\delta}$ to $Y_{0.3}Sr_{0.7}FeO_{3-\delta}$. The difference between oxidised and reduced compounds is a result of cationic reduction, with the difference behaviour with increasing yttrium content a result of increasing redox stability. The increase in the lattice parameters upon reduction decreased with increasing yttrium content, with minimal variation in the lattice parameter of $Y_{0.3}Sr_{0.7}FeO_{3-\delta}$ in both atmospheres, Table 6.3 (b) and 6.5 (b).

(a)		SrFeO$_{3-\delta}$		Y$_{0.05}$Sr$_{0.95}$FeO$_{3-\delta}$			Y$_{0.05}$Sr$_{0.95}$FeO$_{3-\delta}$		
χ^2		2.692		2.277			2.109		
Rp (%)		5.17		4.83			4.49		
wRp (%)		3.83		3.66			3.49		
Primary Phase Fraction		*100 %*		*100 %*			*29 %*		
Space Group		*Immm*		*Icmm*			*Icmm*		
a (Å)		3.890(1)		5.658(1)			5.621(1)		
b (Å)		3.890(1)		15.590(3)			15.588(1)		
c (Å)		20.014(5)		5.524(1)			5.520(1)		
V (Å^3)		302.8(2)		487.3(3)			483.8(1)		
Secondary Phase Fraction		-		-			*71 %*		
Space Group		-		-			*Pm-3m*		
a (Å)		-		-			3.888(1)		
V (Å^3)		-		-			58.8(1)		
Y/Sr	x	0	0	0.0144			0.0146		
	y	0	0	0.1093			0.1095		
	z	0.5	0.318(1)	0.5			0.5		
	U$_{iso}$	0.012(2)	0.014(1)	0.007(1)			0.008(1)		
Fe	x	0		0	0.932		0	0.932	
	y	0		0	0.25		0	0.25	
	z	0.102(3)		0	0.955		0	0.955	
	U$_{iso}$	0.007(1)		0.006(2)	0.001(2)		0.008(6)	0.011(9)	
O	x	0	0	0.25	0.0503	0.86	0.25	0.0503	0.86
	y	0.5	0	0.992	0.1406	0.25	0.992	0.1406	0.25
	z	0.082(7)	0.198(8)	0.25	0	0.625	0.25	0	0.625
	U$_{iso}$	0.014(3)	0.008(5)	0.010(4)	0.009(4)	0.006(1)	0.032(1)	0.012(1)	0.015(1)

328

(b)		$Y_{0.15}Sr_{0.85}FeO_{3-\delta}$	$Y_{0.2}Sr_{0.8}FeO_{3-\delta}$	$Y_{0.25}Sr_{0.75}FeO_{3-\delta}$	$Y_{0.3}Sr_{0.7}FeO_{3-\delta}$
χ^2		2.383	2.733	2.157	3.371
Rp (%)		4.91	5.15	4.61	5.80
wRp (%)		3.69	3.80	3.51	4.11
Space Group		$Pm\text{-}3m$	$Pm\text{-}3m$	$Pm\text{-}3m$	$Pm\text{-}3m$
a (Å)		3.884(1)	3.879(1)	3.878(1)	3.866(1)
V (Å^3)		58.6(1)	58.4(1)	58.3(1)	57.8(1)
Y/Sr	x	0	0	0	0
	y	0	0	0	0
	z	0	0	0	0
	U_{iso}	0.034(1)	0.020(1)	0.033(1)	0.017(1)
Fe	x	0.5	0.5	0.5	0.5
	y	0.5	0.5	0.5	0.5
	z	0.5	0.5	0.5	0.5
	U_{iso}	0.030(1)	0.018(1)	0.009(1)	0.010(1)
O	x	0	0	0	0
	y	0.5	0.5	0.5	0.5
	z	0.5	0.5	0.5	0.5
	U_{iso}	0.090(3)	0.083(3)	0.074(2)	0.067(4)

Table 6.5. Rietveld refinement and lattice parameters from GSAS refinement of $Y_xSr_{1-x}FeO_{3-\delta}$ (x = 0-0.1 (a), x = 0.15-0.3(b))

after reduction at 700 °C in 5% H_2/Ar
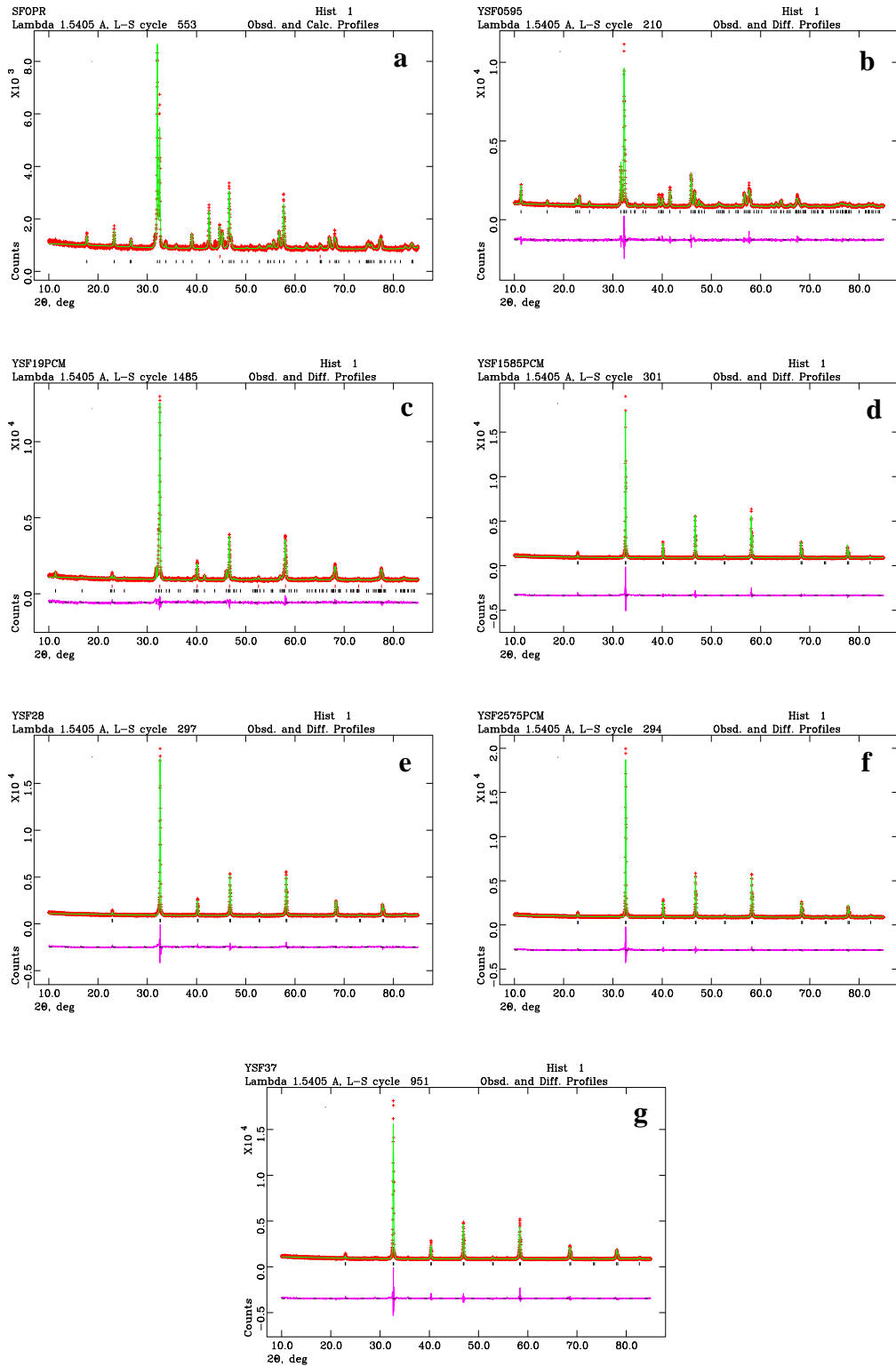
Figure 6.21. GSAS plots for $Y_xSr_{1-x}FeO_{3-\delta}$, x = 0 (a), x = 0.05 (b), x = 0.1 (c), x = 0.15 (d), x = 0.2 (e), x = 0.25 (f) and x = 0.3 (g) after reduction at 700 °C in 5% H_2/Ar

6.2.4. Conclusion

The significant variance in the average radius of the A-site cation, due to the difference in the cationic size of yttrium and strontium, was noted to cause significant irregularities in material properties. Whilst the materials exhibited redox stability from a low dopant concentration, the significantly lower electronic conductivity upon reduction severely limits the utility of these compounds as symmetrical electrode materials for IT-SOFCs. Despite the lower conductivity, $Y_{0.3}Sr_{0.7}FeO_{3-\delta}$ exhibited redox stability and therefore could potentially be utilised as a symmetrical electrode material. Additional investigations into the dopant region $0.3 \leq x \leq 0.4$, may also result in further improvements of the electrical properties whilst maintaining redox stability.

6.3. Conclusion

The structure of lanthanum strontium ferrite did not correlate with the literature for all compounds, although this was attributed to the proximity to phase stability limits and lack of resolution for structural refinement. As was observed previously, the electronic conductivity of $La_xSr_{1-x}FeO_{3-\delta}$ (x = 0.2, 0.4, 0.6) in air was high, > 100 Scm^{-1}, between 300 °C and 700 °C. Minimal variation in the structure of $La_{0.6}Sr_{0.4}FeO_{3-\delta}$ and $La_{0.8}Sr_{0.2}FeO_{3-\delta}$ was observed upon reduction, although a secondary orthorhombic phase observed for both $La_{0.2}Sr_{0.8}FeO_{3-\delta}$ and $La_{0.4}Sr_{0.6}FeO_{3-\delta}$. The formation of the secondary phase significantly decreased the electronic conductivity for both $La_{0.2}Sr_{0.8}FeO_{3-\delta}$ and $La_{0.4}Sr_{0.6}FeO_{3-\delta}$, with only $La_{0.6}Sr_{0.4}FeO_{3-\delta}$ exhibiting electronic conductivity > 30 Scm^{-1} after reduction. Fuel cell testing of lanthanum doped strontium ferrite exhibited significantly reduced performance than was observed for $SrFe_{0.8}Cu_{0.1}Nb_{0.1}O_{3-\delta}$, 116 mWcm^{-2} at 800 °C compared to 306 mWcm^{-2} at 700 °C, however microstructural optimisation and catalytic infiltration may substantially improve the performance of these materials.

Yttrium doping of strontium ferrite formed a two phase cubic perovskite structure for all dopant concentrations up to 30 %. The large A-site cation disorder, cause by the size difference between yttrium and strontium, resulted in a non-linear variation in the lattice parameters. The electronic conductivity of $Y_xSr_{1-x}FeO_{3-\delta}$ (x =

0.05, 0.1, 0.15) in air was sufficient for use as an SOFC cathode material, however a significant reduction in the conductivity, to < 0.1 Scm^{-1}, was observed upon reduction. The conductivity of $Y_{0.3}Sr_{0.7}FeO_{3-\delta}$ was between 7 Scm^{-1} and 18 Scm^{-1} in both air and 5% H_2/Ar, with little variation between oxidising and reducing atmospheres. Redox stability was observed for $Y_xSr_{1-x}FeO_{3-\delta}$ ($x = 0.15, 0.2, 0.25, 0.3$), with oxygen vacancy ordering observed for $SrFeO_{3-\delta}$, $Y_{0.05}Sr_{0.95}FeO_{3-\delta}$ and $Y_{0.1}Sr_{0.9}FeO_{3-\delta}$. A reduction in the desirable properties of yttrium doped strontium ferrites is noted upon comparison to lanthanum doped analogues, likely as a result of the increased A-site disorder, and thus these compounds are of lesser interest as electrode materials for IT-SOFCs.

6.4. References

1. H. Gu, Y. Zheng, R. Ran, Z. Shao, W. Jin, N. Xu and J. Ahn, *Journal of Power Sources*, 2008, **183**, 471-478.

2. Y. Zheng, C. Zhang, R. Ran, R. Cai, Z. Shao and D. Farrusseng, *Acta Materialia*, 2009, **57**, 1165-1175.

3. D. M. Bastidas, S. Tao and J. T. S. Irvine, *Journal of Materials Chemistry*, 2006, **16**, 1603-1605.

4. J. C. Ruiz-Morales, J. Canales-Vázquez, J. Peña-Martínez, D. M. López and P. Núñez, *Electrochimica Acta*, 2006, **52**, 278-284.

5. Y. Zhang, Q. Zhou and T. He, *Journal of Power Sources*, **196**, 76-83.

6. J. M. Ralph, C. Rossignol and R. Kumar *Journal of The Electrochemical Society*, 2003, **150**, A1518-A1522.

7. C. Fu, K. Sun, N. Zhang, X. Chen and D. Zhou, *Electrochimica Acta*, 2007, **52**, 4589-4594.

8. E. Perry Murray, M. J. Sever and S. A. Barnett, *Solid State Ionics*, 2002, **148**, 27-34.

9. Y. Leng, S. H. Chan and Q. Liu, *International Journal of Hydrogen Energy*, 2008, **33**, 3808-3817.

10. Z. Shao and S. M. Haile, *Nature*, 2004, **431**, 170 - 173.

11. M. Lo Faro, D. La Rosa, I. Nicotera, V. Antonucci and A. S. Aricò, *Applied Catalysis B: Environmental*, 2009, **89**, 49-57.

12. M. Arnold, H. Wang and A. Feldhoff, *Journal of Membrane Science*, 2007, **293**, 44-52.

13. S. E. Dann, D. B. Currie, M. T. Weller, M. F. Thomas and A. D. Al-Rawwas, *Journal of Solid State Chemistry*, 1994, **109**, 134-144.

14. M. V. Patrakeev, J. A. Bahteeva, E. B. Mitberg, I. A. Leonidov, V. L. Kozhevnikov and K. R. Poeppelmeier, *Journal of Solid State Chemistry*, 2003, **172**, 219-231.

15. M. V. Patrakeev, A. A. Markov, I. A. Leonidov, V. L. Kozhevnikov and V. V. Kharton, *Solid State Ionics*, 2006, **177**, 1757-1760.

16. G. Xiao, Q. Liu, S. Wang, V. G. Komvokis, M. D. Amiridis, A. Heyden, S. Ma and F. Chen, *Journal of Power Sources*, **202**, 63-69.

17. A. C. Larson and R. B. V. Dreele, *"General Structural Analysis System" Los Alamos National Laboratory Report LAUR*, 1994, 86.

18. M. V. Patrakeev, I. A. Leonidov, V. L. Kozhevnikov and K. R. Poeppelmeier, *Journal of Solid State Chemistry*, 2005, **178**, 921-927.

19. V. V. Vashuk, L. V. Kokhanovskii and I. I. Yushkevich, *Inorganic Materials*, 2000, **36**, 79-83.

20. M. V. Patrakeev, I. A. Leonidov, V. L. Kozhevnikov and V. V. Kharton, *Solid State Sciences*, 2004, **6**, 907-913.

21. S. P. Simner, J. P. Shelton, M. D. Anderson and J. W. Stevenson, *Solid State Ionics*, 2003, **161**, 11-18.

22. E. V. Tsipis, M. V. Patrakeev, V. V. Kharton, A. A. Yaremchenko, G. C. Mather, A. L. Shaula, I. A. Leonidov, V. L. Kozhevnikov and J. R. Frade, *Solid State Sciences*, 2005, **7**, 355-365.

23. H. Hayashi, M. Kanoh, C. J. Quan, H. Inaba, S. Wang, M. Dokiya and H. Tagawa, *Solid State Ionics*, 2000, **132**, 227-233.

24. J. Larminie and A. Dicks, *Fuel Cell Systems Explained*, J. Wiley, 2003.

25. A. Atkinson, S. A. Baron and N. P. Brandon, *Journal of The Electrochemical Society*, 2004, **151**, E186-E193.

26. R. Mukundan, E. L. Brosha and F. H. Garzon, *Electrochemical and Solid-State Letters*, 2004, **7**, A5-A7.

27. X. Li, H. Zhao, W. Shen, F. Gao, X. Huang, Y. Li and Z. Zhu, *Journal of Power Sources*, 2007, **166**, 47-52.

28. O. A. Marina, N. L. Canfield and J. W. Stevenson, *Solid State Ionics*, 2002, **149**, 21-28.

29. S. Koutcheiko, Y. Yoo, A. Petric and I. Davidson, *Ceramics International*, 2006, **32**, 67-72.

30. S. Hui and A. Petric, *Journal of The Electrochemical Society*, 2002, **149**, J1-J10.

31. A. K. Azad, A. K. M. Zakaria, F. U. Ahmed, S. K. Paranjpe and A. Das, *Journal of Magnetism and Magnetic Materials*, 2000, **214**, 251-257.

32.   R. D. Shannon, *Acta Crystallographia Section A*, 1976, **A32**, 751.

33.   L. M. Rodriguez-Martinez and J. P. Attfield, *Physical Review B*, 1996, **54**, R15622-R15625.

34.   L. M. RodrÃ-guez-MartÃ-nez and J. P. Attfield, *Physical Review B*, 2000, **63**, 024424.

35.   M. V. Patrakeev, V. V. Kharton, Y. A. Bakhteeva, A. L. Shaula, I. A. Leonidov, V. L. Kozhevnikov, E. N. Naumovich, A. A. Yaremchenko and F. M. B. Marques, *Solid State Sciences*, 2006, **8**, 476-487.

7. Conclusions and Further Work

This chapter begins with an overview of the work produced in this thesis and draws final conclusions from the data collected. The further work section considers any additional experiments which would have benefited this thesis and explores future experiments which could lead on from this body of work.

7.1. Conclusions

One of the main foci of research into solid oxide fuel cells is the reduction of the operating temperatures, which are currently decreasing at a rate of 100 - 200 °C per decade, with the aim of reducing start-up times and allowing the use of effective materials with thermal stability issues. Whilst double perovskites have previously been investigated as SOFC anode materials between 700 °C and 900 °C [1-3], the effect of low temperature operation on the properties of these materials has not been determined. Research into strontium iron molybdate double perovskites indicated that high temperature reduction was required for induction of high electronic conductivity, limiting the use of these materials at intermediate temperatures. The study collected the data from both $SrCaFe_{1+x}Mo_{1-x}O_{6-\delta}$ (x = 0.2, 0.4, 0.6) and $Sr_{1.6}K_{0.4}Fe_{1+x}Mo_{1-x}O_{6-\delta}$ (x = 0.2, 0.4, 0.6), which demonstrated significantly lower electronic conductivity after reduction at 700 °C compared to reduction at 1200 °C. This indicated that unless pre-reduction of the double perovskite anodes was attained, the fuel cell performance would likely decrease with reductions in the SOFC operating temperature.

Previous investigations in the strontium ferrites indicated a lack of applicability of these materials as anode materials due to poor redox stability at SOFC operating temperatures [4, 5]. Optimisation of the electronic and ionic conductivity of strontium ferrites was observed for the perovskite phase, with B-site doping previously shown to stabilise this structure. Titanium doping was noted to stabilise the perovskite structure from x = 0.1, albeit with a reduction in the electronic conductivity with increasing titanium doping from $SrFe_{0.9}Ti_{0.1}O_{3-\delta}$. The electronic conductivity in reducing atmospheres was not deemed sufficient for effective use as an anode materials, however the redox stability and similar conductivity in both oxidising and

reducing conditions intimates potential for use as a symmetrical electrode material for IT-SOFCs.

Charge compensation mechanisms in strontium ferrites can be utilised to alter the material properties by increasing the charge carrier concentration. Doping with TM^{2+} transition metal dopants at the B-site increased the conductivity in air, however reduction of both $SrFe_{0.7}Mn_{0.2}Ti_{0.1}O_{3-\delta}$ and $SrFe_{0.7}Ni_{0.2}Ti_{0.1}O_{3-\delta}$ exhibited a significant reduction in conductivity and the formation of a secondary phase respectively upon reduction. Both $SrFe_{0.7}Co_{0.2}Ti_{0.1}O_{3-\delta}$ and $SrFe_{0.7}Cu_{0.2}Ti_{0.1}O_{3-\delta}$ exhibited an improvement in the electronic conductivity in both oxidising and reducing atmospheres over $SrFe_{0.9}Ti_{0.1}O_{3-\delta}$, whilst maintaining redox stability. The significant improvement in the conductivity and stability upon doping of $SrFe_{0.9}Ti_{0.1}O_{3-\delta}$ suggests that a more suitable parent compound may produce further improvements in material conductivity and stability.

Replacement of titanium with niobium resulted in an improvement both in the redox stability and electronic conductivity in both oxidising and reducing environments. This research confirmed the promising properties of these materials for use as SOFC materials, previously indicated in research by Anikina *et. al.* [6]. As for $SrFe_{0.9}Ti_{0.1}O_{3-\delta}$, doping of $SrFe_{0.9}Nb_{0.1}O_{3-\delta}$ with TM^{2+} transition metals was utilised to increase the electronic conductivity of these materials. The electronic conductivities of both $SrFe_{0.8}Mn_{0.1}Nb_{0.1}O_{3-\delta}$ and $SrFe_{0.8}Ni_{0.1}Nb_{0.1}O_{3-\delta}$ exhibited a significant reduction in the electronic conductivity, however both $SrFe_{0.8}Co_{0.1}Nb_{0.1}O_{3-\delta}$ and $SrFe_{0.8}Cu_{0.1}Nb_{0.1}O_{3-\delta}$ exhibited an improvement in the electronic conductivity in both oxidising and reducing conditions whilst maintaining redox stability.

Due to the significant increase in the thermal expansion coefficient exhibited by previous cobalt doped perovskites [7 8, 9], copper was posited to be the more suitable dopant for $SrFe_{0.9}Nb_{0.1}O_{3-\delta}$. A series of copper and niobium doped strontium ferrites, $SrFe_{0.9-x}Cu_xNb_{0.1}O_{3-\delta}$ (x = 0 - 0.4), were synthesised to optimise the electronic conductivity and redox stability. Increasing the copper content was noted to reduce the electronic conductivity and redox stability, with $SrFe_{0.8}Cu_{0.1}Nb_{0.1}O_{3-\delta}$ exhibiting the optimum material properties. As $SrFe_{0.8}Cu_{0.1}Nb_{0.1}O_{3-\delta}$ exhibited high electronic conductivity in both oxidising and reducing environments, the utility of the material

as symmetrical electrode for IT-SOFCS was considered. Fuel cell performance of a symmetrical $SrFe_{0.8}Cu_{0.1}Nb_{0.1}O_{3-\delta}$–$Gd_{0.2}Ce_{0.8}O_{2-\delta}$- $SrFe_{0.8}Cu_{0.1}Nb_{0.1}O_{3-\delta}$ fuel cell reached 306 mWcm^{-2} at 700 °C, comparable to previous symmetrical fuel cell performance. The fuel cell performance demonstrates that these symmetrical cells exhibit potential for further utilisation in symmetrical IT-SOFCs.

A-site doping was previously utilised to improve the properties of strontium ferrites for use as SOFC cathode materials, with lanthanum strontium ferrite exhibiting good SOFC cathode performance [10]. As was observed previously, the electronic conductivity of $La_xSr_{1-x}FeO_{3-\delta}$ (x = 0.2, 0.4, 0.6) in air was high, > 100 Scm^{-1}, between 300 °C and 700 °C. Minimal variation in the structure of $La_{0.6}Sr_{0.4}FeO_{3-\delta}$ and $La_{0.8}Sr_{0.2}FeO_{3-\delta}$ was observed upon reduction, although a secondary orthorhombic phase was observed for both $La_{0.2}Sr_{0.8}FeO_{3-\delta}$ and $La_{0.4}Sr_{0.6}FeO_{3-\delta}$. The formation of the secondary phase significantly decreased the electronic conductivity, with only $La_{0.6}Sr_{0.4}FeO_{3-\delta}$ exhibiting electronic conductivity > 30 Scm^{-1}. Fuel cell testing of a 55 wt% $La_{0.6}Sr_{0.4}FeO_{3-\delta}$: 45 wt% $Gd_{0.2}Ce_{0.8}O_{2-\delta}$ symmetrical electrode exhibited significantly reduced performance than was observed for $SrFe_{0.8}Cu_{0.1}Nb_{0.1}O_{3-\delta}$, 116 mWcm^{-2} at 800 °C compared to 306 mWcm^{-2} at 700 °C, however microstructural optimisation and catalytic infiltration may substantially improve the performance of these materials.

Replacement of lanthanum with yttrium was not noted to elicit an improvement in the electronic conductivity or redox stability due to the significant A-site disorder. Whilst structural redox stability was observed for $Y_xSr_{1-x}FeO_{3-\delta}$ (x = 0.15, 0.2, 0.25, 0.3), a significant reduction in the conductivity was observed for $Y_xSr_{1-x}FeO_{3-\delta}$ (x = 0.05, 0.1, 0.15, 0.2), with only $Y_{0.3}Sr_{0.7}FeO_{3-\delta}$ exhibiting minimal variation in the electronic conductivity upon reduction. A reduction in the desirable properties of yttrium doped strontium ferrites is noted upon comparison to lanthanum doped analogues as a result of the increased A-site disorder and thus these compounds are of lesser interest as electrode materials for IT-SOFCs.

7.2. Further Work

Whilst much of the behaviour of the materials and fuel cells was well characterised, additional characterisation techniques could have proved of significant value during materials analysis. Dilatometry measurements are used to determine the thermal expansion coefficient of a material, which would be of value to elucidate the TEC match to common SOFC materials. Dilatometry was not undertaken in the body of work due to lack of access to the equipment, however the data would have been useful in determining optimal anode composite composition during SOFC synthesis.

Scanning electron microscopy of the microstructure of the prepared fuel cells was not included in the thesis due to lack of access to the equipment, however this would have been of significant value when considering fuel cell performance. The importance of optimised electrode microstructure is highlighted in both the introduction, Section 1.2.5, and in the discussion of the fuel cell performance in the literature, Section 1.3.4. Additionally, information on the thickness of the electrode and the electrolyte would have been of worth when discussing the fuel cell performance. Scanning electron microscopy on the fuel cell pellets from this thesis could provide significant information on the effect of the microstructure on fuel cell performance and offer a guideline for further electrode development.

Further research into the potential use of $SrFe_{0.8}Cu_{0.1}Nb_{0.1}O_{3-\delta}$ and $La_{0.6}Sr_{0.4}FeO_{3-\delta}$ as symmetrical electrode materials for IT-SOFCs should concentrate on the production of an optimised electrode structure and possible infiltration of electrode catalysts. As significant improvements in the fuel cell performance of various anode materials have been elicited through infiltration of minor amounts, 0.5 - 10 %, of cerium and precious metal catalysts [11-13], this would be an efficient method for improving fuel cell performance. Similar performance improvements have also been noted for cathodic catalysts, albeit utilising different materials [14]. The infiltration of a composite anodic/cathodic catalyst could significantly improve the utility of symmetrical electrodes by combining the efficiency of specialised electrode materials with the simplified manufacturing of symmetrical electrodes. This research would also

be of interest for the further improvement of reversible SOFCs, potentially improving efficiency and thus the commercial utility of this technology.

In contrast to B-site dopants which reduce the concentration of the iron in the sample whilst altering the Fe^{4+}/Fe_{tot} ratio, A-site dopants can effectively alter the Fe^{4+}/Fe_{tot} ratio without affecting the iron content of the sample. A-site doping of strontium ferrite can therefore, in theory, alter the number of charge carriers more effectively than B-site dopants. B-site doping is more efficient at stabilisation of the perovskite structure of strontium ferrite and improvement of the redox stability of these materials, as a result of disruption of the oxygen vacancy ordering. Further utilisation of both these techniques could potentially result in incremental improvement of material properties.

Substitution of potassium for strontium has been shown to maximise the ionic conductivity of other strontium ferrites, with minimal disruption to the material structure due to the similar atomic radii of the cations. An anode of $Sr_{1.6}K_{0.4}FeMoO_{6-\delta}$ and a cathode of $Sr_{0.9}K_{0.1}FeO_{3-\delta}$ were combined with LSGM to produce an efficient SOFC, with a maximum power density of 766 mWcm^{-2} with H_2 fuel at 800 °C [15]. The anode was later determined to be a dual phase composite of highly conductive $SrMoO_3$ phase and a MIEC $SrFe_{0.6}Mo_{0.4}O_{2.7}$ phase, with the potassium thought to have sublimed from the structure during high temperature synthesis. At lower temperatures the sublimation of the potassium from the compound may not occur, with our own unpublished data intimating that this is the case for strontium manganate. This suggests that potassium doping of either $SrFe_{0.9}Nb_{0.1}O_{3-\delta}$ or $SrFe_{0.8}Cu_{0.1}Nb_{0.1}O_{3-\delta}$ has potential to improve the electronic conductivity without the detrimental effects associated with additional B-site doping.

The importance of optimised microstructures for electrode materials has been extensively investigated, with a variety of techniques used for improvement of the effective porosity [16-21]. Most of these techniques have utilised variations in the manufacturing process to improve the electrode microstructure, however the disorder inherent in the technique still exists. Anodic alumina membranes (AAMs) have been used in the production of ordered arrays of ceramic nanostructures, through infiltration

of AAMs with various ceramic precursors followed by high temperature firing [22, 23]. One of the more significant problems with this technique is the difficulties in the removal of the AAM after formation of the desired nanostructures. The use of phosphoric acid is required to remove the template [23, 24], which has the potential to damage the ceramic material.

Carbon nanotubes (CNTs) are of interest for a multitude of applications due to their stability, conductivity and catalytic activity [25, 26]. As with AAMs, infiltration of carbon nanotubes has been demonstrated as a viable technique for the formation of ceramic nanostructures [27]. A significant volume of work has been on the production of aligned CNT arrays and the various factors which can alter the structure of these arrays [28], although, to the best of our knowledge, no body of work has demonstrated infiltration of an aligned array of carbon nanotubes to form a ceramic counterpart. The stability of carbon nanotubes in air only extends to 750 °C, which is below the conventional temperatures required to form many electrode materials. This provides a solution to the problem of removal of the template observed for AAMs, however the effects on the microstructure of a continuing reaction upon removal of the template cannot be easily predicted. The use of carbon nanotubes as templates for nanostructured anodes exhibits potential for optimisation of the electrode microstructure, however additional work would be required to examine the feasibility of this method.

7.3. References

1. Y.-H. Huang, R. I. Dass, Z.-L. Xing and J. B. Goodenough, *Science*, 2006, **312**, 254-257.

2. P. Zhang, Y.-H. Huang, J.-G. Cheng, Z.-Q. Mao and J. B. Goodenough, *Journal of Power Sources*, **196**, 1738-1743.

3. L. Zhang, Q. Zhou, Q. He and T. He, *Journal of Power Sources*, 2010, **195**, 6356-6366.

4. V. V. Vashuk, L. V. Kokhanovskii and I. I. Yushkevich, *Inorganic Materials*, 2000, **36**, 79-83.

5. M. V. Patrakeev, I. A. Leonidov, V. L. Kozhevnikov and V. V. Kharton, *Solid State Sciences*, 2004, **6**, 907-913.

6. P. V. Anikina, A. A. Markov, M. V. Patrakeev, I. A. Leonidov and V. L. Kozhevnikov, *Solid State Sciences*, 2009, **11**, 1156-1162.

7. L. W. Tai, M. M. Nasrallah, H. U. Anderson, D. M. Sparlin and S. R. Sehlin, *Solid State Ionics*, 1995, **76**, 259-271.

8. J. W. Stevenson, T. R. Armstrong, R. D. Carneim, L. R. Pederson and W. J. Weber, *Journal of The Electrochemical Society*, 1996, **143**, 2722-2729.

9. A. Mai, V. A. C. Haanappel, S. Uhlenbruck, F. Tietz and D. Stöver, *Solid State Ionics*, 2005, **176**, 1341-1350.

10. J. M. Ralph, C. Rossignol and R. Kumar *Journal of The Electrochemical Society*, 2003, **150**, A1518-A1522.

11. M. D. Gross, K. M. Carver, M. A. Deighan, A. Schenkel, B. M. Smith and A. Z. Yee, *Journal of The Electrochemical Society*, 2009, **156**, B540-B545.

12. A. M. Hussain, J. V. T. Høgh, W. Zhang, E. Stamate, K. T. S. Thydén and N. Bonanos, *Journal of Power Sources*, 2012, **212**, 247-253.

13. G. Kim, S. Lee, J. Y. Shin, G. Corre, J. T. S. Irvine, J. M. Vohs and R. J. Gorte, *Electrochemical and Solid-State Letters*, 2009, **12**, B48-B52.

14. H. Uchida, S. Arisaka and M. Watanabe, *Solid State Ionics*, 2000, **135**, 347-351.

15. S.-e. Hou, A. Aguadero, J. A. Alonso and J. B. Goodenough, *Journal of Power Sources*, 2011, **196**, 5478-5484.

16. L. Mingyi, Y. Bo, X. Jingming and C. Jing, *International Journal of Hydrogen Energy*, 2010, **35**, 2670-2674.

17. R. M. C. Clemmer and S. F. Corbin, *Solid State Ionics*, 2004, **166**, 251-259.

18. D. Marrero-López, J. C. Ruiz-Morales, J. Peña-Martínez, J. Canales-Vázquez and P. Núñez, *Journal of Solid State Chemistry*, 2008, **181**, 685-692.

19. F.-Y. Wang, S. Cheng, B.-Z. Wan, C.-H. Chung and M.-J. Chen, *Ceramics International*, 2008, **34**, 1989-1992.

20. A. Sarikaya and F. Dogan, *Ceramics International*, 2013, **39**, 403.

21. L. Nie, J. Liu, Y. Zhang and M. Liu, *Journal of Power Sources*, 2011, **196**, 9975-9979.

22. G. Cao and D. Liu, *Advances in Colloid and Interface Science*, 2008, **136**, 45-64.

23. R.-J. La, Z.-A. Hu, H.-L. Li, X.-L. Shang and Y.-Y. Yang, *Materials Science and Engineering: A*, 2004, **368**, 145-148.

24. Z.-A. Hu, H. Wu, X. Shang, R.-J. LÃ¼ and H.-L. Li, *Materials Research Bulletin*, 2006, **41**, 1045-1051.

25. V. N. Popov, *Materials Science and Engineering: R: Reports*, 2004, **43**, 61-102.

26. T.-W. Chou, L. Gao, E. T. Thostenson, Z. Zhang and J.-H. Byun, *Composites Science and Technology*, **70**, 1-19.

27. L. Gao, X. Wang, H. Tong Chua and S. Kawi, *Journal of Solid State Chemistry*, 2006, **179**, 2036-2040.

28. H. Chen, A. Roy, J.-B. Baek, L. Zhu, J. Qu and L. Dai, *Materials Science and Engineering: R: Reports*, 2010, **70**, 63-91.